Stony Brook University

Molar Topographic Shape as a System for Inferring Functional Morphology and Developmental Patterning in Extant Cercopithecoid Primates

A Dissertation Presented

by

Julia MacKay Winchester

to

The Graduate School

in Partial Fulfillment of the

Requirements

for the Degree of

Doctor of Philosophy

in

Anthropology

(Concentration – Physical Anthropology)

Stony Brook University

May 2016

Stony Brook University

The Graduate School

Julia MacKay Winchester

We, the dissertation committee for the above candidate for the

Doctor of Philosophy degree, hereby recommend

acceptance of this dissertation.

Frederick E. Grine – Dissertation Co-advisor
Professor, Departments of Anthropology and Anatomical Sciences

Jukka Jernvall – Dissertation Co-advisor
Academy Professor, Evolution and Development Group
University of Helsinki

Doug M. Boyer - Chairperson of Defense
Assistant Professor, Department of Evolutionary Anthropology
Duke University

Alistair Evans
Research Fellow, School of Biological Sciences
Monash University

This dissertation is accepted by the Graduate School

Charles Taber
Dean of the Graduate School

Abstract of the Dissertation

Molar Topographic Shape as a System for Inferring Functional Morphology and Developmental Patterning in Extant Cercopithecoid Primates

by

Julia MacKay Winchester

Doctor of Philosophy

in

Anthropology

(Concentration – Physical Anthropology)

Stony Brook University

2016

New imaging technologies are rapidly changing the nature of morphological data by making possible the creation and sharing of large samples of digital scan data, creating a need for high-throughput morphometric methods. A promising example of this can be found in morphological topographic analysis, a suite of algorithms for describing surface shape properties. Topographic methods have been used effectively to address dietary functional morphology of molars in a number of mammal radiations. These methods may be also useful for answering other questions concerning molar shape. Empirical models of mouse molar morphogenesis include predictions concerning molar shape variation that could apply to many mammals. Testing these predictions in primate species may allow consideration of developmental mechanisms of evolutionary change and, relatedly, evolutionary change of developmental mechanisms. This dissertation seeks (1) to develop

new tools for deriving shape properties from morphological data using morphological topographic analysis, (2) to better understand how to apply topographic methods to investigate morphology, (3) to document morphological topography of lower second molars of cercopithecoids in the context of feeding behavior, phylogenetic relationships, allometry, and tooth wear; and (4) to test developmental hypotheses concerning molar size proportions and shape variability on cercopithecoid molar teeth.

Chapter 2 discusses the production of morphological topographic data from anatomical specimens. An application for morphological topographic analysis is introduced. This application, MorphoTester, implements three common topographic metrics: Dirichlet normal energy (DNE, quantifying bending or curvature), relief index (RFI, quantifying relief), and orientation patch count rotated (OPCR, quantifying complexity). The efficacy of the OPCR algorithm here is first assessed because of differences between this method and previous implementations. Topography is then quantified from simple geometric objects to better understand how topography reflects shape. Simple geometric objects simplistically mimic addition of cusps and increases in cusp height. Results suggest that complexity reflects surface features number, and that curvature and relief are both correlated with surface feature shape and number. Surface curvature is more sensitive than relief to interactions between these two factors.

Effects of mesh preparation – surface cropping, simplification, smoothing, and rotation – on quantified topography are then tested using a cercopithecoid M_2 test sample. Occlusal basin cropping maximizes interspecific topographic variability in this sample. Simplification and smoothing both modify surface shape, and topographic metrics change accordingly. DNE and OPCR change in similar ways, befitting their nature as sums

reflecting relatively local aspects of shape. RFI is more conservative to simplification and smoothing as a ratio of two measures which themselves change with simplification and smoothing. Surface rotation changes RFI and OPCR in complex ways, but little change is observed within 5 degrees of rotation. Overall, results indicate that surface preparation is a process of abstraction, and decisions concerning this process must be made while cognizant of the specific sample and research questions involved.

Chapter 3 applies topographic metrics to a large sample of M_2s belonging to a diverse collection of extant cercopithecoid species in order to investigate dietary functional morphology in this radiation. Species are sorted into one of four dietary categories based on food mechanical properties: durophagy, soft-object feeding, moderate elasticophagy, and extreme elasticophagy. The last category includes only *Theropithecus gelada*, which habitually consumes grass components that can be much tougher than the toughest components of other cercopithecoid diets. Possible allometric influences on DNE, RFI, and OPCR are tested using species body mass and specimen M_2 area as body-size proxies. Results suggest that topographic metrics do not scale allometrically in this sample. Topographic metrics are then tested to determine whether they vary significantly between dietary categories. Results of standard statistical analyses indicate that DNE, RFI, and OPCR all vary significantly, but phylogenetically-informed analyses with maximal phylogenetic signal show a lack of significance for OPCR. Overall, cercopithecoid M_2s vary most strongly in surface relief. In addition, predictive models of diet achieve accuracy ratings well above chance but lower than has been observed for other primate radiations. These facts probably relate to cercopithecoid bilophodont molar configuration, with diet-related variation primarily arising through

changes in relief of molar cusps and crests. Comparatively, *Theropithecus gelada* M_2s exhibit similar relief to folivorous colobines but significantly greater curvature, reflecting high columnar cusps and wear-induced enamel bands. This unusual topographic profile is a novel among cercopithecoids and likely represents adaptations to consuming highly fibrous grass components. The analyses above were performed with a sample of relatively less worn M_2s. A second sample with more variably worn M_2s was used to test topographic change across wear. Relief index was used as a wear proxy, and surface curvature and complexity were regressed on relief. Curvature does not seem to be related to relief as a wear proxy, but there is evidence to suggest that M_2 complexity increases as relief decreases. As both relief and complexity are functionally related, this may represent a compensatory balance that helps maintain tooth function through wear.

Chapter 4 tests whether cercopithecoid molar size and shape relationships conform to predictions from models of molar morphogenesis. Empirical studies of mouse molar development have identified several patterning cascades whereby earlier-developing molar teeth control the size, spacing, and shape of subsequent molars and earlier-developing cusps play a similar role for later-developing cusps. A sample of mesiodistal molar lengths from the literature is used to test the prediction that M_3 size relative to M_1 size regressed on M_2 size relative to M_1 size should produce a regression with a slope of 2.0 and an intercept of -1.0, as predicted by the inhibitory cascade model of molar size proportions. Colobines and papionins conform to these expectations, but cercopithecins do not. While in colobines and papionins M_3 is larger than M_2, at least partially because of M_3 hypoconulids, cercopithecins lack M_3 hypoconulids and M_3 is smaller than M_2 in this clade. This is interpreted to reflect an evolutionary modification to

a morphogenetic termination character, causing cercopithecin M_3s to cease development earlier and resulting in a lack of M_3 hypoconulid. But because for all clades M_2 is larger than M_1, it is suggested that morphogenetic processes in all cercopithecoids exhibit an activator/inhibitor balance where activator factors are stronger than inhibitors.

While the inhibitory cascade model includes predictions concerning molar size proportions, the patterning cascade model predicts that later-developing molars and molar cusps should be more variable in shape than earlier-developing molars or cusps. Morphological topographic analysis and geometric morphometric techniques are applied to M_1s, M_2s, and M_3s of *Colobus* and *Cercopithecus* species to test this prediction between molars. Topographic analysis and geometric morphometrics using cusp-tip landmarks of M_3s belonging to 4 species of cercopithecoids are used to test the prediction between M_3 cusps. Geometric morphometric results indicate that more posterior molars are more variable in shape as expected. More posterior M_3 cusps are also more variable in position than more anterior M_3 cusps, both within species and between species. Comparatively, topographic analyses may be less well suited to quantifying levels of morphological variation. Cusp-tip landmarks were also used to test the hypothesis that hypoconulid position can be predicted from non-hypoconulid cusp relationships, and there is some evidence to suggest that contraction of posterior non-hypoconulid cusps relative to anterior cusps is correlated with a less prominent hypoconulid. In general, results demonstrate interrelatedness of molar morphology at various levels, hinting at the presence of presumably ancient mammalian morphogenetic processes combined with derived modifications to developmental processes resulting in morphological change.

This dissertation develops tools for high-throughput morphometrics, and applies these tools to address functional and developmental influences on mandibular molar shape in extant cercopithecoid primates. Taken together, results indicate there is still much to be learned from primate molar morphology. The changing landscape of morphological analysis holds great promise for future insights if our analytical methods are adapted to the large and diverse samples of digital data that increasingly make up the selective environment of research.

Dedicated to my mother, Cherri, and my Nana, Karen, for being my earliest role models, and to my wife, Emily, for always being willing to go on an adventure

"We become what we behold. We shape our tools and thereafter our tools shape us."

John Culkin (1967), summarizing Marshall McLuhan

Table of Contents

List of Tables

Appendix 4

Table A4.1. Species for which mesiodistal length means were gathered from Swindler (2002).

Table A4.2. Specimens comprising 3D surface mesh sample.

Table A4.3. DNE, RFI, and OPCR of M_1s, M_2s, and M_3s for intermolar shape variability analyses.

Table A4.4. Average specimen pairwise landmark distances for M_1s, M_2s, and M_3s for intermolar shape variability analyses.

Table A4.5. DNE, RFI, and OPCR of anterior and posterior sections of M_1s and M_3s for intramolar shape variability analyses.

Table A4.6. Raw cusp-tip landmarks of M_3s for intramolar cusp position variability analyses.

Table A4.7. Cusp-tip landmarks Procrustes-transformed using entire sample (including dummy hypoconulid values).

Table A4.8. 2D and 3D specimen pairwise cusp distances within species for intramolar intraspecies cusp position variability analyses.

Table A4.9. Interspecies pairwise cusp-tip landmark distances for intramolar interspecies cusp position variability analyses.

Table A4.10. Distances between protoconid and metaconid (PM), entoconid and hypoconid (EH), and hypoconulid and geometric centroid of non-hypoconulid cusps (HC).

List of Figures

Chapter 2

List of Institutional Abbreviations

AMNH – American Museum of Natural History, New York

BMNH – The Natural History Museum, London

MNHNP – National Museum of Natural History, Paris

NMNH – Smithsonian National Museum of Natural History, Washington D.C.

SMNK – State Museum of Natural History, Karlsruhe

Acknowledgements

This dissertation has been financially supported by continued support from the National Science Foundation. A Doctoral Dissertation Improvement Grant (BCS-1341120) provided funds for travel, data collection, and scanning. Early in my graduate school career, I was supported by an NSF Graduate Research Fellowship. Additionally, my ability to live and study in Finland was provided by the NSF Nordic Research Opportunity program associated with the Graduate Research Fellowship program.

On a more personal level, there are many people without whom this dissertation would not exist. I am extremely grateful to all of them. In particular, I am very fortunate to have been the recipient of much gracious instruction and encouragement by a number of mentors. As an undergraduate at the University of Arkansas, Peter Ungar and Mike Plavcan together opened my eyes to the study of biological anthropology. Peter taught me that mammal teeth are endlessly fascinating and introduced me to 3D scanning at a time when such technology was relatively uncommon. Mike was my first anatomy instructor, and his infectious enthusiasm and emphasis on thinking in a rigorously quantitative manner have helped make me passionate about morphological inquiry.

On entering graduate school, I have been lucky to benefit from the guidance of a number of learned scholars who in time came to make up my doctoral dissertation committee. Doug Boyer generously allowed me the use of a large dataset for my first graduate level research project, and this data sharing has led to a fruitful collaborative relationship and a continuous and involved mentorship which has sharpened my analytical thinking and taught me how to answer important research questions. I have had

the great fortune to benefit from two advisors whose perspectives have been complementary and invaluable. Jukka Jernvall introduced me to developmental biology and its connections to physical anthropology, nurtured my interest in shape analysis, provided the initial suggestion to create software for topographic analysis, and showed me how to think about broad questions stretching outside of primates. Fred Grine taught me to think about functional morphology in a nuanced way, guided me toward more robust considerations of primate diets, and provided necessary advice on how to apply mathematical shape algorithms to address specific questions concerning primate tooth form. This dissertation reflects the broad array expertise of between these two individuals, and if it succeeds in addressing a diversity of questions it is because of their guidance (though any errors should be of course laid solely at my feet and no one else's). My fourth committee member is Alistair Evans, whose expertise in shape analysis and developmental biology along with generosity in sharing this expertise has continually forced me to think deeper and more carefully about how to study the concept of shape and how to use digital data to do so. His attention to detail has also been of considerable assistance.

Other faculty at Stony Brook have also provided me with guidance over the years. Jack Stern taught me gross anatomy, and I am happy to be part of the pedagogical tradition spread to classrooms all over the country by his instruction. Brigette Demes, Bill Jungers, and Randy Sussman taught me how to teach gross anatomy when I served as a teaching assistant in their anatomy course, and it is very true that teaching anatomy represents the point where anatomical knowledge begins to be cemented permanently. Carola Borries guided me in a hands-on research project early in my graduate education,

and has answered numerous later questions from me concerning cercopithecoid primate feeding behaviors. Gabrielle Russo and Amy Lu both gave valuable insights through a number of productive conversations during the period nearing completion of the dissertation. Anthropology department staff have provided continual assistance and have helped ensure that my procrastinations have not endangered anything too seriously. I'm sincerely thankful to Jean Moreau, Tara Powers, and Megan Alberti for their patience and kindness.

In addition to faculty and staff, my life both professional and personal has benefitted greatly from the lively community of graduate students and post-docs at Stony Brook. My initial graduate student cohort consisting of Stevie Carnation, Stephanie Blatch, Jessica Layfield, and Jen Everhart were instrumental in surviving the first years of graduate school, whether through study groups or "office parties." Stephanie Maiolino and Amanda Kingston provided repeated advice, encouragement, and friendship. In later years, Allison Nesbitt, Carrie Mongle, and Dorien de Vries have been good friends and colleagues, and our lunches together have supplied both interesting research advice and perspectives and a necessary break from dissertation focus. Many others students have provided assistance and made working at Stony Brook an enjoyable environment. This is a partial list, and I ask the forgiveness of any who I may have forgotten: Erin Achilles, Andrea Baden, Matthew Borths, Sharon Doyle, Hillary Duke, Wendy Erb, Peter Fernandez, Katie Goodenberger, James Herrera, Nick Holowka, Simone Hoffman, Jessica Lodwick, Eliot Monaco, Thaddeus Nelson, Abigail Nishimura, Rachel Perlman, Sarah Pilliard, Adam Pritchard, Liz St. Clair, Nathan Thompson, Ian Wallace, Jesse Wolfhagen, Vivek Venkataraman, and Deming Yang.

I also have a debt of gratitude to the University of Helsinki Institute of Biotechnology, where I spent two years as a visiting scholar working Jukka Jernvall's Evo-Devo Laboratory. I can thank the members of that laboratory for helping me to learn developmental biology coming from nearly no knowledge on the subject. The laboratory was also a welcoming and friendly social group, and they helped to make my time in Helsinki not just productive but also exciting and enjoyable. A partial list of these individuals includes Sarah Zohdy, Jackie Moustakas (and her husband Kalle Verho), Laura Säilä-Corfe, Ian Corfe, Addison Kemp, Kate Carter, Elodie Renvoise, Jussi Eronen, Aleksis Karme, and Aki Kallonen. Sarah, Jackie, and Laura I should explicitly thank for their productive research suggestions and for their friendship, and I will not forget the occasional evenings at establishments named only by acronyms. I should also thank my various collaborators around the world not previously mentioned, including Mike Berthaume, Ingrid Daubechies, Laurie Godfrey, Richard Kay, Stephen King, Yaron Lipman, Pat Wright, and others.

And of course, I must extend my sincerest appreciation to the friends and family who have helped me get to where I am. My mother, Cherri, has supported me and loved me my entire life, and I can probably chalk a great deal of what I have accomplished to this point up to the fact that she read to every night as a child, and whole-heartedly nurtured by love of books and learning as soon as I could manage to read them for myself. She has always pushed me to pursue my dreams and to do whatever is necessary to achieve them, and she has always been proud of me no matter how small or large my accomplishments were. It's her support that has made it possible for me to proceed this far. My late grandmother and Nana, Karen, also loved and encouraged me constantly.

Nana taught me independence and when to go your own way, and mottos such as “this too shall pass” or “don’t let the bastards get you down.” She claimed to not be able to understand half the words that came out of my mouth when I tried to explain my research, but she was fiercely proud nonetheless. My siblings, Devan and Tara, have been good friends and have always been charitably interested in hearing about my research. I always look forward to when we can spend more time together. My wife, Emily, is my companion in an adventure that has taken us both back and forth across oceans several times, and I simply cannot describe her nearly unlimited support, patience, and enthusiasm for and with me in the process of creating this dissertation. I could go on for paragraphs about the many ways in which she has been absolutely essential with her help and love, but instead I will simply give one relevant example: Thank you, Emily, for the many dozens of hours you spent with me inserting hundreds of molar row casts into Styrofoam cylinders for μCT scanning in a temporary apartment in Chapel Hill, North Carolina. And for everything else.

Finally, let me say thank you to the many friends who have been there for me over the years. Jeni St. George, Sean Sullivan, Nicola Astles, and Emily (and the passengers of the 1923 Simplon Orient Express; and the Dead Ends Detective Agency; and Anthony, Penny, and Angel; and so on), our evenings playing role-playing games have been a primary source of stress-relief and enjoyment for several years now. Christina Golkin, your friendship has been a great support in stressful times. Katelyn Burgett, Kyle Hill, hannah draper, and Eric Edwards, you are like a second family to me and you all played a direct role in helping bring this dissertation about in providing me lodging for trips to the Smithsonian for data collection, for which I am extremely

grateful. Erica Hankins, your support and enthusiasm for my research has been critical to this being completed. There are so many other friends I could and should name, and I will end here on a partial list with another apology to anyone I may have forgotten: Josh Campbell, Niko Dimitrioğlu, Kaitlin Friedman, Garth Gergerich, Jessica Hankins, Mike Kremen, Shivani Mann, Maxwell McGee, Nathan McNamee, Justin Maurier, David Norris, Natalie Martorell, Brandy Oliver, Callie Rassmussen, Elaine So, Frank Vargas, Rachael Vargas, Emily Walters.

Chapter 1

Introduction

Mammal teeth have long fascinated morphologists. This is partly because dental structures are in many ways unusual or even unique: teeth are the only part of the skeletal system to be regularly exposed to outer environments and the only skeletal tissue to be recruited directly for food parturition; teeth form the first or second part of the digestive system, depending on manual food processing behaviors; and tooth enamel is the most durable tissue of the human body (Bose et al., 1960), resulting in teeth dominating fossil assemblages. Moreover, teeth are associated directly or indirectly with a wide range of topics including evolutionary adaptations, behavior, health, life history, and embryological development (e.g., Szalay and Delson, 1970; Kay, 1978; Seligsohn and Szalay, 1978; Cook and Buikstra, 1979; Grine, 1986, 1988; Jernvall et al., 1998; Weiss et al., 1998; Godfrey et al., 2001; Starling and Stock, 2007; Ungar et al., 2008). Across mammals both extant and extinct, teeth evince an incredible diversity of form. This diversity is perhaps best seen in molars, which recruit a range of morphologies from unicuspate spikes to extremely complex multi-faceted grinding surfaces in order to subdivide food particles prior to swallowing. Because molar shape is directly correlated with an animal's ability to efficiently overcome food mechanical defenses during chewing and also because many of the selective pressures that animals face concern the acquisition of food, there is a wealth of literature concerning molar shape and functional dietary adaptations (Gregory, 1922; Kay and Hiiemae, 1974; Kay, 1975, 1977, 1984; Rosenberger and Kinzey, 1976; Kinzey, 1978; Seligsohn and Szalay, 1978; Kay and

Covert, 1984; Benefit, 1993; Ungar and Kay, 1995; Kirk and Simons, 2001; M'Kirera and Ungar, 2003; Boyer, 2008; Bunn et al., 2011; Winchester et al., 2014). But the study of dental morphology is changing as the result of rapid increases in the affordability and accessibility of digital anatomical surface data over the last two decades (e.g. Morphosource, Boyer et al., 2014). This provides new opportunities and challenges for diagnosing morphology, and makes possible deeper and broader considerations of functional relationships. Digital data also may allow new consideration of hypotheses of molar shape not related to functional morphology, such as predictions from evolutionary-developmental patterning (see Polly [1998, 2005] and Jernvall [2000] for examples of this kind of work not using digital surface meshes). This dissertation seeks to develop new tools for deriving shape properties from morphological digital data, to better understand how to derive shape properties from this data, and to use derived shape properties of extant cercopithecoid molars to investigate hypotheses of functional feeding adaptations and developmental patterning. This chapter will explore the relevant background literature pertaining to this topic before further describing the aims of this dissertation.

1.1: Background

There is a long history of work recognizing that tooth form varies with function. Aristotle observed in The History of Animals that animals with different diets tend to have dissimilar tooth shapes, and he characterized some herbivorous species as having "teeth that do not interlock but have flat opposing crowns." Cuvier (1863) more accurately described molars of many herbivorous mammals as relatively complex

surfaces of infolded enamel compared to the smoother and less complex surfaces of carnivore molars. Cope (1883) inferred selective adaptation from tooth form, interpreting mammalian tooth shape as an adaptation for breaking down food through shearing and crushing. Gregory (1922) applied this paradigm to primates, suggesting that primate molar tooth shapes had evolved as adaptive responses to changes in diet. The concept that primate molar morphology evolved to increase mechanical efficiency through chewing was further developed in the 1970s, as teeth came to be viewed as guides for masticatory movement (Crompton and Sita-Lumsden, 1970; Kay and Hiiemae, 1974). The molars of insectivorous and folivorous primates were recognized to have steep, sharp cusps and crests for shearing and puncturing insect chitin or plant cellulose, respectively. Frugivorous primates were recognized to have flat, blunt cusps for crushing potentially hard fruits, nuts, and seeds (Kay and Hiiemae, 1974; Rosenberger and Kinzey, 1976; Seligsohn and Szalay, 1978; Kinzey, 1978).

The first widely-successful quantitative analysis of functional molar morphology relied on comparisons of relative molar shearing crest lengths (Kay, 1975, 1977, 1984) (Fig. 1). Kay (1975) initially demonstrated that insectivorous and folivorous primates could be distinguished from frugivorous primates in the lengths of the cristid obliqua of the lower second molar and the phase I traverse of the lower second molar hypoconid across the second upper molar during phase I of mastication, dental features involved in shearing function. This conclusion was elaborated to develop the shearing quotient (SQ), a whole-tooth measure of shearing function of lower molars. SQs are measured as the percent deviation between measured actual length of mesiodistal shearing crests and "expected" shearing crest length based on a body-size regression (Anthony and Kay,

1993). To correct for allometric differences due to diet preferences, this body-size regression is often calculated solely from frugivorous species (Kay and Covert, 1984; Anthony and Kay, 1993; Ungar and Kay, 1995). Extant primate species that consume higher proportions of either leaves or insects tend to have higher SQ values, while species that consume fruits or hard objects tend to have lower SQ values.

SQ analyses have been carried out for a variety of living and fossil primate groups. SQ studies of extant primates have considered strepsirrhines (Kay, 1975; Kay and Covert, 1984; Bunn et al., 2011); tarsiers (Bunn et al., 2011); platyrrhines (Anthony and Kay, 1993; Fleagle et al., 1997; Meldrum and Kay, 1997); cercopithecoids (Kay, 1978, 1984; Kay and Covert, 1984); and hominoids (Kay, 1977; Kay and Covert, 1984; Kay, 1984; Ungar and Kay, 1995; Kay and Ungar, 1997). Similar shearing crest measurements, but corrected for body size with a simple ratio to a body-size proxy instead of a body-size regression, have additionally been used to infer dietary preferences in strepsirrhines and tarsiers (Covert, 1986; Strait, 1993a,b). SQs have additionally been used to infer diet in extinct species, with an appropriate living comparison group for deriving body-size regression and behavioral expectations of SQ values. SQs have been applied to fossil taxa such as Eocene anthropoids and prosimians (Kirk and Simons, 2001); Oligocene catarrhines (Rasmussen and Simons, 1980); Miocene platyrrhines (Anthony and Kay, 1993; Fleagle et al., 1997); Miocene hominoids (Kay, 1977; Ungar and Kay, 1995; Kay and Ungar, 1997); and Miocene cercopithecoids (Benefit, 2006). Shearing ratio analyses have been carried out to infer diet in omomyoids and adapiforms as well (Kirk and Simons, 2001; Strait, 2001; Gilbert, 2005).

There are some drawbacks to SQs as a metric for dietary inference from molar teeth. Because SQs are calculated as percent differences from "expected" shearing crest lengths obtained from data-set specific body-size regressions, SQ values are not directly comparable between data-sets unless the species considered in all analyses to be compared possess similar relationships between body size and shearing-crest length. Simply put, SQs are somewhat tied to their originating samples. Additionally, primate teeth begin to wear immediately after occlusion, and the shearing crest landmarks required for SQ are quickly worn past the point of usability (Ungar and M'Kirera, 2003). SQs as a metric cannot adequately account for worn teeth. Measuring shearing crest lengths in species with non-homologous shearing crests can also be a challenge (Bunn et al., 2011). Bunn et al. (2011) noted also that measuring SQs was impossible for certain species such as *Daubentonia*, which has no prominent shearing crests to speak of. For these reasons, there has been recent momentum toward creating new methods of quantifying tooth shape (Reed, 1997; M'Kirera and Ungar, 2003; Evans et al., 2007; Boyer, 2008; Bunn et al., 2011). These methods tend to rely on digital surface representations of anatomical specimens because of recent increases in the fidelity and ease of acquiring digital shape data (Plyusnin, 2008).

1.1.1: Shape quantification from digital surface data

Newer morphological shape quantification methods tend to measure shape from digital representations of anatomical specimens created using a variety of imaging technologies including laser scanners, μCT scanners, visible light scanners, digitizers, and confocal microscopes. The digital representative data created by these techniques can

be produced from tooth specimens directly or from highly accurate epoxy casts created from tooth specimens. Form, accuracy, and detail of digital representative data can vary widely depending on the specific imaging method used. One common form of digital representative data is a collection of points in 3D space (a "point cloud"), which together encode the shape of the external surface of an object.

Most digital surface representations include further information in addition to point cloud data. Geographic Information Systems (GIS) software, used to analyze landscapes and other geographical data, often uses heightmaps or digital elevation models (DEMs): point clouds arranged in a regular XY-plane grid of squares, where each XY-coordinate square can be associated with a Z-axis elevation value. Data arranged in this fashion cannot account for more than one Z-elevation value per XY-coordinate location, as in an overhang or undercut. Other GIS approaches (i.e., Triangulated irregular networks) and many other scientific fields and industries more often encode 3D surface (or shell) shape in a polygon mesh format. In polygon meshes, arbitrary numbers of irregularly spaced 3D point vertices are interconnected with a network of lines or edges. Vertices and edges together comprise polygons, often triangles, which further define surface geometry. Vertex 3D points combined with polygon edges between vertices communicate more information about surface shape than 3D points alone. Polygon edges are Euclidean vectors, in that they are geometric objects with a direction and magnitude. DEMs comparatively do not incorporate vectors. Because they instead rely on discrete grid divisions for heightmap data, these surfaces can be considered raster-based by analogy to 2D images. This distinguishes DEMs from vectorized surface meshes.

Morphological analyses of digital representations of shape have been performed on both DEMs and polygon meshes. Some of the methods used to analyze morphology from digital surfaces have been characterized as shape "specifiers," in that they are approaches that re-encode specific geometric shape from outlines or landmarks in such a way as to quantitatively and often statistically compare geometries between specimens (Evans, 2013). Procrustes-based geometric morphometrics provides a good example of a shape specifier approach, with this approach using Procrustes-aligned landmarks or semi-landmarks to compare landmark shape relationships without the influence of size, rotation, or other non-shape aspects of form (Adams et al., 2004; Lawing and Polly, 2010). These landmarks have various drawbacks, such as a reliance on homologous landmarks and an inability to diagnose more general properties of shape (Evans, 2013). A separate suite of quantitative morphological methods has been developed in order to avoid these limitations, and these techniques focus on what has been called a shape "description" approach (Christopher and Waters, 1974; Funkhouser et al., 2003; Evans, 2013). These methods have also been termed "dental topographic analysis" (M'Kirera and Ungar, 2003), though the terms shape descriptor methods or morphological topographic analysis will be used here to emphasize that these methods need not be limited to dentitions. A history of these morphological topographic analyses will be given.

Reed (1997) collected landmark points using a reflex microscope and interpolated a surface model from those points. He suggested diet might be inferred by measuring areas of cusps and basins from similar models. Zuccotti et al. (1998) used a similar method, measuring over 400 landmark points with an electromagnetic digitizer on

specimens of extant great ape teeth. A method more suitable for smaller teeth was introduced by Jernvall and Selanne (1999) using a laser confocal microscope. This method did not rely on manually selected landmarks and produced a DEM of much higher resolution than previous techniques. The accuracy of DEMs produced by laser confocal microscopes was confirmed by Evans et al. (2001). These methods were not ideal, however, due to the non-automated nature of imaging equipment employed by Reed (1997) and Zuccotti et al. (1998), and limitations of specimen size imposed by the laser confocal microscope used by Jernvall and Selanne (1999) and Evans et al. (2001).

Ungar and Williamson (2000) introduced a technique for creating DEMs using a laser scanner. Laser scanners are relatively automated and capable of capturing high-resolution scans of both large and small teeth. Their technique introduced a metric of molar shape termed relief index (RFI), calculated as the three-dimensional surface area of a tooth divided by the two-dimensional tooth area as projected on the XY plane, multiplied by 100. Unlike SQ, RFI is a whole-tooth measure of molar shape, and is capable of accounting for variably-worn teeth (M'Kirera and Ungar, 2003). Relief index is perhaps unsurprisingly a measure of "relief," that is, the height and steepness of a tooth's cusps and crests. Molar teeth with high, sharp cusps and crests will tend to have high RFI values compared to molars with low, bulbuous cusps. In primates, RFI has been used to investigate dietary preferences in extant strepsirrhines and tarsiers (Boyer, 2008; Bunn et al., 2011); platyrrhines (Ledogar et al., 2013; Guy et al., 2013; Winchester et al., 2014; Guy et al., 2015); cercopithecoids (Ulhaas et al., 2004; Ungar and Bunn, 2008; Bunn and Ungar, 2009; Guy et al., 2013; Guy et al., 2015); and hominoids (M'Kirera and Ungar, 2003; Ungar and M'Kirera, 2003; Guy et al., 2013; Guy et al., 2015). RFI has

additionally been used to consider molar macrowear and dental senescence in mantled howler monkeys and Milne-Edward's sifakas, respectively (Dennis et al., 2004; King et al., 2005). Fossil taxa considered by RFI analyses include hominins (Ungar, 2004, 2007), hominoids (Merceron et al., 2006), and plesiadapids (Boyer et al., 2009).

Relief index is at least somewhat analogous to shearing quotients in that both metrics attempt to quantify the total shearing capacity of a molar (Ungar and M'Kirera, 2003). A recent morphological topographic metric that has considered new elements of shape is orientation patch count (OPC) (Evans et al., 2007; Evans and Jernvall, 2009). OPC is calculated first by deriving contiguous areas of a DEM surface that face one of eight XY orientation arcs, where the XY plane is defined as the occlusal plane, and Z is perpendicular to this plane. Each of the eight XY orientation arcs spans 45° and the first arc is centered on 0°, giving the sequence -22.5° (i.e., 337.5°) – 22.5°, 22.5° – 67.5°, … , 292.5° – 337.5° (i.e., -22.5°). Contiguous DEM surface areas are then counted to determine how many surface regions face a unique aspect compared to their neighbors. This value indicates the complexity of a molar surface – teeth with more complex surfaces due to high number of cusps or high degrees of enamel enfolding will tend to have high OPC values, while simpler teeth with fewer cusps and smoother enamel will have lower OPC values.

Evans et al. (2007) demonstrated using OPC that, despite a wide taxonomic gap, carnivorans and rodents with similar diets exhibited posterior tooth-rows with similar complexity values. Plyusnin et al. (2008) applied machine learning to a variety of topographic and geometric shape variables in order to determine which metrics were ideal for inferring diet in individual teeth and tooth-rows, and concluded that OPC was an

ideal metric for capturing dietary signal in tooth-rows. OPC has also been used to investigate adaptive radiations of multituberculates prior to the Cretaceous-Paleogene mass extinction (Wilson et al., 2012), to elucidate dietary functional ecology of bats (Santana et al., 2011), and to construct computational models of tooth shape and development (Salazar-Ciudad and Marin-Riera, 2013). However, most fossil teeth tend to be isolated and associated tooth rows are relatively uncommon. Evans and Jernvall (2009) introduced a modification of the OPC method suitable for analyzing single teeth termed orientation patch count rotated (OPCR). In primates, OPCR has been used to consider mandibular molar shape in extant strepsirrhines and tarsiers (Bunn et al., 2011), platyrrhines (Ledogar et al., 2013; Winchester et al., 2014) and extinct sub-fossil lemurs (Godfrey et al., 2012). Outside of primates, OPCR has also been used to examine evolutionary transitions in the evolution of horses (Evans and Janis, 2014) and extinct creodonts (Chester et al., 2010).

The most recent addition to morphological topographic methods is Dirichlet normal energy (DNE) (Bunn et al., 2011). DNE uses changes in normal vectors across a triangular mesh representation of a tooth surface to quantify the total amount of bending across a tooth surface. DNE has some similarities to RFI, and teeth with higher, sharper, more bent ("curved" is also used here, but see Ch. 2 for specifics concerning how DNE measures surface curvature) cusps and crests and lower basins will tend to have higher DNE values relative to a (flatter) tooth with low blunt cusps. Bunn et al. (2011) observed that the correlation of RFI and DNE in a sample of primate-heavy euarchontans is relatively high ($R^2 = 0.736$) compared to other correlations between RFI, DNE, OPCR, SQ, and SR metrics. Despite this, DNE has some advantages over RFI such as

independence from 3D model orientation in XYZ space, higher tolerance of variant methods of cropping models, and more accurate dietary prediction of genera (Bunn et al., 2011; Winchester et al., 2014). Within primates, DNE has been calculated for strepsirrhines and tarsiers (Bunn et al., 2011), platyrrhines (Ledogar et al, 2013; Winchester et al., 2014) and sub-fossil lemurs (Godfrey et al., 2012).

With multiple topographic variables available for us, it is a challenge to determine which metric is appropriate for any given situation. Bunn et al. (2011) compared topographic metrics by computing SQs, shearing ratios, RFI, DNE, and OPCR on a wide euarchontan sample and compared and contrasted these metrics for the purpose of dietary inference. There is some degree of overlap between all topographic metrics, with the highest correlation being between SQs and shearing ratios ($R^2 = 0.863$) and the lowest between DNE and OPCR ($R^2 = 0.103$). OPCR in fact overlaps least with other topographic metrics. This is perhaps unsurprising if all metrics capture dietary signal, but the limited correlation of metrics (average R^2 overall = 0.441) suggests that metrics capture different but overlapping aspects of shape variation.

In light of this, Bunn et al. (2011) suggested the ideal way to employ dental-topographic variables would be in a combined fashion. They demonstrated that dietary prediction of "unknown" specimens using discriminant function analyses was much more effective when multiple topographic variables were combined. The most effective metric combination for dietary inference was a combination of all possible variables: SQs, shearing ratios, RFI, DNE, and OPC. RFI, DNE, and OPC alone were less effective at prediction diet but not by a large margin, with an overall success percentage of 79.7% compared to the all-variable analysis' success percentage of 83.1%. Winchester et al.

(2014) found similar results for samples of platyrrhines and strepsirrhines, tarsiers, and platyrrhines considered together. This is worth noting because measuring shearing crests requires more effort and is less automated than RFI, DNE, or OPC, which are all relatively automated.

Topographic analysis of morphology can be used to assess anatomical shape both broadly and deeply. Metrics used in combination capture a multifaceted and complementary assessment of surface shape. Additionally, compared to many other techniques for the assessment of shape, dental topographic analyses rely less on specific landmarks or *a priori* subjective decisions. This "homology-free" nature allows the consideration of highly variable surface (Evans et al., 2007; Boyer, 2008; Bunn et al., 2011). Using these methods it is possible to characterize morphology in diverse samples. In being relatively automated on the level of individual metrics compared to previous techniques, these methods can be considered high-throughput techniques for data acquisition (Plyusnin et al., 2008). The methods need not be limited to dental tissues, though previous research has been largely limited to these structures (but see Plyusnin et al., 2008). While teeth make an excellent model system for the quantification of shape due to the robustness of enamel and the occlusal surface representing a definable surface domain, shape quantification is certainly not limited to the dentition. Given careful selection of desired surface regions, it is reasonable to think that a better understanding of many anatomical elements could be gained through comparative consideration of topographic bending, slope, relief, or complexity. And for dental studies, topographic analyses likely do not need to be limited to questions of molar function. Recent empirical studies of evolutionary-developmental patterning in mice have posited models of tooth

shape morphogenesis that may represent another potential use for morphological topographic analyses.

1.1.2: Molar morphogenesis and evolutionary-developmental patterning

The development of tooth shape, or tooth morphogenesis, is a product of folding and growth of the interface between two tissue types: epithelium and neural-crest originating mesenchyme (Jernvall and Thesleff, 2000a). Tooth morphogenesis is in many ways similar to the development of other epithelial appendages, such as hair or glands (Jernvall and Thesleff, 2000a). As these tissues grow and fold, the inner enamel epithelium gives rise to enamel-producing ameloblast cells while mesenchyme gives rise to dentine-producing odontoblasts. The growth and folding of these tissues seems to be directed by a signaling center known as the primary enamel knot (Jernvall et al., 1994; Jernvall et al., 1996; Vaahtokari et al., 1996). The primary enamel knot is a cluster of non-proliferating cells formed during early tooth morphogenesis in the center of the tooth germ epithelium (Jernvall et al., 1994; Jernvall and Thesleff, 2000b). This cluster of cells expresses a variety of genes and proteins known to be crucial for proper tooth development, and it seems the presence of the primary enamel knot is required for tooth-crown morphogenesis (Jernvall and Thesleff, 2000a).

The development of species-specific cusp patterns occurs in a process mirroring that of overall tooth morphogenesis. The primary enamel knot gives rise to a series of new secondary enamel knots (Jernvall et al., 1994). These secondary enamel knots mark the appearance of future cusp tips, and are similar to primary enamel knots in their non-proliferative nature, expression of factors related to tooth development, and apoptotic

disappearances (Vaahtokari et al., 1996; Coin et al., 1999). Secondary enamel knots appear sequentially in the order of cusp development. The positioning of cusps seems to be determined by elegant control of the timing and location of secondary enamel knots through a patterning cascade (Fig. 3) (Jernvall, 2000).

In this developmental model, the first primary enamel knot to appear (corresponding to the first molar to develop) secretes proteins that encourage the growth of subsequent molars near the primary enamel knot while also secreting proteins that create an "inhibitory field" preventing the development of further molars within a certain proximity (Jernvall and Thesleff, 2000b; Weiss et al., 1998). Additional primary enamel knots marking subsequent molars are initiated at the edge of this inhibitory field. These additional enamel knots have their own inhibition fields, and the number of molars that are initiated depends on the size of earlier-forming teeth, the size of morphogenetic fields, and the time permitted for crown morphogenesis. Initiation of cusps follows a similar pattern, with secondary enamel knots expressing the same growth factors as the primary enamel knot (Jernvall, 1995; Weiss et al., 1998; Jernvall and Thesleff, 2000). Though it is not known whether sequential cusp patterning is maintained by signaling within epithelial or mesenchymal tissues, relative levels of activator and inhibitor signaling should control relative spacing and positioning of developing cusps (Jernvall, 1995, 2000; Weiss et al., 1998; Jernvall and Thesleff, 2000). Later appearing secondary enamel knots mark subsequent cusps, and are initiated at the edge of the inhibitory diffusion gradient. This patterning cascade allows for fine-tuned control of the number and spacing of either molars or molar cusps as changes in the timing and inhibition capability of the first primary or secondary enamel knot will create a cascade of

additional changes in further knots, along with control of overall time of crown morphogenesis.

This patterning-cascade model also has important implications for evolutionary biology. Processes of development determine evolvability, or the capacity to evolve novel morphologies (Jernvall, 2000). A patterning-cascade model provides a potential explanation for the observation of repeated convergent evolution of cusps in mammalian evolution such as the hypocone of upper molars (Hunter and Jernvall, 1995; Jernvall, 2000). This model also makes specific predictions that can be used to indirectly test for this type of developmental patterning in the molars of mammalian populations or species. Specifically, Jernvall (2000) observed that under a patterning-cascade model later-developing cusps should be more variable in form while earlier-developing cusps should be more stable. Alternatively, in the absence of a patterning-cascade model there is little reason why constraints of natural selection against variation in earlier-developing cusps would not also apply to later-developing ones. Jernvall (2000) further documented that this fact was true for 2D YZ (mesiodistal position on molar by height from crown-root junction) position of molars belonging to a population of Lake Ladoga seals (*Phoca hispida ladogensis*), and suggested a developmental process involving a patterning cascade probably evolved early in mammalian evolution. Jernvall and Selanne (2000) documented a similar general pattern in selenodonty, or elongation of cusps, in upper second molars of hedgehogs. Hunter et al. (2010) examined Carabelli cusp expression, size, and symmetry in humans and found support for predictions from the patterning-cascade model. It is unknown whether this pattern holds in non-human primates, but if it did evolve early in mammalian evolution and is present to some degree in modern

humans then there is little reason why it should not. Additionally, it is possible that the specific form of the patterning cascade's effect on cusp variability may differ between mammalian radiations or across evolutionary timespans, but whether this is the case is also unknown. An investigation of these topics in primates would make an ideal test case for these questions.

1.1.3: Molar shape in cercopithecoids

Cercopithecoids make an excellent test case for questions of dietary function and developmental patterning in relation to mandibular molar shape. Species of the cercopithecoid radiation are geographically widespread, behaviorally highly variable, and morphologically very diverse. Cercopithecoids exhibit a wide range of body sizes, locomotive and posture traits, and feeding adaptations. Dentally, extant cercopithecoid upper and lower molars are united in expressing a bilophodont molar configuration with relatively high crowns, four cusps at the margins, and cusp pairs connected with variably raised transverse ridges or lophs (Szalay and Delson, 1979; Strasser and Delson, 1987; Swindler, 2002). Cusp number and configurations are generally similar across the radiation, though M_3s of colobines and papionins express variably present hypoconulids while this cusp is absent in cercopithecins (Swindler, 2002).

Multiple analyses of cercopithecoid molars have documented variation in qualitative shape, shearing potential, or topography. Shearing crests of extant and extinct cercopithecoids have been measured by Benefit (1987, 1993, 2006; Benefit and McCrossin, 1990) and Kay (1978, 1984; Kay and Covert, 1984). RFI of cercopithecoid lower first and second molars has been analyzed by Ungar and Bunn (2008; Bunn and

Ungar, 2009). For both SQs and RFI colobines tend to have higher values compared to cercopithecines as befits their diet higher in leaves. This is consistent with qualitative observations that primates with diets higher in structural carbohydrates tend to have sharper cusps and crests relative to primates with diets with fewer structural carbohydrates (Kay and Hiiemae, 1974; Rosenberger and Kinzey, 1976; Seligsohn and Szalay, 1978; Kinzey, 1978). OPC has been used to compare outer enamel occlusal surfaces and enamel-dentine junctions of molars, though these comparisons were not interpreted in a functional context for cercopithecoids (Skinner et al., 2010; Guy et al., 2015). DNE has not yet been applied to cercopithecoid molar shape diversity.

Compared to most cercopithecoid species, a great deal of attention has been paid to the molar morphology and diet of the gelada baboon *Theropithecus gelada*. *Theropithecus gelada* exhibits a highly unusual diet consisting almost entirely of grass components, some of which express very high toughness values relative to other foods consumed by cercopithecoids, including mature leaves consumed by colobines (Teaford and Lucas, 1994; Lucas, 2004; Venkataraman et al., 2014). *Theropithecus gelada* molars also show a unique molar shape pattern among cercopithecoids with very high crowns, a fast rate of wear, columnar pillars, expanded distal and mesial regions on M_{1-3}, and complex enamel infolding (Jolly, 1972; Meikle, 1977; Swindler, 1983; Jablonski, 1993, 1994; Swindler and Beynon, 1993). It has been suggested that the complicated bands of enamel interspersed with depressions of softer dentin as evinced by worn *T. gelada* molars allows consumption of extremely fibrous and silica-rich grass parts, with relatively durable enamel ridges acting as shearing blades. This morphology has been likened to that of horses or suids (Jolly, 1972). Most of these considerations of *T. gelada*

molar morphology have been qualitative in nature, which makes sense given the difficulty of quantifying the complicated and variable enamel ridging patterns observed in this species. Morphological topographic analyses may represent an ideal method with which to quantify these patterns.

Across all species, considerations of molar morphology in cercopithecoids are often intertwined with questions concerning the origin and purpose of bilophodont molar morphology. Of the two stem fossil cercopithecoid taxa, *Victoriapithecus maccinesi* exhibits bilophodont molars while *Prohylobates* shows incomplete bilophodonty of permanent lower molars (Jablonski and Frost, 2010). The traditional view has held that bilophodonty and the origin of Cercopithecoidea are closely related to increased amounts of folivory, as many lophodont mammals consume leaves (Jolly, 1970; Napier, 1970; Delson 1975; Temerin and Cant, 1983; Andrews and Aiello, 1984; Benefit, 2006). However, more recent analyses of shearing crest lengths and other quantitative morphology of *Victoriapithecus* and other fossil cercopithecoids have suggested that the ancestral condition of both cercopithecoidea and colobidae was fruit and seed consumption, with folivory only a relatively recent novelty in the colobines (Benefit, 1987, 1993, 2006; Benefit and McCrossin, 1990). This may be related to an observation that bilophodont molars of colobines with high cusps and lophs could be equally as well adapted for the consumption of tough seeds as for leaves (Lucas and Teaford, 1993). It is possible that the divergence between cercopithecines and colobines had as much or more to do with adaptations for seed predation than for folivory.

1.2: Aims of this dissertation

The aims of this dissertation are separated into four goals. The first goal is to create a comprehensive open-source software tool for quantitative morphological topographic analysis capable of performing the DNE, RFI, and OPCR methods. The second goal is to use this topographic analysis software to gain a better understanding of how preparation and modification of morphological surface data affects quantified shape, with a focus on comparing previous analyses and providing recommendations for future analyses. The third goal is to use software tools and knowledge of data preparation to deploy high-throughput shape descriptor methods to assess extant cercopithecoid M_2 morphology in the context of adaptations for feeding as well as other factors influential on feeding adaptations such as tooth wear, allometry, and phylogenetic covariance. Finally, the fourth goal of this dissertation is to use shape descriptor and specifier approaches to assess developmental-patterning predictions concerning extant cercopithecoid M_2 size and shape. Dissertation chapter outlines are below, including more detail on predictions and methods for each chapter.

Chapter two discusses the production of shape data from anatomical specimens. This chapter introduces MorphoTester, a free open-source application coded in Python capable of performing topographic metrics DNE, RFI, and OPCR. MorphoTester also includes limited functionality for surface data preparation, with the ability to smooth surface meshes built in. MorphoTester's algorithms for DNE and RFI fully replicate implementations of these methods previously in the literature, but the OPCR implementation uses an approach measuring OPCR from 3D polygonal surface meshes. This 3D-OPCR algorithm is compared to previous OPCR algorithms operating on DEM surfaces using a sample (n = 37) of M_2s belonging to four cercopithecoid species. It is

predicted that 3D-OPCR and DEM-OPCR will be equally effective for differentiating cercopithecoid species. DNE, RFI, and OPCR are then measured from a sample of experimentally modified simple geometric objects that mimic the addition of tooth cusps and increases in tooth cusp height, in order to test a model of topography where OPCR reflects the number of features or "tools" on a tooth surface while DNE and RFI reflect surface feature shape. After this analysis, a number of tests are run to assess the effects of modifying surface pre-processing parameters – including cropping, simplification, smoothing, and alignment – on quantified topography. It is predicted that changes to all pre-processing parameters will have substantial effects on topographic variables.

Chapter three examines M_2 topography of a broad sample of extant cercopithecoid species, and attempts to document relationships between molar topography and dietary food mechanical properties while also accounting for allometry, phylogeny, and tooth wear. The sample for this study consists of 229 M_2s belonging to 23 cercopithecoid species sorted into one of four dietary categories based on dietary food mechanical properties. Teeth in this sample are sorted into two sub-samples: a first sample of 195 relatively less worn M_2s used to examine less worn primary molar morphology, and a second sample of 63 more variably worn M_2s used to examine wear-induced secondary molar morphology. Some M_2s are included in both sub-samples. First, body mass data collected from the literature is used to test whether M_2 area is functionally influenced as well as allometrically influenced, because M_2 area is the most accessible body-size proxy for this sample. After this, M_2 area and body mass data are used to assess whether topographic variables scale allometrically. It is predicted that topographic variables as emergent aspects of shape will not vary with body size.

Topographic variables DNE, RFI, and OPCR for the primary sub-sample are then tested to determine whether and how they vary across dietary categories with standard statistical techniques and phylogenetically-informed methods accounting for phylogenetic covariance. The secondary sub-sample is used to examine whether there is any evidence that molar complexity, a functionally-linked shape attribute, is maintained or enhanced throughout the process of tooth wear. If this is the case, it might signal one way in which teeth are adapted to maintain functionality throughout wear, as has been previously suggested to be the case for both non-primates (e.g., Fortelius, 1985) and primates alike (e.g., Ungar and M'Kirera, 2003; King et al., 2005; Winchester et al., 2012). DNE has previously been observed to decrease with progressive wear in Milne-Edwards' sifakas and mouse lemurs while OPCR has been observed to not decrease with wear in these species (Winchester et al., 2012). Intraspecific cercopithecoid DNE and OPCR are regressed on RFI, which in this intraspecific context is treated as a wear proxy. It is predicted that DNE will decrease as RFI decreases but that OPCR will either increase or not change relative to RFI decrease.

Chapter four tests predictions from empirical models of mouse molar morphogenesis in order to indirectly assess whether cercopithecoid molars develop from similar patterning principles that organize rodent molar morphology. First, a sample of mesiodistal lengths of M_1, M_2, and M_3 of extant cercopithecoids collected from the literature is used to test whether cercopithecoid molar size proportions conform to an inhibitory cascade model of molar tooth initiation and development. It is predicted that cercopithecoid molar size proportions will be similar to expected inhibitory cascade proportions. Subsequent analyses in this chapter consider variability in molar shape.

Because it is possible that shape specifier methods such as geometric morphometrics would be better suited for studying some aspects of shape variability compared to topographic approaches, both shape descriptor and specifier techniques are used and results between them are compared. A sample of 167 surface meshes of M_1s, M_2s, and M_3s is used for these analyses. Of these surface meshes, 132 represent associated M_1 – M_3 toothrows. These associated surfaces are used to test the prediction that molar shape variability increases in more posterior later-developing molars. Both topographic variables and an automated geometric morphometrics approach (*auto3dgm*; Boyer et al., 2015a) are used to quantify molar shape here. The remaining 35 surface meshes are M_3s and are used for analyses specific to M_3. Topographic variables and cusp landmark data are used to test the prediction that more posterior later developing M_3 cusps are more variable in shape, similar to predictions concerning more posterior molars above. Additional attention is paid to the hypoconulid because of its variable presence or absence across cercopithecoid clades. Lastly, cusp landmark data from M_3s of four species of extant cercopithecoids are used to test the prediction that the prominence of hypoconulid cusps or middle distal occlusal surface margins (where hypoconulids are absent) is correlated with the relative constriction of entoconid and hypoconid cusps as a pair compared to protoconid and metaconid cusps as a pair.

Chapter 2

Production of quantitative topographic data from anatomical specimens

2.1: Introduction

Quantity, quality, and diversity of 3D data are likely to grow with time, and with this growth comes the need for high-throughput approaches to the analysis of morphological shape (Plyusnin et al., 2008). Topographic analytical methods that seek to quantify whole-surface morphology represent a potentially promising example of high-throughput shape analysis (Ch. 1). Dental topographic analyses have been used to investigate mammalian molar form-function relationships across taxonomic scales spanning sub-species to mammalian orders (e.g., Ungar and M'Kirera, 2003; Evans et al., 2007; Boyer, 2008; Klukkert et al., 2012a; Winchester et al., 2014). Nevertheless, topographic analyses have often been implemented in ways that can limit wider application. As the name suggests, dental topographic methods have been limited largely to the study of mammalian tooth form. Teeth make an excellent model system for shape quantification with the occlusal surface representing a discretely bounded surface domain. But given careful selection of desired surface regions, it is reasonable to think that a better understanding of many anatomical elements could be gained through comparative consideration of topographic bending, slope, relief, angularity, or complexity. One reason why topographic analyses have not been applied more widely is probably that these methods have so far been limited to dental literature (but see Plyusnin et al., 2008).

Practical factors also increase barriers for use. First, published implementations of topographic metrics often require expensive proprietary software. Implementations of

relief index (RFI) have required software including ArcGIS (Esri) (Ungar and Williamson, 2000; M'Kirera and Ungar, 2003; Ungar and M'Kirera, 2003; Ungar and Bunn, 2008; Bunn and Ungar, 2009) and Avizo/Amira (FEI Visualization Sciences Group) (Boyer, 2008; Bunn et al., 2011; Godfrey et al., 2012; Ledogar et al., 2013; Winchester et al., 2014). Implementations of orientation patch count rotated (OPCR) have required the software SurferManipulator (Evans et al., 2007; Evans and Jernvall, 2009; Boyer et al., 2010; Evans and Janis, 2014). SurferManipulator is a free tool with stand-alone functions for the calculation of OPCR, but it is also designed to interact with the proprietary application Surfer (Golden Software) for data preparation. Dirichlet normal energy (DNE) can be calculated using Teether, a custom-written MATLAB package, but this software has not been made widely available (Bunn et al., 2011). Many topographic studies also use costly software tools to prepare surface data including Avizo/Amira or Geomagic (3D Systems) (Boyer, 2008; Bunn et al., 2011). In fact, different proprietary applications are commonly used for each metric. As a result, monetary and labor costs of applying multiple topographic metrics are high.

In addition, metrics are often performed on digital surface data formats that are not necessarily easily interchangeable. Some analyses of RFI and all analyses of OPCR have measured topography from raster-based gridded elevation data (M'Kirera and Ungar, 2003; Ungar and M'Kirera, 2003; Dennis et al., 2004; Evans et al., 2007; Ungar and Bunn, 2008; Bunn and Ungar, 2009; Bunn et al., 2011; Godfrey et al., 2012; Ledogar et al., 2013; Evans and Janis, 2014; Winchester et al., 2014). Other analyses of RFI and all analyses of DNE have used vector-based triangulated polygon surface meshes (Boyer, 2008; Bunn et al., 2011; Godfrey et al., 2012; Ledogar et al., 2013; Winchester et al.,

2014). This requires different approaches for surface data preparation, which itself increases costs and may introduce unexpected variation into the surface data that topographic analyses seek to quantify. A single tool for performing topographic analyses on a uniform data format would help to minimize these challenges. Here I present an application, MorphoTester, designed to address these challenges and to increase the ease of use and uniformity of topographic analyses.

Using a comprehensive software package for comprehensive execution of topographic analyses on polygonal surface meshes, it is possible to document effects of shape change and data preparation on quantified topography. Topographic metrics are quantitative surface shape descriptors that provide single number measurements of surface shape properties (Evans, 2013). In this way, they are distinct from quantitative representations or reformulations of shape such as 3D geometric morphometric techniques. Topographic metrics quantify emergent morphological characteristics, or in other words characteristics that arise from the interaction of component entities. A consequence of topographic variables measuring emergent characteristics is that these measures are not dependent on specific morphological features. While the shape of individual cusps affects the overall bending across a tooth surface, it is possible to achieve similar degrees of surface bending from many different potential cusp configurations. This is why these methods have been previously described as “homology free” measures of shape (Ungar and M'Kirera, 2003; Evans, 2005; King et al., 2005; Evans et al., 2007). At the same time, this means it may not be immediately clear how to translate quantifications of surface bending, relief, and curvature into an anatomical or cladistic lexicon concerning pinched, flattened, or bulbous cusps, crests, or basins.

Ambiguity in the correlation between topographic variation and traditional lexicon has led to a range of interpretations of topographic metrics. In one study, Ungar and M'Kirera (2003) described average cusp slope and angularity (the derivative of slope) as relating to cusp steepness and jaggedness respectively. In a subsequent analysis they introduced relief index and described it as analogous to shearing quotient approaches, which quantify shearing crest length relative to mesiodistal tooth length (M'Kirera and Ungar, 2003). Teeth with relatively higher relief were indirectly associated with "steeper planes of contact for shearing and slicing" and lower relief teeth were characterized as having "flatter surfaces." Introducing OPCR as a complexity metric, Evans et al. (2007) put forward a model of teeth as "'tools' for breaking down food" and dental complexity as "any measure of the number of features, tools or breakage sites on a tooth." Bunn et al. (2011) extended this approach and suggested a two-axis model where complexity quantifies the number of tools on a tooth surface while relief and curvature reflect the shape of those surface tools. This model, which was expanded by Winchester et al. (2014), suggests that using complementary topographic metrics allows for characterizing at least two axes of emergent tooth shape properties. These models have not been directly tested, though their predictions have been used to interpret molar topography in comparative analyses. In this chapter, I will use custom-made polygonal meshes to chart an experimental topographic morphospace to assess these models.

While it is straightforward to explicitly design experimental simple geometric objects without variation, the same is not true for the creation of digital surface representations of anatomical elements. There are diverse techniques and parametric choices from which to construct a pathway from skeletal material to digital surface

representations that can be morphologically analyzed. This pathway will be generally referred to here as surface or mesh pre-processing. Dental topographic analysis was initially developed at least in part to sidestep choices concerning landmarks and other parameters necessary for more traditional measures of tooth shape (Ungar and M'Kirera, 2003). In contrast, a recent study of platyrrhine dental topography and shearing quotients has suggested that mesh pre-processing parameters represent one way in which topographic analyses are not completely landmark-free (Allen et al., 2015). Certainly implementing topographic analyses requires decisions concerning multiple aspects of surface pre-processing. This includes aspects of surface capture – a variety of scanning technologies and surface data formats exist – or mesh preparation. Steps of mesh preparation form the focus of analyses here, specifically as applied to vector-based polygonal surface meshes.

Mesh pre-processing steps that have been used in previous analyses include choice of surface domain ("cropping"), noise reduction, and mesh alignment. Topographic metrics quantify shape across all surface data present, and for many anatomical elements this requires surface data to be cropped to include only desired surface. Some raster-based analyses of OPCR have not used surface cropping techniques because occlusal alignment of tooth surfaces and heightmap data format together can automatically produce appropriate surface boundaries in some cases (e.g., Evans et al., 2007; Evans and Janis, 2014), but other raster-based analyses of RFI and other topographic measures such as slope or angularity have used cropping techniques to specifically isolate surface regions of interest (e.g., M'Kirera and Ungar, 2003). For comparative analyses, surfaces should be cropped to include similar or possibly

biologically equivalent domains. A number of analyses of second mandibular molars (M_2s) of closely related primate species have cropped all surfaces to the lowest point of the central occlusal basin to achieve this goal (M'Kirera and Ungar, 2003; Ungar and M'Kirera, 2003; Dennis et al., 2004; King et al., 2005; Ungar and Bunn, 2008; Bunn and Ungar, 2009). A study of M_2s of a large sample of prosimians instead cropped specimens to the enamel cervical margin due to significant diversity in occlusal basin morphology across the sample (Boyer, 2008). Subsequent large-scale analyses of platyrrhines have also used this approach for comparison with data from prosimians (Ledogar et al., 2013; Winchester et al., 2014). Little comparative work has been done to assess the effects of surface cropping techniques on inter-species topographic comparisons.

Noise reduction techniques include surface simplification and smoothing. Surface simplification entails the process of reducing the number of polygons forming a surface mesh, while smoothing describes the process of decreasing local shape change around vertices to achieve a "smoother" surface appearance. Boyer (2008) assessed the effect of smoothing on mesh surface area and identified a trend of rapid decrease with initial smoothing followed by an approach toward stability. Some analyses of M_2 topography have arbitrarily chosen to simplify meshes to 10,000 faces and smooth simplified meshes over 100 iterations with a lambda parameter of 0.6 using the software applications Amira or Avizo (FEI Visualization Sciences Group) (Bunn et al., 2011; Ledogar et al., 2013; Winchester et al., 2014). The effects of simplification and smoothing together on topographic values have yet to be tested.

Finally, two of the topographic metrics considered here (RFI and OPCR) are sensitive to mesh orientation in 3D space, with the XY plane needing to be occlusally

aligned for dental analyses. Recently an algorithm has been developed for automatic uniform alignment of surface meshes (*auto3dgm*, Boyer et al., 2015a), and precision of alignment is likely to be higher using an algorithmic approach rather than a manual one (Boyer et al., 2015b). But even when using an algorithmic alignment approach, a user-specified occlusal plane is still required and the accuracy of mesh alignment is therefore still susceptible to inter-observer error. It would be beneficial to know the effects of mesh orientation on quantified topography regardless of alignment method. This chapter seeks to test the effects of three mesh pre-processing parameters: surface cropping, noise reduction, and mesh orientation.

The analyses described here address two main research goals. The first goal is to provide a more comprehensive and automated software tool to perform topographic analyses on anatomical shape data. The second goal is to better document how topographic methods quantify shape and how mesh pre-processing affects quantified topography. Correspondingly, the following research questions are considered:

- Does OPCR measured from polygonal surface meshes better partition species-level differences in molar shape compared to OPCR measured from raster-based digital elevation models?

- Does quantified topography of iteratively modified simple geometric objects conform to previously developed models for understanding topographic metrics?

- How do surface cropping, noise reduction, and mesh orientation affect quantified topography from molar teeth?

2.2: Methods

2.2.1: Study Sample

Investigating how topographic algorithms quantify surface shape requires a reference sample from which to measure topography. Hypothetically, such a sample should be as variable in shape as possible. The sample surfaces themselves and differences between surfaces should also be straightforward to understand, in order to make interpretations of quantified topography from these samples similarly straightforward. At the same time, variability and straightforwardness of sample surfaces must be balanced with the relevance of surface shapes to research questions. Randomly generated 3D points would be highly diverse but not relevant to goals here. As the focus here is on the shape of biological structures, specifically primate dental form, relevance is maximized when shape data represent primate teeth. A large sample of high-resolution digital surfaces representing primate M_2s would be very relevant to research questions address by this dissertation, but quantified topography from this sample may not be very straightforward to interpret. This is for two reasons: 1) noise introduced through surface capture will change quantified topography in unexpected ways (see below), and 2) complex topographic surfaces of primate M_2s exhibit significant change in shape and organization even across a single occlusal surface such that shape can be modified in possibly countless different ways. It is also difficult to experimentally alter mammalian teeth to empirically assess changes in form simultaneously with changes in measures of

topography. This ambitious goal – of connecting changes in phenotype with changes in measures of topography and associating these changes with fitness or other such concepts – has been the target of computational modeling studies informed by evolutionary-developmental findings from experimental mouse populations (e.g., Salazar-Ciudad and Jernvall, 2010; Salazar-Ciudad and Marin-Riera, 2013). These analyses have used developmental models of tooth form and topographic shape measures to assess genotype-phenotype maps and their relationship to morphological fitness, but their conclusions are limited to certain model organisms and the empirical alterations to anatomical form produced by these genetically and developmentally influenced computational models are still complex enough to have reduced straightforwardness for interpreting topography.

This study balances relevance and straightforwardness by using two different samples. The first sample is comprised of biological specimens, while the second sample uses empirically constructed simple geometric objects. The biological sample is an assemblage of M_2s (n = 37) belonging to four species of cercopithecoid primates: three cercopithecine species *Cercopithecus mitis* (*C. mitis*, *n = 10*), *Cercocebus atys* (*Ce. atys*, n = 7), *Theropithecus gelada* (*T. gelada*, n = 9), and one colobine species *Colobus guereza* (*Co. guereza*, n = 10) (Table A2.1, Fig. 2.1). Only unworn or lightly worn specimens were chosen. The relatively small size of this sample was a deliberate choice, as analyses of mesh pre-preprocessing parameters require repeating the mesh preparation process many times. Despite this constraint, the sample was chosen to provide a reasonable degree of variability within primate molar form. These species include both cercopithecoid subfamilies. Among cercopithecines, representatives of both cercopithecin and papionin clades are present. This maximizes phylogenetic variability to the degree

that is possible with four species. These species also have very diverse dietary food mechanical properties (but see Ch. 3 for a functional analysis of topography for a much larger sample). Previous analyses of tooth form in primates have suggested that molar morphology correlates with diet (Gregory, 1922; Kay, 1984; Ungar and M'Kirera, 2003), and so it is reasonable to presume that M_2s belonging to species with diverse diets will also exhibit diverse topographic shape.

The second sample consists of abstract simple geometric objects that have been iteratively modified to produce a continuum of shape from which to measure topography. These simple 3D objects should be instructive for understanding how topography changes with shape transformation. As much of the evolution of mammalian molar form is related to the addition, modification, and/or elimination of cusps and crests, the method for creating simple geometric objects focuses on the addition and modification of abstracted cusp/crest structures. Specifically, simple geometric objects vary by two simplistic parameters: number of cusps and height of cusps. This provides two dimensions of shape change that can be used to directly test previous claims regarding topographic analyses. Additionally, each variable can be independently controlled or varied which will help make results more interpretable.

Simple geometric objects were created using *shapemaker.py* (Appendix 1), which implements two algorithms to create series of iteratively modified shapes. The first of these algorithms is referred to as "Constant-Length." It begins from a default flat rectangular plane of 200 polygons (Fig. 2.2). From this default plane the Constant-Length algorithm produces between one to ten simplistic cusps, where each cusp is comprised of 20 polygon faces joined at an angle to create a ridge. The first cusp initiated is always

placed as far "anterior" as possible on the plane, and any subsequent cusps are placed immediately "posterior" on the plane. Plane length is kept constant for all meshes. All cusps have a height of between six to ten Z-units, and all cusps on a surface have the same height. Constant-Length produces an assemblage of 50 surfaces that together include all possible combinations of one to ten cusps of heights six to ten.

The second shape generation algorithm is referred to as "Delta-Length." The shapes produced by it are similar to those produced by Constant-Length in that they consist of between one to ten simplified cusps with variable heights. The Delta-Length method however introduces cusps with heights from one to ten Z-units. As a result, the Delta-Length assemblage is comprised of 100 meshes instead of 50 as in the previous case. More importantly, the Delta-Length algorithm does not begin with a flat rectangular plane. Instead, meshes are created from a sequence of one to ten 20-polygon cusps laid out in a linear fashion (Fig 2.2). The surface mesh is initiated with the most "anterior" cusp and is terminated with the most "posterior" cusp. Correspondingly, neither mesh length or the total number of polygons comprising each mesh will remain constant. Total number of polygons per mesh will be 20 per cusp up to 10 cusps and 200 polygons.

Both Constant-Length and Delta-Length methods are used here because together they balance relevance and intuitiveness for abstract structures. The mesh assemblage produced by Constant-Length has relatively fewer changing variables compared to Delta-Length, and changes between topographic metrics of Constant-Length meshes should therefore be more easily interpretable in terms of shape modification. But in contrast, the evolutionary history of the addition of major molar features (e.g., the talonid basin) has often been accompanied by an increase in individual molar area. Similarly, experimental

models of mammal molar morphogenesis correlate the development of cusp topography in a developing tooth with an increase in tooth length (Jernvall et al., 1998). An abstract constant-length model of molar crest introduction is less similar to the mammal molar fossil record or to developmental events than a model in which mesh length increases with cusp addition. Topographic results from Delta-Length mesh assemblages may be less easily interpretable, but they are more likely to be understandable in the context of the evolution and development of anatomical form. Topographic results from both algorithms should provide both interpretability and applicability.

2.2.2: MorphoTester

MorphoTester is an application framework for quantifying topographic shape from 3D triangulated polygonal mesh data. It has been created using the Python programming language (van Rossum, 1994) and MorphoTester is free to use as well as open source. As a result, the topographic algorithms included and the base application code may be modified and reused under the terms of a GPL v2.0 (or later) license (see Appendix 2 for more details). Fundamentally, MorphoTester represents a platform for inputting and visualizing polygonal mesh data and executing specific topographic shape algorithms on that data. Output results from topographic algorithms are quantitative descriptors of mesh shape (Evans, 2013). In its default form this application is capable of calculating three topographic metrics: Dirichlet normal energy (DNE, quantifies surface bending) (Bunn et al., 2011), relief index (RFI, quantifies surface relief) (Ungar and M'Kirera, 2003; Boyer, 2008), and orientation patch count rotated (OPCR, quantifies surface complexity) (Evans et al., 2007; Evans and Jernvall, 2009). This framework is

further extendable to include possible future topographic shape algorithms as well. Documentation and source code for MorphoTester are provided in Appendix 2. Current versions of source code and compiled executable files are also available for download at http://morphotester.apotropa.com/.

2.2.3: Accessing MorphoTester

For most users, compiled executable versions of MorphoTester are the easiest way to access the software. Compiled executables are provided for OSX and Windows operating systems. For OSX computers, this software is provided as a single file application bundle that can be run directly and placed in the Applications directory for continued access. MorphoTester for Windows is provided as a directory containing an executable file, *Morpho.exe*, and supporting data files. Users should run *Morpho.exe* to access the software. The program is operated entirely through the graphical user interface, and so no command line interaction is required. Executable versions provide the most direct path to using the program for "out of the box" topographic analysis. Users more familiar with Python can also run the application by interpreting the source code with Python installed. This first requires the installation of dependent Python packages (see below and Appendix 2). If all dependencies have been met, the software can be opened by running the file *Morpho.py* as a script using the Python interpreter. Compiled and source-interpreted versions of MorphoTester have identical functionality. Compilation of source code for OSX and Windows was carried out using the Python packages *py2app* (www.pythonhosted.org/py2app) and *py2exe* (www.py2exe.org) respectively. Configuration files for executable compilation are included in Appendix 2.

In addition to the website given above, MorphoTester source code and compiled executable releases are stored using Github (www.github.com/juliawinchester/morphotester). Github is a major platform for storing and presenting code and code-related materials, and the linked repository is intended to serve as the long-term storage location for this software. The prominence of this platform ensures that these data are protected from the usual vagaries of university and personal webhosting. Additionally, Github has robust tools for communication and collaboration between users. The linked MorphoTester repository is equipped to serve as a central source of reports of software bugs and issues. It is also possible for users to "fork" or clone the software, establishing their own version for addressing problems or expanding features. Changes from software forks may then be merged back into the main repository. This provides interested users with direct access to the MorphoTester source code and easy tools for collaborative development of the software, and provides a direct path for continued maintenance.

When using MorphoTester, mesh data must be provided as Stanford Triangle or Polygon File Format (PLY), a common data format for triangulated polygonal meshes. Non-polygonal surface data such as point clouds can be readily triangulated to create polygon meshes using open source software such as Meshlab (http://meshlab.sourceforge.net/) or proprietary software such as Avizo (FEI Visualization Sciences Group) or Geomagic (3D Systems). PLY format data can be easily converted to and from other common file formats including .obj, .wrl, or .stl using free software such as Meshlab or meshconv (Min, 2015).

Topographic shape can be quantified for individual mesh files, or collections of mesh files can be processed using batch processing. MorphoTester is operated through a graphical user interface (Fig. A2.1). Users can load and visualize surface mesh files to be analyzed or select a directory for batch processing of analyses. Mesh files can be analyzed using any combination of DNE, RFI, and OPCR metrics by enabling or disabling these metrics prior to surface processing. For DNE and OPCR, submenus can be used to change parameters for analysis and enable visualizations of quantified topography on surface meshes. See below for more discussion of analysis parameters in detail. OPCR is visualized by coloring surface patches one of eight colors corresponding to patch orientation (see below). DNE is visualized using a color spectrum map across a surface mesh where warmer colors indicate greater surface bending at a polygon (e.g. Fig. 3 from Bunn et al., 2011). The DNE color map can be adjusted to show bending only relative to the current specimen or relative to an absolute range for comparing curvature between specimens. When processing individual specimens, results of topographic analyses are provided in a text console within the application. When batch processing a directory of specimens, a tab-separated values spreadsheet file listing results of topographic analyses is created in the specimen directory. This file can be opened using most spreadsheet software. Sample data for use with this software and reference topographic results can be downloaded from the above links. MorphoTester software documentation included in Appendix 1 contains more information on how to use this application.

2.2.4: Program structure

Visualization and mathematical functions of MorphoTester are supported by pre-existing open source Python packages. These include the *Numpy* and *Scipy* stack (Van Der Walt and Colbert, 2011), which provides data structures and functions for the large-format multidimensional arrays and matrices that are used to store polygonal mesh data. Mesh visualization is supported by the package *Mayavi* (Ramachandran and Varoquaux, 2011), and this package is integrated with *PyQt4* (riverbankcomputing.com/software/pyqt/intro) and the non-Python open source library *Qt4* (www.qt.io) to implement the graphical user interface. *Matplotlib* (Hunter, 2007) is used for data plotting tasks. A full list of package dependencies can be found in Appendix 2. All of these backend packages have full documentation and so can be leveraged to modify MorphoTester code in a straightforward fashion for future needs.

In addition to being supported by third-party Python packages, this software incorporates and is supplied with Python packages and scripts to provide useful functions for working with triangulated polygonal mesh data. Principal among these is *plython*, a package integrated with MorphoTester that provides objects and methods for inputting, manipulating, and saving triangulated polygonal mesh data within Python. Four other command-line scripts are provided as well: *meshrotate*, which rotates individual PLY-format meshes in XYZ coordinate space; *meshrotate-batch*, which extends *meshrotate* to process multiple files; *PLYtoOFF*, which converts PLY-format mesh data to OFF-format; and *BINtoASC,* which converts PLY-format mesh from binary encoding to ASCII encoding. *BINtoASC* is useful as MorphoTester specifically interprets ASCII encoded PLY-format meshes, while some applications for modifying 3D meshes such as Geomagic only allow saving PLY-format meshes with binary encoding.

The code structure of MorphoTester is split between a primary module containing support for visualization and the user interface (*Morpho.py*) and a series of topographic and supporting modules. These include a module creating a surface mesh object with associated topographic values (*topomesh.py*), three individual modules providing support for calculating topographic metrics, a support module providing functions for the calculation of normal vectors (*normcore.py*), and a second support module providing functions for implicit fair smoothing (*implicitfair.py*). Of the topographic algorithms, support for the calculation of DNE, RFI, and OPCR are provided by the modules *DNE.py*, *RFI.py*, and *OPC.py* respectively. Description of the calculation of these metrics follows.

2.2.5: Dirichlet Normal Energy

DNE can be briefly summarized as a quantification of the degree to which a surface mesh bends (Bunn et al., 2011). It is based on an application of a concept from differential geometry, Dirichlet's energy, applied to the normal map of a mesh. Dirichlet's energy is a measure of the variability of a function, and is termed energy because of applications to energy and action states in physics. DNE is also concerned with variability across a function, with that function being change in position across a three-dimensional surface. Surface variability includes both convexity and concavity, and as a result DNE increases with both types of shape change. In a continuous surface mesh case where surface polygons become arbitrarily small, the DNE method is equivalent to measuring the sum of squares of principal curvatures across a surface. This is in contrast to another recent morphological curvature measure, which averages polygon principal

curvatures and correspondingly returns negative values for concavity and positive values for convexity (Guy et al., 2013; Guy et al., 2015).

Bunn et al. (2011) briefly described the mathematical background for DNE, but here I will expand on the method of the algorithm. DNE is calculated as the sum of energy values across a polygonal mesh surface. Energy value here equals the energy density of a polygon, *e(p)*, multiplied by polygonal face area. The energy density function *e(p)* quantifies change in the normal map around each polygon. While the explicit derivation of this function is given in detail below, it is possible to use a simplified two-dimensional diagram to understand how *e(p)* characterizes amount of bending from change across a surface normal map (Fig. 2.3).

To derive *e(p)*, normal vectors of unit length (i.e., having a magnitude of one) are first derived for each polygon face comprising a mesh. Normal unit vectors for polygonal vertices are then approximated as the normalized average of normal vectors of triangle faces adjacent to each vertex. After producing approximated normal unit vectors for polygonal vertices, it is possible to consider two characterizations of polygon form. The first of these is defined by *u* and *v*, two vectors representing edges of a polygon (put another way, these are vectors representing change in surface position between vertices) (Fig. 2.4). The second is defined by n_u and n_v, which are derivatives of a surface normal map function *n* in the directions *u* and *v*. In a discrete surface mesh these are vectors representing edges of a polygon comprised of the endpoints of normal unit vectors derived from the original polygon (Fig. 2.4).

Using *u* and *v*, it is possible to construct the matrix

$$G = \begin{pmatrix} \langle u, u \rangle & \langle u, u \rangle \\ \langle u, v \rangle & \langle v, v \rangle \end{pmatrix}$$

where $\langle \blacksquare, \blacksquare \rangle$ is a notation indicating the scalar Euclidean inner-product (dot product) of the two values within brackets. These dot products characterize the magnitudes of u and v projected onto themselves and each other, and so G characterizes the spreading out of the original polygon. Similarly, using n_u and n_v it is possible to construct the matrix

$$H = \begin{pmatrix} \langle n_u, n_u \rangle & \langle n_u, n_v \rangle \\ \langle n_u, n_v \rangle & \langle n_v, n_v \rangle \end{pmatrix}$$

which characterizes the spreading out of the polygon normal map analogous to G. The bending of the surface around and at a polygon p is then derived as $e(p) = tr(G^{-1}H)$. The trace of the product of matrices operates similarly to the dot product of vectors, and $e(p)$ can simplistically be considered as the spreading of the polygon normal map relative to the spreading of the original polygon.

Energy per polygon is $e(p)$ multiplied by polygon area. Total DNE is then calculated from the sum of energy values of all polygons across a mesh surface, except for three conditional cases where polygonal energy density may be discarded. (1) The DNE algorithm ignores energy density from polygonal faces whose edges form part of the boundary of a hole in the mesh surface, as vertices related to these edges do not have a full complement of polygonal faces from which to approximate vertex normal vectors. For surfaces created from teeth, a single large inferior hole is often created through "cropping" of unnecessary surface, such as that inferior to the cervical margin (Bunn et al., 2011). (2) Optionally, energy values of polygons can be ignored where G produces a high condition number. Based on the ratio of the largest to smallest singular values in the singular value decomposition of a matrix, matrix condition numbers provide a measure of how close a matrix is to being singular. For G matrices with high condition numbers, very small changes in polygon vertex input are liable to produce large changes in energy

output. Because of this, energy from these polygons is discarded. It is recommended that condition number checking be used when calculating DNE. (3) MorphoTester also allows optional discarding of energy or energy density values above a user specified outlier percentage. This can address surface meshes in which "noisy" polygons produce energy values out of proportion to the overall surface. Outlier removal of energy values above the 99.9^{th} percentile is enabled by default, but these settings can be easily user modified. Consistent outlier removal settings should be used for all specimens in a comparative sample as this setting does affect DNE results.

Higher and lower DNE values represent greater and lesser amounts respectively of bending across a surface. For the example of a primate molar tooth, higher and sharper cusps and crests as well as deeper and more acutely angled basins will produce higher DNE values. DNE is invariant to orientation or scaling of meshes, but quantified surface bending is proportionate to the number of polygons comprising a mesh. This is because DNE is calculated as the sum of polygonal energy densities, and so meshes with greater numbers of polygons will necessarily exhibit higher DNE values than meshes of similar shape with fewer polygons. For analyzing samples of surface meshes, simplifying all meshes to a common number of polygons addresses this variance.

Previous analyses using DNE have employed Teether, a Matlab script, for calculating DNE from polygonal surface data (Bunn et al., 2011; Godfrey et al., 2012; Ledogar et al., 2013; Winchester et al., 2014). Teether has not been made widely available, and MorphoTester replicates the functionality of Teether completely with regards to DNE calculation and visualization. MorphoTester further corrects two errors in the Teether DNE algorithm. The earliest versions of Teether implemented condition

number checking as described above, but did not appropriately discard energy densities from polygons as a result. MorphoTester correctly implements condition number checking. Additionally, Teether forces meshes to be smoothed using an implicit fairing algorithm (Desbrun et al., 1999) prior to DNE calculation. If desired, MorphoTester can optionally perform an implicit fairing smooth for compatibility with Teether. MorphoTester also provides optional removal of energy or energy density values above a user specified percentile as outliers, as described above.

2.2.6: Relief Index

For a mesh, RFI is defined as the ratio of surface area (*3da*) to two-dimensional area projected on a plane parallel to the occlusal plane (*2da*) (Ungar and M'Kirera, 2003; Boyer, 2008). This metric has been calculated variously as $RFI = \frac{3da}{2da} \times 100$ (M'Kirera and Ungar, 2003; Ungar and M'Kirera, 2003; Ungar and Bunn, 2008; Bunn and Ungar, 2009) or as $RFI = ln\left(\frac{\sqrt{3da}}{\sqrt{2da}}\right)$ (Boyer, 2008; Bunn et al., 2011; Ledogar et al., 2013; Winchester et al., 2014). While creating an algorithm to measure *3da* is straightforward since it only requires a summation of individual polygon areas across a surface, exactly measuring *2da* from a complex 3D polygonal mesh is more difficult. While the software SurferManipulator (used to calculate OPC and OPCR from raster-based DEM heightmaps; see below) performs a similar operation on DEM heightmap data, this goal is more challenging with polygonal meshes because of the possible presence of underhanging surface. An algorithm to calculate *2da* from a polygonal mesh must somehow derive a 2D concave hull from a 3D surface mesh with unpredictable geometry. Alpha hull techniques to calculate concave hulls from surface meshes do exist, but they

require one or more parameters regarding hull fitting to be specified prior to hull fitting. Determining parameters that will exactly assign correct convex hulls in every case from potentially extremely variable tooth morphologies was judged impractical. Some previous approaches calculating RFI from polygonal meshes have calculated *2da* by rotating meshes to maximize occlusal position, exporting mesh view as bitmap image, and then using image processing software to measure numbers of pixels in conjunction with a pixel-to-length scalebar (Boyer, 2008; Bunn et al., 2011; Winchester et al., 2014). MorphoTester automates this approach. After calculation, RFI is reported as a simple ratio of *3da* divided by *2da*. *3da* and *2da* are also provided so that RFI can be calculated using any desired formula.

2.2.7: Orientation Patch Count Rotated

Orientation patch count can be defined as the number of regions on a surface ("patches") where adjacent polygons in a patch all face the same "compass" direction (i.e., have similarly angled normal vectors when projected on the XY plane). All previous OPC analyses have sorted polygons into one of eight directional groups, each spanning a 45° arc, and so a perfect sphere should always have a count of eight orientation patches. OPC has been characterized as a surface complexity measure (Evans et al., 2007). OPCR is a modification of the OPC approach designed to be more resistant to potential variation in specimen orientation on the XY plane (Evans and Jernvall, 2009). OPCR addresses this by rotating individual molar specimens eight times across a total arc of 45° (5.625° per rotation), calculating OPC at each rotation. OPCR is the average of these eight variably rotated OPC values.

OPC has been applied to polygonal mesh surfaces (Guy et al., 2013; Guy et al., 2015; Salazar-Ciudad and Marin-Riera, 2013), but OPCR has not. Previous implementations of OPCR have predominantly used the GIS software Surfer (Golden Software) and the application SurferManipulator (Evans et al., 2007). SurferManipulator is designed to interact with Surfer for data preparation, and has stand-alone GIS functions for calculating OPCR (Evans et al., 2007). This approach calculates OPCR from raster-based DEMs, which in this case are comprised of regularly-spaced columns and rows of data which correspond respectively with X and Y points. Each X and Y point pair is associated with at most one Z-axis elevation value, and so the DEMs represent a regularly spaced matrix of elevation information. This heightmap format differs from triangulated polygon meshes in a number of ways, principally in that DEMs cannot store two Z elevation values for one X-by-Y location (as in a sheer wall or an undercut) while polygonal meshes can (Guy et al., 2013). This circumstance may not seem to be an issue for many kinds of anatomical specimens, including teeth, as biological surfaces rarely include perfectly vertical expanses. But a complex specimen exhibiting highly variable surface slope and significant change in height may give rise to surface regions that are intermittently vertical. A polygonal mesh may more accurately characterize a surface like this than a DEM. Additionally, the heightmap data model of the DEM format requires a more static Z-axis orientation compared to polygonal meshes. To increase comparability of metrics and to more accurately describe shape in complex surfaces, MorphoTester diverges from previous implementations of the OPCR metric by quantifying complexity from fully 3D triangulated polygon meshes instead of DEMs. This OPCR algorithm is

introduced here. For clarity, I will refer to the triangulated mesh algorithm as 3D-OPCR and the method used by SurferManipulator as DEM-OPCR.

The 3D-OPCR algorithm requires only one parameter, a minimum patch size. This parameter indicates the minimum size in number of polygons for a patch to be counted toward an OPC value. To calculate OPC, the centroid of the surface mesh is translated to the origin of the XYZ coordinate system. Then normal unit vectors are derived for each polygon face comprising the surface. Normal unit vectors are used to calculate the aspect of each face in the XY plane, and faces are sorted into one of eight groups by aspect. Each group represents an arc of 45 degrees. Contiguous polygons are then sorted into matching aspect groups, and iterative sorting of these arrays is used to construct a list of patches of contiguous polygons of identical aspect grouping. OPC is the number of patches at the minimum patch size or larger. To calculate OPCR this procedure is repeated eight times with the surface mesh being successively rotated 5.625° around the Z-axis, with the total mesh rotation being 45° by the eighth iteration. OPC values from each rotation are then averaged to give an OPCR value.

2.2.8: Statistical Analysis of 3D-OPCR

While the DNE and RFI algorithms used by MorphoTester implement analytical methods previously used in the literature, the 3D-OPCR algorithm has not been applied in prior studies. Because of this, 3D-OPCR as quantified by MorphoTester was compared to DEM-OPCR as measured by SurferManipulator using the cercopithecoid M_2 sample described above. To compare results from 3D-OPCR and DEM-OPCR algorithms, PLY-format surface meshes were first cropped to only include tooth surface above the lowest

point on the central occlusal basin and then simplified and smoothed to remove noise. Meshes were simplified to 10,000 polygons and then smoothed across 100 iterations with a lambda parameter of 0.6 using the Simplifier and SmoothSurface modules of the Amira software (Visualization Sciences Group). 3D-OPCR was then calculated using MorphoTester, with a minimum patch size of 5 polygons. To calculate DEM-OPCR, surface meshes were first converted to raster-based DEM format. This was done by first manually eliminating stacked elevation data by removing all polygonal faces not directly visible from a perspective parallel to the occlusal plane in Amira. After this, SurferManipulator's file conversion tool was employed to convert data to Surfer DEM format. Original triangulated polygon surface meshes and resulting DEMs are presented as Fig. 2.5. SurferManipulator was then used to calculate OPCR from converted DEMs, using previously documented methods (Evans et al., 2007). DEMs were first interpolated to include only 50 rows of data, which effectively normalizes tooth length per specimen. OPCR was then calculated using a minimum patch size of 3.

Minimum patch sizes for MorphoTester and SurferManipulator differ, and the larger minimum patch size for MorphoTester reflects the fact that triangulated polygon meshes as analyzed by MorphoTester encode more finely grained data resolution than the DEMs analyzed by SurferManipulator. While there is no exactly analogous measurement for comparison of resolution between polygon meshes and raster-based DEMs, it can be observed that most 10,000 face polygon meshes used in previous DTA studies contain over 5,000 data point XYZ vertices. Comparatively, the widest specimens in our sample approach 40 columns of XY data, and so after standardizing the number of rows to 50, the maximum number of Z-value elevation data points for a DEM would be 2,000.

Nonetheless, minimum patch size for 3D-OPCR was chosen largely arbitrarily. The DEM-OPCR protocol conforms to a common standard procedure from the literature (Evans et al., 2007; Bunn et al., 2011; Winchester et al., 2014).

After 3D-OPCR and DEM-OPCR were calculated, results were compared using SPSS v.17 (IBM). ANOVAs were run on each treatment using a species factor with *post hoc* pairwise comparison tests run using Tukey's HSD. For all analyses, $\alpha = 0.05$. F-values were compared between treatment ANOVAs as a measure of between-species variance relative to within-species variance, as were numbers of significant *post hoc* comparisons. It is predicted that ANOVAs of 3D-OPCR will exhibit higher F-values and more significant *post hoc* comparisons than ANOVAs of DEM-OPCR. Patterns of differences between 3D-OPCR and DEM-OPCR (DEM-OPCR subtracted from 3D-OPCR; termed ΔOPCR here) were also investigated. Correlations between ΔOPCR and raw 3D-OCPR or DEM-OPCR were tested. An ANOVA was also run on ΔOPCR with a species factor with Tukey's HSD *post hoc* pairwise comparison tests. It is predicted that ΔOPCR will not vary among species.

2.2.9: Simple geometric objects

The simple geometric objects sample was used to empirically document topographic variation as a result of iterative shape modification. Using MorphoTester topographic metrics DNE, RFI, and OPCR were calculated from the assemblages of meshes produced by the algorithms Delta-Length (100 meshes) and Constant-Length (50 meshes) described above. Because the number of polygons comprising Delta-Length meshes is variable and because DNE is sensitive to the number of polygons comprising a

mesh, average DNE or DNE divided by surface polygon number was also calculated and used as a fourth metric for Delta-Length meshes only. Results were then analyzed at the level of individual metrics, such that the following analyses were repeated for each metric. The intent of this experiment was to assess how topographic metrics were affected by change in cusp number or height, at least in the simplistic way that the simple 3D objects used here simulate cusp addition and cusp height increase using angled cusp-like ridges. More explicitly, mesh assemblages were tested to examine the general form of a formula *f(c,h)* where *f* represents topography and *c* and *h* represent cusp number and height respectively. This formula was assessed using a series of linear and power regressions calculated using R.

For each mesh assemblage and topographic metric, regressions were derived for 1) ten sets of data with cusp height as the independent variable and topographic metric as the dependent variable, where data sets were separated by cusp number; and 2) five or ten sets of data (for Constant-Length and Delta-Length respectively) with number of cusps as the independent variable and topographic metric as the dependent variable, with data sets separated by cusp height. The slopes of the first regression group constitute a series of partial derivatives of topographic metrics with respect to cusp height where cusp number is held constant. The slopes of the second regression group are similar, being a series of partial derivatives of topographic metrics with respect to cusp number with cusp height held constant. These partial derivatives allow for characterization of change in topography with respect to only one variable at a time, which permits better determination of the cause of any differences in topography across meshes. R^2 values from linear and power regressions were compared to determine the best formula fit for

each of the total 45 sets of data, and slopes from these regressions were determined to calculate partial derivatives. After this, second order mixed partial derivatives were considered in order to assess 1) the change in topography across the first regression group with respect to cusp number, and 2) the change in topography across the second regression group with respect to cusp height. This was done to characterize the change in topography in the context of one variable with respect to the other variable. It is predicted that OPCR will increase only as number of cusps increase, while RFI and DNE will primarily increase with increase of cusp height.

2.2.10: Mesh pre-processing parameter analyses

Analyses were performed to examine the effect of mesh pre-processing parameter choice on topographic metrics. The cercopithecoid test sample (n = 37) described above was used for these tests. Parametric variation was tested through the creation of multiple duplications of the test sample with altered pre-processing parameters. Sets of duplications were divided between analyses of parameter types so that only one parameter varied per test. Parameters tested included method of surface cropping, methods of noise reduction including smoothing and polygon simplification, and mesh rotation or orientation. All statistical analyses for parametric analyses were performed using the R statistical programming language (R Core Team, 2015).

2.2.10.1: Surface cropping

The effect of surface cropping method on topography was assessed by replicating unprocessed surface scan data three times and employing a different cropping technique

for each replication. The first of these replications was cropped to the occlusal basin and the second was cropped to the cervical margin. The third replicated set was processed using a novel technique of cropping to the inferior-most extent of infolding between the lingual aspects of the protoconid and hypoconid cusps. This point was observable on all species, though variation exists in depth of infolding and presence or absence of a small tubercle located there. Where tubercles were present, surfaces were cropped to include the lowest point of the cleft between tubercle and lingual aspects of protoconid and hypoconid cusps. This cusp-infolding cropping was used as a compromise between occlusal-basin and cervical margin methods, as the distance between the lowest point of the occlusal basin and the cervical margin is substantial in these species relative to strepsirrhines and platyrrhines previously studied by topographic analyses. It is possible that cusp-infolding cropping captures hypothetical functional molar surface adaptations that would be excluded by an occlusal basin crop. Topographic metrics DNE, RFI, and OPCR were measured on each replication using MorphoTester. ANOVAs were then performed per replication using a species factor, and F values were compared between ANOVAs to assess the degree of variation between species compared to variation within species. This analysis seeks to determine which cropping method best distinguishes molar form between these species as measured by topographic metrics.

2.2.10.2: Noise reduction

A directly comparative approach was used to test effects of decimation and smoothing surface mesh topography. One surface mesh of a *Ce. atys* M_2 (AMNH 89373 as listed in Appendix 2, original number of polygons = 332,239) and one surface mesh of

a *T. gelada* M_2 (MNHNP 1963-58 as listed in Appendix 2, original number of polygons = 267,756) were used here. Both surfaces were cropped to include only surface superior to the lowest point of the occlusal basin. From each tooth an array of possible permutations of decimation and smoothing were produced. Each permutation was created from full resolution original data. First, an Amira script (Appendix 2) was used to create an array of differently decimated surfaces for each tooth, with each mesh varying by the number of polygons used as a target for decimation. The polygon number targets for decimation included 2,500, 5,000, 7,500, 10,000, 15,000, 20,000, 30,000, 50,000, 80,000, and 120,000. At each simplification level, a second Amira script (Appendix 2) was used to create an array of smoothed meshes varying by number of smoothing iterations. Smoothing iterations included: 0 (no smoothing), 1, 2, 3, 6, 12, 25, 50, 75, 100, 125, and 150. This resulted in an assemblage of 120 meshes. MorphoTester was used to quantify DNE, RFI, and OPCR for each mesh. Topographic metrics were plotted in two sets similar to analyses of simple geometric objects above. The first set plotted topographic metrics as dependent variables and simplification level as the independent variable, with data sets split by constant smoothing level. The second set was similar with topographic metrics as dependent variables but with smoothing level as independent variable and data sets split by constant simplification level. Percent differences were also calculated between *Ce. atys* and *T. gelada* specimens at each level of decimation by smoothing, and percent differences were then plotted per topographic metrics in the same manner. This allows for consideration of change in either decimation and smoothing in the context of the other factor. Plots were visually examined and judgments were made regarding the changes in topographic shape as a result of noise reduction.

2.2.10.3: Rotation/orientation

Because of the importance of biologically meaningful alignment in topographic analyses using RFI or OPCR, the effect on topography of variation in mesh orientation was assessed. Similar to analyses of noise reduction described above, the study sample for these experiments consisted of one *Ce. atys* M_2 specimen (AMNH 89373 as listed in Appendix 2) and one *T. gelada* M_2 specimen (MNHNP 1963-58 as listed in Appendix 2). Using Amira, these meshes were aligned so that the XY-plane corresponded to an experimenter-assessed occlusal plane for each tooth. After initial alignment, surfaces were cropped to the occlusal basin, decimated to 10,000 polygonal faces, and smoothed over 100 iterations with a lambda parameter of 0.6. A python script *rotatemesh.py* was written to read PLY-format meshes, translate mesh centroids to the coordinate origin, and then rotate meshes around the origin with specified X, Y, and Z degrees of rotation. A wrapper tool *rotatemeshgroup.py* was then written to use *rotatemesh.py* to create samples of variously rotated tooth-scan meshes. For each specimen, mesh files were replicated for all possible combinations of rotation around the X and Y axes increasing by 2 degrees from 0 to 30 degrees. In total this produced 256 variably rotated surface meshes per specimen. A rotation range of 30 degrees was used because when choosing biologically meaningful and homologous alignments for surface meshes, subjective and algorithmic variation in alignments is likely to be significantly less than 30 degrees. Specimens were not moved with respect to the Z axis, which in this case is perpendicular to the occlusal plane. A specimen rotating solely with respect to the Z axis would describe surface "twisting" about the origin, and the measurement of relief should be insensitive to this

variation. Similarly measurement of complexity using OPCR should not be overly affected by this rotation. Though polygon facing will be modified by Z axis rotation, this is unlikely to cause large changes in OPCR due to this measure being an average of OPC values from 8 Z axis rotations across a 45 degree arc.

MorphoTester was used to quantify DNE, RFI, and OPCR from each of the 256 variably rotated M_2 surface meshes per specimen. Percent differences were calculated per topographic metric for each surface relative to the unaligned original mesh. Change in percent difference across the entire 16 x 16 alignment array was then visually assessed and judgments were made. Topographic change in three specific alignment cases was also plotted to better identify dynamics of rotation: 1) rotation around the X axis with no rotation around the Y axis; 2) rotation around the Y axis with no rotation around the X axis; and 3) variation resulting from simultaneous rotation around both X and Y axes.

2.3: Results

The production of anatomical shape data in the context of topographic geometry of mandibular molar teeth was investigated from multiple directions. MorphoTester, a stand-alone application for the quantification of topographic shape was developed. To increase the consistency of topographic metrics measured from a uniform triangulated mesh dataset, a novel 3D-OPCR algorithm was tested comparatively with a previous DEM-OPCR algorithm. Topographic metrics were then used to assess shape in simple geometric objects and in a sample of M_2s belonging to cercopithecoid primates. The parameters used to generate this test cercopithecoid sample were permuted and replications of the sample reflect the diversity of surface shape data resulting from

choices in surface mesh creation protocols. Topographic metrics were calculated from these permutations in order to characterize the effect of parametric choice in mesh pre-processing on topographic shape descriptors. Results from analyses are presented in the order described above.

2.3.1: 3D-OPCR

Descriptive statistics of 3D-OPCR, DEM-OPCR, and ΔOPCR by species are presented in Table 2.1, and represented as Fig. 2.6. For sample M_2s of *Ce. atys* and *T.s gelada*, 3D-OPCR and DEM-OPCR are also graphically presented (Fig. 2.7). Individual specimen data for these metrics are supplied in Table A2.2. Overall mean 3D-OPCR is higher than mean DEM-OPCR. Patterns of mean differences are similar between algorithm treatments. For both treatments, *C. mitis* and *Co. guereza* exhibit lower OPCR compared to *Ce. atys* and *T. gelada*, though for DEM-OPCR this difference is very small while for 3D-OPCR it is much larger. More variance within species can be observed in 3D-OPCR, but 3D-OPCR also evinces a clearer trend of difference between species than DEM-OPCR.

ANOVAs were performed for each treatment using species factors, and the results of ANOVAs support observable trends for 3D-OPCR (Table 2.2). These analyses indicate 3D-OPCR differs significantly between species ($p = 0.005$), but that DEM-OPCR does not ($p = 0.493$). Correspondingly, ANOVA F-values are higher for the 3D-OPCR treatment, showing that the ratio of between-species variance to within-species variance is greater for 3D-OPCR relative to DEM-OPCR. *Post hoc* pairwise comparison tests using Tukey's HSD were also performed. Due to the lack of significance for DEM-

OPCR by ANOVA, only results from 3D-OPCR will be presented (Table 2.3). *Theropithecus gelada* was found to differ significantly in 3D-OPCR from both *C. mitis* and *Co. guereza*. *Cercocebus atys* was not found to significantly differ from any other species by 3D-OPCR.

Significant positive relationships were found between ΔOPCR and both 3D-OPCR and DEM-OPCR (3D-OPCR: $m = 0.736$, $b = -35.972$, $R^2 = 0.864$, $p < 0.001$; DEM-OPCR: $m = 0.703$, $b = -19.806$, $R^2 = 0.122$; $p = 0.036$). ANOVA results indicate that ΔOPCR significantly varies by species, with *post hoc* pairwise comparison tests showing that ΔOPCR of *T. gelada* differs significantly from the three other species considered. No other species pairs differ in ΔOPCR (Tables 2.4, 2.5).

2.3.2: Simple Geometric Objects

Topographic metrics DNE, RFI, and OPCR were quantified across an assemblage of meshes in which simplified cusp-like features of variable heights were added to either a flat constant-length rectangular sheet or a flat growing rectangular sheet with increasing length. Raw DNE, RFI, and OPCR values for Constant-Length and Delta-Length meshes are presented in Table A2.3. Regression parameters are presented for Constant-Length meshes in Table 2.6 and Figure 2.8, and for Delta-Length meshes in Table 2.7 and Figure 2.9. Second-order mixed partial derivative regressions for both mesh assemblages are presented in Table 2.8 and Figure 2.10.

2.3.2.1: Constant-Length Mesh Assemblage

In Fig. 2.8, DNE and RFI are plotted 1) against cusp height with groups separated by cusp number and 2) against cusp number separated by cusp height. The goal of these analyses is to explore the form of a simplified formula $f(c,h)$ where f represents topography and c and h represent cusp number and height respectively. OPCR increments as expected – number of patches increases by two with each additional cusp and is constant with regard to height. This makes sense given that introduced cusps are essentially two flat walls joined at an angled edge (Fig. 2.2). Polygon surfaces that are horizontal (i.e., flat and parallel to the XY axis) were ignored by the 3D-OPCR algorithm. For OPCR, it seems that $f_{OPCR}(c,h) \propto c$, or more descriptively that OPCR increases with respect to cusp number regardless of cusp height.

DNE increases with both addition of new cusps and increase in height. Adding cusps of a given height causes a constant increase in DNE for the first nine cusps. The tenth added cusp contributes a smaller increase than for the previous nine cusps (Fig. 2.8.a.ii). This smaller increase in DNE is explained by the fact that adding a tenth cusp removes a terminal angle between the final cusp and the remaining flat sheet. This terminal edge is present for surfaces with one to nine cusps. For surfaces with ten cusps, the terminal border is now a boundary edge of the sheet and is ignored by the DNE algorithm. Increases in DNE per cusp are greater when cusp height is increased. This shows how DNE quantifies curvature by summing change across a surface normal map. Increasing the number of identically-angled edges around identically-sized polygons across a surface will raise DNE in a straightforward linear manner. Correspondingly, regression group 1 for DNE (DNE by number of cusps separated into height groups) is

better explained by linear regression (Table 2.6). In fact, data sets in this group excluding tenth cusps have a linear R^2 of 1, indicating a perfect linear fit for the data.

Regression group 1 is best characterized linearly, and slopes of linear regressions constitute partial derivatives representing change in DNE by cusp number (DNE_c) at stepped constant heights (Table 2.6). These slopes increase with respect to height, indicating that DNE here is the product of a multiplicative relationship between cusp number and height. The slope of a regression of DNE_c slopes on height is a second order mixed partial derivative (DNE_{ch}) representing how the change in DNE by cusp number itself changes with respect to cusp height (Table 2.8). This second order partial derivative is better represented as a power function rather than a linear function. If DNE was produced from the straightforward interaction of multiplied terms such as $f(c,h) = c*h$ then the second order derivative DNE_{ch} would be a constant. But the greater fit of a power function here indicates that DNE_{ch} includes an h term, and therefore (via integration) that DNE is produced from a more complex interaction of c and h terms. This could result from the h term being raised by a constant power, such that generally speaking $f(c,h) => c*h^n$.

A likely explanation for this arises from the nature of increasing height in the surfaces constructed here with multiple adjacent cusps. Specifically, increasing the height of cusp edges not only affects energy density at that edge (the "peak") but also at the lower edges between adjacent cusps (the "valleys"). Hence increasing height across multiple cusps does not result in a linear increase of energy but rather grows as a power law. At the same time it must be said that the actual relationship of DNE with cusp height and cusp number will be more complicated than the simplistic functions given here. This

is because DNE is a sum of energy values representing change in approximated vertex normal vectors per polygon (see above), and both cusp number and height will interact with this summation formula in various ways. But the simplistic model considered here provides a guide for understanding how DNE responds to shape change in the test case considered here. Further, the trends from this simplistic model should be applicable to other situations as well.

Trends of regression group 2, DNE by cusp height split into cusp number groups, generally support the observations from group 1 (Table 2.6). R^2 values indicate that DNE by cusp height for one cusp is better explained by a linear function compared to a power function. For cusp numbers between two and ten, though, power regressions are a better fit. Additionally, for linear regressions, R^2 values of DNE by cusp height decrease across cusp number groups, indicating that linear models fit the data less well as additional cusps are present on a surface. Inversely, R^2 values generally increase with increasing cusp number for power regressions. The R^2 value for ten cusps is less than the R^2 for nine cusps, but both are still greater than the R^2 for eight cusps. This is interpreted as a result of lessened increase in DNE from the addition of a terminal tenth cusp, as discussed above. Taken together it can be concluded that for one cusp only, DNE increases with height in a linear or nearly linear fashion. As further cusps are added, DNE increases with height as a power function, and the constant power to which DNE is raised also increases with cusp number. Partial derivatives therefore contain *h* terms and are not constants. This is again consistent with an *h^n* term. The lack of constant partial derivatives make it difficult to infer a second order partial derivative (DNE_{hc}) from regression slopes but

given that the functions considered here are continuous, DNE_{hc} should be equal to DNE_{ch} as described above.

RFI also increases with addition of cusps and increases in cusp height (Fig. 2.8, Table 2.6). For both regression groups, linear regression models uniformly fit better than power models. For regression group 2 (RFI by cusp number by height group), R^2 values equal one for all sets of data. This makes sense as the formation of additional cusps from an otherwise flat surface should increase RFI by a constant amount, as two-dimensional area remains the same regardless of cusp number while three-dimensional area is directly proportional to cusp height. Partial derivatives of regression group 1 (RFI by cusp number by height group) increase with height and partial derivatives of regression group 2 (RFI by cusp height by cusp number group) increase with cusp number (Table 2.7). This indicates that like DNE, RFI is produced as the product of *c* and *h* terms. But the multiplication of these factors to generate RFI is more straightforward than the interaction of terms observed for DNE. Unlike DNE, the fact that both regression groups are characterized by linear regressions indicates that changes in RFI by one factor with respect to the other factor occur in a directly multiplicative fashion. This can be seen in the second order mixed partial derivatives, which respectively characterize the change with respect to cusp number of how RFI varies by height (RFI_{hc}) and the change with respect to cusp height of how RFI varies by cusp number (RFI_{ch}) (Table 2.8, Fig 2.10). Whereas the mixed partial derivative of DNE (DNE_{ch}) contains an *h* term, both of the mixed partial derivatives of RFI are constants. Both RFI_{ch} and RFI_{hc} are derivable from regressions and are equal, as would be expected if the RFI formula $f(c,h) = c*h$. Stated

descriptively, RFI in this case is produced as a basic product of cusp number and cusp height.

The relative sensitivity of RFI and DNE to the combined increase in cusp height and cusp number can be examined by comparing mixed partial derivatives of these metrics. RFI_{ch} is *0.091* while DNE_{ch} is *0.654*h*. The presence of the height term in DNEch means that as cusp number and height increases, RFI will increase at a constant rate while the rate of DNE increase will grow. Borrowing analogous concepts, with increasing cusp number and height DNE will continually "accelerate," while RFI increases at a standard "velocity." Because of this, it can be said that DNE is more sensitive to combinations of cusp number and cusp height in the case of this simplistic Constant-Length surface assemblage.

2.3.2.2: Delta-Length mesh assemblage

Topographic metrics DNE, RFI, and OPCR were quantified across meshes with between one to ten variable-height cusps placed sequentially, creating a variable-length series of cusps. Topographic metrics are plotted against cusp number separated by cusp height groups (regression group 1) and against cusp height with groups separated by cusp number (regression group 2) as Fig. 2.9. The primary difference between these meshes and the Constant-Length meshes are the expanding nature of the Delta-Length surfaces.

Results from OPCR and RFI are simpler and will be described first. OPCR results are close to predictions, in that patch counts are moderately above two times the number of cusps independent of cusp height. Cusp features added to the surfaces here each consist of two flat sheets joined at angles to each other and also to surrounding cusp

features. OPCR counts patches of polygons which face similar directions in a circle on the X, Y coordinate plane, and so each cusp feature should possess exactly two OPC patches. OPCR results here show more than two patches per cusp. This can be explained by the eight mesh rotations employed by OPCR, from which OPC is measured and then averaged to produce a final OPCR patch value. The edges of these meshes are located on the X axis. Meshes are rotated 5.625 degrees eight times around the Z axis, achieving in total a 45 degree mesh rotation. When counting patches polygon face directions are sorted into one of eight aspect groups based on 45 degree arcs. The first of these aspect groups begins at 22.5 degrees from the X axis, with successive aspect groups placed at 67.5 degrees, 112.5 degrees, … , 337.5 degrees. After four mesh rotations during the calculating of OPCR, the mesh is rotated 22.5 degrees and correspondingly mesh edges are located both parallel to two of the boundaries between aspect groups and perpendicular to two other aspect group boundaries. Because the X, Y aspect of polygons comprising mesh edges are perpendicular to face-direction group boundaries, small rounding errors in the calculation of aspect direction can result in the over-counting of faces. As a demonstration of this, all patch counts at rotations other than 22.5 degrees return the predicted two patches per cusp.

Regressions of RFI by cusp number split into height groups have slopes close to zero and, in fact, RFI does not change substantially as cusp number is increased (Table 2.7). RFI does change very slightly with increase in cusp number, but this change has no observable positive or negative trend overall. The differences in RFI are likely noise resulting from small variations in the pixel-counting algorithm MorphoTester uses to quantify relief. This result makes sense because RFI is a ratio between 3D and 2D surface

area. When adding identical cusp-like features which themselves have a constant relief, it is logical that addition of further cusps does not affect the overall ratio between 3D and 2D mesh area. RFI does increase as cusp height increases, though slopes of RFI by height are nearly identical regardless of number of cusps. 3D cusp area is proportional to cusp height while increase of height has no effect on 2D surface area of cusps.

Results from DNE for Delta-Length meshes are in some ways similar to results from Constant-Length meshes, though there are also important differences. DNE again increases with both addition of cusps and increase in cusp height. Regressions of group 1 (DNE by cusp number in height groups) are fit linearly with $R^2 = 1$, indicating a perfect fit of the model for the data (Table 2.7). Slopes of these regressions are partial derivatives of DNE with respect to cusp number holding cusp height constant, and regressing these slopes provides a second order mixed partial derivative characterizing how the change in DNE by cusp number itself changes with increasing height. As in the Constant-Length meshes, this mixed partial derivative is better represented as a power function (Table 2.8), suggesting an interaction between cusp number and height in the production of DNE more complicated than a simple multiplicative relationship between these factors (see above for further explanation of this rationale). Additionally, similar to results from the Constant-Length mesh assemblages, regressions of group 2 (DNE by cusp height in cusp number groups) are better explained as power functions except when only one cusp is present (Table 2.7). Slopes of the regressions contain *h* terms and increase across cusp number groups, pointing toward an *h^n* term in a simplified *f(c,h)* formula.

Yet, despite the similarity of results for DNE with the previous mesh assemblage, there is a significant difference between mesh assemblages that has special significance

for DNE. Namely, Constant-Length meshes are constructed from a constant number of polygons across all meshes while polygon counts of Delta-Length meshes increase with cusp number. Since DNE is a sum of energy densities per polygon, meshes with more polygons will be much more likely to evince higher DNE values. This makes interpreting results of direct DNE sums from the Delta-Length assemblage difficult. Instead, it is possibly beneficial to consider the ratio of summed energy densities to the number of mesh polygons. In a sample of meshes in which polygon face numbers have been held constant, DNE/polygon values will express the same trends as standard DNE. DNE/polygon values are used here as an attempt to comparatively examine trends across meshes without standardized numbers of polygons. Results from DNE/polygon are presented in Table 2.7 and regressions are plotted in Fig. 2.9.

Immediately, several differences from standard DNE present themselves. Regressions from group 1 (DNE/polygon by cusp number in height groups) are uniformly better modeled as power functions than linear functions, while regression group 1 for standard DNE were better fit with linear models. Further, for cusp heights one and two DNE/polygon actually decreases as cusps are added. This is contrary to all previous expectations of DNE, as surface bending clearly increases in this meshes as more cusps are added. This results from a peculiar artifact which is specific to the artificial surfaces constructed here. Explaining this fully requires some elaboration on the form of Delta-Length surface meshes. The flat sheets of polygons that comprise these meshes all border at least one cusp. Some of these polygons also intersect with adjacent polygons, forming a “valley,” or are terminal sheets where the non-ridge edge forms part of the outer boundary edge of the surface. All valley and ridge bending angles are equal, and are

produced by symmetric bending of sheets around the ridge or valley. As an example, this means that a 45 degree valley would be formed through two 22.5 degree bends in surrounding sheets.

The decrease of DNE/polygon with additional cusps is caused by polygon sheets adjacent to both ridges and valleys. DNE is quantified as the change in approximated polygon vertex normal vectors (see above), where vertex normal vectors are approximated as the average of normal vectors of faces surrounding each vertex. Vertices of some internal polygons are bounded by 3 polygon faces from one side of a ridge or valley and 3 polygon faces from the other side of a valley or ridge respectively. Because the normal vectors of these faces are symmetric around the Z axis, all vertex normal vectors of these internal polygons are approximated as parallel to the Z axis. In turn there is no change in vertex normal vectors across these polygons, and so the energy density here is zero. These same polygons have positive energy densities in a terminal sheet, and this artifact does not apply to all polygons comprising internal sheets. But because there are more internal polygons than terminal polygons as more cusps are added, for low height cusps the ratio of DNE/polygon face decreases. The trend reverses as cusp height increases because higher cusps cause the remaining internal polygons with positive energy densities to overcome the deficit from zero-energy polygons. This result is unlikely to occur on surfaces outside of these specific circumstances. Evidence of that can be shown in the absence of a similar phenomenon in the Constant-Length meshes.

For cusp heights three and above, DNE/polygon increases with cusp addition. Change in DNE by cusp number is better fit with a power function model than a linear model for all cusp heights. For regression group 2 (DNE by cusp height in cusp number

groups), all sets of data are also better fit with a power model with the exception where only one cusp is present. This is consistent with results for standard DNE values from Delta-Length meshes as well as for the Constant-Length mesh assemblages. Despite the artifactual decrease of DNE/polygon with addition of cusps in a limited case, the generally better fit of power functions to the regression groups here continues to provide support for a complicated interaction between cusp height and cusp number terms for quantified surface bending.

2.3.3: Occlusal cropping

A test sample of cercopithecoid primate M_2s were variably cropped and topographic metrics were quantified from these meshes in order to assess the relative effects of cropping method on topographic shape. Meshes were cropped using occlusal basin, cervical margin, and buccal enamel infolding methods. Topographic DNE, RFI, and OPCR by species are presented in Table 2.9 and Fig. 2.11. Raw topographic metric data per specimen is presented in Appendix Table A2.4. Results will be discussed for DNE followed by RFI and OPCR.

Trends of DNE across species are broadly similar for all treatments. *T. gelada* is highest followed by *Co. guereza*, with *Ce. atys* and *C. mitis* having lower DNE. Means of *Ce. atys* and *C. mitis* are similar, though for occlusal cropping the mean of *Ce. atys* is slightly higher than the mean of *C. mitis* and the reverse is true for cervical and buccal infolding treatments. For all three treatments, DNE significantly varies between species (Table 2.10). For *post hoc* pairwise comparison tests, *T. gelada* differs significantly from *Co. guereza* and *C. mitis* for the occlusal basin and cervical methods, while for buccal

infolding *T. gelada* differs significantly only from *C. mitis* (Table 2.11). In no treatment are *Ce. atys* and *C. mitis* significantly different from each other. Comparing ratios of between-species variability to within-species variability, the occlusal basin method has the highest ANOVA F value ($F = 8.585$, $p < 0.001$), followed by cervical cropping ($F = 6.804$, $p < 0.001$) and buccal infolding ($F = 3.342$, $p = 0.031$). Cropping by occlusal basin maximizes inter-species difference in DNE relative to intra-species difference, followed by cropping to the cervical margin. Buccal enamel infolding crop is the lowest of these three. Mean DNE is also highest for molars cropped to the occlusal basin followed by molars cropped to buccal enamel infolding and then to the cervical margin. This makes sense, given that surface bending across a tooth crown should be lowest on the crown side walls, and therefore DNE should be greater when crown side walls are excluded from a mesh.

Trends of mean RFI across species are not similar between treatments (Table 2.9, Fig. 2.11). For the occlusal basin treatment, *Co. guereza* evinces the highest RFI followed by *T. gelada*, *C. mitis*, and *Ce. atys*. For the cervical method, *Co. guereza* is again highest but followed by *Ce. atys, T. gelada*, and *C. mitis*. For buccal infolding, *T. gelada* is highest followed by *Co. guereza*, *Ce. atys*, and *C. mitis*. RFI only significantly varies across species when cropped by occlusal basin (Table 2.10). The F-values for these treatments in order from highest to lowest are 8.023 (occlusal, $p < 0.001$), 2.152 (buccal infolding, not significant at $p = 0.113$), and 0.285 (cervical, not significant at $p = 0.836$). For *post hoc* pairwise comparison tests for the occlusal basin treatment, *T. gelada* and *Co. guereza* are both significantly higher in relief than *C. mitis* and *Ce. atys.* *Cercopithecus mitis* and *Ce. atys* are again not significantly different from each other,

and neither are *T. gelada* and *Co. guereza.* RFI by treatment is highest for the cervical treatment, followed by buccal infolding and occlusal basin methods. This is the opposite of the order for DNE, and again this is because surfaces that include greater amounts of tooth crown side wall will experience increases in quantified relief.

Trends of mean OPCR across species are similar for all treatments. *Theropithecus gelada* exhibits the highest OPCR followed by *Ce. atys*, with *C. mitis* and *Co. guereza* lowest and nearly equal in all cases. OPCR significantly differs across species for the occlusal basin and cervical methods but not the buccal infolding approach (Table 2.10). ANOVA for the occlusal basin treatment has the highest F value (5.237, $p = 0.005$) followed by cervical (3.304, $p = 0.033$) and buccal infolding (2.613, not significant at $p = 0.068$). Mean OPCR by treatment is highest for the occlusal basin treatment, followed by the buccal infolding and cervical approaches. This is the same trend of mean topography as seen in DNE. For the occlusal basin approach, *post hoc* pairwise comparisons demonstrate that *T. gelada* has significantly higher OPCR than *C. mitis* and *Co. guereza* (Table 2.11). For the cervical approach, *T. gelada* is only significant with *Co. guereza*. For neither treatment does the OPCR of *T. gelada* differ from *Ce. atys.*

2.3.4: Noise reduction

In order to assess the effects of noise reduction parameters on quantified topography, DNE, RFI, and OPCR were quantified from an assemblage of variably decimated (simplified) and smoothed meshes created from one M_2 of *T. gelada* and one of *Ce. atys*. Per specimen and topographic metric, data are presented as two sets: 1) topography across levels of smoothing separated into groups by simplification level, and

2) topography across levels of simplification separated into smoothing levels (Table A2.5, Fig. 2.12). Percent differences between *T. gelada* and *Ce. atys* specimens were also calculated for each decimation and smoothing level. Percent differences are similarly split in two sets (Table A2.5c, Fig. 2.12c). Prior to describing results from topographic metrics, one general statement can be made here regarding anatomical shape data produced by extreme simplification and smoothing. While sufficient simplification and smoothing will cause destructive shape change, meaning that meshes will lose any resemblance to original specimens, no destructive shape change was observed for meshes here even under the highest degrees of smoothing (150 iterations) and/or simplification (2,500 polygons). Even under these extreme conditions, meshes of both *Ce. atys* and *T. gelada* were clearly recognizable compared to original specimens (Fig. 2.13).

2.3.4.1: Topography by smoothing

For data set 1 (topography by smoothing in simplification groups), topographic metrics change across smoothing levels in generally similar ways for both specimens. For DNE, all simplification groups experience an initial substantial decrease in DNE by smoothing which approaches stability once a sufficient number of smoothing iterations has been reached. This point of stability differs according to degree of decimation, with higher polygon-number meshes achieving stability at higher numbers of smoothing iterations. 2,500 polygon meshes achieve stability as early as 12 iterations for *Ce. atys* and 25 iterations for *T. gelada*. Comparatively, meshes decimated to 120,000 faces experience smoothing-related stability in DNE only at 100 smoothing iterations for both species. 10,000 polygon face meshes, which have been used for previous dental

topographic analyses, reach stability at 25 smoothing iterations for *Ce. atys* and 50 iterations for *T. gelada*. As these examples suggest, in general it takes more iterations of smoothing to achieve stability for *T. gelada* than *Ce. atys.* This is likely related to the higher surface bending of this *T. gelada* molar surface compared to this *Ce. atys* specimen. This difference between the two specimens reflects a species-level difference in molar form where M_2s of *T. gelada* generally exhibit higher degrees of surface curvature than M_2s of *Ce. atys*.

Across simplification groups, mean DNE increases with mesh polygon count, which is not surprising given the summed nature of DNE values. Because of this, DNE values divided by polygon number were also considered in an attempt to correct for this difference. It is possible to consider percent differences between minimum and maximum DNE and DNE/polygon values for a given specimen to gauge the degree of divergence between DNE and DNE/polygon treatments across simplification. For unsmoothed meshes, DNE/polygon has smaller percent differences between minimum and maximum values than standard DNE. Percent differences for *Ce. atys* are 63.75% for DNE/polygon and 98.29% for DNE. For *T. gelada*, percent differences are 53.58% for DNE/polygon and 96.97% for DNE. For maximally smoothed meshes, DNE/polygon has similar or greater percent differences between minimum and maximum values compared to standard DNE. For meshes smoothed over 150 iterations, DNE/polygon percent differences are 85.11% and 88.21% for *Ce. atys* and *T. gelada*, while standard DNE percent differences are 86.01% and 82.33% respectively. Similar to standard DNE, DNE/polygon values show a trend of sharp decrease followed by an approach toward stability with increased smoothing. But patterns of mean DNE/polygon by simplification

group differ from standard DNE. For both specimens, after the point of DNE/polygon stability, mean DNE/polygon is higher for less smoothed specimens. Before the point of DNE/polygon stability, trends are more complicated. Meshes exposed to either very low or very high degrees of simplification seem to show the highest DNE/polygon values for unsmoothed meshes. After any amount of initial smoothing, the previously described trend of less-decimated meshes having higher DNE/polygon values predominates.

Change in RFI by iterations of smoothing shows similar trends to DNE, with sharp decrease over initial smoothing levels followed by relative stability. But unlike the stability observed for DNE, after the period of decrease, RFI values actually begin to increase with more iterations of smoothing. The degree of increase is generally small relative to the preceding decrease, though more decimated meshes (i.e., meshes with fewer polygons) show more increase in RFI during this period compared to less decimated meshes. Despite the lower degree of stability in RFI values across smoothing levels, it should be noted that across decimation groups and smoothing levels RFI varies far less than DNE does. For unsmoothed meshes, the percent difference in RFI is 10.60% and 8.11% for *Ce. atys* and *T. gelada* respectively, while for maximally smoothed meshes percent difference of RFI is 1.88% and 2.06% respectively. Even the highest of these percent differences is lower than the lowest of the percent differences of DNE by a factor of five. This means that RFI changes across simplification much less than DNE does.

Trends of OPCR are similar to those of DNE and RFI, in that for both specimens all decimation groups exhibit a period of sharp decrease through initial smoothing steps leading to stabilization of patch counts. Stability is achieved sooner in meshes with fewer polygon faces, and mean OPCR is higher for meshes with more polygon faces regardless

of level of smoothing. This makes sense given the patch counting nature of OPCR. Meshes constructed from higher numbers of polygons provide more topographic surface from which to possibly count clumped patches. In other words, while it is possible for there to be variation in the number of patches that could be counted from eight polygons given variation in relative polygon position, it is only ever possible to count one patch from one polygon. As a result OPCR is higher in meshes with more polygons and as these meshes are modified by smoothing higher polygon meshes require more iterations of smoothing to achieve stability.

2.3.4.2: Topography by simplification

As in data set 1, trends of data set 2 (topography by decimation level separated into groups by smoothing level) are broadly similar for all topographic metrics between both specimens (Table A2.5, Fig. 2.11). All metrics change substantially with decimation, and plots indicate clearly that interactions exist between decimation and smoothing levels. This means that in addition to topographic metrics varying by simplification, simplification of meshes affects topography differently depending on the level of smoothing that post-decimation meshes are exposed to.

For DNE, quantified surface bending decreases as the number of polygonal faces comprising a mesh decreases. As DNE is summed by polygon, this is expected. DNE/polygon values will be considered shortly, but the interaction between decimation and smoothing level is worth noting here. DNE changes with respect to decimation at a faster rate in meshes exposed to lower levels of smoothing. The fastest rate of change in DNE is seen in unsmoothed meshes, followed by meshes smoothed with 1 iteration, and

so on. Meshes smoothed over 150 iterations, the greatest smoothing employed here, experience the least change in DNE by decimation. This suggests that changes in DNE related to mesh simplification are largely related to "unsmoothness" of mesh vertices post-simplification, and that smoothing post-simplification lessens the effects of simplification on quantified surface bending. This makes sense, given that a change in surface polygon number without an attendant change in surface shape should not theoretically cause a change in DNE (since in this case curvature would be evenly distributed among subdivided polygons and curvature summation would remain the same). In other words, mesh simplification and smoothing both change surface mesh shape and topography –DNE in this case – reflects this. In addition, even within groups with constant smoothing levels, the rate of change in DNE decreases for meshes decimated to 20,000 or fewer polygonal faces. The most change in DNE with decimation is seen between meshes decimated to high numbers of polygons (120,000, 80,000, 50,000, etc.). Conversely, the least change in DNE is seen between meshes decimated to low polygon counts (<20,000).

Results from DNE/polygon values have some similarities to those from standard DNE values in that less smoothed meshes experience a higher rate of change, and that rate of change of DNE/polygon itself visibly changes for meshes with 20,000 or fewer polygons. These results are very different from standard DNE values, though, in that DNE/polygon actually increases with simplification for meshes smoothed over 125 or 150 iterations. Meshes with less smoothing also begin to increase at 20,000 or 30,000 polygon counts and below. For all meshes except those that were unsmoothed, this increase means that maximally decimated meshes (2,500 polygons) have DNE/polygon

values higher than minimally decimated meshes (120,000 polygons). This can be understood both as decimation changing local surface shape (i.e., geometric relationships among adjacent polygons, which is what DNE quantifies) and also as polygon number being directly related to changes in local adjacent polygon geometry. What is meant by this second point is this: if a certain amount of curvature is expressed across a mesh with a number of polygons approaching infinity, adjacent geometric changes between meshes will be minimized as surface curves are expressed with progressively higher numbers of polygons. Conversely, if a certain amount of curvature is expressed across a surface where polygon number continually decreases, curves will be expressed by progressively fewer polygons and individual polygons will experience more local geometric change across the surface. If anything, this indicates a limitation of a DNE/polygon approach for attempting to compare meshes with different numbers of polygons. Average DNE by polygon is not necessarily equivalent to standard summed DNE.

RFI also changes with simplification, and there is an interaction between simplification and smoothing levels. RFI of unsmoothed meshes decreases with decimation at a higher rate than for any smoothed meshes. Meshes smoothed 125 or 150 actually increase in relief across decimation before entering a final period of RFI decrease in highly decimated meshes. Boyer (2008) also observed a similar phenomenon. Examination of change in 3D and 2D area by decimation and smoothing reveals that highly smoothed meshes experience some amount of increase in 3D area across decimation, while less smoothed meshes tend to decrease. 2D area remains generally stable until simplification targets reach under 30,000 polygons, where very smoothed meshes begin to increase sharply and other meshes increase to a smaller degree or

decrease. This is all interpreted to reflect change in surface area with very high degrees of smoothing.

Trends of OPCR are surprisingly similar to those of DNE (Table A2.5, Fig. 2.12). OPCR decreases with simplification and less smoothed or unsmoothed meshes experience more change in complexity relative to more smoothed meshes. Also within smoothing groups, rates of change of OPCR decrease in meshes of 20,000 or fewer polygons. Across all decimation levels, meshes with the most smoothing experience the least amount of overall change in OPCR.

2.3.4.3: Percent differences between specimens

In addition to considering effects of noise reduction on topographic metrics within the specimens analyzed here, it is possible to consider changes in topographic metrics between specimens. This is useful because most analyses of anatomical shape are done in a comparative context, whether between individuals, species, or other biologically sorted groups of surfaces. Noise reduction parameters are chosen solely to account for error and variation introduced through the surface creation process, and so are distinct from parameters that indicate a desired anatomical region of study like surface cropping. Ideally, results from topographic analyses would be insensitive to changes in noise reduction parameters. Instead, results indicate that this is not the case. Following from this, it is important to know how to choose noise reduction parameters so as to reduce possible variation introduced by these parameters. If small changes in noise reduction parameters cause topographic differences between surfaces to vary widely, then topographic results are sensitive to parameters in that region. Conversely, if topographic

differences between surfaces do not vary substantially within a range of noise reduction parameters, this means that topography is relatively conservative to parametric choice for that range.

To examine this, percent differences between the two *T. gelada* and *Ce. atys* specimens for each topographic metric are presented across simplification and smoothing (Table A2.5c, Fig. 2.12c). The purpose of these analyses is to find regions of stability where percent differences are relatively stable across smoothing and decimation levels. For DNE, percent differences approach stability for meshes of 20,000 and fewer polygons. The same is true for OPCR with the strongest stability observed for meshes with around 20,000 polygons, although topography is more variable for complexity than bending. Stability decreases somewhat in OPCR in meshes with <15,000 polygons, though meshes with <15,000 polygons are still more stable in OPCR than meshes with 25,000 or more polygons. Compared to DNE and OPCR, RFI changes less across all smoothing and decimation levels. Compared to the approximate range of -30 to 40 percent difference for DNE and -30 to 30 percent difference for OPCR, across all decimation and smoothing levels RFI ranges from 16 to 18 percent difference. Within this tight range, RFI shows some degree of further stabilization for meshes between 10,000 and 50,000 polygons. This different response to percent differences of RFI compared to OPCR or DNE is interpreted as a reflection of the ratio-based nature of RFI compared to summed OPCR and DNE.

2.3.5: Mesh Orientation/Rotation

Topographic metrics were calculated from samples of meshes cropped to the lowest point on the occlusal basin and variably rotated around the X and Y-axes. For specimens of *Ce. atys* and *T. gelada*, percent differences between each rotated mesh and the original unrotated mesh were calculated, and changes in percent differences with rotation were examined for each topographic metric. Results from these analyses are presented as Table 2.12 and Figs. 2.14 and 2.15. Raw topographic metric data from these analyses are provided as Table A2.6. As expected, DNE values do not change with respect to mesh orientation (Table A2.6a). DNE is calculated from individual polygon energy densities, which quantify changes in approximated vertex normal vectors for each polygon relative to changes in vertex vectors per polygon. Mesh rotation changes the orientation of polygons and vertices in the XYZ coordinate system but does not modify polygon position relative to other polygons or polygon vertices relative to other vertexes. Correspondingly, relative change in the local normal map is not altered by a change in mesh rotation and DNE is independent to effects of orientation.

RFI changes with rotation from a manually set occlusal alignment origin for both specimens. Percent differences of RFI increase with rotation around both X and Y axes (Fig. 2.14). As 3D area of meshes is not modified by surface orientation, this indicates that projected surface 2D area decreases with rotation. For *Ce. atys,* rotating only around the Y-axis 30 degrees produces a difference of 19.4%. The matching situation of 30 degrees rotation around the X-axis produces a 20.9% difference in RFI. Rotating around both X- and Y-axes 30 degrees produces a 36.5% difference in RFI. A heatmap of percent differences demonstrates that intermediate degrees of rotation follow these trends, with degree of rotation around either X- or Y-axes contributing to an increase in

percent difference of RFI values (Fig. 2.14). Within 6 degrees of rotation around either axis, percent difference of RFI is at most 2.08%. Beyond that point, percent differences increase more rapidly. Percent differences of RFI with rotation are specifically plotted for the three distinct sets described above: rotation around the Y-axis alone, rotation around the X-axis alone, and simultaneous rotation around X- and Y-axes (Table 2.12, Fig. 2.15). Slopes of power-modeled regressions of these lines provide information about the rate of change in RFI with rotation of these axes. As might be expected, the highest slope is found for simultaneous X- and Y-axis rotation. Rotation around X- and Y-axes respectively are similar, but X-axis rotation increases percent difference of RFI at a faster rate than Y-axis rotation. I will return to explain this difference shortly, after describing results for *T. gelada.*

For the *T. gelada* specimen, rotation changes percent differences of RFI less than for *Ce. atys*. A 30 degree rotation around the X-axis by itself produces a 12.8% difference in RFI, and 30 degree rotation around the Y-axis alone produces a 7.4% difference. 30 degree rotation around X- and Y-axes together results in an 18.5% difference in RFI values. As in *Ce. atys*, plots of percent difference of RFI are presented for X-axis rotation, Y-axis rotation, and rotation around X and Y-axes simultaneously (Fig. 2.15). X- and Y-axis rotations both contribute to an increase in RFI so that rotation around both axes produces more change in RFI values than rotation of either axis alone. Rotation around the X-axis also results in a faster rate of change in RFI than the Y axis, as seen in *Ce. atys.* It is interesting that for rotation around the Y-axis alone for *T. gelada*, RFI actually decreases slightly before increasing. In other words, 2D area of surface meshes increases before decreasing steadily. No similar trend is observed for *Ce. atys*. The

reasons for this are discussed below. But the general trend of RFI increase (2D area decrease) holds for most rotations, and at 10 degrees of rotation the highest observed percent difference in RFI is under 2% (Table A2.6).

Comparing rates of RFI change between specimens, an unexpected result is that the fastest rate of change in percent differences of RFI (that of simultaneous X and Y-axis rotation) for *T. gelada* is actually lower than the slowest rate of change for *Ce. atys* (Y-axis rotation). This result and the difference in rate of change between X and Y-axes for both specimens can be explained with some mathematical modeling of mesh rotation. As previously observed, increase in RFI here reflects a decrease in 2D mesh area. The difference between *T. gelada* and *Ce. atys* can therefore be rephrased as *T. gelada* experiences less decrease in 2D mesh area (or even a slight increase in 2D area for rotation around the Y axis alone) with rotation relative to *Ce. atys*. In order to explain this, it is necessary to describe some similarities or differences in form between these specimens (Table 2.13). First, this *T. gelada* specimen has a greater overall relief as measured by RFI from an occlusal plane alignment (0.387) compared to *Ce. atys* (0.306). Second, both specimens have similar ratios of average surface height (measured as the Z-axis difference between surface vertex positions and an XY occlusally aligned plane intersecting the lowest point on the occlusal basin) and mesiodistal length (*Ce. atys* = 0.296, *T. gelada* = 0.323) or buccolingual width (*Ce. atys* = 0.234, *T. gelada* = 0.221). With these facts in mind, it is possible to construct a simplistic mathematical model to understand change in 2D area in the context of these parameters.

A simplified two-dimensional model is used here where one-dimensional width projected on the x-axis (p) of a rotated rectangle is used as a proxy for projected 2D area

in the three-dimensional case. For a two-dimensional rectangle with variable width (w) and height (h) exposed to variable rotation (θ) a function $p(w,h,\theta)$ can be constructed as

$$p(w,h,\theta) = \sqrt{w^2 + h^2}\,\cos\left(\frac{\pi}{2} - \theta - \tan^{-1}\frac{w}{h}\right)$$

where w, h, and θ all have initial values of zero and only increment positively. In order to easily observe trends from this function, I will assign width an arbitrary value of 2 to limit the equation to two variables. This is justifiable because the ratio of h/w is much more important to this model than the absolute values of w or h. Because the known h/w ratios in the M_2 specimens are equal to or less than approximately 0.3, h will be limited to $0.3w$ and is therefore bounded inclusively to [0, 0.6]. Rotation from 0 to 90 degrees is plotted from this model, bounding θ to [0, π/6] (Fig. 2.16). As 30 degrees of rotation is the range empirically investigated above, the first third of this plotted range is most noteworthy. The variable of interest here is negative change in p (analogous to projected 2D area) over θ for different values of h. For all values of h considered, p decreases from origin to 90 degrees of rotation. The rate of change of p is, however, more negative for lower h, and consequently at 90 degrees of rotation p is lower for lower h. This is exacerbated by a tendency for higher h values to first increase in p with rotation before decreasing. This can be understood by considering a spotlight that is directly overhead a floating square casting a shadow on the ground – if the square rotates, the shadow will increase in length before decreasing back to initial length, and the function of shadow length will be sinusoidal. The trend of greater decrease in p with lower h explains the

greater decrease in 2D area in the lower *Ce. atys* compared to the taller *T. gelada*. The initial increase in 2D area for *T. gelada* for Y-axis rotation is also explained by this.

It is worth saying, though, that lower specimens will not always experience greater change in RFI with rotation relative to taller specimens. This behavior with rotation is limited to specimens with an absolutely low ratio of height to length or width. This is illustrated by the floating square example above, if the floating square is replaced with a floating rectangle. For rectangles with height greater than length, relatively taller rectangles will grow shadows faster than relatively shorter rectangles. Using the p function given above, trends of p with rotation differ for rectangles with a height to width ratio that is relatively larger than those considered here (e.g. $h/w > 0.5$, though this is not the minimum bound for this behavior). For this case, the initial increase described for relatively higher h mentioned above takes precedence and p instead increases across 30 degrees of rotation. The rate of change of p with θ is here proportional to h, such that higher h results in more positive change in p. Applying this to anatomical tooth models, surfaces with relatively large height to length or width ratios – such as those produced by cervical margin cropping methods – will experience decrease in RFI (increase in 2D area) with rotation instead of the increase in RFI (decrease in 2D area) seen here. And for those surfaces with generally large height to width or length ratios, surfaces in that group that are relatively taller will experience more change in RFI from rotation than relatively shorter surfaces. This is in contrast to the M_2 surfaces observed here with generally small height to width or length ratios, in which surfaces that are relatively taller experience less change in RFI from rotation than relatively shorter surfaces.

While results from RFI require significant explanation to be understood fully, trends of RFI are consistent with power functions and so can be understood through modeling as described above. Trends of OPCR are much more irregular (Table A2.6, Fig. 2.14). While RFI mostly increases with rotation as would be expected from relief of a generally wide and low surface, OPCR increases and decreases unpredictably with rotation. The region of highest positive percent difference in OPCR differs substantially between *Ce. atys* and *T. gelada*, being 0 degrees X-axis and 4 degrees Y-axis rotation (PD = 3.3%) for *Ce. atys* and 18 degrees X-axis and 10 degrees Y-axis rotation (PD = 14.6%) for *T. gelada*. For *Ce. atys*, 30 degrees of rotation on the Y-axis produces a -14% difference while the same on the X-axis produces a -11% difference. Simultaneous 30 degree rotations of the X and Y-axes results in a -25% difference in OPCR. This is actually not the greatest negative percent difference for *Ce. atys*, which is -27% difference at 30 degrees rotation on the Y-axis and 16 degrees rotation on the X-axis. For *T. gelada*, 30 degrees of rotation on the Y-axis produces a -4.1% difference in OPCR while the same on the X-axis produces a 4.6% difference. Rotation of both X and Y-axes for *T. gelada* results in a -12.5% difference in OPCR, the greatest negative percent difference for this specimen for all rotations. Within 6 degrees of rotation differences are relatively smaller, between 5.9% to -1.1% difference in OPCR. In general, these results show that while OPCR responds unpredictably to mesh rotation, the greatest magnitude of change in OPCR is found with high degrees of mesh rotation.

2.4: Discussion

2.4.1: MorphoTester

The software presented here provides a direct and unified approach to perform topographic shape analyses on 3D anatomical specimen data. Topographical analyses of molar teeth have shown great promise for providing new ways to quantify complex aspects of surface shape. This is especially likely to be true in contexts where functional adaptations may be more strongly linked to overall "emergent" geometry than to the arrays of discrete features comprising that geometry (see below). Tooth form may represent a good example of this (Salazar-Ciudad and Marín-Riera, 2013), but it is unlikely to be the only suitable subject. If multiple distinct morphological configurations can be adapted to address functional challenges, then holistic homology-free shape descriptors are likely to be an effective quantitative tool for better understanding anatomical form-function relationships more broadly. MorphoTester is an open source freeware application implementing complementary topographic analyses measured from a standard data format. As a result, this software provides a more comprehensive and direct method for applying topography to questions of morphology.

Included methods for quantifying surface bending (DNE) and relief (RFI) replicate previous implementations of these metrics. This tool allows the capture of quantitative descriptors of shape that are comparable to previous studies in a more automated and less time-intensive manner than previously possible. Using MorphoTester, DNE can also be quantified from surfaces with finer resolution (more polygon faces) than is possible for the Teether Matlab tool used by Bunn et al. (2011). In the case of surface complexity (OPCR), MorphoTester provides a new implementation for measuring complexity from triangulated polygon surface data instead of DEMs. This 3D-OPCR approach may have advantages over previous DEM-OPCR methods due to measuring

complexity from higher-resolution data compared to a common previously-used DEM data resolution (though the DEM-OPCR method is not limited by resolution), and results here suggest this method may be more capable of distinguishing certain kinds of surfaces than previous approaches (see below).

MorphoTester in a more general sense serves as a modifiable application framework for visualizing 3D triangulated polygon surface data and performing quantitative analyses on surface mesh data. The source code and topographic algorithms included in this software and all dependent third-party packages are compliant with open source licenses that allow use and modification by third parties. Compared to some previous methods that rely on expensive proprietary software, this application is a complete open source solution for topographic analysis. MorphoTester and its components can also be continually developed to take advantage of future topographic methods and shape measurement algorithms. Visualization of 3D data can be modified to provide better graphical illustrations of relevant surface shape characteristics and quantified topography. As a high level programming language, Python is straightforward to understand and to work with. The flexibility of Python allows this code to be interpreted or compiled, providing respectively direct access to code objects and functions as well as broad and immediate access by a wide range of users. This adaptability means that the software provided here can grow to incorporate future advances in the study of topographic shape, and that its code could be modified for other scientific tools as appropriate.

As affordability and accessibility of scanning technologies increase over time, morphologists are beginning to have access to progressively larger datasets of highly

accurate 3D surfaces representing anatomical elements. To make sense of progressively expanding assemblages of 3D morphological data and to most efficiently derive scientific insights from these data, it will be necessary to have high-throughput analytical tools designed to work with large datasets to extract as much information as possible. These techniques are currently being developed, but in some cases their wider application is hampered by high labor and financial costs associated with proprietary software and a diversity of methodological pathways from data to results. The free open source software presented here allows more automated and comprehensive application of morphological analytic methods. It has been designed to capture detailed descriptive quantification of complementary aspects of shape from complicated anatomical surfaces and to do so across large datasets including diverse morphological variation. In this context, this application is an evolutionary step toward tools for deeper and broader considerations of morphological phenotypic variation.

2.4.2: 3D-OPCR

Results from this study suggest that complexity as measured by the OPCR metric performed on triangulated polygon surface meshes (3D-OPCR) is at least as effective at partitioning differences in molar complexity as an OPCR metric performed on DEM data. 3D-OPCR is capable of distinguishing between the species considered here, while DEM-OPCR is not. The lack of statistical significance of DEM-OPCR in this case is interesting, given that DEM-OPCR has been shown to distinguish mammalian taxa with differing diets in other primate radiations including strepsirrhines and platyrrhines, as well as in carnivorans, rodents, and chiropterans (Evans et al., 2007; Bunn et al., 2011;

Santana et al., 2011; Winchester et al., 2014). It is probable that the statistical significance by 3D-OPCR and lack thereof by DEM-OPCR is related to a difference in how *Theropithecus gelada* M_2 complexity was characterized relative to other species. For 3D-OPCR, *T. gelada* M_2s were significantly more complex than M_2s of *Cercopithecus mitis* or *Colobus guereza*, while DEM-OPCR was not found to significantly vary between species. Also while *T. gelada* was not found to significantly differ from *Cercocebus atys* in 3D-OPCR, mean 3D-OPCR does differ more between these species (10.64) than DEM-OPCR (-0.9). These results can be explained in several ways.

First, differences between treatments may reflect factors extrinsic to the molar specimens considered here. For relatively fine-resolution triangular polygon mesh data, the approach used here to convert polygonal meshes to DEM format may entail a loss of information which in this case reduces variation in complexity as quantified by DEM-OPCR. It is true that in converting data from a triangulated polygonal mesh to a DEM, some surface polygons are discarded. Probably more important is the fact that the DEM data was simplified to a much coarser resolution, having approximately one-fifth the number of surface data points compared to 3D-OPCR (see above and Fig. 3). A reduction in variation of quantified complexity for the more simplified DEMs is supported by the relatively lower variance within and between species observed for DEM-OPCR. It must be noted that this high degree of DEM simplification is not necessary for calculating DEM-OPCR, and it is certainly possible to measure OPCR from DEMs with finer resolution. In fact, a recent analysis of dental complexity in fossil horses has shown that clearer evolutionary trends are apparent with increasingly fine DEM resolution (Evans and Janis, 2014). At the same time a number of analyses of complexity of individual

molars have employed the level of simplification used here (Evans et al., 2007; Bunn et al., 2011; Godfrey et al., 2012; Ledogar et al., 2013; Evans and Janis, 2014; Winchester et al., 2014), and so these results are relevant to a common method of applying DEM-OPCR.

It is also possible that differences between treatments reflect factors intrinsic to the molar morphology of the species considered here. Namely, it is possible that magnitudes of differences between 3D-OPCR and DEM-OPCR are correlated with molar complexity or other shape aspects. This could explain significant differences between *T. gelada* and *Cercopithecus mitis* or *Colobus guereza* for 3D-OPCR where no similar differences were found for DEM-OPCR. Molars of *T. gelada* exhibit a morphology marked by complicated enamel infolding and rapid changes of slope compared to other species considered here, though this degree of enamel infolding is not as complicated as that of other species previously considered by DEM-OPCR (e.g., Evans and Janis, 2014). But for the species considered here to compare 3D-OPCR and DEM-OPCR, it is possible that loss of surface information and greater degrees of simplification associated with the DEM-OPCR approach used here affect quantified complexity for *T. gelada* to a greater degree than for other species. This is supported by the finding that differences between 3D-OPCR and DEM-OPCR are significantly greater in specimens with higher 3D-OPCR or DEM-OPCR values, and that *T. gelada* shows a greater difference between treatments than any other species considered here.

If this does explain differences in patterns between 3D-OPCR and DEM-OPCR, observations here may be related to a recent finding that relief index values of molars of high-relief insectivorous strepsirrhines were more varied after being oriented to a

common orientation by an automatic algorithm relative to lower-relief molars of other species (Boyer et al., 2015b). That is, surfaces with high crowns or otherwise significant vertical extent (i.e., having great change in the Z axis) may be more sensitive to modifications of surface data related to the Z axis. Removing stacked elevation data in the Z axis is more likely to affect surfaces with more complex vertical area, and equal modifications of occlusal plane orientation in high and low crowned teeth may affect relief more in high-crowned teeth. Taken together, these results suggests that topographic analysis is a powerful tool to quantitatively describe anatomical shape; at the same time, however, serious consideration of methodology is necessary to characterize results. Choice of pathway from specimen to quantified data is likely to affect observations in ways that are non-trivial and sometimes difficult to predict.

2.4.3: Simple geometric objects

Complexity (OPCR) has been described as reflecting numbers of tooth surface tools, while relief (RFI) and bending (DNE) have been described as reflecting tooth surface tool shape (Evans et al., 2007; Bunn et al., 2011; Godfrey et al., 2012; Ledogar et al., 2013; Winchester et al., 2014). The accuracy of this model was examined with a sample of progressively modified simple geometric meshes. These meshes simulate the addition of simplistic variably tall cusp-like ridges. OPCR results from this sample reinforce the idea that complexity is a measure of the number of surface mesh features. The introduction of OPCR by Evans et al. (2007) explicitly links the OPCR algorithm to a number of tools model of shape quantification. In fact, in introducing the OPCR method, Evans et al. (2007) give more consideration to modeling tooth form than any of

the studies introducing the other metrics considered here (RFI: Ungar and M'Kirera, 2003; Boyer, 2008; DNE: Bunn et al., 2011). It is perhaps unsurprising then that complexity closely follows expectations.

Results from surface bending and relief are more complicated in that number and shape of surface mesh features can together influence both RFI and DNE. Specifically, bending and relief increase as the result of multiplicative interactive relationships between cusp number and cusp height in certain simulations. This partially undermines the prediction that relief and surface bending will primarily reflect surface feature shape. It is also partially inconsistent with the model of topographic results and tooth form initially developed by Bunn et al. (2011) and subsequently used and furthered by other analyses (Godfrey et al., 2012; Ledogar et al., 2013; Winchester et al., 2014). At the same time it is true that relative to complexity as a measure of feature number alone, bending and relief more reflect surface feature shape even if they are also affected by feature number in this simplistic model. Beyond this, RFI and DNE reflect surface feature number in a different manner from OPCR. This can be seen in low correlations previously observed between these metrics (DNE and OPCR, $R^2 = 0.103$; RFI and OPCR, $R^2 = 0.118$), the lowest correlations observed out of any of the topographic or shearing crest-related variable pairs tested by Bunn et al. (2011). It should also be said that in the case of actual tooth morphologies, complexity can also reflect surface feature shape – a pinched crest will exhibit less complexity than a hemispherical cusp, for example.

While surface relief and bending are both produced from an interaction of feature number and shape factors, there are significant differences in how these factors produce

them. DNE is more sensitive to the interaction of these factors than RFI. Multiple cusps increasing in height (or the progressive addition of relatively tall cusps) causes surface bending to increase at a much greater rate than relief. This is because surface relief increases linearly with the addition of cusps or increase in cusp height, while surface bending increases linearly with cusp height for one cusp and exponentially for more than one cusp. For the simple models used here, this is due to addition of surface features or increases of feature height producing changes in cusp "tip" angles and also in the angles of valleys between adjacent cusps, and all of these changes in angle contributing to increase in DNE. The addition of a new cusp creates either an intercuspal valley with positive energy where previously energy was zero, or a more sharply bent intercuspal valley from a more bluntly bent angle between cusp and flat surface. Increasing cusp height sharpens bending angles at these intercuspal valleys and interfaces between a cusp and flat surface. Resulting from this, adding a cusp increases energy density at multiple points of bending. Raising the height of a particular cusp increases energy values at both the cusp tip and the valleys adjacent to that cusp. When multiple cusp heights are raised, cusp tip energy increases as a product of single cusp height. But energy values of intercuspal valleys are influenced by the two cusps adjacent to the valley, and so these energy values increase as a product of two cusp heights. In summation, while relief and surface bending both increase due to a combination of surface feature number and shape factors, bending is much more sensitive to interactions between these factors. It can be concluded that surfaces that emphasize many steep or sharp surface features will likely cause greater increases in a measure of bending than a measure of relief. Additionally, it should be recognized that it is not increase in cusp height per se that increases quantified

bending in these surfaces. Rather, increases in cusp height in these simulations create sharper angles at cusp-like ridge "tip" edges and intercuspal valleys, and DNE increases as a result of these sharper angles. Relief meanwhile does increase as a result of cusp height, with taller cusps having increased surface area with no change to 2D projected area.

These distinction between RFI and DNE highlights significant differences between these metrics, despite their high correlations in some instances (e.g. prosimian primates, $R^2 = 0.736$ [Bunn et al., 2011]). DNE can be described as a relatively "local" measure of surface shape while RFI is better described as relatively "global." DNE sums energy values across individual surface polygons to measure degrees of bending around each polygon comprising a mesh. Each per-polygon energy value is a quantification of bending around a local domain defined by the target polygon and each polygon adjacent to it (i.e., sharing a vertex with it). Energy values across a mesh form a surface-wide aggregation of local domain bending per polygon. As a sum of these energy densities, DNE provides a globalized or whole-surface characterization of local bending. If a surface mesh is modified to increase overall bending, quantification of overall bending is accomplished by a summing individualized local increases in bending across a surface. Comparatively, surface relief is a ratio between 3D surface area and 2D surface area projected on the XY plane. Surface areas are themselves summations of areas of surface polygons, and so RFI is a relative index of two globalized or whole-surface properties. Relief more directly reflects overall surface shape compared to bending's summary of local surface shape change across a surface.

This difference between relief and bending has consequences. To start, it should be noted that OPCR as a complexity metric is a local surface shape descriptor like DNE. Complexity is quantified as a sum of patches across a mesh that have different orientations. These patches are examples of local surface domains as breaks between patches relate to change in local polygon position. The total number of patches across a surface is similar to DNE in that it is a globalized summary of local shape domains. Even at a more basic level, DNE and OPCR share similarities in being summations compared to RFI being a ratio measure. Complexity and bending as summations are more sensitive to surface mesh polygon number than relief as a global property. Compared to RFI, both DNE and OPCR increase with mesh polygon number and increase at a faster rate as mesh polygon number changes (see section 2.3.4 above). RFI is relatively insensitive to mesh polygon number. In fact, it is reasonable to expect that mesh simplification with minimal or no change in surface shape as a result of simplification would result in minimal or no differences in quantified surface relief.

Differences between global and local topographic metrics also suggest that it might be possible to derive a global measure of surface bending or complexity that would be less sensitive to factors such as mesh polygon number. Analyses presented throughout this chapter have attempted to create such a global measure of surface curvature by testing average surface bending per polygon (DNE/polygon). Due to certain artifacts relating to perfectly symmetrical surface edges, DNE/polygon was not the most effective metric when applied to simple geometric objects. Results from DNE/polygon of simple geometric objects do still reinforce the conclusion that surface bending is produced from a complex interaction between surface feature number and shape factors. The advantages

and weaknesses of DNE/polygon as a bending metric are discussed further in section 2.4.4.2 below.

Aside from distinctions between global and local shape metrics, the sensitivity of RFI and DNE to a combination of feature number and shape factors may explain the high degree of accuracy shown by these metrics for predicting diet in samples of extant prosimians and platyrrhines (Bunn et al., 2011; Winchester et al., 2014). It is interesting that while both metrics showed relatively high accuracy in diet prediction for both groups in isolation, only DNE was effective in predicting dietary food preferences when both groups were considered together (Winchester et al., 2014). This may be related to DNE's relatively higher sensitivity to interactions between feature number and shape factors. It is possible that, in general, DNE may be more effective than RFI at predicting functional differences between samples of teeth where sample specimens exhibit more variability in morphological configuration compared to samples of teeth with more generally similar morphology. Samples with high morphological variability could be expected to evince significant interrelated variation in both the number and shape of surface features of molar crowns, and it may be the case that DNE more strongly reflects these differences. Comparatively, RFI may be more effective at characterizing shape in samples of molar teeth with more similarity in overall morphological configuration, especially if differences between teeth with similar configurations are largely expressed in terms of height and steepness of cusps with little change to feature shape aside from steepness or feature number. This could be seen as an explanation for RFI being a slightly better predictor of dietary category in a sample of eight platyrrhine genera, and DNE being a slightly better predictor in a diverse sample of prosimian molars. The cercopithecoid

sample considered in the next chapter of this dissertation exhibits an overall similar bilophodont molar configuration, and correspondingly RFI explains more M_2 shape variance than DNE (see Ch. 3).

OPCR being a measure of feature number may also be related to the relatively lower effectiveness of complexity for predicting diet in samples of extant prosimians, platyrrhines, or cercopithecoids (Bunn et al., 2011; Winchester et al., 2014, Ch. 3) because of overall morphological similarity within these samples. At the same time, complexity has been effective in distinguishing a broader and more trophic-level set of dietary categories in a sample of rodents and carnivorans with much broader taxonomic diversity (Evans et al., 2007), though this analysis was performed on tooth rows instead of individual teeth as in the analyses above. This may suggest that complexity reflects a relatively high level or gross scale measurement of tooth configuration compared to quantifying relief or bending. A gross scale measurement could be expected to be well suited for characterizing extremely diverse tooth forms, such as those across mammalian orders. At the same time, a metric like that might be less effective for distinguishing differences between teeth with similar morphologies. This dovetails with the observations above for surface bending and relief, and suggests that it is worthwhile to consider scales of difference between morphologies in addition to specific shape differences.

2.4.4: Analyses of pre-processing parameters

2.4.4.1: Mesh cropping

Meshes were cropped to three different levels including the occlusal basin, cervical margin, and point of infolding of buccal enamel between occlusal and cervical

margins, and effects of cropping methods on topographic variables were assessed. The buccal enamel infolding method was attempted as a compromise between occlusal-basin and cervical-margin cropping, to capture possible shape differences below the occlusal basin while still being easily replicable and hypothetically similar between species. Results suggest that topographic variables measured from occlusal-basin cropped meshes detect more variance between cercopithecoid species here than either the cervical margin or buccal infolding cropping procedures. Between the cervical margin and buccal infolding methods, cervical margin cropping tended to characterize more variation. Results from buccal infolding cropping reflect the least variance of all three treatments, and trends between species relating to buccal enamel infolding cropping often differ from other treatments. It is inferred from this that the landmark used for this cropping approach, the lowest point of buccal enamel infolding on the molar crown, is substantially variable between the four species considered here and is not informative for the purposes of standardized mesh cropping. It can be concluded that this is not an effective method for cropping surface meshes.

Given the relatively high variability captured by topographic variables from occlusal basin cropping, most of the topographic differences between these species in molar crown morphology seem to exist above the lowest point of the occlusal basin. This is perhaps not surprising given the common bilophodont molar configuration across cercopithecoids. Different cropping methods highlight specific surface regions and therefore highlight specific molar shape domains. For example, cervical margin cropping highlights degrees of whole-tooth hypsodonty more than occlusal basin cropping. It is interesting that surface relief does not differ significantly between species for cervical

margin cropping. If theoretically teeth of all species here were the same size and the height from cervical margin to central occlusal basin were identical, it would be reasonable to expect that relief of cervical-margin cropped teeth would have similar trends to occlusal-basin cropping but perhaps with lower magnitudes of difference. Instead, trends differ for cervical margin relief. This suggests that differences in hypsodonty between species play a role in changing trends across cropping methods. At the same time, if this sort of hypsodonty were functionally related, one might expect *T. gelada* to exhibit high relief from cervical margin cropping. *Theropithecus gelada* has relatively lower relief, though folivorous *Co. guereza* has the highest relief by cervical margin cropping.

Surface bending and complexity are both relatively robust to cervical margin and occlusal basin cropping approaches. DNE and OPCR differ significantly for both treatments and have similar trends of differences. Meanwhile, RFI is significantly different for occlusal basin cropping but not for cervical margin cropping, and trends between species vary between treatments. This comparison of RFI between occlusal basin and cervical margin cropping represents the first comparative test between the two most prominent cropping methods in the literature, and the differences between the two approaches are surprising. It is at least possible to say that there is likely not a single surface cropping technique that is appropriate for all molar crown samples for analyses of molar form-function relationships, much less for all research questions. Differences in molar configuration across samples, including where primary differences in molar form are located on the crown, will likely bias samples to being more effectively cropped using one technique or another.

Yet, while molar morphology will likely mean that certain cropping techniques will capture greater variation for a given sample, comparability of samples must also be considered. Studies of dental topography in closely related species have been able to use occlusal basin cropping techniques because of the certainty of homology for occlusal basins given the restricted phylogenetic distance of study species (M'Kirera and Ungar, 2003; Ungar and M'Kirera, 2003; Ungar and Bunn, 2008; Bunn and Ungar, 2009; Klukkert et al., 2012a, b). A study of a diverse sample of strepsirrhines and tarsiers used cervical margin cropping because of a lack of certainty regarding homology or uniformity in occlusal basins for the species considered (Boyer, 2008). Some subsequent dental topographic analyses have been designed for comparability with this prosimian sample, and so have also used cervical margin cropping (Bunn et al., 2011; Godfrey et al., 2012; Ledogar et al., 2013; Winchester et al., 2014). It may be the case that cervical margin cropping is more appropriate for taxonomically very broad samples that are intended to be compared with other large samples. In any case, choice of cropping parameter sharply constrains the comparability of topographic results. Making a choice of cropping technique requires balancing opposing factors such as sample-specific variability or inter-sample comparability. The cercopithecoids considered in this dissertation express a generally similar bilophodont molar configuration, where differences between species are primarily located above a central occlusal basin. As a result, occlusal basin cropping captures the most shape variability between these species. As the primary interest of these analyses is to better understand molar form-function relationships in extant cercopithecoids and to create a comparative dataset for future analyses of extinct

cercopithecoid paleoecology, this cropping technique is justified despite lessened comparability with other previously published dental topographic samples.

It is generally recommended that future dental topographic analyses should explicitly consider the balance of sample-specific and comparative factors discussed here. But applying this approach may cause some to wonder about the possibility of circular reasoning – that it is necessary to visually examine specimens to subjectively gauge differences before instituting a cropping paradigm that will most strongly reflect the differences observed. Instead it should be remembered that an ideal level of tooth cropping is not in itself a biological property. Due to technological and methodological limitations, it is necessary to study digital representations that are abstractions of anatomical specimens from reality. Choice of parameters for mesh pre-processing represents an example of constructing a pathway of abstraction for deriving quantitative data from complex 3D skeletal elements. In this sense, choosing a cropping approach is similar to making decisions regarding appropriate sample sizes and must be done while being cognizant of both the nature of the study specimens and the sorts of research questions being asked in a given study.

2.4.4.2: Noise reduction

As expected, noise reduction techniques including simplification and smoothing have a substantial and consistent effect on dental topography. More than this, the presence of both simplification and smoothing affects quantified topography in a complicated manner rather than producing straightforward additive effect. In other words, levels of simplification affect how topographic metrics change across smoothing and vice

versa. Nonetheless, it is possible to make some general observations for surface mesh noise reduction. First, it is clear that significant amounts of noise reduction cause substantial changes in mesh surface shape. Fortunately, destructive shape change has not been observed in these analyses, even at extreme levels of simplification (reduction to 2,500 polygons) and smoothing (150 iterations). The most simplified and smoothed meshes of this sample are still immediately recognizable as the original teeth (Fig. 2.13). Further observations will be discussed for smoothing and then for simplification.

Surface bending and complexity both decrease with progressive smoothing, which makes sense given that mesh smoothing reduces local vertex shape variation. Surface relief also decreases with smoothing, though with successive smoothing some amount of relief increase occurs in more simplified meshes. All topographic metrics change the most from an unsmoothed state to 50 iterations of smoothing. After this point, all metrics enter a state of relative stability where metric change with smoothing is less significant. A number of previous studies of dental topography using polygon surface meshes have used 100 iterations of smoothing in Amira or Avizo applications as standard (Boyer, 2008; Bunn et al., 2011; Ledogar et al., 2013; Winchester et al., 2014). Analyses here indicate that 100 iterations of smoothing is well inside the region of stability observed here. This degree of smoothing is likely a good standard for future analyses assuming specimens broadly similar to those from previous analyses.

In the two specimens considered here, surface relief is much less affected than bending or complexity by changes in mesh polygon number and smoothness. RFI seems relatively insensitive to levels of simplification and smoothing, and so results of surface relief are likely to be robust regardless of mesh noise reduction techniques. This is in line

with suggestions made regarding RFI in section 2.4.3 above. This observation also has promising implications for comparing studies of relief from polygon surface meshes (e.g. Boyer, 2008; Chapter 3) to studies of relief from raster-based DEM formats (e.g. Ungar and M'Kirera, 2003; Bunn and Ungar, 2009). It does mean, though, that relatively more care must be taken regarding mesh pre-processing when interpreting results from surface bending or complexity. This has implications for differences observed between 3D-OPCR and DEM-OPCR algorithms. Although it is difficult to directly compare data resolutions in surface meshes and DEMs, the DEM data contain fewer points relative to the surface meshes analyzed and results here (and elsewhere, see also Evans and Janis [2014]) suggest numbers of data points comprising surfaces play a large role in influencing OPCR variation.

Comparing the *Ce. atys* and *T. gelada* specimens considered here, surface DNE and OPCR require more iterations of smoothing to achieve stability in *T. gelada* than in *Ce. atys*. The same is not true for RFI. *Theropithecus gelada* also has higher surface curvature and complexity than *Ce. atys*. It may be the case that surfaces with higher local shape change will take longer to achieve stability through smoothing procedures compared to surfaces with lower local shape change. As a demonstration of this, consider two spherical surface meshes where vertex positions have shifted at random distances tangential to the spherical surface. If the vertices of one sphere are perturbed to a greater degree, then that sphere should exhibit higher overall local surface curvature and complexity compared to the sphere with less local shape change. The more perturbed sphere should also require more smoothing to achieve a perfectly spherical form, as well.

Mean surface bending and complexity across smoothing levels is correlated with the number of polygons that form surface meshes. In other words, surfaces with more polygon faces tend to have higher DNE and OPCR, and successive levels of decimation decrease these metrics. Average RFI also decreases with progressive decimation, but the range of change in RFI is very small compared to DNE or OPCR. Again this points to surface relief being relatively robust to mesh noise reduction. This also highlights the difference between the local natures of DNE and OPCR as metrics compared to the global nature of RFI (see above).

Analyses of surface simplification and smoothing attempted to derive a more global measure of surface bending by assessing average DNE per polygon in addition to standard DNE. Average DNE per polygon varies less by simplification level than standard DNE, and experiences smoothing stability in a similar way to standard DNE. It is interesting to note, however, that mean DNE/polygon is actually smaller in surface meshes with more polygon faces. This is the opposite of the trend from standard DNE. The reason for this is that on a surface with a given degree of curvature, increasing the number of polygons comprising the surface effectively decreases the proportion of that curvature expressed by any given triangle. Representing a smoothly curving surface with sufficiently many triangles allows individual triangles to be nearly parallel with each other, while doing the same with very few triangles requires more sharp angling between adjacent triangles. While DNE/polygon is less sensitive to mesh polygon number than standard DNE, it still changes non-trivially with mesh simplification. Because of this, DNE/polygon is probably not an effective substitute for standard DNE for comparing surface meshes with widely different numbers of polygons. It could however be used as a

metric to compare samples of meshes with a small range of possible polygon counts, because in this case, triangles can be assumed to express similar degrees of curvature. For such meshes, DNE/polygon would primarily correct for small differences in standard DNE resulting from mesh polygon number. At the same time, in such a sample results from DNE/polygon should be broadly similar to standard DNE due to the small range of mesh polygon counts.

In addition to making descriptive observations of the effects of mesh simplification on topography, it is possible to make suggestions for future analyses that incorporate simplification as a pre-processing step. Results from percent differences of topographic metrics between *Ce. atys* and *T. gelada* specimens can be used to inform these suggestions. None of the topographic metrics considered here is completely insensitive to simplification. Despite this, it is possible to gauge ranges of simplified mesh polygon numbers where there is relatively smaller change in percent difference of topographic metrics. Within these ranges of simplification, topographic metrics will produce more similar results than would be the case for meshes outside of this range. As a result, topographic comparisons will be more stable between studies if these studies have simplified meshes within this overall range. In general, percent differences for both DNE and OPCR are relatively stable for surfaces with 2,500 – 30,000 polygons. Compared to DNE and OPCR, percent differences for RFI are much more stable at all levels of decimation. Within RFI, percent differences are highly stable for meshes of 2,500 – 50,000 polygons. This fits with the pattern of other results from this chapter suggesting that RFI is relatively insensitive to mesh pre-processing compared to DNE or OPCR. But these results suggest that it is optimal to simplify specimens to some degree

prior to calculating RFI. For all three metrics, simplification to 10,000 polygons is located well within regions of stability for percent differences. Because of this, meshes in Chapters 3 and 4 will be simplified to 10,000 polygons prior to shape measurement for all analyses.

2.4.4.3: Mesh rotation/orientation

For the *Ce. atys* and *T. gelada* specimens considered here, quantified surface relief and complexity respond differently to variable mesh rotation around the X- and Y-axes. Rotation around the Z-axis rotation was not considered here, as it would not substantially change either RFI or OPCR results. With the exception of an initial slight decrease in relief for rotation around the Y-axis alone for the *T. gelada* specimen, RFI increases with mesh rotation for both specimens around both axes. This indicates that mesh rotation generally decreases 2D projected area in connection with the overall low average relief of these specimens. Measured surface complexity changes more unpredictably, experiencing both increases and decreases across mesh rotation. Unlike RFI, where occlusal alignment seems to mostly approximate a local maximum of projected 2D area, occlusal alignment seems to be neither a local minimum nor maximum for OPCR. There is little reason to expect occlusal alignment to be a local extreme for OPCR, but this means that alignment across a mesh sample may introduce random variation in complexity where this might not be the case for relief. For both metrics, magnitude of variation changes with greater rotation. Corresponding to this, relief experiences very minor change up to 10 degrees of rotation. OPCR is more sensitive to alignment but relatively less variation is seen up to 6 degrees of rotation. As in analyses

discussed above, RFI seems to be relatively robust against mesh pre-processing. It is reasonable to believe that variation introduced through alignment, whether manual or algorithmic (*auto3dgm*; Boyer et al., 2015a), is likely to produce error rates of <10%. Also, error rates are likely to be lower for algorithmic alignment compared to manual procedures (Boyer et al., 2015b). Because of this, differences in quantified topography due to mesh rotation are likely to be minimal.

Despite this, it is worth considering further the differences between *Ce. atys* and *T. gelada* specimens in RFI across alignment, because they have implications regarding possible systematic error in mesh alignment procedures related to phylogenetic or functional factors. Results from these specimens and simplistic mathematical modeling suggest that for specimens with absolutely low average relief, RFI will increase faster with change in alignment for specimens with relatively low relief compared to specimens with relatively high relief. For specimens with relatively high relief, RFI may decrease before increasing. But for specimens with absolutely high relief, RFI should decrease with rotation and relatively taller specimens will decrease at a faster rate than relatively short specimens. Absolute relief here indicates differences between overall tooth mesh height across species, such as a difference between cercopithecoid M_2s cropped to the cervical margin (high absolute relief) or the occlusal basin (low absolute relief). Differences in absolute relief are likely to occur between samples of teeth. Relative relief indicates differences between species with a sample, such as *T. gelada* evincing more relief than *Ce. atys*. What all this means is that for equivalent amounts of alignment, specimens with different degrees of relief will experience different degrees of change in quantified relief. In other words, changes of alignment may introduce systematic error in

quantified relief based on relative relief between specimens. This may explain a recent observation from a comparative study of relief of manually and algorithmically aligned M_2s belonging to strepsirrhines primates (Boyer et al., 2015b). Boyer et al. (2015b) compared RFI between alignment procedures for prosimian primates with similar diets, and found that insectivorous taxa show different relief between manual and algorithmic alignment treatments where no similar difference was found for other dietary categories. Insectivorous taxa also exhibit the most relief compared to other dietary groups in their sample. If the *auto3dgm* automatic alignment algorithm used in that study performed similar degrees of alignment in each specimen, the greater difference for the insectivorous taxa between alignment treatments could be explained by systematic error introduced through alignment affecting species with the steepest molar cusps and crests.

2.5: Conclusions

This chapter has discussed the production of anatomical shape data from 3D scans of molar specimens and the quantitative description of whole surface form by morphological topographic analysis. A software application for performing morphological topographic analysis and a method for quantifying complexity from 3D triangulated polygon meshes have been introduced. The performance of topographic metrics has been gauged on simple geometric objects to better understand quantitative shape description measures. Mesh pre-processing steps including cropping, noise reduction, and orientation have been examined to describe their effects on both anatomical shape data and quantified topographic shape. Conclusions will be discussed first for topographic tools and then for mesh pre-processing parameters.

MorphoTester is an open source, stand-alone application for measuring topography from surface meshes using the methods DNE (bending), RFI (relief), and OPCR (complexity). This software represents a step toward more comprehensive and automated tools for quantitative phenotypic analysis. DNE, RFI, and OPCR quantitatively describe surface shape properties, and their descriptions of shape can be understood using at least two frameworks or models. One model has been used previously in the literature, and describes OPCR as a measure of the number of features on a tooth surface while DNE and RFI quantify the shape of features on a tooth surface. Observations here indicate DNE and RFI reflect both number and shape of tooth surface features, with DNE being more sensitive to interactions between these factors. Based on these observations, it is perhaps more accurate to rephrase this framework as: OPCR reflects number of surface features, RFI most strongly reflects feature shape, and DNE most strongly reflects combinations of these factors. Results from this chapter have also indicated a second framework that is somewhat orthogonal to the first. DNE and OPCR both summarize whole surface shape properties as a summation of local changes in surface shape. In contrast, RFI characterizes global surface relief as a ratio between globalized surface shape properties. This means that curvature and complexity are measured through relatively local metrics quantifying overall shape as a collection of changes across relatively small domains of surface geometry. Relief is measured through a relatively global approach characterizing whole surface domains. This has implications for how these metrics respond to shape data pre-processing, as DNE and OPCR are more sensitive to variation in mesh preparation.

Before applying topographic metrics to 3D digital shape data representing molar teeth or other anatomical elements, one must first have accurate 3D digital shape data (one must also first invent the universe [Sagan, 1980]). The particular shape data format considered in this dissertation is the triangulated polygon mesh, which has been used effectively in a range of morphological methodologies including geometric morphometrics (e.g., Boyer et al., 2015). To produce a triangulated polygon mesh from an anatomical element, a procedural pathway from specimen to data is required. This pathway includes steps for specimen preparation, scanning, and mesh pre-processing. It is this last step that is the second focus of this chapter, as mesh pre-processing requires decisions regarding multiple parameters that have direct effects on topographic results. Types of mesh pre-processing include surface cropping, noise reduction, and alignment. One conclusion that can be made here is that there is no such thing as an ideal mesh pre-processing parameter set. Instead, these parameters make up a process of abstraction that is necessary for transforming a real biological specimen into a form more amenable to being easily and directly quantified for the purposes of analysis. To make decisions regarding these parameters, a researcher must be aware of the nature of the specimen and the research questions to be investigated using topographic methods.

As an example of this, consider a tooth surface marked with extreme enamel crenulations, such as an unworn pitheciine molar. Degrees of surface noise reduction that are optimal for non-pitheciine species may result in so much simplification and smoothing in a pitheciine specimen that enamel crenulations are “polished” to the point of removal. Even in less extreme cases, surface noise reduction may distort topographic shape signals relating to features such as crenulated enamel. At the same time, surface

noise is inevitably introduced during the process of mesh creation (given current scanning and processing modalities), and so it is necessary to reduce random noise-related error in topographic results. In this case, a researcher must make decisions regarding pre-processing parameters, while balancing the opposing factors of surface noise and the granularity or scale of features of interest. Similar balances must be struck for other aspects of mesh pre-processing as well. Results from this study indicate that the effects of mesh pre-processing on topographic shape results are themselves related to topographic form in a somewhat circular fashion. This demonstrates the need for nuanced understanding of the specimens under consideration, research questions, and techniques of mesh preparation and analysis prior to forming decisions regarding specimen to data pathways.

Preparing meshes for topographic analyses requires the choice of a number of parameters and approaches, and it has been suggested that these parametric choices are in some ways equivalent to choices of landmarks that must be made for more traditional methods of molar shape quantification, such as shearing quotient analyses (Allen et al., 2015). Topographic analysis was initially developed to be less reliant on landmarks than previous methods, and the parametric choices required for topographic analysis are not fully comparable to the types of decisions required in earlier approaches. Unlike landmarks, most of the pre-processing decisions required for topographic analysis are more dependent on techniques of data acquisition or post-processing analysis, and so are only partially concerned with biological concepts. For example, parameters such as smoothing level or mesh alignment procedure do not depend on careful considerations of identifiability and homology as anatomical landmark characters do. These parameters

must be given significant thought, but they sidestep theoretical discussions regarding character choice and quality. This means that these parameters can be more easily applied to diverse samples with highly variable morphologies. This is one way in which these methods are well characterized as high-throughput morphometric techniques (Plyusnin et al., 2008). Additionally, most of the pre-processing decisions that must be made for topographic analyses must also be made for any quantitative technique that relies on digital data. As an example, Bunn et al. (2011) performed error testing of noise reduction techniques on the measurement of shearing quotients from digital data. In this sense, topographic analysis requires fewer parameters compared to many approaches, including traditional methods taking advantage of increasingly large digital datasets.

Nonetheless, there are two mesh pre-processing parameters that topographic analyses are especially linked to and reliant on. These include mesh cropping, as topographic metrics quantify shape across all surface represented by a particular mesh, and mesh rotation in the case of RFI and OPCR. These parameters also represent the most "landmark-like" decisions required for topographic analysis. Surface cropping techniques and decisions regarding how to locate occlusal planes on tooth surfaces are probably most effective if these represent biologically equivalent surfaces regions between species. In this context, it should be recognized that topographic analyses are not truly "homology-free" as has been previously suggested (Ungar and M'Kirera, 2003; Evans, 2005; King et al., 2005; Evans et al., 2007). But compared to other available techniques, morphological topographic analysis is certainly "homology-light." The ability of these methods to be applied to highly variable morphological samples with relatively

strong automation suggests that they are valuable tools for more comprehensive and high-throughput quantitative phenotypic analysis.

Table 2.1. Descriptive statistics of 3D-OPCR and DEM-OPCR by species.

		DEM-OPCR		3D-OPCR		ΔOPCR	
Species	*n*	Mean	S.D.	Mean	S.D.	Mean	S.D.
Cercocebys atys	7	57.41	6.932	75.71	13.798	18.30	9.133
Cercopithecus mitis	10	56.10	3.026	69.75	7.961	13.65	6.320
Colobus guereza	10	54.10	4.001	70.91	9.134	16.81	6.739
Theropithecus gelada	9	56.51	4.534	86.35	8.992	29.83	6.091
Total	36	55.90	4.571	75.38	11.601	19.48	9.182

Table 2.2. ANOVA on OPCR treatments with species factor.

Treatment	*n*	MSE b	MSE w	*df*	*F*	*p*
DEM-OPCR	36	17.389	21.226	35	0.819	0.493
3D-OPCR	36	533.285	97.202	35	5.486	0.004

Table 2.3. Pairwise post hoc comparisons of 3D-OPCR between species.

	Cercopithecus mitis	*Colobus guereza*	*Theropithecus gelada*
Cercocebus atys	5.964 (0.614)	4.802 (0.757)	10.633 (0.162)
Cercopithecus mitis		1.162 (0.993)	**16.597 (0.005)**
Colobus guereza			**15.435 (0.009)**

* Bold indicates significance with $p < 0.05$.

Table 2.4. ANOVA on ΔOPCR with species factor.

n	MS b	MS w	*df*	*F*	*P*
36	461.819	48.921	35	9.440	<0.001

*MS b: mean square between species; MS w: mean square error within species

Table 2.5. Pairwise *post-hoc* comparisons of ΔOPCR between species.

	Cercopithecus mitis	*Colobus guereza*	*Theropithecus gelada*
Cercocebus atys	4.654 (0.539)	1.491 (0.972)	**11.530 (0.013)**
Cercopithecus mitis		3.163 (0.744)	**16.183 (<0.001)**
Colobus guereza			**13.021 (0.002)**

*Cell values given as absolute mean differences between species, with Tukey's HSD *p* following in parentheses. Bold indicates $p < 0.05$.

Table 2.6. Regression parameters for Constant-Length simple geometric objects by DNE and RFI.

a. DNE

i. Cusp height by DNE separated by number of features.

	Linear			Power		
Number of features	Slope (m)	Intercept	R^2	m	Exponent	R^2
1	**1.463**	**0.544**	**0.998**	1.999	0.836	0.997
2	3.895	-2.353	0.986	**2.221**	**1.265**	**0.996**
3	6.327	-5.249	0.981	**2.506**	**1.471**	**0.998**
4	8.759	-8.146	0.979	**2.806**	**1.599**	**0.999**
5	11.191	-11.042	0.977	**3.109**	**1.686**	**0.999**
6	13.622	-13.938	0.976	**3.415**	**1.751**	**1.000**
7	16.054	-16.834	0.976	**3.722**	**1.801**	**1.000**
8	18.486	-19.731	0.975	**4.028**	**1.841**	**1.000**
9	20.918	-22.617	0.975	**4.335**	**1.873**	**1.000**
10	22.973	-25.507	0.973	**4.390**	**1.923**	**1.000**

ii. Number of cusps by DNE separated by height of cusps.

	Linear			Power		
Cusp height	Slope (m)	Intercept	R^2	m	Exponent	R^2
1	**0.278**	**1.792**	**0.994**	1.869	0.360	0.966
2	**1.458**	**2.195**	**0.998**	3.250	0.690	0.991
3	3.637	1.362	0.999	**4.659**	**0.900**	**0.999**
4	6.513	0.014	1.000	**6.375**	**1.012**	**1.000**
5	**9.807**	**-1.585**	**1.000**	8.309	1.075	0.999

b. RFI

i. Cusp height by RFI separated by number of features.

	Linear			Power		
Number of features	Slope (m)	Intercept	R^2	m	Exponent	R^2
1	**0.906**	**0.421**	**0.999**	1.331	0.797	0.993
2	**0.816**	**0.477**	**0.999**	1.289	0.763	0.992
3	**0.725**	**0.524**	**0.999**	1.249	0.725	0.990
4	**0.634**	**0.588**	**0.999**	1.208	0.681	0.988
5	**0.544**	**0.644**	**0.999**	1.168	0.682	0.986
6	**0.453**	**0.700**	**0.999**	1.129	0.573	0.982

7	**0.363**	**0.756**	**0.999**	1.091	0.505	0.978
8	**0.272**	**0.812**	**0.999**	1.056	0.422	0.972
9	**0.181**	**0.867**	**0.999**	1.023	0.319	0.964
10	**0.091**	**0.924**	**0.999**	0.996	0.185	0.951

ii. Number of cusps by RFI separated by height of cusps.

	Linear			Power		
Cusp height	Slope (m)	Intercept	R^2	m	Exponent	R^2
1	**0.041**	**0.979**	**1.000**	0.976	0.135	0.927
2	**0.121**	**0.979**	**1.000**	1.012	0.306	0.952
3	**0.212**	**0.979**	**1.000**	1.079	0.426	0.966
4	**0.306**	**0.979**	**1.000**	1.158	0.510	0.975
5	**0.401**	**0.979**	**1.000**	1.245	0.573	0.981

Table 2.7. Second order mixed partial derivatives of DNE and RFI, calculated as regression of linear regression slopes from Tables 2.6 and 2.7 (see text).

a. Constant-Length assemblage

	Linear			Power		
Metric	Slope (m)	Intercept	R^2	m	Exponent	R^2
DNE	2.411	-2.895	0.971	**0.294**	**2.229**	**0.998**
RFI (by height in feature groups)	**0.091**	**0.000**	**1.000**	0.091	1.000	1.000
RFI (by feature in height groups)	**0.091**	**-0.056**	**0.999**	0.043	1.426	0.997

b. Delta-Length assemblage

	Linear			Power		
Metric	Slope (m)	Intercept	R^2	m	Exponent	R^2
DNE	3.269	-0.529	0.987	**0.363**	**1.975**	**0.991**
RFI (by height in feature groups)	**-0.001**	**0.954**	**0.164**	**0.953**	**-0.002**	**0.083**
RFI (by feature in height groups)	**-0.001**	**0.000**	**0.990**	*		

* A power regression can't be derived for RFI (by feature in height groups) as slopes of linear regressions include negative values.

Table 2.8. Regression parameters for Delta-Length simple geometric objects by DNE, DNE/polygon, and RFI.
a. DNE

i. Cusp height by DNE separated by number of features.

	Linear			Power		
Number of features	Slope (m)	Intercept	R^2	m	Exponent	R^2
1	**1.497**	**-0.631**	**0.985**	1.474	0.954	0.971
2	4.765	-5.916	0.986	**1.811**	**1.368**	**0.994**
3	8.034	-11.202	0.987	**2.190**	**1.525**	**0.998**
4	11.303	-16.488	0.987	**2.569**	**1.614**	**0.999**
5	14.572	-21.774	0.987	**2.944**	**1.672**	**0.999**
6	17.841	-27.060	0.987	**3.318**	**1.713**	**0.998**
7	21.110	-32.345	0.987	**3.690**	**1.744**	**0.998**
8	24.379	-37.361	0.987	**4.060**	**1.768**	**0.998**
9	27.648	-42.917	0.987	**4.429**	**1.788**	**0.997**
10	30.916	-48.203	0.987	**4.797**	**1.804**	**0.997**

ii. Number of cusps by DNE separated by height of cusps.

	Linear			Power		
Cusp height	Slope (m)	Intercept	R^2	m	Exponent	R^2
1	**0.290**	**1.512**	**1.000**	1.636	0.400	0.963
2	**1.502**	**1.227**	**1.000**	2.534	0.788	0.995
3	**3.705**	**-0.123**	**1.000**	3.603	1.012	1.000
4	**6.597**	**-1.829**	**1.000**	5.069	1.116	0.998
5	**9.902**	**-3.690**	**1.000**	6.814	1.166	0.997
6	**13.450**	**5.626**	**1.000**	8.736	1.193	0.996
7	**17.143**	**-7.600**	**1.000**	10.769	1.208	0.995
8	**20.926**	**9.594**	**1.000**	12.875	1.218	0.994
9	**24.767**	**-11.598**	**1.000**	15.032	1.225	0.994
10	**28.648**	**-13.607**	**1.000**	17.222	1.229	0.994

b. DNE/polygon

i. Cusp height by DNE/polygon separated by number of features.

	Linear			Power		
Number of features	Slope (m)	Intercept	R^2	m	Exponent	R^2
1	**0.075**	**-0.032**	**0.985**	0.074	0.954	0.971
2	0.119	-0.148	0.986	**0.045**	**1.368**	**0.994**
3	0.134	-0.187	0.987	**0.037**	**1.525**	**0.998**
4	0.141	-0.206	0.987	**0.032**	**1.614**	**0.999**
5	0.146	-0.218	0.987	**0.029**	**1.672**	**0.999**
6	0.149	-0.226	0.987	**0.028**	**1.713**	**0.998**
7	0.151	-0.231	0.987	**0.026**	**1.744**	**0.998**
8	0.152	-0.235	0.987	**0.025**	**1.768**	**0.998**
9	0.154	-0.238	0.987	**0.025**	**1.788**	**0.997**

10	0.155	-0.241	0.987	**0.024**	**1.804**	**0.997**

ii. Number of cusps by DNE/polygon separated by height of cusps.

	Linear			Power		
Cusp height	Slope (m)	Intercept	R^2	m	Exponent	R^2
1	-0.006	0.067	0.654	**0.082**	**-0.600**	**0.983**
2	-0.005	0.118	0.654	**0.127**	**-0.213**	**0.935**
3	0.001	0.181	0.653	**0.180**	**0.012**	**0.893**
4	0.007	0.266	0.654	**0.254**	**0.116**	**0.872**
5	0.014	0.366	0.654	**0.341**	**0.166**	**0.861**
6	0.021	0.476	0.654	**0.437**	**0.193**	**0.855**
7	0.028	0.591	0.654	**0.538**	**0.208**	**0.852**
8	0.036	0.710	0.654	**0.644**	**0.218**	**0.850**
9	0.043	0.832	0.654	**0.752**	**0.225**	**0.848**
10	0.050	0.956	0.654	**0.861**	**0.229**	**0.847**

c. RFI

i. Cusp height by RFI separated by number of features.

	Linear			Power		
Number of features	Slope (m)	Intercept	R^2	m	Exponent	R^2
1	**0.947**	**0.303**	**1.000**	1.260	0.872	0.994
2	**0.959**	**0.307**	**1.000**	1.276	0.872	0.994
3	**0.954**	**0.305**	**1.000**	1.269	0.872	0.994
4	**0.949**	**0.303**	**1.000**	1.262	0.872	0.994
5	**0.957**	**0.305**	**1.000**	1.272	0.872	0.994
6	**0.945**	**0.302**	**1.000**	1.257	0.872	0.994
7	**0.952**	**0.305**	**1.000**	1.267	0.872	0.994
8	**0.945**	**0.302**	**1.000**	1.257	0.872	0.994
9	**0.949**	**0.303**	**1.000**	1.262	0.872	0.994
10	**0.948**	**0.303**	**1.000**	1.261	0.872	0.994

ii. Number of cusps by RFI separated by height of cusps.

	Linear			Power		
Cusp height	Slope (m)	Intercept	R^2	m	Exponent	R^2
1	**0.000**	**1.393**	**0.158**	1.392	-0.002	0.080
2	**-0.002**	**2.203**	**0.174**	2.202	-0.002	0.091
3	**-0.002**	**3.116**	**0.170**	3.113	-0.002	0.087
4	**-0.003**	**4.063**	**0.169**	4.060	-0.002	0.087
5	**-0.004**	**5.024**	**0.168**	5.020	-0.002	0.086

6	**-0.004**	**5.993**	**0.164**	5.989	-0.002	0.084
7	**-0.005**	**6.967**	**0.166**	6.961	-0.002	0.084
8	**-0.006**	**7.944**	**0.169**	7.938	-0.002	0.087
9	**-0.006**	**8.922**	**0.167**	8.916	-0.002	0.086
10	**-0.007**	**9.902**	**0.165**	9.894	-0.002	0.083

Table 2.9. Descriptive statistics of metrics by species per cropping treatment.

a. DNE

		OC		CC		BC	
Species	n	Mean	S.D.	Mean	S.D.	Mean	S.D.
Cercocebys atys	7	196.557	14.730	197.170	21.464	205.693	28.724
Cercopithecus mitis	10	200.202	31.095	195.254	25.330	199.850	32.925
Colobus guereza	10	216.874	17.092	215.861	18.129	216.762	16.889
Theropithecus gelada	9	243.863	17.342	233.954	12.195	233.930	16.989
Total	36	215.040	27.848	210.371	24.730	214.204	27.107

b. RFI

		OC		CC		BC	
Species	n	Mean	S.D.	Mean	S.D.	Mean	S.D.
Cercocebys atys	7	0.280	0.028	0.519	0.055	0.450	0.062
Cercopithecus mitis	10	0.303	0.035	0.511	0.026	0.411	0.050
Colobus guereza	10	0.359	0.025	0.521	0.030	0.460	0.030
Theropithecus gelada	9	0.354	0.060	0.505	0.055	0.460	0.056
Total	36	0.327	0.050	0.514	0.040	0.444	0.052

c. OPCR

		OC		CC		BC	
Species	n	Mean	S.D.	Mean	S.D.	Mean	S.D.
Cercocebys atys	7	75.964	13.792	64.232	9.658	67.286	10.832
Cercopithecus mitis	10	70.138	8.399	60.675	5.661	64.475	8.527
Colobus guereza	10	70.913	9.134	59.388	6.691	62.100	8.030
Theropithecus gelada	9	86.347	8.992	69.438	7.523	73.028	8.676
Total	36	75.538	11.628	63.021	7.996	66.500	9.507

Table 2.10. ANOVAs of topographic metrics with species factor per cropping treatment.

a. DNE

Treatment	n	MSE b	MSE w	df	F	*p*

Occlusal basin crop (OC)	**36**	**4034.483**	**469.971**	**35**	**8.585**	**<0.001**
Cervical crop (CC)	36	2751.969	404.451	35	6.804	0.001
Buccal infolding crop (BC)	36	2045.023	611.972	35	3.342	0.031

b. RFI

Treatment	n	MSE b	MSE w	df	F	*p*
Occlusal basin crop (OC)	**36**	**0.013**	**0.002**	**35**	**8.023**	**<0.001**
Cervical crop (CC)	36	<0.001	0.002	35	0.285	0.836
Buccal infolding crop (BC)	36	0.005	0.002	35	2.152	0.113

c. OPCR

Treatment	n	MSE b	MSE w	df	F	*p*
Occlusal basin crop (OC)	**36**	**519.477**	**99.187**	**35**	**5.237**	**0.005**
Cervical crop (CC)	36	175.567	53.132	35	3.304	0.033
Buccal infolding crop (BC)	36	207.478	79.401	35	2.613	0.068

Table 2.11. Pairwise post hoc comparisons of topographic metrics between species per cropping treatment.

a. DNE

i. OC

	Cercopithecus mitis	*Colobus guereza*	*Theropithecus gelada*
Cercocebus atys	-3.645 (0.986)	-20.317 (0.248)	**-47.306 (0.001)**
Cercopithecus mitis		-16.672 (0.331)	**-43.661 (0.001)**
Colobus guereza			**-26.989 (0.050)**

i. CC

	Cercopithecus mitis	*Colobus guereza*	*Theropithecus gelada*
Cercocebus atys	1.916 (0.997)	-18.691 (0.255)	**-36.784 (0.007)**
Cercopithecus mitis		-20.607 (0.122)	**-38.701 (0.002)**
Colobus guereza			-18.094 (0.250)

i. BC

	Cercopithecus mitis	*Colobus guereza*	*Theropithecus gelada*
Cercocebus atys	5.843 (0.963)	-11.070 (0.801)	-28.238 (0.128)
Cercopithecus mitis		-16.912 (0.433)	**-34.080 (0.026)**
Colobus guereza			-17.168 (0.443)

b. RFI

i. OC

	Cercopithecus mitis	*Colobus guereza*	*Theropithecus gelada*
Cercocebus atys	-0.023 (0.650)	**-0.079 (0.002)**	**-0.074 (0.004)**
Cercopithecus mitis		**-0.056 (0.018)**	**-0.051 (0.041)**
Colobus guereza			0.005 (0.993)

i. CC

	Cercopithecus mitis	*Colobus guereza*	*Theropithecus gelada*
Cercocebus atys	0.007 (0.983)	-0.003 (0.999)	0.014 (0.915)
Cercopithecus mitis		-0.010 (0.945)	0.006 (0.988)
Colobus guereza			0.017 (0.831)

i. BC

	Cercopithecus mitis	*Colobus guereza*	*Theropithecus gelada*
Cercocebus atys	0.039 (0.407)	-0.010 (0.974)	-0.010 (0.975)
Cercopithecus mitis		-0.049 (0.144)	-0.049 (0.161)
Colobus guereza			-0.001 (1.000)

c. OPCR

i. OC

	Cercopithecus mitis	*Colobus guereza*	*Theropithecus gelada*
Cercocebus atys	5.827 (0.639)	5.051 (0.734)	10.383 (0.185)
Cercopithecus mitis		-0.775 (0.998)	**-16.210 (0.006)**
Colobus guereza			**-15.435 (0.010)**

i. CC

	Cercopithecus mitis	*Colobus guereza*	*Theropithecus gelada*
Cercocebus atys	3.557 (0.756)	4.845 (0.540)	-5.205 (0.521)
Cercopithecus mitis		1.288 (0.979)	-8.763 (0.074)
Colobus guereza			**-10.050 (0.032)**

i. BC

	Cercopithecus mitis	*Colobus guereza*	*Theropithecus gelada*

Cercocebus atys	2.811 (0.918)	5.186 (0.643)	-5.742 (0.583)
Cercopithecus mitis		2.375 (0.933)	-8.553 (0.178)
Colobus guereza			-10.928 (0.055)

Table 2.12. Regression parameters for *Cercocebus atys* and *Theropithecus gelada RFI* across a) rotation of X axis alone, b) rotation of Y axis alone, and c) simultaneous rotation of X and Y axes.

Specimen	Regression set	m	Exponent	R^2
Cercocebus atys 89373	Rotation of X axis	0.057	1.735	1.000
Cercocebus atys 89373	Rotation of Y axis	0.025	1.967	0.999
Cercocebus atys 89373	Rotation of X and Y axes	0.086	1.785	1.000
Theropithecus gelada 1963-58	Rotation of X axis	0.107	1.377	0.998
Theropithecus gelada 1963-58	Rotation of Y axis	0.328	0.875	0.917
Theropithecus gelada 1963-58	Rotation of X and Y axes	0.097	1.510	0.997

Table 2.13. Mean tooth height from lowest point of occlusal basin, buccolingual width, mesiodistal length, and RFI for *Cercocebus atys* and *Theropithecus gelada* specimens.

Specimen	Mean height	B-L width	M-D length	Height/width	Height/length	RFI
Cercocebus atys 89373	1.960	6.630	8.370	0.300	0.230	0.308
Theropithecus gelada 1963-58	3.030	9.380	13.710	0.320	0.220	0.387

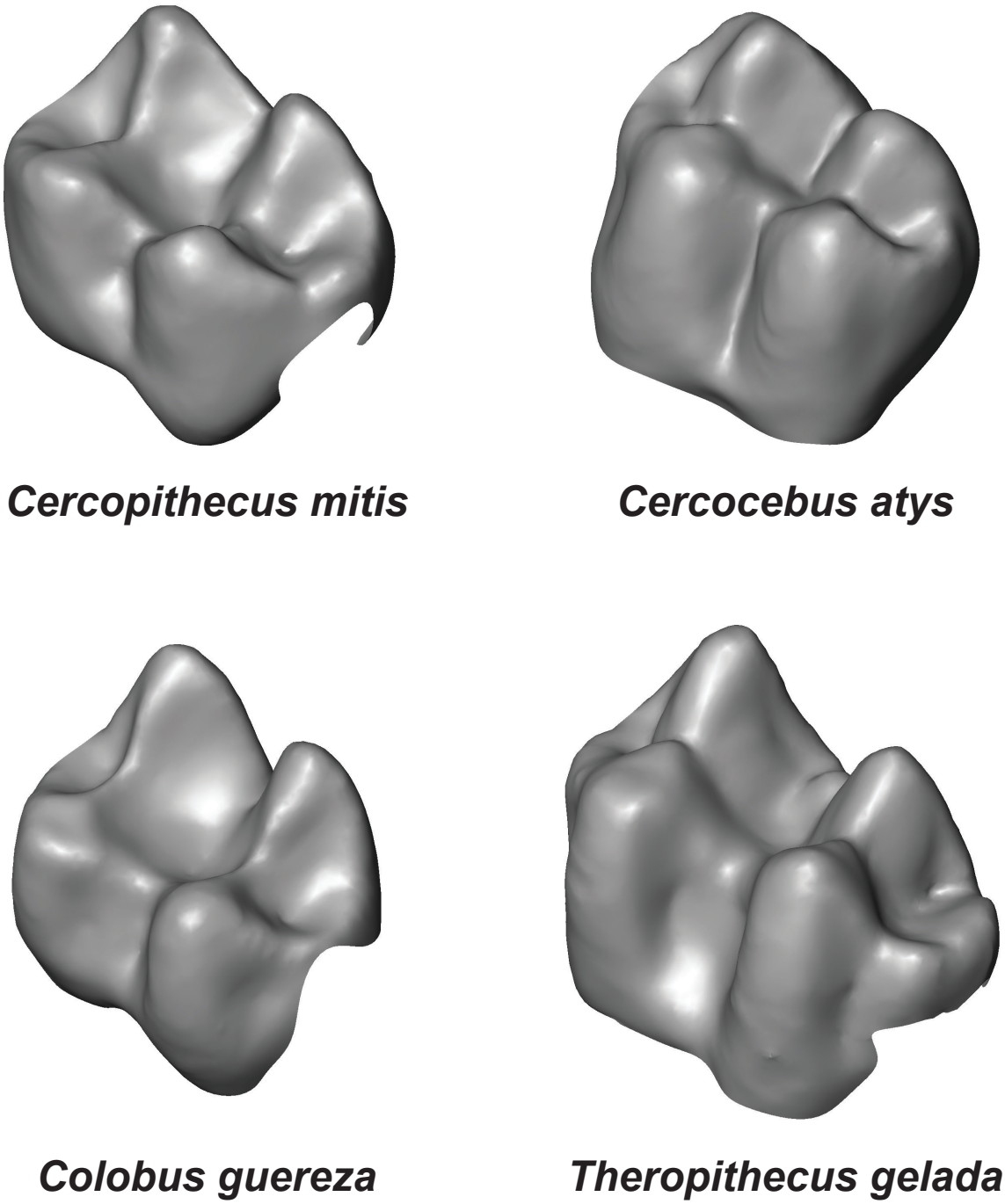

Fig 2.1. Specimens representing the four species of the cercopithecoid M_2 test sample. Specimen numbers (as given in Appendix 2): *Cercopithecus mitis* - AMNH 52364, *Cercocebus atys* - AMNH 89373, *Colobus guereza* - BMNH 28.11.11.2, *Theropithecus gelada* MNHNP 1963-58. M_2s are not presented to scale, buccal and distal aspects are toward bottom-left and bottom-right respectively.

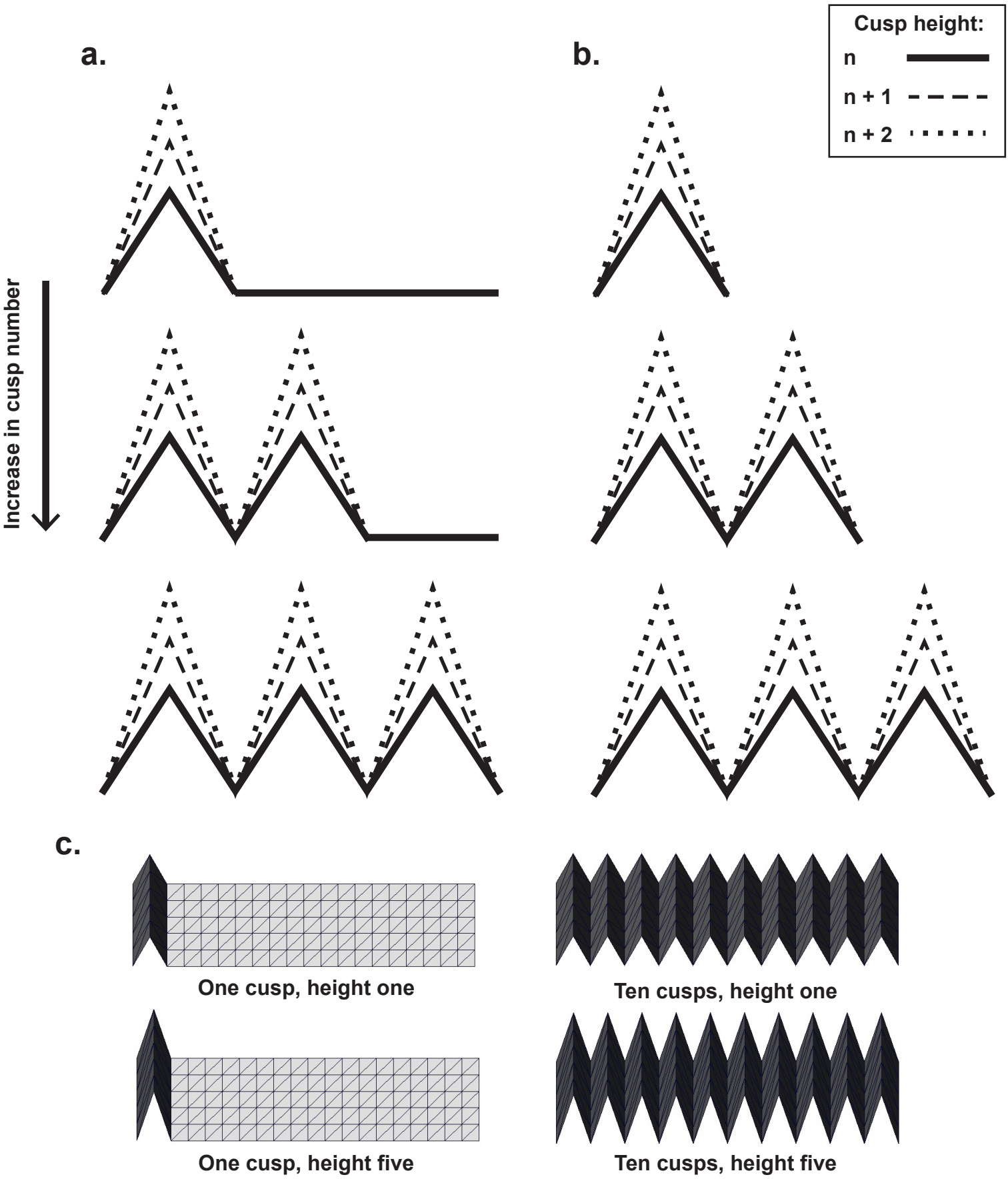

Fig. 2.2. Two-dimensional representation of surface meshes generated by (a) Constant-Length and (b) Delta-Length algorithm components of *shapemaker.py*. Number of cusps and steps of height are limited to three here. The Constant-Length algorithm introduces crests of varying height to a flat rectangular plane, while the Delta-Length algorithm creates crests without a pre-existing surface. Height is constant for all crests per individual generated mesh, and maximum crest numbers are identical between algorithms. (c) Example Constant-Length meshes.

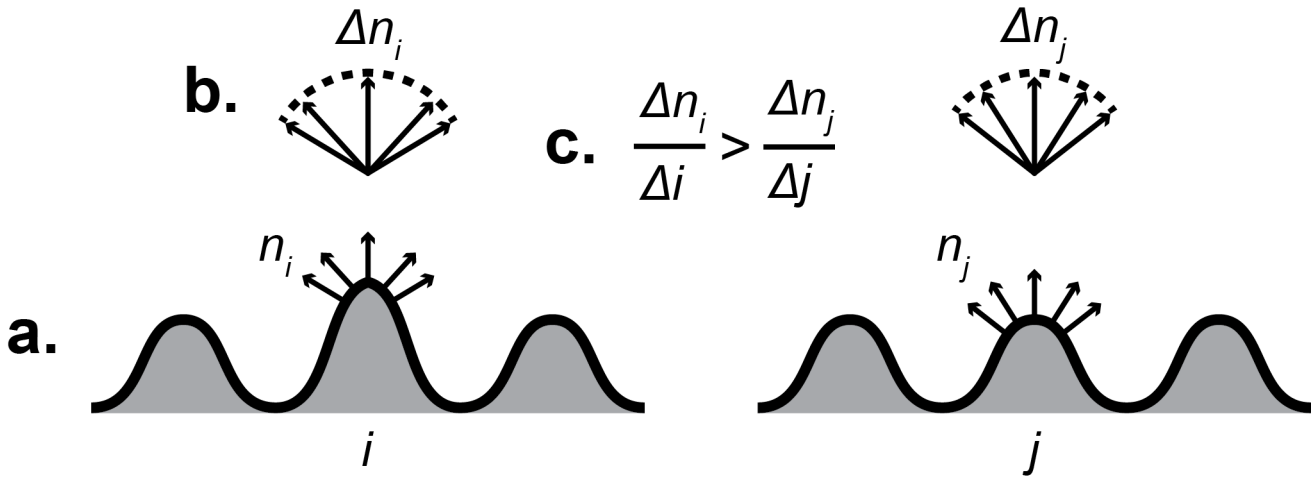

Fig 2.3. A simplistic two-dimensional diagram describing shape quantification using the Dirichlet normal energy method. (a) Given two surfaces *i* and *j*, normal vectors of magnitude one are derived for equal-length regions of interest. End-points of normal vectors define n_i and n_j, the normal maps of *i* and *j* respectively. (b) Δn represents the change in position of end-points of normal vectors, or the change in the normal map. Superimposing origin points of normal vectors corrects Δn for the change in surface position (Δi or Δj). Arc length of superimposed normal vectors reflects degree of surface bending. (c) Stated explicitly, surface bending for a region of interest can be said to be characterized by change in the normal map (Δn) relative to change in surface position (Δi or Δj). Surface i shows greater bending. For the three-dimensional polygon mesh case used here, regions of interest are individual polygon vertices (see text for more details).

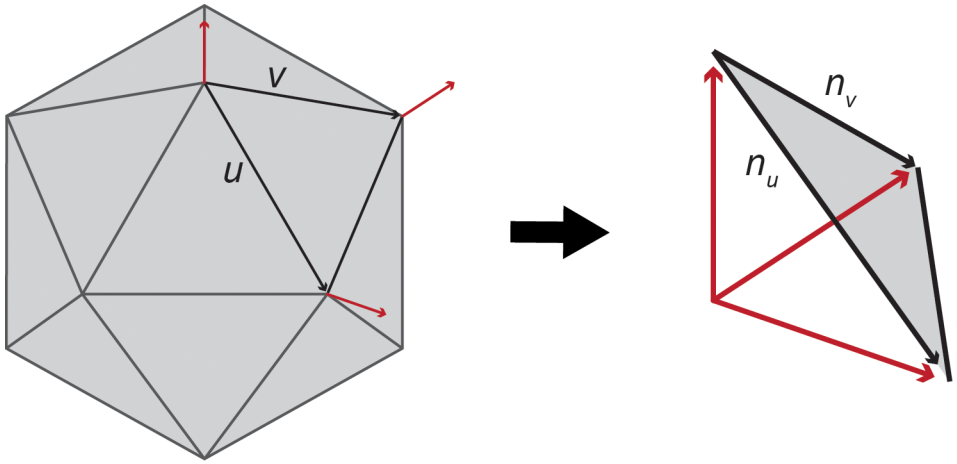

Fig 2.4. Diagram demonstrating edge vectors *u* and *v* of given polygon and approximated normal vectors (red) for polygon vertices. End-points of vertex normals form a polygon with edge vectors n_u and n_v. Translating vertex normals to a common origin point visualizes spreading of n_u and n_v relative to spreading of *u* and *v*. Polygons on more curved surfaces will produce greater relative spreading of n_u and n_v. The function *e(p)* quantifies relative spreading to calculate degree of surface bending per polygon.

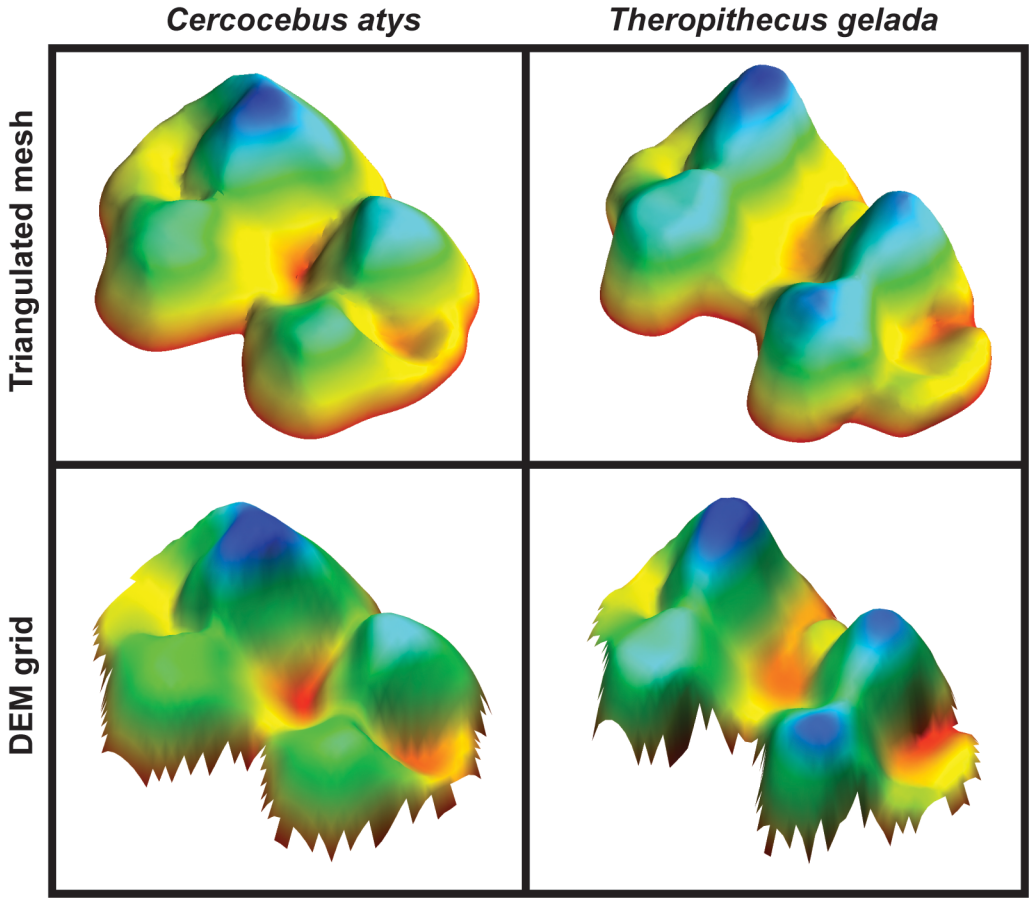

Fig 2.5. Comparison of triangulated mesh and DEM grid formats of second mandibular molar tooth surfaces for species *Cercocebus atys* and *Theropithecus gelada*. Teeth are presented in oblique perspective, with distal and buccal aspects toward bottom-right and bottom-left respectively. Color scaling reflects elevation. Triangulated mesh data is used for calculation of 3D-OPCR and DEM grid data is used for calculation of DEM-OPCR. Triangulated mesh data used here represent molar surface at a relatively finer resolution compared to DEM data.

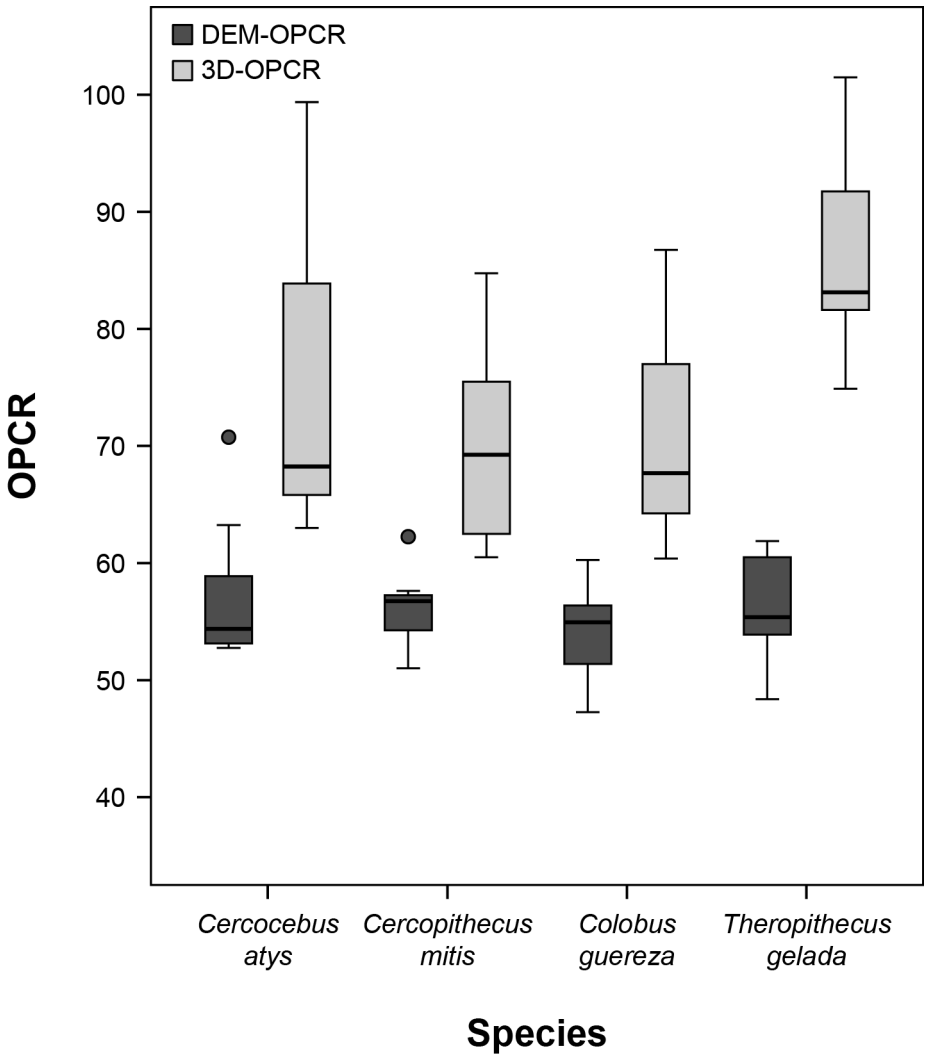

Fig 2.6. Box plot of DEM-OPCR and 3D-OPCR by species.

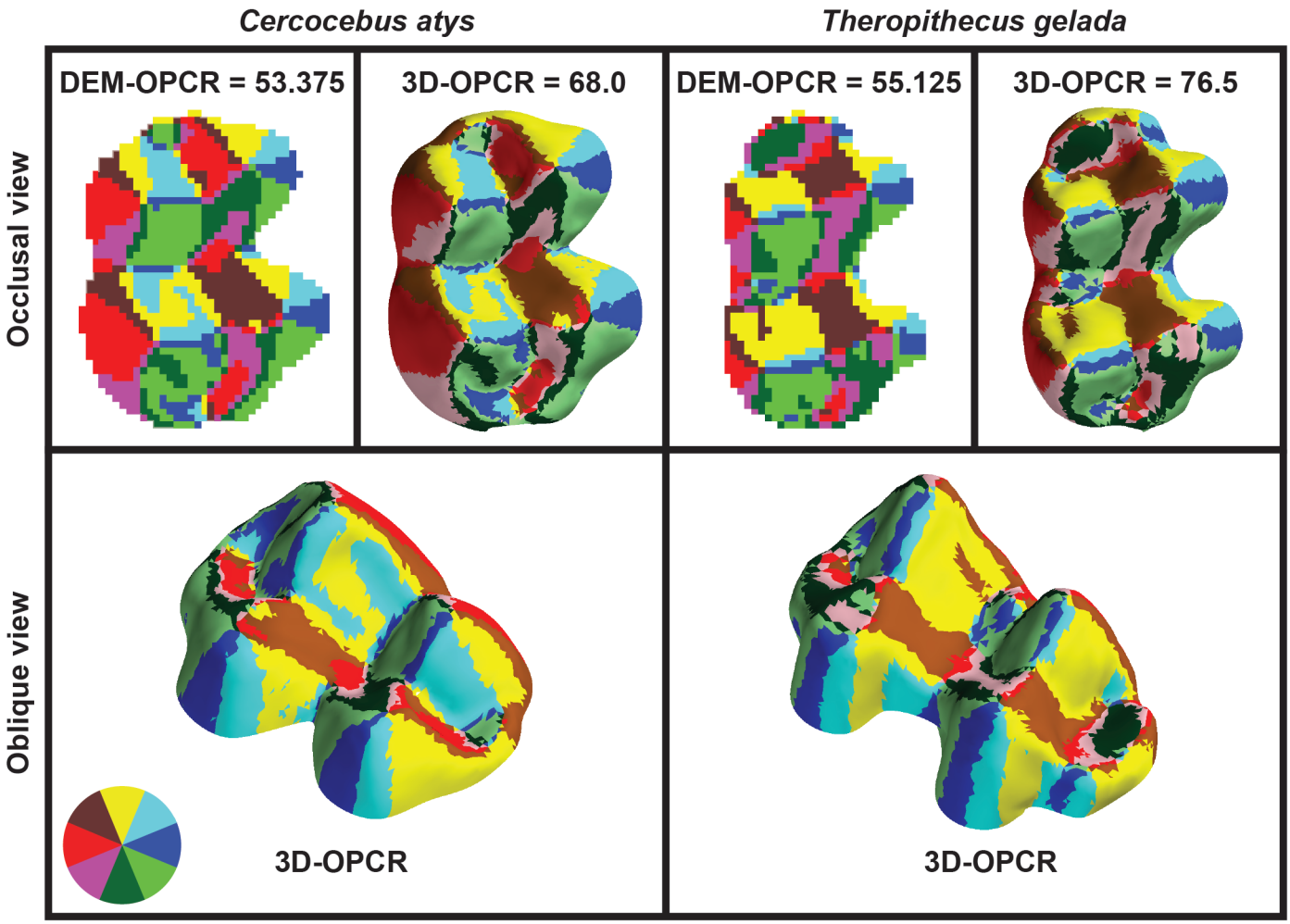

Fig 2.7. Results of DEM-OPCR and 3D-OPCR algorithms applied to molar tooth surfaces from Fig. 2.5. Results from both algorithms are presented in occlusal perspective, with distal aspect at top and buccal aspect toward right. 3D-OPCR results are also shown in oblique perspective, with distal and buccal aspects toward bottom-right and bottom-left respectively. Color wheel at bottom left indicates patch aspect direction for occlusal perspective. 3D-OPCR results are presented with surface shading while DEM-OPCR results are not.

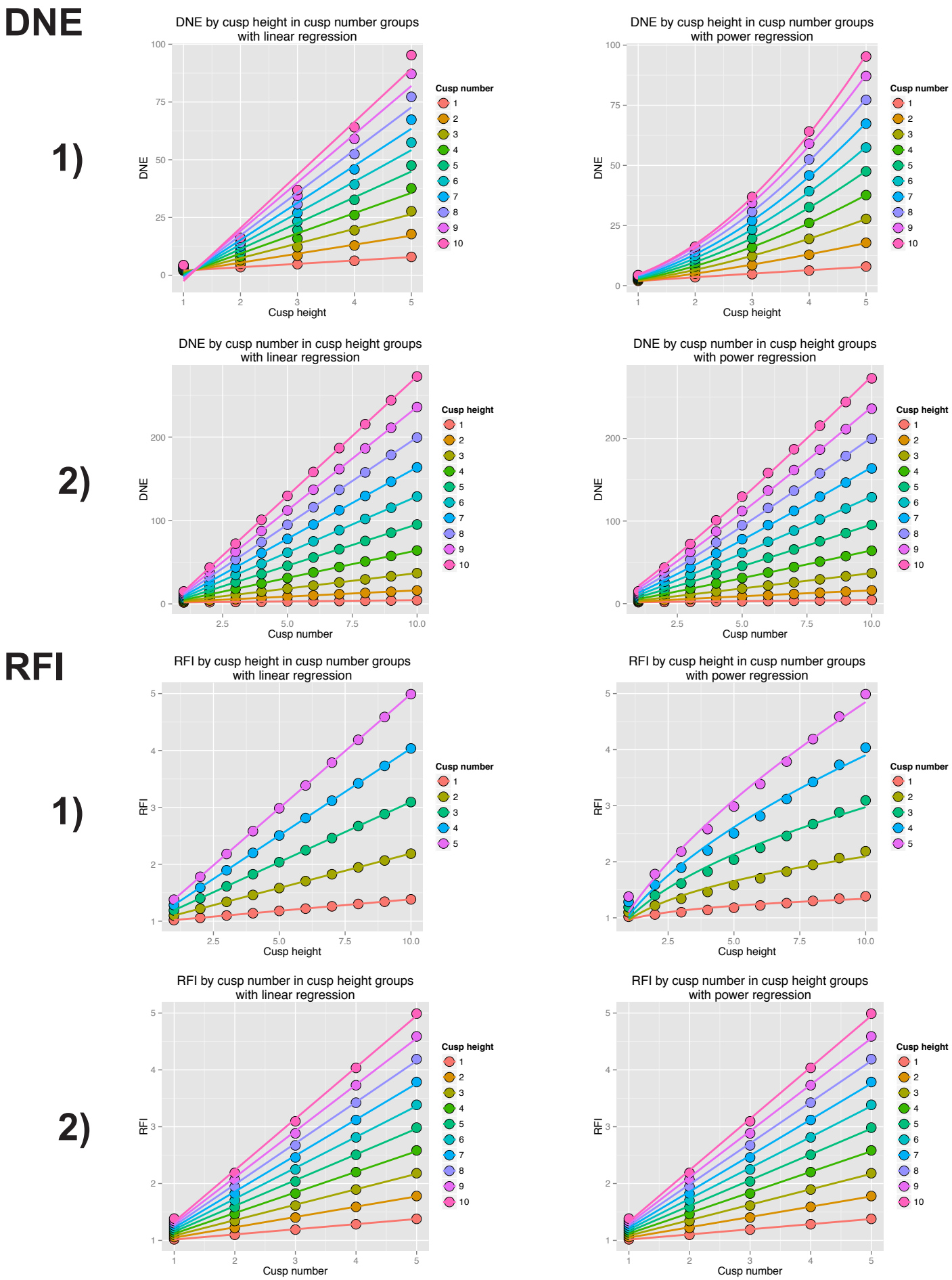

Fig 2.8. Scatter plots of topographic metrics (DNE, RFI) across cusp height and number factors for constant-length simple geometric objects. Plots are divided into groups of 1) metrics by cusp height split into sets by constant cusp number, and 2) metrics by cusp number split into sets by constant cusp height. Regressions are given for both linear and power models.

DNE

1)

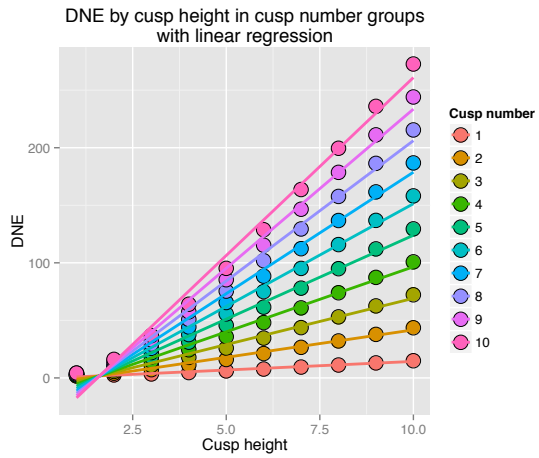

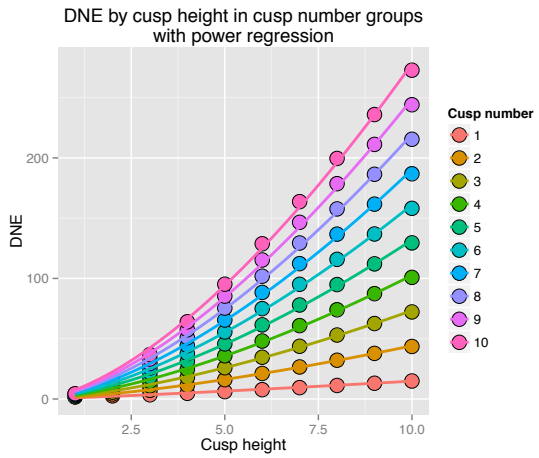

2)

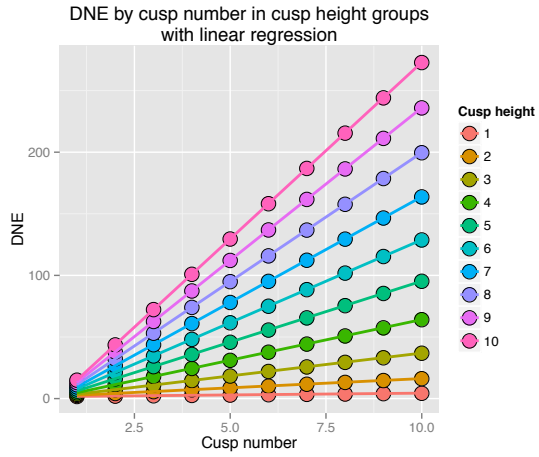

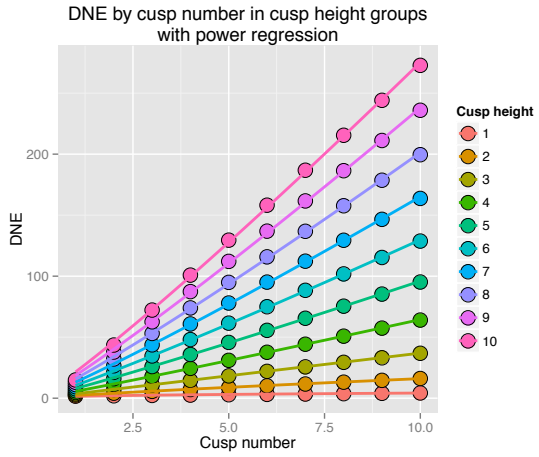

DNE/ Polygon

1)

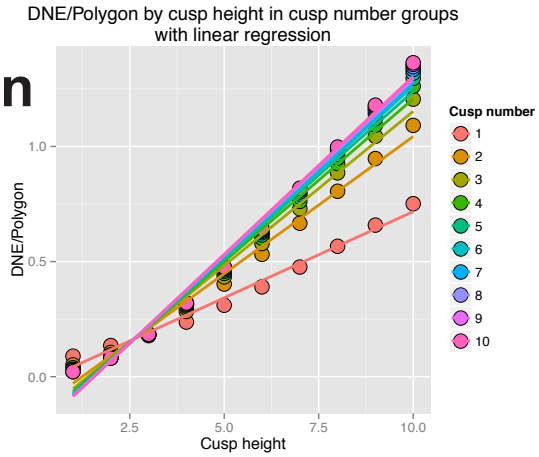

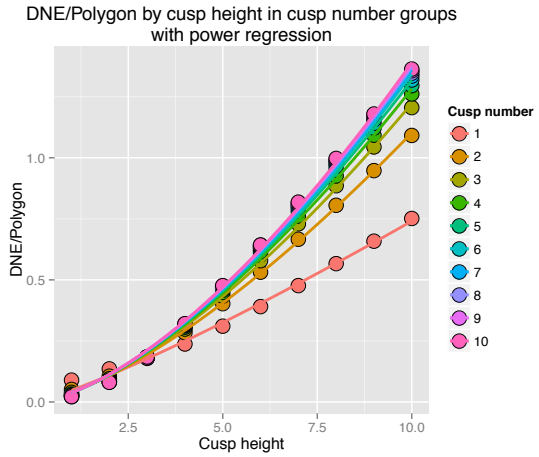

2)

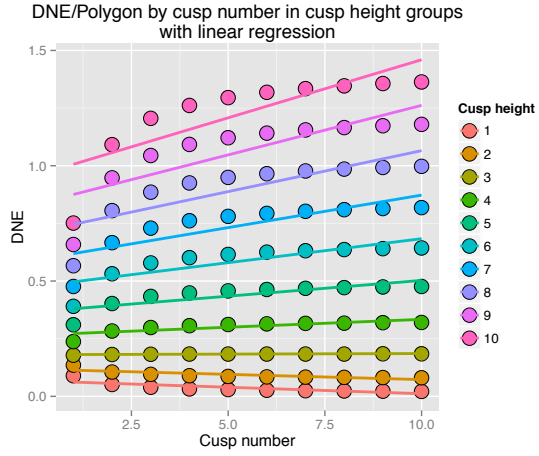

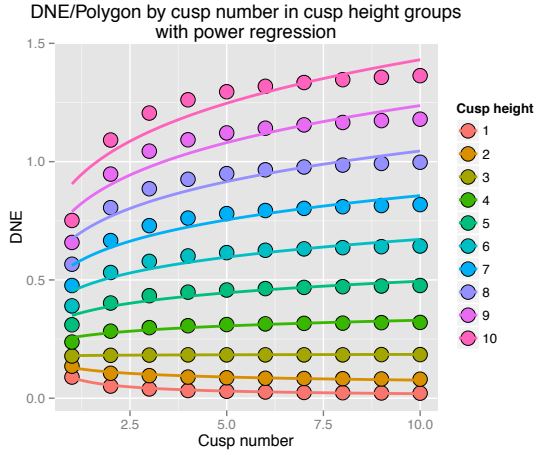

Fig 2.9. Scatter plots of topographic metrics (DNE, DNE/Polygon, RFI) across cusp height and number factors for delta-length simple geometric objects. Plots are divided into groups of 1) metrics by cusp height split into sets by constant cusp number, and 2) metrics by cusp number split into sets by constant cusp height. Regressions are given for both linear and power models.

RFI

1)

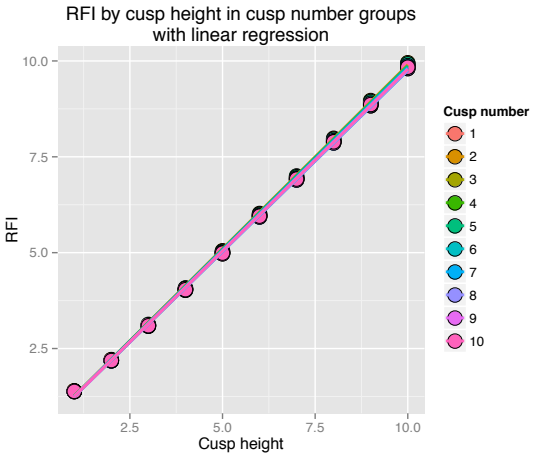

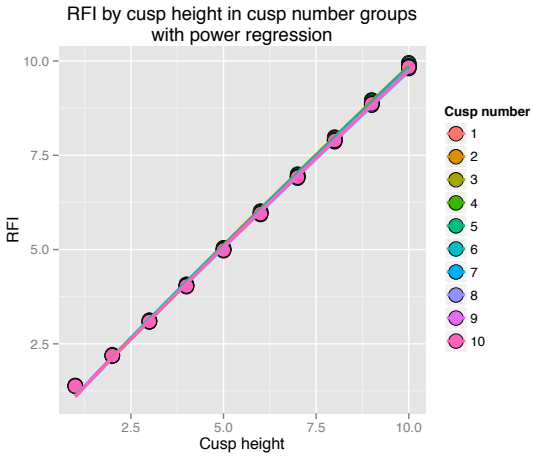

2)

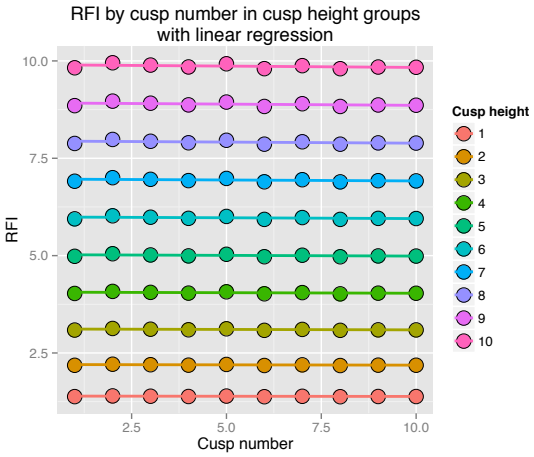

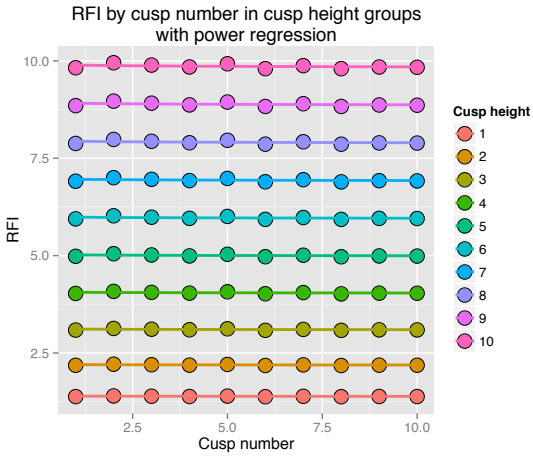

Fig 2.9. Scatter plots of topographic metrics (DNE, DNE/Polygon, RFI) across cusp height and number factors for delta-length simple geometric objects. Plots are divided into groups of 1) metrics by cusp height split into sets by constant cusp number, and 2) metrics by cusp number split into sets by constant cusp height. Regressions are given for both linear and power models.

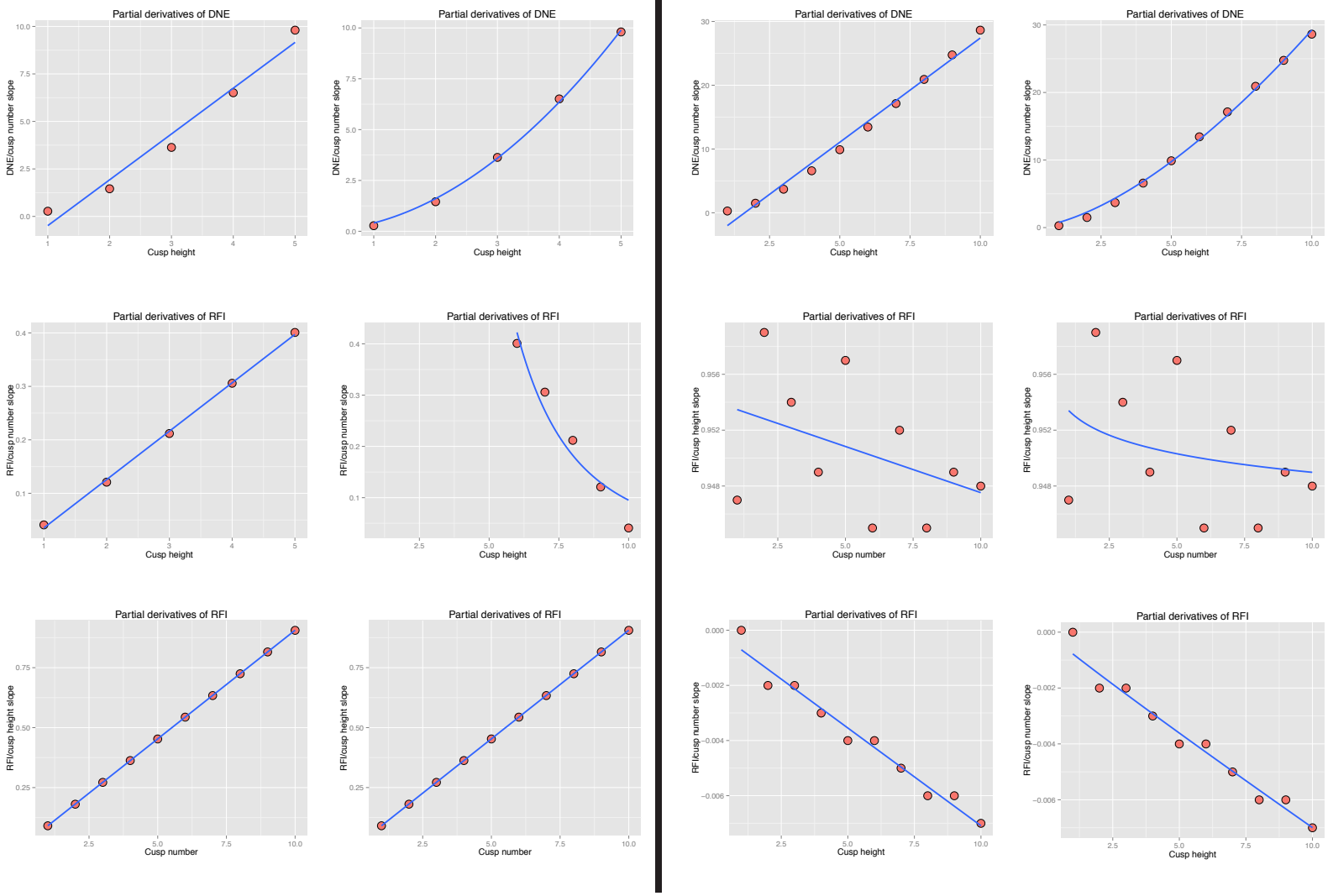

Fig 2.10. Partial derivatives of DNE and RFI with respect to cusp height and number factors (linear regression slopes from Figs. 2.8 and 2.9). Regression slopes of partial derivatives are second-order partial derivatives of topographic metrics, and represent change in topographic metrics with respect to both cusp height and number. See text for details, including protocol for choosing slopes from Figs. 2.8 and 2.9.

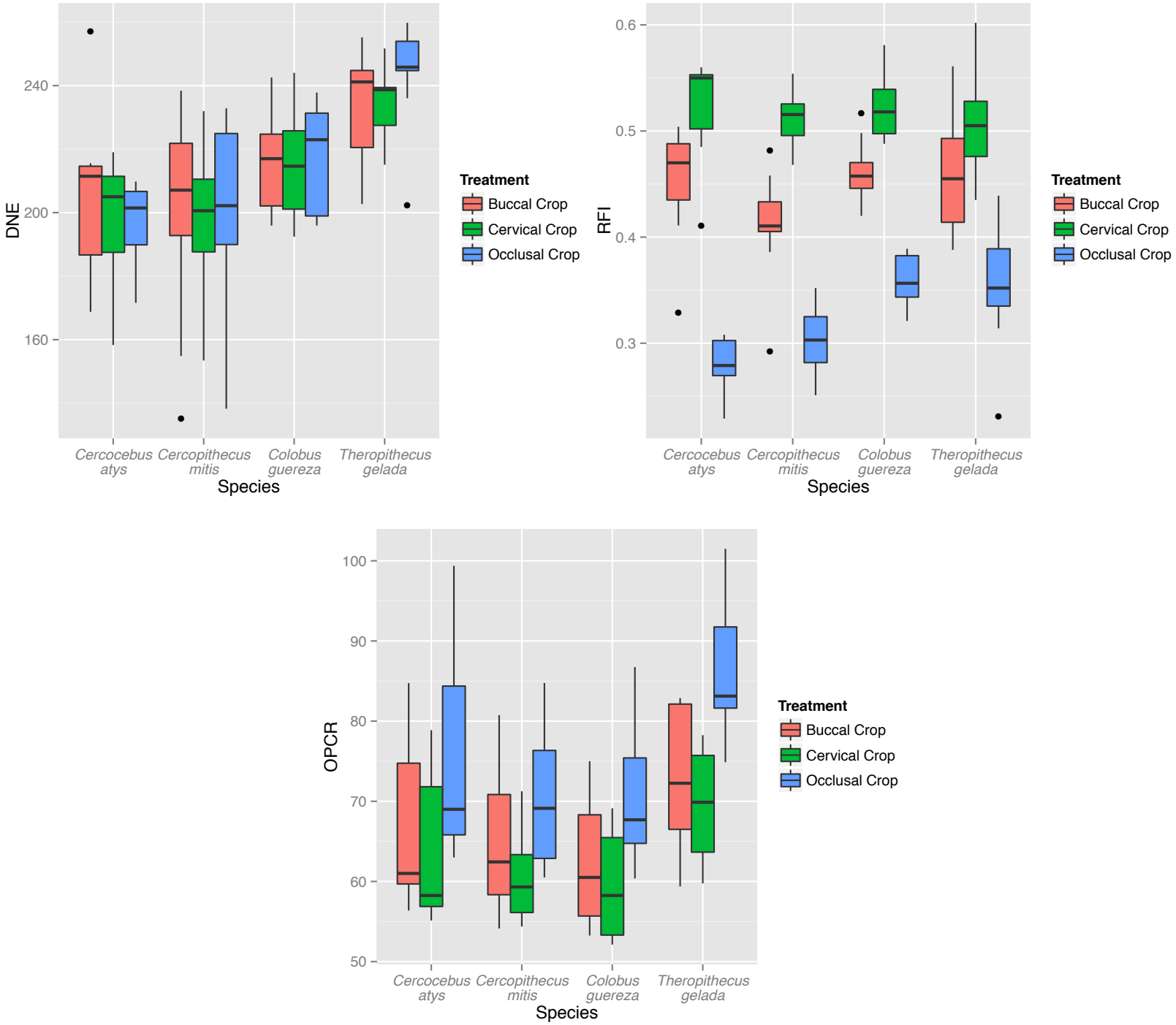

Fig 2.11. Box plots by species and occlusal cropping treatment per topographic metric (DNE, RFI, OPCR).

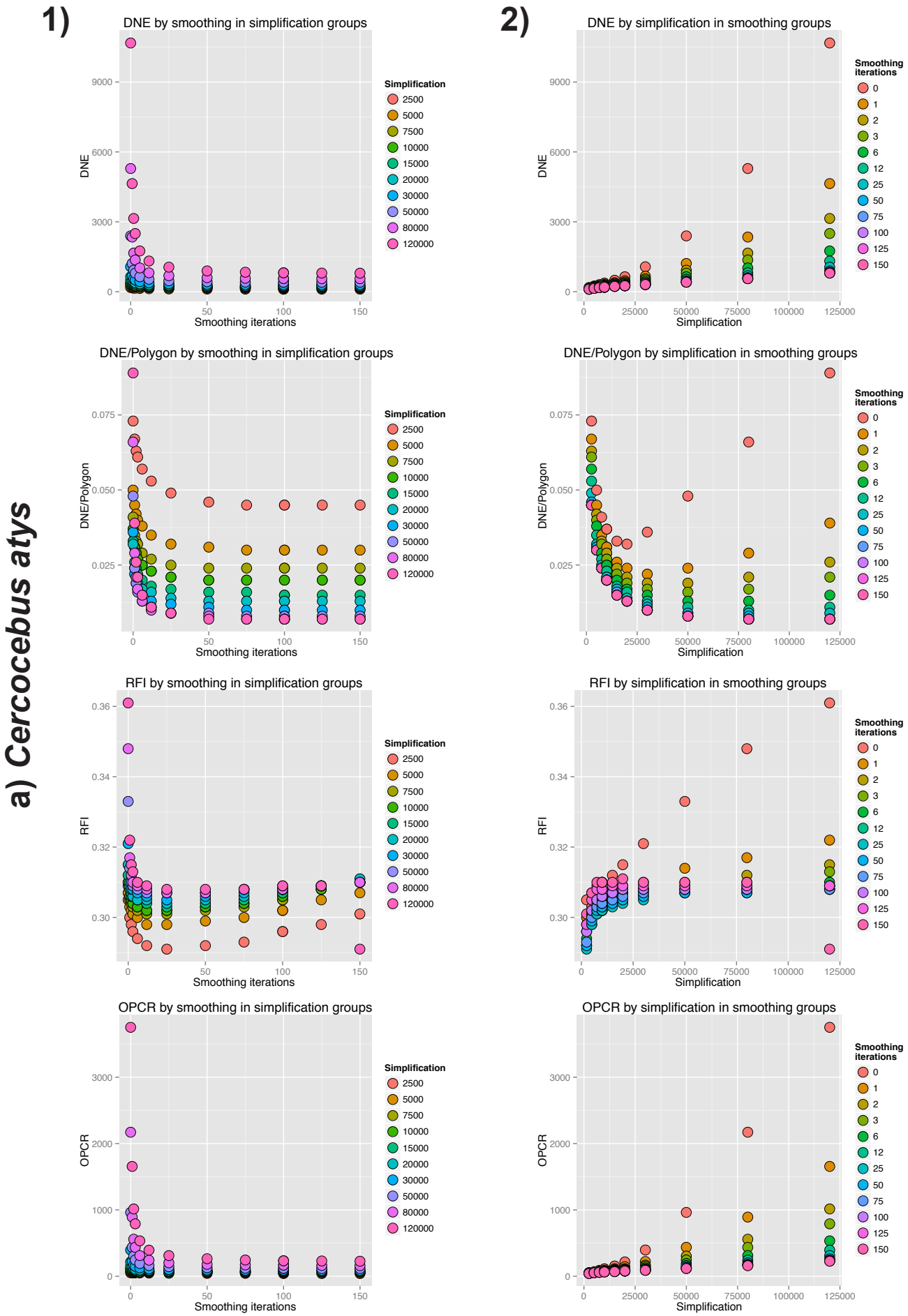

Fig 2.12. Scatter plots of topographic metrics (DNE, DNE/Polygon, RFI, OPCR) across smoothing iterations and simplification level factors for a) *Cercocebus atys* and b) *Theropithecus gelada* specimens. Plots are divided into groups of 1) metrics by smoothing iterations split into sets by constant simplification level, and 2) metrics by simplification level split into sets by constant smoothing iterations. c) Percent differences between specimens per topographic metrics, split into groups 1) and 2) as above.

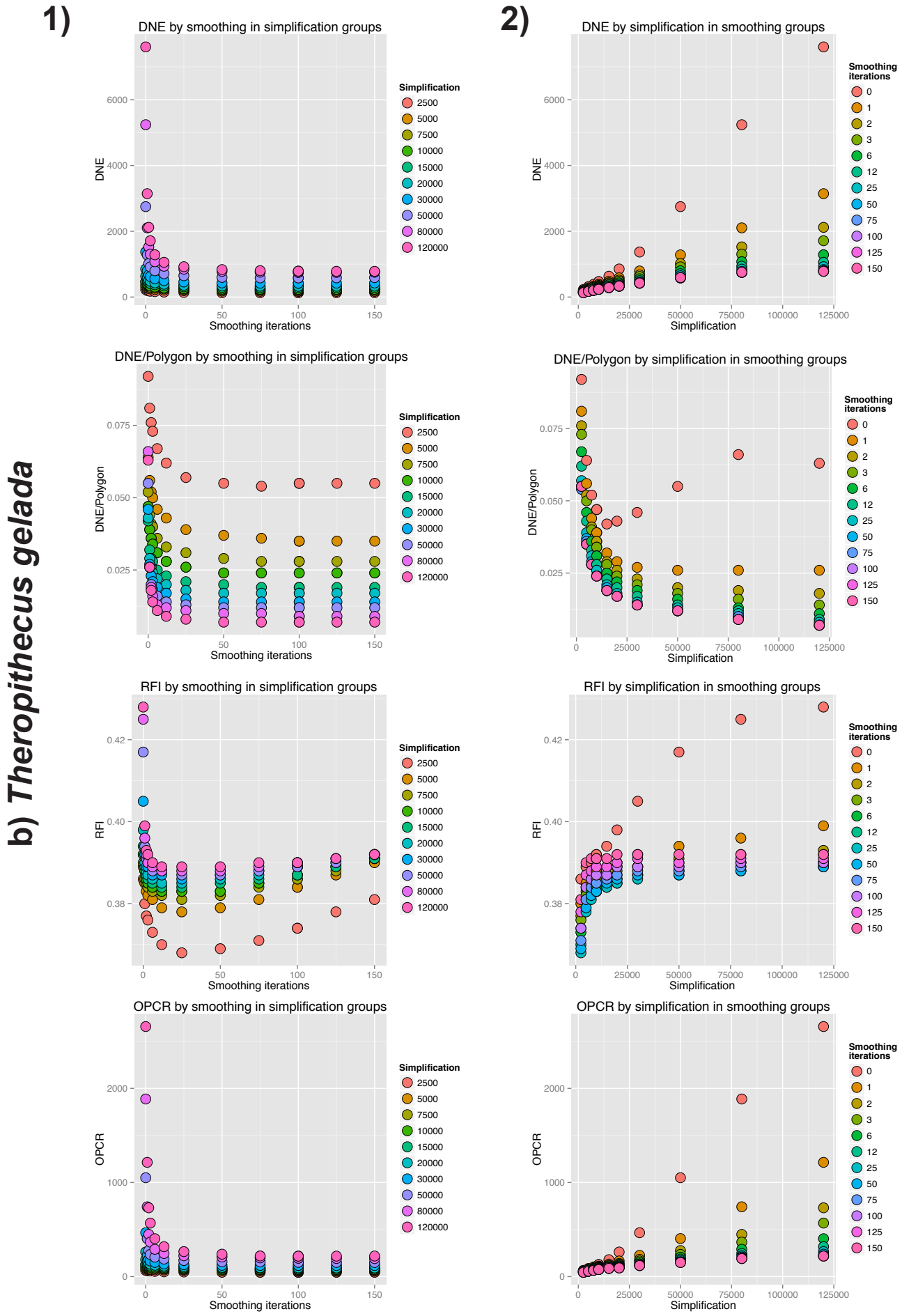

Fig 2.12. Scatter plots of topographic metrics (DNE, DNE/Polygon, RFI, OPCR) across smoothing iterations and simplification level factors for a) *Cercocebus atys* and b) *Theropithecus gelada* specimens. Plots are divided into groups of 1) metrics by smoothing iterations split into sets by constant simplification level, and 2) metrics by simplification level split into sets by constant smoothing iterations. c) Percent differences between specimens per topographic metrics, split into groups 1) and 2) as above.

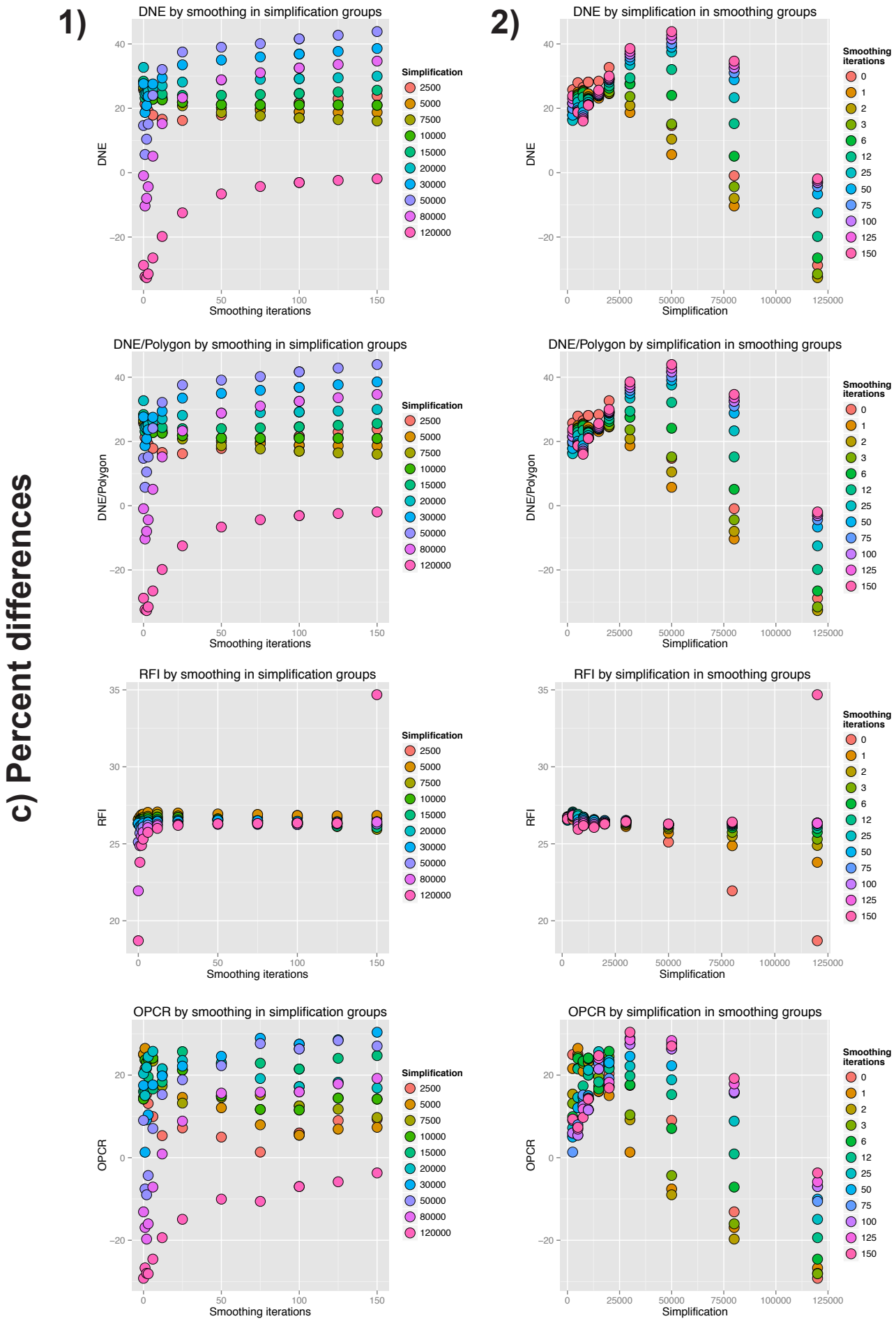

Fig 2.12. Scatter plots of topographic metrics (DNE, DNE/Polygon, RFI, OPCR) across smoothing iterations and simplification level factors for a) *Cercocebus atys* and b) *Theropithecus gelada* specimens. Plots are divided into groups of 1) metrics by smoothing iterations split into sets by constant simplification level, and 2) metrics by simplification level split into sets by constant smoothing iterations. c) Percent differences between specimens per topographic metrics, split into groups 1) and 2) as above.

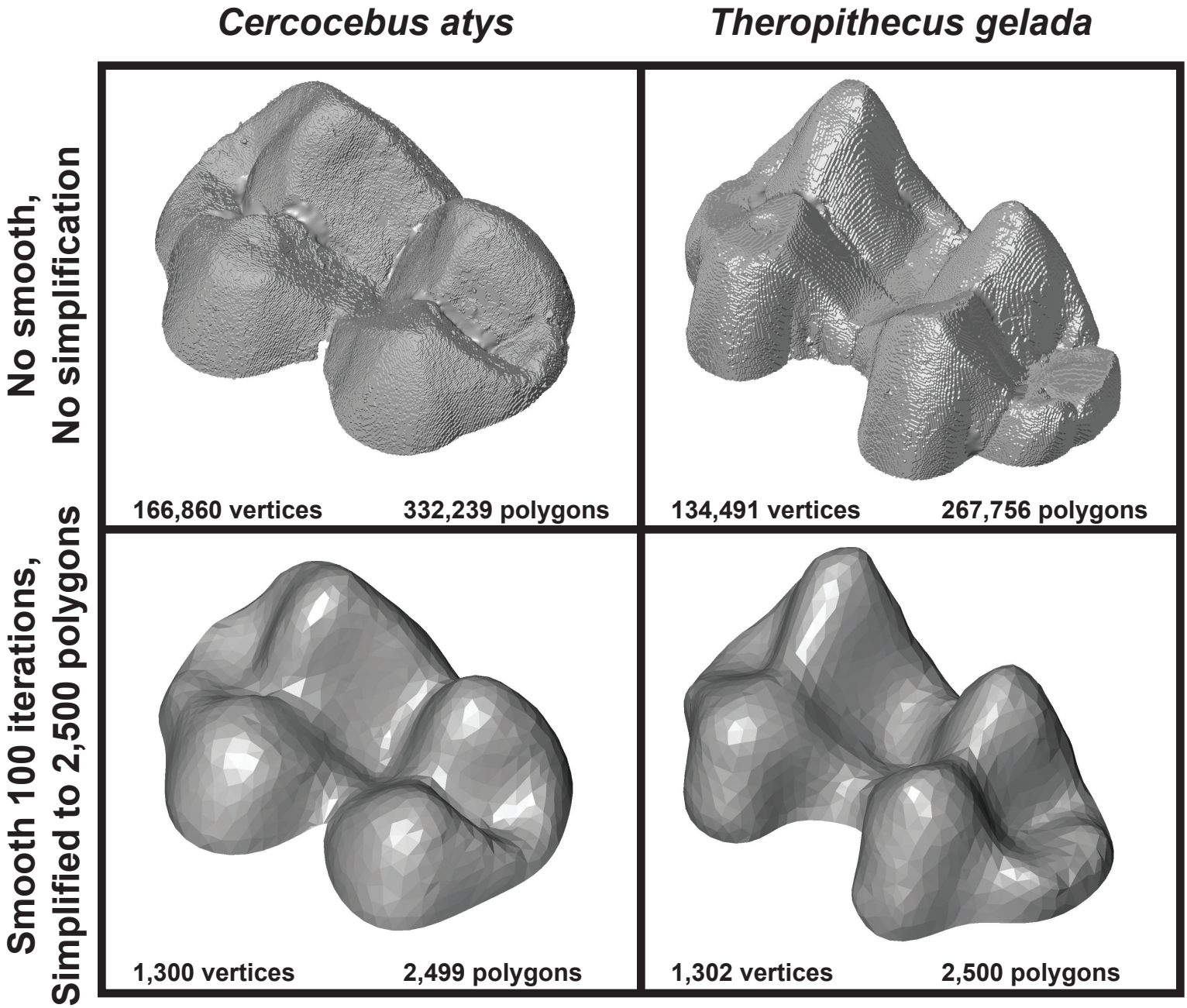

Fig 2.13. Original unsmoothed and unsimplified surfaces of M_2s of *Ce. atys* and *T. gelada* compared to maximally smoothed and simplified surfaces. Though the process of simplification and smoothing entail significant shape change, maximally smoothed and simplified surfaces are still recognizable as original teeth.

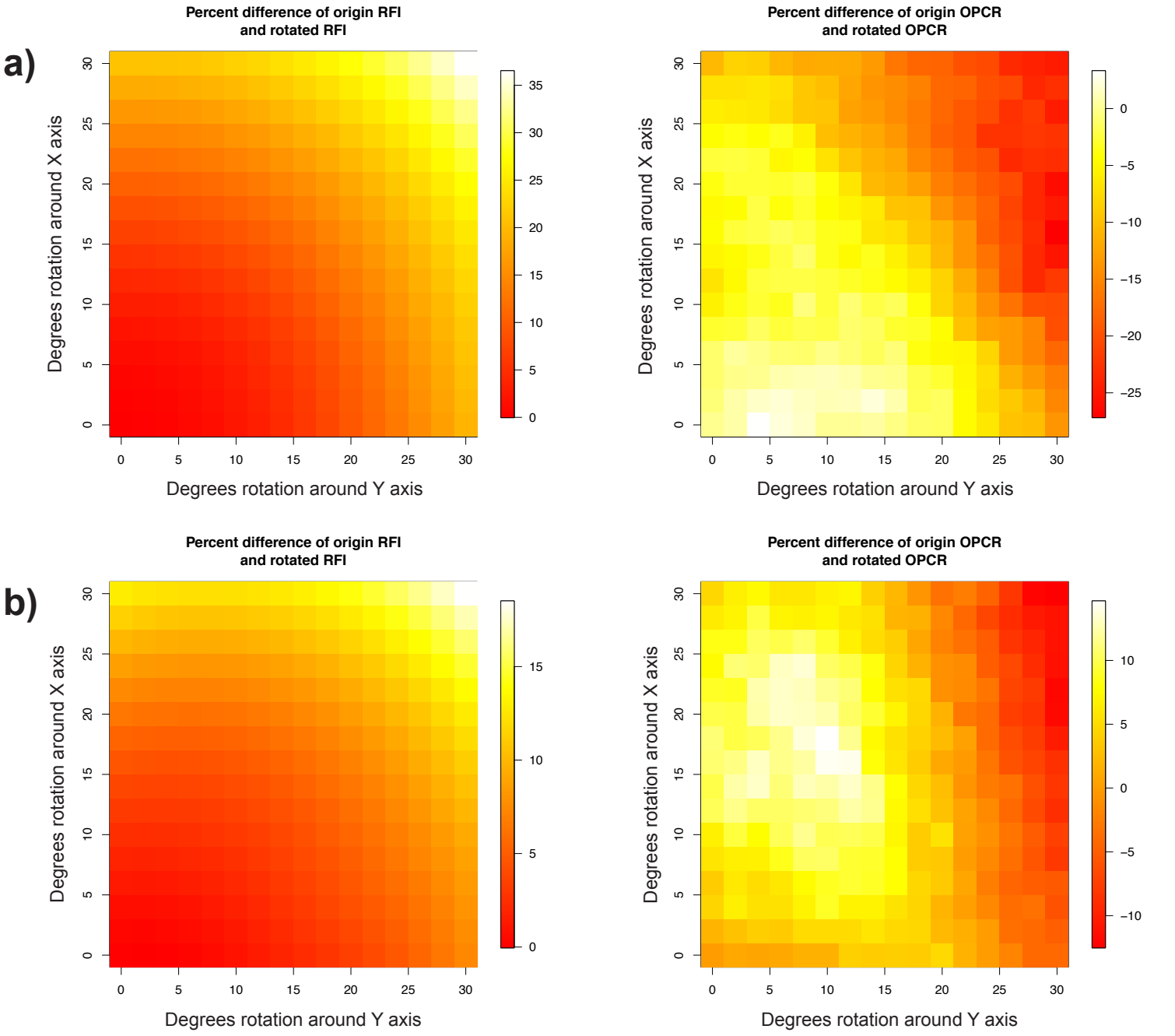

Fig 2.14. Color maps for RFI and OPCR showing percent differences between original metric values and metric values after rotation around X and/or Y axes for a) *Cercocebus atys* and b) *Theropithecus gelada* specimens.

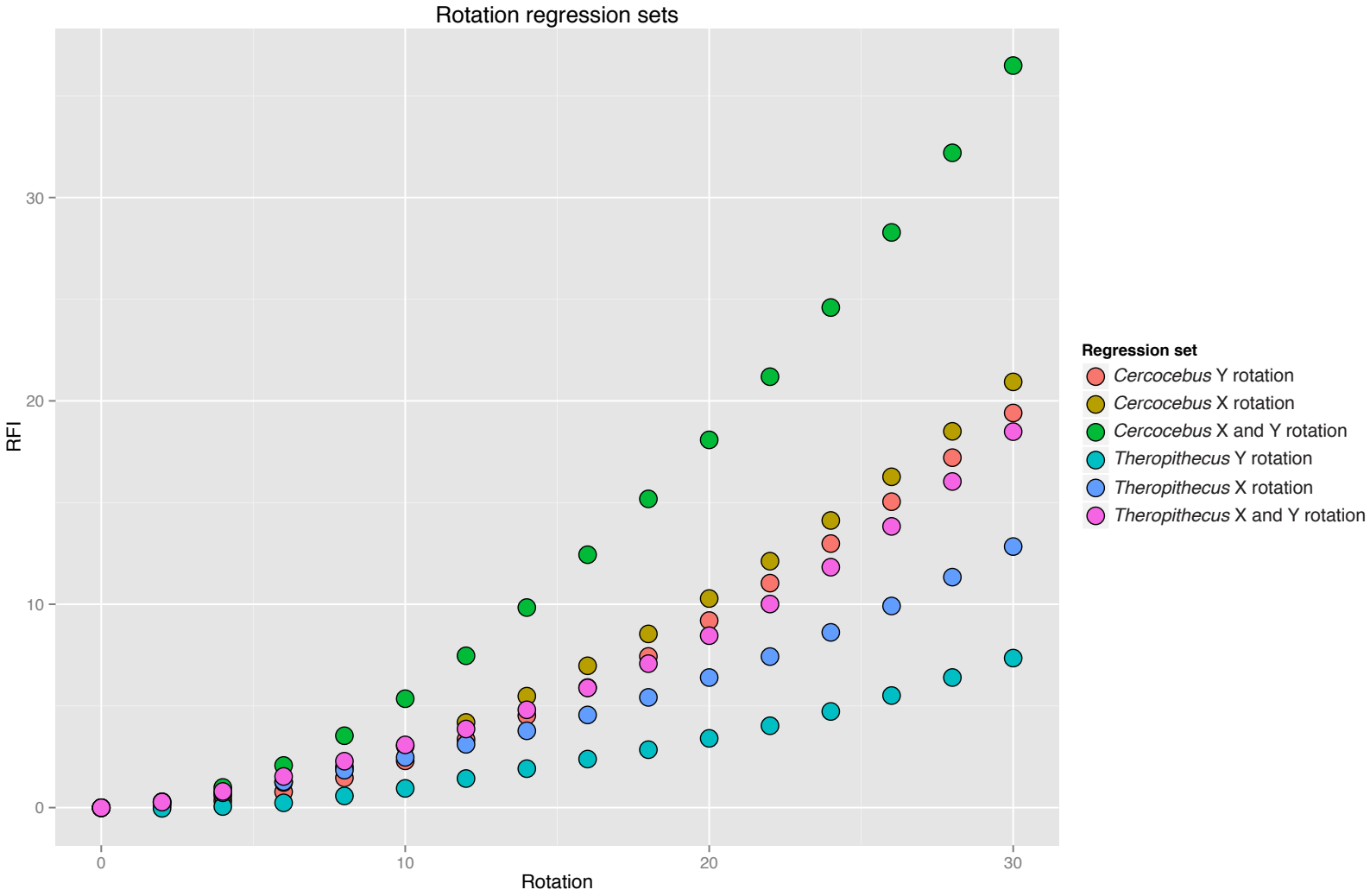

Fig 2.15. Scatter plots of RFI by mesh rotation for *Cercocebus atys* and *Theropithecus gelada* specimens for special rotation cases: rotation around the Y axis alone, rotation around the X axis alone, and rotation around X and Y axes simultaneously.

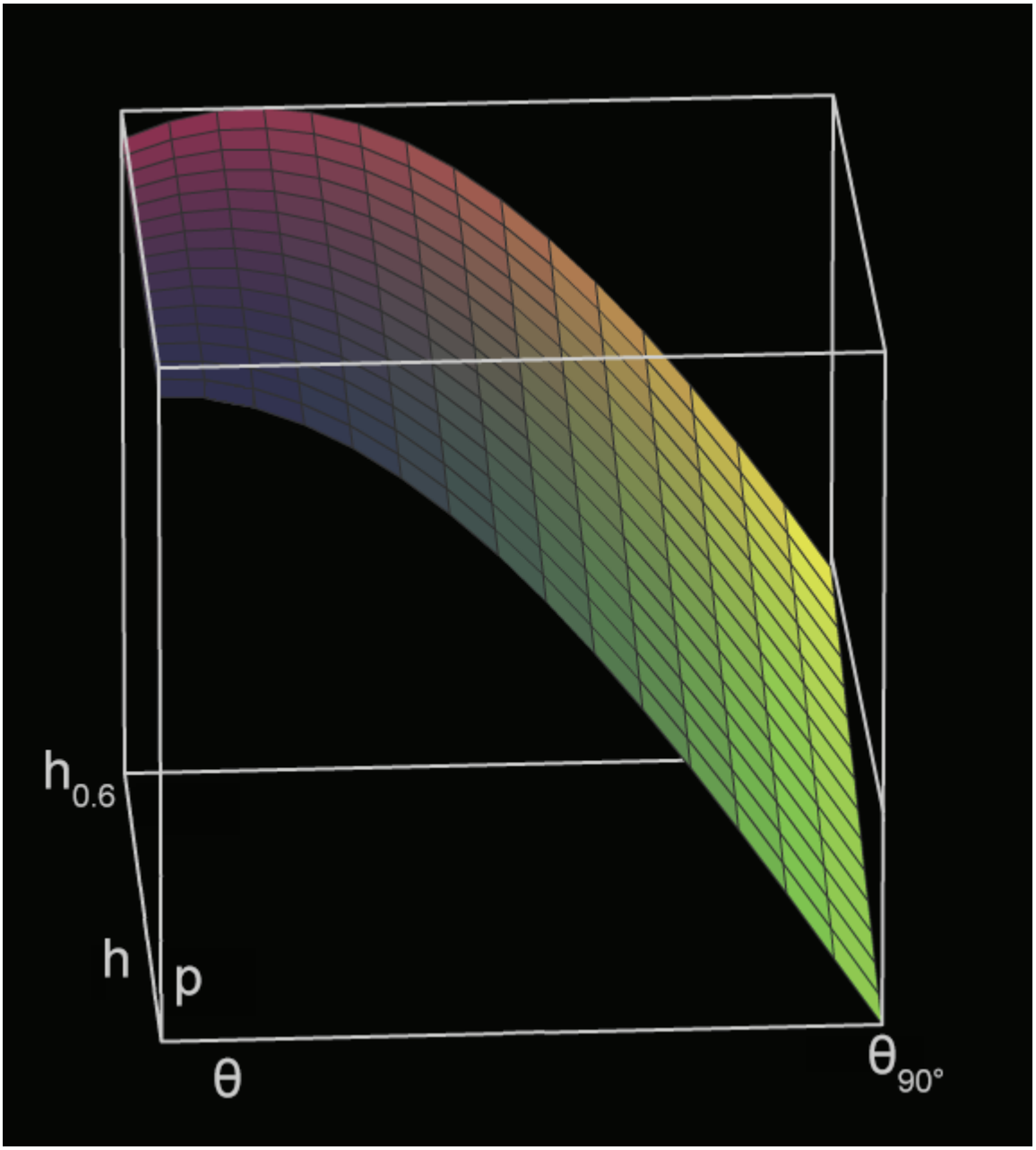

FIg 2.16. Three-dimensional plot of simplified 2D shape rotation model. See text for details on formula and plot variable ranges. Variables are as follows: *p*, width of a two-dimensional rotating rectangle with a width of 2 and a height of *h*; *h*, height of the rectangle plotted from 0 to 0.6; *θ*, angle of rotation of rectangle from 0 to 90 degrees.

Chapter 3

Diet and dental topography in extant cercopithecoids

3.1: Introduction

Cercopithecoid molars are of interest to functional morphologists because characterization of dental shape may yield insights into the selective pressures that affect molar form, the evolutionary transitions that have led to current morphological diversity, and the functional ecology of extant species. Techniques that quantitatively characterize morphology, including morphological topographic analysis, are well suited to address questions of molar shape (Ch. 1, 2). One traditional method for quantifying molar form, the shearing quotient, has been applied to cercopithecoid species in a number of studies (Kay, 1975, 1977, 1978, 1981, 1984; Kay and Covert, 1984; Kay and Hylander, 1978; Benefit, 1987; Benefit and McCrossin, 1990). A good example of these studies is Benefit and McCrossin (1990), where shearing quotients and a dietary folivory/frugivory index were assessed for a diverse sample of extant cercopithecoids and used to predict folivory/frugivory diet proportions in fossil taxa. Other studies have used morphological topographic analyses to quantify lower mandibular molar (M_2) shape in cercopithecoids (Ungar and Bunn, 2008; Bunn and Ungar, 2009; Kullmer et al., 2009; Guy et al., 2013; Guy et al., 2015). Some of these analyses have had small sample sizes either because they had a primary focus on developing analytic techniques (Kullmer et al., 2009; Guy et al., 2013) or because cercopithecoids represented a relatively small proportion of a larger sample of other primate groups (Guy et al., 2015). Because of this, interpretations of cercopithecoid functional dental morphology from these studies are limited. Two

morphological topographic analyses have focused specifically on Old World monkeys. Ungar and Bunn (2008; Bunn and Ungar, 2009) investigated surface slope, relief, and angularity in four cercopithecoid species. They found significant differences between "frugivorous" cercopithecines and "folivorous" colobines, with colobine species exhibiting higher surface slope and relief across wear relative to cercopithecines.

The cercopithecoid radiation has not been investigated with high-throughput techniques of morphological analysis as deeply or broadly as some other primate radiations, such as strepsirrhines (Boyer, 2008; Bunn et al., 2011) or platyrrhines (Ledogar et al., 2013; Winchester et al., 2014). Moreover, previous functional analyses have often not addressed certain factors that should be considered before confident conclusions can be drawn regarding molar form-function relationships. Allometry and phylogeny represent factors that influence molar morphology in conjunction with function, and it is necessary to distinguish phylogenetic or allometric effects on molar shape from functional effects. At the same time, dietary food mechanical properties and the process of tooth wear complicate our understanding of dental functional dynamics. A robust assessment of cercopithecoid dental morphology should consider all of these factors. The study presented here uses a diverse sample of extant cercopithecoids to examine molar topography in a phylogenetic context explicitly addressing dietary food material properties, allometry, and tooth wear. Because of this, each of these four factors will be discussed in turn.

Most functional morphological analyses of cercopithecoid molar shape seek to link dietary behaviors with presumed adaptations of molar teeth for overcoming mechanical defenses of foods. An increasingly large literature is available concerning

dietary preferences of cercopithecoid species and mechanical properties of dietary food items. Even so, the large majority of primate analyses of molar shape tend to sort species into categories based on dietary food item preferences: "insectivory," "frugivory," "folivory," etc. There are several issues with using this diet categorization approach for analyses of molar function, with the largest being that these categories are not actually functional in nature. Within each of these categories there is a significant diversity in mechanical properties (Yamashita, 1996; Venkataraman et al., 2014). Dietary behaviors also tend to vary greatly across time, place, and individuals even with species (e.g. Chapman et al., 2002), which undermines the precision of dietary categories that attempt to differentiate species by consistent broad differences in feeding behavior. Nonetheless, categorical bins have advantages for broad-sample analyses of molar morphology and the use of food item preference categories can be justified for a number of reasons. In any diverse sample of primates, there is necessarily variability in the detail available in the literature regarding diets of study species. In order to characterize broad trends within a radiation, it is necessary to consider some species with poorly documented dietary behaviors. Studies of food mechanical properties are far less common than studies of food item preferences, and detailed information on dietary variability between study sites, populations, and seasons is simply not available for most species. An advantage of categorical bins is they allow semi-quantitative assessment of diet and can account for partial information. But for cercopithecoid species it is possible to design categorical bins with a stronger emphasis on food mechanical properties, which should be more strongly functionally related than food item preference categorization. Yamashita (1996) described one framework for accomplishing this goal, separating Malagasy lemur species

into three diet categories based on food material properties. These categories were durophagy for species that habitually consume hard food objects, elasticophagy for species that habitually consume tough food objects, and soft/brittle food feeding for species that consume soft, brittle food objects. A modification of this approach is used here.

Studies of cercopithecoid molar form-function relationships have also often not considered phylogenetic interrelatedness in depth. Because species are interrelated they cannot be considered independent units for statistical analysis (Felsenstein, 1985). This is especially problematic in combination with dietary categories that split all cercopithecoid species into "frugivorous" and "folivorous" bins, because typically all frugivores are cercopithecines and all but one folivore are colobines. In this case it is difficult to determine to what degree differences between dietary categories are functional in nature or are the product of possibly non-functional morphological differences that were present in the respective common ancestors of extant cercopithecines and colobines. This issue is compounded by the relatively restricted samples used by previous analyses since consideration of phylogenetic influence often requires a diverse sample of taxa. A diverse sample of cercopithecoid species would allow a more robust estimation of phylogenetic and functional causes of morphological variation.

While some topographic analyses of non-cercopithecoid primate radiations have considered phylogeny (Boyer, 2008; Winchester et al., 2014), only one topographic analysis of primate molar morphology has previously investigated whether topographic signals are allometrically influenced. Boyer (2008) tested correlation between surface area and 2D projected area in a broad sample of euarchontans dominated by strepsirrhine

species, because allometric influences on relief index should produce a non-isometric relationship between surface area and a measure of absolute size such as 2D projected area. Surface area was indeed found to scale with isometry with 2D projected area, and it was concluded that relief index is not allometrically influenced in the species considered (Boyer, 2008). Yet there are possible reasons why molar topography could be affected by body size, not least because neither surface curvature (DNE) or complexity (OPCR) have been assessed for allometric signal in primates. Some occlusal traits that contribute to molar shape such as shearing crests have been found to be negatively allometrically scaled with respect to metabolic rate (Kay, 1975, 1978). Energy requirements for primate species scale with body size and variably sized species face different challenges regarding food processing (Kleiber, 1961; Kay, 1975). At the very least, a larger tooth has more space for tooth surface features compared to a smaller tooth (and vice versa), and this may create selective pressures for modifications of molar occlusal shape in large or small individuals. This situation is complicated by the fact that molar tooth size is itself functionally influenced in some cases as well as scaling positively allometrically (Kay, 1975, 1978; Gingerich and Smith, 1985; Strait, 1993a). Kay (1975, 1978) and Strait (1993a) have observed for all primates and small-bodied prosimians respectively that folivorous and/or insectivorous species tend to have larger molars for their body sizes and frugivorous species tend to have smaller molars for their body sizes. Additionally, a comparative study of second mandibular molar (M_2) topography of strepsirrhine and platyrrhines has found that platyrrhine species have smaller M_2s relative to body size but greater M_2 relief compared to strepsirrhine species (Winchester et al., 2014). This has been suggested to represent two different functional solutions –

increasing molar relief or size – to the same problem of maintaining the longevity of tooth function in the face of progressive enamel wear. Both of these findings point to the possibility of complicated relationships between molar shape, molar size, body size, and function. Despite this, topographic metrics have not been tested directly to assess whether they scale with body size. If molar topography is found to vary allometrically, this will be something that topographic analyses need to address.

Compared to phylogeny or allometry, tooth wear has been addressed by more dental topographic analyses (Ungar and M'Kirera, 2003; M'Kirera and Ungar, 2003; Dennis et al., 2004; King et al., 2005; Ungar and Bunn, 2008; Bunn and Ungar, 2009; Winchester et al., 2011). For four species of cercopithecoids, surface slope and relief were observed to decrease in more worn M_1s and M_2s. In fact, one of the original motivators driving the development of topographic analysis was a desire to more robustly account for variably worn assemblages of molar teeth than is generally possible with more traditional morphometric methods such as shearing quotients (Ungar and M'Kirera, 2003). In addition to greatly increasing possible sample sizes due to being able to measure variably worn teeth, quantitative shape measures capable of accounting for wear allow for testing of the hypothesis that primate teeth are adapted to wear in a manner that maintains functionality over time (M'Kirera and Ungar, 2003). This idea suggests that adaptations of tooth surfaces may not be simply spatial in nature but also temporal, which would make sense given the non-regenerative and long-lived nature of tooth tissues. The development of functional wear-produced secondary molar morphology has been solidly demonstrated in some mammals such as ungulates (e.g., Fortelius, 1985), but whether or not a similar phenomenon occurs in primates is more difficult to say based on current

evidence. One would expect to be able to find some functionally-linked aspect of molar shape that would either not change through wear or would increase as a result of wear, in the same way that shearing bands occur in greater number in more worn horse teeth (Rensberger et al., 1984). Some evidence from dental topographic studies may support this hypothesis. While surface slope and relief have been observed to decrease with wear, an angularity measure (the derivative of slope, or the average change in surface slope across a surface) has been found in some cases to not be significantly modified by the process of wear (Ungar and M'Kirera, 2003, Bunn and Ungar, 2008). A longitudinal study of M_2 relief, curvature, and complexity in mouse lemurs and Verreaux's siafakas found that M_2 relief and curvature decrease through wear (and age) but that complexity does not (Winchester et al., 2011). Complexity and angularity have both been interpreted as functionally related and so these emergent morphological properties may represent functional aspects of shape conserved through wear. Yet at the same time, complexity has been one of the topographic metrics mostly weakly correlated with function in primates, and analyses of angularity have produced mixed results. More work is needed here to reach firmer conclusions.

Tooth wear and its relationship to function should also be considered in a comparative context among taxa. Hominoid and cercopithecoid M_2 relief decreases with progressive tooth wear, but for most wear stages relief differences between species seem to be maintained. M_2s of *Gorilla gorilla* exhibit more relief than M_2s of *Pan troglodytes* whether those M_2s are unworn or moderately worn, even though average relief for both species decreases from unworn to moderately worn states of wear (Ungar and M'Kirera, 2003; M'Kirera and Ungar, 2003). This has also been observed for M_2s of

cercopithecoids, though the picture is more complicated for M1 (Ungar and Bunn, 2008; Bunn and Ungar, 2009). And the same trend has been observed in a longitudinal study of mouse lemurs and Verreaux's siafakas, with *Microcebus* M_2s having generally less relief than *Propithecus* throughout the process of wear (Winchester et al., 2011). This maintenance of difference may not hold for extreme wear, where the eradication of cusp topography and the creation of large dentine basins surrounded by enamel rims may cause species with previously distinct shape to converge topographically (M'Kirera and Ungar, 2003; Bunn and Ungar, 2008). In these comparative contexts, relief has been interpreted to indicate differences in functional adaptations for feeding between species as well as changes in tooth morphology across wear within species. Observations of maintenance of relief across the process of tooth wear necessarily relies on a lack of interaction between these relief signals.

Extant cercopithecoid primates make an excellent test case for a broad-scale functional topographic analysis incorporating and addressing all of the above factors. Cercopithecoid species are taxonomically, geographically, and dietarily diverse. Moreover, current knowledge of cercopithecoid dietary behaviors suggests a nuanced breadth in food item choices and mechanical properties that belies traditional divisions of these species into "frugivorous" and "folivorous" categories. Examples of this include recognition of obligate hard object feeding in some papionin species (Daegling et al., 2011; McGraw and Daegling, 2012), obligate consumption of extremely tough grass components in *Theropithecus gelada* (Venkataraman et al., 2014), surprising amounts of folivory among guenons like *Cercopithecus mitis* (Chapman et al., 2002), and seed predation in *Colobus satanas* (Poulsen et al., 2002). Yet despite this dietary variation,

extant cercopithecoids are united in exhibiting a derived bilophodont molar configuration. Neither strepsirrhine nor platyrrhine primates have this level of similarity in molar occlusal organization, and so cercopithecoids constitute an excellent group from which to test the ability of topographic methods to detect possibly subtle functional signals in molar shape. Cercopithecoid species also span a wide range of body sizes, meaning they are ideal to investigate possible allometric influences on morphology.

The study presented here quantifies cercopithecoid M_2 topographic shape in the context of dietary food mechanical properties using phylogenetically-informed methods to investigate molar form-function relationships in this clade. Relationships between M_2 topography and allometry and wear are also considered. Hypotheses of this study include:

- Cercopithecoid dental topography reflects dietary food mechanical properties, even after taking phylogeny into account.

- Molar topography does not scale allometrically.

- Molar shape maintains functionality for overcoming food mechanical defenses throughout all but the final stages of progressive wear.

3.2: Methods

3.2.1: Study Sample

The sample for this study consists of 229 M_2s belonging to 23 cercopithecoid species (Table A3.1). This sample represents a significant proportion of cercopithecoid

phylogenetic diversity. Out of the 22 currently recognized cercopithecoid genera, 19 are present in this sample. *Erythrocebus* is not included in this sample, but the closely related *Chlorocebus* is represented. *Erythrocebus* and *Chlorocebus* likely represent a clade to the exclusion of all other species (Disotell, 2000). *Simias* is also absent but the closely related genus *Nasalis* is present, and these genera also likely form a clade (Disotell, 2000). As a result, minimal phylogenetic diversity is lost by the absence of these species in the sample. *Rungwecebus* is also absent, which is not surprising given the very recent discovery of this genus (Davenport et al., 2006). This sample represents both likely clades within cercopithecinae – cercopithecins and papionins – as well as both African and Asian groups within the colobinae. Species considered here also have considerable diversity in both body size and behavior. Mean body masses for species here range from 1.6 kg for females of *Miopithecus* to 31.6 kg for males of *Mandrillus* (data collected from Smith and Jungers [1997], original citations located there). Behaviorally, the species here exhibit considerable diversity in locomotive, social, and feeding adaptations.

To derive this sample of 229 M_2s belonging to 23 species, approximately 500 M_2 specimens were accessed directly from the collections of natural history museums in the United States, United Kingdom, and France (see Table A3.1 for list of museums). An additional 116 M_2 specimens were also graciously provided to JMW by Doug M. Boyer and Elizabeth M. St Clair. This initial assemblage of M_2s covers at least 56 cercopithecoid species and includes all cercopithecoid genera except *Rungwecebus*. Because the majority of specimens included M_1 and this dissertation focuses on the entire molar tooth row in addition to M_2 (see Ch. 3), a quantitative wear score was recorded for each M_1 in this assemblage. Wear scores range from 0 to 5 and increase in increments of

0.5 from less worn to more worn states. A score of 0 indicates a tooth prior to functional occlusion, and 5 indicates a near-total obliteration of occlusal morphology, typically resulting in a single large central dentin basin surrounded by marginal enamel rims. A score of 0.5 indicates no visible significant wear on a tooth surface, and a score of 1.0 indicates at most a "pin-prick" dentin exposure on cusps. Beyond this, increasing scores indicate progressive wearing down of cusps and crests and increases in dentin exposure. Importantly, though, for each specimen increasing wear scores between 0.5 and 5 were scored relative to other specimens of that species and not relative to the entire sample. In other words, wear scores are useful for charting M_1 tooth wear relative to other specimens within a species. These scores were used to collect specimens for each species that together represent a wide range of wear states but which nonetheless primarily consist of relatively less worn molars. This method also sidesteps issues of possible differences in wear processes between species. But this does mean that these wear scores should not be used to compare specimens between species. Wear scores for the 229 M_2s used in these analyses are included in Table A3.2.

The 23 species in the sample were chosen from this larger assemblage, with the intent to maximize phylogenetic disparity while also allowing for efficient analysis. For each species chosen, approximately 10 specimens were selected when possible. When fewer than 10 specimens were available for a species, as many were used as possible. Direct visual examination of M_2s and M_1 wear scores (because M_2 wear should still be linked to the degree of M_1 wear) were used to assess degree of M_2 wear, and extreme degrees of wear were avoided. Descriptive statistics of M_1 wear scores per species are

provided as Table 3.1a. This sample was used to assess dental topography of primary M_2 morphology in the context of feeding behavior.

To consider secondary M_2 morphology resulting from wear and to compare changes in topographic metrics through wear, a secondary smaller sample was established of 63 M_2s with more variable wear from five cercopithecoid species (Table A3.1, secondary sample). Four of the species are also included in the primary sample: *Colobus guereza*, *Macaca fascicularis*, *Papio cynocephalus*, and *Theropithecus gelada*. For *C. guereza*, *M. fascicularis*, and *T. gelada*, both means and standard deviations of M_1 wear scores are greater than those from the primary sample. The same specimens are used for *Papio cynocephalus* in both samples. *Cercopithecus campbelli* is the final specimen in the secondary variably worn sample. This species is not in the primary sample, though a congener (*Cercopithecus mitis*) is. *Cercopithecus campbelli* was used because available specimens showed more visible variation in wear states compared to *C. mitis* in terms of both less worn and more worn M_2s. Therefore, using *C. campbelli* in this sample provides a better characterization of possible wear states in *Cercopithecus*. Descriptive statistics of M_1 wear scores for the secondary variably worn sample are provided in Table 3.1b.

Species were sorted into four dietary categories based on observations of feeding behavior present in the literature (Table 3.2, Fig. 3.1). The dietary categories used in this study are hard object feeding, soft object feeding, moderately-tough object feeding, and extremely-tough object feeding. In contrast to previous analyses that have sorted species into dietary categories based on gross dietary food type (frugivory, folivory, etc.) this approach sorts species into categories based on mechanical properties of food items. The

categories represent a modification of the method of Yamashita (1996). Hard object feeding describes the habitual consumption of foods that exhibit high hardness or simultaneous high hardness and toughness. Examples of food items that fall into this category include seeds, nuts, or unripe fruits with high hardness values, such as the extremely hard *Sacoglottis gabonensis* seeds that *Cercocebus atys* is known to feed on in the Tai Forest of Cote d'Ivoire (Daegling et al., 2011). Moderately-tough object feeding describes the habitual consumption of foods with low hardness and moderate to high toughness as measured by mechanical tests such as scissors or wedge tests (Lucas et al., 2001). Extremely-tough object feeding describes the habitual consumption of foods with low hardness and with high to extreme fracture toughness values. The two tough object feeding categories primarily distinguish between the folivorous diets of colobines and the obligate grass consumption of *T. gelada*, since significant differences between fracture toughness values of food items have been observed between *T. gelada* and colobines (Venkataraman et al., 2014). Moderately-tough object feeding colobines tend to have diets marked by the presence of moderately tough leaves, both young and mature (e.g., Davies et al., 1999). In some cases colobines are also known to predate substantially on tough seeds, and most species also supplement diets with unripe or ripe fruits (Teaford and Lucas, 1994; Davies et al., 1998). Soft object feeding describes the habitual consumption of foods that are neither high in hardness or toughness, and includes species that do not fall into any other category. This category of foods mostly includes ripe fruits with low hardness and toughness values such as the *Uvariopsis congensis* fruits consumed by *Cercopithecus mitis* (Chapman et al., 2002), but can also include other less frequently consumed food items such as invertebrates without hard exoskeletons.

Dietary categories are assigned here using a balance of estimated food material properties for common dietary food objects compared to estimated food material properties for uncommon dietary food objects. As with most primate species, analyses of feeding and food material properties suggest that some cercopithecoid species often consume foods with wide ranges of material properties (Wieczkowski, 2009). Behavioral observations also suggest that many primates prefer to consume less mechanically resistant foods, falling back on more resistant foods when other more preferable foods are not present (Lambert et al., 2004). Mechanical properties of uncommon food objects affect dietary categorization when uncommon food objects are observed to represent a substantial portion of all foods consumed for a species. Otherwise, mechanical properties of common food items guide dietary categorization. The subjectivity of this approach is recognized. Ideally it would be possible to create a quantitative index of food item mechanical properties to describe primate diets. However, doing so is currently impractical for the cercopithecoids considered here. The literature lacks detailed dietary observations for some genera, such as *Mandrillus* or *Lophocebus* (McGraw and Daegling, 2012; McGraw et al., 2012). And paradoxically species with very detailed dietary observations such as *Cercopithecus mitis* show incredible feeding diversity across populations, geography, and seasons (Chapman et al., 2002). Qualitative dietary categorizations allow for characterizing both subjective descriptions of diet and quantitative observations of dietary diversity.

Because of the diversity of diets in this sample, it is worth commenting on the categorization of certain species. The high diversity of feeding object choice in *C. mitis* has already been mentioned, but even across this diversity the large majority of food

objects are unlikely to be mechanically resistant in terms of either hardness or toughness (Chapman et al., 2002). The same is true of all cercopithecins considered here, and so these species are categorized as soft object feeders. *Miopithecus ogouensis*, which may be a cercopithecin or a sister taxon to cercopithecins, is assigned as a soft object feeder. Despite this, *Miopithecus* also consumes a non-trivial number of insects with chitinous shells (Guatier-Hion, 1988). This may be related to the small size of this species. Three papionin species – *Cercocebus atys*, *Mandrillus sphinx*, and *Lophocebus albigena* – are considered hard object feeding. *Cercocebus atys* diets have been recorded to habitually contain nuts and seeds with extremely high hardness values, and similar qualitative observations have been made for species of *Mandrillus* and *Lophocebus* (Daegling et al., 2011; McGraw and Daegling, 2012; McGraw et al., 2012). It is possible that *C. atys* represents an extreme example of hard object feeding, but *Mandrillus* and *Lophocebus* diets likely exhibit more hardness than those of soft object feeding guenons. Colobine species are assigned to the moderately-tough object feeding category. This represents not just the folivory with which these species are commonly described, but also the fact that these species have been observed to consume other types of food items with moderate to high toughness. For example, *Colobus guereza* has been observed at some sites to consume a very high number of high-toughness seeds (Poulsen et al., 2002). *Rhinopithecus* and *Colobus* species respectively have been observed to habitually feed on lichen and flowers, food items which have greater toughness than some young leaves that comprise a large portion of many colobine diets (Davies et al., 1999; Grueter et al., 2009).

3.2.2: Specimen acquisition and preparation

Specimen post-canine tooth rows were accessed from the collections of natural history museums in the United States, United Kingdom, and France (Table A3.1). Highly accurate molds of post-canine tooth rows were created using President Jet MicroSystem impression material (Coltene Whaledent). Plastic replica casts of tooth rows were then produced from molds using a two-part Epotek 301 epoxy (Epoxy Technology) combined with a gray pigment for opacity. Toothrow casts were digitally imaged using a Nikon XTH 225 ST μCT scanner. After μCT scan reconstruction, image Z-slice stacks were processed and triangulated to produce polygon surface meshes using Amira (FEI Visage Imaging Group). Surface meshes were pre-processed using guidelines from Chapter 2 of this dissertation while attempting to maintain comparability with previous dental topographic analyses (Fig. 3.2). M_2s were first isolated from toothrow surface scans. M_2 surfaces were then manually oriented so that the mesh XY-plane corresponded with the occlusal plane. After orientation, surfaces were cropped to include only surface polygons above the lowest point of an occlusal basin. This method maximizes inter-species variability for cercopithecoids (Ch. 2). Cropped meshes were simplified to 10,000 faces and smoothed 100 iterations with a Pagel's ʎ value of 0.6 using the Simplifier and SmoothSurface modules of Amira. The simplification algorithm used here attempts to simplify surface polygons to a target number, here 10,000, but there is some small degree of variation in the actual simplified numbers of polygons.

After simplification and smoothing, certain non-biological artifacts were present on some surfaces. These artifacts are the result of either casting, scanning, or the triangulation of surface meshes from μCT image stacks. For example, small bubbles on

M_2 surfaces can result from casting. Triangulation of surface meshes from μCT image stacks can produce erroneously sharp angles or pits across a surface. Geomagic (3D Systems) was used to remove these artifacts and to fill in subsequent surface holes resulting from artifact removal. In some cases, this resulted in surface meshes that were composed of polygon numbers either below or above 10,000. The average number of polygons for surface meshes in this sample is 9,994 with a standard deviation of 134 faces (Table A3.2).

3.2.3: Variables measured

Topographic variables Dirichlet normal energy (DNE), relief index (RFI), orientation patch count rotated (OPCR), two-dimensional area (2DA), and three-dimensional area (3DA) were calculated from each prepared M_2 surface mesh using the MorphoTester application (Ch. 2). DNE characterizes local surface bending across a surface mesh by quantifying change across the surface normal map. DNE was measured in MorphoTester with condition number checking, outlier removal based on energy values (energy density * polygon area) at the 99.9^{th} percentile, and with no implicit fairing smooth. As noted above, there is some variation in numbers of polygons comprising meshes in this sample. Because of this, DNE values calculated by MorphoTester were divided by mesh polygon number prior to analyses. This means that DNE values in this chapter are equivalent to the "DNE/polygon" values from Chapter 2 of this dissertation. This is justifiable because of the fairly low variance in mesh polygon number for surfaces here (Ch. 2). Nonetheless, both polygon numbers per surface mesh and standard unadjusted DNE values are provided in raw data tables (Table A3.2). RFI is

a ratio between mesh surface area over the 2D area of the surface's projection onto the XY plane. This metric characterizes surface relief. OPCR characterizes surface complexity by counting contiguous patches of surface sharing the same facing. OPCR was measured in MorphoTester using a minimum patch size of five. Thinking of tooth surfaces as collections of surface features acting as tools to break down foods, topographic metrics can be thought of as quantifying number or shape of surface features. OPCR largely quantifies surface feature number, RFI most strongly reflects surface feature shape, and DNE relatively reflects combinations of surface feature shape and number (Ch. 2). A second way that topographic results can be understood is that DNE and OPCR summarize whole surface shape variation local to polygons or vertices (the discrete smallest elements of shape in polygonal meshes) where RFI reflects shape as a ratio of global shape properties. 2DA was also used as a body size proxy for analyses of allometry and discriminant function analyses. For analyses of allometry, mean body masses by species for males and females were also collected from the literature for use as a second body size proxy (Table 3.3).

3.2.4: Statistical analyses

All statistical analyses were carried out using R version 3.2.2 (R Core Team, 2015). Alpha levels for all analyses were 0.05 except where otherwise noted. Statistical analyses tested for effects of allometry, diet, phylogeny, and wear proxy on topographic variables. These tests will be described in that order.

Allometry

Possible allometric influences on topography were investigated. It is predicted that topographic variables will not be influenced by allometry. Each specimen in this sample has an associated 2DA, and this variable could be used as a body size proxy for tests of allometry. But it is possible that molar area itself carries a functional signal; that is, it is possible that species that consume a particular diet may have larger molars relative to their body size compared to species that regularly consume other foods. Since dental topography is predicted to be correlated with function in cercopithecoids, using a body size proxy that is itself functionally correlated may obscure relationships between topography and allometry. Because of this, an analysis was carried out to first examine functional correlations of 2DA relative to body size. A "criterion of subtraction" approach was used for this test. A species-level regression was created using natural log of species mean 2DA as the dependent variable and natural log of average mean male and female body mass per species as the independent variable. Species mean body masses were entered into the regression and returned values were retransformed from logarithmic to arithmetic space. These returned values were used as an "expected 2DA" for each sample species. Relative 2DA was calculated as the percent difference of species mean 2DA and expected 2DA. A standard ANOVA with diet category factor was then performed on species-level relative 2DA values, followed by a phylogenetically-informed ANOVA also using a diet category factor.

Because of results from the tests above, analyses of allometric influences on topographic variables were run using both M_2 area and species mean body masses as body size proxies. A set of linear regressions was created using the natural log of species mean topographic variables as the dependent variables and the natural log of species

mean body mass as the dependent variable. A second set of specimen-level linear regressions were also created using natural log of topographic variables as dependent variables and natural log of 2DA as the independent variable. Regressions were tested for significance to assess whether topographic variables are affected by allometry.

Diet

Whether and how dental topography varies by diet between cercopithecoid species is a major focus of this study. It is predicted that dental topography will vary between species, in that DNE and RFI will increase from hard object feeding to extremely-tough object feeding but that the opposite trend will be observed for OPCR. To test this prediction, ANOVAs were performed on topographic variables DNE, RFI, and OPCR with diet category and species factors. Post-hoc pairwise comparison tests were run from these ANOVAs using Tukey's Honest Significant Difference (HSD) method to assess significant differences in topography between pairs of individual species. For each topographic variable, the number of significant post-hoc pairwise comparisons between species with dissimilar diets were compared to significant post-hoc pairwise comparisons between species in the same diet category. This provides an assessment of intra-species topographic variation between diet categories compared to within diet categories.

An additional ANOVA was also run on topographic variables using a clade factor instead of a species factor in order to examine how topography varies by higher-order phylogenetic groupings. The clades for this analysis were cercopithecins, papionins, and colobines. *Allenopithecus nigroviridis* may represent a cercopithecine or a sister taxon to cercopithecins, but for the purposes of this analyses this species was included in the

cercopithecin clade. Post-hoc pairwise comparison HSD tests were also run to assess differences in topography between specific clades.

Phylogenetically-informed analyses

Dietary categories and phylogenetic groupings of cercopithecoid species do not seem to be independent in this sample. As an example, all species in the moderately-tough object feeding category are colobines, and conversely all cercopithecins sit within the soft object feeding category. This raises concerns that any differences observed in topography between dietary categories relate more to phylogenetic influences than functional adaptations for feeding. Possible phylogenetic influences are investigated through the use of phylogenetically-informed analyses, specifically a phyloANOVA. A consensus phylogram for primates trimmed to include only sample species was downloaded from 10ktrees.fas.harvard.edu to serve as the tree data for phylogenetic analyses (Arnold et al., 2010). Phylogenetically-informed ANOVA approaches model evolution using a GLS method and use evolutionary models to account for phylogenetic relationships when testing for significant differences in traits across factor groups. This analysis uses the phylogenetic ANOVA functions present in the caper (Comparative Analyses of Phylogenetics and Evolution in R) package (Orme, 2012). These functions autocorrelate residuals from diet category means to phylogenetic tree branch lengths. Group trait means and standard errors are then adjusted by this correlation model. A trait found to be significantly different between factor groups by phylogenetic ANOVA is judged to differ even after accounting for phylogenetic interrelationships. Conversely, results which show significance by standard ANOVA but lack significance by

phylogenetic ANOVA suggest that differences between groups may be a consequence of phylogenetic influences such as taxon over-sampling.

As phylogenetic ANOVA implemented by caper can only be run on species mean data, phylogenetic ANOVAs were run for species mean topographic variables using a diet group factor. A Pagel's ʎ parameter is required for PGLS models of evolution, and analyses were initially run using a maximum-likelihood estimate of best-fit Pagel's ʎ parameter. Likelihood ratio tests were also carried out to assess whether Pagel's ʎs for each topographic variable was significantly different from 0 and 1. If Pagel's ʎ is significantly different from 0 and 1, this provides some degree of confidence regarding Pagel's ʎ estimation (presuming Pagel's ʎ is not 0 or 1). However, because the number of species here (22) is relatively small for analyses of this type, resulting probability profiles of maximum-likelihood Pagel's ʎ were not stabilized. Correspondingly, estimates of Pagel's ʎ were often not significantly different from either 0 or 1, suggesting that Pagel's ʎ cannot be confidently estimated for this dataset (see Results below). Since Pagel's ʎ provides an estimate of phylogenetic signal, this makes testing this dataset for phylogenetic influences on M_2 topography difficult.

Despite these issues, analyses can still be run, though they should be interpreted conservatively, acknowledging the methodological limitations. Two analyses were run on species mean topographic variables across dietary groups. The first of these was a standard non-phylogenetic ANOVA. Results of this analysis will be identical to those of a phylogenetic ANOVA where Pagel's ʎ equals 0. The second analysis was a phylogenetic ANOVA with estimated Pagel's ʎ of 1. Trait evolution where Pagel's ʎ equals one can be modeled as Brownian motion and suggests maximized phylogenetic

influences on a trait. If significant differences in topographic variables across functional groups are indicated by standard ANOVA and phylogenetic ANOVA where Pagel's ʎ equals one, this suggests that differences between dietary categories persist even while accounting for maximal phylogenetic signal. This approach allows a reasonably robust verification of trait differences after accounting for phylogeny if both ANOVAs are significant, since probable actual phylogenetic signal for dental topography is represented best by a Pagel's ʎ value between 0 and 1.

Discriminant function analysis

In addition to descriptive analyses of differences between species or diet categories, it is possible to construct and test predictive models of diet. This provides another avenue for insight into how dental topography varies with diet across cercopithecoids. These analyses can also be used to create a model of dietary prediction for paleoecological inferences of fossil taxa, presuming extinct taxa are closely related enough to cercopithecoids that assumptions of the predictive model are likely to apply. Discriminant function analysis (DFA) was used to construct diet models. A number of DFAs were created with dietary category as the dependent factor variable and one to four independent variables. Possible independent variables include DNE, RFI, OPCR, and 2DA as a body size proxy. All possible combinations of variables were tested, entering all variables simultaneously. Dietary predictive success was evaluated using a "leave one out" jack-knife procedure, with prior probabilities of group membership determined by group sizes. This means that specimens are by default more likely to be assigned to dietary category groups with more specimens than groups with fewer specimens prior to

the influence of predictive variables. This procedure repeatedly constructs predictive models from all sample specimens except one, and then predicts the dietary category of the missing "unknown" specimen. After cycling through the sample using each specimen as unknown, overall accuracy of models for predicting diet can be estimated. To assess predictive models of topography, predictive success of different combinations of topographic and body size variables were compared. Percentages of overall variation explained by discriminant functions and correlations of discriminant functions to topographic and body size variables (comprising a "structure matrix") were also examined.

Wear proxy analyses

Differences in relief between specimens within species are assumed to reflect both variability relating to unworn primary M_2 morphology and secondary changes on molar morphology by progressive wear. For a sample of variably worn teeth that includes significantly worn M_2s, large differences in intra-species wear likely reflect degree of wear more strongly than idiosyncratic variability in primary morphology. Proceeding from this, it should be to possible to use relief index of M_2s as an intra-species wear proxy in order to examine changes in surface DNE and OPCR through progressive wear. In contrast to the larger main sample used in previous analyses, these tests used the smaller sample of variably worn M_2s ($n = 63$) belonging to five cercopithecoid species. Linear regressions were constructed for each species using DNE and OPCR as dependent variables and RFI as the independent variable. ANCOVAs were also run to test for differences in DNE and OPCR between diet groups using RFI as a covariate.

Relationships between DNE or OPCR and RFI were also tested for each species using regressions and correlation coefficients, using a Bonferroni multiple comparisons correction to judge correlation significance.

3.3: Results

Topographic variables DNE, RFI, OPCR, 2DA, and 3DA were calculated for sample specimens for a primary sample of relatively less worn M_2s and a secondary smaller sample of variably worn M_2s. Descriptive statistics of topographic variables DNE, RFI, and OPCR are given for species, clades, and dietary categories as Table 3.4 for the primary sample and Table 3.5 for the secondary sample. DNE and OPCR are visualized for example specimens in Figs. 3.3 and 3.4. Raw data for topographic variables are presented in Tables A3.2 and A3.3.

3.3.1: Allometry

Before assessing allometric influences on topographic variables, possible correlations between dietary function and 2D M_2 area (2DA, the most easily accessible body size proxy) were investigated. M_2 areas relative to an expected body mass/molar area regression were calculated using a criterion of subtraction approach, and an ANOVA was run on relative M_2 area using a diet factor (Fig. 3.5). Descriptive statistics of relative M_2 area are described in Table 3.6 and raw data for relative M_2 area are available as Table A3.4. ANOVA indicates that M_2 area does vary significantly between dietary groups ($p = 0.007$), with extremely-tough object feeders (*Theropithecus gelada*) and soft object feeders (cercopithecins, *Macaca spp.*, and *Papio cynocephalus*) exhibiting larger

M_2s relative to body mass compared to moderately-tough object feeders (colobines) and hard object feeders (*Cercocebus*, *Lophocebus*, and *Mandrillus*) (Table 3.7).

Functional influences on relative M_2 area were also investigated in a phylogenetically-informed context. A phylogenetically-informed ANOVA was run with Pagel's ʎ value estimated with a maximum-likelihood approach. This Pagel's ʎ value was significantly different from one ($p = 0.012$) but not significantly different from zero ($p = 1$) and the probability profile for this estimation does not show an observable peak between zero and one (Table 3.8, Fig 3.6). This indicates that Pagel's ʎ cannot be confidently estimated for this analysis (see below for further discussion on this problem) and so a second phylogenetically-informed ANOVA was run with Pagel's ʎ set to one. When phylogenetic signal is assumed to be one, relative M_2 area does not vary significantly between diet groups ($p < 0.125$) (Table 3.9). It is possible that with a larger sample, Pagel's ʎ could be more confidently estimated and a phylogenetically-informed ANOVA using this estimated Pagel's ʎ would indicate that relative M_2 area does vary by diet when taking phylogeny into account. Had the phyloANOVA here indicated significance where Pagel's ʎ is manually set to one, this would be a robust demonstration of relative M_2 area varying by diet.

Because of mixed indications regarding functional influences on 2DA as a body size proxy, two sets of analyses were run to assess possible correlations between allometry and topographic variables. First species mean level analyses were run using mean body mass, and then individual specimen level analyses were run using relative M_2 area. Species mean data regressions of mean topographic variables by mean body mass are detailed in Table 3.10a and presented as Figure 3.7. No topographic variable was

significantly associated with mean body mass (DNE: p = 0.707; RFI: p = 0.889; OPCR: p = 0.586). Individual specimen data regressions of topographic variables DNE, RFI, OPCR by 2D M_2 area are detailed in Table 3.10b and presented as Figure 3.8. None of these regressions were found to be significant, though the regression of RFI on M_2 area does seem to approach significance with p = 0.0586. Both DNE and OPCR can be confidently said to not be significantly related to M_2 area for this dataset (DNE: p = 0.828; OPCR: p = 0.604).

3.3.2: Standard ANOVAs

Results from ANOVAs of topographic variables with diet factors indicate that DNE, RFI, and OPCR all vary significantly across the dietary categories considered here with $p < 0.001$ for each variable (Table 3.11). Topographic variables by dietary category are graphically presented as Fig. 3.9. While all variables were found to significantly vary by diet, *F* values of ANOVAs were highest for RFI followed by DNE and OPCR (RFI *F*: 59.517; DNE *F*: 12.107; OPCR *F*: 10.108). Results of post-hoc Tukey's HSD pairwise comparison tests are provided as Table 3.12. For DNE, all dietary categories are significantly different except hard object feeding and soft object feeding. For RFI, all dietary categories are significantly different except moderately-tough object feeding and extremely-tough object feeding. Stated another way, M_2s of *Theropithecus gelada* exhibit more surface curvature than M_2s of colobines, but relief values are more similar between these groups. M_2s of hard object feeding papionins evince less relief than soft object feeding papionins and guenons, but surface curvature is more similar between these groups. For OPCR, moderately-tough object feeding differs from all other dietary

categories, but no other significant differences are present. M_2s of moderately-tough object feeding colobines are less complex than M_2s of species from all three other diet groups. M_2s of extremely-tough object feeding *T. gelada* do exhibit the highest OPCR of all dietary categories, but no significant differences are found between this group and hard object feeding or soft object feeding.

Results from ANOVAs of topographic variables with species factors indicate that DNE, RFI, and OPCR all vary significantly across species with $p < 0.001$ for each variable (Table 3.13). Topographic variables by species are graphically presented as Fig. 3.10. In general, differences in topographic variables by species track with differences by dietary category group. Moderately-tough object feeder *Nasalis larvatus* has the highest mean DNE in the sample (246.686) and hard object feeding *Lophocebus albigena* has the lowest (193.758). Soft object feeder *Macaca fascicularis* has the highest mean OPCR in the sample (87.438) and moderately-tough object feeder *Semnopithecus entellus* has the lowest (63.962). Moderately-tough object feeder *Piliocolobus badius* exhibits the highest mean RFI in the sample (0.402) and soft object feeder *Papio cynocephalus* has the lowest (0.255). Extremely-tough object feeder *T. gelada* is noteworthy because it shows the second highest mean DNE (246.563) and the second highest mean OPCR (85.239) in the sample with mean RFI (0.351) similar to the colobine mean (0.360).

Post-hoc pairwise comparisons of topographic variables between species are presented as Table 3.14. The number of significant differences between species both across and within dietary categories are given as Table 3.15. In addition to the numbers of significant differences between species classified by diet, this table also provides total possible species pairs for each diet group combination and percentages of all possible

species pairs that were found to be significantly different for topographic variables. Comparing overall percentages of significantly different species pairs between topographic variables (Table 3.15), RFI was the most effective at partitioning inter-species variation in this sample with 72 significant species pairs (31.17%), with 71 of those being comparisons between species with different diets and only 1 between species in the same diet category. OPCR was the second most effective at partitioning inter-species variation in general with 17 significant species pairs (7.36%), with 14 being comparisons between diets and 3 species pairs with the same diets. DNE was least effective in terms of number of significant species pairs with 11 pairs (4.76%), though all of these pairs are between diets. It is also possible to compare numbers of significant inter-species pairs between diet group pairs to assess species-level variation of topography in the context of diet. For DNE, most significant differences are found between extremely-tough object feeder *T. gelada* and the other three diet groups, especially hard object feeders or soft object feeders. Hard object feeding and soft object feeding species are also not generally differentiated from each other by DNE. Neither are hard object feeding and soft object feeding species differentiated substantially from each other for RFI. Instead, RFI features a pattern whereby hard object feeding and soft object feeding species together differ from moderate and extremely-tough object feeding species. In absolute numbers, most interspecies pairs are between soft object feeding species and moderately-tough object feeding species, but this is influenced by the high number of species in these dietary groups. High proportions of hard object feeding (100%) and soft object feeding (42.85%) species are also differentiated from *T. gelada.*

For OPCR, all between diet inter-species pairs involve moderately-tough object feeding species being distinguished from species in the three other diet groups.

Results from ANOVAs of topographic variables by clade factor show that DNE, RFI, and OPCR vary between colobines, cercopithecins, and papionins (Table 3.16, Figure 3.11). RFI has the greatest inter-clade variability relative to intra-clade variability ($F = 60.18$, $p < 0.001$) followed by OPCR ($F = 16.65$, $p < 0.001$) and DNE ($F = 3.431$, $p = 0.002$). Post-hoc Tukey's HSD pairwise comparison tests were also run (Table 3.17). For RFI, colobines show significantly higher relief than either papionins or guenons. Guenons show higher relief than papionins as well, though this difference is not significant ($p = 0.126$). DNE is similar to RFI in trend with highest surface curvature seen in colobines followed by guenons and papionins. Pairwise comparisons show that for DNE only the difference between colobines and papionins is statistically significant, however. For OPCR, colobines have significantly lower surface complexity than either papionins or guenons. Papionins have greater surface complexity than guenons, though again this is not significant ($p = 0.111$).

3.3.3: Phylogenetically-informed analyses

Phylogenetically-informed ANOVAs were carried out to assess whether differences of topographic variables between diet groups retain significance after accounting for phylogenetic relationships. First, a phylogenetic ANOVA was run on species means of topographic variables using a maximum-likelihood protocol to estimate Pagel's λ values. Likelihood ratio tests were also run to assess whether Pagel's λ is significantly different from 0 and 1 to ensure confidence of Pagel's λ estimation (Table

3.18). For DNE, likelihood ratio tests show that estimated Pagel's ʎ is significantly different from one ($p < 0.001$) but not significantly different from zero ($p = 1$). For RFI, estimated Pagel's ʎ does not differ significantly from one ($p = 0.067$) or zero ($p = 1$). For OPCR, estimated Pagel's ʎ is significantly different from one ($p = 0.002$) but not significantly different from zero ($p = 1$). These analyses were run on species mean topographic variables, which means that each analysis had a sample size of 22. The Pagel's ʎ measure used here can have relatively low power to detect phylogenetic signal when fewer than 30 data points are used in analyses (Freckleton et al., 2002). These results suggest that Pagel's ʎs cannot be confidently estimated for this sample, likely because of the small sample size of species means. This is supported by probability profile plots for Pagel's ʎ estimation for each topographic variable (Figure 3.12). A well estimated Pagel's ʎ value should show a visible peak in probability with decreases in probability for Pagel's ʎ values both above and below the peak estimated value. A flat profile or a continually increasing trend with no peak suggest that Pagel's ʎ is not being well estimated for this sample.

Because of this lack of confidence in Pagel's ʎ estimation, a more robust but less informative method was used. This included standard species mean ANOVAs (equivalent to phylogenetically-informed ANOVA where Pagel's ʎ equals zero) and phylogenetically-informed ANOVAs with Pagel's ʎ manually assigned as one. Standard species mean ANOVAs are presented as Table 3.19 and Figure 3.13. Topographic variables DNE and RFI vary across diet groups with unambiguous significance (DNE: $p=0.004$; RFI: $p < 0.001$). ANOVAs of OPCR show borderline significance with $p = 0.05$. Post-hoc pairwise comparisons were run for this analysis using only three diet

groups: hard object feeding, soft object feeding, and moderately-tough object feeding (Table 3.20). This is because the extremely-tough object feeding group only contains *T. gelada*, and so for species mean analyses this diet group only possesses one value. Relief and curvature of moderately-tough object feeders are significantly greater than relief and curvature of hard object feeders or soft object feeders. Complexity of moderately-tough object feeders complexity is significantly less than that of soft object feeders. No other diet group pairs are significant by pairwise comparison tests.

For phylogenetically-informed ANOVAs of topographic variables by diet factor where Pagel's λ equals one, autocorrelated diet group means are generally similar to those from standard ANOVAs (Table 3.21). Trends of increase between diet groups are the same as those of standard ANOVAs. DNE and RFI are found to vary significantly between diet groups even with phylogenetic relationships have been accounted for. OPCR, however, loses significance ($p = 0.673$) when accounting for phylogeny.

3.3.4: Discriminant function analyses

To test the ability of dental topographic variables to accurately predict diet and to create predictive models for paleoecological inference, a set of discriminant function analyses (DFAs) were run classifying diet food material property category per specimen using topographic variables DNE, RFI, OPCR, and M_2 2D area as a body size proxy (Tables 3.22, 3.23, 3.24; Figs. 3.14, 3.15). Predictive accuracy ranged from 52.2% for DNE alone to 67.8% for all topographic variables combined with M_2 area (Table 3.22). For DFAs using single topographic variables in isolation DNE was the least accurate (52.2%) compared to OPCR (53.3%) or RFI (60.6%), though all accuracy rates are

notably better than chance. M_2 area alone predicts diet with 52.8% accuracy. Predictive accuracy is improved for each topographic variable when M_2 area is also considered. RFI is still the most effective for these analyses (65.6%), with DNE second (58.3%) and OPCR third (54.4%) in effectiveness. In fact, for all topographic variable combinations adding M_2 area increases predictive accuracy.

All discriminant function analyses with two or more variables show a first discriminant function that explains a large majority of sample variance and a second discriminant function that explains a much smaller proportion, with the exception of the DFA including DNE, OPCR, and M_2 area (DF1: 53.1%, DF2: 43.51%) (Table 3.23). For DFAs accounting for body size, M_2 area is the variable most heavily weighted on DF2 or less commonly DF1 (Table 3.24). If present, RFI tends to be the variable most heavily weighted on DF1. When DNE and RFI are combined both variables tend to be most heavily weighted on DF1, with RFI more strongly weighted. When OPCR is present with DNE or RFI it tends to be weighted on DF2 or DF3 (if present in model). For the DFA including DNE, RFI, and OPCR, DF1 is most heavily weighted on RFI, DF2 is most weighted by OPCR, and DF3 is most weighted by DNE (though DNE and OPCR both contribute non-trivially to DF1 and DF2). For the DFA including all variables, DF1 is most weighted by RFI and DNE, DF2 is weighted by M_2 area, and DF3 is weighted by OPCR.

Results from DFAs can be parsed further by examining predictive accuracy for specific dietary categories (Table 3.22). But before doing so it is worthwhile to note sample sizes per diet grouping. This sample included 27 specimens assigned to hard object feeding, 55 for soft object feeding, 86 for moderately-tough object feeding, and 11

for extremely-tough object feeding. DFAs were constructed using prior probabilities based on group size such that without any information from topographic or body size variables, specimens would be more likely to be sorted into larger groups. It is reasonable to expect therefore that larger groups will have higher rates of predictive success, and divergences from this null expectation should be given special attention. Across all analyses, the largest diet groups experience the highest predictive accuracy, with moderately-tough object feeding being accurately classified at a rate of 86.3% and soft object feeding being predicted with 55.0% accuracy. But the smallest diet group, extremely-tough object feeding, is actually more successfully classified on average with 38.2% compared to hard object feeding with 15.79%. Classification accuracy for hard object feeding across all analyses is actually quite close to the null expectation of 15.1%. However, averaging classification rates across all analyses can be somewhat deceptive with predictive accuracy of hard object feeding ranging from 0% (DNE alone) to 44.4% (all variables) compared to moderately-tough object feeding ranging from 80.5% (OPCR and M_2 area) to 88.5% (DNE and RFI).

On the level of individual analyses, it is generally true that increasing the number of variables in a DFA improves its predictive accuracy. The DFA including all variables has either the highest predictive accuracy or close to it for three of the four diet groups. The single exception to this is for extremely-tough object feeding where the all-variable DFA reaches 63.6% predictive accuracy while a DFA using M_2 area alone reaches 72.7% and a DFA using DNE and M_2 area achieves 90.9% accuracy. Given results from DFAs and ANOVAs (see above), this result is likely explained as a combination of two facts: that RFI explains more significant variance related to diet across this sample than any

other topographic variable, and that *T. gelada* evinces M_2 relief similar to colobines but unusually high M_2 curvature and body size. For the all-variable DFA, DF1 is most heavily weighted by RFI and ANOVAs generally show greater *F* values for RFI compared to DNE or OPCR (see above). RFI has the most statistical power for differentiating diet in this sample, and the all-variable DFA weights classification results by RFI accordingly. But RFI of the extremely-tough object feeding group is not significantly different from the moderately-tough object feeding group, and so the all-variable DFA classifies *T. gelada* at a lower rate than a DFA using M_2 area alone. In fact, the 63.6% accuracy of the all-variable DFA for extremely-tough object feeding is identical to the performance from a DFA using RFI and M_2 area. Meanwhile, a DFA using DNE and M_2 area successfully classifies 90.9% for extremely-tough object feeding specimens. This suggests that while *T. gelada* has distinct DNE from species in other diet groups, this difference is being downweighted in the combined DFA because of DNE's lessened explanatory power across the entire sample relative to RFI. At the same time, it should be noted that DFAs using either DNE or RFI alone produce no accurate classifications for extremely-tough object feeding. The large body size of *T. gelada* must be leveraged alongside topographic variables to achieve successful prediction. But when this is done, DNE is more successful for classifying extremely-tough object feeding than RFI.

3.3.5: Wear proxy analyses

M_2 surface curvature and complexity were regressed on surface relief across five species with the goal of examining topographic change across gross tooth wear. Whole

sample regressions of DNE and OPCR by RFI show that OPCR significantly decreases with increase of RFI but that DNE is not significantly correlated with RFI across this sub-sample (Table 3.25, Figure 3.16).

To take possible inter-species differences into account, ANCOVAs of DNE and OPCR were run using a species factor with RFI as covariate (Table 3.26, Figure 3.16). The ANCOVA of OPCR shows that OPCR across species has a significant negative relationship with RFI. As RFI decreases, OPCR increases. No significant interaction is found between species and RFI on OPCR, which indicates that slopes of RFI by OPCR do not differ between species considered. There is a significant effect of species on OPCR, which shows that Y-axis intercepts of OPCR by RFI regressions do differ between species even if regression slopes do not. This means that OPCR increases at a similar rate with RFI decrease for all species, but at the same time there are species-specific differences in OPCR that are generally maintained between species as OPCR changes. Significant differences in Y-axis intercepts are interpreted as reflecting inter-species differences in unworn primary M_2 morphology. This is further supported by inter-species differences being observed in both mean RFI and OPCR above. Although the whole-sample regression indicates that DNE has no significant relationship with RFI, an ANCOVA suggests that DNE has a significant positive relationship with RFI at $p = 0.041$ with a significant effect from species and no evidence for interaction between these factors.

To more fully examine intra-species relationships between DNE or OPCR with RFI, regressions of DNE and OPCR on RFI were constructed for each of the five species considered here (Table 3.27). No regressions of DNE on RFI yielded significant results

for any species. For OPCR, *Papio cynocephalus* and *Theropithecus gelada* showed a significant negative relationship between OPCR and RFI. Results from *Colobus guereza* also seem to approach marginal significance with $p = 0.021$ where the Bonferroni-corrected critical significance level is $p < 0.01$.

3.4: Discussion

3.4.1: Allometry

If topographic variables scale allometrically then this may need to be addressed prior to drawing conclusions for relationships between topography and masticatory function. The most accessible per-specimen body size proxy for this study is M_2 area, but M_2 size has been shown to be influenced by dietary preference as well as body size (Kay, 1975; Gingerich and Smith, 1985; Strait, 1993). Therefore possible functional effects on M_2 area were investigated prior to assessing allometry in topographic variables.

Results indicate little if any evidence for functional influences on relative M_2 area in the cercopithecoids considered here. When species-mean M_2 area is measured relative to body mass using a criterion of subtraction, extremely-tough object feeders and soft object feeders have significantly larger M_2s for their body size compared to moderately-tough object feeders and hard object feeders. However, these dietary groups contain respectively one species and an entire sub-family, which raises the question of whether phylogenetic differences between cercopithecoid clades represent a better explanation for differences in M_2 size. Specifically, comparing clades cercopithecins have greater relative M_2 area than papionins, while colobines may have smaller relative M_2 area. A phylogenetically-informed analysis maximizing possible phylogenetic covariation in

relative M_2 area does not indicate that relative M_2 area varies between diet groups. Phylogenetic covariation was maximized for this analysis because the number of species included in the sample here does not allow for a confident estimation of phylogenetic signal (this is a theme that will be returned to throughout this discussion). It is possible that in a larger sample where phylogenetic covariation could be more confidently estimated, differences between dietary groups could be detected when accounting for phylogeny. At the same time, results below indicate that even when maximizing phylogenetic covariation, surface curvature and relief continue to differ significantly between diet groups. Had relative M_2 area been found to vary significantly between diet groups after maximizing phylogenetic signal, this would represent a robust indication of functional influences on M_2 size relative to body size (absolute M_2 size predicts diet with 52.8% accuracy, but is largely a body size measure; see below). But it did not, and therefore no such conclusion can be made here.

Additionally, it can be observed that the trends observed between diet groups here do not match conclusions from other studies of relative M_2 size in primates. Kay (1975) found that primate folivores and insectivores have larger molars than would be expected based on their body size while frugivores have relative smaller molars. The term folivore could possibly be applied to the extremely-tough object feeder *Theropithecus gelada*, but this does not address "folivorous" moderately-tough object feeding colobines exhibiting relatively small molars compared to "frugivorous" soft object feeders. Strait (1993) found similar trends in prosimian faunivores and frugivores, though she could not address folivory in her analyses due to her sample being made up of small-bodied species. Given both the weakness of the evidence found here for functional influences on M_2 area and

the contradictions between that evidence and other primate studies, the null hypothesis of no functional influence on M_2 area is conservatively not rejected.

To provide the best possible assessment of potential allometric influences on M_2 topography, topographic variables were tested for allometric influences using species-mean body mass and per-specimen M_2 area. Species-mean M_2 topography does not seem to scale with body mass here. Similarly, there is no evidence to suggest that surface curvature or complexity scale with M_2 area. Surface relief has a negative relationship with M_2 area that approaches but does not reach significance. If surface relief were to be shown to negatively scale with M_2 area, this would be interesting in light of Ungar and M'Kirera's (2003) suggestion that relief index quantifies a surface property very similar to relative molar shearing crest length. A specific shearing crest, the cristid obliqua, has previously been shown to be negatively allometric with respect to metabolic rate (Kay, 1975). But again this relationship is only marginally significant at best.

A seeming lack of allometric influences on topography is interesting, given that primate energy requirements and food processing needs scale with body size (e.g., Kleiber, 1961; Kay, 1975; Hayssen and Lacy, 1985; Ross et al., 2009). In primates, size-related changes in feeding can include modifications to daily feeding time, chew cycle duration, food volume per chew, or daily food volume, and size-related changes in feeding seem to relate to size-related changes in food material properties (Ross et al., 2009). Any of these changes to feeding behavior could be possibly linked to topographic adaptations, whether topography allows new feeding behaviors or permits symplesiomorphic feeding behaviors at larger or smaller body sizes. And yet results show no evidence for a relationship between topographic variables and body size proxies.

There are multiple possible explanations for this. It is possible that tooth shape divorced from size is adapted primarily to mechanical defenses of food in a way that is insensitive to body size scaling (aside from differently-sized species being able to exploit food tissues with different mechanical properties). Lucas' (2004) extensive engineering model of tooth size and shape suggests a framework in which tooth shape is determined by mechanical properties of food materials and not by properties such as particle size or volume. Lucas (2004) in fact suggests generally different causes of tooth size and shape scaling, though he also notes the difficulty of measuring shape independent of tooth size. Compared to more traditional morphometric techniques, topographic metrics may actually represent a quantitative description of shape more divorced from size than has previously been possible. At least, topographic metrics such as surface curvature and complexity seem to reflect relatively "emergent" properties of surface shape compared to more traditional methods such as shearing quotients (Ch. 2). This could possibly explain the lack of significance found here when testing surface curvature and complexity for allometric influences.

Alternatively, it is possible that cercopithecoids represent a poor sample on which to test allometry. Radiations such as strepsirrhines or platyrrhines exhibit a relatively wider range of molar cusp configurations. As an example, some species exhibit M_2s with large reductions in either topographic relief or size (*Daubentonia* and *Callithrix,* respectively) and other species approach cercopithecoid-like bilophodont configurations (*Propithecus* and *Alouatta*). Comparatively, cercopithecoid M_2s exhibit a common bilophodont molar configuration, although there is still significant morphological variation between bilophodont M_2s. Cercopithecoid bilophodonty and its relationship to

dental topography will be discussed further below, but it is possible that a primate sample with more variation in molar shape would show allometric changes in surface topography. If that were the case, it would also need to be explained against the fact that cercopithecoids show a diverse array of body sizes and dietary behaviors. In any case, results here suggest that it is possible to test for functionally-related differences in molar topography between cercopithecoid species without accounting for allometry.

3.4.2: Molar topography and diet

Second mandibular molar topography of extant cercopithecoids varies according to the mechanical properties of consumed food items. Most of this variation in topography is expressed as change in surface relief compared to change in curvature or complexity. Cercopithecoid M_2s typically exhibit a bilophodont configuration of two pairs of cusps connected by variably prominent lophs, and results here indicate that most diet-correlated changes in tooth morphology are caused by the raising of cusps, lophs, and shearing crests in tough object feeding species compared to hard object feeding or soft object feeding species. This raising and sharpening results in increased surface relief. This generally matches conclusions from more traditional methods of characterizing morphology (Lucas and Teaford, 1994). M_2s of hard object feeding species also show less surface relief than soft object feeding species, which is consistent with topographic analyses from strepsirrhines and platyrrhines (Winchester et al., 2014). Moderately-tough object feeding colobines and extremely-tough object feeding *T. gelada* do not show any difference in relief, contra predictions. Like surface relief, curvature also significantly varies across cercopithecoid diet groups. Species that consume more foods with higher

Young's modulus values have M_2s that have more bent surfaces, likely from sharper and more elaborate cusps, crests, and lophs. Surface relief and curvature do not have identical patterns of differences between diet groups. *Theropithecus gelada* M_2s are more curved than those of colobines, while hard object feeding and soft object feeding groups do not differ significantly in M_2 surface curvature. Nonetheless, both surface curvature and relief can be observed to vary across diet groups even when maximum possible phylogenetic covariance is taken into account (i.e., when PGLS analyses are run with Pagel's λ set to one), providing solid support for these aspects of molar topography being strongly associated with dietary behavior in these species.

Compared to surface curvature and relief, there is less evidence to suggest that molar complexity is correlated with diet in cercopithecoid M_2s. Standard analyses indicate that complexity does vary between cercopithecoid diet groups, with moderately-tough object feeding colobines expressing less complex molars compared to any other diet group. But because of the distribution of species within the dietary groups considered here, this result can be restated simply as colobine species having less complex M_2s than cercopithecine species. Correspondingly, a phylogenetically-informed analysis indicates that surface complexity does not vary between diet groups when phylogenetic relationships are accounted for. It is possible that differences in complexity here reflect differences between the respective common ancestor species of the cercopithecine and colobine clades. This of course would not mean that complexity is not necessarily a functional indicator, as differences in complexity between cercopithecine and colobine common ancestors could be related to long-standing differences in dietary behaviors as is often thought to have been the case for these clades (Benefit and McCrossin, 1990).

Results from topography across cercopithecoids can be compared to other dental topographic analyses of primate groups such as prosimians or platyrrhines (e.g., Boyer, 2008; Bunn et al., 2011; Winchester et al., 2014). Comparing *F* values from ANOVAs between analyses and topographic variables can provide an indication of which aspects of shape best explain inter-species shape variation in each group. The cercopithecoid pattern could be summarized as one where the most variation is explained by relief followed by curvature, and where complexity shows mixed results. This is reasonably similar to the pattern observed for both platyrrhines and prosimians, where surface relief followed closely by surface curvature capture the most inter-species variation relative to intra-species variation (Bunn et al., 2011; Winchester et al., 2014). Surface relief and curvature did have nearly equal *F* values for platyrrhines (RFI: F = 75.139; DNE: F = 72.695), however, while these values are notably dissimilar in cercopithecoids (RFI: F = 55.39; DNE: F = 12.8). Prosimian *F* values sit between these extremes (RFI: F = 87.260; DNE: F = 79.205) (Bunn et al., 2011). For analyses of all three groups, complexity was found to characterize less variation than surface relief or curvature. Complexity in platyrrhines and strepsirrhines was also observed to not significantly vary between diet groups when phylogenetically-informed analyses were used (Winchester et al., 2014).

From the trends of variation in cercopithecoids, platyrrhines, and prosimians it is possible to suggest that across these very diverse radiations, most change in M_2 topography correlated with diet is expressed through modifications of surface relief and curvature. Compared to relief, complexity plays a smaller role in diet-linked morphological variation here. Topographic complexity relates to the number of features or tools on a tooth surface while relief and curvature both relate to a combination of

feature number and feature shape, with curvature being relatively more sensitive to combinations of these factors (Ch. 2). Within these primate groups, modifications of tooth shape related to diet likely occur mostly through changing the shapes and positions of cusps and crests in conjunction with adding or removing small cuspules or other surface features and not through modifying gross-scale molar configuration which would be more strongly captured by a complexity measure. If complexity is better equipped to quantify relatively gross scale changes in morphological organization, this metric might give more insights from a sample considering morphological changes across primate radiations instead of within them. This would be consistent with complexity being shown to carry functional signal in extremely diverse mammalian samples (Evans et al., 2007; Zohdy et al., 2008). And this is not to say that complexity does not correlate with function in the primate radiations considered thus far. To the contrary, complexity is capable of strongly reflecting unusual molar morphologies seemingly adapted for consuming highly fibrous and tough food items in species such as bamboo lemurs (Bunn et al., 2011) or pitheciine seed predators (Ledogar et al., 2013; Winchester et al., 2014). This topic will be returned to shortly below.

In addition to discussing differences in topography between diet groups, it is possible to consider dental topography of certain sample species in the context of diet. *Miopithecus ogouensis* is a cercopithecin characterized as a soft object feeder, but *M. ogouensis* M_2s show the third highest mean surface curvature in the entire sample. Quantified mean curvature for this species is greater than any other soft object feeding species, though the degree of difference is not statistically significant. *Miopithecus ogouensis* also shows high RFI, though this species is joined here by possible

cercopithecin sister taxon *Allenopithecus nigroviridis*. *Miopithecus* represents the smallest cercopithecoid genus and, unlike other cercopithecines, at least a third of the diet of this genus is comprised of arthropods (Gautier-Hion, 1988). Increased intake of tough arthropod shells rich in structural carbohydrates may explain higher bending and relief in the M_2s of this species. If so, this could represent an example of morphological diversity among cercopithecins reflecting an already recognized diversity of diet in this clade.

Among moderately-tough object feeding colobines, this sample includes two closely-related species pairs where differences in feeding behaviors might suggest that differences in dental topography should be found. *Colobus satanas* has been observed to feed almost exclusively on hard and fibrous seeds in some populations while congener *Colobus guereza* occasionally predates on seeds but more commonly subsists on soft and tough fibrous leaf tissue (Poulsen et al., 2002; Fashing et al., 2007). *Colobus satanas* evinces greater complexity and lower relief compared to *C. guereza*, which is in line with expectations of topography, though these differences are again not statistically significant. Surface curvature between these species is very similar. A second pair of Asian colobine species, *Presbytis melalophos* and *Trachypithecus obscurus*, might also be expected to differ in dental topography given that *P. melalophos* has been characterized as substantially more frugivorous than *Trachypithecus obscuris* (Fashing, 2007). Despite this, and against expectations, *P. melalophos* has greater surface relief and complexity than *Trachypithecus obscurus*, though these differences are again non-significant.

In terms of both molar topography and dietary behaviors, perhaps the most unusual species in this sample is the gelada baboon, *T. gelada*. This species has a diet that

consists almost entirely of grass components, some of which have very high Young's modulus values (Venkataraman et al., 2014). Certainly these grass components are more mechanically resistant than the leaves and other materials that make up colobine diets. *Theropithecus gelada* also has unique topographic characteristics compared to the rest of this sample, with M_2s that express surface relief similar to colobines but higher than hard object feeding or soft object feeding species, surface complexity similar to hard object feeding or soft object feeding species, and surface curvature that is higher than any other diet group. Compared to probably the most closely related species in this sample, *Papio cynocephalus*, M_2s of *T. gelada* have significantly greater curvature and relief and similar complexity. In a qualitative sense, *T. gelada* molars have an unusual combination of high crowns, infolded enamel ridges, and columnar shape. As significant effort has been given to qualitative descriptions of *T. gelada* molar shape, it is worth comparing and contrasting one such description with the topographic characteristics observed here. Jolly (1972) provides a detailed assessment:

> "In Colobinae, the major cusps are linked by high cross-lophs, and there is a tendency to reduce structures mesial and distal to the principal cusp-pairs. The effective surface is therefore made up of a series of sharp transverse ridges, upper interlocking with lower, a pattern which persists until an advanced stage of wear, and is presumably related functionally to chopping foliage. In the molars of *Theropithecus*, extreme crown height and relief is associated with *additional* clefts and fossae, especially mesial and distal to the major cusps, with the formation of a prominent *longitudinal* ridge, and with a wear pattern in which the

> occlusal surface of the molar crown is reduced to a plane surface at an early stage. Clearly a different adaptive pattern is involved, in which the grinding surface is provided by the pattern of enamel ridges, the remains of the walls of the cusps and inter-cusp crests, which project from the exposed dentine in the worn tooth surface. […]
>
> "The adaptive advantage of the *Theropithecus* molar over the bunodont *Papio* type is first that, the greater complexity of invaginations provides more enamel ridges on the surface of worn tooth; second, that the more parallel-sided and deeper inter-cusp clefts and basins prolong the presence of these enamel ridges to a more advanced stage of wear, and third, that the high crowns provide more material to be abraded and thus postpone dental obsolescence even further." (Jolly, 1972, pp. 112 – 113) [italics from original]

Molar topography offers a method for quantitatively making comparisons between species to enrich qualitative descriptions such as this. The "additional clefts and fossae" increase overall surface convexity and concavity across this surface and so are reflected in greater surface curvature compared to colobines. Additional surface features present on *T. gelada* molars also may result in greater complexity relative to colobines. But interestingly, when quantifying complexity as a number of directional-facing patches there is no difference between *Papio* and *T. gelada* in M_2 complexity. Of course, "complexity" as used by Jolly (1972) and OPCR patch-count complexity do not need to refer to the same property. Indeed, degree of surface bending could just as easily be said

to represent complexity. But it does raise questions as to what causes this similarity in patch-count complexity between *Papio* and *T. gelada* that is distinct from colobines. It is possible that *Papio* achieves high complexity through a different morphological route than *T. gelada*. Perhaps among cercopithecoids, bunodont teeth are more likely to exhibit higher patch counts because a flatter irregular dome might be expected to show more variation in directional facing than one that is more raised. But there are some similarities between these species that might also give rise to greater complexity. Both species have relatively larger M_2s for their body size, which could possibly allow for greater surface complexity. Also it is possible that *Papio* and *T. gelada* both feature greater elaboration of M_2 surface regions mesial and distal to the four primary cusps relative to colobines. Compared to *Papio*, though, *T. gelada* certainly exhibits more elaboration. Combining the quantitative and qualitative descriptions of shape here, it is suggested that *T. gelada* M_2s have greater relief and curvature than *Papio* due to a simultaneous increase in the number of tooth surface features – the clefts, fossae, and ridges above – and greater bending of surface features. Because surface curvature is highly sensitive to combinations of changes in surface feature number and shape, this results in *T. gelada* having high surface curvature compared to both *Papio* and most colobines. This combination of factors also leaves *T. gelada* with similar complexity to *Papio* but higher relief, and similar relief to most colobines but higher complexity.

Certainly the molar morphology of *T. gelada* is related to the grass components that make up the majority of the diet of this species. Some parts of the grass species consumed by *T. gelada* exhibit substantially greater fracture toughness than any foods habitually consumed by other cercopithecoid species, including mature leaves consumed

by colobines (Lucas, 2004; Venkataraman et al., 2014). This diet is unique among cercopithecoids, and so it is perhaps not surprising that the topographic characteristics – the specific pattern of surface curvature, relief, and complexity – for this species are also unique in this sample. These topographic characteristics may represent a morphological adaptation for consuming grass components that is novel among cercopithecoids. In having the second highest mean OPCR in this sample, complexity in *T. gelada* relative to the rest of this sample is somewhat similar to the bamboo-feeding *Prolemur simus* having the greatest complexity in a prosimian sample (Bunn et al., 2011). Though complexity was quantified using a 3D-OPCR method here compared to the DEM-OPCR used by Bunn et al. (2011), comparing complexity of *T. gelada* relative to other cercopithecoids with complexity of *P. simus* relative to other prosimians seems reasonable. Bamboo is extremely fibrous and mechanically resistant, similar to some of the grass components consumed by *T. gelada*. But compared to the rest of the prosimian sample, *P. simus* showed average surface curvature and relief. In a sample of platyrrhines, pitheciine seed predator M_2s had the highest complexity in the sample but low curvature and relief (Winchester et al., 2014). No other primate species whose dental topography has been assessed has been found to have topographic characteristics similar to *T. gelada*. Perhaps this is related to how unusual the diet of this species is. In qualitatively describing *T. gelada* molar shape, Jolly (1972) suggested possible comparisons could be made with horses, cows, pigs, elephants, or rodents. Perhaps quantitative topographic comparisons with these groups are necessary to fully make sense of *T. gelada* molar morphology.

3.4.3: Predictive models of diet

A discriminant function analysis of diet of cercopithecoid specimens using all topographic variables (DNE, RFI, and OPCR) as well as M_2 area was able to achieve an overall prediction success rate of 67.8%. This is substantially above chance, but this degree of accuracy is below that achieved for prosimians (91.9%), platyrrhines (80.2%), or a combined sample including both prosimians and platyrrhines (74.6%) for analyses using the same variable set (Winchester et al., 2014). A principle reason for this lack of accuracy is the complete overlap between hard object feeding and soft object feeding categories for this DFA. This overlap persists across every DFA tested here. Though M_2 relief does differ significantly between hard object feeding and soft object feeding categories (see above), DFAs indicate very little differentiation between these diet categories. This is interpreted to reflect a general similarity in M_2 shape between species in the hard object feeding or soft object feeding categories. In other words, evidence here does not provide much support for hard object feeding cercopithecoids having distinct M_2 topography. This is an unexpected result. It may be the case that functional signals of cercopithecoid hard object feeding lay outside the realm of quantified M_2 topography, or that indications of hard object feeding may be more readily found in post-canine tooth size or premolar shape. In fact, it has been observed that *Cercocebus atys* individuals typically process extremely hard *Sacoglottis gabonensis* seeds using pre-molar loading (Daegling et al., 2011). It could also be that the bilophodont configuration of cercopithecoids can be recruited to consume hard food objects without a specific need for additional topographic adaptations.

Aside from overlaps between soft object feeding and hard object feeding, the most effective DFA here is reasonably accurate at separating moderately-tough object

feeders from either extremely-tough object feeders or hard object feeders/soft object feeders (as a combined unit). Similarly extremely-tough object feeding *T. gelada* is well differentiated from other diet groups, though this is accomplished through a combination of high M_2 curvature and large body size via large M_2 area. Given the overall similarity in molar configuration among cercopithecoid species, the degree of success of the DFAs here is generally respectable.

3.4.4: Molar topography and wear

Relief index has been shown in multiple analyses to decrease across progressive wear within species (Ungar and M'Kirera, 2003; M'Kirera and Ungar, 2003; Dennis et al., 2004; King et al., 2005; Boyer, 2008; Ungar and Bunn, 2008; Bunn and Ungar, 2009; Winchester et al., 2011). Because of this, relief index was used as a wear proxy within species to test for possible changes in surface curvature or complexity as teeth wear down. A restricted sample of variably worn M_2s belonging to five species (*Cercopithecus campbelli*, *Colobus guereza*, *Macaca fascicularis*, *Papio cynocephalus*, and *Theropithecus gelada*) was used for this analysis. There is weak evidence for a positive relationship between DNE and RFI, but results suggest more strongly a negative relationship between OPCR and RFI. Whole-sample regressions, an analysis of co-variance, and certain species-specific regressions indicate that within cercopithecoid species, M_2 complexity increases as relief decreases. The slope of this relationship does not significantly differ between species per an analysis of covariance, but Y-intercepts of these slopes do differ between species. This suggests that though OPCR increases as relief decreases in a similar way in all species, species M_2s have different initial

complexity values. Moreover, this indicates that inter-species differences in complexity values are more or less maintained even as complexity values increase through the process of wear. *Theropithecus gelada* has the highest complexity of the species considered here. Four of the five M_2s with the greatest complexity in the variably worn sample (and among those with the lowest relief) belong to *T. gelada* (the other belongs to *Colobus guereza*). When regressions were tested on the level of individual species, a significant relationship between M_2 complexity and relief was only found for *T. gelada* and *Papio cynocephalus*.

It is not surprising that the strongest signals for a relationship between M_2 complexity and relief were generally found for *T. gelada*. Gelada baboons consume extremely tough grasses and their diet includes non-trivial quantities of silicate from surface grit, and *T. gelada* M_2s have been observed to undergo significant wear more quickly than other cercopithecoid species (Jolly, 1972). *Theropithecus gelada* molar adaptations may share certain similarities with those of ungulates or other grazing mammals, in that progressive wear may have the potential to increase or at least maintain tooth functionality through the exposure of enamel ridges that serve as functional shearing or grinding structures. This secondary tooth morphology in turn may ensure the ability to consume tough food materials as part of a highly abrasive diet. This idea is relatively easy to demonstrate for ungulates, but it is more difficult to derive quantitative support for this hypothesis for *T. gelada* or other primates. Results from analyses here suggest that M_2 complexity represents a quantitative morphological trait that is maintained or possibly enhanced through the process of wear. Complexity has been repeatedly demonstrated to be functionally related in various mammalian groups (Evans

et al., 2007; Bunn et al., 2011; Santana et al., 2011; Evans and Janis, 2014; Winchester et al., 2014), and so it is reasonable to believe that molar complexity does play a role in determining molar functional efficiency or potential. For *T. gelada*, progressive wear reduces cusp height and leads to the exposure of significant enamel infolding which increases quantified surface complexity while decreasing surface relief. Trade-offs between surface relief and complexity through wear may quantify a compensatory balance that ensures tooth functionality and delays dental senescence.

Being able to quantify these morphological characteristics allows for this phenomenon to be tested for cercopithecoid or other primate species that do not exhibit the obvious and marked enamel infolding of *T. gelada*. Results from analysis of covariance suggest a balance between relief and complexity across five species (*Cercopithecus mitis*, *Colobus guereza*, *Macaca fascicularis*, *Papio cynocephalus*, and *Theropithecus gelada*). Results from species-specific regressions also provide additional evidence for this phenomenon in *Papio cynocephalus*. It is also tempting to note that for species-specific regressions, *Colobus guereza* M_2 complexity is related to relief at $p = 0.02$ where the Bonferroni-corrected alpha level for these analyses was $p < 0.01$. It is possible that larger sample sizes and accounting for wear in a more quantitative manner would show further evidence. More work is needed to answer that question. It is also possible that the reduced efficacy of complexity to differentiate cercopithecoid diets in topographic analyses is related to an emphasis on relatively unworn primary M_2 morphology in these analyses, and that for more worn teeth complexity would show a stronger diet-linked signal. In this context, it should be pointed out that in any case, results here show at least some support for the idea that M_2 complexity may represent a

functionally-linked trait conserved through wear in some species such as *T. gelada* or *Papio cynocephalus*.

3.5: Conclusions

This chapter has considered dental functional morphology of extant cercopithecoids in the context of presumed dietary adaptations. Morphology of cercopithecoid M_2s has been analyzed using techniques from morphological topographic analysis that together quantify M_2 surface relief, curvature, and complexity. Cercopithecoid M_2 topography varies across species and reflects mechanical properties of dietary food items, with moderate and extremely-tough object feeders (i.e., *T. gelada*) exhibiting generally greater surface relief and curvature than hard object feeders or soft object feeders. *T. gelada* has greater surface curvature than moderately-tough object feeders, and hard object feeders have less surface relief than soft object feeders. In general, cercopithecoid M_2s vary mostly in relief, reflecting raising of cusps, crests, and lophs, though high surface curvature in *T. gelada* may indicate a novel solution among cercopithecoids for the habitual consumption of extremely tough grass components. While there is a risk that differences between cercopithecoids may reflect phylogeny rather than function, results from phylogenetically-informed analyses support these conclusions. The same cannot be said for complexity, which by phylogenetically-informed analyses does not significantly differ between dietary categories when maximal possible phylogenetic influence is taken into account. It is true, though, that colobines (moderately-tough object feeders) have less complex M_2s compared to cercopithecines (which together comprise hard object feeders, soft object feeders, and extremely-tough

object feeders). But this may be the result of offsets in M_2 complexity between the last common ancestors of the colobine and cercopithecine clades rather than the result of dietary adaptations in species belonging to these clades. Of course, it is possible that such theoretical phylogenetic offsets could have been the result of ancient dietary differences and corresponding molar adaptations in these last common ancestors, but the analyses here do not speak to this question.

This is not to say that complexity is not important for cercopithecoid molar function. The results described above primarily relate to relatively less worn primary M_2 morphology. An additional set of analyses considering more variably worn secondary M_2 morphology suggests that complexity may be maintained or even increase as tooth wear progresses. Complexity increases significantly with increasing intra-species relief, used here as a wear proxy. Given that complexity has been repeatedly shown to be functionally linked with more fibrous or herbivorous diets in other mammals, it is not unreasonable to think that increased complexity in worn cercopithecoid M_2s could help to compensate for decreased relief in the process of food parturition. When the secondary sample is considered against the larger primary sample, the most worn M_2s from the secondary sample exhibit complexity greater than almost any teeth from the primary sample. It is possible that more dietary-linked variation in complexity would be observed if more variably worn M_2s were considered. If this were the case, it would be additional evidence suggesting the existence of functionally maintained secondary M_2 morphology in cercopithecoid primates.

In addition to wear, the relationship of dental topography to allometric scaling was considered. Evidence here suggests that surface relief, curvature, and complexity do

not scale with body size in cercopithecoid M_2s. This seems to conform with a previous observation that M_2 relief does not scale with body size in prosimians (Boyer, 2008). The idea that dental topographic variables may not be affected by allometry is intriguing given that at least some of the tooth surface features that help to contribute to topography do show scaling. This may be additional support for dental topographic variables being capable of measuring emergent morphological shape properties which are not constrained by some of the same factors as component morphological features. In any case, it is possibly worthwhile for future dental topographic analyses involving a broad sample to consider allometry. This is straightforward for analyses involving relief indices since performing this metric requires the measurement of two-dimensional molar area, a body size proxy. Though at the same time, functional influences on M_2 area in addition to allometric influences should also be considered since it is possible that functional influences may obscure the use of this body size proxy for investigating allometry in topographic variables that are strongly functionally linked.

Allometry, wear, and phylogeny are all potentially important factors affecting molar topography, and a broad sample of extant cercopithecoids provides a suitable sample for investigating these factors in combination with functional dental morphology. These results address dental ecology for living cercopithecoid species, and provide a comparative dataset against which to infer the paleoecology of fossil taxa. But morphological topographic analyses may also be useful for addressing topics outside of functional morphology. The next chapter of this dissertation will bring this approach to bear on questions of evolutionary-developmental processes.

Table 3.1. Descriptive statistics of M_2 wear scores for primary (generally less worn) and secondary (more variably worn) samples.

a. Primary sample

Species	**n**	**Mean**	**S.D.**
Allenopithecus nigroviridis	6	1.667	0.931
Cercocebus atys	7	2.214	1.150
Cercopithecus mitis	10	1.500	0.527
Chlorocebus aethiops	10	2.250	1.034
Colobus guereza	10	1.550	0.497
Colobus satanas	7	1.357	1.069
Lophocebus albigena	10	1.250	0.540
Macaca fascicularis	10	2.350	0.530
Macaca sylvanus	8	2.938	1.613
Mandrillus sphinx	10	2.900	1.729
Miopithecus ogouensis	9	1.556	0.635
Nasalis larvatus	10	3.150	0.709
Papio cynocephalus	9	1.889	0.961
Piliocolobus badius	5	1.700	0.274
Presbytis melalophos	11	1.455	0.472
Procolobus verus	7	2.571	1.305
Pygathrix nigripes	8	2.500	1.134
Rhinopithecus roxellana	9	2.111	1.294
Semnopithecus entellus	10	2.250	0.825
Theropithecus gelada	9	3.556	0.846
Trachypithecus (Kasi) vetulus	9	2.056	1.286
Trachypithecus obscuris	9	2.778	1.543

b. Secondary Sample

Species	**n**	**Mean**	**S.D.**
Cercopithecus campbelli	8	1.313	0.704
Colobus guereza	15	2.033	1.008
Macaca fascicularis	15	2.367	1.302
Papio cynocephalus	9	1.889	0.961
Theropithecus gelada	18	3.842	1.225

Table 3.2. Dietary food material property categories assigned to sample species.

Species	Diet Group	References
Cercocebus atys	Hard object feeding	Bergmüller, unpublished data (cited in McGraw, 1998); Bergmüller et al., unpublished data (cited in Range and Noë, 2002); Daegling et al., 2011; McGraw et al., 2011
Lophocebus albigena		Chalmers, 1968; Waser, 1977; Tutin et al., 1997; Olupot, 1998; Poulsen et al., 2001; Lambert et al., 2004; McGraw et al., 2012
Mandrillus sphinx		Hoshino, 1985; Lahm, 1986; Caldecott et al., 1996; Rogers et al., 1996; McGraw and Daegling, 2012
Allenopithecus nigroviridis	Soft object feeding	Gautier-Hion, 1988; Zeeve, 1991
Cercopithecus campbelli		Gautier-Hion, 1988; Buzzard, 2006
Cercopithecus mitis		Cords, 1986; Butynski, 1990; Lawes et al., 1990, Lawes, 1991; Beeson et al., 1996; Kaplin and Moermond, 2000; Kaplin, 2001; Lambert, 2002
Chlorocebus aethiops		Wrangham and Waterman, 1981; Whitten, 1983; Isbell et al., 1998
Macaca		Wheatley, 1980; Yeager, 1996

fascicularis		
Macaca sylvanus		Hanya et al., 2011
Miopithecus ogouensis		Gautier-Hion, 1988
Papio cynocephalus		Post, 1982; Stacey, 1986; Norton et al., 1987; Bentley-Condit, unpublished data (cited in Swedell, 2007)
Colobus guereza	Moderately-tough object feeding	Oates, 1997; Fashing, 2001; Fashing et al., 2007
Colobus satanas		McKey et al., 1981; Oates, 1994; Gautier-Hion et al., 1997; Poulsen et al., 2002
Nasalis larvatus		Bennett and Sebastian, 1988; Yeagar, 1989, unpublished data (cited in Fashing, 2007); Matsuda et al., 2009
Piliocolobus badius		Davies et al., 1999
Presbytis melalophos		Curtin, 1980; Bennett, 1983; Johns, 1983
Procolobus verus		Davies et al., 1999
Pygathrix nigripes		Duc et al., 2009
Rhinopithecus roxellana		Grueter et al., 2009; Poirier and Hu, 1983; Su et al., 1998; Li, 2006
Semnopithecus entellus		Hladik, 1977; Newton 1987, 1992; Kar-Gupta and Kumar, 1994
Trachypithecus obscurus		Curtin, 1980; MacKinnon and MacKinnon, 1980
Trachypithecus (Kasi) vetulus		Hladik, 1977
Theropithecus	Extremely-	Dunbar and Dunbar, 1974; Dunbar, 1977; Wrangham,

gelada	tough object feeding	1976; Hunter, 2001; Iwamoto, 1979; Venkataraman, 2014

Table 3.3. Species body mass data.

Species	Mean body mass female	Mean body mass male	Both sexes body mass mean
Allenopithecus nigroviridis	3.44	6.04	4.74
Cercocebus atys	6.20	11.00	8.60
Cercopithecus mitis	4.36	7.70	6.03
Chlorocebus aethiops	3.46	5.02	4.24
Colobus guereza	8.55	11.70	10.12
Colobus satanas	7.42	10.40	8.91
Lophocebus albigena	6.02	8.25	7.14
Macaca fascicularis	3.59	5.36	4.48
Macaca sylvanus		11.10	11.10
Mandrillus sphinx	12.90	31.60	22.25
Miopithecus ogouensis	1.56	1.94	1.75
Nasalis larvatus	9.82	20.40	15.11
Papio cynocephalus	11.03	19.50	15.26
Piliocolobus badius	8.21	8.36	8.29
Presbytis melalophos	6.47	6.59	6.53
Procolobus verus	4.20	4.70	4.45
Pygathrix nemaeus	8.44	11.00	9.72
Rhinopithecus roxellana	11.60	17.90	14.75
Semnopithecus entellus	10.53	14.53	12.53
Theropithecus gelada	11.70	19.00	15.35
Trachypithecus obscurus	6.26	7.90	7.08

Trachypithecus (Kasi) vetulus	11.20	12.00	11.60

* All units provided as kg. Body mass per sex was calculated as the average of all body mass values present for non-provisioned populations of each species in Smith and Jungers (1997). Between one and three body mass measures were available for both sexes for all species, with the exception of female *Macaca sylvanus* where only an estimate for a provisioned population was provided. Both sexes mean body mass was calculated as the average of mean male and female body mass values, with the exception of *Macaca sylvanus* where mean male body mass was used.

Table 3.4. Descriptive statistics of topographic variables and M_2 area by species, clade, and diet categories for primary (relatively less worn) sample.

a. Species

		DNE		RFI		OPCR		2DA		3DA	
Species	n	Mean	S.D.	Mean	S.D.	Mean	S.D.	Mean	S.D.	Mean	S.D.
Allenopithecus nigroviridis	6	196.126	32.215	0.323	0.044	69.771	8.559	24.744	2.248	49.530	8.322
Cercocebus atys	7	198.277	15.267	0.280	0.028	75.714	13.798	41.282	12.301	72.411	22.537
Cercopithecus mitis	10	202.017	31.214	0.303	0.034	69.750	7.961	28.176	5.138	51.822	10.267
Chlorocebus aethiops	10	194.164	25.379	0.276	0.038	81.963	12.508	26.915	3.550	46.889	6.973
Colobus guereza	10	216.351	17.062	0.359	0.025	70.913	9.134	35.304	3.036	72.471	7.546
Colobus satanas	7	218.982	13.466	0.326	0.023	78.143	7.172	31.724	1.242	60.903	3.807
Lophocebus albigena	10	193.031	18.549	0.259	0.025	79.038	5.816	31.488	4.114	52.884	7.128
Macaca fascicularis	10	212.696	18.364	0.293	0.030	87.438	7.851	29.419	2.310	52.999	5.342
Macaca sylvanus	8	196.012	23.014	0.279	0.039	84.969	13.442	53.423	5.698	94.762	14.717
Mandrillus sphinx	10	212.924	26.049	0.267	0.041	84.313	8.682	81.052	11.382	138.692	24.040

Miopithecus ogouensis	9	228.591	22.509	0.324	0.052	84.840	18.316	10.740	0.676	20.656	2.722
Nasalis larvatus	10	240.672	45.530	0.390	0.033	73.988	10.848	43.300	3.099	94.753	9.730
Papio cynocephalus	9	197.123	22.812	0.255	0.037	83.792	6.787	87.036	6.769	145.034	13.992
Piliocolobus badius	5	244.823	10.644	0.402	0.022	69.825	9.084	33.794	4.788	75.700	11.650
Presbytis melalophos	11	234.781	18.973	0.367	0.035	74.705	9.050	24.521	1.893	51.277	6.404
Procolobus verus	7	216.252	32.594	0.372	0.034	67.875	11.506	22.222	1.995	46.000	6.040
Pygathrix nigripes	8	221.393	10.775	0.327	0.022	80.625	12.903	34.393	2.282	64.524	4.992
Rhinopithecus roxellana	9	208.524	38.781	0.348	0.035	66.931	5.773	53.632	6.752	107.765	15.822
Semnopithecus entellus	10	204.641	28.158	0.363	0.031	63.963	3.198	45.823	6.302	94.807	14.314
Theropithecus gelada	11	245.863	20.572	0.351	0.057	85.239	8.537	86.129	11.546	174.626	30.141
Trachypithecus obscurus	9	224.522	21.388	0.349	0.051	75.958	11.377	27.140	2.358	55.033	8.749
Trachypithecus (Kasi) vetulus	9	226.148	31.186	0.360	0.055	79.417	12.616	27.830	1.945	56.256	6.196

b. Diet

		DNE		RFI		OPCR		2DA		3DA	
Diet	n	Mean	S.D.	Mean	S.D.	Mean	S.D.	Mean	S.D.	Mean	S.D.
Hard object feeding	27	201.759	22.097	0.267	0.032	80.130	9.704	52.384	24.553	89.727	43.126
Soft object feeding	62	203.852	26.121	0.292	0.043	81.544	13.183	37.010	24.277	65.366	39.909
Moderately-tough object feeding	95	222.725	28.984	0.360	0.039	72.920	10.550	34.875	10.107	71.567	21.903
Extremely-tough	11	245.863	20.572	0.351	0.057	85.239	8.537	86.129	11.546	174.626	30.141

Object feeding

c. Clade

		DNE		RFI		OPCR		2DA		3DA	
Clade	n	Mean	S.D.	Mean	S.D.	Mean	S.D.	Mean	S.D.	Mean	S.D.
Cercopithecin	35	204.724	29.547	0.303	0.045	78.500	14.953	22.621	8.052	41.862	14.937
Colobine	95	222.725	28.984	0.360	0.039	72.920	10.550	34.875	10.107	71.567	21.903
Papionin	65	209.768	27.085	0.285	0.049	83.221	9.580	59.582	26.100	106.909	50.733

Table 3.5. Descriptive statistics of topographic variables and M_2 area by species for secondary (variably worn) sample.

a. Species

		DNE		RFI		OPCR		2DA		3DA	
Species	n	Mean	S.D.	Mean	S.D.	Mean	S.D.	Mean	S.D.	Mean	S.D.
Cercopithecus campbelli	7	209.912	33.963	0.298	0.022	75.518	7.874	21.728	0.915	39.417	1.857
Colobus guereza	15	212.099	19.130	0.324	0.056	75.808	12.717	35.938	4.235	69.138	10.928
Macaca fascicularis	14	226.422	29.952	0.288	0.040	85.962	7.807	31.058	3.551	56.101	10.578
Papio cynocephalus	9	197.123	22.812	0.255	0.037	83.792	6.787	87.036	6.769	145.034	13.992
Theropithecus gelada	19	247.835	22.001	0.315	0.068	87.559	11.396	86.530	9.442	163.421	26.691

b. Diet

		DNE		RFI		OPCR		2DA		3DA	
Diet	n	Mean	S.D.	Mean	S.D.	Mean	S.D.	Mean	S.D.	Mean	S.D.
Soft object feeding	30	213.344	30.778	0.279	0.039	82.767	8.413	46.179	28.476	79.674	46.270
Moderately-tough object feeding	15	212.099	19.130	0.324	0.056	75.808	12.717	35.938	4.235	69.138	10.928

Extremely-tough object feeding	19	247.835	22.001	0.315	0.068	87.559	11.396	86.530	9.442	163.421	26.691

c. Clade

		DNE		RFI		OPCR		2DA		3DA	
Clade	n	Mean	S.D.	Mean	S.D.	Mean	S.D.	Mean	S.D.	Mean	S.D.
Cercopithecin	7	209.912	33.963	0.298	0.022	75.518	7.874	21.728	0.915	39.417	1.857
Colobine	15	212.099	19.130	0.324	0.056	75.808	12.717	35.938	4.235	69.138	10.928
Papionin	42	229.914	31.456	0.293	0.058	86.226	9.388	69.053	27.204	125.357	52.225

Table 3.6. Descriptive statistics of species-mean relative M_2 area across species and diet groups.

a. Species

Species	Relative M_2 area
Allenopithecus nigroviridis	-1.278701669
Cercocebus atys	7.069427297
Cercopithecus mitis	-5.540726387
Chlorocebus aethiops	102.7712518
Colobus guereza	-18.61146072
Colobus satanas	-19.79832298
Lophocebus albigena	-6.527009167
Macaca fascicularis	22.35629866
Macaca sylvanus	104.3753087
Mandrillus sphinx	5.739321932
Miopithecus ogouensis	-11.94170644
Nasalis larvatus	-25.2769137
Papio cynocephalus	49.11328178

Piliocolobus badius	-9.952995127
Presbytis melalophos	-22.39537991
Procolobus verus	-7.200705929
Pygathrix nemaeus	-18.3525308
Rhinopithecus roxellana	-5.819188025
Semnopithecus entellus	-9.479587029
Theropithecus gelada	46.94993149
Trachypithecus (Kasi) johnii	-41.85911332
Trachypithecus obscurus	-18.9824715

b. Diet

Diet	n	Mean relative M_2 area
Hard object feeding	3	2.093913354
Soft object feeding	7	37.12214378
Moderately-tough object feeding	11	-17.97533355
Extremely-tough object feeding	1	46.94993149

Table 3.7. ANOVA of species-mean relative M_2 area across diet groups.

	df	Sum of squares	Mean squares	*F*	*p*
Diet	3	14813	4938	5.535	0.007
Residuals	18	16058	892		

Table 3.8. Profile probabilities of maximum-likelihood estimated lambda for phyloANOVA of species-mean relative M_2.

	Lambda	*p*
Lower bound	0	1
Upper bound	1	0.012
Estimate	0	

Table 3.9. PhyloANOVA of species-mean relative M_2 area across diet groups, lambda = 1.

a. ANOVA terms

	df	*F*	*p*
Diet	3	2.183	0.125
Residuals	18		

b. Auto-correlated diet group means

Diet	Mean
Hard object feeding	-8.350
Soft object feeding	37.915
Moderately-tough object feeding	-17.123
Extremely-tough object feeding	40.924

Table 3.10. Regressions of topographic variables on body size proxy variables.

a. Species mean regressions of topographic variables by body mass.

Variable	R^2	*p*
DNE	0.007	0.707
RFI	0.001	0.889
OPCR	0.015	0.586

b. Individual specimen regressions of topographic variables by 2D projected M2 area.

Variable	R^2	*p*

DNE	<0.001	0.828
RFI	0.019	0.0587
OPCR	0.001	0.604

Table 3.11. ANOVA of topographic variables across diet categories.

Topographic variable		*df*	Sum of squares	Mean squares	*F*	*p*
DNE	Diet	3	27485	9162	12.8	<0.001
	Residuals	178	127384	716		
RFI	Diet	3	0.2778	0.09259	55.39	<0.001
	Residuals	185	0.3093	0.00167		
OPCR	Diet	3	3848	1282.8	10.11	<0.001
	Residuals	191	24240	126.9		

Table 3.12. Post-hoc pairwise comparisons of topographic variables across diet categories.

a. DNE

	Hard object feeding	Moderately-tough object feeding	Extremely-tough object feeding
Hard object feeding	2.094 (0.987)	**20.966 (0.003)**	**44.104 (<0.001)**
Soft object feeding		**18.873 (<0.001)**	**42.010 (<0.001)**
Moderately-tough object feeding			**23.137 (0.038)**

b. RFI

	Hard object feeding	Moderately-tough object feeding	Extremely-tough object feeding

Hard object feeding	0.024 (0.056)	**0.093 (<0.001)**	**0.083 (<0.001)**
Soft object feeding		**0.069 (<0.001)**	**0.059 (<0.001)**
Moderately-tough object feeding			-0.009 (0.887)

c. OPCR

	Hard object feeding	Moderately-tough object feeding	Extremely-tough object feeding
Hard object feeding	1.415 (0.948)	**-7.210 (0.019)**	5.109 (0.585)
Soft object feeding		**-8.625 (<0.001)**	3.694 (0.748)
Moderately-tough object feeding			**12.319 (0.004)**

* Bold indicates significance at $p < 0.05$.

Table 3.13. ANOVA of topographic variables across species.

Topographic variable		*df*	Sum of squares	Mean squares	*F*	*p*
DNE	Species	21	49756	2369	3.607	<0.001
	Residuals	160	105112	657		
RFI	Species	21	0.3478	0.01656	11.56	<0.001
	Residuals	167	0.2392	0.001433		
OPCR	Species	21	10123	482.1	4.642	<0.001
	Residuals	173	17966	103.8		

Table 3.14. Post-hoc pairwise comparisons of topographic variables between species.

a. DNE

i. Mean differences between species

	Allenopithecus nigroviridis	*Cercocebus atys*	*Cercopithecus mitis*	*Chlorocebus aethiops*	*Colobus guereza*	*Colobus satanas*	*Lophocebus albigena*	*Macaca fascicularis*	*Macaca sylvanus*	*Mandrillus sphinx*	*Miopithecus ogouensis*
Allenopithecus nigroviridis	NA	NA	NA	NA	NA	NA	NA	NA	NA	NA	NA
Cercocebus atys	2.151	NA	NA	NA	NA	NA	NA	NA	NA	NA	NA

Cercopithecus mitis	5.891	3.740	NA	NA	NA	NA	NA	NA	NA	NA	NA
Chlorocebus aethiops	-1.962	-4.113	-7.853	NA	NA	NA	NA	NA	NA	NA	NA
Colobus guereza	20.226	18.074	14.334	22.188	NA	NA	NA	NA	NA	NA	NA
Colobus satanas	22.857	20.706	16.966	24.819	2.631	NA	NA	NA	NA	NA	NA
Lophocebus albigena	-3.094	-5.245	-8.986	-1.132	-23.320	-25.951	NA	NA	NA	NA	NA
Macaca fascicularis	16.570	14.419	10.679	18.532	-3.655	-6.287	19.664	NA	NA	NA	NA
Macaca sylvanus	-0.114	-2.265	-6.005	1.848	-20.340	-22.971	2.980	-16.684	NA	NA	NA
Mandrillus spinx	16.798	14.647	10.907	18.760	-3.427	-6.058	19.893	0.228	16.912	NA	NA
Miopithecus ogouensis	32.465	30.314	26.574	34.427	12.239	9.608	35.559	15.895	32.579	15.667	NA
Nasalis larvatus	44.546	42.395	38.655	46.508	24.320	21.689	47.640	27.976	44.660	27.748	12.081
Papio cynocephalus	0.997	-1.154	-4.894	2.959	-19.228	-21.859	4.092	-15.573	1.111	-15.801	-31.468
Piliocolobus badius	48.697	46.546	42.806	50.659	28.472	25.841	51.792	32.127	48.811	31.899	16.232
Presbytis melalophos	38.655	36.504	32.764	40.617	18.429	15.798	41.749	22.085	38.769	21.857	6.190
Procolobus verus	20.126	17.975	14.235	22.088	-0.099	-2.731	23.220	3.556	20.240	3.328	-12.339
Pygathrix nigripes	25.267	23.116	19.376	27.229	5.042	2.410	28.361	8.697	25.381	8.469	-7.198
Rhinopithecus roxellana	12.398	10.247	6.507	14.360	-7.827	-10.458	15.493	-4.172	12.513	-4.400	-20.067
Semnopithecus entellus	8.515	6.364	2.624	10.477	-11.710	-14.342	11.609	-8.055	8.629	-8.283	-23.950
Theropithecus gelada	49.737	47.586	43.846	51.699	29.511	26.880	52.831	33.167	49.851	32.939	17.272
Trachypithecus obscurus	28.396	26.245	22.505	30.358	8.171	5.539	31.490	11.826	28.510	11.598	-4.069
Trachypithecus (Kasi) vetulus	30.023	27.872	24.131	31.985	9.797	7.166	33.117	13.453	30.137	13.224	-2.442

	Nasalis larvatus	*Papio cynocephalus*	*Piliocolobus badius*	*Presbytis melalophos*	*Procolobus verus*	*Pygathrix nigripes*	*Rhinopithecus roxellana*	*Semnopithecus entellus*	*Theropithecus gelada*	*Trachypithecus obscurus*	*Trachypithecus (Kasi) vetulus*
Allenopithecus nigroviridis	NA	NA	NA	NA	NA	NA	NA	NA	NA	NA	NA
Cercocebus atys	NA	NA	NA	NA	NA	NA	NA	NA	NA	NA	NA
Cercopithecus mitis	NA	NA	NA	NA	NA	NA	NA	NA	NA	NA	NA

Chlorocebus aethiops	NA	NA	NA	NA	NA	NA	NA	NA	NA	NA	NA
Colobus guereza	NA	NA	NA	NA	NA	NA	NA	NA	NA	NA	NA
Colobus satanas	NA	NA	NA	NA	NA	NA	NA	NA	NA	NA	NA
Lophocebus albigena	NA	NA	NA	NA	NA	NA	NA	NA	NA	NA	NA
Macaca fascicularis	NA	NA	NA	NA	NA	NA	NA	NA	NA	NA	NA
Macaca sylvanus	NA	NA	NA	NA	NA	NA	NA	NA	NA	NA	NA
Mandrillus spinx	NA	NA	NA	NA	NA	NA	NA	NA	NA	NA	NA
Miopithecus ogouensis	NA	NA	NA	NA	NA	NA	NA	NA	NA	NA	NA
Nasalis larvatus	NA	NA	NA	NA	NA	NA	NA	NA	NA	NA	NA
Papio cynocephalus	-43.549	NA	NA	NA	NA	NA	NA	NA	NA	NA	NA
Piliocolobus badius	4.151	47.700	NA	NA	NA	NA	NA	NA	NA	NA	NA
Presbytis melalophos	-5.891	37.658	-10.042	NA	NA	NA	NA	NA	NA	NA	NA
Procolobus verus	-24.420	19.129	-28.571	-18.529	NA	NA	NA	NA	NA	NA	NA
Pygathrix nigripes	-19.279	24.270	-23.430	-13.388	5.141	NA	NA	NA	NA	NA	NA
Rhinopithecus roxellana	-32.148	11.401	-36.299	-26.256	-7.728	-12.869	NA	NA	NA	NA	NA
Semnopithecus entellus	-36.031	7.518	-40.182	-30.140	-11.611	-16.752	-3.883	NA	NA	NA	NA
Theropithecus gelada	5.191	48.739	1.039	11.082	29.611	24.470	37.338	41.222	NA	NA	NA
Trachypithecus obscurus	-16.150	27.399	-20.301	-10.259	8.270	3.129	15.998	19.881	-21.341	NA	NA
Trachypithecus (Kasi) vetulus	-14.523	29.025	-18.675	-8.632	9.897	4.756	17.624	21.508	-19.714	1.626	NA

ii. Pairwise comparison *p* values

	Allenopithecus nigroviridis	*Cercocebus atys*	*Cercopithecus mitis*	*Chlorocebus aethiops*	*Colobus guereza*	*Colobus satanas*	*Lophocebus albigena*	*Macaca fascicularis*	*Macaca sylvanus*	*Mandrillus sphinx*	*Miopithecus ogouensis*
Allenopithecus nigroviridis	NA	NA	NA	NA	NA	NA	NA	NA	NA	NA	NA
Cercocebus atys	1.000	NA	NA	NA	NA	NA	NA	NA	NA	NA	NA
Cercopithecus mitis	1.000	1.000	NA	NA	NA	NA	NA	NA	NA	NA	NA

Chlorocebus aethiops	1.000	1.000	1.000	NA	NA	NA	NA	NA	NA	NA	NA
Colobus guereza	0.999	0.998	1.000	0.943	NA	NA	NA	NA	NA	NA	NA
Colobus satanas	0.998	0.996	0.999	0.934	1.000	NA	NA	NA	NA	NA	NA
Lophocebus albigena	1.000	1.000	1.000	1.000	0.910	0.903	NA	NA	NA	NA	NA
Macaca fascicularis	1.000	1.000	1.000	0.992	1.000	1.000	0.984	NA	NA	NA	NA
Macaca sylvanus	1.000	1.000	1.000	1.000	0.992	0.987	1.000	0.999	NA	NA	NA
Mandrillus spinx	1.000	1.000	1.000	0.990	1.000	1.000	0.981	1.000	0.999	NA	NA
Miopithecus ogouensis	0.915	0.826	0.882	0.461	1.000	1.000	0.396	1.000	0.721	1.000	NA
Nasalis larvatus	0.314	0.118	0.113	**0.013**	0.873	0.983	**0.009**	0.676	0.072	0.691	1.000
Papio cynocephalus	1.000	1.000	1.000	1.000	0.991	0.986	1.000	0.999	1.000	0.999	0.680
Piliocolobus badius	0.384	0.222	0.249	0.058	0.913	0.983	**0.045**	0.781	0.154	0.791	1.000
Presbytis melalophos	0.595	0.345	0.366	0.070	0.992	1.000	0.052	0.945	0.238	0.950	1.000
Procolobus verus	1.000	1.000	1.000	0.988	1.000	1.000	0.979	1.000	0.998	1.000	1.000
Pygathrix nigripes	0.996	0.991	0.998	0.902	1.000	1.000	0.863	1.000	0.975	1.000	1.000
Rhinopithecus roxellana	1.000	1.000	1.000	1.000	1.000	1.000	0.999	1.000	1.000	1.000	0.995
Semnopithecus entellus	1.000	1.000	1.000	1.000	1.000	1.000	1.000	1.000	1.000	1.000	0.953
Theropithecus gelada	0.129	**0.028**	**0.022**	**0.002**	0.529	0.850	**0.001**	0.299	**0.015**	0.312	0.999
Trachypithecus obscurus	0.971	0.930	0.963	0.635	1.000	1.000	0.564	1.000	0.860	1.000	1.000
Trachypithecus (Kasi) vetulus	0.970	0.937	0.968	0.694	1.000	1.000	0.631	1.000	0.877	1.000	1.000

	Nasalis larvatus	*Papio cynocephalus*	*Piliocolobus badius*	*Presbytis melalophos*	*Procolobus verus*	*Pygathrix nigripes*	*Rhinopithecus roxellana*	*Semnopithecus entellus*	*Theropithecus gelada*	*Trachypithecus obscurus*	*Trachypithecus (Kasi) vetulus*
Allenopithecus nigroviridis	NA	NA	NA	NA	NA	NA	NA	NA	NA	NA	NA
Cercocebus atys	NA	NA	NA	NA	NA	NA	NA	NA	NA	NA	NA
Cercopithecus mitis	NA	NA	NA	NA	NA	NA	NA	NA	NA	NA	NA
Chlorocebus aethiops	NA	NA	NA	NA	NA	NA	NA	NA	NA	NA	NA

Colobus guereza	NA	NA	NA	NA	NA	NA	NA	NA	NA	NA	NA
Colobus satanas	NA	NA	NA	NA	NA	NA	NA	NA	NA	NA	NA
Lophocebus albigena	NA	NA	NA	NA	NA	NA	NA	NA	NA	NA	NA
Macaca fascicularis	NA	NA	NA	NA	NA	NA	NA	NA	NA	NA	NA
Macaca sylvanus	NA	NA	NA	NA	NA	NA	NA	NA	NA	NA	NA
Mandrillus spinx	NA	NA	NA	NA	NA	NA	NA	NA	NA	NA	NA
Miopithecus ogouensis	NA	NA	NA	NA	NA	NA	NA	NA	NA	NA	NA
Nasalis larvatus	NA	NA	NA	NA	NA	NA	NA	NA	NA	NA	NA
Papio cynocephalus	**0.044**	NA	NA	NA	NA	NA	NA	NA	NA	NA	NA
Piliocolobus badius	1.000	0.124	NA	NA	NA	NA	NA	NA	NA	NA	NA
Presbytis melalophos	1.000	0.177	1.000	NA	NA	NA	NA	NA	NA	NA	NA
Procolobus verus	0.964	0.999	0.965	0.999	NA	NA	NA	NA	NA	NA	NA
Pygathrix nigripes	0.998	0.973	0.997	1.000	1.000	NA	NA	NA	NA	NA	NA
Rhinopithecus roxellana	0.458	1.000	0.603	0.817	1.000	1.000	NA	NA	NA	NA	NA
Semnopithecus entellus	0.201	1.000	0.363	0.533	1.000	1.000	1.000	NA	NA	NA	NA
Theropithecus gelada	1.000	**0.007**	1.000	1.000	0.789	0.956	0.159	**0.046**	NA	NA	NA
Trachypithecus obscurus	0.999	0.833	0.999	1.000	1.000	1.000	1.000	0.991	0.974	NA	NA
Trachypithecus (Kasi) vetulus	1.000	0.860	1.000	1.000	1.000	1.000	1.000	0.991	0.996	1.000	NA

b. RFI

i. Mean differences between species

	Allenopithecus nigroviridis	*Cercocebus atys*	*Cercopithecus mitis*	*Chlorocebus aethiops*	*Colobus guereza*	*Colobus satanas*	*Lophocebus albigena*	*Macaca fascicularis*	*Macaca sylvanus*	*Mandrillus sphinx*	*Miopithecus ogouensis*
Allenopithecus nigroviridis	NA	NA	NA	NA	NA	NA	NA	NA	NA	NA	NA
Cercocebus atys	-0.043	NA	NA	NA	NA	NA	NA	NA	NA	NA	NA

Cercopithecus mitis	-0.021	0.023	NA	NA	NA	NA	NA	NA	NA	NA	NA
Chlorocebus aethiops	-0.047	-0.004	-0.027	NA	NA	NA	NA	NA	NA	NA	NA
Colobus guereza	0.036	0.079	0.056	0.083	NA	NA	NA	NA	NA	NA	NA
Colobus satanas	0.002	0.046	0.023	0.050	-0.033	NA	NA	NA	NA	NA	NA
Lophocebus albigena	-0.064	-0.021	-0.043	-0.017	-0.100	-0.066	NA	NA	NA	NA	NA
Macaca fascicularis	-0.030	0.014	-0.009	0.017	-0.065	-0.032	0.034	NA	NA	NA	NA
Macaca sylvanus	-0.045	-0.001	-0.024	0.002	-0.080	-0.047	0.019	-0.015	NA	NA	NA
Mandrillus spinx	-0.056	-0.013	-0.036	-0.009	-0.092	-0.059	0.008	-0.027	-0.012	NA	NA
Miopithecus ogouensis	0.001	0.044	0.021	0.048	-0.035	-0.002	0.064	0.030	0.045	0.057	NA
Nasalis larvatus	0.067	0.111	0.088	0.114	0.032	0.065	0.131	0.097	0.112	0.124	0.067
Papio cynocephalus	-0.069	-0.025	-0.048	-0.021	-0.104	-0.071	-0.005	-0.039	-0.024	-0.012	-0.069
Piliocolobus badius	0.079	0.122	0.100	0.126	0.043	0.077	0.143	0.109	0.124	0.135	0.079
Presbytis melalophos	0.044	0.087	0.064	0.091	0.008	0.041	0.107	0.073	0.088	0.100	0.043
Procolobus verus	0.048	0.092	0.069	0.095	0.013	0.046	0.112	0.078	0.093	0.105	0.048
Pygathrix nigripes	0.004	0.047	0.024	0.051	-0.032	0.001	0.068	0.033	0.048	0.060	0.003
Rhinopithecus roxellana	0.025	0.068	0.045	0.072	-0.011	0.022	0.088	0.054	0.069	0.081	0.024
Semnopithecus entellus	0.040	0.083	0.060	0.087	0.004	0.037	0.104	0.069	0.084	0.096	0.039
Theropithecus gelada	0.028	0.071	0.048	0.075	-0.008	0.025	0.092	0.057	0.072	0.084	0.027
Trachypithecus obscurus	0.026	0.069	0.047	0.073	-0.009	0.024	0.090	0.056	0.071	0.083	0.026
Trachypithecus (Kasi) vetulus	0.037	0.080	0.058	0.084	0.001	0.035	0.101	0.067	0.082	0.093	0.037

	Nasalis larvatus	*Papio cynocephalus*	*Piliocolobus badius*	*Presbytis melalophos*	*Procolobus verus*	*Pygathrix nigripes*	*Rhinopithecus roxellana*	*Semnopithecus entellus*	*Theropithecus gelada*	*Trachypithecus obscurus*	*Trachypithecus (Kasi) vetulus*
Allenopithecus nigroviridis	NA	NA	NA	NA	NA	NA	NA	NA	NA	NA	NA
Cercocebus atys	NA	NA	NA	NA	NA	NA	NA	NA	NA	NA	NA
Cercopithecus mitis	NA	NA	NA	NA	NA	NA	NA	NA	NA	NA	NA

Chlorocebus aethiops	NA	NA	NA	NA	NA	NA	NA	NA	NA	NA	NA
Colobus guereza	NA	NA	NA	NA	NA	NA	NA	NA	NA	NA	NA
Colobus satanas	NA	NA	NA	NA	NA	NA	NA	NA	NA	NA	NA
Lophocebus albigena	NA	NA	NA	NA	NA	NA	NA	NA	NA	NA	NA
Macaca fascicularis	NA	NA	NA	NA	NA	NA	NA	NA	NA	NA	NA
Macaca sylvanus	NA	NA	NA	NA	NA	NA	NA	NA	NA	NA	NA
Mandrillus spinx	NA	NA	NA	NA	NA	NA	NA	NA	NA	NA	NA
Miopithecus ogouensis	NA	NA	NA	NA	NA	NA	NA	NA	NA	NA	NA
Nasalis larvatus	NA	NA	NA	NA	NA	NA	NA	NA	NA	NA	NA
Papio cynocephalus	-0.136	NA	NA	NA	NA	NA	NA	NA	NA	NA	NA
Piliocolobus badius	0.012	0.148	NA	NA	NA	NA	NA	NA	NA	NA	NA
Presbytis melalophos	-0.024	0.112	-0.036	NA	NA	NA	NA	NA	NA	NA	NA
Procolobus verus	-0.019	0.117	-0.031	0.005	NA	NA	NA	NA	NA	NA	NA
Pygathrix nigripes	-0.064	0.072	-0.076	-0.040	-0.045	NA	NA	NA	NA	NA	NA
Rhinopithecus roxellana	-0.043	0.093	-0.055	-0.019	-0.024	0.021	NA	NA	NA	NA	NA
Semnopithecus entellus	-0.028	0.108	-0.039	-0.004	-0.009	0.036	0.015	NA	NA	NA	NA
Theropithecus gelada	-0.040	0.096	-0.051	-0.016	-0.021	0.024	0.003	-0.012	NA	NA	NA
Trachypithecus obscurus	-0.041	0.095	-0.053	-0.017	-0.022	0.023	0.002	-0.014	-0.002	NA	NA
Trachypithecus (Kasi) vetulus	-0.030	0.106	-0.042	-0.006	-0.011	0.034	0.013	-0.003	0.009	0.011	NA

ii. Pairwise comparison *p* values

	Allenopithecus nigroviridis	*Cercocebus atys*	*Cercopithecus mitis*	*Chlorocebus aethiops*	*Colobus guereza*	*Colobus satanas*	*Lophocebus albigena*	*Macaca fascicularis*	*Macaca sylvanus*	*Mandrillus sphinx*	*Miopithecus ogouensis*
Allenopithecus nigroviridis	NA	NA	NA	NA	NA	NA	NA	NA	NA	NA	NA
Cercocebus atys	0.938	NA	NA	NA	NA	NA	NA	NA	NA	NA	NA
Cercopithecus mitis	1.000	1.000	NA	NA	NA	NA	NA	NA	NA	NA	NA

Chlorocebus aethiops	0.794	1.000	0.994	NA	NA	NA	NA	NA	NA	NA	NA
Colobus guereza	0.983	**0.007**	0.129	**0.000**	NA	NA	NA	NA	NA	NA	NA
Colobus satanas	1.000	0.798	1.000	0.514	0.975	NA	NA	NA	NA	NA	NA
Lophocebus albigena	0.229	1.000	0.581	1.000	**0.000**	0.066	NA	NA	NA	NA	NA
Macaca fascicularis	0.998	1.000	1.000	1.000	**0.025**	0.982	0.915	NA	NA	NA	NA
Macaca sylvanus	0.919	1.000	1.000	1.000	**0.005**	0.756	1.000	1.000	NA	NA	NA
Mandrillus spinx	0.468	1.000	0.877	1.000	**0.000**	0.197	1.000	0.994	1.000	NA	NA
Miopithecus ogouensis	1.000	0.776	1.000	0.454	0.915	1.000	**0.042**	0.981	0.730	0.148	NA
Nasalis larvatus	0.157	**0.000**	**0.000**	**0.000**	0.960	0.085	**0.000**	**0.000**	**0.000**	**0.000**	**0.028**
Papio cynocephalus	0.157	0.999	0.435	1.000	**0.000**	**0.040**	1.000	0.816	1.000	1.000	**0.025**
Piliocolobus badius	0.135	**0.000**	**0.001**	**0.000**	0.887	0.089	**0.000**	**0.000**	**0.000**	**0.000**	**0.040**
Presbytis melalophos	0.869	**0.001**	0.025	**0.000**	1.000	0.809	**0.000**	**0.003**	**0.001**	**0.000**	0.611
Procolobus verus	0.878	**0.004**	0.073	**0.001**	1.000	0.844	**0.000**	**0.016**	**0.003**	**0.000**	0.706
Pygathrix nigripes	1.000	0.820	1.000	0.565	0.990	1.000	0.090	0.985	0.782	0.241	1.000
Rhinopithecus roxellana	1.000	0.068	0.565	**0.011**	1.000	1.000	**0.000**	0.213	0.055	**0.001**	0.999
Semnopithecus entellus	0.948	**0.003**	0.066	**0.000**	1.000	0.924	**0.000**	**0.011**	**0.002**	**0.000**	0.802
Theropithecus gelada	0.999	**0.024**	0.326	**0.002**	1.000	0.999	**0.000**	0.085	**0.019**	**0.000**	0.993
Trachypithecus obscurus	1.000	**0.052**	0.490	**0.007**	1.000	1.000	**0.000**	0.169	**0.042**	**0.001**	0.998
Trachypithecus (Kasi) vetulus	0.983	**0.011**	0.171	**0.001**	1.000	0.977	**0.000**	**0.040**	**0.009**	**0.000**	0.927

	Nasalis larvatus	*Papio cynocephalus*	*Piliocolobus badius*	*Presbytis melalophos*	*Procolobus verus*	*Pygathrix nigripes*	*Rhinopithecus roxellana*	*Semnopithecus entellus*	*Theropithecus gelada*	*Trachypithecus obscurus*	*Trachypithecus (Kasi) vetulus*
Allenopithecus nigroviridis	NA	NA	NA	NA	NA	NA	NA	NA	NA	NA	NA
Cercocebus atys	NA	NA	NA	NA	NA	NA	NA	NA	NA	NA	NA
Cercopithecus mitis	NA	NA	NA	NA	NA	NA	NA	NA	NA	NA	NA
Chlorocebus aethiops	NA	NA	NA	NA	NA	NA	NA	NA	NA	NA	NA

Colobus guereza	NA	NA	NA	NA	NA	NA	NA	NA	NA	NA	NA
Colobus satanas	NA	NA	NA	NA	NA	NA	NA	NA	NA	NA	NA
Lophocebus albigena	NA	NA	NA	NA	NA	NA	NA	NA	NA	NA	NA
Macaca fascicularis	NA	NA	NA	NA	NA	NA	NA	NA	NA	NA	NA
Macaca sylvanus	NA	NA	NA	NA	NA	NA	NA	NA	NA	NA	NA
Mandrillus spinx	NA	NA	NA	NA	NA	NA	NA	NA	NA	NA	NA
Miopithecus ogouensis	NA	NA	NA	NA	NA	NA	NA	NA	NA	NA	NA
Nasalis larvatus	NA	NA	NA	NA	NA	NA	NA	NA	NA	NA	NA
Papio cynocephalus	**0.000**	NA	NA	NA	NA	NA	NA	NA	NA	NA	NA
Piliocolobus badius	1.000	**0.000**	NA	NA	NA	NA	NA	NA	NA	NA	NA
Presbytis melalophos	0.998	**0.000**	0.981	NA	NA	NA	NA	NA	NA	NA	NA
Procolobus verus	1.000	**0.000**	0.999	1.000	NA	NA	NA	NA	NA	NA	NA
Pygathrix nigripes	0.151	0.057	0.138	0.892	0.904	NA	NA	NA	NA	NA	NA
Rhinopithecus roxellana	0.663	0.000	0.567	1.000	1.000	1.000	NA	NA	NA	NA	NA
Semnopithecus entellus	0.991	**0.000**	0.953	1.000	1.000	0.963	1.000	NA	NA	NA	NA
Theropithecus gelada	0.713	**0.000**	0.620	1.000	1.000	1.000	1.000	1.000	NA	NA	NA
Trachypithecus obscurus	0.733	**0.000**	0.628	1.000	1.000	1.000	1.000	1.000	1.000	NA	NA
Trachypithecus (Kasi) vetulus	0.987	**0.000**	0.940	1.000	1.000	0.990	1.000	1.000	1.000	1.000	NA

c. OPCR

i. Mean differences between species

	Allenopithecus nigroviridis	*Cercocebus atys*	*Cercopithecus mitis*	*Chlorocebus aethiops*	*Colobus guereza*	*Colobus satanas*	*Lophocebus albigena*	*Macaca fascicularis*	*Macaca sylvanus*	*Mandrillus sphinx*	*Miopithecus ogouensis*
Allenopithecus nigroviridis	NA	NA	NA	NA	NA	NA	NA	NA	NA	NA	NA
Cercocebus atys	5.943	NA	NA	NA	NA	NA	NA	NA	NA	NA	NA

Cercopithecus mitis	-0.021	-5.964	NA	NA	NA	NA	NA	NA	NA	NA	NA
Chlorocebus aethiops	12.192	6.248	12.212	NA	NA	NA	NA	NA	NA	NA	NA
Colobus guereza	1.142	-4.802	1.162	-11.050	NA	NA	NA	NA	NA	NA	NA
Colobus satanas	8.372	2.429	8.393	-3.820	7.230	NA	NA	NA	NA	NA	NA
Lophocebus albigena	9.267	3.323	9.287	-2.925	8.125	0.895	NA	NA	NA	NA	NA
Macaca fascicularis	17.667	11.723	17.687	5.475	16.525	9.295	8.400	NA	NA	NA	NA
Macaca sylvanus	15.198	9.254	15.219	3.006	14.056	6.826	5.931	-2.469	NA	NA	NA
Mandrillus spinx	14.542	8.598	14.562	2.350	13.400	6.170	5.275	-3.125	-0.656	NA	NA
Miopithecus ogouensis	20.424	14.480	20.444	8.232	19.282	12.052	11.157	2.757	5.226	5.882	NA
Nasalis larvatus	4.217	-1.727	4.237	-7.975	3.075	-4.155	-5.050	-13.450	-10.981	-10.325	-16.207
Papio cynocephalus	14.021	8.077	14.042	1.829	12.879	5.649	4.754	-3.646	-1.177	-0.521	-6.403
Piliocolobus badius	0.054	-5.889	0.075	-12.138	-1.087	-8.318	-9.212	-17.612	-15.144	-14.488	-20.369
Presbytis melalophos	4.934	-1.010	4.955	-7.258	3.792	-3.438	-4.333	-12.733	-10.264	-9.608	-15.490
Procolobus verus	-1.896	-7.839	-1.875	-14.087	-3.037	-10.268	-11.163	-19.562	-17.094	-16.438	-22.319
Pygathrix nigripes	10.854	4.911	10.875	-1.337	9.713	2.482	1.588	-6.812	-4.344	-3.687	-9.569
Rhinopithecus roxellana	-2.840	-8.784	-2.819	-15.032	-3.982	-11.212	-12.107	-20.507	-18.038	-17.382	-23.264
Semnopithecus entellus	-5.808	-11.752	-5.788	-18.000	-6.950	-14.180	-15.075	-23.475	-21.006	-20.350	-26.232
Theropithecus gelada	15.468	9.524	15.489	3.276	14.326	7.096	6.201	-2.199	0.270	0.926	-4.956
Trachypithecus obscurus	6.188	0.244	6.208	-6.004	5.046	-2.185	-3.079	-11.479	-9.010	-8.354	-14.236
Trachypithecus (Kasi) vetulus	9.646	3.702	9.667	-2.546	8.504	1.274	0.379	-8.021	-5.552	-4.896	-10.778

	Nasalis larvatus	*Papio cynocephalus*	*Piliocolobus badius*	*Presbytis melalophos*	*Procolobus verus*	*Pygathrix nigripes*	*Rhinopithecus roxellana*	*Semnopithecus entellus*	*Theropithecus gelada*	*Trachypithecus obscurus*	*Trachypithecus (Kasi) vetulus*
Allenopithecus nigroviridis	NA	NA	NA	NA	NA	NA	NA	NA	NA	NA	NA
Cercocebus atys	NA	NA	NA	NA	NA	NA	NA	NA	NA	NA	NA
Cercopithecus mitis	NA	NA	NA	NA	NA	NA	NA	NA	NA	NA	NA

Chlorocebus aethiops	NA	NA	NA	NA	NA	NA	NA	NA	NA	NA	NA
Colobus guereza	NA	NA	NA	NA	NA	NA	NA	NA	NA	NA	NA
Colobus satanas	NA	NA	NA	NA	NA	NA	NA	NA	NA	NA	NA
Lophocebus albigena	NA	NA	NA	NA	NA	NA	NA	NA	NA	NA	NA
Macaca fascicularis	NA	NA	NA	NA	NA	NA	NA	NA	NA	NA	NA
Macaca sylvanus	NA	NA	NA	NA	NA	NA	NA	NA	NA	NA	NA
Mandrillus spinx	NA	NA	NA	NA	NA	NA	NA	NA	NA	NA	NA
Miopithecus ogouensis	NA	NA	NA	NA	NA	NA	NA	NA	NA	NA	NA
Nasalis larvatus	NA	NA	NA	NA	NA	NA	NA	NA	NA	NA	NA
Papio cynocephalus	9.804	NA	NA	NA	NA	NA	NA	NA	NA	NA	NA
Piliocolobus badius	-4.162	-13.967	NA	NA	NA	NA	NA	NA	NA	NA	NA
Presbytis melalophos	0.717	-9.087	4.880	NA	NA	NA	NA	NA	NA	NA	NA
Procolobus verus	-6.112	-15.917	-1.950	-6.830	NA	NA	NA	NA	NA	NA	NA
Pygathrix nigripes	6.638	-3.167	10.800	5.920	12.750	NA	NA	NA	NA	NA	NA
Rhinopithecus roxellana	-7.057	-16.861	-2.894	-7.774	-0.944	-13.694	NA	NA	NA	NA	NA
Semnopithecus entellus	-10.025	-19.829	-5.863	-10.742	-3.913	-16.663	-2.968	NA	NA	NA	NA
Theropithecus gelada	11.251	1.447	15.414	10.534	17.364	4.614	18.308	21.276	NA	NA	NA
Trachypithecus obscurus	1.971	-7.833	6.133	1.254	8.083	-4.667	9.028	11.996	-9.280	NA	NA
Trachypithecus (Kasi) vetulus	5.429	-4.375	9.592	4.712	11.542	-1.208	12.486	15.454	-5.822	3.458	NA

ii. Pairwise comparison *p* values

	Allenopithecus nigroviridis	*Cercocebus atys*	*Cercopithecus mitis*	*Chlorocebus aethiops*	*Colobus guereza*	*Colobus satanas*	*Lophocebus albigena*	*Macaca fascicularis*	*Macaca sylvanus*	*Mandrillus sphinx*	*Miopithecus ogouensis*
Allenopithecus nigroviridis	NA	NA	NA	NA	NA	NA	NA	NA	NA	NA	NA
Cercocebus atys	1.000	NA	NA	NA	NA	NA	NA	NA	NA	NA	NA
Cercopithecus mitis	1.000	1.000	NA	NA	NA	NA	NA	NA	NA	NA	NA

Chlorocebus aethiops	0.763	1.000	0.495	NA	NA	NA	NA	NA	NA	NA	NA
Colobus guereza	1.000	1.000	1.000	0.688	NA	NA	NA	NA	NA	NA	NA
Colobus satanas	0.997	1.000	0.988	1.000	0.998	NA	NA	NA	NA	NA	NA
Lophocebus albigena	0.978	1.000	0.910	1.000	0.975	1.000	NA	NA	NA	NA	NA
Macaca fascicularis	0.117	0.751	**0.024**	1.000	0.054	0.963	0.965	NA	NA	NA	NA
Macaca sylvanus	0.434	0.979	0.198	1.000	0.332	1.000	1.000	1.000	NA	NA	NA
Mandrillus spinx	0.432	0.984	0.177	1.000	0.312	1.000	1.000	1.000	1.000	NA	NA
Miopithecus ogouensis	**0.031**	0.392	**0.004**	0.979	**0.010**	0.743	0.718	1.000	1.000	1.000	NA
Nasalis larvatus	1.000	1.000	1.000	0.980	1.000	1.000	1.000	0.305	0.792	0.796	0.088
Papio cynocephalus	0.548	0.994	0.276	1.000	0.442	1.000	1.000	1.000	1.000	1.000	0.999
Piliocolobus badius	1.000	1.000	1.000	0.848	1.000	0.999	0.990	0.194	0.551	0.559	0.061
Presbytis melalophos	1.000	1.000	1.000	0.991	1.000	1.000	1.000	0.364	0.851	0.856	0.109
Procolobus verus	1.000	0.998	1.000	0.402	1.000	0.956	0.821	**0.023**	0.158	0.146	**0.004**
Pygathrix nigripes	0.932	1.000	0.805	1.000	0.920	1.000	1.000	0.999	1.000	1.000	0.944
Rhinopithecus roxellana	1.000	0.984	1.000	0.170	1.000	0.843	0.567	**0.004**	0.051	**0.041**	**0.001**
Semnopithecus entellus	1.000	0.748	1.000	**0.019**	0.996	0.389	0.133	**0.000**	**0.004**	**0.003**	**0.000**
Theropithecus gelada	0.281	0.944	0.083	1.000	0.167	0.998	0.999	1.000	1.000	1.000	1.000
Trachypithecus obscurus	1.000	1.000	0.999	1.000	1.000	1.000	1.000	0.669	0.969	0.975	0.297
Trachypithecus (Kasi) vetulus	0.973	1.000	0.899	1.000	0.970	1.000	1.000	0.984	1.000	1.000	0.809

	Nasalis larvatus	*Papio cynocephalus*	*Piliocolobus badius*	*Presbytis melalophos*	*Procolobus verus*	*Pygathrix nigripes*	*Rhinopithecus roxellana*	*Semnopithecus entellus*	*Theropithecus gelada*	*Trachypithecus obscurus*	*Trachypithecus (Kasi) vetulus*
Allenopithecus nigroviridis	NA	NA	NA	NA	NA	NA	NA	NA	NA	NA	NA
Cercocebus atys	NA	NA	NA	NA	NA	NA	NA	NA	NA	NA	NA
Cercopithecus mitis	NA	NA	NA	NA	NA	NA	NA	NA	NA	NA	NA
Chlorocebus aethiops	NA	NA	NA	NA	NA	NA	NA	NA	NA	NA	NA

Colobus guereza	NA	NA	NA	NA	NA	NA	NA	NA	NA	NA	NA
Colobus satanas	NA	NA	NA	NA	NA	NA	NA	NA	NA	NA	NA
Lophocebus albigena	NA	NA	NA	NA	NA	NA	NA	NA	NA	NA	NA
Macaca fascicularis	NA	NA	NA	NA	NA	NA	NA	NA	NA	NA	NA
Macaca sylvanus	NA	NA	NA	NA	NA	NA	NA	NA	NA	NA	NA
Mandrillus spinx	NA	NA	NA	NA	NA	NA	NA	NA	NA	NA	NA
Miopithecus ogouensis	NA	NA	NA	NA	NA	NA	NA	NA	NA	NA	NA
Nasalis larvatus	NA	NA	NA	NA	NA	NA	NA	NA	NA	NA	NA
Papio cynocephalus	0.887	NA	NA	NA	NA	NA	NA	NA	NA	NA	NA
Piliocolobus badius	1.000	0.664	NA	NA	NA	NA	NA	NA	NA	NA	NA
Presbytis melalophos	1.000	0.929	1.000	NA	NA	NA	NA	NA	NA	NA	NA
Procolobus verus	1.000	0.222	1.000	0.999	NA	NA	NA	NA	NA	NA	NA
Pygathrix nigripes	0.999	1.000	0.962	1.000	0.693	NA	NA	NA	NA	NA	NA
Rhinopithecus roxellana	0.997	0.076	1.000	0.986	1.000	0.431	NA	NA	NA	NA	NA
Semnopithecus entellus	0.834	**0.007**	1.000	0.697	1.000	0.091	1.000	NA	NA	NA	NA
Theropithecus gelada	0.612	1.000	0.403	0.689	0.073	1.000	**0.016**	**0.001**	NA	NA	NA
Trachypithecus obscurus	1.000	0.991	1.000	1.000	0.994	1.000	0.957	0.585	0.914	NA	NA
Trachypithecus (Kasi) vetulus	1.000	1.000	0.987	1.000	0.807	1.000	0.556	0.136	1.000	1.000	NA

Table 3.15. Summary of significant species pairwise comparisons of dental topographic variables sorted by diet category, with total number of all possible species pairwise comparisons for reference. Numbers before the slash indicate number of significant differences between species, numbers after the slash indicate number of total possible comparisons between species. Numbers in parentheses indicate the percentage of between-species comparisons that are significant compared to all possible between-species comparisons.

a. DNE

	Hard object feeding	Soft object feeding	Moderately-tough object feeding	Extremely-tough object feeding

Hard object feeding	0/3 (0%)	0/21 (0%)	2/33 (6.06%)	2/3 (66.67%)
Soft object feeding		0/21 (0%)	2/77 (2.60%)	4/7 (57.14%)
Moderately-tough object feeding			0/55 (0%)	1/11 (9.09%)
Extremely-tough object feeding				NA

b. RFI

	Hard object feeding	Soft object feeding	Moderately-tough object feeding	Extremely-tough object feeding
Hard object feeding	0/3 (0%)	1/21 (4.76%)	25/33 (75.76%)	3/3 (100%)
Soft object feeding		1/21 (4.76%)	39/77 (50.65%)	3/7 (42.86%)
Moderately-tough object feeding			0/55 (0%)	0/11 (0%)
Extremely-tough object feeding				NA

c. OPCR

	Hard object feeding	Soft object feeding	Moderately-tough object feeding	Extremely-tough object feeding
Hard object feeding	0/3 (0%)	0/21 (0%)	2/33 (6.06%)	0/3 (0%)
Soft object feeding		3/21 (14.29%)	10/77 (12.99%)	0/7 (0%)
Moderately-tough object feeding			0/55 (0%)	2/11 (18.18%)
Extremely-tough object feeding				NA

Table 3.16. ANOVAs of topographic variables across clade.

Topographic variable		df	Sum of squares	Mean squares	F	p
DNE	Clade	2	10216	5108	6.321	0.00223
	Residuals	179	144653	808		
RFI	Clade	2	0.2306	0.11531	60.18	<0.001
	Residuals	186	0.3564	0.00192		
OPCR	Clade	2	4151	2075.7	16.65	<0.001
	Residuals	192	23947	124.7		

Table 3.17. Post-hoc pairwise comparisons of topographic variables between clades.

a. DNE

	Colobine	Papionin
Cercopithecin	**18.001 (0.008)**	5.044 (0.697)
Colobine		**-12.958 (0.017)**

b. RFI

	Colobine	Papionin
Cercopithecin	**0.057 (<0.001)**	-0.018 (0.126)
Colobine		**-0.075 (<0.001)**

c. OPCR

	Colobine	Papionin
Cercopithecin	**-5.580 (0.033)**	4.721 (0.111)
Colobine		**10.301 (<0.001)**

Table 3.18. Profile probabilities of maximum-likelihood estimated lambda for phyloANOVAs of topographic variables by diet.

	DNE		RFI		OPCR	
	Lambda	*p*	Lambda	*p*	Lambda	*p*
Lower bound	0	1	0	1	0	1
Upper bound	1	<0.001	1	0.067	1	0.002
Estimate	0		0		0	

Table 3.19. ANOVA of species-mean topographic variables by diet (analogous to phyloANOVA with lambda = 0).

Topographic variable		*df*	Sum of squares	Mean squares	*F*	*p*
DNE	Diet	3	3413	1137.7	6.348	0.004
	Residuals	18	3226	179.2		
RFI	Diet	3	0.031612	0.010537	19.85	<0.001
	Residuals	18	0.009556	0.000531		
OPCR	Diet	3	390	129.99	3.17	0.0496
	Residuals	18	738.2	41.01		

Table 3.20. Post-hoc pairwise comparisons of species-mean topographic variables across diet categories.

a. DNE

	Soft object feeding	Moderately-tough object feeding	Extremely-tough object feeding
Hard object feeding	2.407 (0.994)	23.761 (0.061)	43.060 (0.054)
Soft object feeding		**21.353 (0.019)**	**40.652 (0.049)**
Moderately-tough object feeding			19.299 (0.527)

b. RFI

	Soft object feeding	Moderately-tough object feeding	Extremely-tough object feeding
Hard object feeding	0.025 (0.434)	**0.092 (<0.001)**	**0.094 (0.011)**
Soft object feeding		**0.067 (<0.001)**	**0.070 (0.049)**
Moderately-tough object feeding			0.003 (0.999)

c. OPCR

	Soft object feeding	Moderately-tough object feeding	Extremely-tough object feeding
Hard object feeding	1.437 (0.988)	-6.748 (0.394)	5.551 (0.875)
Soft object feeding		-8.185 (0.071)	4.114 (0.930)
Moderately-tough object feeding			12.299 (0.288)

* Bold indicates significance at $p < 0.05$.

Table 3.21. PhyloANOVA of species-mean topographic variables by diet, lambda = 1.

a. ANOVA terms

Topographic variables		*df*	*F*	*p*
DNE	Diet	3	4.903	0.012
	Residuals	18		
RFI	Diet	3	11.92	<0.001
	Residuals	18		
OPCR	Diet	3	0.5517	0.654
	Residuals	18		

b. Autocorrelated diet means

Diet	DNE	RFI	OPCR
Durophagy	202.694	0.284	77.891
Soft object feeding	205.408	0.294	81.57
Moderate elasticophagy	225.245	0.362	72.696
Extreme elasticophagy	251.34	0.388	83.696

Table 3.22. Discriminant function analyses cross-validated predictive accuracy.

Variable set	Accuracy	Diet category accuracy			
		Hard object feeding	Soft object feeding	Moderately-tough object feeding	Extremely-tough object feeding
DNE	52.2	0	38.1	83.9	0
LnRFI	60.6	3.7	58.2	87.4	0
OPCR	53.3	0	43.6	82.8	0
Ln2DA	52.8	0	0	100	72.7
DNE+LnRFI	62.2	11.1	58.2	88.5	0
DNE+OPCR	60.6	0	61.8	86.2	0
DNE+Ln2DA	58.3	18.5	30.9	83.9	90.9
LnRFI+OPCR	62.2	14.8	58.2	87.4	0
LnRFI+Ln2DA	65.6	25.9	52.7	86.2	63.6
OPCR+Ln2DA	54.4	11.1	32.7	80.5	63.6
DNE+LnRFI+OPCR	63.3	25.9	56.4	87.4	0
DNE+LnRFI+Ln2DA	65	25.9	54.5	83.9	63.6
DNE+OPCR+Ln2DA	64.4	22.2	47.3	86.2	81.8
LnRFI+OPCR+Ln2DA	66.7	33.3	52.7	85.1	72.7
DNE+LnRFI+OPCR+Ln2DA	67.8	44.4	52.7	85.1	63.6

Table 3.23. Percentage of variance explained by discriminant functions for DFAs with more than one variable.

Variable set	DF1	DF2	DF3
DNE+LnRFI	94.1	5.9	
DNE+OPCR	82.07	17.93	
DNE+Ln2DA	78.21	21.79	
LnRFI+OPCR	91.58	8.42	
LnRFI+Ln2DA	76.03	23.97	
OPCR+Ln2DA	74.34	25.66	
DNE+LnRFI+OPCR	89.58	8.03	2.39
DNE+LnRFI+Ln2DA	71.65	27.83	0.52
DNE+OPCR+Ln2DA	53.05	43.51	3.43
LnRFI+OPCR+Ln2DA	70.7	25.95	3.34
DNE+LnRFI+OPCR+Ln2DA	69.88	26.28	3.84

Table 3.24. DFA variable correlation (structure) matrices for DFAs with more than one variable.

Variable Set	Variables	DF1	DF2	DF3
DNE+LnRFI	DNE	0.502	**0.865**	
	LnRFI	**0.999**	0.054	
DNE+OPCR	DNE	**0.651**	-0.759	
	OPCR	-0.623	**-0.782**	
DNE+Ln2DA	DNE	0.547	**-0.837**	
	Ln2DA	**0.831**	0.556	
LnRFI+OPCR	LnRFI	**0.995**	0.095	
	OPCR	-0.431	**-0.903**	
LnRFI+Ln2DA	LnRFI	**0.984**	-0.179	
	Ln2DA	0.067	**0.998**	
OPCR+Ln2DA	OPCR	-0.51	**-0.86**	

	Ln2DA	**-0.883**	0.469	
DNE+LnRFI+OPCR	DNE	0.504	0.58	**-0.639**
	LnRFI	**0.986**	-0.075	-0.146
	OPCR	-0.429	**0.887**	0.172
DNE+LnRFI+Ln2DA	DNE	0.53	0.284	**0.799**
	LnRFI	**0.985**	-0.151	0.084
	Ln2DA	0.059	**0.923**	-0.38
DNE + OPCR + Ln2DA	DNE	0.662	-0.259	**0.703**
	OPCR	-0.15	**0.722**	0.675
	Ln2DA	**0.674**	0.603	-0.425
LnRFI + OPCR + Ln2DA	LnRFI	**0.965**	-0.26	-0.04
	OPCR	-0.378	0.452	**0.807**
	Ln2DA	0.111	**0.91**	-0.4
DNE + LnRFI + OPCR + Ln2DA	DNE	0.536	0.258	0.159
	LnRFI	**0.964**	-0.204	-0.108
	OPCR	-0.384	0.41	**0.802**
	Ln2DA	0.083	**0.904**	-0.287

* Values given as correlations between individual variables and discriminant functions. Bold indicates the absolute greatest correlation for each discriminant function per analysis.

Table 3.25. Regressions of DNE and OPCR on RFI across secondary (variably worn) sample.

Variable	*m*	*b*	R^2	*p*
DNE	119.59	187.45	0.049	0.083
OPCR	-109.402	115.491	0.297	<0.001

Table 3.26. ANCOVA of DNE and OPCR by species with RFI as covariate.

Variable		*df*	Sum of squares	Mean squares	*F*	*p*
DNE	RFI	1	2749	2749	4.381	0.041

	Species	4	18700	4675	7.451	<0.001
	RFI * Species	4	1846	462	0.736	0.572
	Residuals	53	33257	627		
OPCR	RFI	1	2300	2300.5	32.696	<0.001
	Species	4	1665	416.2	5.915	<0.001
	RFI * Species	4	49	12.3	0.175	0.950
	Residuals	53	3729	70.4		

Table 3.27. Species regressions of DNE and OPCR on RFI for secondary (variably worn) sample.

Species	Variable	*m*	*b*	R^2	*p*
Cercopithecus mitis	DNE	-117.7	244.9	0.006	0.870
	OPCR	-174.56	127.49	0.2431	0.261
Colobus guereza	DNE	115.05	174.81	0.112	0.222
	OPCR	-134.11	119.27	0.346	0.021
Macaca fascicularis	DNE	214.00	164.78	0.082	0.342
	OPCR	-89.45	111.73	0.212	0.113
Papio cynocephalus	DNE	280.41	125.73	0.207	0.218
	OPCR	-151.23	122.3	0.682	**0.006**
Theropithecus gelada	DNE	-27.5	256.5	0.007	0.7313
	OPCR	-113.964	123.458	0.456	**0.002**

*Bold indicates significance, Bonferroni corrected alpha = 0.01.

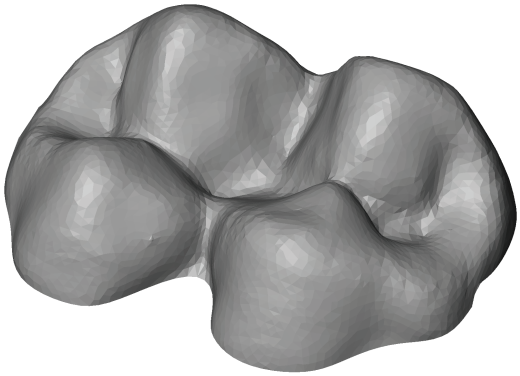

Hard object feeding
(*Cercocebys atys*)

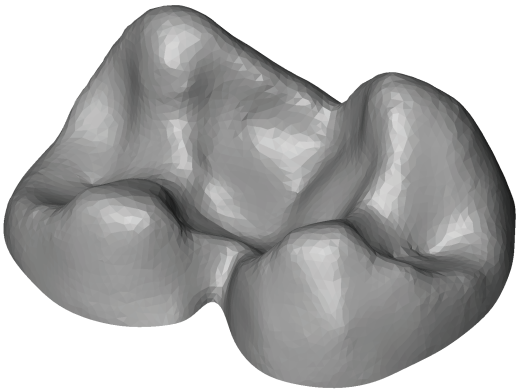

Soft object feeding
(*Cercopithecus mitis*)

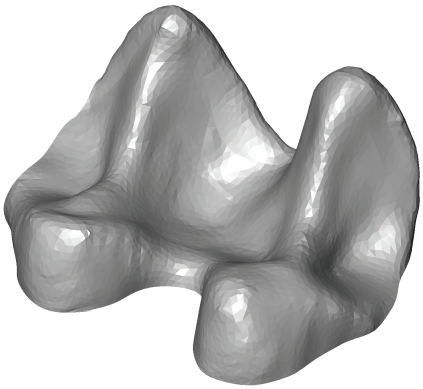

Moderately-tough
object feeding
(*Presbytis melalophos*)

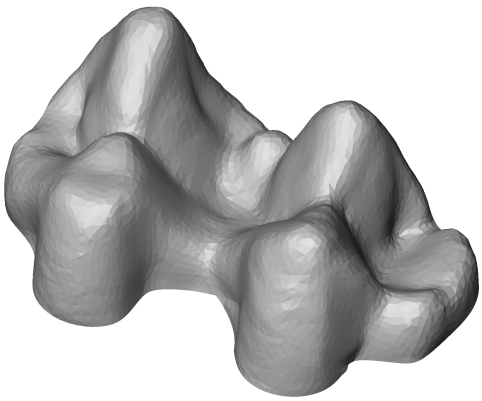

Extremely-tough
object feeding
(*Theropithecus gelada*)

Fig 3.1. Example M_2s of cercopithecoid species sorted into dietary food mechanical property categories.

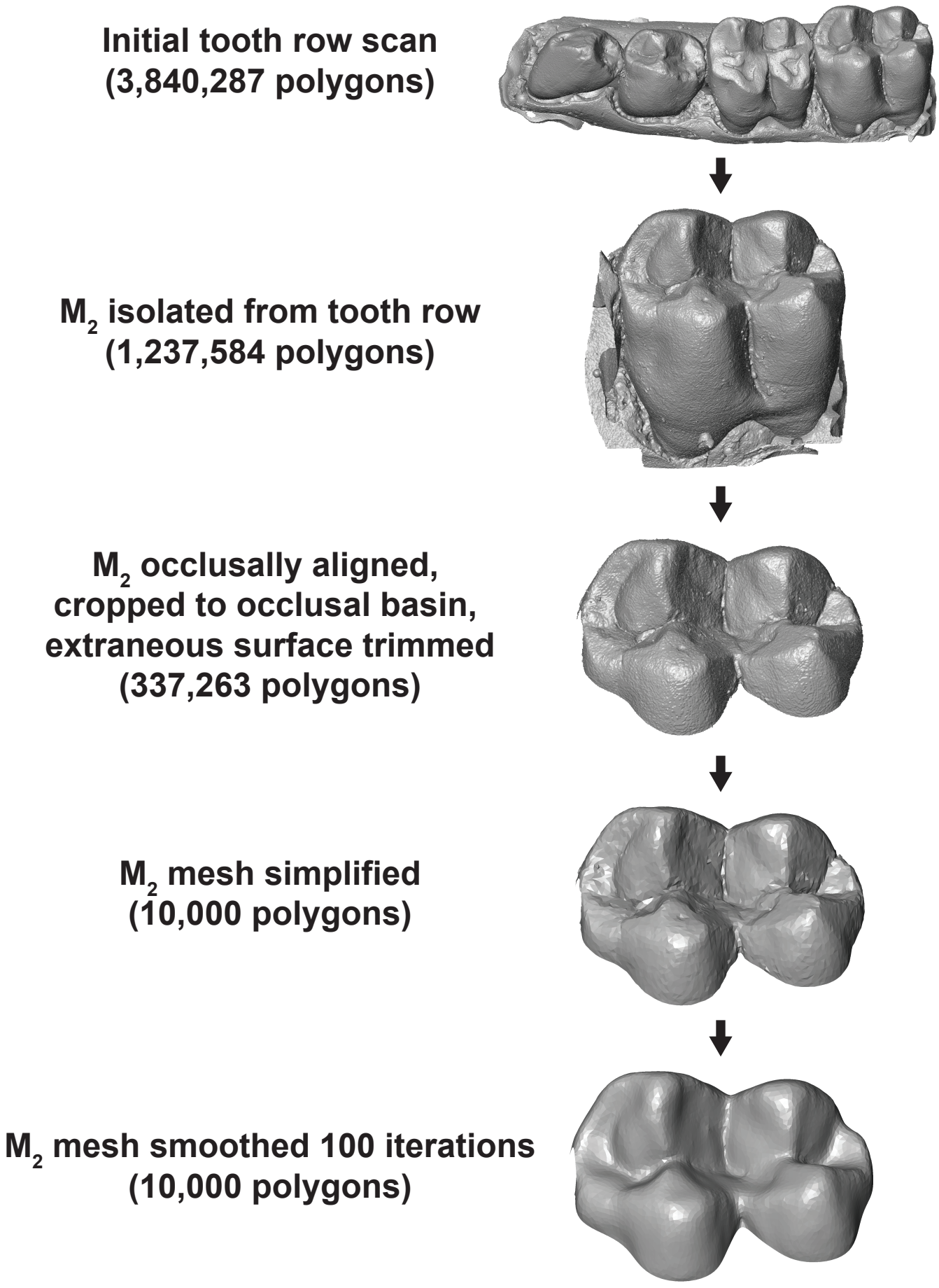

Fig 3.2. Post-scanning mesh preparation procedure. See Chapter 2 for further details. *Cercocebus atys* specimen number 89373 shown for reference.

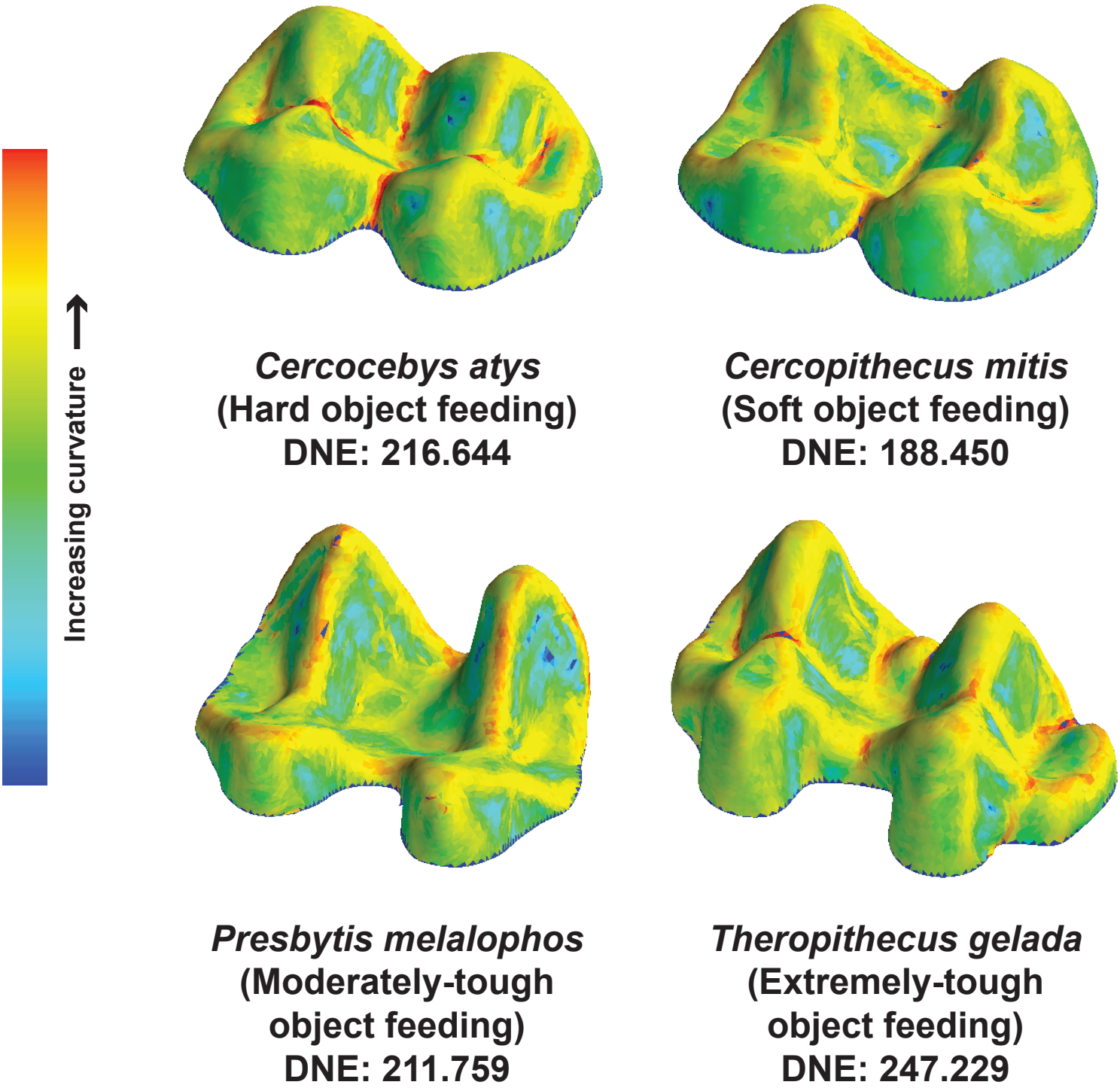

Fig 3.3. DNE visualized on reference cercopithecoid M_2 specimens. Warmer colors indicate greater degrees of local curvature. All specimens are presented using a uniform color scale, and similar colors therefore indicate similar degrees of local curvature between specimens.

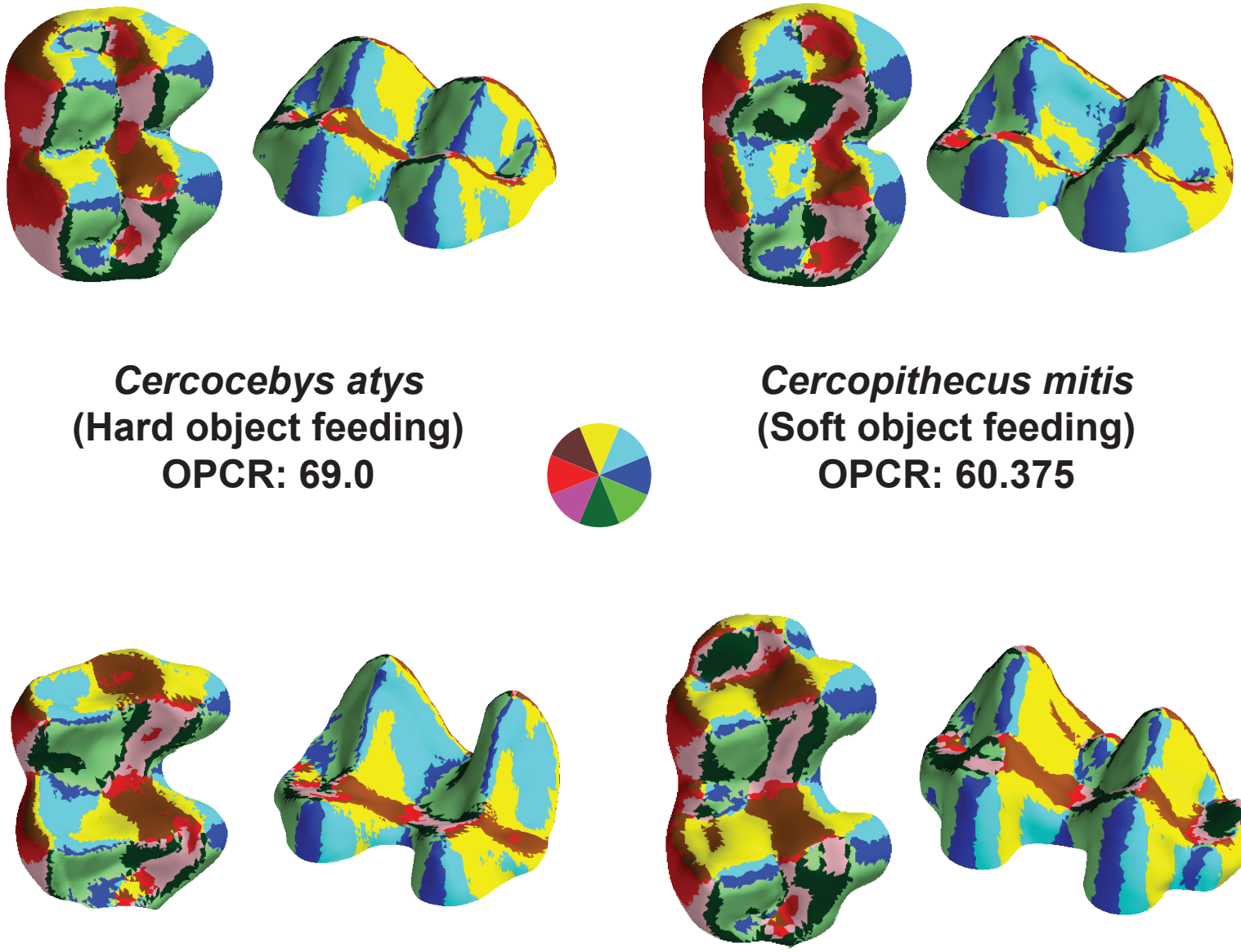

Fig 3.4. OPCR visualized on reference cercopithecoid M_2 specimens. For each species, occlusal (left) and oblique (right) perspectives are shown. For oblique perspective distal aspect is toward bottom-right and buccal aspect is toward bottom-left. Color wheel in center indicates patch facing by color for occlusal perspective.

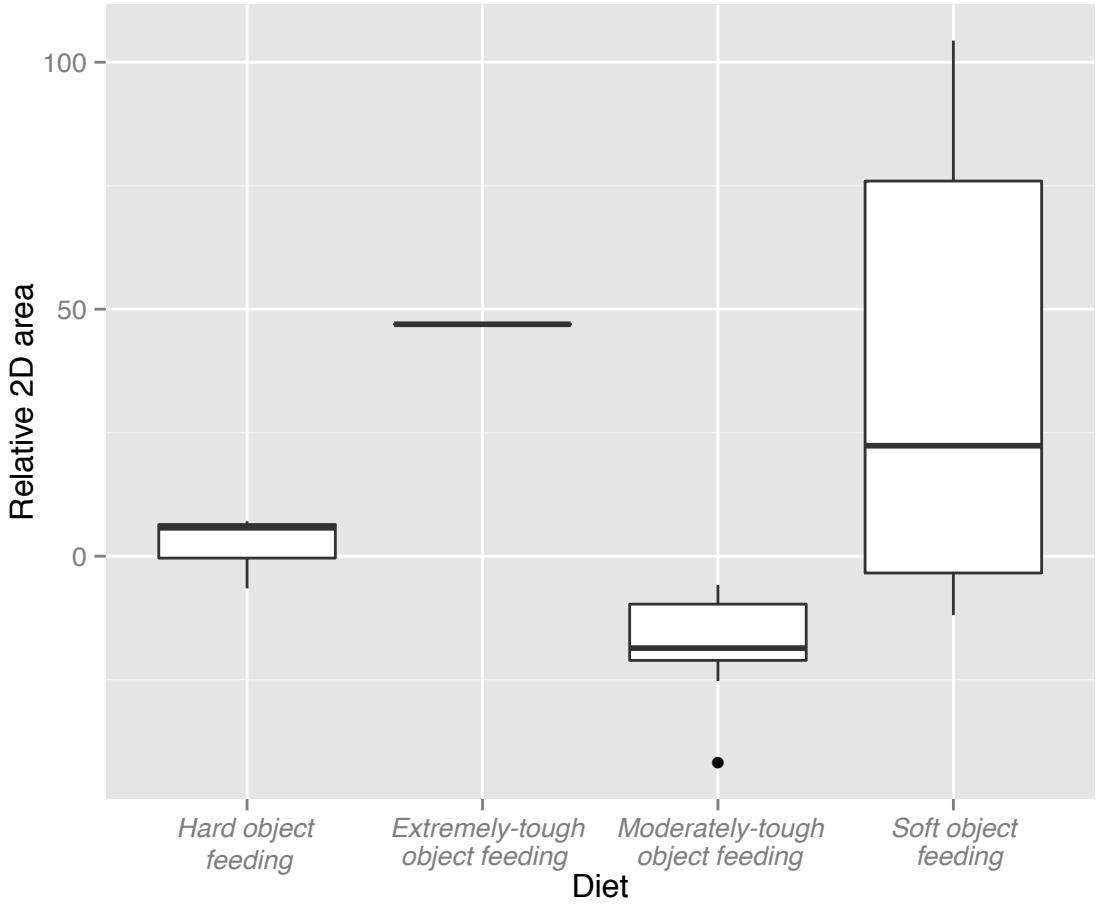

Fig 3.5. Box plot of relative M_2 2D area by diet group.

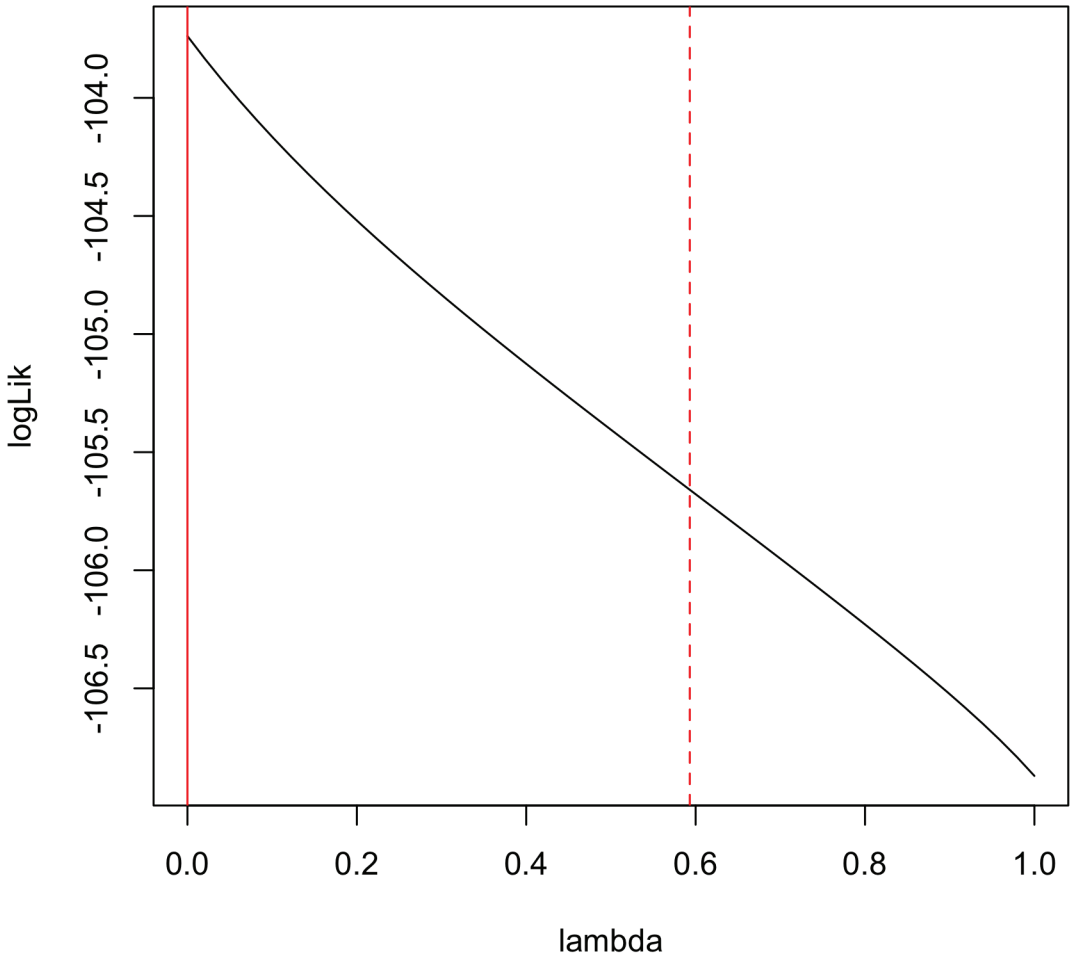

Fig 3.6. Log-Likelihood profile of lambda for relative M_2 area.

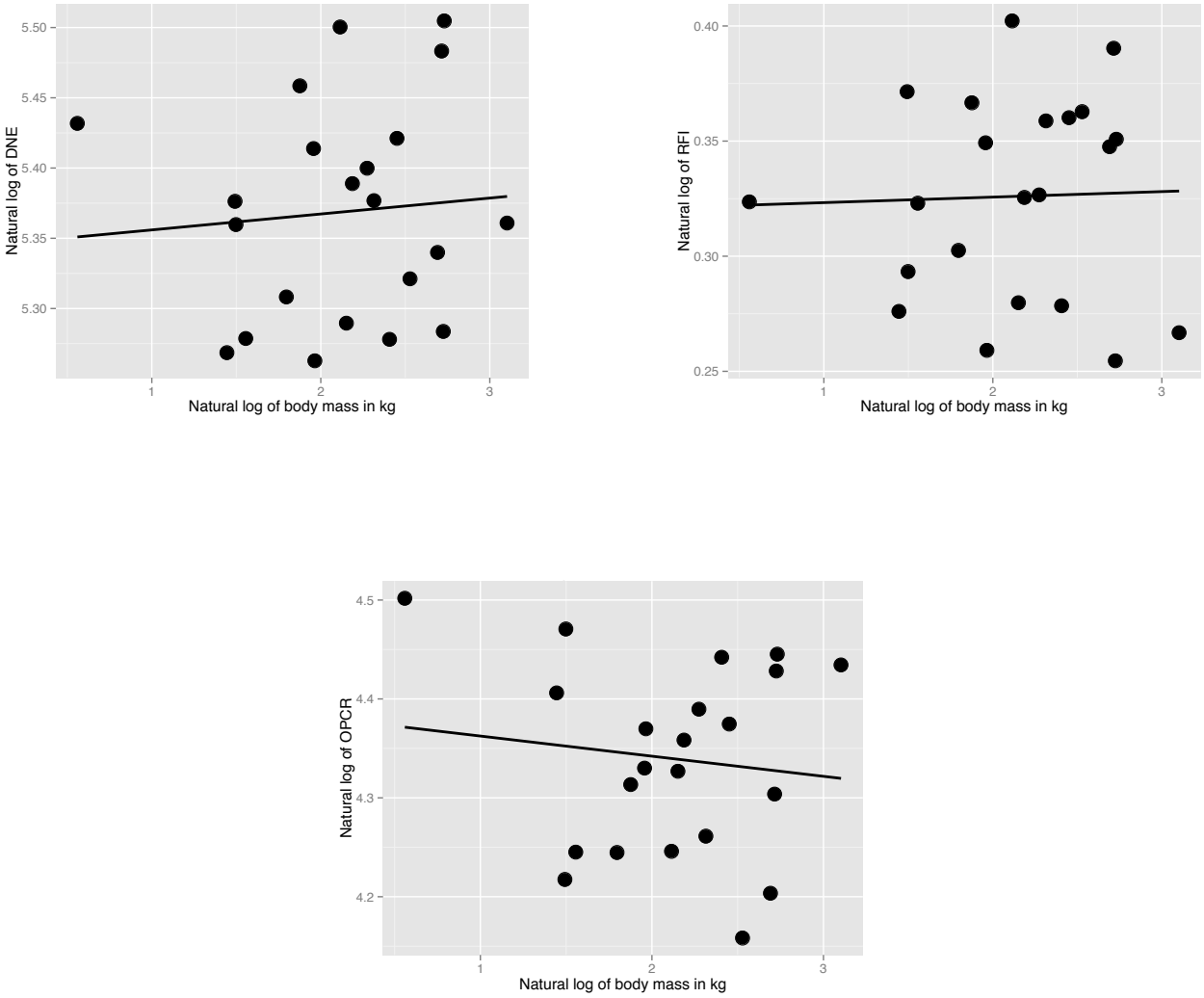

Fig 3.7. Regressions of species-mean topographic variables on body mass.

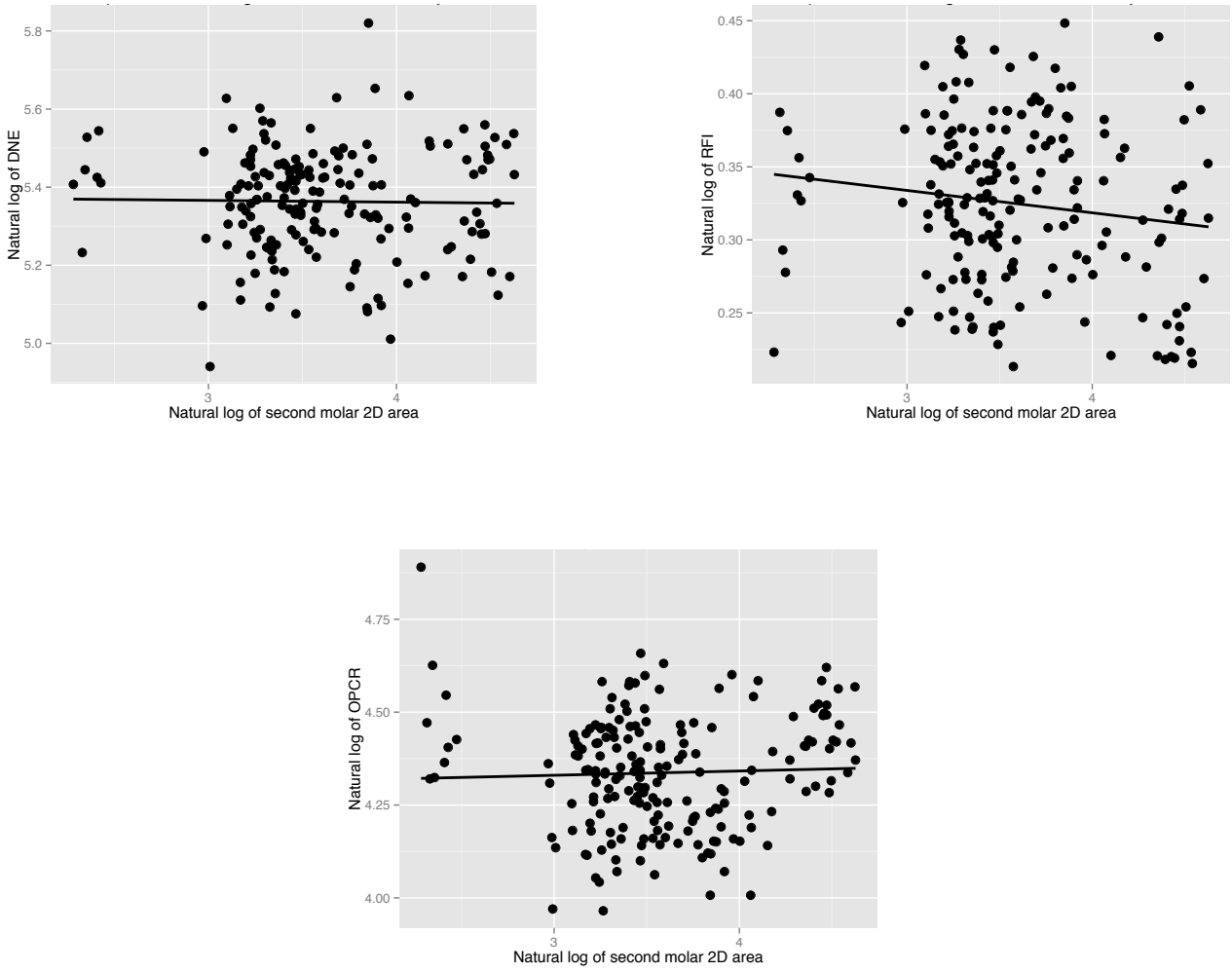

Fig 3.8. Regressions of specimen-level topographic variables on M_2 2D area.

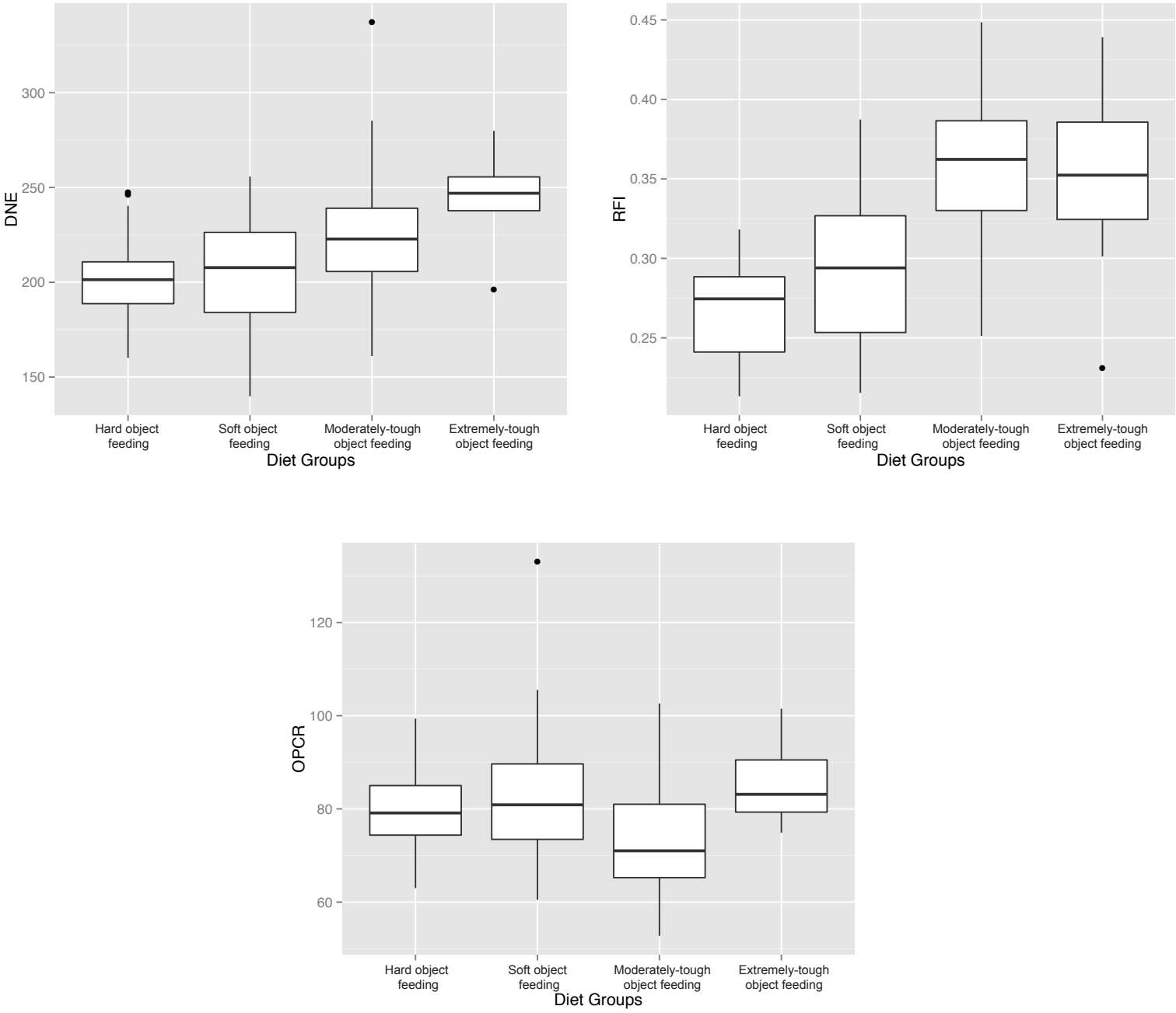

Fig 3.9. Box plots of topographic variables (DNE, RFI, OPCR) by diet.

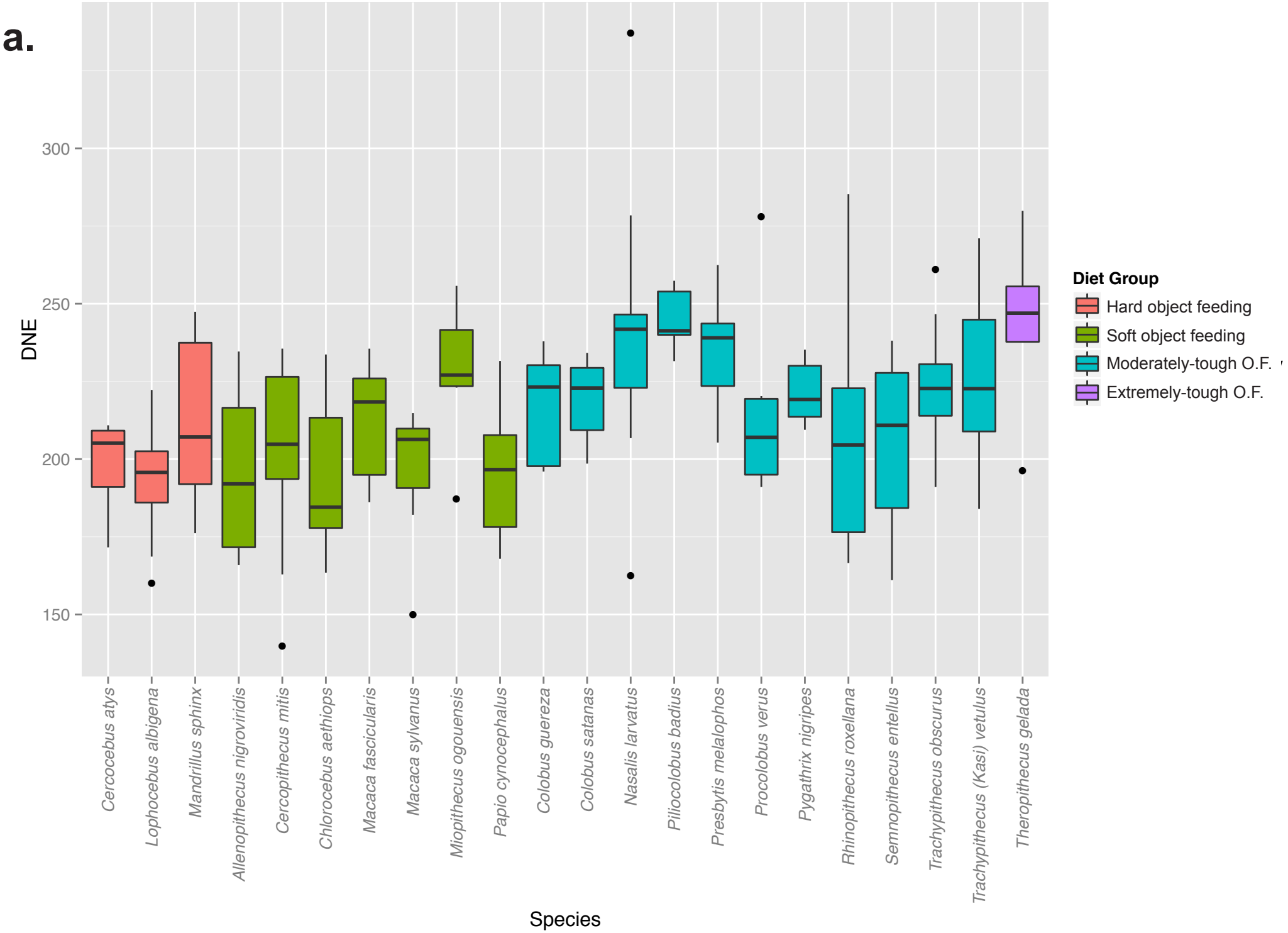

Fig 3.10a. Box plots of topographic variables (a: DNE, b: RFI, c: OPCR) by species and diet.

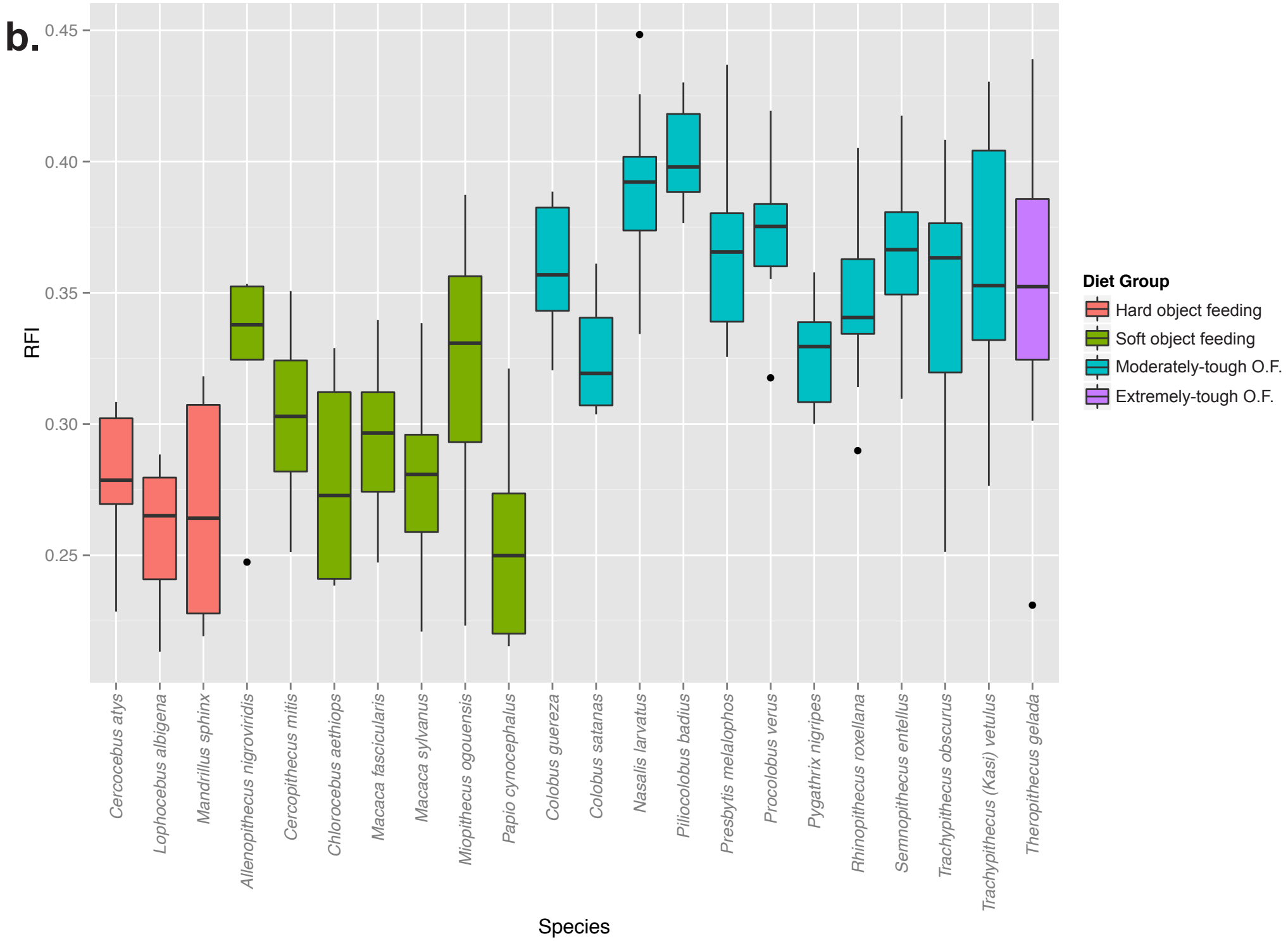

Fig 3.10b. Box plots of topographic variables (a: DNE, b: RFI, c: OPCR) by species and diet.

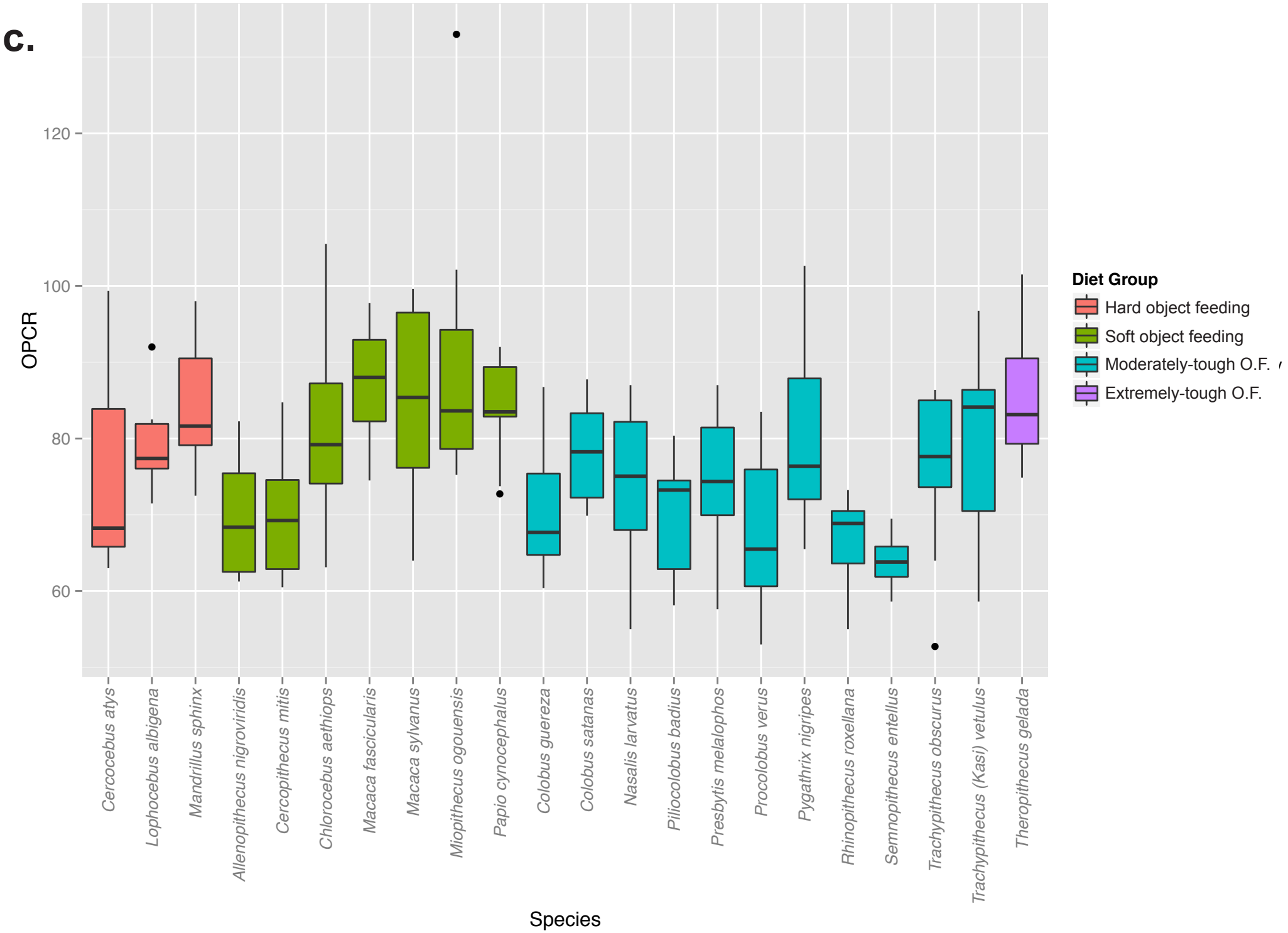

Fig 3.10c. Box plots of topographic variables (a: DNE, b: RFI, c: OPCR) by species and diet.

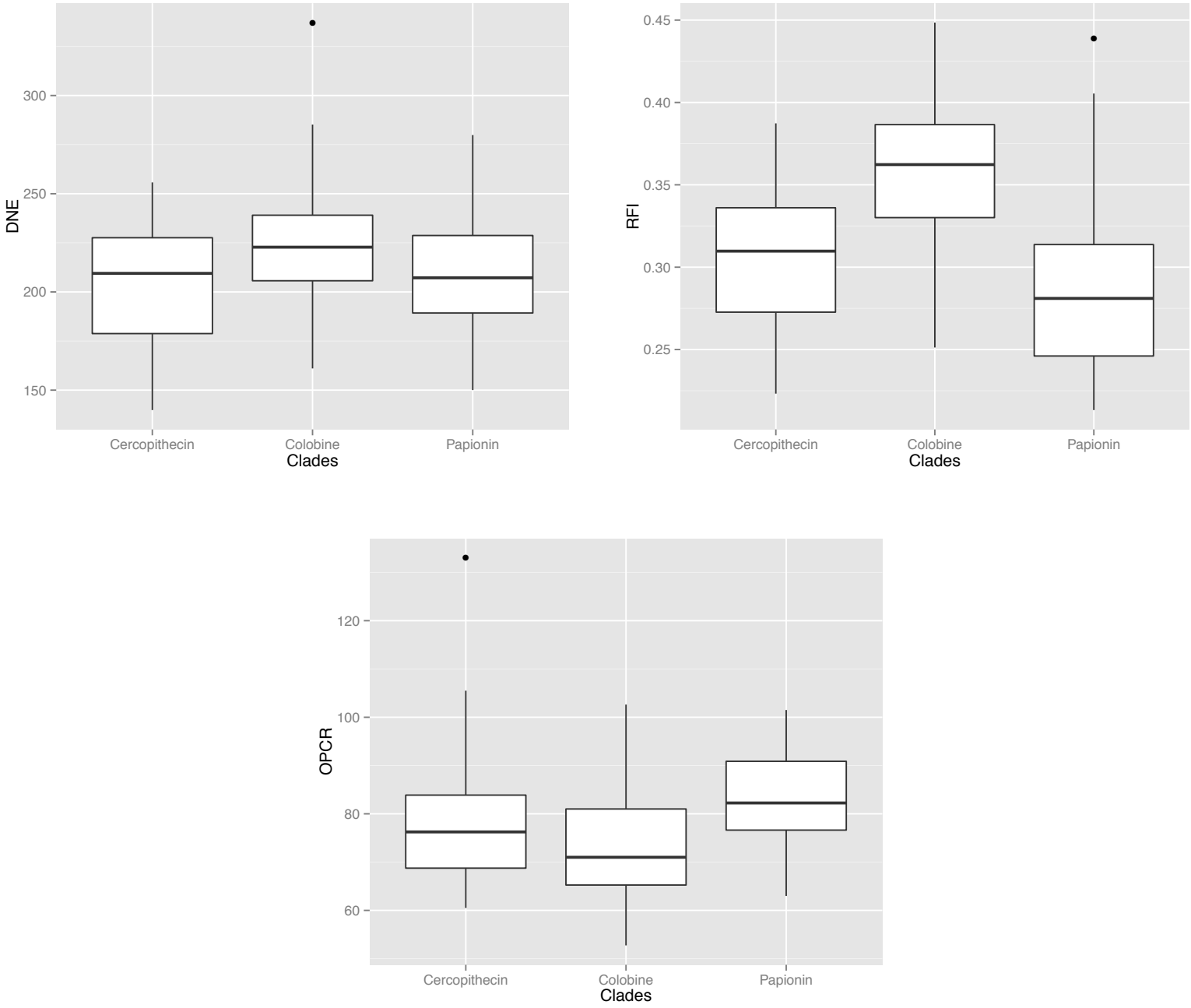

Fig 3.11. Box plots of topographic variables (DNE, RFI, OPCR) by clade.

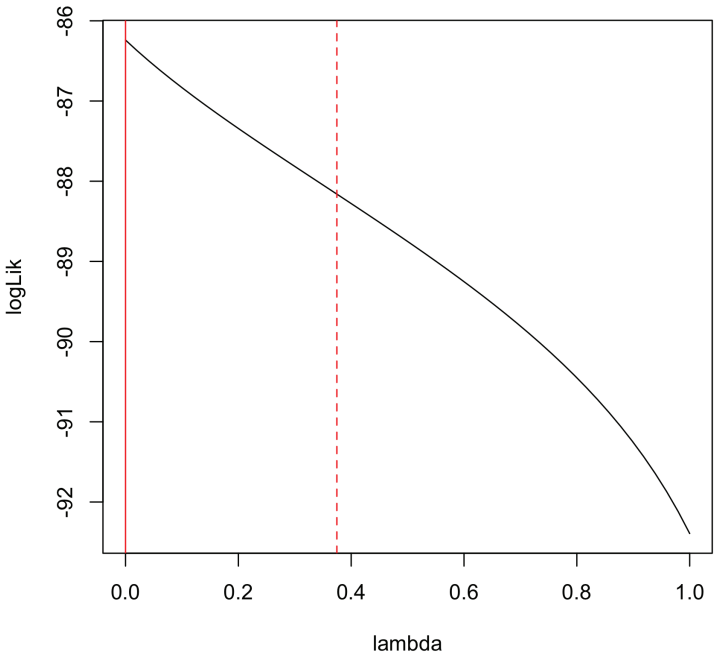

a. DNE

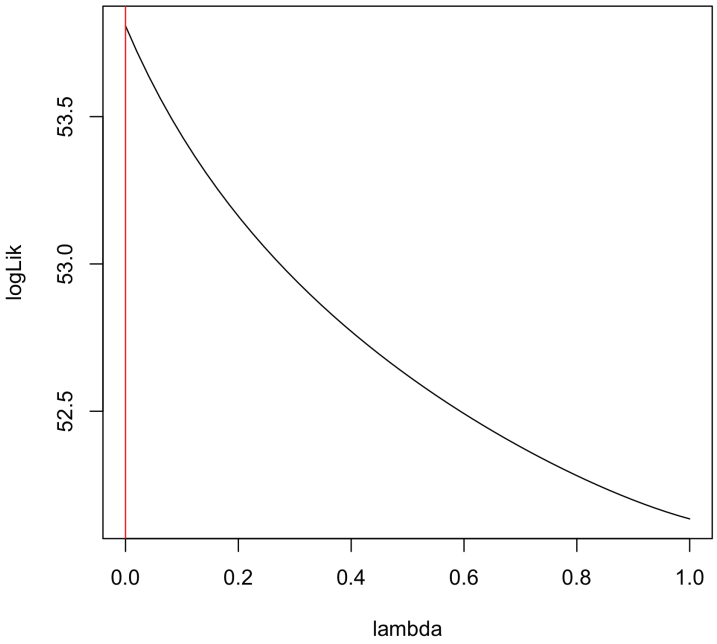

b. RFI

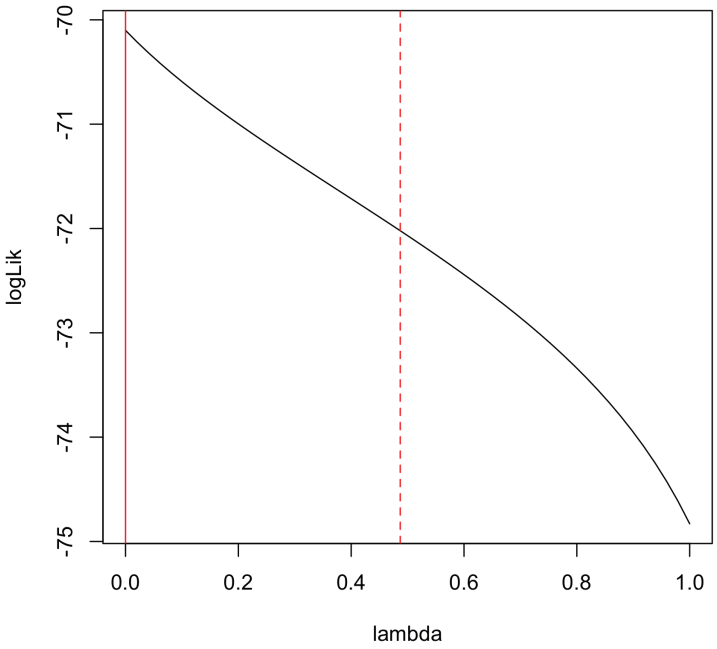

c. OPCR

Fig 3.12. Log-Likelihood profile plots of lambda for phylogenetic analyses of topographic variables by diet

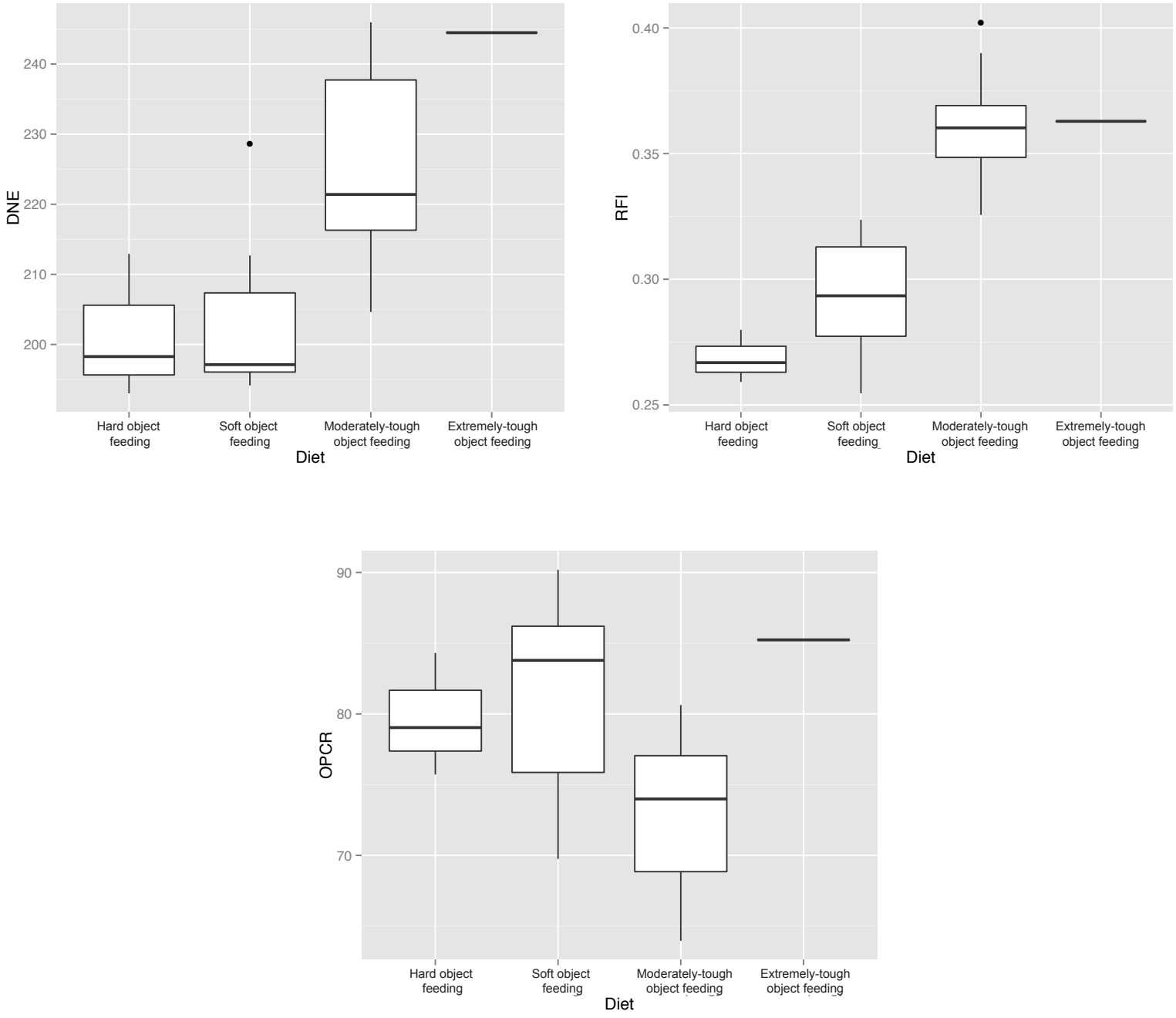

Fig 3.13. Box plots of species-mean topographic variables (DNE, RFI, OPCR) by diet.

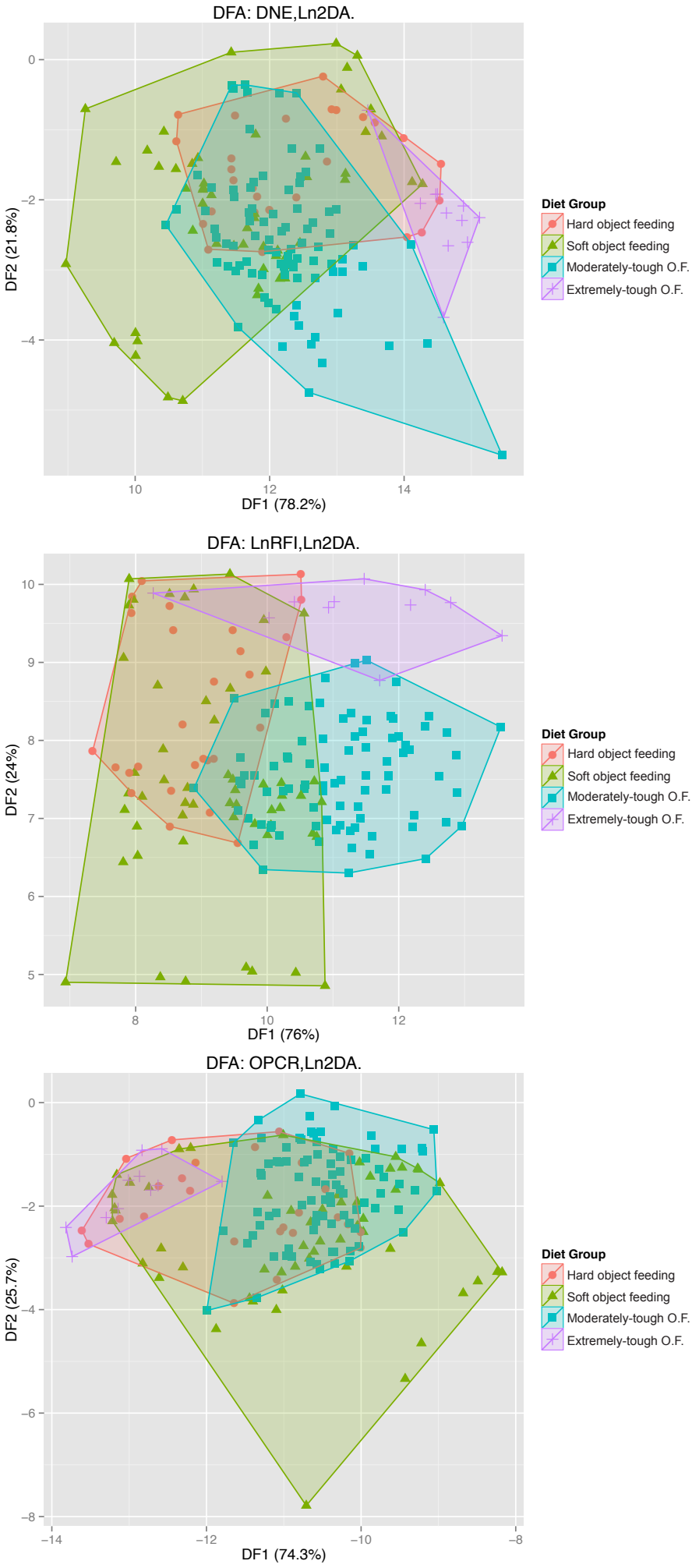

Fig 3.14a. DFAs of each topographic variable combined with M_2 2D area. Percentage of variance explained by discriminant functions given on axes.

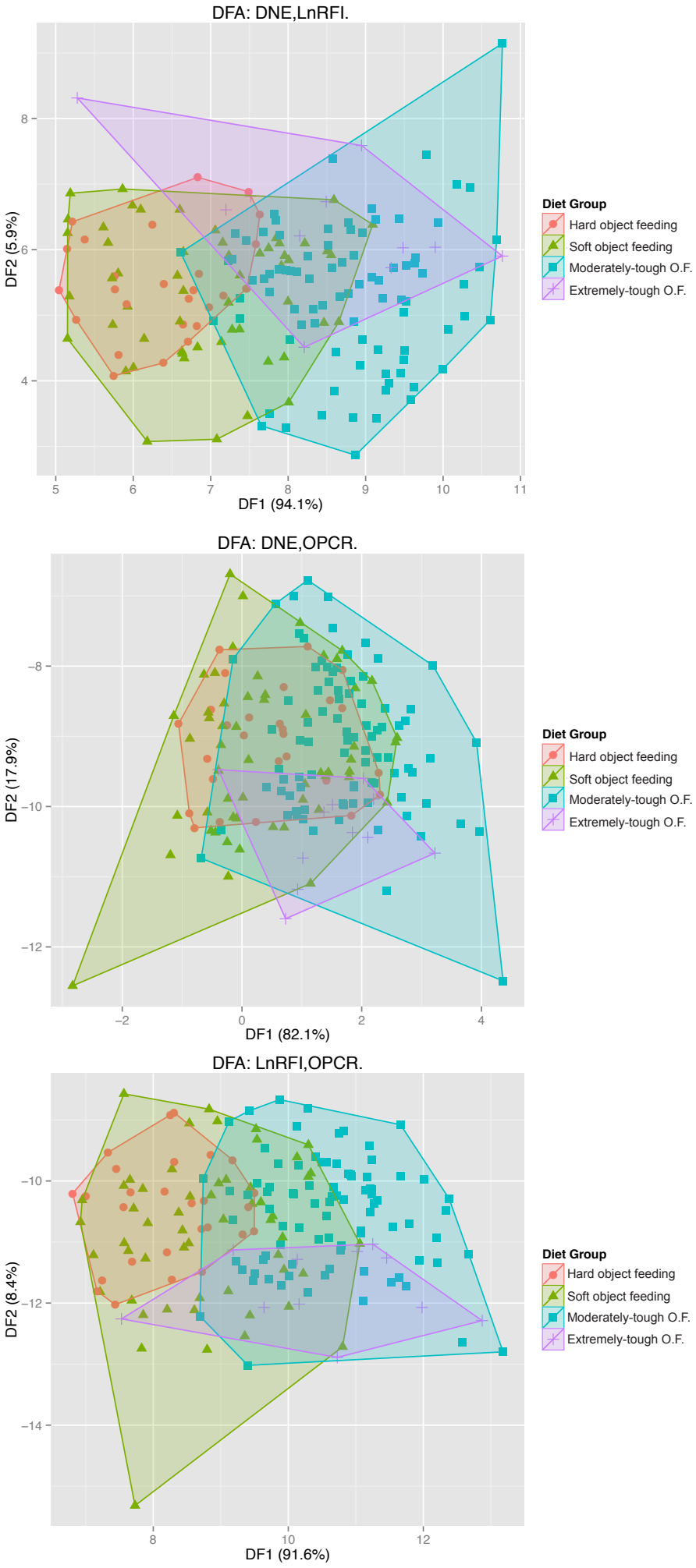

Fig 3.14b. DFAs of topographic variables combined in pairs without M_2 2D area. Percentage of variance explained by discriminant functions given on axes.

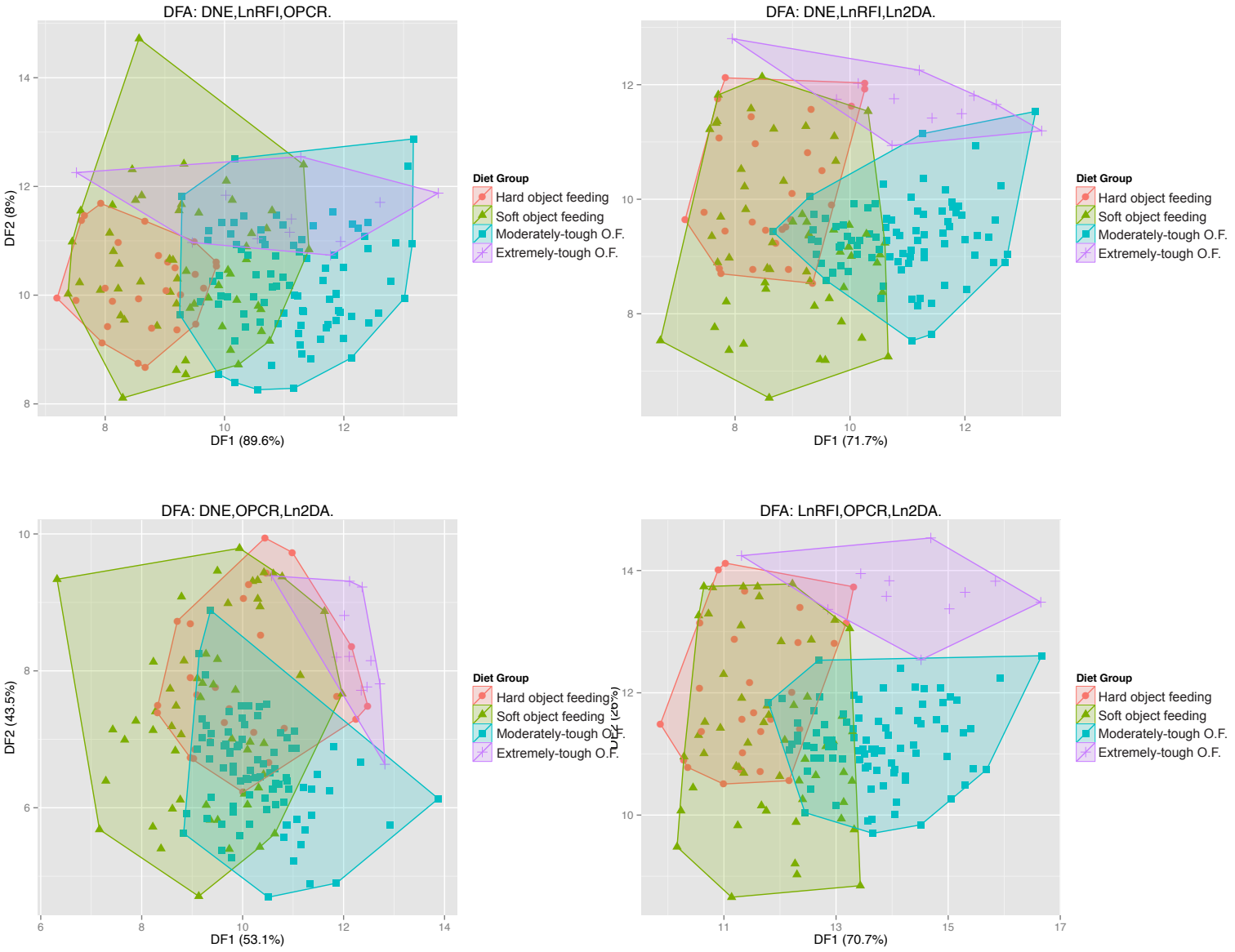

Fig 3.14c. DFAs of all possible combinations of three variables from DNE, RFI, OPCR, and M_2 2D area. Percentage of variance explained by discriminant functions given on axes.

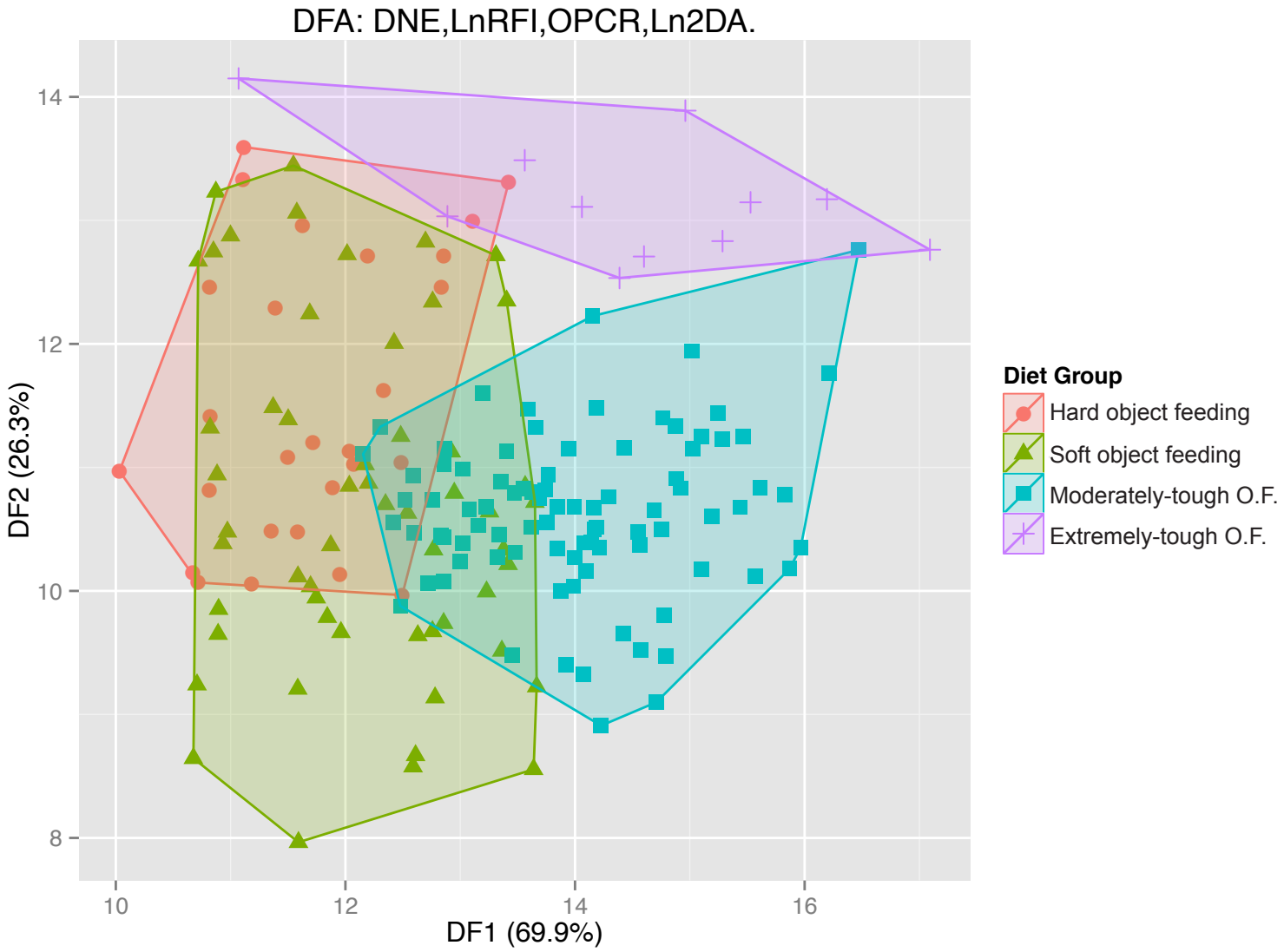

Fig 3.14d. DFA of all variables combined (DNE, RFI, OPCR, and M_2 2D area). Percentage explained by discriminant functions given on axes.

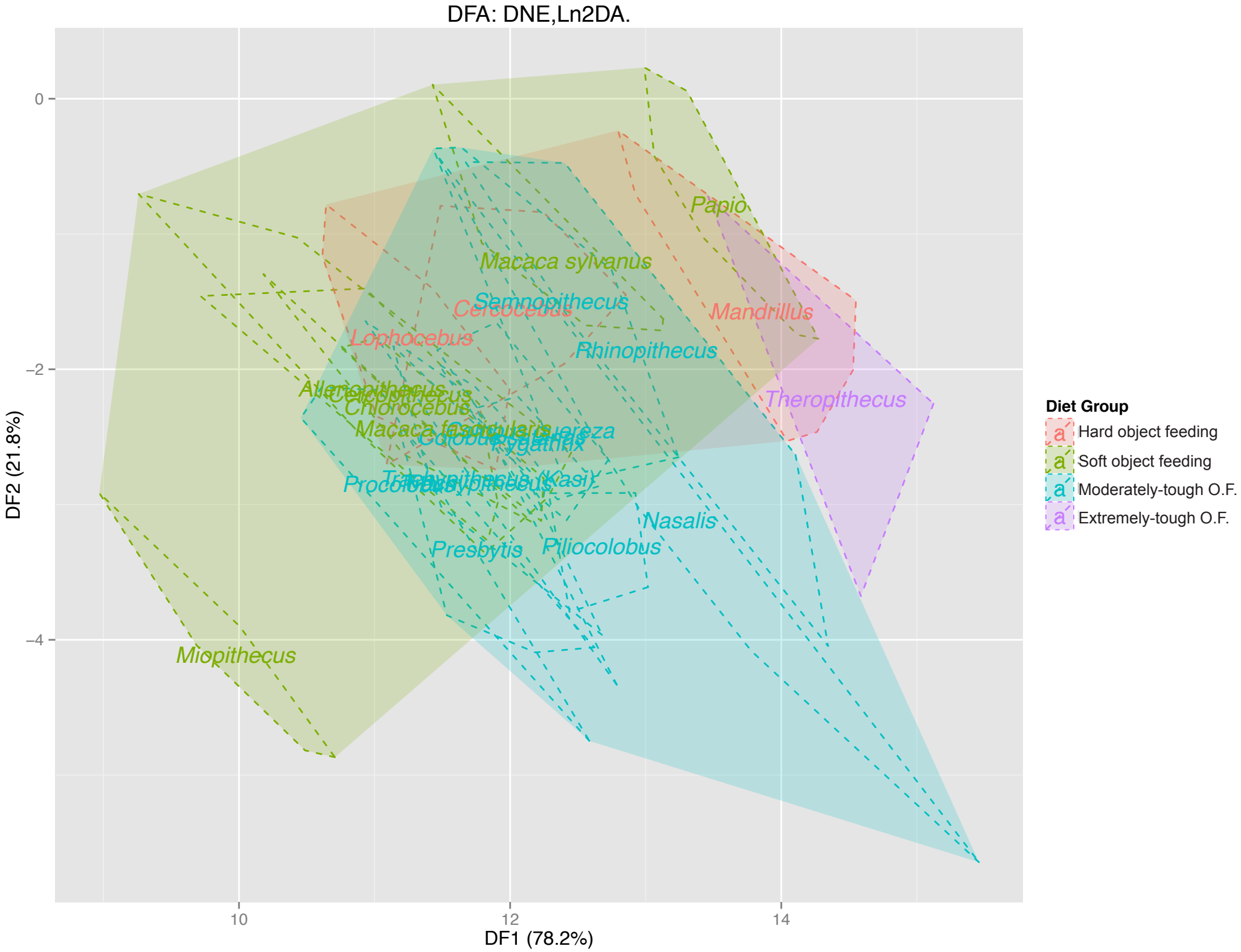

Fig 3.15a. DFA of DNE and M_2 2D area with diet groups and species outlined with convex hulls. Percentage variation explained on axes.

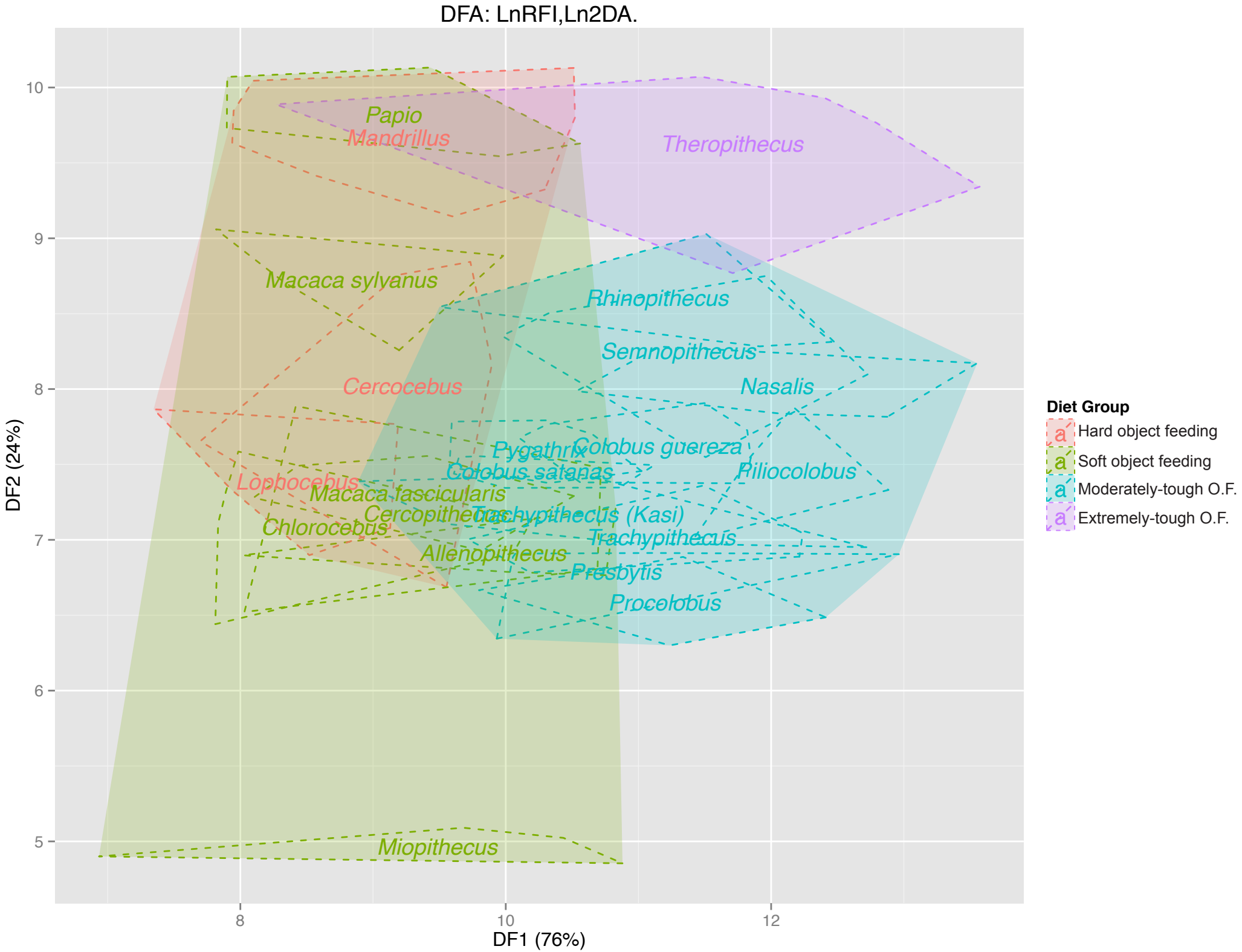

Fig 3.15b. DFA of RFI and M_2 2D area with diet groups and species outlined with convex hulls. Percentage variation explained on axes.

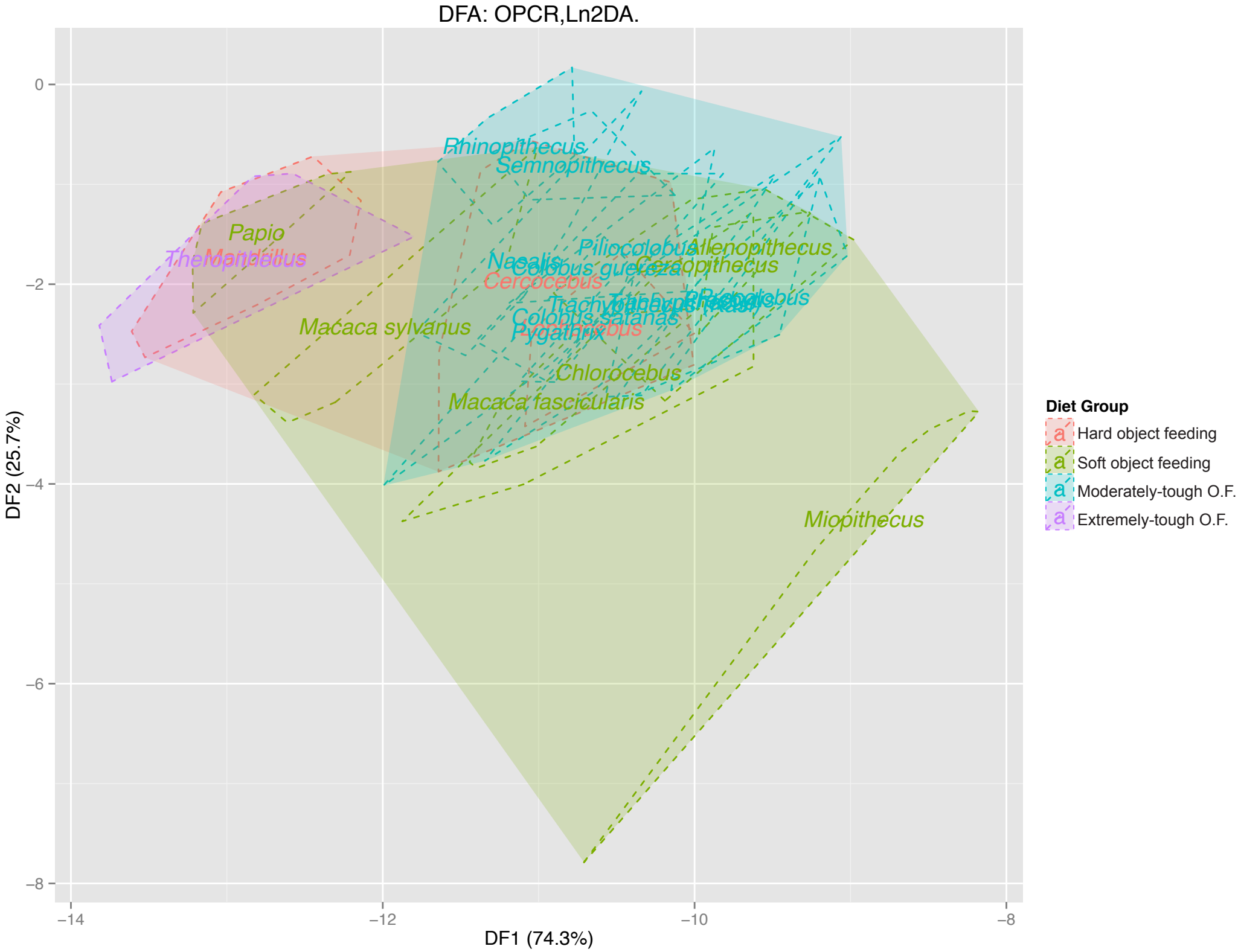

Fig 3.15c. DFA of OPCR and M_2 2D area with diet groups and species outlined with convex hulls. Percentage variation explained on axes.

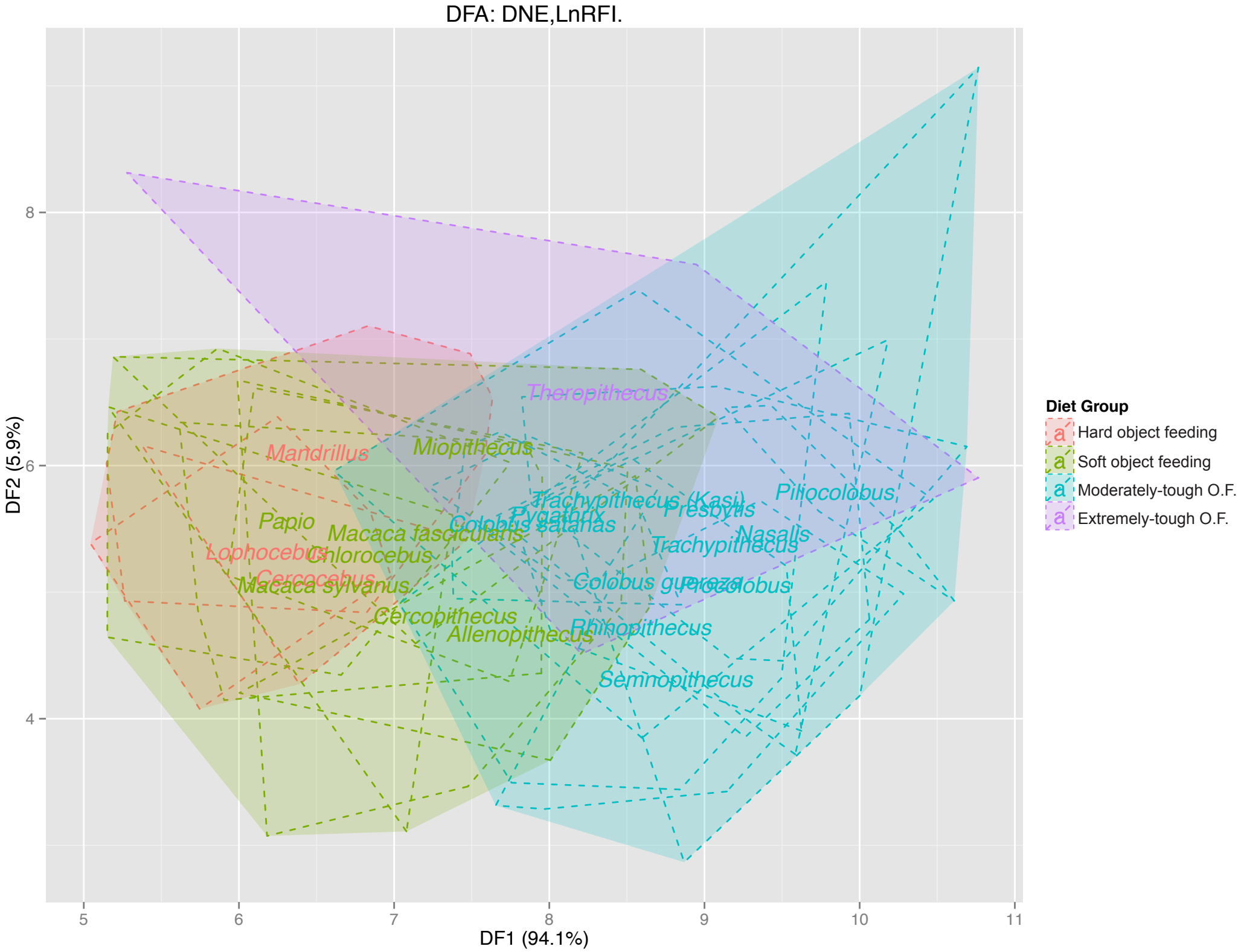

Fig 3.15d. DFA of DNE and RFI with diet groups and species outlined with convex hulls. Percentage variation explained on axes.

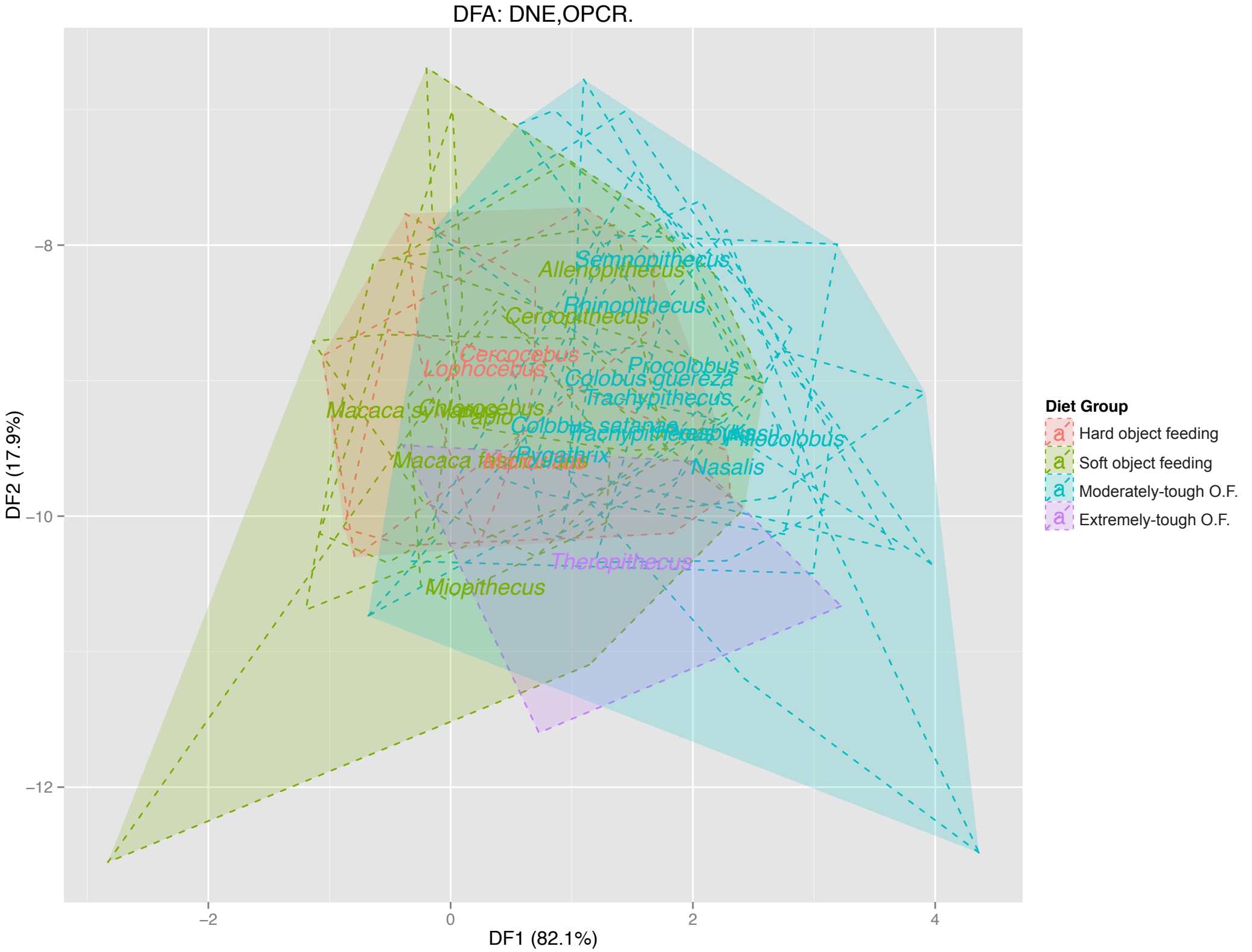

Fig 3.15e. DFA of DNE and OPCR with diet groups and species outlined with convex hulls. Percentage variation explained on axes.

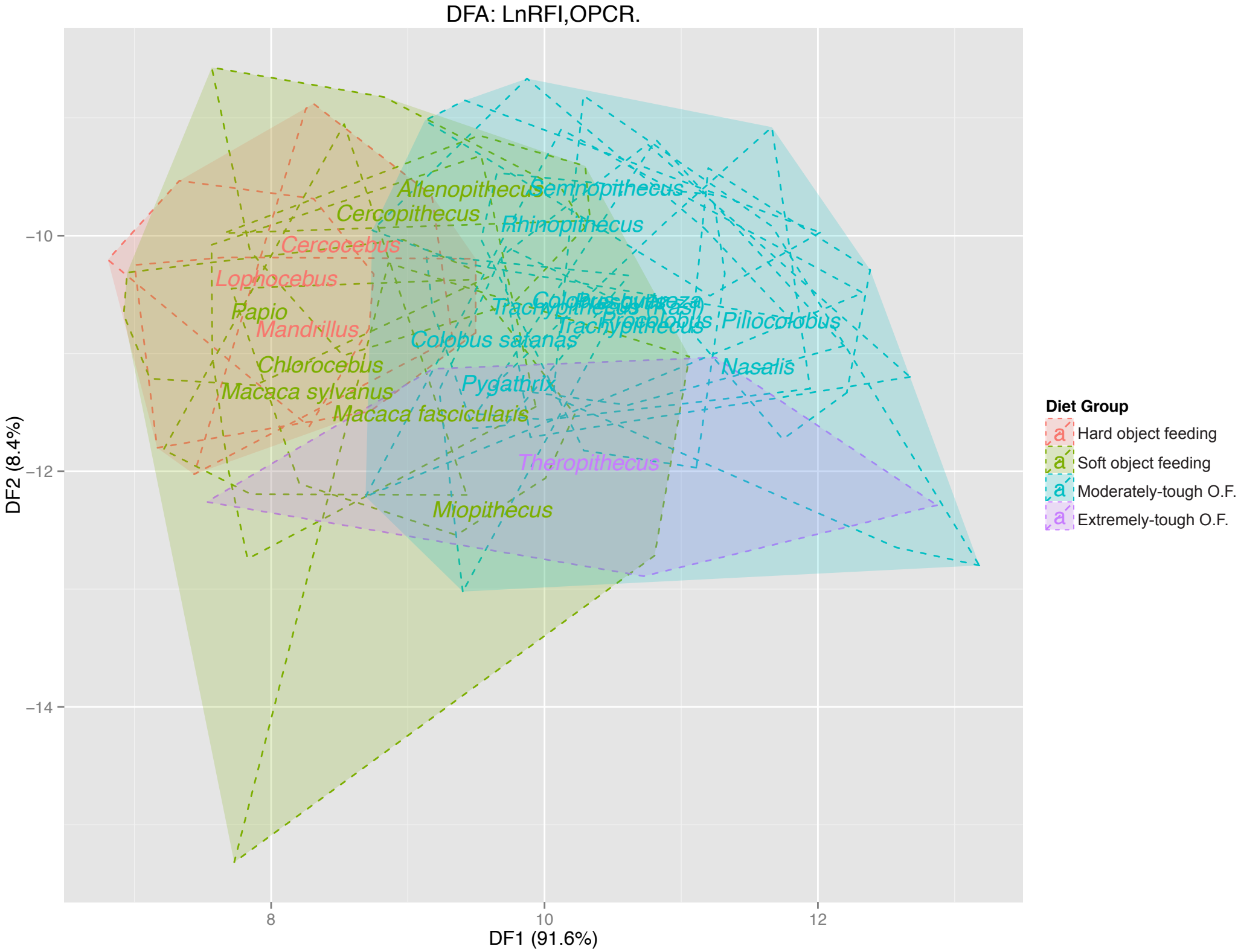

Fig 3.15f. DFA of RFI and OPCR with diet groups and species outlined with convex hulls. Percentage variation explained on axes.

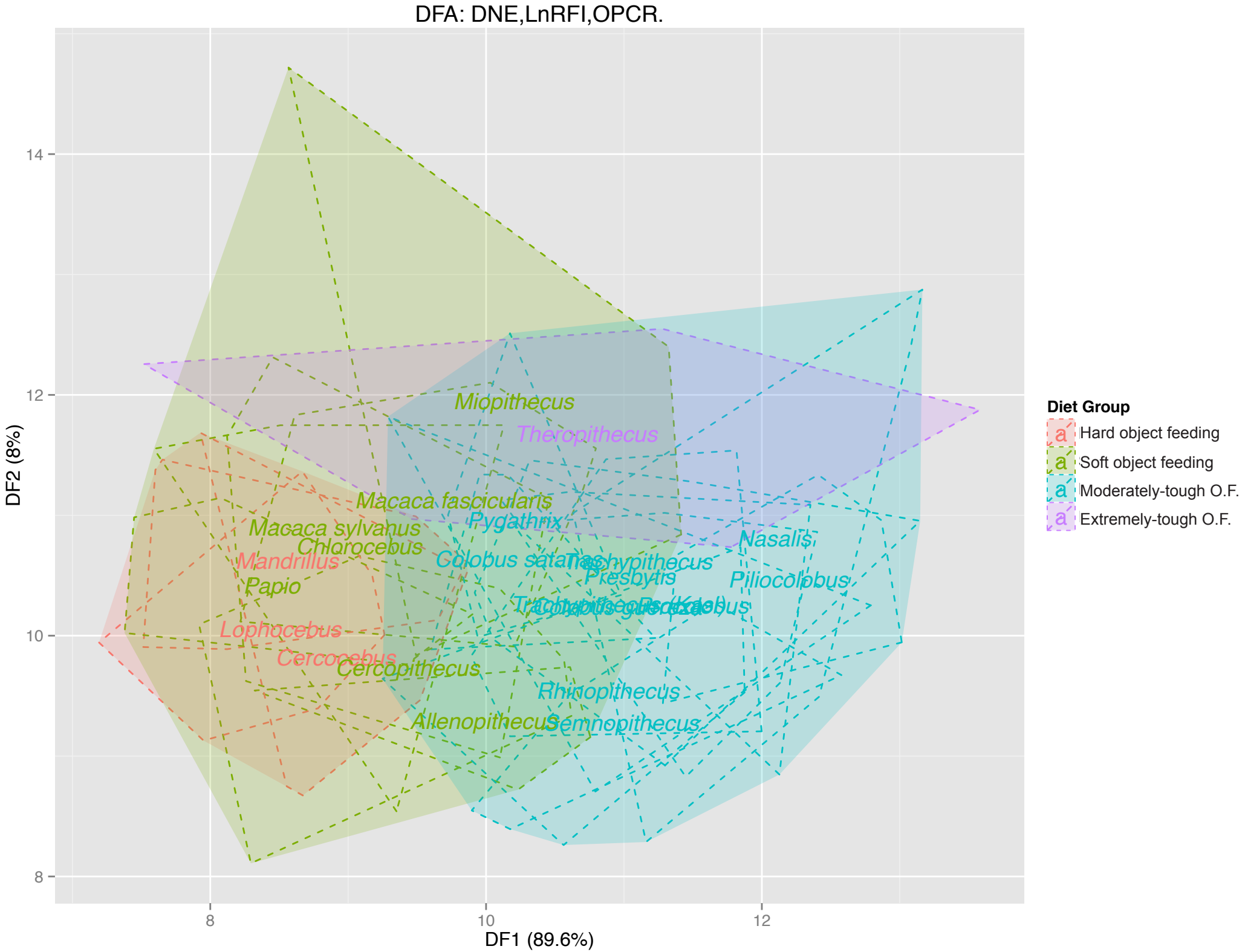

Fig 3.15g. DFA of DNE, RFI, and OPCR with diet groups and species outlined with convex hulls. Percentage variation explained on axes.

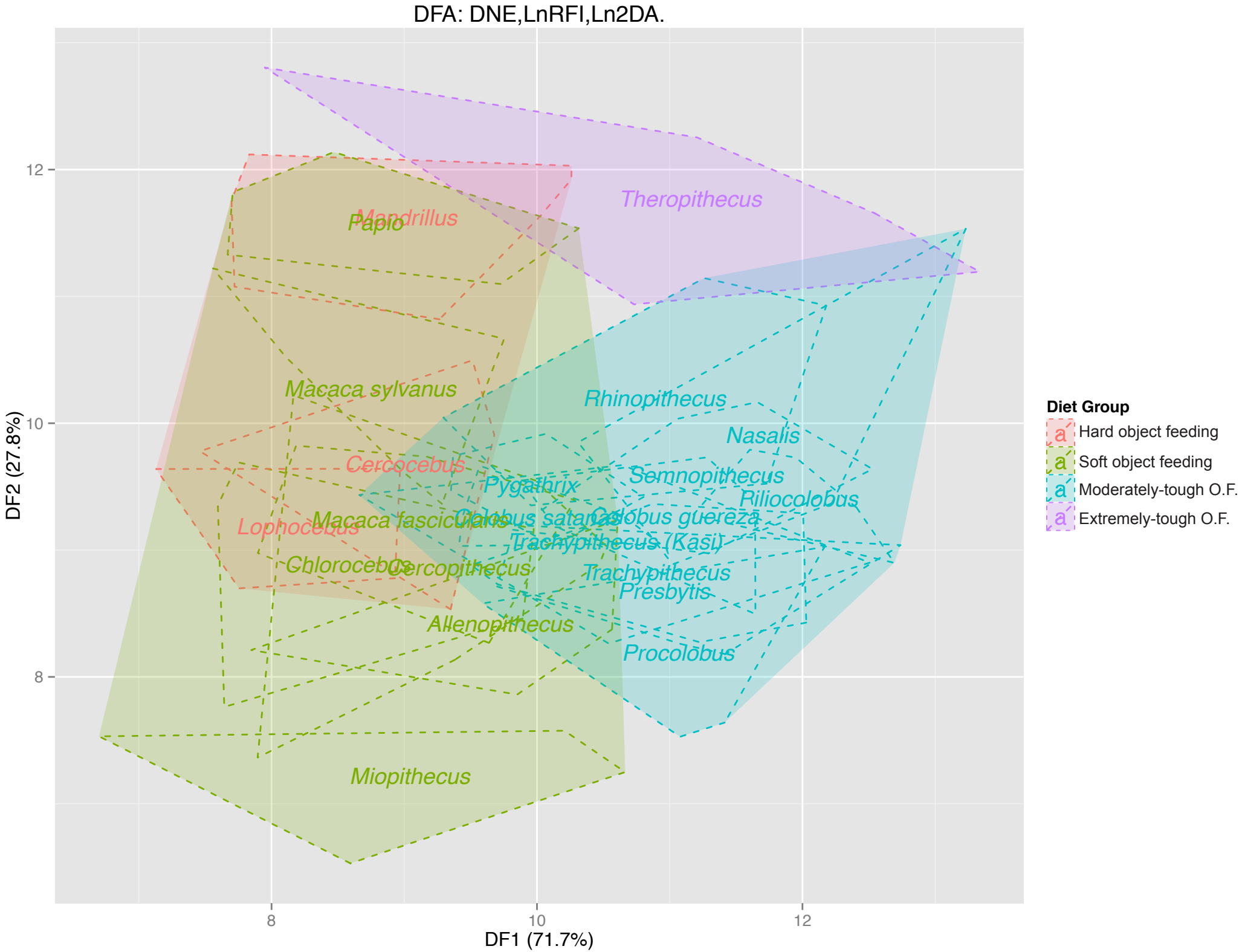

Fig 3.15h. DFA of DNE, RFI, and M_2 2D area with diet groups and species outlined with convex hulls. Percentage variation explained on axes.

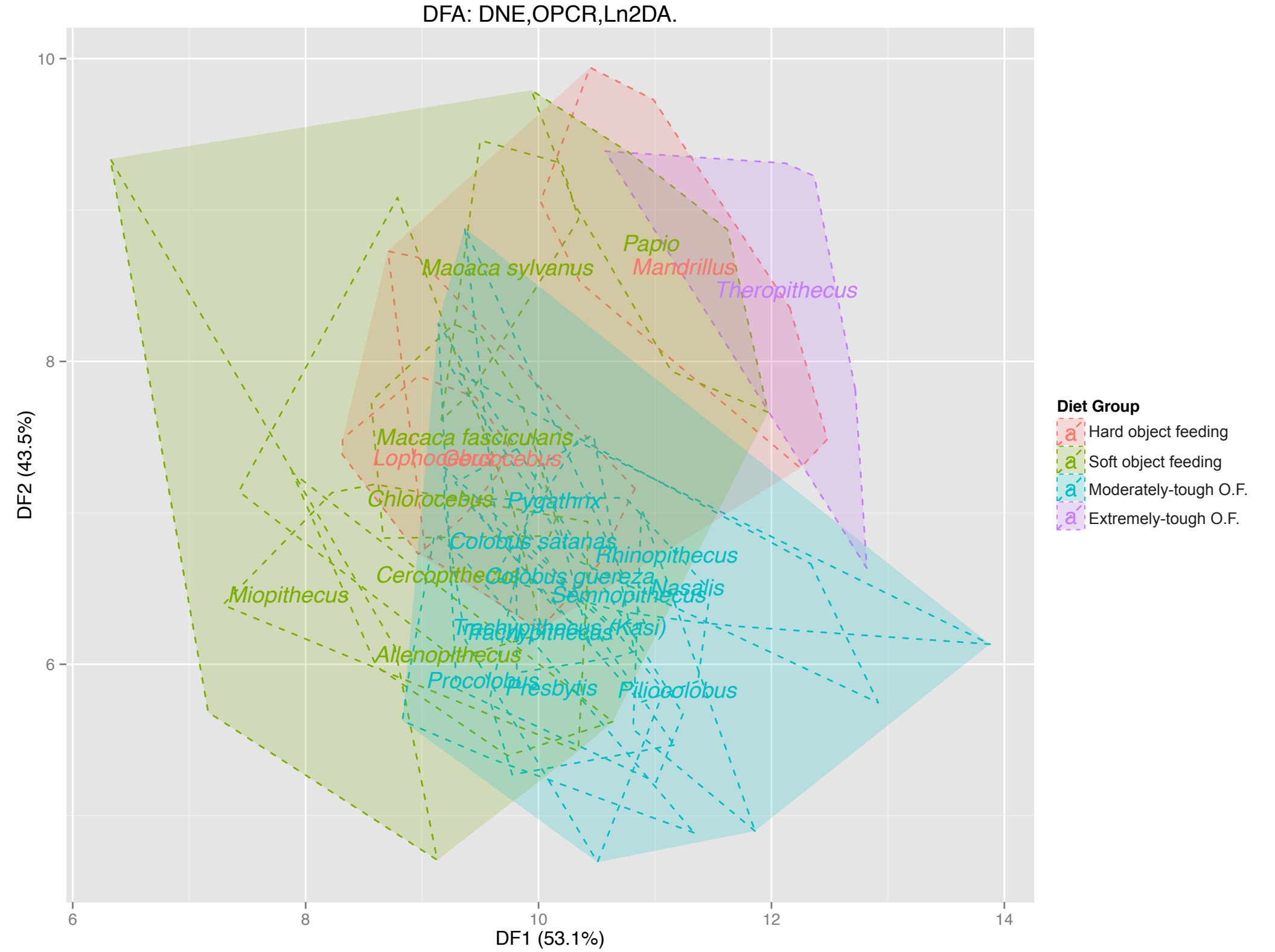

Fig 3.15i. DFA of DNE, OPCR, and M_2 2D area with diet groups and species outlined with convex hulls. Percentage variation explained on axes.

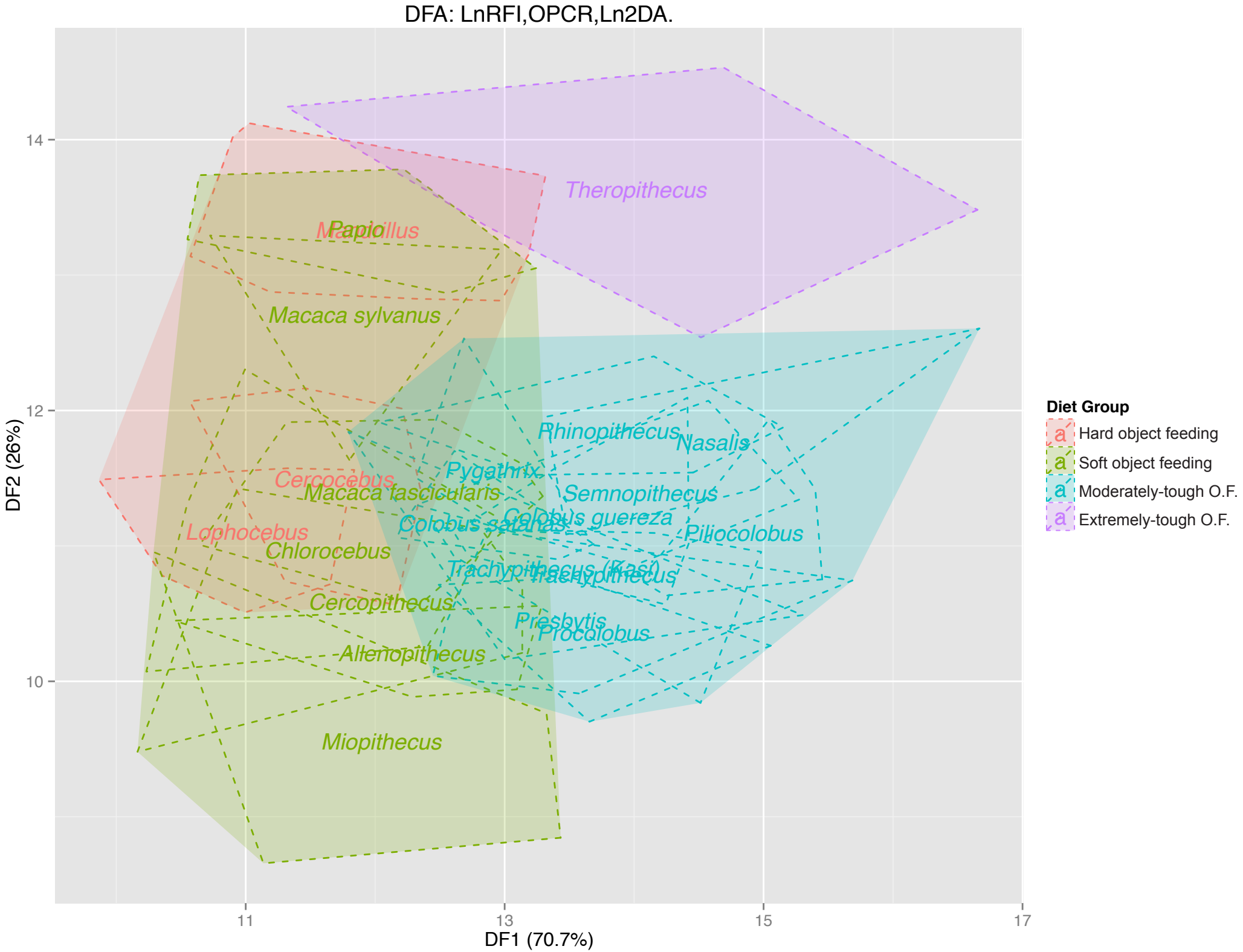

Fig 3.15j. DFA of RFI, OPCR, and M_2 2D area with diet groups and species outlined with convex hulls. Percentage variation explained on axes.

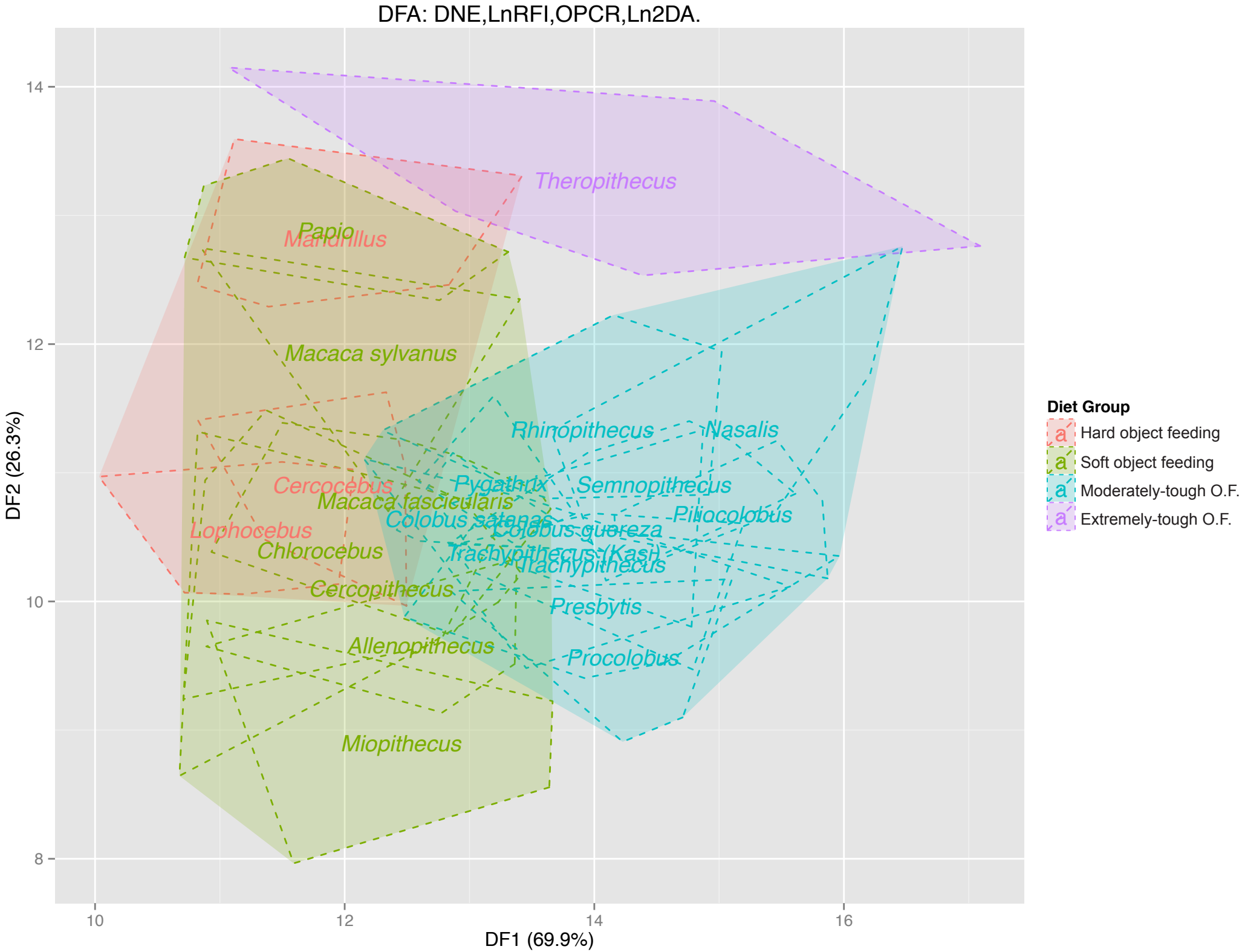

Fig 3.15k. DFA of DNE, RFI, OPCR, and M_2 2D area with diet groups and species outlined with convex hulls. Percentage variation on axes.

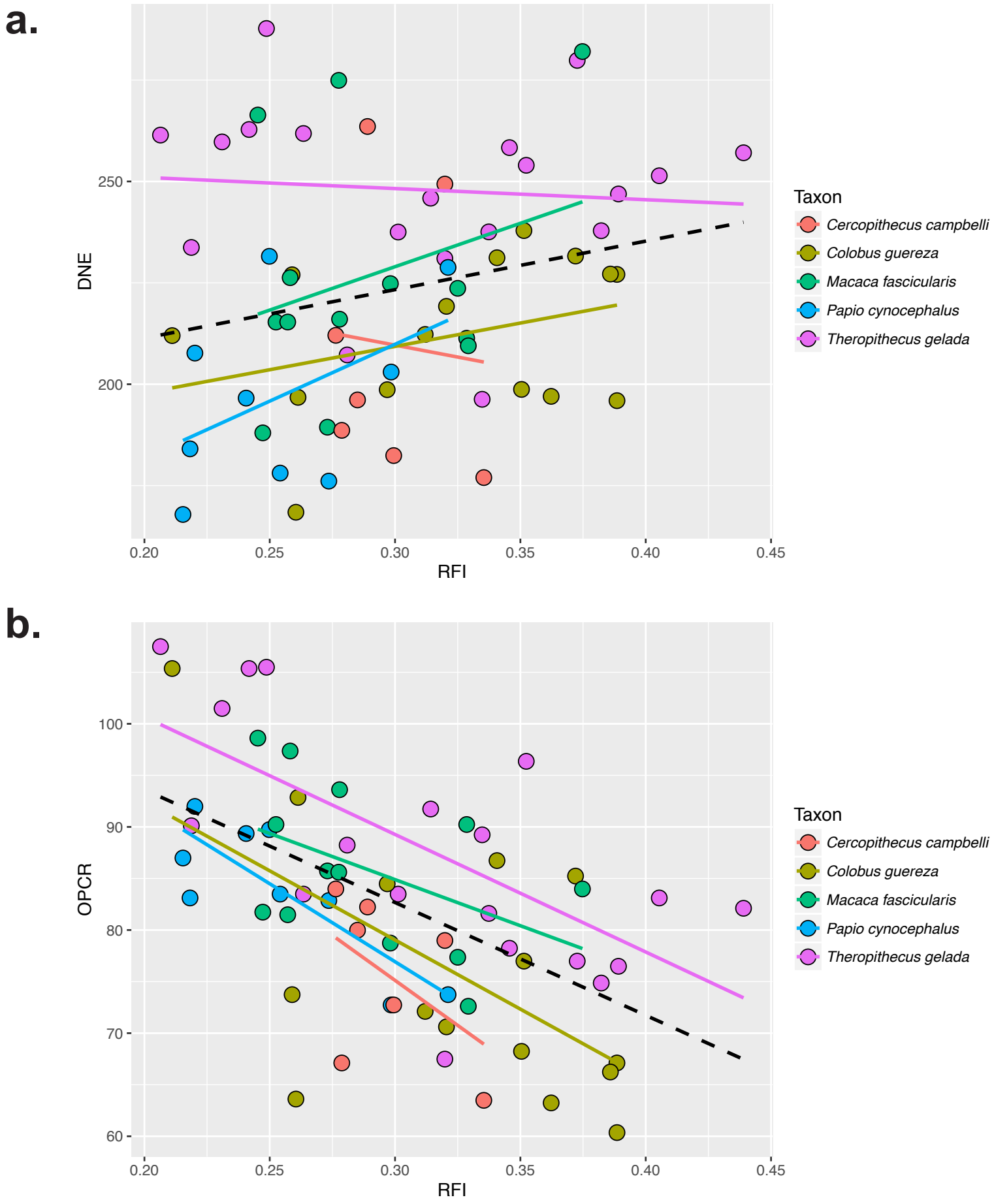

Fig 3.16. Regressions of (a) OPCR and (b) DNE by RFI. Sample species are differentiated by color. Dashed black line displays trend for all species combined, colored solid lines indicate trends for specific species.

Chapter 4

Developmental patterning and molar form in extant cercopithecoids

4.1: Introduction

Previous chapters have discussed production of digital data from anatomical specimens (Ch. 2), quantification of shape from this data using morphological topographic analyses (Ch. 2), and relationships between quantified molar topography and dietary food mechanical properties in extant cercopithecoids (Ch. 3). Those studies, like most considerations of dental morphology, were largely concerned with quantifying shape from post-eruptive molar teeth where development of the molar crown is already complete. But it is likely that to better understand molar shape it will be necessary to recognize and comprehend the developmental morphogenetic processes that lead to the formation of tooth shape. Developmental pathways outline the ranges of possible morphological variation that may be produced through natural selection (Jernvall, 1995; Gerhart and Kirschner, 1997), and understanding morphogenesis allows a clearer understanding of how adaptive evolutionary transitions may have been accomplished (Polly, 1998a; Jernvall, 2000). At the same time, developmental processes themselves are also subject to evolutionary modifications (e.g., Salazar-Ciudad and Jernvall, 2004). As a result, comparative analyses of morphology in a developmental context may shed light on evolutionary modifications to developmental pathways between species which will in turn further increase our understanding of the production of morphology.

Despite this potential, it is impractical to study dental morphogenesis in cercopithecoid species directly for various reasons. Fortunately, it is possible to use

predictions from recent empirical models of tooth development in rodents to attempt to infer aspects of molar morphogenesis in cercopithecoids. In doing so it may be possible to indirectly investigate the developmental processes that have produced the diversity of bilophodont cercopithecoid molar teeth specifically and primate molar teeth more generally, including those of humans and extinct hominins (e.g., Evans et al., 2016). The predictions of empirical models of mouse tooth morphogenesis are specifically relevant to this dissertation as many of them concern molar shape, especially molar shape variability. While morphological topographic analyses have historically been used to investigate molar shape in the context of dietary functional relationships (Ch. 1), there is no *prima facie* reason why they cannot be used for other purposes. One study assessing complexity of enamel-dentin junctions in combination with outer enamel surfaces has already considered one developmental process, namely the deposition of enamel and dentin (Skinner et al., 2010). Molar topographic analyses may therefore provide an apt suite of methods for investigating predictions of molar shape variability from developmental models. If the opposite is true and topographic methods are not well suited to detecting differences in shape variability compared to other shape quantification methods such as landmark-based approaches, this may still be instructive regarding strengths and weaknesses of different approaches for quantifying morphology.

Empirical models of mouse molar morphogenesis are more fully detailed in Chapter 1 of this dissertation, but key principles of molar development will be briefly reviewed here. Teeth develop from the interface of epithelial and mesenchymal tissues (Butler, 1956). Proliferation and folding of epithelial tissue for a given molar tooth seems to be initiated by a primary enamel knot, a non-mitotic signaling center expressing

various proteins that both inhibit and activate the development of further primary knots (Jernvall et al., 1994; Vaahtokari 1996; Jernvall et al., 1998; Jernvall and Thesleff, 2000a,b). The primary enamel knot of a subsequent molar develops at the margins of the inhibitory field of the initial knot, and the subsequent knot also expresses inhibitors and activators that affect the initiation of molars yet to develop (Jernvall et al., 2000; Salazar-Ciudad and Jernvall, 2002; Kassai et al., 2005; Kavanagh et al., 2007). The balance of inhibitors and activators expressed by a primary enamel knot and/or surrounding tissues provides an elegant mechanism for initiating multiple molar teeth while ensuring sufficient spacing between molars. A consequence of this "inhibitory cascade" model is that modifications to the inhibitor/activator balance in the first molar will have a compounding effect on subsequent molars (Kavanagh et al., 2007).

Cusps within molars seem to develop from a similar "patterning cascade," with equivalent compounding results on subsequent cusps (Weiss et al., 1998; Jernvall and Thesleff, 2000b; Jernvall, 2000). In mouse molars the primary knot defines the initial tooth crown epithelial base area, which expands primarily longitudinally (mesio-distally) and secondarily horizontally (bucco-lingually). Before disappearing apoptotically, the primary knot gives rise to the first in a sequence of secondary enamel knots (Jernvall et al., 1994; Jernvall and Thesleff, 2000b). Secondary enamel knots are similar to primary enamel knots in being non-proliferative signaling centers that express inhibitors and activator, helping to space and organize future cusps. In the lower molars of mice, the first secondary knot corresponds to the protoconid cusp (Jernvall et al., 2000; Jernvall and Thesleff, 2000b). Shortly after the appearance of the first secondary knot, another secondary knot develops directly lingual to the first and marks the appearance of the

metaconid cusp. Later, a second pair of secondary enamel knots, marking the appearance of third and fourth cusps, appear distal to the first two. Much like for the first pair of secondary enamel knots, the knots of the second pair are parallel buccolingually and appear to both develop either roughly simultaneously or at very similar points in the developmental schedule (Jernvall et al., 2000; Jernvall and Thesleff, 2000b). The number of cusps that can be initiated on a developing tooth surface is limited by the inhibitor/activator balance of secondary enamel knots starting with the first of these knots, the available tooth crown epithelial base area, and by the length of time from the appearance of the primary enamel knot to the termination of crown morphogenesis and the initiation of root formation (Jernvall, 1995; Jernvall and Thesleff, 2000a,b; Jernvall and Jung, 2000). Much like for the individual molars, spacing of cusps is determined by the balance of inhibitors and activators expressed by secondary knots and modifications in this balance for the first secondary knot have cascading compounded effects on subsequent cusps (Jernvall, 2000; Jernvall et al., 2000).

These developmental models make several predictions that can be tested from fully developed cercopithecoid molars. Of these, the inhibitory cascade (IC) model of tooth development and its predictions for molar size proportions have so far received the most attention in mammals (Kavanagh et al., 2007; Polly, 2007; Asahari, 2013; Halliday and Goswami, 2013; Bernal et al., 2013; Schroer and Wood, 2015; Evans et al., 2016; see Ch. 1 for more details). Specifically, Kavanagh et al. (2007) reason that if molar teeth are developed from a balance of activators and inhibitors, then a ratio of third molar size to first molar size regressed on a ratio of second molar size to first molar size should produce a linear regression with a slope of 2.0 and an intercept of -1.0. There is some

evidence that predictions of this model are supported for some clades of primates (Lucas et al., 1986; Bernal et al., 2013; Schroer and Wood, 2015; also see Ch. 1 for further discussion). This prediction is tested for cercopithecoids in this chapter because it is straightforward to assess and provides vital context to subsequent analyses, but the focus of this chapter is on shape variability more than molar proportion patterning specifically.

Inhibitory cascade and patterning cascade models respectively make predictions regarding inter-tooth and intra-tooth (inter-cusp) shape variability. If the balance of inhibitors and activators in initial enamel knots has compounding effects on later-developing molars or molar cusps, then it should be the case that later-developing molars or molar cusps are more variable in form. For example, under this model the initiation of the hypoconulid cusp is affected by the development of the protoconid but protoconid initiation is not affected by hypoconulid development. Later-developing molars or molar cusps are affected by greater numbers of developmental events relating to earlier-developing molars or molar cusps respectively, and small amounts of variation across these events should combine to produce overall greater variability in later-developing structures. It is possible to test this prediction both 1) within species, to address whether later-developing molars or molar cusps are more variable in a given species; and 2) between species, to address whether observed morphological differences between species occur more frequently in later-developing teeth or cusps. Put another way, this latter prediction asks whether morphological differences between species are more likely to be accumulated across later-developing structures. This is related to Hunter and Jernvall's (1995) observation that the hypocone has been repeatedly evolved and lost across

mammals, but it should be possible to use novel shape quantification techniques to address this question in a more granular fashion addressing all molar cusps.

It is also possible to use these developmental models to investigate molar cusp shape patterning; that is, whether the locations of cusps on the molar surface follow certain regular developmentally-derived rules that suggest the pattern of cusp locations is determined by an inhibitor/activator cascade. Jernvall (2000) applied these concepts to investigate molar cusp number and prominence in a population of Lake Ladoga seals (*Phoca hispida ladogensis*), concluding that cusp number and prominence in these seals is explained by a patterning cascade model that cumulatively increases and guides height variation in shorter marginal cusps. Specifically, later-developing molar cusps were found be more variable in height than earlier-developing cusps, and the position of later-developing cusps was found to be guided by two-dimensional angular relationships between earlier-developing cusps. This indicates that the positions of molar cusps across a molar in these seals are in part determined by relationships between earlier-developing cusps, and this finding not only demonstrates the non-independence of tooth cusps as characters but also represents one way in which developmental principles can be used to explain morphological organization. In other words, exploring cusp patterning in a developmental context may provide a better understanding of the morphogenetic rules by which morphological configurations arise. Developmental patterning is a major component of evolvability, and so knowledge of developmental patterning is valuable for recognizing evolutionary-developmental dynamics in extant species and the fossil record.

Correspondingly, it would be valuable to be able to test for developmental relationships between molar cusps in cercopithecoids. These primates represent a more

complex test case than the Lake Ladoga seals discussed above. Compared to these seals, cercopithecoids experience less variation in cusp number and variation in cusp number is principally found in the presence or absence of an M_3 hypoconulid. Additionally, molar cusps in the seals considered by Jernvall (2000) are arranged in a single mesiodistal line allowing the use of 2D methods for analysis. Cercopithecoids comparatively exhibit complicated 3D bilophodont organization. Despite these challenges, having a greater understanding of the developmental processes that lead to M_3 hypoconulid absence, presence, or prominence would be valuable. By considering certain aspects of empirical models of mouse molar morphogenesis, it is possible to develop predictions that would allow testing of cercopithecoid M_3 cusp patterning.

To begin with, mice and cercopithecoids both possess two pairs of buccolingually parallel cusps, where one set is mesially positioned related to the other (Jernvall and Thesleff, 2000b; Jernval et al., 2000). Evidence from cusp calcification for cercopithecoids suggests that the mesial pair (protoconid and metaconid) develops prior to the distal pair (entoconid and hypoconid), again similar to mice (Butler, 1956; Swindler, 1961; Swindler and McCoy, 1964; Turner, 1963; Kraus and Jordan, 1965; Oka and Kraus, 1969; Tarrant and Swindler, 1972; Corrucini, 1979; Siebert and Swindler, 1991; Swindler and Beynon, 1993). It is possible that cercopithecoids experience short intervals between the development of protoconid and metaconid together and entoconid and hypoconid together, similar to mice. In mice, parallel cusp pairs seem to experience some degree of buccolingual migration away from each other due to intercuspal epithelial proliferation and folding and the growth of the tooth crown base area (Jernvall and Thesleff, 2000b). This again may also be the case in cercopithecoids. It is possible that

low inhibition and/or high activation in cercopithecoids could lead to a shorter time interval between mesial cusp pair and distal cusp pair development, providing for a) greater migration of the distal cusp pair with tooth crown base area expansion, leading to greater distances between distal cusps; and b) the presence or increased development of hypoconulid cusps, provided enough epithelial base area and time until the termination of crown morphogenesis. If increased distances between the distal cusp pair of entoconid and hypoconid correlate with the prominence of the hypoconulid cusp, this suggests possible developmental patterning relationships that guide the development of the M_3 talonid basin and component cusps. This possible relationship will be tested here.

The study presented here quantifies cercopithecoid molar shape through topographic and geometric morphometric methods to test the hypothesis that inhibitory and patterning cascade models of dental morphogenesis organize molar crown and molar cusp form. Molar size is also assessed to supplement conclusions from quantified shape and to test the related hypothesis that cercopithecoid molar proportions are controlled by an inhibitory cascade mechanism. Specific hypotheses of this study include:

- Relative molar proportions are the product of cascading morphogenetic processes modeled by an inhibitory cascade framework.

- Later-developing molars and molar cusps are affected by more developmental events than earlier developing molars or molar cusps, respectively, as outlined by inhibitory and patterning cascade models. As

a result, more posterior molars and molar cusps should be generally more variable in shape.

- Within individual molars, relative cusp positions are organized according to the principles of a patterning cascade model of molar cusp morphogenesis.

4.2: Methods and Materials

All statistical analyses were carried out using R version 3.2.2 (R Core Team, 2015) unless otherwise stated.

4.2.1: Study samples

Two samples were used in this study. One sample consists of linear mesiodistal (MD) lengths taken from first, second, and third mandibular molar teeth (M_1, M_2, M_3) belonging to a diverse collection of cercopithecoid primates. These measurements were published by Swindler (2002), and data were gathered from there. MD length for each tooth was measured as the maximum mesiodistal diameter on the occlusal plane between contact points (Swindler, 2002). MD length means represent data from 1,135 individuals in total. Mean MD lengths per species were used in this study to test developmental hypotheses of relative inter-molar proportions in cercopithecoids. Table A4.1 contains a list of species for which data was gathered from Swindler (2002).

A second sample was used to test developmental hypotheses of inter- and intra-molar shape variability. This sample consists of 167 3D surface meshes of M_1s, M_2s, and

M_3s belonging to 79 cercopithecoid individuals across four genera (*Cercopithecus*, *Colobus, Macaca*, and *Presbytis*) (Fig 4.1, Table A4.2). Of the cercopithecoid specimens, 22 *Cercopithecus* and 22 *Colobus* specimens are represented by associated $M_1 – M_3$ meshes (total *n* for all teeth = 132), comprising complete left or right molar toothrows for these specimens. *Cercopithecus* specimens include individuals from species *C. campbelli*, *C. mitis*, and *C. mona*. *Colobus* specimens include individuals from species *Co. guereza*, *Co. polykomos*, and *Co. satanas*. Associated toothrow meshes belonging to these two genera were used to test developmental hypotheses of inter-molar shape variability.

In addition to the 132 associated $M_1 – M_3$ toothrow meshes, this sample also includes 35 additional M_3 surface meshes for M_3-specific analyses. These meshes were collected from specimens belonging to four species: *C. mitis* (*n* = 3), *Co. guereza* (*n* = 5), *Macaca fascicularis* (*n* = 18), and *Presbytis melalophos* (*n* = 11). These were combined with 7 *C. mitis* M_3 surfaces and 7 *Co. guereza* M_3 surfaces from the toothrow specimens described above to create a sub-sample for testing M_3 intra-molar shape variability. The four species in this sub-sample were selected because together they represent a range of M_3 hypoconulid character states. *C. mitis* lacks an M_3 hypoconulid, while *P. melalophos* exhibits a small variable hypoconulid and *Co. guereza* and *M. fascicularis* both express relatively large hypoconulids (Swindler, 2002; Willis and Swindler, 2004).

All meshes were prepared according to the suggested method from Ch. 2 of this dissertation. In short, individual teeth were 1) isolated from tooth rows, 2) aligned to an occlusal plane, 3) cropped to include only tooth surface above the lowest point on the occlusal basin, 4) simplified to 10,000 polygons, and 5) smoothed across 100 iterations. Any modifications to this procedure for specific analyses are described below.

4.2.2: Inhibitory cascade analyses

The developmental inhibitory cascade model makes certain predictions regarding relative molar size along the toothrow. Principal among these predictions is that a ratio of M_3 size to M_1 size regressed against a ratio of M_2 size to M_1 size should produce a positive relationship with a slope of 2.0 and an intercept of -1.0. MD lengths were used to test whether these predictions are supported for the cercopithecoid radiation. Mean M_2/M_1 and M_3/M_1 MD length ratios were calculated for each species from MD means, and regressions of mean M_2/M_1 ratios on mean M_3/M_1 ratios were created for all cercopithecoids and for three clades within cercopithecoids: guenons, papionins, and colobines. Each regression was tested for significance, and expected slope (2.0) and intercept (-1.0) values were compared against 95% confidence intervals of estimated model slopes and intercepts. It is predicted that expected values will fall within 95% confidence intervals of model values.

4.2.3: Inter-molar shape variability

Developmental models predict that later-developing molars should be more variable in shape than earlier-developing molars. Two approaches were used to test this prediction for cercopithecoid mandibular molars: morphological topographic analyses and an automated-landmark geometric morphometric method. Both of these approaches used the 132 associated $M_1 – M_3$ toothrow meshes described above.

Topographic metrics Dirichlet normal energy (DNE, quantifying surface bending), relief index (RFI, quantifying surface relief), and orientation patch count

rotated (OPCR, quantifying surface complexity) were calculated from prepared surface meshes for each M_1, M_2, or M_3 specimen using the application MorphoTester (Ch. 2). For calculating DNE, condition number checking and outlier removal at 99.9% were used while implicit fair smoothing was not. For calculating OPCR, minimum patch count was set to 5. Differences between tooth classes (M_1, M_2, M_3) and genera were assessed for each topographic variable using two-way ANOVAs with genus and tooth class factors. Due to interactions between genus and tooth class factors for RFI and OPCR, additional ANOVAs by tooth class were run for each genus. Homogeneity of variances between tooth classes was tested for topographic variables using Levene's and Bartlett's tests of homoscedasticity. Separate analyses were run for each genus. It is predicted that M_3s will be more variable in quantified surface curvature, relief, and complexity than M_2s and M_1s, and that M_2s will in turn be more variable than M_1s.

In addition to techniques of morphological topographic analysis, inter-molar variability was also assessed using a landmark-based geometric morphometric approach. Compared to topographic measures, which are whole-surface shape descriptors, landmark-based morphometric techniques quantitatively characterize shape (Evans, 2013). Because of this distinction, these techniques may be differently able to appropriately quantify shape variation. Sets of 128 landmarks were automatically generated from M_1, M_2, and M_3 surface meshes using the *auto3dgm* algorithm (Boyer et al., 2015a). This algorithm takes an assemblage of surface meshes as input, automatically aligns surface meshes to a common orientation in 3D space using principal components techniques, and generates a set of mathematically corresponding landmarks across input meshes (Fig. 4.2). Generated landmarks are output in two forms: size-scaled representing

variation in shape only, and size-unscaled representing variation in size and shape. Both sets of landmarks were analyzed for this study.

While the standard *auto3dgm* algorithm uses eight possible principal component XYZ alignments to create a set of possible orientations from which to uniformly align input surfaces in 3D space, erroneous specimen mirroring was found to occur when this was used for the specimens from this sample. As a result, the *auto3dgm* source code was modified to eliminate initial principal component alignments involving mirroring (i.e., any alignment producing a rotation matrix with a determinant of negative one). The modified version of the *auto3dgm* algorithm is included in Appendix 1. This modified algorithm uses four principal component XYZ alignments to uniformly align surfaces instead of eight. Modified *auto3dgm* was applied to surface meshes split into groups by genus (*Cercopithecus*, *Colobus*) and tooth class (M_1, M_2, M_3). As noted above, *auto3dgm* produces landmarks in both scaled and unscaled formats. Running *auto3dgm* on the six surface mesh sets therefore resulted in twelve sets of 128 landmarks with each landmark set specific to a genus, tooth class, and scaled or unscaled format. Because this method generates landmarks that maximize quantified shape variation for the specific set of surfaces provided to the algorithm, individual landmarks are not directly comparable between landmark sets. Within a landmark set, though, individual landmarks represent mathematically corresponding points that can be compared between specimens within the set.

Molar shape variability was quantified from automatically-generated landmarks by calculating Procrustes distances between specimens for M_1s, M_2s, and M_3s of *Cercopithecus* and *Colobus*. Each of the twelve landmark sets generated by *auto3dgm*

were loaded into the application Morphologika (O'Higgins and Jones, 1998). This application was used first to Procrustes align landmarks with mirroring disabled and, for unscaled landmark sets only, size-scaling disabled. For each landmark set, Procrustes distances were derived for each pair of specimens. For a specimen pair, Procrustes distance was calculated as the square root of a sum of squares of differences in position for equivalent landmarks. With 22 molar specimens per set, this yielded 231 total Procrustes distances per set across 12 sets.

Means of Procrustes distances per set can be compared between sets as a measure of shape variability. If for example *Cercopithecus* M_3s are more variable in shape as a tooth class than *Cercopithecus* M_1s, then Procrustes distances between M_3 specimens should be greater on average than Procrustes distances between M_1 specimens. The use of size-scaled and size-unscaled landmark sets further helps to establish whether possible differences between tooth classes are the result of tooth shape alone or tooth shape and size acting together. If differences between *Cercopithecus* M_3 and M_1 were seen in size-unscaled landmark sets but not in size-scaled sets, it cannot be concluded that differences in molar shape variability have been observed independent from possible variability related to different molar sizes.

For each genus, two ANOVAs were run on size-scaled and size-unscaled data testing whether Procrustes distances differ between tooth classes. With 231 Procrustes distances per tooth class per genus per scaled and unscaled sets, this means that each ANOVA comparing M_1, M_2, and M_3 involved 693 total Procrustes distances. *Post hoc* pairwise comparison tests were also run using Tukey's HSD to further partition possible differences between tooth classes.

4.2.4: Intra-molar shape variability

Somewhat analogously to developmental models of molar row development, hypotheses of individual molar morphogenesis predict that later-developing cusps within a molar should be more variable in position and form than earlier-developing cusps. Because molar cusp morphogenesis proceeds from mesial to distal, it is generally the case that more distal cusps develop later (Jernvall, 1995). Specifically, for cercopithecoid molars it is predicted that cusps in order of ascending variability should be protoconid, metaconid, hypoconid, entoconid, and (where present) hypoconulid. This prediction was tested using analyses of morphological topography and cusp position landmarks.

Topographic metrics DNE, RFI, and OPCR were calculated from a collection of M_1s (n = 22) and M_3s (n = 22) belonging to *Co. guereza*, *Co. polykomos*, and *Co. satanas* (Table A4.1). These same specimens were also used in section 4.2.1 above. Because the topographic metrics used here quantify shape across all surface present in a given 3D object file, obtaining topography of specific molar regions requires modifications of surface meshes to include only the region of interest. As developing consistent protocols for cropping individual cusps was found to be impractical, molars were separated into mesial and distal portions for topographic calculation. Mesial molar portions included protoconid and metaconid cusps while distal portions included hypoconid, entoconid, and (for M_3) hypoconulid cusps. Molar surfaces were bisected by defining a line originating from the lingual occlusal surface margin at a point halfway between the metaconid and entoconid and terminating at the furthest extent of the cristid obliqua on the buccal occlusal surface margin (Fig 4.3). Bisection lines were kept straight except as necessary

to run between contours of the metaconid and/or entoconid near line origins. All polygons falling on or mesial to the line were assigned to the mesial division, and all polygons distal to the line were assigned to the distal division.

The software Amira (Visage Imaging Group) was used to bisect surface meshes. Bisection lines were drawn and all polygons on or mesial to the line were selected using the Edit Surface module. All mesial polygons were removed from the surface, and remaining distal surface was exported as a separate mesh. Previously removed mesial polygons were then recovered, distal polygons were selected and removed using the Invert Surface Highlights function, and mesial surface was exported as a separate mesh. Topographic variables DNE, RFI, and OPCR were calculated from each mesial and distal mesh for each M_1 and M_3 using MorphoTester and the parameters described above. For each tooth class, topographic variables of mesial and distal molar halves were tested for homogeneity of variance using Levene's and Bartlett's tests. Differences in mean topographic variables were also assessed using two-way ANOVAs with tooth class and mesial/distal division factors.

Because landmark-based methods may be better or worse for quantifying shape-related variation in molar form than topographic methods, cusp landmark data were collected for a sample of 51 M_3s belonging to four species: *C. mitis*, *Co. guereza*, *M. fascicularis*, and *P. melalophos* (Table A4.1). For each molar, XYZ point coordinate data for all cusp tips were gathered using Amira, sampling the protoconid first followed by metaconid, entoconid, hypoconid, and hypoconulid (if present). For *C. mitis* where hypoconulids were not present, the midpoint of the distal occlusal margin between entoconid and hypoconid cusps was collected instead. This was done to both better align

landmarks between species and to allow a test of hypoconulid/distal occlusal margin prominence in relation to relative cusp constriction (see section 4.2.5 below). Resulting landmark data were imported into Morphologika and Procrustes superimposed with size-scaling and mirroring enabled. Procrustes-aligned XYZ landmark data were used for two sets of analyses. The first set of analyses was strictly intraspecific and tested the prediction that for a given species, later-developing cusps are more variable in cusp tip position. The second set of analyses compared species to test the prediction that between species, differences in cusp positions should be primarily observed in later-developing cusps.

For intraspecific analyses pairwise cusp tip landmark distances between specimens were calculated in two formats, 3D and 2D (XY distance excluding Z-axis). This was done to attempt to account for the effect of light wear on cusp tips. Distances were calculated for each cusp between cusp tip landmarks for all possible pairs of specimens within each species. For example, from 18 *Macaca fascicularis* specimens 153 pairwise cusp tip landmark distances were calculated for each cusp, and in total from all 5 cusps 765 landmark distances were derived for this species. In order to assess whether choice of 2D or 3D distance affects patterns of differences between pairwise landmark distances across cusps, two-way ANOVAs were carried out for each species with cusp and 2D/3D treatment factors. No interaction was observed between cusp and 2D/3D treatment, and further analyses were carried out for both pairwise distance treatments. For each treatment, two-way ANOVAs were performed with species and cusp factors. Both of these analyses indicated interaction between factors, and so one-way ANOVAs were run for each species to test whether pairwise landmark distances vary between cusps.

Post hoc pairwise comparison tests were subsequently run as appropriate using Tukey's HSD.

For the interspecific analyses, species were split into six possible two-species pairs. For each species pair, 3D cusp landmark distances were calculated between all specimens of the first species and all specimens of the second. As an example, because there were 11 *P. melalophos* and 12 *Co. guereza* specimens in this sample, for each of the five cusps, 132 (11 * 12) pairwise landmark distances were generated for this pair of species. For species pair comparisons with *C. mitis,* which lacks a hypoconulid, pairwise landmark distances were calculated for the four remaining cusps. Six Bonferroni-corrected ANOVAs (corrected $\alpha = 0.0083$) were then run for species-pairs to assess whether interspecific pairwise landmark distances vary by cusp. *Post hoc* pairwise comparison Tukey's HSD tests were run to further partition differences. Pairwise comparisons were also Bonferroni-adjusted for significance, having an adjusted alpha of 0.001. It is predicted that between species pairwise landmark distances will vary by cusp and that later-developing cusps will evince greater pairwise landmark distances.

4.2.5: Hypoconulid prominence

Developmental hypotheses of molar morphogenesis suggest not only that later-developing cusps will be more variable than earlier-developing cusps, but also that the developmental processes of earlier-developing cusps should affect the form and position of later-developing cusps. It is predicted that hypoconulid prominence will correlate with a ratio of the distance between the entoconid and hypoconid relative to the distance between the protoconid and metaconid. Stated differently, it is predicted that greater

restriction of the entoconid-hypoconid relative to the protoconid-metaconid will be related to smaller or absent hypoconulids.

Analyses testing this prediction used the cusp tip landmark data described above, including the distal occlusal margin landmark for *C. mitis* as a "dummy" hypoconulid. This allowed *C. mitis* to be compared with other sample species for tests of "hypoconulid" prominence. Given that hypoconulids of the other three species considered here typically protrude as distal "heels" from occlusal surfaces, and that hypoconulid cusp tips tend to occupy one of the most extreme distal positions on the occlusal surface, it could be suggested that the analyses here are testing prominence of distal molar expansion more than hypoconulid prominence as such. Certainly the dummy hypoconulid point measured from *C. mitis* specimens is not evolutionarily homologous to the actual hypoconulids measured. But considered from a developmental perspective, this approach is defensible. Molar models of morphogenesis suggest that cusps are not independent characters but are rather the product of a cascade of knock-on developmental pathway events. The appearance or disappearance of a fifth molar cusp is likely the product of a sufficiently low inhibitory field and a sufficiently active excitatory field combined with available basement membrane and time for formation. In this context, distal expansion of a molar surface and the appearance of a fifth molar cusp are likely closely related. Therefore, it is valuable to be able to compare distal heel prominence in *C. mitis* with hypoconulid prominence in the other species analyzed here. In any case, the use of dummy hypoconulid values for *C. mitis* specimens should at least not affect results within or between species that do possess M_3 hypoconulids.

Hypoconulid or distal occlusal margin prominence (termed HC for short) is calculated as the distance between the hypoconulid or distal occlusal margin landmark and the centroid geometric center of the protoconid, metaconid, entoconid, and hypoconid landmarks. An ANOVA was run to assess differences in HC prominence between species, and post-hoc pairwise comparison tests were subsequently performed using Tukey's HSD. Distances were calculated between protoconid and metaconid (PM) and between entoconid and hypoconid (EH), and from these distances a PM/EH ratio was generated. A second ANOVA was performed to assess whether and how PM/EH ratios differ between species, with following post-hoc Tukey's HSD as well. Results from these two ANOVAs were compared to gauge whether clear trends across species could be observed. It is predicted that species with greater PM/EH ratios should display less hypoconulid prominence. Possible intraspecific relationships between hypoconulid prominence and relative cusp retraction were also analyzed. An ANCOVA was run to test HC by species with PM/EH as a covariate. Because of factor interactions in the ANCOVA, HC was regressed on PM/EH ratio for each species. These regressions were tested for significance. It is predicted that species will demonstrate a significant negative relationship between hypoconulid prominence and relative cusp restriction.

4.3: Results

4.3.1: Inhibitory cascade analyses

Ratios of M_2 mesiodistal (MD) length over M_1 MD length were regressed on ratios of M_3 MD length over M_1 MD length to test predictions of an inhibitory cascade model of molar development. Estimated regression models are presented in Table 4.1 and

plotted as Figure 4.4. Regressions including all cercopithecoids, colobines alone, and papionins alone were found to be significant with a positive relationship between M_2/M_1 MD length and M_3/M_1 MD length as predicted. Across these regressions, slopes ranged from 1.847 to 2.399 and intercepts ranged from -1.366 to -0.729. Predicted slope and intercept values were 2.0 and -1.0 respectively, and for all of these regressions predicted values fall within the 95% confidence intervals of model value estimates. It is concluded that model predictions are supported for these groups. On the other hand, for guenons a significant relationship was not observed between M_2/M_1 MD length and M_3/M_1 MD length ($p = 0.296$, slope = 0.433, intercept = 0.588). For this non-significant regression, predicted slope and intercept values do fall outside of 95% confidence intervals.

4.3.2: Inter-molar shape variability

Differences in shape variability across *Cercopithecus* and *Colobus* mandibular molars were assessed using techniques of morphological topographic analysis and geometric morphometrics. Topographic analyses will be discussed first, followed by morphometric analyses.

Topographic variables DNE (curvature), RFI (relief), and OPCR (complexity) were calculated from M_1s, M_2s, and M_3s of *Cercopithecus* and *Colobus*. Raw topographic variable data can be found in Table A4.3. Descriptive statistics are presented as Table 4.2, and topographic variables are plotted in Figure 4.5. It can be observed that DNE and RFI tend to increase from first through third molars, while OPCR decreases in *Cercopithecus* and is irregular in *Colobus*. Results from ANOVAs support this, indicating that all topographic variables differ significantly between tooth classes for both

genera (Table 4.3). A lack of factor interaction shows that the pattern of differences in DNE between tooth classes is relatively similar for both genera, but patterns of differences by tooth class in RFI and OPCR are different between genera. Most importantly, Levene's and Bartlett's tests show no evidence for significant differences in variances of topography between tooth classes for either genus or any topographic variable (Table 4.4). Instead, the null hypothesis of equal variances in topographic variables between tooth classes is supported here. Beyond this, trends of variability for topographic variables are generally opposite to predictions, with M_1s tending to have the highest standard deviations for DNE, RFI, and OPCR followed by M_2s and lastly by M_3s (Table 4.2, Fig. 4.5).

ANOVAs were run on Procrustes distances for M_1s, M_2s, and M_3s, to determine whether later-developing teeth are more variable in shape as predicted. Raw data for these analyses is included in Table A4.4, descriptive statistics are shown as Table 4.5, and results of ANOVAs are given as Table 4.6. Box plots of Procrustes distances for scaled and unscaled landmark sets are presented in Figure 4.6. Results from analyses of unscaled landmarks may relate to changes in shape or size, while results from scaled analyses specifically reflect shape-related variation. Plots show that Procrustes distances increase for both genera from M_1 to M_2 to M_3, regardless of whether data was scaled or unscaled. Results from ANOVA support this, indicating that Procrustes distance differs significantly between molar tooth classes for both *Cercopithecus* and *Colobus* whether scaled or unscaled. Post-hoc pairwise comparison tests show that for unscaled data of both genera, all tooth classes are significantly different from each other (Table 4.7). For scaled data for both genera, M_3 has significantly larger Procrustes distances than either

M_1 or M_2 while M_2 is not significantly more variable than M_1. M_2 exhibiting significantly larger Procrustes distances than M_1 for unscaled data but not for scaled data could be explained as a result of size differences. For both of these genera, M_2s are generally larger than M_1s, and size-related shape variation may influence pairwise distances here. At the same time, results from scaled analyses show that even when shape is tested while accounting for differences in size, M_3 is significantly more variable via pairwise landmark distances than either M_1 or M_2. Predictions are robustly upheld here.

4.3.3: Intra-molar shape variability

To investigate whether later-developing cusps express relatively more variability, two types of analyses were performed: morphological topographic analyses characterizing cusp shape and morphometric analyses characterizing cusp position. Topographic variables DNE, RFI, and OPCR were calculated from separated mesial and distal surface regions of M_1s and M_3s belonging to *Co. guereza*, *Co. polykomos*, and *Co. satanas*. Raw topographic variable data can be found in Table A4.5, and descriptive statistics for DNE, RFI, and OPCR are presented as Table 4.8. Box plots of topographic variables for mesial and distal regions of each tooth class are provided as Figure 4.7. Results of two-way ANOVAs of topographic variables by tooth class and surface region factors show no significant factor interactions (Table 4.9). This indicates that topographic variables vary (or do not vary) between mesial and distal surface regions in a similar manner for both M_1 and M_3. M_3 mesial and distal surface regions were found to evince significantly greater DNE, RFI, and OPCR relative to M_1 mesial and distal surface regions (consistent with results discussed in section 4.3.2 above). For both M_1 and M_3,

mesial surface regions express significantly lower RFI but higher OPCR compared to distal surface regions. DNE does not significantly differ between mesial and distal surface regions.

Barlett's and Levene's tests of homogeneity of variances were used to test the predictions discussed above (Table 4.10). Contrary to expectations, mesial surface regions of M_1 show significantly greater variability than distal surface regions by Bartlett's test. Greater variability in mesial surface regions of M_1 is also supported by possibly marginal significance ($p = 0.062$) by Levene's test. If marginal significance is judged as $0.05 > p < 0.10$, Levene's test also indicates that DNE of M_3 mesial surface regions is more variable than distal surface regions with $p = 0.09$. No other comparisons are significantly different in variability. Predictions of later-developing cusps being more variable in topographic shape are not supported by analyses here.

Morphometric analyses were used to test predictions as applied to cusp positions. Cusp tip landmark data were collected for a sample including *C. mitis*, *Co. guereza*, *M. fascicularis*, and *P. melalophos*, and pairwise cusp-tip landmark distances were calculated as the variable of interest. Raw cusp tip landmark data for all species are supplied in Table A4.6, and Procrustes-aligned landmark data are included as Table A4.7. These data were used to assess patterns of intramolar variability in two analyses, one with a focus within species and a second focusing on differences between species.

For the intraspecific analysis of intramolar variability, 2D and 3D pairwise cusp-tip landmark distances were calculated between specimens within each of the four species considered. Raw 2D and 3D pairwise landmark distances are located in Table A4.8. Descriptive statistics of pairwise landmark distances are given as Table 4.11, and box

plots of landmark distances per cusp for each species are presented as Figure 4.8. ANOVAs testing effects of cusp and 2D/3D distance calculation methods on landmark distances show no significant interactions between cusp and 2D/3D treatment for any species, although *C. mitis* approaches significance with $p = 0.061$ (Table 4.12, Figure 4.9). As could be expected, cusp-tip pairwise landmark 3D distances are significantly longer than 2D distances for all species. Two-way ANOVAs for 2D and 3D distances testing cusp and species factors do show significant interactions, suggesting that 2D and 3D pairwise landmark distances vary across cusps differently for the species considered here (Table 4.13). As a result, separate ANOVAs were run for each sample species.

ANOVAs of 2D pairwise cusp-tip landmark distances by cusp are presented for each species as Table 4.14 and Figure 4.8. All species show significant differences in 2D pairwise landmark distances between cusps, indicating that for all species some cusps are more variably positioned (i.e., have larger pairwise landmark distances) across specimens and some cusps are less variably positioned (i.e., have smaller pairwise landmark distances). For all species, there is a general trend where more distal cusps tend to have larger cusp-tip pairwise distances. For 2 of the 3 species that have hypoconulid cusps, that cusp is the most variably positioned. Tukey's HSD post-hoc pairwise comparisons help to elucidate patterns of significant differences in 2D distances (Table 4.15). For *C. mitis*, entoconid and hypoconid cusps have significantly larger pairwise distances than protoconid or metaconid cusps respectively, and the entoconid has significantly larger pairwise distances than hypoconid. For *Co. guereza*, the entoconid, hypoconid, and hypoconulid cusps all have significantly larger pairwise distances than the metaconid, and the hypoconid and hypoconulid cusps have larger pairwise distances than the

protoconid. For *M. fascicularis*, entoconid, hypoconid, and hypoconulid cusps all have significantly larger pairwise distances than the protoconid cusp. For *P. melalophos*, the metaconid and entoconid cusps have significantly larger pairwise distances than the protoconid, and the entoconid has significantly larger pairwise distances than the hypoconid. Therefore compared to other species, *P. melalophos* shows more differences between adjacent mesial or distal cusps.

ANOVAs of 3D pairwise cusp-tip landmark distances by cusp are presented for each species as Table 4.16 and Figure 4.9. As for 2D distances, all species show significant differences in cusp-tip pairwise distances across cusps and trends generally indicate that more distal cusps are more variably positioned within each species. Tukey's HSD post-hoc pairwise comparisons partition significant differences between cusps per species (Table 4.17). For *C. mitis*, the entoconid and hypoconid are significantly more variable than the protoconid, and the entoconid is significantly more variable than the metaconid. For *Co. guereza*, the entoconid, hypoconid, and hypoconulid are all significantly more variable than the protoconid and the hypoconulid is also significantly more variable than the metaconid. For *M. fascicularis,* entoconid and hypoconid cusps show significantly longer pairwise distances compared to protoconid just as for 2D distances, but three more significant differences are also present: hypoconulid cusps have significantly longer pairwise distances than protoconid or metaconid, and hypoconid cusps have significantly longer pairwise distances than metaconid. All significant differences for *P. melalophos* are between distal cusps, with entoconid and hypoconulid cusps both having longer pairwise distances than hypoconid. Mean pairwise distances for hypoconulid and entoconid are longer than metaconid or protoconid though not

significantly so, and hypoconids have the shortest 3D pairwise distances for this species. While patterns of difference in pairwise landmark distances between cusps are complex for the species considered, predictions of later-developing cusps being more variably positioned than earlier-developing cusps is still generally supported here for both 2D and 3D cusp-tip distances.

While intraspecific analyses of intramolar variability calculated 2D and 3D cusp-tip pairwise landmark distances within each species considered, interspecific analyses calculated pairwise landmark distances as 3D distances between cusp tips between species pairs. Raw pairwise landmark distances for the six species pairs considered here are given as Table A4.9. Descriptive statistics for these pairwise distances are supplied as Table 4.18 and box plots are presented as Figure 4.10. Bonferroni-corrected ANOVAs and Tukey's HSD post-hoc pairwise comparisons for each ANOVA (Bonferroni-corrected for 48 total post-hoc corrections) are shown in Tables 4.19 and 4.20 respectively. ANOVAs indicate that pairwise distances vary significantly across cusps for every species pair considered here. Trends of cusp pairwise distances are similar for all species with distal cusps being more variable than mesial cusps. For the three species pairs including *C. mitis* (where hypoconulid position was not considered), Tukey's HSD post hoc tests indicate significant differences between all cusps except for bucco-lingual cusp pairs protoconid – metaconid and hypoconid – entoconid (the latter still being significantly different in *C. mitis/Co. guereza*). For *Co. guereza*/*P. melalophos*, the hypoconulid is the most variable followed by the entoconid, hypoconid, metaconid, and protoconid. All cusps are significantly different from each other by HSD except for protoconid – metaconid, hypoconid – metaconid, and hypoconid – protoconid. The trend

of *Co. guereza*/*M. fascicularis* is similar, with entoconid as the most variable followed by hypoconid, hypoconulid, metaconid, and protoconid. All cusps are significantly different except protoconid – metaconid, entoconid – hypoconid, hypoconulid – metaconid, and hypoconulid – hypoconid. For *M. fascicularis/P. melalophos,* the hypoconulid is again the most variable, followed by the hypoconid, protoconid, and metaconid, with the entoconid actually the least variable in position for this species pair. All cusps are significantly different except protoconid – metaconid and entoconid – metaconid.

Some general patterns can be discerned from the interspecific results here. First, with only one exception distal entoconid, hypoconid, and hypoconulid cusps are more variable in position between species than mesial protoconid and metaconid cusps. This is consistent with predictions of later-developing, more distal cusps being more variable than relatively mesial cusps. For the two species pairs involving *P. melalophos* and another species with a hypoconulid (*Co. guereza* and *M. fascicularis*), the distal-most hypoconulid is the most variable cusp between species. This is likely explained by *Co. guereza* and *M. fascicularis* having well-developed hypoconulids compared to *P. melalophos*' smaller and more often variably expressed hypoconulid (see section 4.3.4 below for more details on this). This also explains why for the species pair *Co. guereza/M. fascicularis*, the hypoconulid is observed to be less variable between species than the entoconid and hypoconid. It is also worth pointing out that the two cusps with the most similar cusp-tip pairwise landmark distances between species (i.e., the cusp pair with the fewest number of significant post-hoc comparisons) are the protoconid and the metaconid. These cusps were found to not significantly differ in interspecific cusp-tip pairwise differences in any of the species pairs considered here. The second-most similar

pair of cusps are the entoconid and the hypoconid, which were only observed to significantly differ in *C. mitis/Co. guereza, Co. guereza/P. melalophos*, and *M. fascicularis/P. melalophos*. Both pairs of cusps share a molar surface "loph" respectively, and it is consistent with predictions that the more variable cusp "loph" pair is the more distal one.

4.3.4: Hypoconulid prominence and distal cusp constriction

To test the prediction that more constricted hypoconid and entoconid cusp pairs relative to protoconid and metaconid cusp pairs are related to less prominent hypoconulid cusps, cusp tip data (Table A4.7) were collected and combined with a set of "dummy hypoconulid" middle distal occlusal margin landmarks for *C. mitis*, and distances between cusps were calculated. Table A4.10 includes raw data for protoconid – metaconid distance (P-M), entoconid – hypoconid distance (E-H), geometric centroids for all non-hypoconulid cusps, and hypoconulid/occlusal margin – centroid distance ("HC" prominence). Descriptive statistics for these variables as well as for the ratio of PM/EH are given in Table 4.21. PM/EH ratios provide a measure of relative distal cusp constriction.

An ANOVA testing PH/EH ratios by species indicates that relative distal cusp constriction differs significantly between species (Table 4.22, Fig. 4.11). The most constricted distal cusps belong to *C. mitis,* followed by *P. melalophos*, *M. fascicularis*, and *Co. guereza*. Post hoc pairwise comparisons show that all species differ significantly from each other except for *P. melalophos* and *M. fascicularis*, and *M. fascicularis* and *Co. guereza*. An ANOVA testing HC prominence by species also demonstrates

significance differences between species, and the trend of HC prominence is similar to the trend PH/EH ratio but in reverse (Table 4.22, Fig. 4.12). *M. fascicularis* has the most prominent hypoconulid cusps, followed by *Co. guereza*, *P. melalophos*, and *C. mitis* without a hypoconulid (measuring the distal occlusal margin instead). Post hoc pairwise comparisons show that all species differ significantly except *C. mitis* and *P. melalophos*, and *Co. guereza* and *M. fascicularis*. This means that the hypoconulid of *P. melalophos* is not significantly further away from a centroid defined by all other cusps than is the midpoint of the distal occlusal margin in *C. mitis*. A regression of HC prominence by PM/EH ratio across the entire sample indicates a significant negative relationship as predicted (Table 4.24, Fig 4.13).

An ANCOVA was also performed to account for the effect of species on HC prominence with PH/EH ratios as covariate (Table 4.25, Fig. 4.13). This ANCOVA shows significant interaction between species and PM/EH covariate. This means that slopes of regressions between HC prominence and PM/EH ratios likely vary between species. As result, regressions were performed for each species individually (Table 4.26, Fig. 4.13). For *C. mitis* and *P. melalophos*, there is a negative relationship between HC prominence and PM/EH ratio with clear and near significance respectively (*C. mitis*: $p = 0.029$; *P. melalophos*: $p = 0.055$). For *Co. guereza*, there is also a negative relationship between HC prominence and PM/EH ratio, but this relationship is not significant ($p = 0.110$). For *M. fascicularis* on the other hand, there is a significant positive relationship ($p = 0.032$). This is however largely because of a specimen (*M. fascicularis* 385) with unusually high HC prominence (1.28) and PM/EH ratio (1.43). If this specimen is considered an outlier and the regression is recalculated excluding it, then *M. fascicularis*

loses significance (p = 0.377). It can also be noted that if the ANCOVA is performed again excluding this potential outlier, the p-value for interaction between species and covariate crosses the significance threshold (including outlier: p = 0.002; excluding outlier: p = 0.067), though the shift in p-values is still relatively minor.

4.4: Discussion

4.4.1: Inhibitory cascade in primates

The developmental predictions of the inhibitory cascade model indicate that, for a typical mammal, M_3 size relative to M_1 should be significantly explained by M_2 size relative to M_1 with slope of 2.0 and an intercept of -1.0. Results here initially suggest that cercopithecoids as a whole conform to the developmental predictions of the inhibitory cascade model, in that a whole-sample regression of M_3/M_1 mesiodistal length by M_2/M_1 mesiodistal length is consistent with the expected slope and intercept. Partitioning data further by clade however reveals that colobines and papionins are indeed consistent with predictions but that guenons are not. Colobines and papionins both have a general molar size equation of $M_1 < M_2 < M_3$, which as noted by Kavanagh et al. (2007) suggests an activator/inhibitor balance marked by relatively weak levels of inhibition. It should be noted that the analyses performed here represent a strictly interspecific test of this model using species means as data points. Across colobine and papionin species, species-mean level relative M_2 and M_3 sizes correlate as predicted. Since data points here represent species means, these results should not be assumed to apply to changes in relative molar size among individuals within species. In any case, the observation of a $M_1 < M_2 < M_3$ molar size pattern in colobines and papionins is not new and has been noticed by a

number of previous studies (e.g., Swindler, 2002; Willis and Swindler, 2004). What is new is that significant correlations of relative molar size fit a predictive developmental model of molar tooth formation. This suggests that various characteristics of cercopithecoid molars such as size are not independent and are instead tightly linked by a cascade effect.

Compared to colobines and papionins, guenon relative molar size does not support Kavanagh et al.'s (2007) prediction. This was also noticed by Schroer and Wood (2015) in a genus-level analysis where individual specimen occlusal area was the variable of interest (they also noticed cercopithecoids' general conformation to the IC model). But the focus of that analysis was on general trends and specifically applying IC model predictions to hominins, and as a result they did not consider this observation concerning guenons in detail. Guenons have a molar size pattern of $M_1 < M_2 > M_3$, and data here indicate that guenon M_3 size relative to M_1 expands less quickly (or not at all) as M_2 size relative to M_1 increases. Kavanagh et al. (2007) provided one possible explanation for a $M_1 < M_2 > M_3$ size pattern involving both relatively low levels of inhibition and an early arrest of M_3 development. This explanation invokes two different and possibly independent developmental characters, with activator/inhibitor balance being an initiation character and the cessation of M_3 development being a termination character. Developmental characters have been discussed specifically in the context of molar cusp development by Jernvall and colleagues (Jernvall, 1995, 2000; Jernvall and Jung, 2000), but these ideas should be expandable to molar row development as well. An activator/inhibitor balance is hypothetically established at the initiation of molar development and its effects are felt throughout the molar row by continuing cascade

effects, while global termination of molar formation is orthogonal to this in that it sets the time at which crown morphogenetic processes cease.

A molar size pattern of $M_1 < M_2 > M_3$ involves relatively weak inhibition to explain larger M_2 relative to M_1 and earlier M_3 crown termination to explain smaller M_3. This explanation is adopted here for guenons, especially in light of the idea that colobines and papionins both also show weak levels of inhibition. But an alternative developmental explanation can be found in the idea of a reversing of the inhibitory cascade at a certain tooth, leading to progressively smaller teeth distal to the tooth marking the reversal point (Evans et al., 2016). Apes and hominins not belonging to the genus *Homo* exhibit molar size patterns in which M2 or M3 is the largest tooth in the mandibular postcanine dentition with more mesial teeth smaller, but *Homo* seems to have undergone an evolutionary developmental shift toward M_1 or M_2 being the largest teeth with both mesial and distal teeth progressively smaller (Evans et al., 2016). This has been interpreted as evidence for an inhibitory cascade pattern that reverses the characteristic size pattern around a certain tooth. Developmentally this produces, from mesial to distal, progressively larger teeth up to the point of reversal and then progressively smaller teeth subsequently (Evans et al., 2016). Neither the mechanisms for this reversal of the inhibitory cascade or for termination characters guiding the cessation of M_3 morphogenesis are known.

Comparing these clades, it can also be noted that the primary morphological difference between guenon M_3s and those of colobines and papionins is that guenons lack M_3 hypoconulids. Stem cercopithecoids *Victoriapithecus* and *Prohylobates* possess M_3 hypoconulids (Benefit and McCrossin, 2008), and so it is reasonable to suggest that an

M_3 hypoconulid, a molar size pattern of $M_1 < M_2 < M_3$, and an inhibitory cascade with weak inhibition levels may all represent related primitive conditions for the cercopithecoid clade. A derived loss of M_3 hypoconulids in guenons may have been accomplished by an evolutionary modification for earlier M_3 crown termination or alternately an inhibitory cascade pattern reversal in conjunction with symplesiomorphic weak inhibition.

Also, while no specific connection is necessarily suggested here, it is interesting to note that from what little is known of comparative life history variables there is evidence to suggest that guenon molars may have an absolutely faster (i.e., not relative to body size) developmental schedule than colobines or papionins. Some observations of gestation lengths place guenons as among the fastest of all cercopithecoids, and an observation of dental eruption schedules from captive vervet monkeys (*Chlorocebus aethiops*) notes that vervet dental eruption is faster in absolute time than *Trachypithecus cristatus*, another quickly-developing primate (Harvey and Clutton-Brock, 1985; Bolter, 2011). Also overall developmental schedules correlate to body sizes (or other related variables, e.g. Godfrey et al., 2001), and guenons are among the smallest of all cercopithecoids (Smith and Jungers, 1997). It is tempting to suppose that the possible existence of absolutely shorter developmental schedules in guenons compared to other cercopithecoids may in some way be related to guenons possibly having an earlier termination of molar morphogenesis. Nonetheless, more work will be required in order to say whether there are connections between body size or overall developmental schedules and aspects of molar morphogenesis as considered here.

4.4.2: Inter-molar shape variability

Analyses considered in section 4.4.1 above are principally concerned with molar size, but all subsequent discussion will concern results regarding molar shape. A patterning cascade model of development suggests that more distal molars should be more variable in shape because they develop later than mesial molars and are affected by mesial molar developmental events. There is strong support for this prediction from analyses of automated 3D geometric morphometric landmarks, but no support is found from topographic analyses. This is a trend that will continue for intra-molar shape variability as well, and possible explanations will be considered in section 4.4.5 below. For automated landmark analyses, both *Cercopithecus* and *Colobus* M_3s are significantly more variable than M_1s or M_2s regardless of whether data has been scaled or unscaled. For unscaled data accounting for both size and shape, M_2s of both species are also significantly more variable than M_1s. As differences in scaled data concern only shape and not size, this is a more direct indicator that more distal molars in these species are indeed more variable in shape.

Distal molar teeth have been observed to be more variable than mesial molar teeth in various mammals by a number of observers using coefficients of variation calculated from size measurements such as mesiodistal lengths, buccolingual widths, or occlusal areas calculated as the product of mesiodistal and buccolingual distances (Van Valen, 1962; Gould and Garwood, 1969; Yablokov, 1974; Gingerich, 1974; Gingerich and Ryan, 1979; Gingerich and Schoeninger, 1979; Gingerich and Winkler, 1979; Pengilly, 1984; Cope, 1993; Plavcan, 1993). Yet despite the number of studies that have applied CVs to this problem, there are non-trivial issues with CVs where the apparent variability

of small traits may be inflated (Polly, 1998b). Polly's (1998b) re-analysis of tooth variability using a regression approach has suggested that previously observed differences in variability between molars are artifactual, resulting from a negative correlation between CV and mean variable size. This is because CVs are calculated as the ratio of variable standard deviation to variable mean, and measurement error contributes uniformly to estimated variance, resulting in artificially inflated CVs when trait mean value is very small (Polly, 1998b). At the same time, Polly (1998b) suggested that at least some aspects of earlier findings might still be found to be accurate when measures of shape rather than size were used to examine the topic. The automated landmark analyses used here quantify shape and are largely capable of accounting for effects of size. And in fact, the results here support the variability observations of the previous studies using CVs. It is theoretically still possible that size plays a confounding role here and helps to produce the pattern of variability observed, but this seems unlikely given that *Cercopithecus* M_3s are actually smaller in size than either M_2s or M_1s of this species.

Finding that more distal molars are more variable in shape than mesial molars does support developmental predictions, but other explanations have also been posited to explain this phenomenon. Of these explanations, the one that is most applicable to molar teeth is the idea that tooth variability is inversely proportional to occlusal complexity (Gingerich and Schoeninger, 1979). This hypothesis argues that occlusal complexity places a constraint on variability because teeth with more complex occlusal surfaces must be less variable in order to achieve functional occlusion. While topographic analyses do not support predictions of variability between molars, central tendencies of topographic variables can still be used in conjunction with automated landmarks to assess this

hypothesis. For both *Cercopithecus* and *Colobus*, more distal teeth have occlusal surfaces that evince greater amounts of total surface bending and relief. Distal molars of *Cercopithecus* have higher numbers of occlusal "complexity" (in the sense of total surface patches, see Chapter 3 for more discussion on how this is not the same as older uses of the term "complexity"), *Colobus* shows a reverse trend. Taken together, topographic variables do not support the idea that a more complex occlusal surface should be accompanied by lower shape variability. If anything, the opposite is supported here. A developmental hypothesis is more strongly supported here, given that patterning cascade models do not have any expectations regarding molar surface complexity.

4.4.3: Intra-molar shape variability

Similar to analyses of inter-molar shape variability discussed above, there is strong support for predictions of a patterning cascade across M_3 cusps from cusp-tip landmark analyses but not from topographic analyses. Differences between these methods are considered in section 4.4.5 below. Using cusp-tip landmarks, both intraspecific and interspecific tests of cusp variability were performed. From the intraspecific test, analyses of cusp tip variability suggest that for each species more distal cusps are generally more variable in position. For all species and for almost all cusps with only one exception, protoconid and metaconid cusps are less variable than entoconid, hypoconid, or hypoconulid cusps. The one exception to this is the hypoconid of *P. melalophos*, which is similar to the protoconid and metaconid in variability. Of all cusp pairs across all species, the entoconid and hypoconulid and the protoconid and metaconid respectively are most similar in variability, but second in terms of similarity of variability is the distal cusp pair

entoconid and hypoconid. There is a definite trend of increasing variability across distal cusps within species. At the most conservative, it can be said that there is strong support for a difference in variability between the mesial cusp pair (protoconid and metaconid) and the three distal cusps (entoconid, hypoconid, and hypoconulid). The data also suggest a secondary specific lack of variability between the distal entoconid and hypoconid cusp pair.

The interspecific test of these predictions assesses whether differences between species are more likely to be found in more distal later-developing molars than mesial molars. As in the intraspecific test, there is strong support for more distal cusps being more variable in position. There is again a general trend in which for all pairs of species that were compared, mesial trigonid basin cusps protoconid and metaconid are less variable in position between species than distal talonid basin cusps entoconid, hypoconid, and protoconid. Gauging post-hoc comparisons of cusps across all species pair comparisons, the most similar cusps in terms of variability are again the protoconid and metaconid followed by entoconid and hypoconid. There is support here for dividing M_3 cusps into one of three groups based on similar variabilities between species: a) a mesial cusp pair including protoconid and metaconid, b) a distal cusp pair including entoconid and hypoconid, and c) the distal-most hypoconulid. Variability of the hypoconulid between species is interesting for the three species pairs which included this cusp (*Co. guereza – M. fascicularis*, *Co. guereza – P. melalophos,* and *M. fascicularis – P. melalophos*). Hypoconulid variability between *Co. guereza* and *M. fascicularis* is less than that of the entoconid, though still greater than the protoconid or metaconid. But for *Co. guereza – P. melalophos* or *M. fascicularis – P. melalophos*, hypoconulid variability

is the highest of all cusps. This has to do with *P. melalophos* having small variably expressed hypoconulids (Willis and Swindler, 2004) and *Co. guereza* and *M. fascicularis* having larger, more similar hypoconulids. Comparisons of hypoconulids between *P. melalophos* and either *Co. guereza* or *M. fascicularis* capture these differences between hypoconulid expression while comparisons between *Co. guereza* and *M. fascicularis* do not.

Results from analyses here can be compared to a number of previous considerations of mammalian molar cusp variability. Intraspecific trends of increasing cusp position variability for more distal cusps within cercopithecoid species are consistent with Corruccini's (1979) observation that more distal hominoid molar cusp diameters are more variable as measured from coefficients of variation. The interspecific trend observed here of molar cusp differences between species occurring more in distal cusps can be placed alongside Hunter and Jernvall's (1995) observation that the hypocone has been convergently evolved on upper molars more than 20 times throughout mammalian evolution. Though lower molars were considered here, both results are consistent with developmental predictions. Additionally compared to Hunter and Jernvall's (1995) qualitative approach to determining hypocone character states, the method used here allows for quantification of variability for all cusps across a molar surface. This provides the ability to estimate patterns of variability change across molars.

In this regard this study is actually most similar to Polly's (1998a) analysis of molar cusp-tip landmark position in M_1s and M_2s of two evolutionary lineages of viverravid carnivorans. As in this study, that work included intraspecific analyses and interspecific analyses. But unlike the cercopithecoids considered here, viverravids

expressed a trend in which more mesial trigonid cusps were more variable than distal talonid cusps. Increased variability was explained as the product of viverravid trigonids being generally higher than talonids. Cusp height increase in molar morphogenesis can be accomplished through increased intercuspal growth which may result in increased cusp variability (Jernvall, 1995; Polly, 1998a). More straightforward and expected trends of increasing distal cusp variability from the cercopithecoids here may in this context be related to relatively similar trigonid and talonid heights for this group. Alternately it is possible that differences between results in these studies result from how cusp-tip landmark position variability was quantified. Polly (1998a) used squared summed distances from geometric centroids for cusp landmarks, while this study used specimen cusp-tip pairwise landmark distances. Regardless of this difference in approaches, though, results here are similar to those of Polly (1998a) in that they support Smith et al.'s (1985) suggestion that evolutionary differences between species will most likely be found in characters that express high degrees of variability. In cercopithecoids these are later-developing distal cusps, as is expected from a patterning cascade model of development.

4.4.4: Hypoconulid prominence and distal cusp constriction

Compared to analyses of molar size or molar cusp position variability, support is more modest for a relationship between hypoconulid prominence and distal cusp spreading relative to mesial cusp spreading. The evidence that is present more strongly supports the idea of an interspecific relationship between these traits than an intraspecific correlation. There is a significant trend between species where *C. mitis* evinces the most relative

distal cusp constriction followed by *P. melalophos*, *M. fascicularis*, and *Co. guereza*. M_3 hypoconulids are absent in *C. mitis,* and *P. melalophos* shows a significantly less prominent hypoconulid cusp than either *M. fascicularis* or *Co. guereza*. It is interesting to note that the distance between *P. melalophos*' hypoconulid and the centroid of all other cusps is not actually significantly greater than a similar distance for *C. mitis* between the M_3 distal margin and cusp centroid. Meanwhile, *Co. guereza* has high relative distal cusp spreading and a prominent hypoconulid. The most prominent hypoconulids in this sample actually belong to *M. fascicularis*, but this species expresses distal cusp spreading only slightly lower than that of *P. melalophos*. This distinction between *M. fascicularis* and the other three study species continues into the intraspecific correlation analyses. For *C. mitis*, *Co. guereza*, and *P. melalophos* there exist (marginally significant) negative relationships between relative distal cusp constriction and M_3 distal margin or hypoconulid prominence, as expected. Comparatively *M. fascicularis* shows a significant positive relationship.

There are several possible reasons for this to be the case. It is possible that the observed positive relationship for *M. fascicularis* is artifactual and may disappear if a larger sample size is used. In fact larger sample sizes for all of the species considered here will likely elucidate whether a predicted relationship between relative distal cusp constriction and hypoconulid prominence does exist and if so what form it takes. The M_3s of *M. fascicularis* express the largest hypoconulids on average of all species studied here but they also show moderate degrees of relative distal cusp constriction. It should also be noted that unlike any other species considered, *M. fascicularis* M_3s often express one to three additional small cuspules distal to the entoconid or hypoconid and mesial to the

hypoconulid. It is possible that *M. fascicularis* experiences some modification to developmental processes that allows the formation of not only large hypoconulids but occasionally also additional cusps combined with moderate degrees of relative distal cusp constriction. This could take the form of lowered levels of inhibition during molar morphogenesis, as an example. It is also possible that cercopithecines in general experience moderate to high degrees of relative distal cusp constriction, indicating more need for consideration of phylogenetic influences on developmental patterning. If this is the case though it clearly does not divide cercopithecines and colobines cleanly given that *P. melalophos* exhibits high distal cusp constriction in conjunction with very small hypoconulids.

Yet even with the *M. fascicularis* results being contrary to expectations between individuals within this species, it still more or less fits expected trends between species. It would be interesting to study other cercopithecoid species with either very diminutive or very prominent hypoconulids in order to assess further this possible patterning relationship between cusp construction and hypoconulid prominence. At the least, these data suggest that it is unlikely that any cercopithecoid M_3 expressing a hypoconulid will exhibit relative distal cusp constriction greater than that observed here for *C. mitis*, and vice versa it is unlikely that any cercopithecoid M_3 with this level of distal cusp constriction will exhibit a hypoconulid.

4.4.5: Comparing methods of shape quantification

A pattern can be seen in results here where geometric morphometric techniques strongly support predictions regarding shape variability while morphological topographic

variables DNE (bending), RFI (relief), and OPCR (complexity) detect no significant differences in variability. Both approaches were performed on the same specimens, and this result is surprising given the effectiveness of topographic analyses for quantifying functional morphological characters (Ch. 3). The stark difference in levels of variability indicated by these two approaches requires explanation. Two possible reasons will be given here, the first being considered less likely and the second being considered more likely. There is a statistical difference between how results from GM and topographic analyses were tested. Bartlett's and Levene's tests of homogeneity of variances were used to assess levels of variability in topographic variables, while specimen pairwise landmark distances were calculated and then tested with analyses of central tendencies such as ANOVAs or post hoc pairwise comparison tests. A landmark with more variation between specimens should have a greater mean pairwise distance between landmarks of all specimens considered, allowing the use of the mean to compare variability in this instance. It is possible that differences in statistical power between tests of homoscedasticity and tests of central tendencies have produced the different results observed here. This is unlikely, though, given that standard deviations of topographic variables tend to run counter to expected trends for both analyses of inter-molar variance and intra-molar cusp variance. More likely is that the divergence in results here reflects a substantive difference between these shape quantification approaches that should be addressed in order to best make quantitative judgments from anatomical data.

Specifically, it may be the case that topographic methods are less well suited for studying variation between individuals within species than GM methods. A primary distinction between how GM and topographic methods approach shape quantification is

that GM approaches are “shape specifiers” where topographic metrics are “shape descriptors” (Evans, 2013). In other words GM landmark approaches re-codify shape into a more comparable form between specimens. Specimens in a GM study are represented by standardized sets of 2D or 3D data points that actually represent surface shape and position (such as cusp tip points in some analyses here). The standardization of this data allows comparison between specimens to rigorously diagnose differences in morphology through differences in landmark positions and proportions. This can also be applied to study variation (e.g., Polly, 1998a for a developmental example). Topographic variables on the other hand quantify emergent properties of a surface. An emergent property describes a larger pattern or entity that arises from smaller or simpler component entities. Topographic metrics quantify emergent aspects of whole surface shape as single quantitative values. A consequence of this is that multiple morphological configurations can give rise to the same topographic value. As an example, two separate cusps of a given height can yield the same relief value as a single cusp with twice the height, even though these are clearly very different in shape. This is an advantage in studies of dental function where emergent shape properties may be more correlated with selective fitness than any particular component morphology (Salazar-Ciudad and Marin-Riera, 2013). But it may represent a disadvantage for using these methods to study variation if that variation gives rise to a range of morphologies that produce the same or similar emergent topographic shape properties. I consider this the more likely explanation for the difference in results by GM and topographic approaches here, but a broader analysis of the differences between these shape quantification methods would be valuable. Given the previous analyses of topographic metrics performed in this dissertation (Ch. 2), it is possible to

make some guesses as to the relative sensitivity of topographic metrics to detecting variability. DNE is strongly sensitive to interactions of shape factors such as surface feature shape and feature number, RFI is weakly sensitive to those interactions, and OPCR is primarily responsive to surface feature number alone. As a result, it may be the case that DNE will more actively reflect shape variation than the other two metrics. It is true that for comparisons of variability between M_1, M_2, and M_3, *Cercopithecus* M_3 DNE is the only topographic value that has a higher standard deviation than either M_1 or M_2.

4.5: Conclusions

The analyses in this chapter together provide multiple avenues of support for the idea that developmental patterning cascades originally discovered empirically in mouse studies also play a role in governing molar development in cercopithecoid primates. An inhibitory cascade model of molar size patterning accurately predicts relative molar size in colobines and papionins, suggesting a developmental scheme involving weak inhibition between primary enamel knots initiating molar morphogenesis. Guenons do not conform to this model's predictions, but instead compared to other cercopithecoids show a molar size pattern that suggests weak inhibition combined with an earlier termination point of molar morphogenesis or a reversal of inhibitory cascade size patterning. The evolutionary modification of termination characters or inhibitory cascade size patterning represent possible developmental mechanisms for the derived loss of hypoconulid cusps observed in guenons. There may also be connections between these processes and factors such as body size or life history, though this is speculative for now. Molar shape variability also conforms to patterning cascade expectations, with both distal

molars and distal cusps within M_3 being more variable in shape and position than mesial molars or molar cusps. Conclusions regarding molar cusp variability are supported for both intraspecific and interspecific levels. Later-developing molar cusps are more variable within species, and differences between species are more often observed in later-developing cusps. This is a specific example supporting a general prediction concerning developmental constraints (Smith et al., 1985). There is also moderate support for a patterning relationship between relative distal molar cusp constriction and hypoconulid prominence. This suggests it may be possible to not only predict size or variability, but to chart spatial patterns of development in such a way so as to understand how molar shape relationships are formed.

These results as a group suggest that the formation of molar teeth in cercopithecoid primates is controlled by elegant developmental processes that organize many aspects of molar morphogenesis. These developmental processes seem to play a role in managing or guiding multiple hierarchical levels of morphological form, from relatively broad factors such as molar size to relatively intricate factors such as relative cusp positioning. Interrelated patterning cascades also exist at various developmental hierarchical levels, for example from primary enamel knots initiating molars in sequence to the successions of secondary enamel knots that initiate cusp positions and are produced because of primary knot activity. All this points to the idea that not only are molar characters interdependent, but that the diversity of molar characters may be related to each other through relatively straightforward patterning rules that together comprise a set of tools from which morphological variation can arise. Moreover, the fact that cercopithecoid molars conform to predictions made from empirical studies of mouse

molar morphogenesis may hint that these elegant developmental patterning processes represent ancient shared derived traits among mammals. This is not to say that there are not species or clade-specific modifications to these patterning pathways, since results here may provide evidence for an example of just such a modification concerning hypoconulid loss in guenons. But rather the flexibility of proposed patterning cascade models allows the generation of an extremely diverse theoretical set of molar morphologies, and this may represent the simple but flexible basic mechanism through which dental development is carried out in mammals including primates and rodents.

Examining whether and to what degree fully formed cercopithecoid molars behave according to predictions from patterning cascade models is also an important goal because of the samples to which this analysis can be applied. Directly studying molar morphogenesis through experimental approaches in primates such as the ones studied in this chapter is inadvisable not only just because of the relatively long gestation lengths primates tend to undergo compared to mice but also because of clear ethical issues. As a result, testing predictions from empirical mouse models of molar development provides a relatively rare window into early-stage dental morphogenesis in these animals. Being able to compare tooth development in mice and primates increases the total understanding that we have concerning both groups. On top of this, developmental predictions concerning fully formed teeth represent perhaps the only way to study these processes in extinct species. Being able to extend our knowledge of development to fossils provides a key way of fulfilling the two central goals of evolutionary-developmental biology: studying how developmental processes constrain the types of morphologies available for selection to act on throughout evolution, and studying how developmental processing have

themselves changed across time, modifying the available tools with which to create morphology. For cercopithecoid primates, the analyses of developmental patterning in extant species completed here represent a comparative dataset from which to judge future inferences regarding extinct groups.

Comparing results from this chapter with analyses discussed in previous chapters, one additional conclusion seems apparent: that techniques of topographic analysis have not proved as effective as landmark-based morphometric techniques for quantifying developmentally-linked molar shape variation. This is interpreted to be caused by topographic methods possibly producing similar results from divergent morphological configurations where landmark methods would not behave similarly. While a deeper investigation is needed to test this tentative idea, this work is valuable in that it presents one of the first attempts to use morphological topographic analysis for a purpose other than detecting functional signatures in morphology (but see Skinner et al., 2010). And the weakness of topography here compared to geometric morphometrics has produced a testable prediction concerning substantive differences between the two. It is important to know the relative capabilities of three-dimensional shape quantification techniques, especially automated high-throughput approaches such as topographic analysis or automated 3D landmarks. The quantity and quality of 3D anatomical specimen shape data has increased rapidly in the recent past, and this trend is only like to multiply moving forward, and high-throughput shape quantification methods are necessary to efficiently parse this growing sea change in morphological data. When using these methods, only a rigorous understanding of shape quantification methods will make it possible to accurately interpret these continuously growing data sets.

Table 4.1. Regressions of M_3/M_1 mesiodistal length by M_2/M_1 mesiodistal length.

Clade	Slope	S.E.	Intercept	S.E.	p
Cercopithecoids	1.847	0.532	-0.777	0.578	0.001
Colobines	1.894	0.485	-0.729	0.516	0.001
Guenons	0.433	0.396	0.588	0.426	0.300
Papionins	2.399	1.041	-1.366	1.168	0.037

Table 4.2. Descriptive statistics of topographic variables DNE, RFI, and OPCR of M_1, M_2, and M_3.

			DNE		RFI		OPCR	
Genus	**Tooth**	**n**	**mean**	**S.D.**	**mean**	**S.D.**	**mean**	**S.D.**
Cercopithecus	M_1	22	178.155	53.519	0.237	0.044	83.182	15.621
	M_2	22	206.972	45.610	0.294	0.032	72.636	10.980
	M_3	22	250.568	64.168	0.335	0.029	70.551	12.453
Colobus	M_1	22	218.100	67.997	0.305	0.035	75.670	9.352
	M_2	22	224.810	35.134	0.337	0.030	75.324	8.461
	M_3	22	280.217	48.843	0.353	0.033	82.665	8.262

Table 4.3. ANOVAs of DNE, RFI, and OPCR by tooth class (M_1, M_2, M_3).

a. ANOVAs by tooth class and genus factors

i. DNE

Factor	df	SS	MS	F	p
Genus	1	28029	28029	9.718	0.002
Tooth type	2	106927	53463	18.536	<0.001
Genus*Tooth type	2	2692	1346	0.467	0.628

ii. RFI

Factor	df	SS	MS	F	p
Genus	1	0.06103	0.06103	51.884	<0.001
Tooth type	2	0.11958	0.05979	50.831	<0.001
Genus*Tooth type	2	0.01414	0.00707	6.009	0.003

iii. OPCR

Factor	df	SS	MS	F	p
Genus	1	195	194.8	1.565	0.213
Tooth type	2	653	326.2	2.622	0.077

Genus*Tooth type	2	2119	1059.7	8.512	<0.001

b. ANOVAs by tooth class for each genus for RFI and OPCR

Genus	**Variable**	**df**	**SS**	**MS**	**F**	**p**
Cercopithecus	RFI	2	0.10752	0.05376	42.21	<0.001
	OPCR	2	2017	1008.7	5.823	0.005
Colobus	RFI	2	0.02619	0.013097	12.14	<0.001
	OPCR	2	755	377.4	4.981	0.01

Table 4.4. Bartlett and Levene's tests of DNE, RFI, and OPCR for M_1, M_2, and M_3.

a. Bartlett's tests

	DNE			**RFI**			**OPCR**		
Genus	**K^2**	**df**	**p**	**K^2**	**df**	**p**	**K^2**	**df**	**p**
Cercopithecus	2.3935	2	0.3022	4.0062	2	0.1349	2.6809	2	0.2617
Colobus	8.6632	2	0.01315	0.45019	2	0.7984	0.36264	2	0.8342

b. Levene's tests

	DNE		**RFI**		**OPCR**	
Genus	**W**	**p**	**W**	**p**	**W**	**p**
Cercopithecus	1.068	0.350	4.888	0.011	2.224	0.117
Colobus	0.953	0.391	0.488	0.616	0.039	0.962

Table 4.5. Descriptive statistics of Procrustes distances of *auto3dgm* landmarks for M_1, M_2, and M_3.

		Scaled (shape only)			**Unscaled (size and shape)**		
Genus	**Tooth**	**n**	**Mean**	**S.D.**	**n**	**Mean**	**SD**
Cercopithecus	M_1	231	0.249	0.054	231	0.57	0.157
	M_2	231	0.252	0.045	231	0.635	0.147
	M_3	231	0.298	0.069	231	0.71	0.189
Colobus	M_1	231	0.255	0.053	231	0.663	0.132
	M_2	231	0.26	0.046	231	0.750	0.146
	M_3	231	0.276	0.06	231	0.893	0.207

Table 4.6. ANOVAs of Procrustes distances by tooth class (M_1, M_2, M_3).

Genus	**Scaling**	**df**	**SS**	**MS**	**F**	**p**
Cercopithecus	Scaled	2	0.357	0.178	55.22	<0.001
	Unscaled	2	2.254	1.127	41.58	<0.001

Colobus	Scaled	2	0.058	0.029	10.21	<0.001
	Unscaled	2	6.2	3.100	114.2	<0.001

Table 4.7. Tukey's HSD post-hoc comparisons of Procrustes distances by tooth class.

a. *Cercopithecus*

i. Scaled

	M_2	M_3
M_1	0.003 (0.841)	**0.050 (<0.001)**
M_2		**0.047 (<0.001)**

ii. Unscaled

	M_2	M_3
M_1	**0.065 (<0.001)**	**0.140 (<0.001)**
M_2		**0.075 (<0.001)**

b. *Colobus*

i. Scaled

	M_2	M_3
M_1	0.006 (0.497)	**0.022 (<0.001)**
M_2		**0.016 (0.004)**

ii. Unscaled

	M_2	M_3
M_1	**0.087 (<0.001)**	**0.229 (<0.001)**
M_2		**0.142 (<0.001)**

Table 4.8. Descriptive statistics of topographic variables DNE, RFI, and OPCR of anterior and posterior portions of Colobus M_1 and M_3.

			DNE		**RFI**		**OPCR**	
Tooth	**Portion**	**n**	**mean**	**S.D.**	**mean**	**S.D.**	**mean**	**S.D.**
M_1	Anterior	22	151.936	55.703	0.318	0.037	53.125	10.931
	Posterior	22	136.44	28.142	0.296	0.038	57.017	10.62
M_3	Anterior	22	228.626	106.718	0.364	0.031	58.358	13.771
	Posterior	22	224.911	73.077	0.348	0.034	66.034	10.337

Table 4.9. ANOVAs of DNE, RFI, and OPCR of anterior and posterior portions of *Colobus* M_1 and M_3.

i. DNE

Factor	df	SS	MS	F	p
Tooth	1	150029	150029	29.098	<0.001
Portion	1	2030	2030	0.394	0.532
Tooth*Portion	1	763	763	0.148	0.701

ii. RFI

Factor	df	SS	MS	F	p
Tooth	1	0.05258	0.05258	42.815	<0.001
Portion	1	0.00813	0.00813	6.624	0.012
Tooth*Portion	1	0.00022	0.00022	0.182	0.671

iii. OPCR

Factor	df	SS	MS	F	p
Tooth	1	1117	1116.8	8.448	0.00467
Portion	1	736	736	5.568	0.02061
Tooth*Portion	1	79	78.8	0.596	0.44237

Table 4.10. Bartlett and Levene's tests of DNE, RFI, and OPCR for anterior and posterior portions of *Colobus* M_1 and M_3.

a. Bartlett's test

	DNE			RFI			OPCR		
Tooth Class	**K^2**	**df**	**p**	**K^2**	**df**	**p**	**K^2**	**df**	**p**
M_1	8.9	1	0.003	0.009	1	0.924	0.017	1	0.896
M_3	2.8734	1	0.09	0.244	1	0.621	1.665	1	0.2

b. Levene's test

	DNE		RFI		OPCR	
Tooth	**W**	**p**	**W**	**p**	**W**	**p**
M_1	3.6849	0.062	0.035666	0.851	<0.001	0.998
M_2	1.762	0.1915	0.567	0.456	0.728	0.398

Table 4.11. Descriptive statistics of 2D and 3D intraspecies pairwise cusp-tip landmark distances.

a. 2D

Species	Cusp	n	mean	S.D.
C. mitis	Protoconid	45	0.031	0.015
	Metaconid	45	0.028	0.015
	Entoconid	45	0.031	0.016
	Hypoconid	45	0.043	0.027
Co. guereza	Protoconid	66	0.030	0.014
	Metaconid	66	0.021	0.013
	Entoconid	66	0.037	0.023
	Hypoconid	66	0.041	0.023
	Hypoconulid	66	0.041	0.021
M. fascicularis	Protoconid	153	0.028	0.017
	Metaconid	153	0.032	0.016
	Entoconid	153	0.034	0.018
	Hypoconid	153	0.034	0.021
	Hypoconulid	153	0.034	0.017
P. melalophos	Protoconid	55	0.031	0.019
	Metaconid	55	0.043	0.021
	Entoconid	55	0.048	0.022
	Hypoconid	55	0.032	0.016
	Hypoconulid	55	0.041	0.020

b. 3D

Species	Cusp	n	mean	S.D.
C. mitis	Protoconid	45	0.039	0.015
	Metaconid	45	0.041	0.016
	Entoconid	45	0.054	0.025
	Hypoconid	45	0.052	0.029
Co. guereza	Protoconid	66	0.037	0.016
	Metaconid	66	0.041	0.019
	Entoconid	66	0.051	0.026
	Hypoconid	66	0.052	0.025
	Hypoconulid	66	0.059	0.031
M. fascicularis	Protoconid	153	0.036	0.017
	Metaconid	153	0.039	0.018
	Entoconid	153	0.043	0.018
	Hypoconid	153	0.048	0.021
	Hypoconulid	153	0.045	0.019
P. melalophos	Protoconid	55	0.047	0.025

	Metaconid	55	0.051	0.019
	Entoconid	55	0.056	0.022
	Hypoconid	55	0.042	0.020
	Hypoconulid	55	0.055	0.024

Table 4.12. ANOVAs of cusp-tip pairwise landmark distances by cusp and 2D/3D format factors.

Species	**Factor**	**df**	**SS**	**MS**	**F**	**p**
C. mitis	Cusp	3	0.011	0.004	8.671	<0.001
	2D/3D	1	0.016	0.016	37.780	<0.001
	Cusp * 2D/3D	3	0.003	0.001	2.475	0.061
Co. guereza	Cusp	4	0.037	0.009	19.820	<0.001
	2D/3D	1	0.031	0.031	66.630	<0.001
	Cusp * 2D/3D	4	0.003	<0.001	1.740	0.139
M. fascicularis	Cusp	4	0.016	0.004	12.231	<0.001
	2D/3D	1	0.041	0.041	123.262	<0.001
	Cusp * 2D/3D	4	0.002	<0.001	1.637	0.162
P. melalophos	Cusp	4	0.018	0.004	10.234	<0.001
	2D/3D	1	0.017	0.017	38.094	<0.001
	Cusp * 2D/3D	4	0.001	<0.001	0.821	0.512

Table 4.13. ANOVAs of 2D and 3D cusp-tip pairwise landmark distances by cusp and species factors.

Variable	**Factor**	**df**	**SS**	**MS**	**F**	**p**
2D distance	Cusp	4	0.017	0.004	12.482	<0.001
	Species	3	0.010	0.003	9.462	<0.001
	Cusp * Species	11	0.025	0.002	6.529	<0.001
3D distance	Cusp	4	0.032	0.008	18.437	<0.001
	Species	3	0.016	0.005	12.284	<0.001
	Cusp * Species	11	0.018	0.002	3.708	<0.001

Table 4.14. ANOVAs of 2D cusp-tip pairwise landmark distance by cusp for each species.

Species	df	SS	MS	F	p
C. mitis	3	0.006	0.002	5.814	0.001
Co. guereza	4	0.019	0.005	13.320	<0.001
M. fascicularis	4	0.005	0.001	3.748	0.005
P. melalophos	4	0.011	0.003	7.227	<0.001

Table 4.15. Tukey HSD post-poc comparisons of 2D cusp-tip pairwise landmark distances by cusp for each species.

a. *C. mitis*

	Metaconid	Entoconid	Hypoconid
Protoconid	0.003 (0.831)	0.001 (1.000)	**0.012 (0.014)**
Metaconid		0.004 (0.779)	**0.015 (0.001)**
Entoconid			**0.012 (0.019)**

b. *Co. guereza*

	Metaconid	Entoconid	Hypoconid	Hypoconulid
Protoconid	0.009 (0.081)	0.007 (0.183)	**0.011 (0.006)**	**0.012 (0.005)**
Metaconid		**0.016 (<0.001)**	**0.020 (<0.001)**	**0.020 (<0.001)**
Entoconid			0.004 (0.735)	0.004 (0.704)
Hypoconid				<0.001 (1.000)

c. *M. fascicularis*

	Metaconid	Entoconid	Hypoconid	Hypoconulid
Protoconid	0.004 (0.256)	**0.006 (0.015)**	**0.006 (0.014)**	**0.006 (0.016)**
Metaconid		0.002 (0.791)	0.002 (0.785)	0.002 (0.811)
Entoconid			<0.001 (1.000)	<0.001 (1.000)
Hypoconid				<0.001 (1.000)

d. *P. melalophos*

	Metaconid	Entoconid	Hypoconid	Hypoconulid
Protoconid	**0.012 (0.012)**	**0.017 (<0.001)**	0.001 (0.998)	0.010 (0.089)
Metaconid		0.004 (0.774)	0.011 (0.028)	0.003 (0.952)
Entoconid			**0.016 (<0.001)**	0.007 (0.331)
Hypoconid				0.008 (0.171)

Table 4.16. ANOVAs of 3D cusp-tip pairwise landmark distance by cusp for each species.

Species	df	SS	MS	F	p
C. mitis	3	0.008	0.003	5.398	0.001
Co. guereza	4	0.021	0.005	9.173	<0.001
M. fascicularis	4	0.014	0.003	9.806	<0.001
P. melalophos	4	0.008	0.002	4.160	0.003

Table 4.17. Tukey HSD post-poc comparisons of 3D cusp-tip pairwise landmark distances by cusp for each species. Values are given as absolute difference between group means followed by *p* values in parenthesis. Significant results ($p < 0.05$) are bolded.

a. *C. mitis*

	Metaconid	Entoconid	Hypoconid
Protoconid	0.002 (0.970)	**0.015 (0.007)**	**0.013 (0.030)**
Metaconid		**0.013 (0.027)**	0.011 (0.093)
Entoconid			0.002 (0.962)

b. *Co. guereza*

	Metaconid	Entoconid	Hypoconid	Hypoconulid
Protoconid	0.004 (0.892)	**0.014 (0.006)**	**0.015 (0.003)**	**0.022 (<0.001)**
Metaconid		0.010 (0.095)	0.011 (0.056)	**0.018 (<0.001)**
Entoconid			0.001 (1.000)	0.008 (0.341)
Hypoconid				0.007 (0.467)

c. *M. fascicularis*

	Metaconid	**Entoconid**	**Hypoconid**	**Hypoconulid**
Protoconid	0.002 (0.766)	**0.007 (0.013)**	**0.012 (<0.001)**	**0.009 (<0.001)**
Metaconid		0.004 (0.267)	**0.009 (<0.001)**	**0.006 (0.028)**
Entoconid			0.005 (0.140)	0.002 (0.881)
Hypoconid				0.003 (0.643)

d. *P. melalophos*

	Metaconid	**Entoconid**	**Hypoconid**	**Hypoconulid**
Protoconid	0.004 (0.870)	0.010 (0.144)	0.005 (0.749)	0.008 (0.290)
Metaconid		0.006 (0.662)	0.009 (0.194)	0.004 (0.859)
Entoconid			**0.015 (0.005)**	0.001 (0.997)
Hypoconid				**0.013 (0.015)**

Table 4.18. Descriptive statistics of interspecies pairwise cusp-tip landmark distances.

Species Pair	**n**	**Cusp**	**Mean**	**S.D.**
C. mitis - *Co. guereza*	**120**	**Protoconid**	**0.058**	**0.018**
		Metaconid	**0.063**	**0.022**
		Entoconid	**0.125**	**0.036**
		Hypoconid	**0.079**	**0.029**
C. mitis - *M. fascicularis*	**180**	**Protoconid**	**0.068**	**0.025**

		Metaconid	**0.072**	**0.022**
		Entoconid	**0.100**	**0.027**
		Hypoconid	**0.091**	**0.026**
C. mitis - P. melalophos	**110**	**Protoconid**	**0.052**	**0.024**
		Metaconid	**0.053**	**0.021**
		Entoconid	**0.073**	**0.028**
		Hypoconid	**0.078**	**0.027**
Co. guereza - M. fascicularis	**216**	**Protoconid**	**0.045**	**0.019**
		Metaconid	**0.047**	**0.024**
		Entoconid	**0.067**	**0.025**
		Hypoconid	**0.064**	**0.027**
		Hypoconulid	**0.055**	**0.029**
Co. guereza - P. melalophos	**132**	**Protoconid**	**0.057**	**0.032**
		Metaconid	**0.061**	**0.026**
		Entoconid	**0.086**	**0.029**
		Hypoconid	**0.065**	**0.020**
		Hypoconulid	**0.104**	**0.028**
M. fascicularis - P. melalophos	**198**	**Protoconid**	**0.079**	**0.035**
		Metaconid	**0.077**	**0.032**
		Entoconid	**0.067**	**0.026**
		Hypoconid	**0.095**	**0.024**
		Hypoconulid	**0.118**	**0.029**

Table 4.19. ANOVAs of interspecies cusp-tip pairwise landmark distances for each species pair.

Species Pair	**df**	**MS**	**SS**	**F**	**p**
C. mitis - Co. guereza	3	0.330	0.110	151.30	<0.001
C. mitis - M. fascicularis	3	0.123	0.041	65.20	<0.001
C. mitis - P. melalophos	3	0.059	0.020	31.03	<0.001
Co. guereza - M. fascicularis	4	0.081	0.020	32.02	<0.001
Co. guereza - P. melalophos	4	0.208	0.052	70.20	<0.001
M. fascicularis - P. melalophos	4	0.312	0.078	89.46	<0.001

Table 4.20. Tukey HSD post-hoc comparisons of interspecies cusp-tip pairwise landmark distances for each species pair. Values are given as absolute difference between group means followed by *p* values in parenthesis. Significant results ($p < \$0.05$) are bolded.

a. *C. mitis - Co. guereza*

	Metaconid	Entoconid	Hypoconid
Protoconid	0.005 (0.562)	**0.066 (<0.001)**	**0.020 (<0.001)**

Metaconid		**0.062 (<0.001)**	**0.016 (<0.001)**
Entoconid			**0.046 (<0.001)**

b. *C. mitis - M. fascicularis*

	Metaconid	Entoconid	Hypoconid
Protoconid	0.003 (0.609)	**0.031 (<0.001)**	**0.023 (<0.001)**
Metaconid		**0.028 (<0.001)**	**0.020 (<0.001)**
Entoconid			**0.008 (0.013)**

c. *C. mitis - P. melalophos*

	Metaconid	Entoconid	Hypoconid
Protoconid	0.002 (0.967)	**0.021 (<0.001)**	**0.026 (<0.001)**
Metaconid		**0.020 (<0.001)**	**0.025 (<0.001)**
Entoconid			0.005 (0.468)

d. *Co. guereza - M. fascicularis*

	Metaconid	Entoconid	Hypoconid	Hypoconulid
Protoconid	0.002 (0.887)	**0.022 (<0.001)**	**0.019 (<0.001)**	**0.010 (<0.001)**
Metaconid		**0.019 (<0.001)**	**0.017 (<0.001)**	0.008 (0.006)
Entoconid			0.003 (0.787)	**0.011 (<0.001)**
Hypoconid				0.008 (0.004)

e. *Co. guereza - P. melalophos*

	Metaconid	Entoconid	Hypoconid	Hypoconulid
Protoconid	0.004 (0.736)	**0.029 (<0.001)**	0.008 (0.111)	**0.047 (<0.001)**
Metaconid		**0.025 (<0.001)**	0.004 (0.755)	**0.043 (<0.001)**
Entoconid			**0.021 (<0.001)**	**0.018 (<0.001)**
Hypoconid				**0.039 (<0.001)**

f. *M. fascicularis - P. melalophos*

	Metaconid	Entoconid	Hypoconid	Hypoconulid
Protoconid	0.001 (0.992)	**0.011 (0.001)**	**0.016 (<0.001)**	**0.039 (<0.001)**
Metaconid		0.010 (0.006)	**0.018 (<0.001)**	**0.041 (<0.001)**
Entoconid			**0.028 (<0.001)**	**0.051 (<0.001)**
Hypoconid				**0.023 (<0.001)**

Table 4.21. Descriptive statistics of intercuspal M_3 distances.

		PM		EH		PM/EH		HC	
Species	**n**	**mean**	**S.D.**	**mean**	**S.D.**	**mean**	**S.D.**	**mean**	**S.D.**
C. mitis	10	0.630	0.038	0.494	0.027	1.281	0.128	0.987	0.073
Co. guereza	12	0.570	0.033	0.557	0.035	1.026	0.071	1.145	0.061
M. fascicularis	18	0.529	0.037	0.473	0.039	1.124	0.111	1.192	0.043
P. melalophos	11	0.656	0.055	0.571	0.031	1.153	0.115	1.003	0.058

Table 4.22. ANOVA and Tukey HSD post-hocs of PM/EH by species.

a. ANOVA

df	**SS**	**MS**	**F**	**p**
3	0.361	0.12	10.33	<0.001

b. Tukey HSD

	Co. guereza	*M. fascicularis*	*P. melalophos*
C. mitis	**-0.255 (<0.001)**	**-0.157 (0.003)**	**-0.127 (0.046)**
Co. guereza		0.098 (0.082)	**0.128 (0.033)**
M. fascicularis			0.029 (0.893)

Table 4.23. ANOVA and Tukey HSD post-hocs of hypoconulid prominence.

a. ANOVA

df	**SS**	**MS**	**F**	**p**
3	0.41	0.137	41.52	<0.001

b. Tukey HSD

	Co. guereza	M. fascicularis	P. melalophos
C. mitis	**0.159 (<0.001)**	**0.206 (<0.001)**	0.016 (0.913)
Co. guereza		0.047 (0.138)	**-0.142 (<0.001)**
M. fascicularis			**-0.189 (<0.001)**

Table 4.24. Regression of hypoconulid prominence by relative posterior cusp restriction.

Slope	**S.E.**	**Intercept**	**S.E.**	**p**
-0.376	0.099	1.528	0.114	<0.001

Table 4.25. ANCOVA of hypoconulid prominence (HC) by species with relative posterior cusp restriction (PM/EH) covariate.

Factor	**df**	**SS**	**MS**	**F**	**p**

Species	3	0.41	0.137	57.256	<0.001
PM/EH	1	0.011	0.011	4.782	0.034
Species * PM/EH	3	0.041	0.014	5.676	0.002

Table 4.26. Regressions of hypoconulid prominence by relative posterior cusp restriction for each species.

Species	**Slope**	**S.E.**	**Intercept**	**S.E.**	**p**
C. mitis	-0.388	0.146	1.483	0.188	0.029
Co.guereza	-0.416	0.237	1.572	0.244	0.11
M. fascicularis	0.198	0.084	0.97	0.095	0.032
P. melalophos	-0.3	0.136	1.349	0.158	0.055

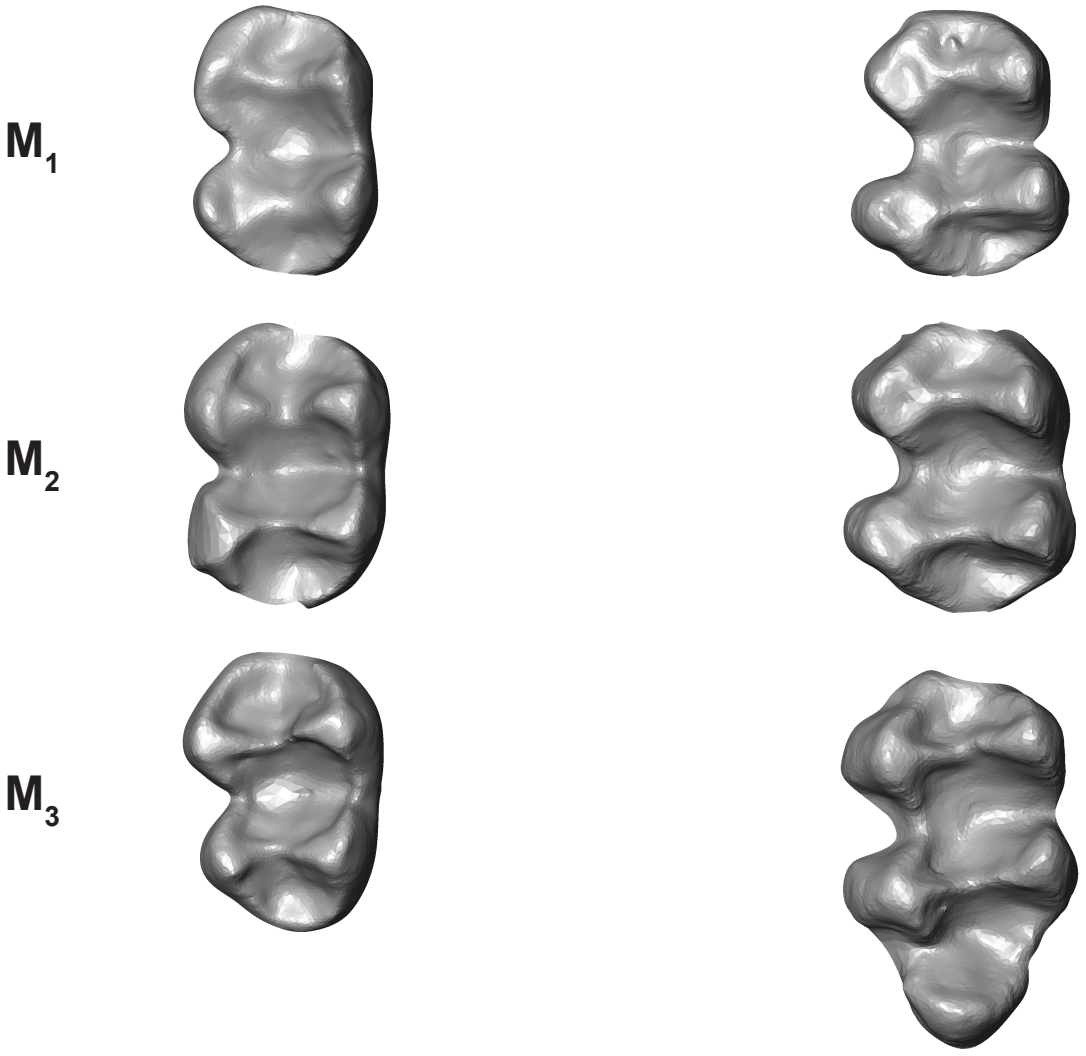

Fig 4.1. Representative specimens for study sample. Specimens are scaled so that buccolingual widths of M_3s are approximately equal between species. As a result, teeth are not scaled consistently between species. For museum attribution codes, see Appenidix 4.

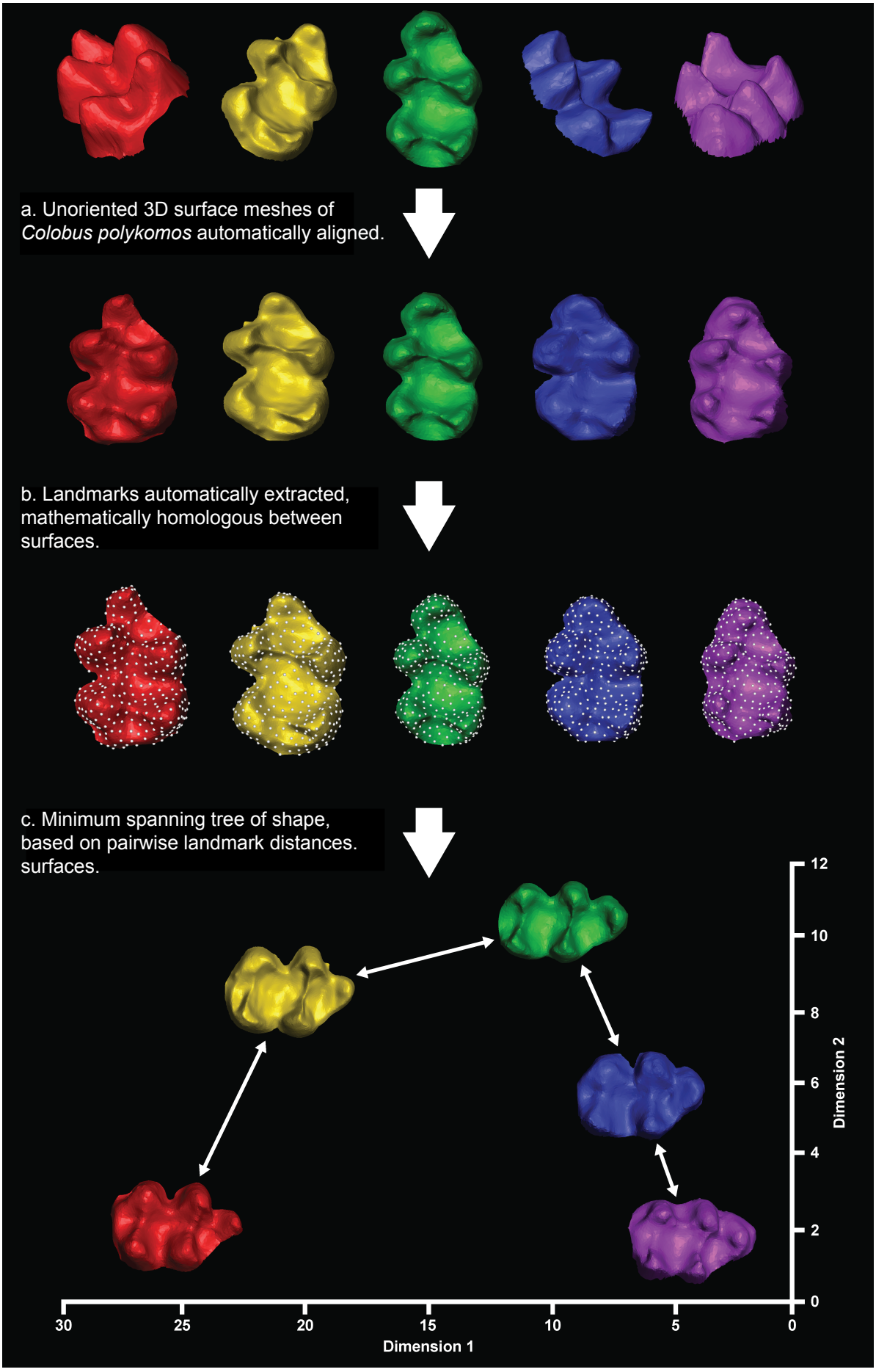

Fig 4.2. Demonstration of process for shape alignment of 3D surfaces and automatic creation of mathematically homologous landmarks by the *auto3dgm* software. Part c. depicts a minimum spanning tree of example specimens based on average pairwise landmark distance.

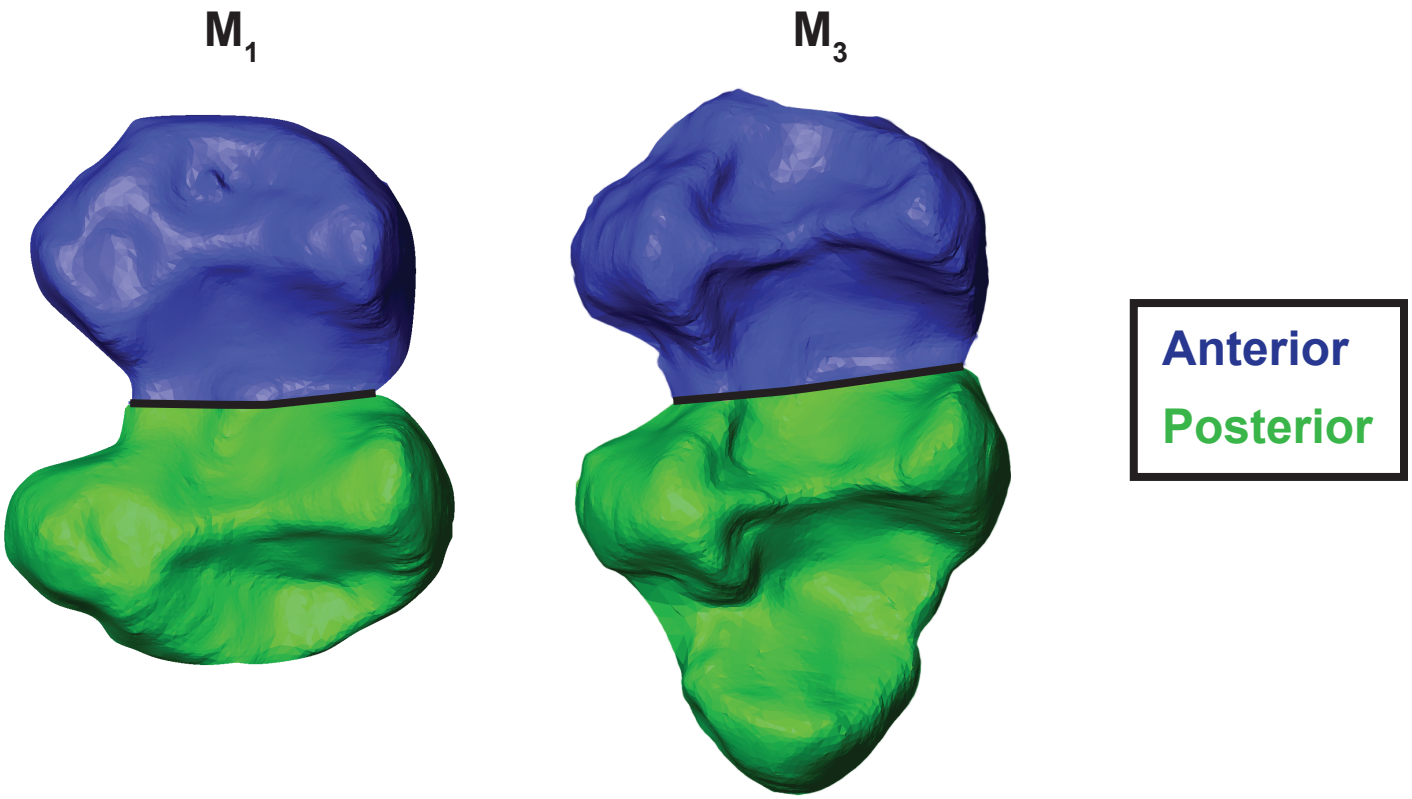

Fig 4.3. Sectioning of Colobus M_1 and M_3 into anterior and posterior divisions. Black line indicates line of division between sections. See text for details on how lines of division were derived. Specimens shown here (*Colobus guereza* BMNH 1938.9.9.4 M_1 and M_3) are also depicted in Fig. 4.1.

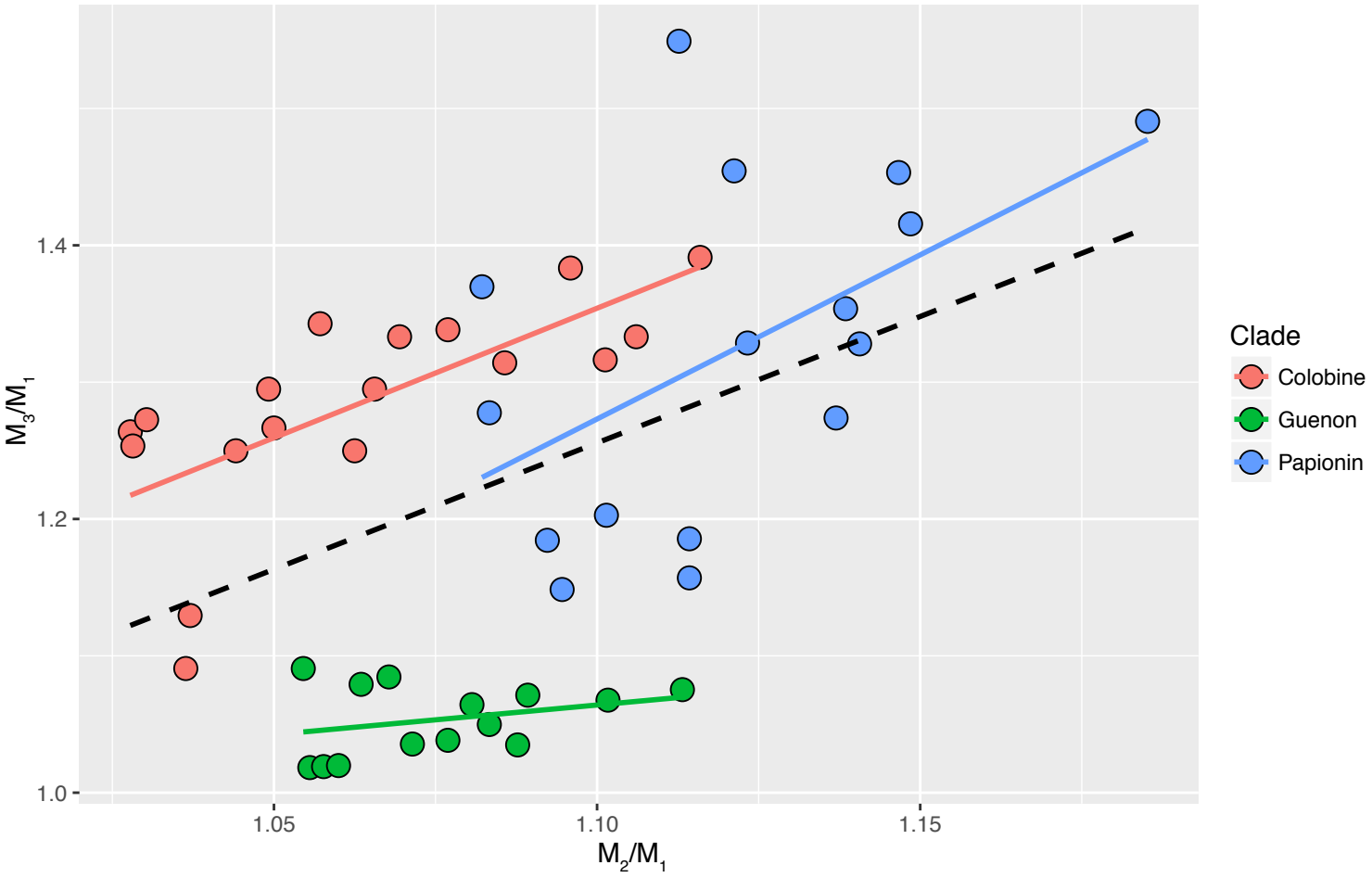

Fig 4.4. Regressions of M_3/M_1 mesiodistal lengths by M_2/M_1 mesiodistal lengths to test predictions of the inibitory cascade model of molar tooth development.

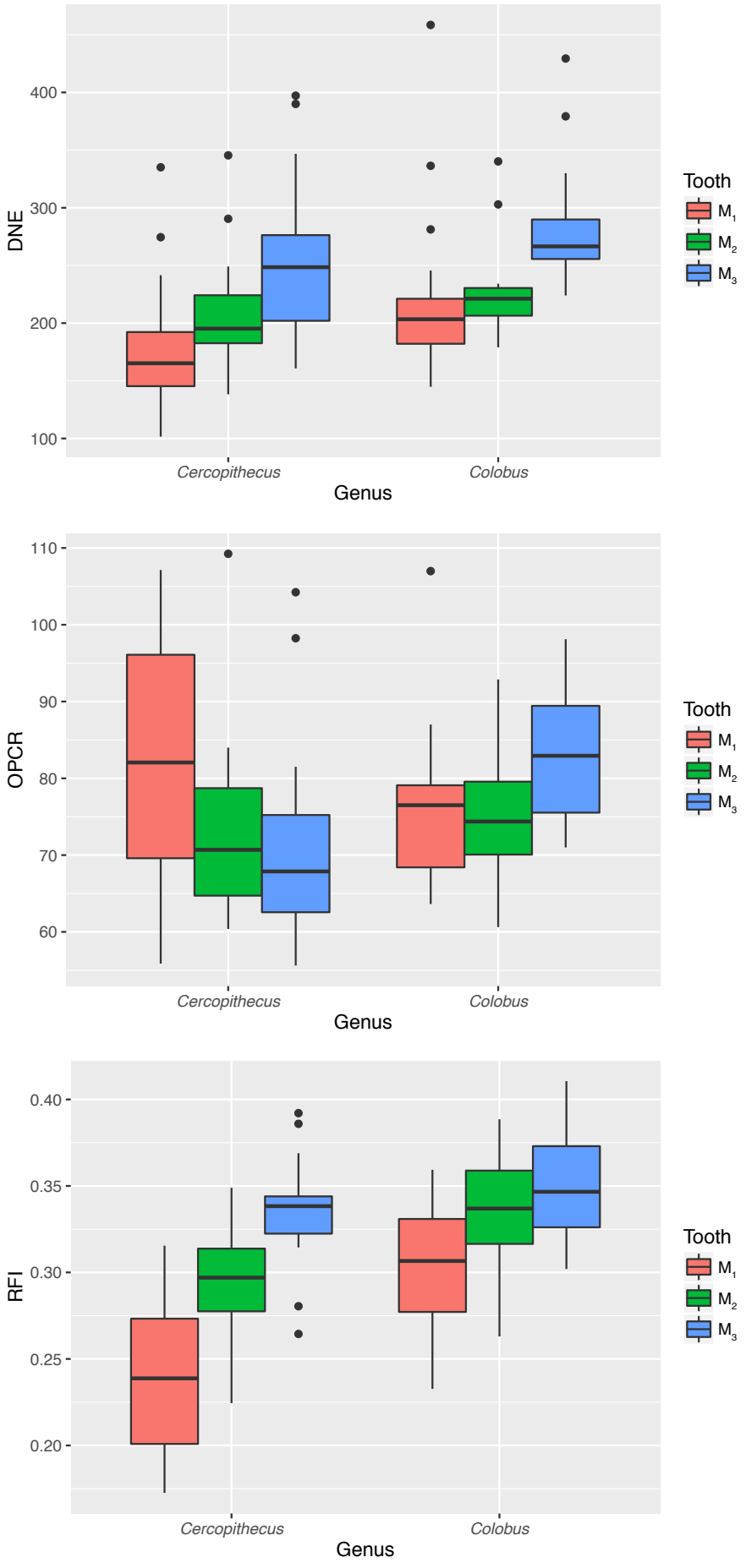

Fig 4.5. Box plots of topographic variables (DNE, RFI, OPCR) of M_1, M_2, and M_3 for *Cercopithecus* and *Colobus*.

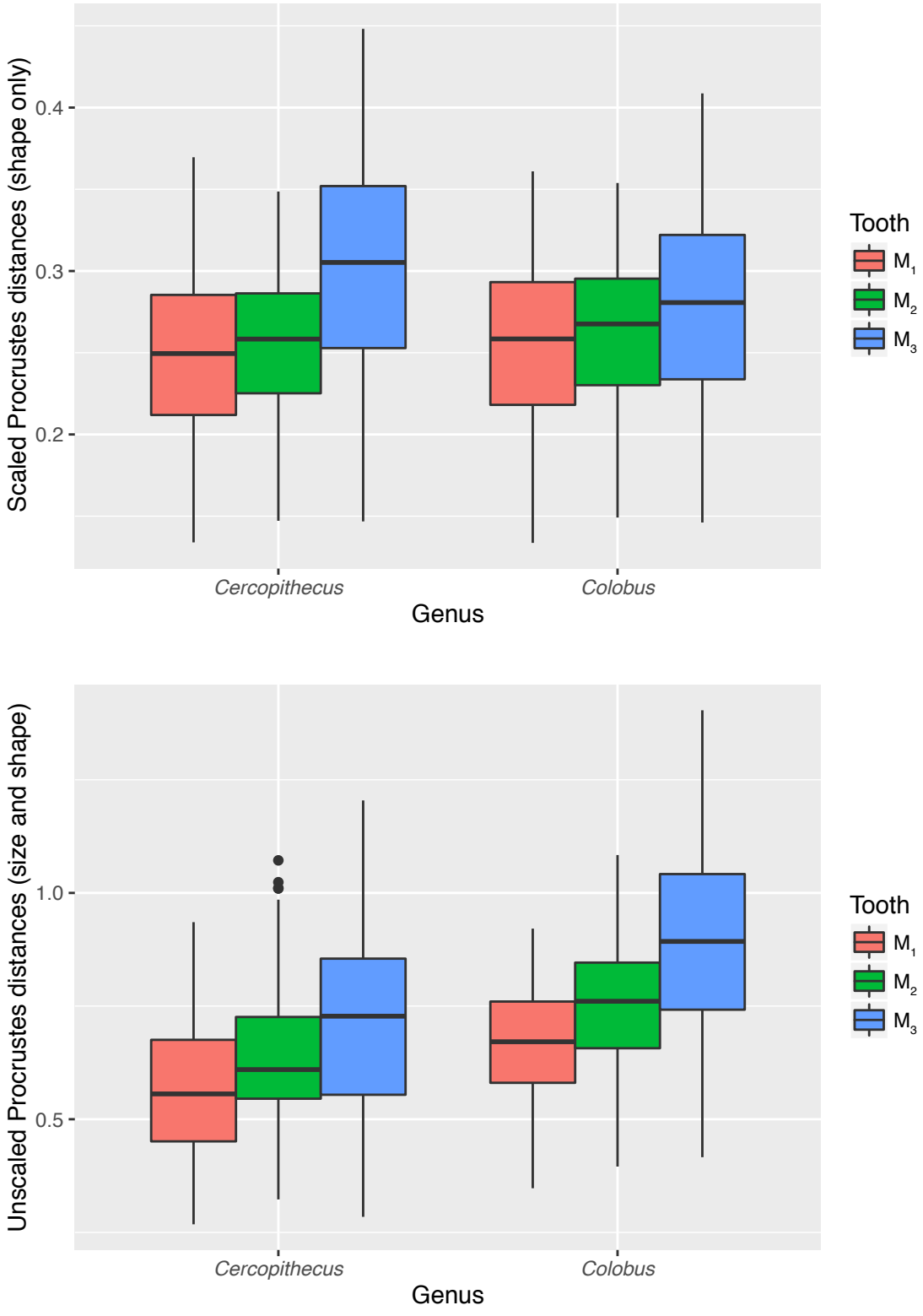

Fig 4.6. Scaled and unscaled Procrustes distances for M_1, M_2, and M_3 of *Cercopithecus* and *Colobus*.

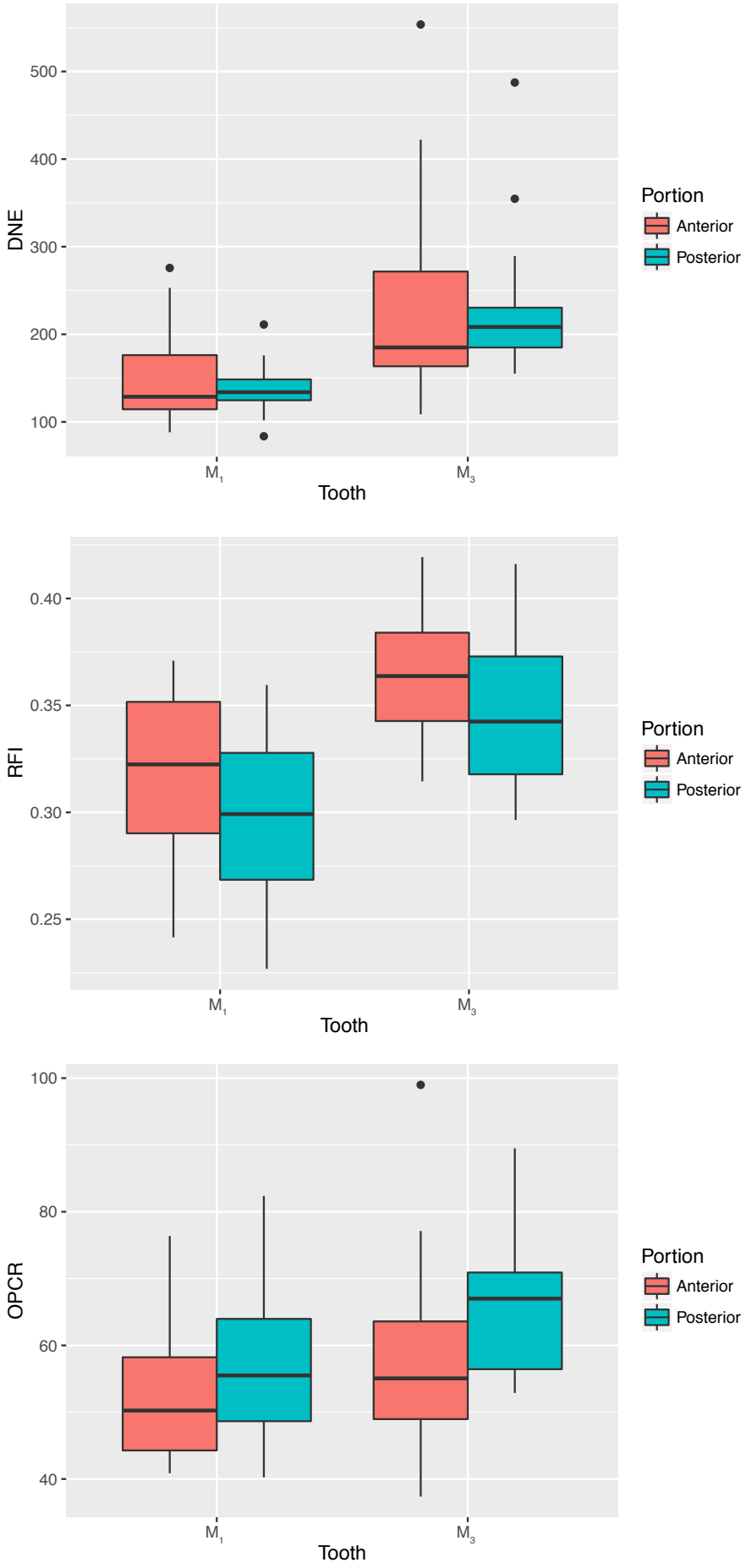

Fig 4.7. Box plot of topographic variables (RFI, DNE, OPCR) of anterior and posterior sections of *Colobus* M_1 and M_3.

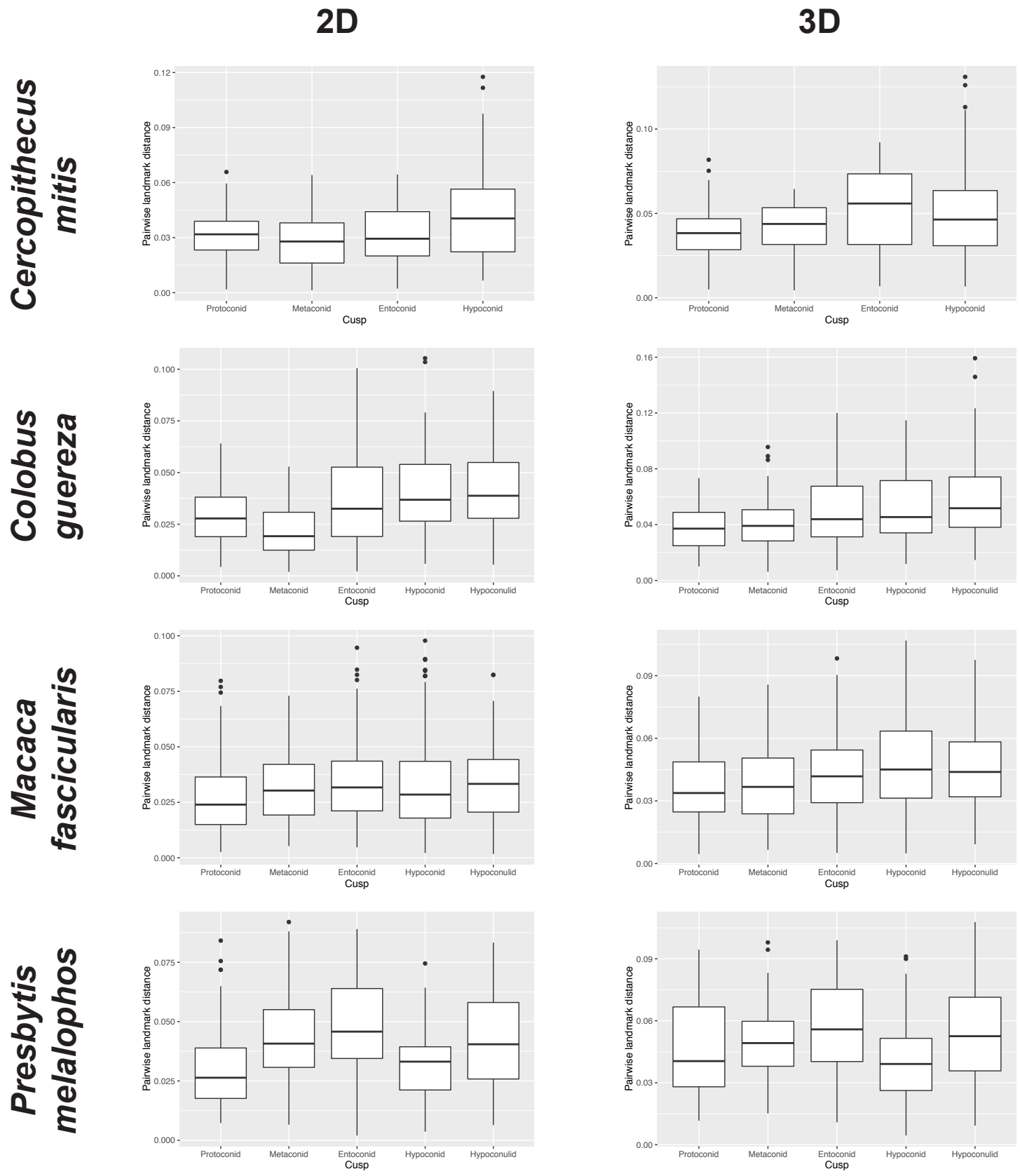

Fig 4.8. Box plots of 2D and 3D intraspecies pairwise cusp-tip landmark distances.

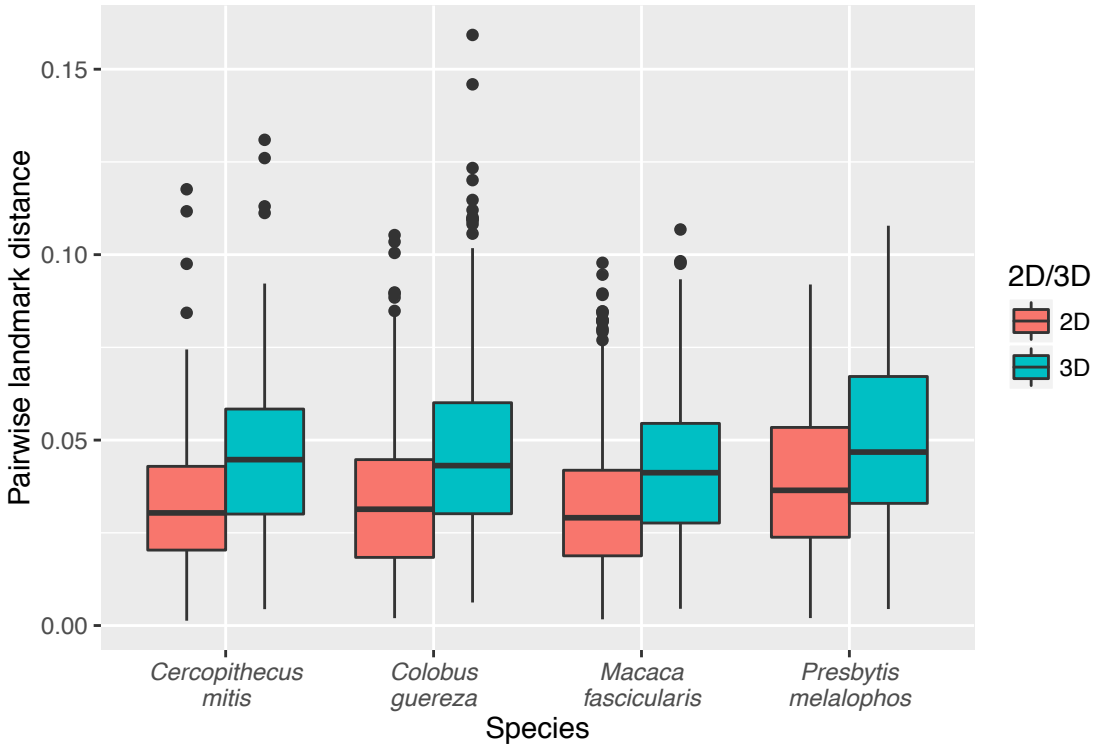

Fig 4.9. Box plot of 2D and 3D intraspecies pairwise cusp-tip landmark distances, demonstrating differences in pairwise landmark distances by 2D/3D treatment for each species.

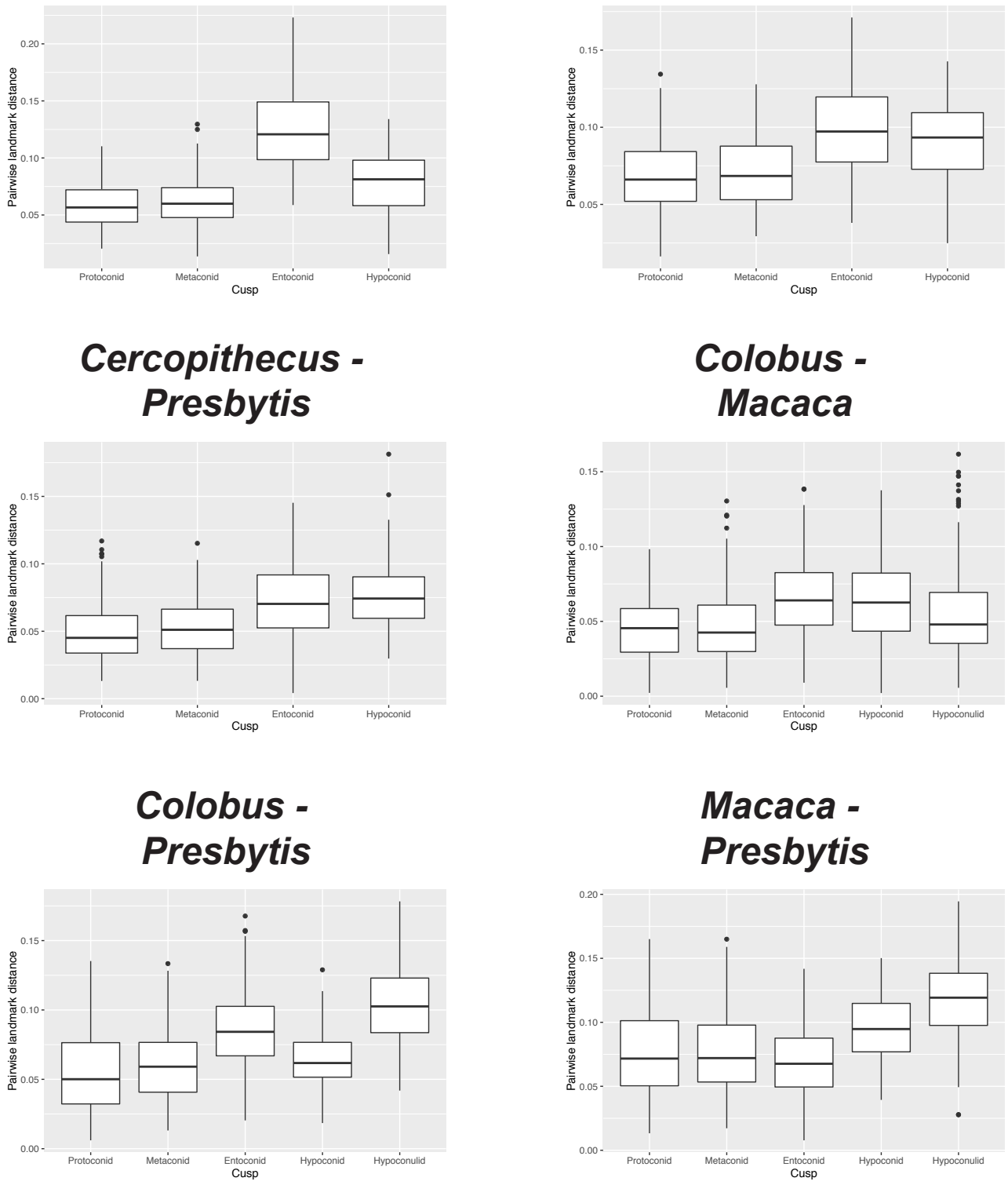

Fig 4.10. Box plots of interspecies pairwise cusp-tip landmark distances by cusp for pairs of species.

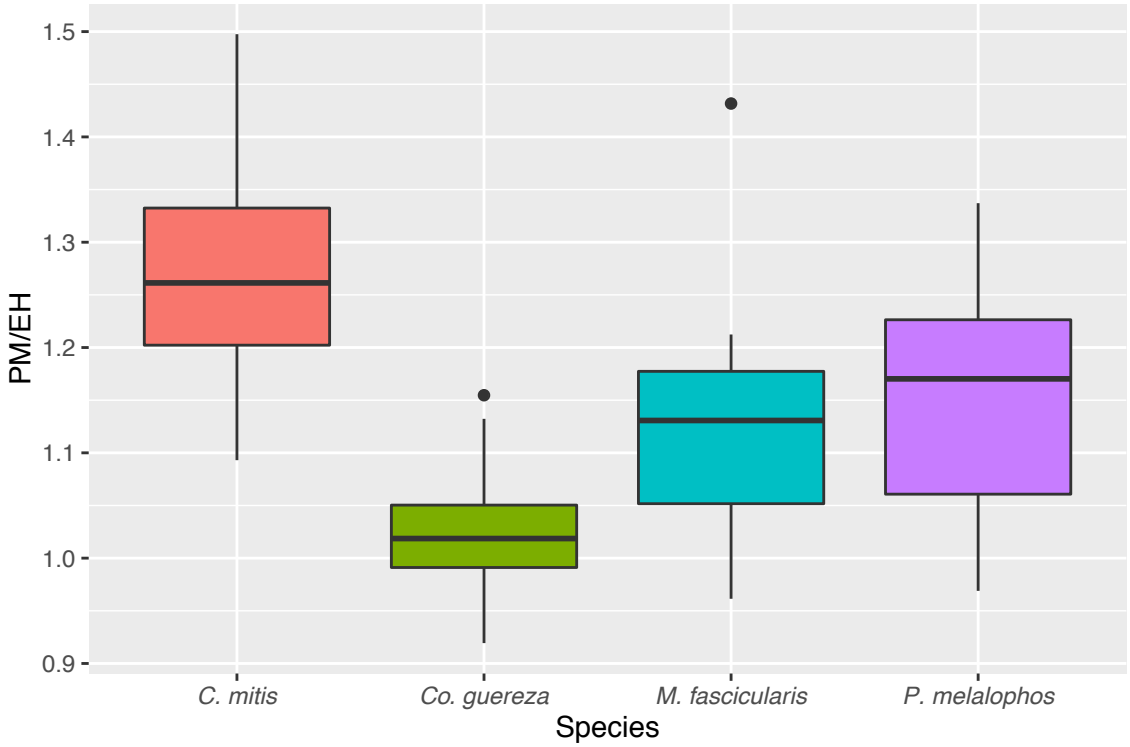

Fig 4.11. Box plots of PM/EH (ratio of distance from protoconid to metaconid over distance from entoconid to hypoconid) by species. PM/EH provides a measure of posterior cusp constriction relative to anterior cusp constriction.

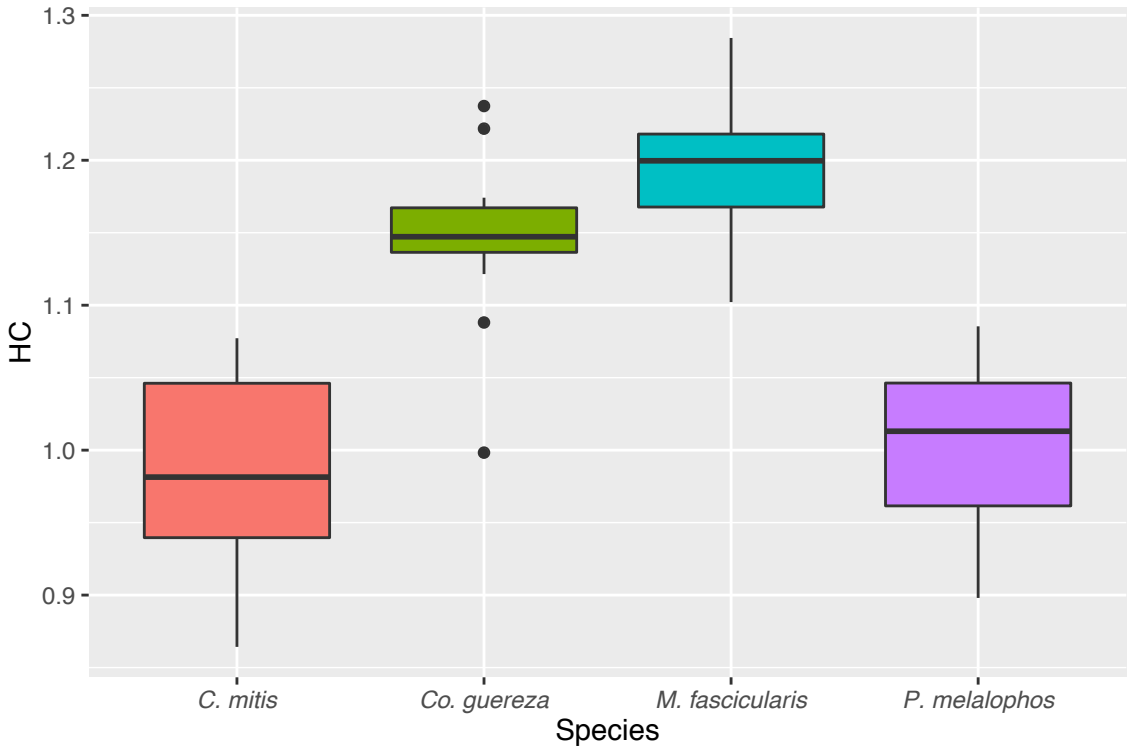

Fig 4.12. Box plots of HC, the distance of the hypoconulid or middle distal occlusal margin (for C. mitis) from the geometric centroid of the protoconid, metaconid, entoconid, and hypoconid. HC provides a measure of hypoconulid prominence.

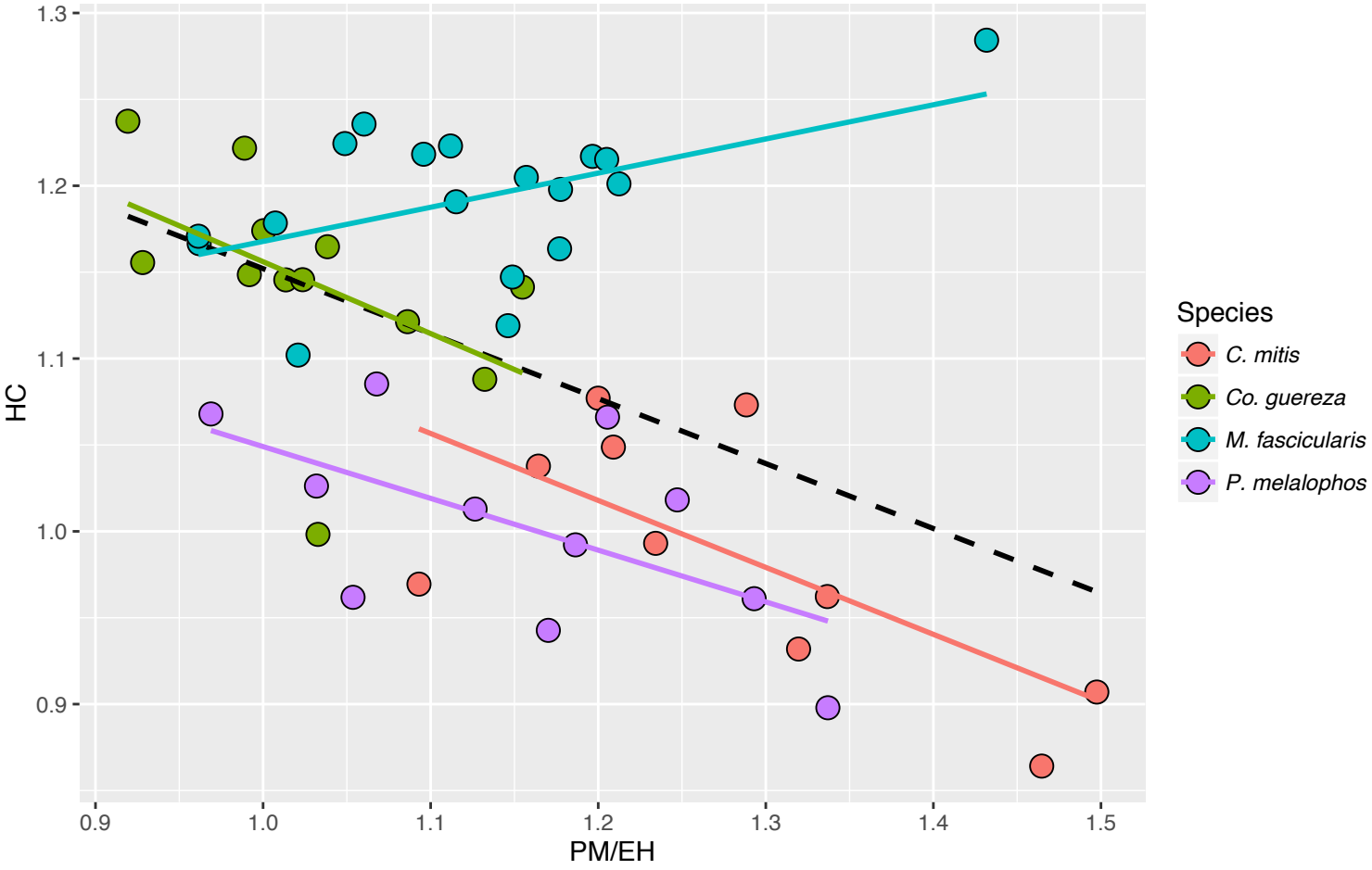

Fig 4.13. Regression of HC (distance of hypoconulid from geometric centroid of other major cusps) by PM/EH (ratio of distance from protoconid to metaconid over distance from entoconid to hypoconid). Dashed black line indicates trend line for all species combined.

Chapter 5

Conclusions

The goals of this dissertation were to construct more comprehensive open-source software tools for morphological topographic analysis, to better understand the effects of surface mesh pre-processing parameters on quantified topography, and to use developed tools and understanding to assess extant cercopithecoid second mandibular molar topography in the context of dietary food mechanical-processing and evolutionary-developmental patterning models. Molar surface shape has been an active research subject dating back to the beginning of systematic biology and anthropology, and a wealth of interpretations have been made concerning dental morphology (e.g., Cuvier, 1863; Cope, 1883; Gregory, 1922; Kay and Hiiemae, 1974; Kay, 1975, 1977, 1984; Rosenberger and Kinzey, 1976; Kinzey, 1978; Seligsohn and Szalay, 1978; Kay and Covert, 1984; Benefit, 1993; Ungar and Kay, 1995; Kirk and Simons, 2001; M'Kirera and Ungar, 2003; Boyer, 2008; Bunn et al., 2011; Winchester et al., 2014). Despite this, the last several decades have seen technological innovations that have revolutionized our ability to both survey and understand morphological shape. New imaging technologies such as laser or μCT scanners allow for the creation of highly accurate digital surface representations of anatomical specimens. Increasing affordability and availability of these technologies has led to continuous growth in the quantity and quality of digital surface datasets representing molar teeth and other anatomical elements (e.g., *MorphoSource*, Boyer et al., 2014). Interpreting these increasingly large dataset requires quantitative morphological methods well suited to quickly processing specimens while extracting as

much as information as possible, or in other words techniques of "high-throughput morphometrics" (Plyusnin et al., 2008). Morphological topographic analysis is a promising new approach for relatively automated morphometric shape description (e.g., Ungar and M'Kirera, 2003; Evans et al., 2007; Boyer, 2008; Bunn et al., 2011; Evans, 2013). This dissertation seeks to improve tools for the analysis of topography, to better understand the application of topographic methods, and to apply these shape descriptor techniques to address molar form-function relationships and developmental relationships. Each chapter will be summarized here, with a discussion of its findings and significance.

The goal of Chapter 2 was to produce improved tools for morphological topographic analysis and to better understand how surface mesh pre-processing parameters affect quantified topography. Previous implementations of morphological topographic analysis have used a diversity of software packages to perform topographic algorithms, but some of these implementations involve software that is either not widely available (e.g., Bunn et al., 2011) or proprietary and expensive (e.g., Boyer, 2008). Also there is reason to believe that the power of morphological topographic analysis is improved when multiple metrics are combined (Bunn et al., 2011; Winchester et al., 2011). Perhaps more importantly, implementations of topographic metrics sometimes use surface mesh data formats that are not necessarily interchangeable, with some approaches using digital elevation models (DEMs) created from Geographic Information Systems software (Ungar and M'Kirera, 2003; Evans et al., 2007) and others using triangulated polygon surface meshes (Boyer, 2008; Bunn et al, 2011). A single free open source application capable of measuring multiple topographic metrics from a uniform surface mesh data format would be advantageous. Chapter two introduces MorphoTester, an

open-source application capable of measuring Dirichlet normal energy (DNE, quantifies surface curvature) (Bunn et al., 2011), relief index (RFI, quantifies surface relief) (Ungar and M'Kirera, 2003; Boyer, 2008), and orientation patch count rotated (OPCR, quantifies surface complexity) (Evans et al., 2007; Evans and Jernvall, 2009) from triangulated polygon surface meshes.

The implementations of DNE and RFI used by MorphoTester completely replicate or extend previous uses of these metrics in the literature, but the OPCR implementation uses an algorithm distinct from much previous work in quantifying complexity from polygon meshes instead of from DEMs. A sample of second mandibular molars (M_2s) belonging to four species of extant cercopithecoids was used to compare OPCR values produced by the MorphoTester algorithm to OPCR values produced by the application SurferManipulator (Evans et al., 2007). Results from these comparisons suggest that OPCR as measured by MorphoTester is at least as capable of distinguishing species-level differences in M_2 complexity as OPCR measured by SurferManipulator, and in fact may be more capable of distinguishing inter-species differences in complexity relative to intra-species differences. This is most likely explained by a difference in mesh resolution. Polygonal meshes used here encode shape as 10,000 triangular polygons with 5,000 to 6,000 vertices, and tend to contain approximately three times the number of raw 3D data points compared to DEMs produced using a standard SurferManipulator procedure. A similar phenomenon was found when the effect of data resolution within SurferManipulator was previously tested (Evans and Janis, 2014). At the same time, it is also true that differences between OPCR values as calculated by MorphoTester and SurferManipulator seem correlated with absolute complexity, such that species such as *T.*

gelada with greater complexity compared to other species exhibit greater differences between OPCR values by treatment. Because DEM-based approaches such as SurferManipulator may be less well equipped to consider undulating vertical surfaces or surfaces with undercuts, this may indicate that rapid vertical surface change across a tooth surface may cause greater differences in OPCR calculated from DEMs and polygonal surfaces, relative to differences in OPCR by treatment for flatter teeth.

Topographic variables were measured on a sample of simple geometric objects that mimic addition of cusps and increases in cusp height in order to empirically test how quantified topography changes with intuitive modification of shape. As expected, OPCR increases only with addition of cusps and not with increase of cusp height. RFI and DNE increase with both addition of cusps and increase of cusp height. There is a difference between these metrics, however, in the degree to which they respond to interactions of cusp addition and increased cusp height. RFI increases at a linear rate when both cusp addition and cusp height are present, while DNE increases as a power function. This is likely due to increases in cusp height for multiple cusps resulting in curvature increases at multiple points across a surface mesh, and these multiple curving inflections having interaction effects on DNE. Previous models of topographic metrics have suggested that OPCR reflects tooth surface feature number and RFI and DNE reflect surface feature shape (Evans et al., 2007; Bunn et al., 2011; Winchester et al., 2014). Results here suggest a modification to this: that OPCR indeed reflects tooth surface feature number, that relatively RFI most strongly reflects surface feature shape, and relatively DNE most strongly reflects interactions between surface feature number and shape.

In addition to surface mesh data format affecting how topography is quantified, the procedure used to prepare or pre-process meshes has a significant effect on quantified topography (Boyer, 2008; Bunn et al., 2011). Mesh pre-processing steps considered here include surface cropping, simplification, smoothing, and alignment in 3D space. The sample of extant cercopithecoid M_2s mentioned above was used to test effects of these parameters on topographic values. To test cropping methods, sample M_2s were duplicated and variably cropped to include a) surface above the lowest point on the central occlusal basin, b) surface above the cervical margin, and c) surface above a point of infolding on the buccal enamel wall. For all topographic variables, occlusal-basin cropping captures more inter-species difference relative to intra-species difference than either of the other cropping treatments. Previous approaches have used occlusal basin cropping in small samples of closely related species in order to ensure similarity in preserved surface (Ungar and M'Kirera, 2003; M'Kirera and Ungar, 2003; Ungar and Bunn, 2008; Bunn and Ungar, 2009; Klukkert et al., 2012), while others have used cervical-margin cropping on broad samples of prosimians and platyrrhines because for these samples the similarity of occlusal basin cropping could not be ensured (Boyer, 2008; Bunn et al., 2011; Winchester et al., 2014). Results here from a broad sample of cercopithecoids can be interpreted to suggest that occlusal-basin cropping may be most effective at capturing relative inter-species difference where molar configurations between species are relatively similar (such as for bilophodont cercopithecoid M_2s) while cervical-margin cropping may be more effective for samples with highly variable molar configurations (such as strepsirrhine M_2s). One M_2 of *Theropithecus gelada* and one M_2 of *Cercocebus atys* were used to test simplification and smoothing by variably simplifying and

smoothing these M_2s. Results from these analyses are complicated, but it is clear that simplification and smoothing both substantially affect topographic variables, and that simplification and smoothing factors interact in how they affect topography. Nonetheless, it is possible to identify ranges of simplification and smoothing parameters in which changes in quantified topography are minimized. This range does include a common previously used mesh pre-processing protocol involving simplifying meshes to a 10,000 polygon target and carrying out 100 iterations of post-simplification smoothing in Amira/Avizo. These same M_2s were also variably rotated in space along X- and Y-axes, and topographic variables were measured throughout alignment. DNE is independent of alignment as expected, while RFI and OPCR change significantly. Within 5% rotation, however, change in both of these metrics is minimized, and this degree of difference is likely greater than would be experienced with either manual or algorithmic mesh alignment. There is also some evidence to suggest that relative tooth height between species may affect how RFI changes with rotation, and this is possibly connected to a recent observation of shape being related to more variable automatic alignment compared to manual alignment (Boyer et al., 2015b).

Results from analyses of surface mesh cropping, simplification, and smoothing suggest a primary take-home message: that the production of quantitative topographic data from anatomical specimens requires a process of abstraction, and that choices in data processing must be made in the context of sample specimens and research questions. Current imaging technology and software allows for highly accurate digital representations of anatomical surfaces, but these representations can not be perfectly accurate for a variety of reasons including noise and introduced artifacts. Given current

computing standards, efficient high-throughput morphometrics on consumer-level hardware typically requires some level of simplification of data, and this simplification has the benefit of addressing introduced noise or other non-biological surface information. The need to address artifactual noise and to process surfaces efficiently must be balanced against surface scan accuracy, and as a result there is no universally applicable ideal standard for mesh processing protocols or parameters. Rather, choices regarding the pathway from anatomical specimen to quantitative shape data are highly context dependent. It does seem for many samples that the previously used approach involving simplification to 10,000 polygons and 100 iterations of post-simplification smoothing will likely be adequate, but this is by no means guaranteed for all primate M_2s let alone other anatomical elements.

The goal of chapter three was to use the tools and information produced by chapter two to assess molar form function relationships in extant cercopithecoids in the context of allometry, tooth wear, and phylogeny. Morphological topographic analyses have been used to investigate relationships between molar shape and dietary food items in large samples of strepsirrhines and tarsiers (Boyer, 2008; Bunn et al., 2011), and platyrrhines (Winchester et al., 2014), but cercopithecoids have thus far only been investigated in relatively smaller groups (Ungar and Bunn, 2008; Bunn and Ungar, 2009; Kullmar, 2009; Guy et al., 2013; Guy et al., 2015). Some of these analyses have considered tooth wear (Ungar and Bunn, 2008; Bunn and Ungar, 2009; Winchester et al., 2012), but fewer have considered phylogenetic covariation (Boyer, 2008; Winchester et al., 2014) and none have assessed whether topographic variables scale allometrically.

A sample of 229 polygon surface meshes of M_2s belonging to 23 extant cercopithecoid species was used for these analyses, split into a primary sample of relatively less worn M_2s to investigate less worn primary M_2 morphology and a secondary sample of more variably worn M2s to investigate possible secondary M_2 morphology induced through wear. Species in this sample were sorted into one of four categories based on dietary food mechanical properties: hard object feeding, soft object feeding, moderately-tough object feeding, and extremely-tough object feeding. A sample of species means of mesiodistal tooth lengths was also collected from the literature (Swindler, 2002) in order to better assess allometric scaling. Before testing allometry, possible functional influences on 2D M_2 area were first examined. Standard statistical and phylogenetically-informed analyses suggested mixed evidence concerning whether 2D M_2 area was affected by dietary function as well as allometry, and so allometry was examined on a per-specimen level with 2D M_2 area and on a species-mean area with body mass data. Neither body size proxy was significantly associated with any topographic variables. This suggests that quantified molar topography does not scale allometrically, at least in extant cercopithecoids. This is interesting because certain molar surface features that contribute to topographic shape such as the cristid obliqua do scale negatively with metabolic rates in many primates (Kay, 1978). Topographic metrics measure emergent shape aspects that reflect shape properties arising from collections of surface features (Evans, 2013; Salazar-Ciudad and Marin-Riera, 2013), and it is possible that higher-order shape quantification such as this may not scale allometrically even when the features comprising molar surfaces do.

Given that topographic variables considered here do not seem to scale allometrically, it is possible to analyze differences between species, clades, dietary food material property categories without addressing allometry. Standard statistical and phylogenetically-informed analyses were used to investigate this. Results suggest that cercopithecoid M_2 topography varies between species in a way that reflects dietary food mechanical properties. Cercopithecoid M_2s vary most strongly by relief, which makes sense given the common bilophodont molar configuration of these teeth. Moderate and extremely-tough object feeders display increased relief corresponding to heightened cusps and crests relative to soft object feeders and durophages. These teeth also vary in curvature, with extremely-tough object feeders evincing M_2s with more curvature compared to moderately-tough object feeders, and both of those having more bent M_2 surfaces than soft object feeders and durophages. Extremely-tough object feeding here is represented only by the species *Theropithecus gelada*, which has an unusual diet consisting almost entirely of extremely fibrous and tough grass components and an equally unusual molar configuration among cercopithecoids, with high columnar cusps, fast rates of wear, and complex wear-induced enamel bands (Jolly, 1972; Venkataraman et al., 2014). The high curvature of *Theropithecus gelada* is likely a quantitative reflection of the unusual M_2 morphology of this species, and the specific profile of topographic variables for this species may represent a novel solution among cercopithecoids for consuming such a fibrous diet. Complexity is more complicated in cercopithecoids, with extremely-tough object feeders, soft object feeders and durophages all showing greater complexity than moderately-tough object feeders. An accurate estimate of phylogenetic signal could not be made for this sample, but when possible

phylogenetic covariation is maximized inter-species differences in complexity are no longer indicated as significant even though they remain significant for curvature and relief. This may indicate that differences in complexity are the result of phylogeny and not function, with the common ancestor of guenons and papionins possibly exhibiting a degree of M_2 complexity greater than that of the common ancestor of colobines.

An array of discriminant function analyses were carried out to determine which collection of variables most accurately predicts diet for individual specimens. The most accurate combination proved to be all topographic variables and 2D M_2 area, which is consistent with previous considerations of predictive dietary accuracy of topography excluding shearing quotients and ratios (Bunn et al., 2011; Winchester et al., 2014). This supports the idea that the three topographic metrics used here quantify different aspects of surface shape, and using them in combination increases their power (Bunn et al., 2011). It is curious that the highest predictive accuracy for this cercopithecoid sample using all topographic variables and M_2 area (67.8%) is lower than for a sample that combined platyrrhines, strepsirrhines, and tarsiers together (74.6%). There are a number of explanations for this. Analyses done here suggest minimal differentiation between hard object feeding and soft object feeding diet groups. Also extremely-tough object feeding *T. gelada* is most accurately distinguished from moderately-tough object feeding colobines only when DNE and M_2 size are weighted in an analysis, and the most overall successful all-variable analysis here downweights DNE and therefore does not distinguish these groups most accurately. For *T. gelada*, this again suggests this species exhibits unusually high M_2 curvature among cercopithecoids reflecting its unique morphological features in combination with very large body size. But the overall lack of

predictive accuracy – though still substantially greater than chance – probably most likely reflects the common bilophodont molar configuration shared by all extant cercopithecoids. This is compared to a range of molar configurations, including approaches toward bilophodonty, which are seen in strepsirrhines and platyrrhines. On a functional level, this may also suggest that the bilophodont cercopithecoid molar configuration is well suited for breaking down a wide variety of foods with varying mechanical properties. Observed topographic differences between species may reflect adjustments to reflect feeding specialization from an initially broadly capable bilophodont design, and these adjustments may be relatively subtle compared to at least some other primate radiations. This would be consistent with observations that cercopithecoid diets can vary significantly over time or between populations and geography (Chapman et al., 2002).

The previous analyses considered primary M_2 morphology; that is, differences in molar morphology of relatively less worn M_2s. It is also possible that the process of tooth wear is itself adapted to produce worn tooth morphologies that maintain or even improve tooth function across the wear process. This latter phenomenon has been demonstrated for ungulates (e.g., Fortelius, 1985) but is more difficult to assess in primates. Surface relief and curvature have been demonstrated to decrease through wear in some primates species, but surface angularity (a DEM-based metric, the derivative of average surface slope or the degree of change in surface slope across a surface) and complexity have been observed to not change through wear (M'Kirera and Ungar, 2003; Bunn and Ungar, 2009; Winchester et al., 2012). It should be said that surface angularity and complexity are likely to be positively correlated, given that the addition of cusps, cuspules, crests, or

other surface features will generally result in more change in slope across a tooth surface. Angularity is more easily measured from DEM data, given that it needs a plane from which to define slope and DEM heightmaps provide a definite reference plane and regular XY-coordinate grids from which to measure equivalent amounts of slope across a surface. But complexity can be measured from a polygon mesh, and so complexity was tested here.

Instead of wear scores or actual ages as have been used in previous studies, these analyses used intra-species RFI as a wear proxy. This is because previous studies of topographic variables through wear have consistently indicated that relief within species decreases in more worn M_2s (M'Kirera and Ungar, 2003; Dennis et al., 2004; King et al., 2005; Bunn and Ungar, 2009; Winchester et al., 2012). Inter-species RFI is here considered to reflect differences in molar relief resulting either from species-level or idiosyncratic differences in primary unworn morphology or secondary differences introduced through wear, but intra-species RFI of highly variably worn teeth is assumed to reflect modifications to M_2 morphology introduced by wear in addition to idiosyncratic variation. Using intra-species RFI as a wear proxy, there is evidence here to suggest that complexity has a negative relationship with wear. In other words, as relief decreases through the process of wear, complexity seems to increase. The strongest evidence for this is in *T. gelada*, which makes sense given previous qualitative interpretations of complex wear-induced enamel bands in this species serving as compensatory features for grass consumption, similar to ungulates (Jolly, 1972; Meikle, 1977; Swindler, 1983; Jablonski, 1993, 1994; Swindler and Beynon, 1993). It should be said that results here are different from previous considerations of angularity and complexity with regard to wear,

in that those studies found a lack of relationship between angularity and complexity with wear while results here suggest a negative relationship. This could reflect a compensatory balance where relief is decreased through wear as complexity increases, permitting some degree of maintenance of tooth function.

While most considerations of molar topography to date have been functional in nature similar to chapter three, chapter four assessed cercopithecoid molar shape to test predictions from models of molar morphogenesis. The last several decades have seen a sharp increase in our knowledge concerning the embryonic developmental processes that organize and produce morphology (Jernvall et al., 1994; Jernvall, 1995; Thesleff and Sahlberg, 1996; Jernvall et al., 1998; Jernvall, 2000; Jernvall and Selänne, 1999; Jernvall and Thesleff, 2000a,b, 2012; Thesleff et al., 2001; Kavanagh et al., 2007). Molar teeth, especially in mice, have provided an excellent model system for these experiments and resulting from this, predictive models of certain aspects of mouse molar morphogenesis have been developed. The inhibitory cascade model suggests that initiation and growth of molars in a molar row are initiated by a non-proliferative signaling center known as a primary enamel knot, which expresses proteins to both encourage and inhibit the development of subsequent enamel knots denoting later-developing molars (Thesleff et al., 2001; Kavanagh et al., 2007). The strength and dispersion of activators and inhibitors released by enamel knots and surrounding tissues allow a first molar to determine the spacing and relative size of subsequent molars, and with certain assumptions concerning the balance of these factors it is possible to develop predictions of relative molar size (Kavanagh et al., 2007). Also, because later-developing molars are affected by more developmental events and possible perturbations than earlier-developing molars because

of cascading morphogenetic processes, this model suggests that later-developing posterior molars should be more variable in form for embryological reasons (Jernvall et al., 1994; Jernvall, 1995; Polly, 1998; Jernvall, 2000). Molar cusps develop in a similar cascading fashion, with primary enamel knots in mice giving rise to secondary enamel knots denoting the presence of mesial protoconid and metaconid cusps (Jernvall and Thesleff, 2000a). These secondary enamel knots also release inhibitor and activator proteins that space the development of more distal later developing cusps. Following from this, it can be predicted that later-developing cusps should be more variable in form than earlier-developing cusps, and the form of earlier-developing cusps should affect the positioning of later-developing cusps (Polly, 1998; Jernvall, 2000). This chapter tested these predictions for cercopithecoid M_2s, using samples of mesiodistal tooth lengths collected from the literature, surface meshes of associated $M_{1\text{-}3}$ toothrows for examining inter-molar shape variability, and surface meshes of isolated M_3s for examining intra-molar cusp position variability.

Assuming that molar size is produced by a cascading series of inhibitor and activator proteins released by primary enamel knots, it can be predicted that a ratio of M_3 size over M_1 size regression on M_2 size over M_1 size (i.e., relative M_3 size regressed on relative M_1 size) should most often result in a linear regression with a slope of 2.0 and an intercept of -1.0 (Kavanagh et al., 2007). Colobine and papionins regressions are consistent with this prediction, which is consistent with the only other consideration of cercopithecoid inhibitory cascades thus far published (Schroer and Wood, 2015). But this prediction lies outside 95% confidence intervals for a cercopithecin regression, suggesting that this prediction does not hold for guenons. Guenons have a molar size

ratio where M_1s are smaller than or similar in size to M_2s, and M_3s are smaller than M_2s. Kavanagh et al. (2007) suggested that this size pattern may be generated via an inhibitor/activator balance marked by greater activation (causing $M_1 < M_2$) combined with an earlier termination of morphogenesis (causing $M_2 > M_3$). This is interpreted to be the cause of cercopithecins not fitting predictions here, especially given that cercopithecins lack M_3 hypoconulids where colobines and papionins possess visibly present hypoconulids. Under this molar morphogenesis model, M_3 hypoconulids should result from sufficiently high levels of activator proteins combined with enough space on a developing molar tooth and enough time for activator proteins from previous secondary enamel knots to initiate a secondary enamel knot denoting a hypoconulid. Both colobines and papionins should also have an inhibitor/activator balance marked by high levels of activation, given that the molar size pattern in these clades is $M_1 < M_2 < M_3$. A modification to the timing of the termination of molar morphogenesis could represent a developmental method by which to achieve the lack of an M_3 hypoconulid in guenons.

The prediction that later-developing molars are more variable in shape was tested by both topographic variables and a geometric morphometric algorithm for automated landmark placement (*auto3dgm*, Boyer et al., 2015a). This is because topographic variables, being quantifiers of emergent aspects of surface shape, may not actually be as capable as geometric morphometric shape specifier methods at diagnosing variability in the components that comprise topographic shape. And in fact, GM landmark analyses showed evidence for M_3s being significantly more variable in shape (and shape and size together) compared to M_1s and M_2s, while no significant differences were observed for topographic variables. A similar result was found for analyses of intra-molar cusp

variability, with topography of mesial and distal portions not different in variability while cusp-tip landmark analyses found evidence for more distal cusps being more variable both within and between species. This means that not only are more distal cusps more variably placed in the species considered here, but morphological differences in cusp position between species are more likely to be encountered in more distal later developing cusps. These results have bearing on microevolutionary and macroevolutionary scales, respectively, and the macroevolutionary results can be compared to Hunter and Jernvall's (1995) observation of repeated convergent evolution of the hypocone in mammals. These analyses also provide an interesting comparison of the relative abilities of shape descriptor and shape specifier methods. Multiple possible morphological configurations could theoretically give rise to a single given DNE, RFI, or OPCR value while it would be much more difficult for multiple morphological configurations to give rise to a similar set of landmarks for GM analyses. This also demonstrates the value of applying topographic techniques to non-functional questions, because it can increase understanding of how morphological topographic analysis reflects shape diversity. Cusp position relationships are also explored in this chapter, and there is some evidence to suggest that hypoconulid prominence may be negatively related to constriction of posterior cusps relative to constriction of anterior cusps, but more work is needed on this topic.

The results obtained from this dissertation provide numerous opportunities for further work. The open source expandable nature of MorphoTester means that this software can be adapted in order to apply possible new topographic algorithms or to address unforeseen needs. Consideration of the effects of pre-processing parameters on

quantified topography should provide some guidance for future work on how differences in mesh pre-processing may affect topographic variables. Future work could further consider how changes in mesh pre-processing will affect quantified topographic differences along functional lines – in other words, for species with different diets and molar shape, how does mesh processing affect differences in quantified topography? In conjunction with this, more consideration of how pre-processing affects molars with small-scale features, such as enamel crenulations, would be valuable. It is possible that the most common simplification target of 10,000 triangles may obscure or eliminate some subtler features on surface meshes. The extant cercopithecoid topographic sample provides a comparative dataset against which to compare fossil cercopithecoids in order to infer paleoecology. Additionally, these results suggest that further studies should consider allometry and tooth wear more actively. Considering allometry will likely confirm whether or not the seeming independence of topographic variables from allometry observed here is the case for other primate radiations. Considering tooth wear more directly, likely with a better quantitative accounting for wear state, will allow testing of the observation here that complexity seems to increase as relief decreases in cercopithecoid M_2s. And finally, results from analyses of developmental patterning suggest the need for a much broader developmental consideration of molar shape and cusp position in cercopithecoids and other primates. Inter- and intra-molar shape variability analyses here used only four species because of the time necessary to carry out shape quantification, but as techniques improve it should be possible to increase sample sizes greatly and carry out a more systematic survey of whether and how cercopithecoids conform to empirical models of molar morphogenesis.

This dissertation provides new tools for morphological topographic analysis, increases our knowledge of how to use these methods, and applies topographic techniques to questions of cercopithecoid molar form-function relationships and evolutionary-developmental patterning. Chapter two provides new software and the most thorough consideration of the production of surface mesh data for topographic analysis published to date. Chapter three investigates M_2 topography of a broad sample of extant cercopithecoids, and constitutes a large extant sample of comparative data similar to that previously published for strepsirrhines and tarsiers (Boyer, 2008; Bunn et al., 2011) or platyrrhines (Winchester et al., 2014). Moreover, this analysis represents the most directly functional consideration of dietary food mechanical properties as part of a topographic analysis. It also addresses factors that influence dental topography and molar function such as allometry, tooth wear, and phylogeny. Chapter four applies topographic metrics to an entirely new question, that of developmental patterning, and suggests that cercopithecoids generally seem to conform to empirical mouse models of molar development but that at the same time there is variation within cercopithecoids and developmental patterns may possibly be affected by body size or other factors. This chapter also provides a comparison between topographic and geometric techniques of shape quantification. Considered in total, this dissertation supports and extends the idea that high-throughput techniques of shape quantification in general, and morphological topographic analysis in particular, represent a powerful new approach for gaining a better understanding of morphology in many contexts.

References

Adams DC, Rohlf FJ, Slice DE. 2004. Geometric morphometrics: ten years of progress following the 'revolution.' Ital J Zool 71:5-16.

Allen KL, Cooke SB, Gonzales LA, Kay RF. 2015. Dietary Inference from Upper and Lower Molar Morphology in Platyrrhine Primates. PLoS ONE 10:e0118732.

Andrews P, Aiello L. 1984. An evolutionary model for feeding and positional behavior. In: Chivers DJ, Wood BA, Bilsborough A, editors. Food Acquisition and Processing in Primates. New York: Plenum Press. p. 422–460.

Anthony RL, Kay RF. 1993. Tooth form and diet in ateline and alouattine primates: reflections on the comparative method. Am J Sci 293A:356–382

Aristotle. 1965. The History of Animals. Peck AL, editor. New York: Loeb Classical Library.

Arnold C, Matthews LJ, Nunn CL. 2010. The 10kTrees website: a new online resource for primate phylogeny. Evol Anthropol 19:114-118.

Asahara M. 2013. Unique inhibitory cascade pattern of molars in canids contributing to their potential to evolutionary plasticity of diet. Ecol Evol 3:278-285.

Beeson M, Tame S, Keeming E, Lea SEG. 1996. Food habits of guenons (*Cercopithecus spp.*) in Afro-montane forest. Afr J Ecol 34:202-210.

Benefit BR. 1987. The molar morphology, natural history, and phylogenetic position of the middle Miocene monkey Victoriapithecus. Ph.D. dissertation, New York University.

Benefit BR. 1993. The permanent dentition and phylogenetic position of *Victoriapithecus* from Maboko Island, Kenya. J Hum Evol 25:83–172.

Benefit BR. 2006. Old World monkey origins and diversification: an evolutionary study of diet and dentition. In: Whitehead PF, Jolly CJ, editors. Old World Monkeys. New York: Cambridge University Press. p 133–179.

Benefit BR, McCrossin ML. 1990. Diet, species diversity and distribution of African fossil baboons. Kroeber Anthropol Soc Papers 71/72:77–93.

Benefit BR, McCrossin ML. 2008. The Victoriapithecidae, Cercopithecoidea. In: Hartwig WC, editor. The Primate Fossil Record. Cambridge: Cambridge University Press. p. 241-254.

Bennett EL, Sebastian AC. 1988. Social organization and ecology of proboscis monkeys (*Nasalis larvatus*) in mixed coastal forest in Sarawak. Int J Primatol 9:233-255.

Bernal V, Gonzalez PN, Perez SI. 2013. Developmental processes, evolvability, and dental diversification of New World Monkeys. Evol Biol 40:532-541.

Bolter DR. 2011. A comparative study of growth patterns in crested langurs and vervet monkeys. Anat Res Int article ID 948671. p. 1-12.

Bose AK, Blackwell RQ, Fosdick LS. 1960. The fractionation of human tooth enamel on the basis of density. J Dent Res 39:141-149.

Boyer DM. 2008. Relief index of second mandibular molars is a correlate of diet among prosimian primates and other euarchontan mammals. J Hum Evol 55:1118–1137.

Boyer DM, Evans AR, Jernvall J. 2010. Evidence of dietary differentiation among late Paleocene-early Eocene plesiadapids (Mammalia, primates). Am J Phys Anthropol 142:194–210.

Boyer DM, Kaufman S, Gunnell GF, Rosenberger AL, Delson E. 2014. Managing 3D digital data sets of morphology: MorphoSource is a new project-based data archiving and distribution tool. Am J Phys Anthropol 153:85.

Boyer DM, Puente J, Gladman JT, Glynn C, Mukherjee S, Yapuncich GS, Daubechies I. 2015a. A new fully automated approach for aligning and comparing shapes. Anat Rec 298:249-276.

Boyer DM, Winchester J, Glynn C, Puente J. 2015b. Detailed anatomical orientations for certain types of morphometric measurements can be determined automatically with geometric algorithms. Anat Rec: 298:1816-1823.

Bunn JM, Ungar PS. 2009. Dental topography and diets of four old world monkey species. Am J Primatol 71:466–477.

Bunn JM, Boyer DM, Lipman Y, St. Clair EM, Jernvall J, Daubechies I. 2011. Comparing Dirichlet normal surface energy of tooth crowns, a new technique of molar shape quantification for dietary inference, with previous methods in isolation and in combination. Am J Phys Anthropol 145:247–261.

Butler PM. 1956. The ontogeny of molar patterns. Biol Rev 31:30-70.

Butynski TM. 1990. Comparative ecology of blue monkeys (*Cercopithecus mitis*) in high and low density subpopulations. Ecol Monogr: 1-26.

Buzzard PJ. 2006. Ranging patterns in relation to seasonality and frugivory among *Cercopithecus campbelli*, *C. petaurista*, and *C. diana* in the Tai forest. Int J Primatol 27:559-573.

Caldecott JO, Feistner ATC, Gadsby EL. 1996. A comparison of ecological strategies of pig-tailed macaques, mandrills and drills. In: Fa JE, Lindburg DG, editors. Evolution and Ecology of Macaque Societies. Cambridge: Cambridge University Press. p. 73-94.

Chalmers NR. 1968. Group composition, ecology, and daily activities of free living mangabeys in Uganda. Fol Primatol 8:247-262.

Chapman CA, Chapman LJ, Cords M, Gathua JM, Gautier-Hion A, Lambert JE, Rode K, Tutin CEG, White JLT. Variation in the diets of *Cercopithecus* species: differences within forests, among forests, and across species. In: Glenn ME, Cords M, editors. The Guenons: Diversity and Adaptation in African Monkeys. New York: Kluwer Academic Publishers. p. 325-350.

Chester SGB, Bloch JI, Secord R, Boyer DM. A small bodied species of Palaeonictis (Creodonta, Oxyaenidae) from the Paleocene-Eocene thermal maximum. J Mamm Evol 17:227-243.

Christopher RA, Waters JA. 1974. Fourier series as a quantitative descriptor of miospore shape. J Paleontol 48:697-709.

Cook DC, Buikstra JE. 1979. Health and differential survival in prehistoric populations: prenatal dental defects. Am J Phys Anthropol 51:649-664.

Coin R, Lesot H, Vonesch JL, Haikel Y, Ruch JV. 1999. Aspects of cell proliferation kinetics of the inner dental epithelium during mouse molar and incisor morphogenesis: a reappraisal of the role of the enamel knot area. Int J Dev Biol 43:261–269.

Cope DA. 1993. Measures of dental variation as indicators of multiple taxa in samples of sympatric *Cercopithecus* species. In: Kimbel WH, Martin LB, editors. Species, Species Concepts, and Primate Evolution. New York: Plenum Press. p. 211-237.

Cope ED. 1883. On the trituberculate type of molar tooth in the Mammalia. Pal Bull No 37 Proc Amer Philos Soc 21:324–326.

Cords M. 1986. Interspecific and intraspecific variation in diet of two forest guenons, *Cercopithecus ascanius* and *C. mitis*. J Anim Ecol 55: 811-827.

Corruccini RS. 1979. Molar cusp-size variability in relation to odontogenesis in hominoid primates. Arch Oral Biol 24_633-634.

Covert HH. 1986. Biology of early Cenozoic primates. In: Swindler DR, Erwin J, editors. Comparative primate biology, Volume 1: systematics, evolution and anatomy. New York: Alan R. Liss. p 335–359.

Crompton AW, Sita-Lumsden AG. 1970. Functional significance of therian molar pattern. Nature 227:197–199.

Curtin SH. 1980. Dusky and Banded Leaf Monkeys. In: Chivers DJ. Malayan Forest Primates: Ten Years' Study in Tropical Rain Forest. New York: Springer. p. 107-146.

Cuvier G. 1963. The Animal Kingdom. London: Bohn.

Daegling DJ, McGraw WS, Ungar PS, Pampush JD, Vick AE, Bitty EA. 2011. Hard-object feeding in sooty mangabeys (*Cercoebus atys*) and interpretations of early hominin feeding ecology. PLoS ONE 6:e23095.

Davenport TR, Stanley WT, Sargis EJ, De Luca DW, Mpunga NE, Machaga SJ, Olson LE. 2006. A new genus of African monkey, *Rungwecebus*: morphology, ecology, and molecular phylogenetics. Science 312:1378-1381.

Davies AG, Oates JF, Dasilva GL. 1999. Patterns of frugivory in three West African colobine monkeys. Int J Primatol 20:327-357.

Dennis JC, Ungar PS, Teaford MF, Glander KE. 2004. Dental topography and molar wear in *Alouatta palliata* from Costa Rica. Am J Phys Anthropol 125:152–161.

Delson E. 1975. Evolutionary history of the Cercopithecidae. In: Szalay FS, editor. Contributions to primatology, Volume 5: approaches to primate paleobiology. Basel: S. Karger. p 167– 217.

Desbrun M, Meyer M, Schroder P, Barr AH. 1999. Implicit fairing of irregular meshes using diffusion and curvature flow. SIGGRAPH 99.

Disotell TR. 2000. The molecular systematics of the Cercopithecidae. In: Whitehead PF, Jolly CJ, editors. Old World Monkeys. Cambridge: Cambridge University Press. p. 29-56.

Duc HM, Baxter GS, Page MJ. 2009. Diet of *Pygathrix nigripes* in Southern Vietnam. Int J Primatol 30:15-28.

Dunbar RIM. 1977. Feeding ecology of gelada baboons: a preliminary report. In: Clutton-Brock TH, editor. Primate Ecology: Studies of Feeding and Ranging Behaviour in Lemurs, Monkeys, and Apes. London: Academic Press. p. 251-75.

Dunbar RIM, Dunbar EP. 1974. Ecological relations and niche separation between sympatric terrestrial primates in Ethiopia. Fol Primatol 21:36-60.

Evans AR. 2005. Connecting morphology, function, and tooth wear in microchiropterans. Biol J Linn Soc 85: 81-96.

Evans AR. 2013. Shape descriptors as ecometrics in dental ecology. Hystrix 24:133-140.

Evans AR, Janis CM. 2014. The evolution of high dental complexity in the horse lineage. Ann Zool Fennici 51:73-79.

Evans AR, Jernvall J. 2009. Patterns and constraints in carnivoran and rodent dental complexity and tooth size. J Vert Paleo 29:24A.

Evans AR, Harper IS, Sanson GD. 2001. Confocal imaging, visualization and 3-D surface measurement of small mammalian teeth. J Micros 204: 108–119.

Evans AR, Wilson GP, Fortelius M, Jernvall J. 2007. High-level similarity of dentitions in carnivorans and rodents. Nature 445:78–81.

Evans AR, Daly ES, Catlett KS, Paul KS, King SJ, Skinner MM, Nesse HP, Hublin JJ, Townsend GC, Schwartz GT, Jernvall J. 2016. A simple rule governs the evolution and development of hominin tooth size. Nature 530:477-480.

Fashing PJ. 2001. Feeding ecology of guerezas in the Kakamega Forest, Kenya: the importance of Moraceae fruit in their diet. Int J Primatol 22:579-609.

Fashing PJ. 2007. African colobine monkeys. In: Campbell C, Fuentes A, MacKinnon KC, Bearder SK, Stumpf RM, editors. Primates in Perspective. Oxford: Oxford University Press. p. 201-224.

Fashing PJ, Dierenfeld ES, Mowry CB. 2007. Influence of plant and soil chemistry on food selection, ranging patterns, and biomass of *Colobus guereza* in Kakamega Forest, Kenya. Int J Primatol 28:673-703.

Felsenstein J. 1985. Confidence limits on phylogenies: an approach using the bootstrap. Evolution 39:783-791.

Fleagle JG, Kay RF, Anthony MRL. 1997. Fossil new world monkeys. In: Kay RF, Madden RH, Cifelli RL, Flynn JJ, editors. Vertebrate paleontology in the Neotropics. Washington D.C.: Smithsonian Institution. p 473–495.

Fortelius M. 1985. Ungulate cheek teeth: developmental, functional, and evolutionary interrelations. Acta Zool Fenn 180:1-76.

Freckleton RP, Harvey PH, Pagel M. 2002. Phylogenetic analysis and comparative data: a test and review of evidence. Am Nat 160:712-726.

Funkhouser T, Min P, Kazhdan M, Chen J, Halderman A, Dobkin D. 2003. A search engine for 3D models. ACM T Graphic 22:83-105.

Gautier-Hion A. 1988. The diet and dietary habits of forest guenons. In: Gautier-Hion A, Bourliere F, Gautier JP, Kingdon J, editors. A Primate Radiation. Evolutionary Biology of the African Guenons. Cambridge: Cambridge University Press. p. 257-283.

Gautier-Hion A, Gautier JP, Moungazi A. 1997. Do black Colobus in mixed-species groups benefit from increased foraging efficiency? C R Acad Sci Paris 320:67-71.

Gerhart J, Kirschner M. 1997 Cells, embryos, and evolution. New York: Blackwell.

Gilbert CC. 2005. Dietary ecospace and the diversity of euprimates during the early and middle Miocene. Am J Phys Anthropol 126:237-249.

Gingerich PD. 1974. Size variability of the teeth in living mammals and the diagnosis of closely related sympatric fossil species. J Paleontol 48:895-903.

Gingerich PD, Ryan AS. 1979. Dental and cranial variation in living Indriidae. Primates 20:141-159.

Gingerich PD, Schoeninger MJ. 1979. Patterns of tooth size variability in the dentition of primates. Am J Phys Anthropol 51:457-466.

Gingerich PD, Smith BH. 1985. Allometric scaling in the dentition of primates and insectivores. In: Jungers WL, editor. Size and Scaling in Primate Biology. New York: Plenum Press. p. 257-272.

Gingerich PD, Winkler DA. 1979. Patterns of variation and correlation in the dentition of the fox, *Vulpes vulpes*. J Mammal 60:691-704.

Godfrey LR, Samonds KE, Jungers WL, Sutherland MR. 2001. Teeth, brains, and primate life histories. Am J Phys Anthropol 114:192-214.

Godfrey LR, Winchester JM, King SJ, Boyer DM, Jernvall J. 2012. Dental topography indicates ecological contraction of lemur communities. Am J Phys Anthropol 148:215-227.

Gould SJ, Garwood RA. 1969. Levels of integration in mammalian dentitions: an analysis of correlations in *Nesophontes micrus* (Insectivora) and *Oryzomys couesi* (Rodentia). Evolution 23:276-300.

Gregory WK. 1922. The Origin and Evolution of the Human Dentition. Baltimore: Williams and Wilkins. 548p.

Grine FE. 1986. Dental evidence for dietary differences in *Australopithecus* and *Paranthropus*: a quantitative analysis of permanent molar microwear. J Hum Evol 15:783-822.

Grine FE, editor. 1988. Evolutionary History of "Robust" Australopithecines. New York: de Gruyter.

Grueter CC, Li D, Ren B, Wei F, Xiang Z, van Schaik CP. 2009. Fallback foods of temperate-living primates: a case study on snub-nosed monkeys. Am J Phys Anthropol 140:700-715.

Guy F, Gouvard F, Boistel R, Euriat A, Lazzari V. 2013. Prospective in (primate) dental analysis through tooth 3D topographical quantification. PLoS ONE 8(6):e66142.

Guy F, Lazzari V, Gilissen E, Thiery G. 2015. To what extent is primate second molar enamel occlusal morphology shaped by the enamel-dentine junction? PLoS ONE 10(9): e0138802.

Halliday TJD, Goswami A. 2013. Testing the inhibitory cascade model in Mesozoic and Cenozoic mammaliforms. BMC Evol Biol 13:79.

Hanya G, Menard N, Qarro M, Ibn Tattou M, Fuse M, Vallet D, Yamada A, Go M, Hino T, Tsujino R, Agetsuma N, Wada K. 2011. Dietary adaptations of temperate primates: comparisons of Japanese and Barbary macaques. J Primatol 52:187-198.

Harjunmaa E, Kallonen A, Voutilainen M, Hamalainen K, Mikkola ML, Jernvall J. 2012. On the difficulty of increasing dental complexity. Nature 483(7389):324-327.

Harvey PH, Clutton-Brock TH. 1985. Life history variation in primates. Evolution 39: 559-581.

Hayssen V, Lacy RC. 1985. Basal metabolic rates in mammals: taxonomic differences in the allometry of BMR and body mass. Comp Biochem Physiol 81A:741-754.

Hladik CM. 1977. A comparative study of feeding strategies of two sympatric species of leaf monkeys: *Presbytis senex* and *Presbytis entellus*. In: Clutton Brock TH, editor. Primate Ecology. London: Academic Press. p. 323-353.

Hoshino J. 1985. Feeding ecology of mandrills (*Mandrillus sphinx*) in Campo animal reserve, Cameroon. Primates 26:248-273.

Hunter CP. 2001. Ecological determinants of gelada ranging patterns (*Theropithecus gelada*). Ph.D. dissertation, University of Liverpool.

Hunter JD. 2007. Matplotlib: A 2D graphics environment. Comput Sci Eng 9:90–95.

Hunter JP, Jernvall J. 1995. The hypocone as a key innovation in mammalian evolution. Proc Natl Acad Sci USA 92:10718–10722.

Hunter JP, Guatelli-Steinberg D, Weston TC, Durner R, Betsinger TK. 2010. Model of tooth morphogenesis predicts carabelli cusp expression, size, and symmetry in humans. PLoS ONE 5(7): e11844.

Isbell LA, Pruetz JD, Young TP. Movements of vervets (*Cercopithecus aethiops*) and patas monkeys (*Erythrocebus patas*) as estimators of food resource size, density, and distribution. Beh Ecol Sociobiol 42:123-133.

Iwamoto T. 1979. Ecological and sociological studies of gelada baboons. Feeding ecology. Contrib Primatol 16:279-330.

Jablonski NG. 1993. Evolution of the masticatory apparatus in *Theropithecus*. In: Jablonski NG, editor. *Theropithecus*: The Rise and Fall of a Primate Genus. Cambridge: Cambridge University Press. p. 209-224.

Jablonski NG. 1994. Convergent evolution in the dentition of grazing Macropodine marsupials and the grass-eating Cercopithecine primate *Theropithecus gelada*. J R Soc West Aust 77:37-43.

Jablonski NG, Frost S. 2010. Cercopithecoidea. In: Werdelin L, Sanders WJ, editors. Cenozoic mammals of Africa. Berkeley and London: Univ. of California Press. p. 393-428.

Jernvall J. 1995. Mammalian molar cusp patterns: developmental mechanism of diversity. Acta Zool Fenn 198:1-61.

Jernvall J. 2000. Linking development with generation of novelty in mammalian teeth. Proc Natl Acad Sci USA 97:2641–2645.

Jernvall J, Jung HS. 2000. Genotype, phenotype, and developmental biology of molar tooth characters. Yearb Phys Anthropol 43:171-190.

Jernvall J, Selänne L. 1999. Laser confocal microscopy and geographic information systems in the study of dental morphology. Paleontologica Electronica 2: 18.

Jernvall J, Thesleff I. 2000a. Return of lost structure in the developmental control of tooth shape. In: Teaford MF, Smith MM, Ferguson MWJ, editors. Development, function, and evolution of teeth. Cambridge: Cambridge University Press. p 13–21.

Jernvall J, Thesleff I. 2000b. Reiterative signaling and patterning during mammalian tooth morphogenesis. Mech Dev 92:19–29.

Jernvall J, Thesleff I. 2012. Tooth shape formation and tooth renewal: evolving with the same signals. Development 139:3487-3497.

Jernvall J, Kettunen P, Karavanova I, Martin LB, Thesleff I. 1994. Evidence for the role of the enamel knot as a control center in mammalian tooth cusp formation: non-dividing cells express growth stimulating Fgf-4 gene. Int J Dev Biol 38:463–469.

Jernvall J, Hunter JP, Fortelius M. 1996. Molar tooth diversity, disparity, and ecology in

Cenozoic ungulate radiations. Science 274:1489–1492.

Jernvall J, Åberg T, Kettunen P, Keränen S, Thesleff I. 1998. The life history of an embryonic signaling center: BMP-4 induces *p21* and is associated with apoptosis in the mouse tooth enamel knot. Development 125:161-169.

Jernvall J, Keränen SVE, Thesleff I. 2000. Evolutionary modification of development in mammalian teeth: quantifying gene expression patterns and topography. Proc Nat Acad Sci USA 97:14444-14448.

Jolly CJ. 1970. The large African monkeys as an adaptive array. In: Napier JR, Napier PH, editors. Old World Monkeys: Evolution, Systematics and Behavior. New York: Academic Press. p. 141–174.

Jolly CJ. 1972. The classification and natural history of *Theropithecus* (*Simopithecus*) (Andrews, 1916) baboons of the African Plio-Pleistocene. Bull Br Mus Nat Hist (Geol) 22:1-123.

Kaplin BA. 2001. Ranging behavior of two species of guenons (*Cercopithecus l'hoesti* and *C. mitis doggetti*) in the Nyungwe Forest Reserve, Rwanda. Int J Primatol 22:521-548.

Kaplin BA, Moermond TC. 2000. Foraging ecology of the mountain monkey (*Cercopithecus l'hoesti*): implications for its evolutionary history and use of disturbed forest. Am J Primatol 50:227-246.

Kar-Gupta K, Kumar A. 1994. Leaf chemistry and food selection by common langurs (*Presbytis entellus*) in Rajaji National Park, Uttar Pradesh, India. Int J Primatol 15:75-93.

Kassai Y, Munne P, Hotta Y, Penttilä E, Kavanagh K, Ohbayashi N, Takada S, Thesleff I, Jernvall J, Itoh N. 2005. Regulation of mammalian tooth cusp patterning by ectodin. Science 309:2067-2070.

Kavanagh KD, Evans AR, Jernvall J. 2007. Predicting evolutionary patterns of mammalian teeth from development. Nature 449:427-432.

Kay RF. 1975. The functional adaptations of primate molar teeth. Am J Phys Anthropol 43:195–216.

Kay RF. 1977. Evolution of molar occlusion in Cercopithecidae and early catarrhines. Am J Phys Anthropol 46:327–352.

Kay RF. 1978. Molar structure and diet in extant Cercopithecidae. In: Butler P, editor. Development, function, and evolution of teeth. London: Academic Press. p 309–339.

Kay RF. 1981. The nut-crackers – a new theory of the adaptations of the Ramapithecinae.

Am J Phys Anthropol 55:141-151.

Kay RF. 1984. On the use of anatomical features to infer foraging behavior in extinct primates. In: Rodman PS, Cant JGH, editors. Adaptations for foraging in nonhuman primates. New York: Columbia University Press. p 21–53.

Kay RF, Covert HH. 1984. Anatomy and behavior of extinct primates. In: Chivers DJ, Wood BA, Bilsborough A, editors. Food acquisition and processing in primates. New York: Plenum Press. p 467–508.

Kay RF, Hylander WL. 1978. The dental structure of mammalian folivores with special reference to Primates and Phalangeroidea (Marsupialia). In: Montgomery GG, editor. The Biology of Arboreal Folivores. Washington, D.C.: Smithsonian Institution Press. p. 173-191.

Kay RF, Hiemae KM. 1974. Jaw movement and tooth use in recent and fossil primates. Am J Phys Anthropol 40:227–256.

Kay RF, Ungar PS. 1997. Dental evidence for diet in some Miocene catarrhines with comments on the effects of phylogeny on the interpretation of adaptation. In: Begun DR, Ward C, Rose M, editors. Function, phylogeny, and fossils: hominoid evolution and adaptations. New York: Plenum Press. p 131–151.

King SJ, Arrigo-Nelson SJ, Pochron ST, Semprebon GM, Godfrey LR, Wright PC, Jernvall J. 2005. Dental senescence in a long-lived primate links infant survival to rainfall. Proc Natl Acad Sci USA 102:16579–16583.

Kinzey WG. 1978. Feeding behavior and molar features in two species of titi monkey. In: Chivers DJ, Herbert J, editors. Recent advances in primatology, Volume 1: behavior. New York: Academic Press. p 373–385.

Kirk EC, Simons EL. 2001. Diets of fossil primates from the Fayum Depression of Egypt: a quantitative analysis of molar shearing. J Hum Evol 40:203–229.

Kleiber M. 1961. The Fire of Life. New York: Wiley.

Klukkert ZS, Teaford MF, Ungar PS. 2012a. A dental topographic analysis of chimpanzees. Am J Phys Anthropol 148:276–284.

Klukkert ZS, Dennis JC, M'Kirera F, Ungar PS. 2012b. Dental topographic analysis of the molar teeth of primates. Methods Mol Biol 915:145–152.

Kullmer OT, Benazzi S, Fiorenza L, Schulz D, Bacso S, Winzen O. 2009. Technical note: occlusal fingerprint analysis: quantification of tooth wear pattern. Am J Phys Anthropol 139:600-605.

Kraus BS, Jordan RE. 1965. The Human Dentition Before Birth. Philadelphia: Lea and Febiger.

Lahm SA. 1986. Diet and habitat preference of *Mandrillus sphinx* in Gabon: implications of foraging strategy. Am J Primatol 11:9-26.

Lambert JE. 2002. Digestive retention times in forest guenons (*Cercopithecus spp.*) with reference to chimpanzees (*Pan troglodytes*). Int J Primatol 23:1169-1185.

Lambert JE, Chapman CA, Wrangham RW, Conklin-Brittain NL. 2004. Hardness of cercopithecine foods: implications for the critical function of enamel thickness in exploiting fallback foods. Am J Phys Anthropol 125: 363-368.

Lawes MJ. 1991. Diet of samango monkeys (*Cercopithecus mitis erythrarchus*) in the Cape Vidal dune forest, South Africa. J Zool 224:149-173.

Lawes MJ, Henzi SP, Perrin MR. Diet and feeding behaviour of samango monkeys (*Cercopithecus mitis labiatus*) in Ngoye forest, South Africa. Fol Primatol 54:57-69.

Lawing AM, Polly PD. 2010. Geometric morphometrics: recent applications to the study of evolution and development. J Zool 280:1-7.

Ledogar JA, Winchester JM, St. Clair EM, Boyer DM. 2013. Diet and dental topography in pitheciine seed predators. Am J Phys Anthropol 150:107-121.

Li Y. 2006. Seasonal variation of diet and food availability in a group of Sichuan snub-nosed monkeys in Shennongia Nature Reserve, China. Am J Primatol 68:217-233.

Lucas PW. 2004. Dental Functional Morphology: How Teeth Work. Cambridge: Cambridge University Press.

Lucas PW, Teaford MF. 1994. Functional morphology of colobine teeth. In: Davies AG, Oates JF, editors. Colobine Monkeys: Their Ecology, Behaviour and Evolution. Cambridge: Cambridge University Press. p. 173-203.

Lucas PW, Corlett RT, Luke DA. 1986. Postcanine tooth size and diet in anthropoid primates. Z Morphol Anthropol 76:253-276.

Lucas PW, Beta T, Darvell BW, Dominy NJ, Essackjee HC, Lee PKD, Osorio D, Ramsden L, Yamashita N, Yuen TDB. 2001. Field kit to characterize physical, chemical, and spatial aspects of potential primate foods. Fol Primatol 72:11-25.

M'Kirera F, Ungar PS. 2003. Occlusal relief changes with molar wear in *Pan troglodytes troglodytes* and *Gorilla gorilla gorilla*. Am J Primatol 60:31–41.

MacKinnon JR, MacKinnon KS. 1980. Niche differentiation in a primate community. In: Chivers DJ. Malayan Forest Primates: Ten Years' Study in Tropical Rain Forest. New York: Springer. p. 167-190.

Matsuda I, Tuuga A, Higashi S. 2009. The feeding ecology and activity budget of proboscis monkeys. Am J Primatol 71:478-492.

McGraw WS. 1998. Comparative locomotion and habitat use of six monkeys in the Tai Forest, Ivory Coast. Am J Phys Anthropol 105:493-510.

McGraw WS, Daegling JD. 2012. Primate feeding and foraging: integrating studies of behavior and morphology. Annu Rev Anthropol 41:203-219.

McGraw WS, Vick AE, Daegling DJ. 2011. Sex and age differences in the diet and ingestive behaviors of sooty mangabeys (*Cercocebus atys*) in the Tai Forest, Ivory Coast. Am J Phys Anthropol 144:140-153.

McGraw WS, Pampush JD, Daegling DJ. 2012. Brief communication: enamel thickness and durophagy in mangabeys revisited. Am J Phys Anthropol 147:326-333.

McKey DB, Gartlan JS, Waterman PG, Choo GM. Food selection by black colobus monkeys (*Colobus satanas*) in relation to plant chemistry. Biol J Linn Soc 16:115-146.

Meikle WE. 1977. Molar wear stages in *Theropithecus gelada*. Kroeber Anthropol Soc Papers 50:21–25.

Meldrum DJ, Kay RF. 1997. *Nuciruptor rubricae*, a new pitheciine seed predator from the Miocene of Colombia. Am J Phys Anthropol 102:407–427.

Merceron G, Taylor S, Scott R, Chaimanee Y, Jaeger JJ. 2006. Dietary characterization of the hominoid *Khoratpithecus* (Miocene of Thailand): evidence from dental topographic and microwear texture analyses. Naturwissenschaften 93:329–333.

Min P. 2015. *meshconv* (software). Available from: http://www.cs.princeton.edu/~min/meshconv/.

Napier JR. 1970. Paleoecology and catarrhine evolution. In: Napier JR, Napier PH, editors. Old World Monkeys: Evolution, Systematics and Behavior. New York: Academic Press. p. 53–96.

Newton PN. 1987. The social organization of forest Hanuman langurs (*Presbytis entellus*). Int J Primatol 8:199-232.

Newton P. 1992. Feeding and ranging patterns of forest hanuman langurs (*Presbytis entellus*). Int J Primatol 13:245-285.

Norton GW, Rhine RJ, Wynn GW, Wynn RD. 1987. Baboon diet: a five-year study of stability and variability in the plant feeding and habitat of the yellow baboons (*Papio cynocephalus*) at Mikumi National Park, Tanzania. Fol Primatol 48:78-120.

O'Higgins P, Jones N. 1998. Facial growth in *Cercocebus torquatus*: an application of three dimensional geometric morphometric techniques to the study of morphological variation. J Anat 193:251-272.

Oates JF. 1994. The natural history of African colobines. In: Oates JF, Davies AG, editors. Colobine Monkeys. Cambridge: Cambridge University Press. p. 75-128.

Oka SW, Kraus BS. 1969. The circumnatal status of molar crown maturation among the Hominoidea. Arch Oral Biol 14:639-655.

Olupot W. 1998. Long-term variation in mangabeys (*Cercocebus albigena johnstoni*, Lydekker) feeding in Kibale National Park, Uganda. Afr J Ecol 36:96-101.

Orme D, Freckleton R, Thomas G, Petzoldt T, Fritz S, Isaac N, Pearse W. 2012. caper: Comparative Analyses of Phylogenetics and Evolution in R. R package version 0.5. Available from: http://CRAN.R-project.org/package=caper

Pengilly D. 1984. Developmental versus functional explanations for patterns of variability and correlation in the dentitions of foxes. J Mammal 65:34-43.

Plavcan JM. 1993. Canine size and shape in male anthropoid primates. Am J Phys Anthropol 92:201-2016.

Poirier FE, Hu HX. 1983. *Macaca mulatta* and *Rhinopithecus* in China: preliminary research results. Curr Anthropol 24:387-388.

Polly PD. 1998a. Variability, selection, and constraints: development and evolution in Viverravid (Carnivora, Mammalia) molar morphology. Paleobiology 24:409-429.

Polly PD. 1998b. Variability in mammalian dentitions: size-related bias in the coefficient of variation. Biol J Linn Soc 64:83-99.

Polly PD. 2005. Development and phenotypical correlation: the evolution of tooth shape in *Sorex araneus*. Evol Dev 7:29-41.

Polly PD. 2007. Evolutionary biology: development with a bite. Nature 449:413-415.

Post DG. 1982. Feeding behavior of yellow baboons (*Papio cynocephalus*) in the Amboseli National Park, Kenya. Int J Primatol 3:403-30.

Poulsen JR, Clark CJ, Smith TB. 2001. Seasonal variation in the feeding ecology of the gray-cheeked mangabeys (*Lophocebus albigena*) in Cameroon. Am J Primatol 54:91-105.

Poulsen JR, Clark CJ, Connor EF, Smith TB. 2002. Differential resource use by primates and hornbills: implications for seed dispersal. Ecology 83:228-240.

Plyusnin I, Evans AR, Karme A, Glonis A, Jernvall J. 2008. Automated 3D phenotype analysis using data mining. PLoS One 3:1–9.

R Core Team. 2015. R: A language and environment for statistical computing. https://www.R-project.org/

Ramachandran P, Varoquaux G. 2011. Mayavi: 3D visualization of scientific data. Comput Sci Eng 13:40–51.

Range F, Noë R. 2002. Familiarity and dominance relations among female sooty mangabeys in the Taï National Park. Am J Primatol 56:137-153.

Rasmussen DT, Simons EL. 1992. Paleobiology of the oligopithecines, the earliest known anthropoid primates. Int J Primatol 13:477–508.

Reed DNO. 1997. Contour mapping as a new method for interpreting diet from tooth morphology. Am J Phys Anthropol 102(24):194.

Rensberger JM, Forsten A, Fortelius M. 1984. Function evolution of the cheek tooth pattern and chewing directin in Tertiary horses. Paleobiology 10:439-452.

Rogers ME, Abernethy KA, Fontaine B, Wickings EJ, White LJ, Tutin CE. 1996. Ten days in the life of a mandrill horde in the Lope Reserve, Gabon. Am J Primatol 40:297-313.

Rosenberger AL, Kinzey WG. 1976. Functional patterns of molar occlusion in platyrrhine primates. Am J Phys Anthropol 45:281–297.

Ross CF, Washington RL, Eckhardt A, Reed DA, Vogel ER, Dominy NJ, Machanda ZP. 2009. Ecological consequences of scaling of chew cycle duration and daily feeding time in Primates. J Hum Evol 56:570-585.

Sagan C. 1980. Cosmos. New York: Random House.

Salazar-Ciudad I, Jernvall J. 2002. A gene network model accounting for development and evolution of mammalian teeth. Proc Nat Acad Sci USA 99:8116-8120.

Salazar-Ciudad I, Jernvall J. 2004. How different types of pattern formation mechanisms affect the evolution of form and development. Evol Dev 6:6-16.

Salazar-Ciudad I, Jernvall J. 2010. A computational model of teeth and the developmental origins of morphological variation. Nature 464:583-587.

Salazar-Ciudad I, Marin-Riera M. 2013. Adaptive dynamics under development-based genotype-phenotype maps. Nature 497:361-365.

Santana SE, Strait S, Dumont ER. 2011. The better to eat you with: functional correlates of tooth structure in bats. Func Ecol 25:839-847.

Schroer K, Wood B. 2015. Modeling the dental development of fossil hominins through the inhibitory cascade. J Anat 226:150-162.

Seligsohn D, Szalay FS. 1978. Relationship between natural selection and dental morphology: tooth function and diet in *Lepilemur* and *Hapalemur*. In: Butler PM, Joysey KA, editors. Development, function and evolution of teeth. New York: Academic Press. p 289–307.

Siebert JR, Swindler DR. 1991. Perinatal dental development in the chimpanzee (*Pan troglodytes*). Am J Phys Anthropol 86:287-294.

Skinner MM, Evans AR, Smith T, Jernvall J, Tafforeau P, Kupczik K, Olejniczak AJ, Rosas A, Radovcic J, Thackery JF, Toussaint M, Hublin JJ. 2010. Contributions of enamel-dentine junction shape and enamel deposition to primate molar crown complexity. Am J Phys Anthropol 142: 157–163.

Smith JM, Burian R, Kauffman S, Alberch P, Campbell J, Goodwin B, Lande R, Raup D, Wolpert L. 1985. Developmental constraints and evolution: a perspective from the Mountain Lake conference on development and evolution. Q Rev Biol 60:265-287.

Smith RJ, Jungers WL. 1997. Body mass in comparative primatology. J Hum Evol 32:523-559.

Stacey PB. 1986. Group size and foraging efficiency in yellow baboons. Beh Ecol Sociobiol 18:175-187.

Starling AP, Stock JT. 2007. Dental indicators of health and stress in early Egyptian and Nubian agriculturalists: a difficult transition and gradual recovery. Am J Phys Anthropol 134:520-528.

Strait SG. 1993a. Differences in occlusal morphology and molar size in frugivores and faunivores. J Hum Evol 25:471–484.

Strait SG. 1993b. Molar morphology and food texture among small-bodied insectivorous mammals. J Mammal 74:391–402.

Strait SG. 2001. Dietary reconstruction of small-bodied omomyoid primates. J Vert Paleontol 21:322–334.

Strasser E, Delson E. 1987. Cladistic analysis of cercopithecid relationships. J Hum Evol 16: 81-99.

Su Y, Ren R, Yan K, Li J, Zhou Y, Zhu Z, Hu Z, Hu Y. 1998. Preliminary survey of the home range and ranging behavior of golden monkeys (*Rhinopithecus roxellana*) in Shennongjia National Natural Research, Hubei, China. In: Jablonski NG, editor. The Natural History of the Doucs and Snub-Nosed Monkeys. Singapore: World Scientific Press. p. 255-268.

Swindler DR. 1961. Calcification of the permanent first mandibular molar in rhesus monkeys. Science 134:566.

Swindler DR. 1983. Variation and homology of the primate hypoconulid. Folia primatol 41:112-123.

Swindler DR. 2002. Primate dentition. Cambridge: Cambridge University Press.

Swindler DR, Beynon AD. 1993. The development and microstructure of the dentition of *Theropithecus*. In: Jablonski NG, editor. *Theropithecus*: The Rise and Fall of a Primate Genus. Cambridge: Cambridge University Press. p. 351-381.

Swindler DR, McCoy HA. 1964. Calcification of deciduous teeth in rhesus monkeys. Science 144:1243-1244.

Szalay FS, Delson E. 1979. Evolutionary History of the Primates. San Diego: Academic Press.

Tarrant LH, Swindler DR. 1972. The state of the deciduous dentition of a chimpanzee fetus (*Pan troglodytes*). J Dent Res 51:677.

Temerin LA, Cant JGH. 1983. The evolutionary divergence of Old World monkeys and apes. Am Nat 122: 335–351.

Thesleff I, Sahlberg C. Growth factors as inductive signals regulating tooth morphogenesis. Semin Cell Dev Biol 7:185-193.

Thesleff I, Keränen S, Jernvall J. 2001. Enamel knots as signaling centers linking tooth morphogenesis and odontoblast differentiation. Adv Dent Res 15:14-18.

Turner E. 1963. Crown development in human deciduous molar teeth. Arch Oral Biol 8:523-540.

Tutin CE, Ham RM, White LJ, Harrison MJ. 1997. The primate community of the Lopé Reserve, Gabon: diets, responses to fruit scarcity, and effects on biomass. Am J Primatol 42:1-24.

Ulhaas L, Kullmer O, Schrenk F, Henke W. 2004. A new 3-d approach to determine functional morphology of cercopithecoid molars. Ann Anat 186:487–493.

Ungar PS. 2004. Dental topography and diets of *Australopithecus afarensis* and early *Homo*. J Hum Evol 46:605–622.

Ungar PS. 2007. Dental topography and human evolution: with comments on the diets of *Australopithecus africanus* and *Paranthropus robustus*. In: Bailey S, Hublin JJ, editors. Dental perspectives on human evolution: state of the art research in dental anthropology. New York: Springer-Verlag. p 321–343

Ungar PS, Bunn JM. 2008. Primate dental topographic analysis and functional morphology. In: Irish JD, Nelson GC, editors. Technique and application in dental anthropology. New York: Cambridge University Press. p 253–265.

Ungar PS, Kay RF. 1995. The dietary adaptations of European Miocene catarrhines. Proc Natl Acad Sci USA 92:5479–5481.

Ungar PS, M'Kirera F. 2003. A solution to the worn tooth conundrum in primate functional anatomy. Proc Natl Acad Sci USA 100:3874–3877.

Ungar PS, Williamson M. 2000. Exploring the effects of tooth wear on functional morphology: a preliminary study using dental topographic analysis. Paleontologica Electronica 3:18.

Ungar PS, Grine FE, Teaford MF. 2008. Dental microwear and diet of the Plio-Pleistocene hominin *Paranthropus boisei*. PLoS ONE 3(4): e2044.

Vaahtokari A, Åberg T, Jernvall J, Keränen S, Thesleff I. 1996. The enamel knot as a signaling center in the developing mouse tooth. Mech Dev 54:39–43.

Van Der Walt S, Colbert SC. 2011. The NumPy array: a structure for efficient numerical computation. Comput Sci Eng 13:22–30.

van Rossum G. 1994. Python Reference Manual. Available from: http://www.cs.cmu.edu/afs/cs.cmu.edu/project/gwydion-1/OldFiles/OldFiles/python/Doc/ref.ps

Van Valen L. 1962. Growth fields in the dentition of *Peromyscus*. Evolution 16:272-277.

Venkataraman VV, Glowacka H, Fritz J, Clauss M, Seyoum C, Nguyen N, Fashing PJ. 2014. Effects of dietary fracture toughness and dental wear on chewing efficiency in geladas (*Theropithecus gelada*). Am J Phys Anthropol 155:17-32.

Waser 77

Weiss K, Stock D, Zhao Z. 1998. Dynamic interactions and the evolutionary genetics of dental patterning. Crit Rev Oral Biol Med 9:369–398.

Wheatley BP. 1980. Feeding and ranging of East Bornean *Macaca fascicularis*. In: Lindburg DG, editor. The Macaques. New York: Van Nostrand Reinhold Co. p. 215-246.

Whitten PL. 1983. Diet and dominance among female vervet monkeys (*Cercopithecus aethiops*). Am J Primatol 5:139-159.

Wieczkowski J. 2009. Brief communication: puncture and crushing resistance scores of Tana river mangabeys (*Cercocebus galeritus*) diet items. Am J Phys Anthropol 140:572-577.

Willis MS, Swindler DR. 2004. Molar size and shape variations among Asian colobines. Am J Phys Anthropol 125:51-60.

Wilson GP, Evans AR, Corfe IJ, Smits PD, Fortelius M, Jernvall J. 2012. Adaptive radiation of multituberculate mammals before the extinction of dinosaurs. Nature 483:457-460.

Winchester JM, Zohdy S, King S, Wright PC, Jernvall J. 2011. Testing for tooth wear resistant measures of diet in primates. J Vert Paleo 31(S2): 79-80.

Winchester JM, Boyer DM, St. Clair EM, Gosselin-Ildari AD, Cooke SB, Ledogar JA. 2014. Dental topography of platyrrhines and prosimians: convergence and contrasts. Am J Phys Anthropol 153:29-44.

Wrangham RW. 1976. Aspects of feeding and social behaviour in gelada baboons. Mimeo report to Science Research Council, London.

Wrangham RW, Waterman PG. 1981. Feeding behaviour of vervet monkeys on *Acacia tortilis* and *Acacia xanthrophloea*: with special reference to reproductive strategies and tannin production. J Anim Ecol 50:715-731.

Yablokov AV. 1974. Variability of Mammals. New Delhi: Amerind Publishing Company.

Yamashita N. 1996. Seasonality and site specificity of mechanical dietary patterns in two Malagasy lemur families (Lemuridae and Indriidae). Int J Primatol 17:355-387.

Yeager CP. 1996. Feeding ecology of the long-tailed macaque (*Macaca fascicularis*) in Kalimantan Tengah, Indonesia. Int J Primatol 17:51-62.

Zeeve SR. 1991. Behavior and ecology of primates in the Lomako Forest, Zaire. Ph.D. dissertation, State University of New York, Stony Brook.

Zohdy S, Evans AR, Wright PC, Jernvall J. 2008. Roughing it: what it takes for *Hapalemur*, bears, and rodents to chew bamboo. Am J Phys Anthropol 135:228.

Zuccotti LF, Williamson MD, Limp WF, Ungar PS. 1998. Modeling primate occlusal topography using geographic information systems technology. Am J Phy Anthropol 107:137–142.

Appendix 1: Source code and scripts

A1.1: List of contents

A1.2: Source code and scripts referenced in chapter two

A1.2.1: MorphoTester

MorphoTester is a scientific computing application for the quantification of topographic metrics from polygonal surfaces representing anatomical specimens. This software is fully described in chapter one. Source code for MorphoTester, current at the time of writing (4/11/2016), will be provided below. As this software continues to be maintained and updated as of the date of writing, more recent source code versions may be found at this software's official repository (https://github.com/JuliaWinchester/morphotester).

Source code files are listed alphabetically and include:

i. *__init__.py*: Python package initialization file
ii. *DNE.py*: Dirichlet normal energy algorithm
iii. *implicitfair.py*: Functions for implicit fairing smooth
iv. *Morpho.py*: Main application classes
v. *normcore.py*: Functions for calculating normal vectors
vi. *OPC.py*: Orientation patch count rotated algorithm
vii. *plython.py*: Module for creation and saving of .ply polygonal meshes
viii. *render.py*: Functions for plotting 2D outline of 3D surface mesh
ix. *RFI.py*: Relief index algorithm
x. *topomesh.py*: Class for storing polygonal surface meshes and associated topographic data

i. *__init__.py*: Python package initialization file

```
'''
Created on Oct 2, 2015

A scientific computing application for measuring topographic shape in 3D data.
To run MorphoTester, execute Morpho.py as a script.

MorphoTester is licensed under the GPL license. See LICENSE.txt for further details.

@author: Julia M. Winchester
'''

__version__ = '1.0'

__requires__ = ['Image', 'matplotlib', 'mayavi', 'numpy', 'PyQt4', 'scipy', 'sip',
'traits', 'traitsui', 'tvtk']
```

ii. *DNE.py*: Dirichlet normal energy algorithm

```
'''
Created on Feb 1, 2012

This module calculates Dirichlet Normal Energy for a provided 3D mesh using
the MeshDNE class. See Bunn et al. (2011) and Winchester (2016) for
further details on method.

@author: Julia M. Winchester
'''

import implicitfair
import normcore
from copy import copy as pcopy
from numpy import zeros, transpose, nonzero, sqrt, sum, trace, mat, array, dot, isnan,
copy, array_equal
from numpy.linalg import cond, LinAlgError
from scipy.sparse import lil_matrix
from scipy.stats import scoreatpercentile
from collections import defaultdict

class MeshDNE(object):
    """Class for calculating and storing Dirichlet normal energy values for polygonal
    mesh data.

    When instanced, this class calculates Dirichlet normal energy and associated
    variables and stores them. All attributes listed below are populated on
    instantiation.

    Args:
        TopoMesh (TopoMesh object): Triangulated polygon mesh data.
        dosmooth (bool): Whether or not mesh should be smoothed prior to DNE
            calculation.
        smoothit (int): Number of iterations for smoothing.
        smoothstep (float): Step size for smoothing
        docondition (bool): Whether or not to perform matrix condition number
            checking as part of DNE calculation.
        dooutlier (bool): Whether or not to perform outlier removal as part of
            DNE calculation.
        outlierperc (float): Percentile above which to remove energy outliers.
        outliertype (bool): Whether to remove outliers as energy*face values
            (true) or energy values (false).

    Attributes:
        Mesh (TopoMesh object): Triangulated polygon mesh data.
        vert_tri_dict (dict): Associates vertex index keys with related
            face index values.
        edgeverts (ndarray): Pairs of vertices that form surface boundary edges.
        fnormal (ndarray): Normalized unit normals of surface polygons.
        vnormal (ndarray): Normalized approximated unit normals of surface
            vertices (approximated as average of normals of associated faces).
        e (ndarray): Energy density values of surface polygons.
        facearea (ndarray): Surface polygon areas.
        equantity (ndarray): e * facearea for surface polygons.
        DNE (float): Summation of equantity.
        high_condition_faces (list): Surface polygons with high matrix condition
            numbers. If condition number check is on, these are not counted
            toward DNE.
        outlier_faces (list): Surfaces with outlier energy values. If outlier
            removal is on, these are not counted toward DNE.
        boundary_faces (list): Polygons forming mesh edges. Not counted toward
            DNE.
        nan_faces (list): Any polygons resulting in NAN e values.
        filename (string): Filename of current mesh. Unused for now.
    """
    def __init__(self, TopoMesh, dosmooth, smoothit, smoothstep, docondition, dooutlier,
        outlierperc, outliertype, fname):
```

```
        self.Mesh = TopoMesh
        self.dosmooth = dosmooth
        self.smoothit = smoothit
        self.smoothstep = smoothstep
        self.docondition = docondition
        self.dooutlier = dooutlier
        self.outlierperc = float(outlierperc)
        self.outliertype = outliertype
        self.fname = fname

        self.vert_tri_dict = None
        self.edgeverts = None
        self.fnormal = None
        self.vnormal = None
        self.e = None
        self.facearea = None
        self.equantity = None
        self.DNE = None

        self.high_condition_faces = list()
        self.outlier_faces = list()
        self.boundary_faces = list()
        self.nan_faces = list()

        self.calcdne()

    def calcdne(self):
        """Method for calculating surface Dirichlet normal energy and populating instance
        variables."""
        # creation of dictionary of vertex keys and face values
        self._get_vert_tri_dict()

        # optional implicit smooth of mesh
        if self.dosmooth == 1:
            self.Mesh = pcopy(self.Mesh)
            self.Mesh.vertices = implicitfair.smooth(self.Mesh.vertices, self.Mesh.faces,
                int(self.smoothit), float(self.smoothstep), self.vert_tri_dict)
            if self.Mesh.vertices == "!":
                print "Cholesky error"
                return "!"

        # creation of array of vertices per edge
        self._get_edge_verts()
        # list of boundary faces
        self._get_boundary_faces()

        # arrays of normalized face normals and vertex normals approximated from adjacent
        faces
        self.vnormal, self.fnormal = normcore.computenormal(self.Mesh.vertices,
            self.Mesh.faces, self.Mesh.triverts, self.vert_tri_dict)
        # array of e(p) and face area for polygons across mesh

        self._energize_surface()

        self._sumdne()

    def _energize_surface(self):
        """Calculates energy values and polygon areas across a surface."""
        energy_and_facearea = array([self._energy(face, i) for i, face in
            enumerate(self.Mesh.faces)])
        self.e = energy_and_facearea[:,0]
        self.facearea = energy_and_facearea[:,1]

    def _energy(self, face, i):
        """Returns energy value and polygon area for a provided polygon."""

        TV1 = array([self.Mesh.vertices[face[0]], self.Mesh.vertices[face[1]],
            self.Mesh.vertices[face[2]]])
```

```
    TV2 = array([self.vnormal[face[0]],self.vnormal[face[1]],self.vnormal[face[2]]])

    if array_equal(TV1[0], TV1[1]) or array_equal(TV1[0], TV1[2]) or
        array_equal(TV1[1], TV1[2]):
        print "Warning: Duplicate vertices in polygon %s." % i
        print "Ignoring this polygon for energy calculation, but editing surface to
            remove duplicate vertices prior to DNE calculation is encouraged."
        return [0,1]

    b1 = TV1[1] - TV1[0]
    b2 = TV1[2] - TV1[0]

    g = array(([dot(b1,b1), dot(b1,b2)],[dot(b2,b1), dot(b2,b2)]))

    if self.docondition:
            if cond(g) > 10**5:
                self.high_condition_faces.append([i, cond(g)])
                return [0,1]

    c1 = TV2[1] - TV2[0]
    c2 = TV2[2] - TV2[0]

    fstarh = array(([dot(c1,c1), dot(c1,c2)], [dot(c2,c1), dot(c2,c2)]))

    gm = mat(g)

    try:
        gminv = gm.I
    except LinAlgError as err:
        condition = cond(g)
        if condition > 10**5:
            err.args += ('G matrix for polygon %s is singular and an inverse cannot
                 be determined. Condition number is %s, turning condition number
                 checking on will cause this polygon to be ignored for energy
                 calculation.' % (i, cond(g)),)
            raise
        else:
            err.args += ('G matrix for polygon %s is singular and an inverse cannot
                be determined. Condition number is %s, turning condition number
                checking on will not cause this polygon to be ignored for energy
                calculation. Further mesh processing is advised.' % (i, cond(g)),)
            raise

    e = trace((gminv*fstarh))
    facearea = 0.5 * sqrt(g[0,0]*g[1,1]-g[0,1]*g[1,0])

    if isnan(e):
        self.nan_faces.append(i)

    return [e,facearea]

def _sumdne(self):
    """Sums energy values * face areas, ignoring certain kinds of polygons depending
        on parameters."""
    # ignore energy of boundary faces
    self.e[self.boundary_faces] = 0

    # energy density is e(p) * area of polygon
    self.equantity = array([x*y for x, y in zip(self.e, self.facearea)])

    # optional removal of top outliers, percentile for outliers is user settable
    if self.dooutlier:
        self._outlierremove()

    self.DNE = round(sum(self.equantity),3)

def _outlierremove(self):
    """Flags outlier faces based on parameters and removes associated energy
```

```
        values."""
    switcharoo = [self.e, self.equantity]
    percentile = scoreatpercentile(switcharoo[self.outliertype], self.outlierperc)
    for i, energy in enumerate(switcharoo[self.outliertype]):
        if energy > percentile or isnan(energy):
            self.outlier_faces.append([i, energy, self.facearea[i]])
            self.equantity[i] = 0

def _get_vert_tri_dict(self):
    """Generates dictionary associating vertex index keys with related polygon index
        values."""
    self.vert_tri_dict = defaultdict(list)

    for findex, face in enumerate(self.Mesh.faces):
        for vertex in face:
            self.vert_tri_dict[vertex].append(findex)

def _get_edge_verts(self):
    """Generates pairs of vertices comprising surface edges."""
    M = lil_matrix((self.Mesh.nvert,self.Mesh.nvert))

    nedge = 0

    for face in self.Mesh.faces:
        v1, v2, v3 = face

        if M[v1,v2] == 0:
            nedge += 1
            M[v1,v2] = nedge
            M[v2,v1] = nedge

        if M[v3,v1] == 0:
            nedge += 1
            M[v1,v3] = nedge
            M[v3,v1] = nedge

        if M[v2,v3] == 0:
            nedge += 1
            M[v3,v2] = nedge
            M[v2,v3] = nedge

    self.edgeverts = zeros([nedge,2], int)

    nonzeroarray = transpose(nonzero(M))

    for entry in nonzeroarray:
        self.edgeverts[M[entry[0],entry[1]]-1] = [entry[0],entry[1]]

def _get_boundary_faces(self):
    """Generates list of polygons comprising surface edges."""
    self.boundary_faces = list()

    for verts in self.edgeverts:
        f1, f2 = [self.vert_tri_dict[vert] for vert in verts]
        cf = [x for x in f2 for y in f1 if x == y]

        if len(cf) == 1:
            self.boundary_faces.append(cf[0])

    self.boundary_faces = list(set(self.boundary_faces))
```

iii. *implicitfair.py*: Functions for implicit fairing smooth

```
'''
Created on Oct 10, 2012

Contains functions for executing an implicit fairing smooth on a 3D mesh.

@author: Julia M. Winchester
'''

from math import acos, tan
from numpy import sqrt, spacing, diag, mat
from numpy.linalg import cholesky, solve, LinAlgError
from scipy.sparse import identity, lil_matrix

def clamp(n, minn, maxn):
    return max(min(maxn, n), minn)

def My_Angle(u,v):
    du = sqrt(sum(u**2))
    dv = sqrt(sum(v**2))
    du = max(du,spacing(1))
    dv = max(dv,spacing(1))

    x = sum(u*v) / (du*dv)
    x = clamp(x, -1.0, 1.0)
    angle = acos(x)
    return angle

def laplaciantension(vertex, faceindex, vert_tri_dict):
    n = len(vertex)
    L = lil_matrix((n,n))
    ring = vert_tri_dict

    for i in range(0,n):
        for b in ring[i]:
            bf = faceindex[b]
            if bf[0] == i:
                v = (bf[1],bf[2])
            else:
                if bf[1] == i:
                    v = (bf[0],bf[2])
                else:
                    if bf[2] == i:
                        v = (bf[0],bf[1])
                    else:
                        print "Problem in face ring."
            j = v[0]
            k = v[1]
            vi = vertex[i]
            vj = vertex[j]
            vk = vertex[k]

            # angles
            alpha = My_Angle(vk-vi, vk-vj)
            beta = My_Angle(vj-vi, vj-vk)

            # add weight
            if alpha == 0:
                cot_alpha = 0
            else:
                cot_alpha = 1/tan(alpha)

            if beta == 0:
                cot_beta = 0
            else:
                cot_beta = 1/tan(beta)
```

```
            L[i,j] = L[i,j] + cot_alpha
            L[i,k] = L[i,k] + cot_beta

    a = L.sum(axis=1)
    b = [float(i) for i in a]
    L = L - diag(b)

    return L

def smooth(vertex, faceindex, iternum, stepsize, vert_tri_dict):
    L = laplaciantension(vertex, faceindex, vert_tri_dict)
    sparseidentity = identity(len(vertex))

    tochol = sparseidentity - (stepsize*L)
    tochol = mat(tochol)

    try:
        R = cholesky(tochol).T # Upper-triangular matrix cholesky decomposition (.T makes
            it upper, normally it spits out lower)
    except LinAlgError:
        print "Cholesky decomposition cannot be computed, mesh matrix is not positive
            definite."
        return "!"

    for k in range(0,iternum):
        Q = solve(R.H, vertex)
        vertex = solve(R,Q)

    return vertex
```

iv. *Morpho.py*: Main application classes

```
'''
Created on Jun 17, 2012

This module activates MorphoTester, a scientific computing application for measuring
topographic shape of 3D anatomical data. It should be run as a script from the
command line. It contains the application GUI and calls subsequent modules plython, DNE,
RFI, and OPCR.

@author: Julia M. Winchester
'''

import os
os.environ['ETS_TOOLKIT'] = 'qt4'
os.environ['QT_API'] = 'pyqt'

import sys
import sip
sip.setapi('QString', 2)

import topomesh

from math import log
from numpy import array, amax, amin, rint, empty, nan, isfinite
from traits.api import HasTraits, Instance
from traitsui.api import View, Item
from mayavi.core.ui.api import MlabSceneModel
from tvtk.pyface.scene_editor import SceneEditor
from PyQt4 import QtGui

class MainWidget(QtGui.QWidget):
    """ Class for primary UI window."""

    def __init__(self):
        super(MainWidget, self).__init__()

        self.open_file_dialog_path ='/'
        self.open_directory_dialog_path = '/'
        self.initUI()

    def initUI(self):
        """ Creates primary UI layout and widgets.

        Displays MayaviView 3D viewer pane. Opens submenus for file selection, directory
        selection, and DNE/OPCR options. Executes calculation of topography and
        visualization of calculated topography.
        """
        #=====================================================================
        # Tab layout
        #=====================================================================
        self.tab_widget = QtGui.QTabWidget()

        self.tab1 = QtGui.QWidget()
        self.tab1layout = QtGui.QGridLayout()
        self.tab1layout.setSpacing(10)
        self.tab1.setLayout(self.tab1layout)

        self.tab2 = QtGui.QWidget()
        self.tab2layout = QtGui.QGridLayout()
        self.tab2layout.setSpacing(10)
        self.tab2.setLayout(self.tab2layout)

        self.tab_widget.addTab(self.tab1, "Shape metrics")
        self.tab_widget.addTab(self.tab2, "Mesh tools")

        #=====================================================================
        # UI widgets
```

```
#=============================================================================
self.openbutton = QtGui.QPushButton("Open File")
self.opendirbutton = QtGui.QPushButton("Open Directory")
self.openlabel = QtGui.QLabel("")

# Topography and options window widgets
self.dnecheck = QtGui.QCheckBox("DNE")
self.dnecheck.toggle()
self.dnebutton = QtGui.QPushButton("Options")

self.rficheck = QtGui.QCheckBox("RFI")
self.rficheck.toggle()

self.opcrcheck = QtGui.QCheckBox("OPCR")
self.opcrcheck.toggle()
self.opcrbutton = QtGui.QPushButton("Options")

# Topography calculation buttons
self.calcfilebutton = QtGui.QPushButton("Process File")
self.calcdirbutton = QtGui.QPushButton("Process Directory")

# Contents of mesh tools tab
self.implicit_fair_check = QtGui.QCheckBox("Implicit fair smooth")

self.implicit_fair_iterations_label = QtGui.QLabel("Iterations")
self.implicit_fair_iterations = QtGui.QLineEdit("3")

self.implicit_fair_step_size_label = QtGui.QLabel("Step size")
self.implicit_fair_step_size = QtGui.QLineEdit("0.1")

self.implicit_fair_label = QtGui.QLabel("This will output implicit faired
    meshes.")
self.implicit_fair_label2 = QtGui.QLabel("For single files, this will update
    current mesh in view.")

self.implicit_fair_file = QtGui.QPushButton("Process File")
self.implicit_fair_dir = QtGui.QPushButton("Process Directory")

# Output log
self.morpholog = QtGui.QTextEdit()
self.morpholog.setReadOnly(1)

# 3D view
self.mayaviview = MayaviView(0,1)
self.threedview = self.mayaviview.edit_traits().control

#=============================================================================
# GUI behavior
#=============================================================================
self.openbutton.clicked.connect(self.OpenFileDialog)
self.opendirbutton.clicked.connect(self.OpenDirDialog)

self.calcfilebutton.clicked.connect(self.CalcFile)
self.calcdirbutton.clicked.connect(self.CalcDir)

self.implicit_fair_file.clicked.connect(self.fair_file)
self.implicit_fair_dir.clicked.connect(self.fair_directory)

# Options submenu buttons
self.DNEOptionsWindow = DNEOptionsWindow(self)
self.dnebutton.clicked.connect(self.DNEOptionsWindow.show)
self.OPCROptionsWindow = OPCROptionsWindow(self)
self.opcrbutton.clicked.connect(self.OPCROptionsWindow.show)

#=============================================================================
# UI grid layout
#=============================================================================
grid = QtGui.QGridLayout()
```

```
        grid.setSpacing(10)

        grid.addWidget(self.openbutton, 0, 0)
        grid.addWidget(self.openlabel, 1, 0)
        grid.addWidget(self.opendirbutton, 0, 1)

        grid.addWidget(self.tab_widget, 2, 0, 14, 2)

        self.tab1layout.addWidget(self.dnecheck, 0, 0)
        self.tab1layout.addWidget(self.dnebutton, 0, 1)
        self.tab1layout.addWidget(self.rficheck, 1, 0)
        self.tab1layout.addWidget(self.opcrcheck, 2, 0)
        self.tab1layout.addWidget(self.opcrbutton, 2, 1)

        self.tab1layout.addWidget(self.calcfilebutton, 10,0)
        self.tab1layout.addWidget(self.calcdirbutton, 10,1)

        self.tab2layout.addWidget(self.implicit_fair_check, 0, 0)
        self.tab2layout.addWidget(self.implicit_fair_iterations_label, 1, 0)
        self.tab2layout.addWidget(self.implicit_fair_iterations, 1, 1)
        self.tab2layout.addWidget(self.implicit_fair_step_size_label, 2, 0)
        self.tab2layout.addWidget(self.implicit_fair_step_size, 2, 1)
        self.tab2layout.addWidget(self.implicit_fair_label, 3, 0, 1, 2)
        self.tab2layout.addWidget(self.implicit_fair_label2, 4, 0, 1, 2)

        self.tab2layout.addWidget(self.implicit_fair_file, 10, 0)
        self.tab2layout.addWidget(self.implicit_fair_dir, 10, 1)

        grid.addWidget(self.morpholog, 16, 0, 2, 4)
        grid.addWidget(self.threedview, 0, 2, 16, 2)

        self.setLayout(grid)

        self.sizeHint()
        self.setWindowTitle('MorphoTester')

        sys.stdout = OutLog(self.morpholog, sys.stdout)
        sys.stderr = OutLog(self.morpholog, sys.stderr, QtGui.QColor(255,0,0))

    def OpenFileDialog(self):
        """Method for loading .ply surface mesh files."""
        filepath = QtGui.QFileDialog.getOpenFileName(self, 'Open File',
            self.open_file_dialog_path)
        self.filepath = filepath
        self.open_file_dialog_path = os.path.dirname(filepath)

        if not len(filepath):
            return

        print "Opening file..."
        filename = os.path.split(filepath)[1]
        self.openlabel.setText(filename)
        self.filename = filename
        self.TopoMesh = topomesh.TopoMesh(filepath)
        self.mayaviview = MayaviView(self.TopoMesh.mesh,1)
        print "File open!"

    def OpenDirDialog(self):
        """Method for selecting a directory for batch processing of .ply surface mesh
            files."""
        self.dirpath = QtGui.QFileDialog.getExistingDirectory(self, 'Open Directory',
            self.open_directory_dialog_path)
        self.open_directory_dialog_path = self.dirpath

        if not len(self.dirpath):
            return

        print "Opening directory..."
```

```
        self.openlabel.setText(".."+self.dirpath[-20:])
        self.mayaviview = MayaviView(0,1)

    def ProcessSurface(self):
        """Method for processing surface mesh data to acquire topographic variables."""

        if self.dnecheck.isChecked():
            self.TopoMesh.GenerateDNE(self.DNEOptionsWindow.fairvgroup.isChecked(),
                                      self.DNEOptionsWindow.dneiteration.text(),
                                      self.DNEOptionsWindow.dnestepsize.text(),
                                      self.DNEOptionsWindow.dneconditioncontrolcheck.
                                          isChecked(),
                                      self.DNEOptionsWindow.outliervgroup.isChecked(),
                                      self.DNEOptionsWindow.dneoutlierval.text(),
                                      self.DNEOptionsWindow.dneoutliertype1.isChecked(),
                                      self.filename)

        if self.rficheck.isChecked():
            self.TopoMesh.GenerateRFI()

        if self.opcrcheck.isChecked():
            self.TopoMesh.GenerateOPCR(self.OPCROptionsWindow.opcrminpatch.text())

    def CalcFile(self):
        """Method for processing a single surface mesh object.

        Connected to Process File Button."""
        if not self.dnecheck.isChecked() and not self.rficheck.isChecked() and not
            self.opcrcheck.isChecked():
            print "No topographic variables have been selected for analysis."
        self.ProcessSurface()

        if self.dnecheck.isChecked():
            print "\nDNE calculation details:"
            if self.TopoMesh.DNE == "!":
                print "\nDNE could not be calculated due to cholesky factorization
                    error."
            else:
                if self.DNEOptionsWindow.outliervgroup.isChecked():
                    print "\nPolygons removed as outliers:"
                    for face in self.TopoMesh.outlierfaces:
                        print "Polygon: %s\tEnergy: %s\tArea %s" % (face[0], face[1],
                            face[2])
                if self.DNEOptionsWindow.dneconditioncontrolcheck.isChecked():
                    print "\nPolygons removed for high matrix condition numbers:"
                    for face in self.TopoMesh.conditionfaces:
                        print "Polygon: %s\tMatrix condition number: %s" % (face[0],
                            face[1])
                print "\nNumber of edge polygons ignored: %s" %
                    len(self.TopoMesh.boundaryfaces)

        print "\n--------------------"
        print "RESULTS"
        print "File name: %s" % self.openlabel.text()
        print "Mesh face number: %s" % self.TopoMesh.nface
        if self.dnecheck.isChecked():
            if self.TopoMesh.DNE == "!":
                print "\nError (Cholesky factorization error)"
            else:
                print "\nDNE: %s" % self.TopoMesh.DNE
                if self.DNEOptionsWindow.visvgroup.isChecked():
                    MayaviView.VisualizeDNE(self.mayaviview, self.TopoMesh.DNEscalars,
                    self.DNEOptionsWindow.dnerelvischeck.isChecked(),
                    float(self.DNEOptionsWindow.dneabsminval.text()),
                    float(self.DNEOptionsWindow.dneabsmaxval.text()))
        if self.rficheck.isChecked():
            print "\nRFI: %s" % self.TopoMesh.RFI
            print "Surface area: %s" % self.TopoMesh.surfarea
```

```
            print "Outline area: %s" % self.TopoMesh.projarea
        if self.opcrcheck.isChecked():
            print "\nOPCR: %s" % self.TopoMesh.OPCR
            print "OPC at each rotation: %s" % self.TopoMesh.OPClist
            if self.OPCROptionsWindow.visualizeopcrcheck.isChecked():
                MayaviView.VisualizeOPCR(self.mayaviview, self.TopoMesh.OPCscalars,
                self.TopoMesh.nface)
        print "--------------------"
        if self.OPCROptionsWindow.visualizeopcrcheck.isChecked() and
            self.DNEOptionsWindow.visvgroup.isChecked() and self.dnecheck.isChecked() and
            self.opcrcheck.isChecked():
            print "DNE and OPCR visualization both requested. Defaulting to OPCR
                visualization."

    def CalcDir(self):
        """Method for batch processing a directory of .ply surface mesh files.

        Connected to Process Directory button."""
        if not self.dnecheck.isChecked() and not self.rficheck.isChecked() and not
            self.opcrcheck.isChecked():
            print "No topographic variables have been selected for analysis."
            return

        resultsfile = open(os.path.join(self.dirpath,'morphoresults.txt'),'w')
        resultsfile.write("Filename\tMesh Face Number\tDNE\tRFI\tSurface Area\tOutline
            Area\tOPCR\n")

        for filename in os.listdir(self.dirpath):
            if filename[-3:] == "ply":
                self.filename = filename
                print "Processing " + filename + "..."
                self.TopoMesh = topomesh.TopoMesh(os.path.join(self.dirpath,filename))
                self.ProcessSurface()
                resultsfile.write("%s\t%s\t%s\t%s\t%s\t%s\t%s\n" % (filename,
                    self.TopoMesh.nface, self.TopoMesh.DNE, self.TopoMesh.RFI,
                    self.TopoMesh.surfarea, self.TopoMesh.projarea, self.TopoMesh.OPCR))
                print "\n--------------------\n"
            else:
                print filename + "does not have a .ply extension, skipping to next file."
        resultsfile.close()

    def fair_file(self):
        print "Implicit fairing " + self.filename + "..."
        self.fair_mesh(self.filepath)
        self.mayaviview.VisualizeMesh(self.TopoMesh.mesh, 1)

    def fair_directory(self):
        for filename in os.listdir(self.dirpath):
            if filename[-3:] == "ply":
                print "Implicit fairing " + filename + "..."
                self.TopoMesh = topomesh.TopoMesh(os.path.join(self.dirpath,filename))
                self.fair_mesh(os.path.join(self.dirpath,filename))

    def fair_mesh(self, filepath):
        self.TopoMesh.implicit_fair_mesh(int(self.implicit_fair_iterations.text()),
                                         float(self.implicit_fair_step_size.text()))
        filename = os.path.split(filepath)[1]
        fairdir = os.path.join(os.path.dirname(filepath), 'faired-mesh', '')
        if not os.path.exists(fairdir):
            os.mkdir(fairdir)
        self.TopoMesh.SaveArray(os.path.join(fairdir, (filename[:-4] + "-faired.ply")))

class MayaviView(HasTraits):
    """Class for 3D visualization of polygonal meshes and related 2D decorators.

    Initializes 3D viewer and displays a 3D polygonal mesh if provided with a data
    object.
```

```
Args:
    plotmesh (bool): If true, plots model from MainWidget.TopoMesh class.
    clearscreen (bool): If true, clears figure before plotting model.

Attributes:
    Class:
        scene: MlabSceneModel instance.
        view: Mayavi view of scene.
    __init__():
        plot: Mayavi figure plot of visualized mesh.
"""
scene = Instance(MlabSceneModel, ())

# The layout of the panel created by Traits
view = View(Item('scene', editor=SceneEditor(), resizable=True, show_label=False),
    resizable=True)

def __init__(self, model, clearscreen):
    HasTraits.__init__(self)

    self.model = model
    self.plot = self.VisualizeMesh(self.model, clearscreen)

def VisualizeMesh(self, model, clearscreen):
    """Method for creating a Mayavi figure plot of visualized 3D polygonal mesh."""
    if clearscreen:
        self.plot = self.scene.mlab.clf()

    if not model:
        self.plot = self.scene.mlab.points3d(0,0,0,opacity=0.0)
    else:
        triangles = model[2]
        x, y, z = model[0][:,0], model[0][:,1], model[0][:,2]

        self.plot = self.scene.mlab.triangular_mesh(x, y, z, triangles)

    return self.plot

def Interpolate(self, i, j, steps):
    """Interpolates sets of numbers between designated end point number sets."""
    onestep = steps+1
    ijrange = j.astype(float) - i.astype(float)
    fillarray = rint(array([ijrange/(onestep)*s+i.astype(float) for s in
        range(onestep)[1:]]))
    if (fillarray < 0).any():
        fillarray = array([abs(x[::-1]) if (x < 0).any() else x for x in
            fillarray.T]).T
    return fillarray

def RelativeLut(self, lut, lmin, lmax):
    """Given a LUT (255x4 array of colors), creates a new LUT from segment of
        original LUT using interpolation."""
    cutlut = lut[int(round(lmin*255)):int(round(lmax*255))]
    newlut = empty([len(lut), 4]) # New null LUT of 255 length
    newlut[:] = nan
    for i, nugget in enumerate(cutlut):
        newlut[int(float((len(lut)-1))/float((len(cutlut)-1))*float(i))] = nugget
    somelut = [i for i, x in enumerate(newlut) if isfinite(x).all()]
    pairlut = zip(somelut[:-1], somelut[1:])
    for pair in pairlut:
        if pair[1]-pair[0]-1 < 1:
            continue
        newlut[pair[0]+1:pair[1]] = self.Interpolate(newlut[pair[0]],
            newlut[pair[1]], (pair[1]-pair[0]-1))
    return newlut

def VisualizeScalars(self, scalars, customlut=None, scale='linear', colorbar=1):
    """Method for visualizing scalar data on polygonal mesh using optional color LUT
```

```
        and linear or log scaling."""
        self.visplot = self.VisualizeMesh(self.model,1)

        self.visplot.mlab_source.dataset.cell_data.scalars = scalars
        self.visplot.mlab_source.dataset.cell_data.scalars.name = 'Cell data'
        self.visplot.mlab_source.update()

        self.visplot2 = self.scene.mlab.pipeline.set_active_attribute(self.visplot,
            cell_scalars='Cell data')
        self.visplot3 = self.scene.mlab.pipeline.surface(self.visplot2)

        if customlut is None:
            self.visplot3.module_manager.scalar_lut_manager.lut_mode = 'blue-red'
        else:
            self.visplot3.module_manager.scalar_lut_manager.lut.table = customlut

        self.visplot3.module_manager.scalar_lut_manager.lut.scale = scale

        if colorbar:
            self.scene.mlab.colorbar(object=self.visplot3, orientation='vertical')

        self.scene.mlab.draw()

        return self.visplot3

    def VisualizeDNE(self, edens, isrelative, absmin, absmax):
        """Visualizes energy density across polygonal mesh."""
        # For visualizing on log scale, transforms all 0 values (boundary and outlier
        faces) to lowest non-zero energy on polygon
        apple = sorted(set(edens))[1]
        eve = [apple if not x else x for x in edens]
        emin = amin(eve)
        emax = amax(eve)

        if isrelative:
            self.plot3 = self.VisualizeScalars(eve, scale='log10')
        else:
            eve = [absmin if x<absmin else x for x in eve]
            eve = [absmax if x>absmax else x for x in eve]

            if absmin == 0.0:
                absmin = 1e-08

            if absmin < emin:
                lutmin = (log(emin) - log(absmin))/(log(absmax) - log(absmin))
            else:
                lutmin = 0.0
            if absmax > emax:
                lutmax = (log(emax)-log(absmin))/(log(absmax) - log(absmin))
            else: lutmax = 1.0

            abslut = self.plot.module_manager.scalar_lut_manager.lut.table.to_array()
            rellut = self.RelativeLut(abslut, lutmin, lutmax)
            self.plot3 = self.VisualizeScalars(eve, customlut=rellut, scale='log10')

    def VisualizeOPCR(self,hexcolormap,facelength):
        """Visualizes patches across polygonal mesh."""
        strdictb = {'#000000': 0.0, '#FF0000': 0.167, '#964B00': 0.278, '#FFFF00': 0.388,
            '#00FFFF': 0.5, '#0000FF': 0.612, '#90EE90': 0.722, '#014421': 0.833,
            '#FFC0CB': 1.0}
        strdict =  {'#FF0000': 0.0, '#964B00': 0.188, '#FFFF00': 0.314, '#00FFFF': 0.439,
            '#0000FF': 0.536, '#90EE90': 0.686, '#014421': 0.812, '#FFC0CB': 1.0}

        if "#000000" in hexcolormap:
            opcrcolorscalars = array([strdictb[key] for key in hexcolormap])

            colors = [(0,0,0,255),(255,0,0,255),(150,75,0,255),(255,255,0,255),
                (0,255,255,255),(0,0,255,255),(144,238,144,255),(1,68,33,255),
```

```
                (255,192,203,255)]
            arclen = [28,29,28,28,29,28,28,29,28]

            opcrcolorlut = [colors[i] for i in range(9) for j in range(arclen[i])]

        else:
            opcrcolorscalars = array([strdict[key] for key in hexcolormap])

            colors = [(255,0,0,255),(150,75,0,255),(255,255,0,255),(0,255,255,255),
                (0,0,255,255),(144,238,144,255),(1,68,33,255),(255,192,203,255)]
            arclen = [32,32,32,32,31,32,32,32]
            opcrcolorlut = [colors[i] for i in range(8) for j in range(arclen[i])]

        self.plot3 = self.VisualizeScalars(opcrcolorscalars, opcrcolorlut,
            scale='linear', colorbar=0)

class DNEOptionsWindow(QtGui.QDialog):
    """Submenu for selecting optional parameters for DNE calculation."""
    def __init__(self, parent=None):
        super(DNEOptionsWindow, self).__init__(parent)
        #=====================================================================
        # Submenu layout
        #=====================================================================
        self.layout = QtGui.QVBoxLayout()
        self.layout.setSpacing(25)

        #=====================================================================
        # Submenu widgets
        #=====================================================================
        self.OKbutton = QtGui.QPushButton("OK")
        self.OKbutton.clicked.connect(self.OKClose)

        # Matrix condition number controls
        self.dneconditioncontrolcheck = QtGui.QCheckBox("Condition number checking")
        self.dneconditioncontrolcheck.toggle()

        # Outlier removal controls
        self.dneoutliervallabel = QtGui.QLabel("Percentile")
        self.dneoutlierval = QtGui.QLineEdit("99.9")
        self.dneoutlierval.setFixedWidth(40)
        self.outlierhbox = HBoxWidget([self.dneoutliervallabel, self.dneoutlierval],
            spacing=6)

        self.dneoutliertype1 = QtGui.QCheckBox("Energy x area")
        self.dneoutliertype1.toggle()
        self.dneoutliertype2 = QtGui.QCheckBox("Energy")
        self.dneoutlierbuttons = QtGui.QButtonGroup()
        self.dneoutlierbuttons.addButton(self.dneoutliertype1)
        self.dneoutlierbuttons.addButton(self.dneoutliertype2)
        self.outliervgroup = VGroupBoxWidget('Outlier removal', [self.dneoutliertype1,
            self.dneoutliertype2, self.outlierhbox])

        # Smoothing controls
        self.dneiterationlabel = QtGui.QLabel("Iterations")
        self.dneiteration = QtGui.QLineEdit("3")
        self.dneiteration.setFixedWidth(40)
        self.fairithbox = HBoxWidget([self.dneiterationlabel, self.dneiteration])

        self.dnestepsizelabel = QtGui.QLabel("Step size")
        self.dnestepsize = QtGui.QLineEdit("0.1")
        self.dnestepsize.setFixedWidth(40)
        self.fairesthbox = HBoxWidget([self.dnestepsizelabel, self.dnestepsize])

        self.fairvgroup = VGroupBoxWidget('Implicit fair smooth', [self.fairithbox,
            self.fairesthbox])
        self.fairvgroup.setChecked(0)

        # Visualization control widgets
```

```
        self.dneabsmaxlabel = QtGui.QLabel("Max")
        self.dneabsmaxval = QtGui.QLineEdit("1.0")
        self.dneabsmaxval.setFixedWidth(40)
        self.dneabsminlabel = QtGui.QLabel("Min")
        self.dneabsminval = QtGui.QLineEdit("0.0")
        self.dneabsminval.setFixedWidth(40)
        self.vishbox = HBoxWidget([self.dneabsminlabel, self.dneabsminval,
            self.dneabsmaxlabel, self.dneabsmaxval])

        self.dnerelvischeck = QtGui.QCheckBox("Relative scale")
        self.dnerelvischeck.toggle()
        self.dneabsvischeck = QtGui.QCheckBox("Absolute scale")
        self.dnevisbuttons = QtGui.QButtonGroup()
        self.dnevisbuttons.addButton(self.dnerelvischeck)
        self.dnevisbuttons.addButton(self.dneabsvischeck)
        self.visvgroup = VGroupBoxWidget('Visualize DNE', [self.dnerelvischeck,
            self.dneabsvischeck, self.vishbox])
        self.visvgroup.setChecked(0)

        #=======================================================================
        # Building the submenu layout
        #=======================================================================
        self.layout.addWidget(self.dneconditioncontrolcheck)

        self.layout.addWidget(self.outliervgroup)
        self.layout.addWidget(self.fairvgroup)
        self.layout.addWidget(self.visvgroup)

        self.layout.addWidget(self.OKbutton)
        self.setLayout(self.layout)

        self.setSizePolicy(0, 0)

        self.setWindowTitle('DNE Options')

    def OKClose(self):
        """Closes submenu on OK."""
        self.close()

class OPCROptionsWindow(QtGui.QDialog):
    """Submenu for selecting optional parameters for OPCR calculation."""
    def __init__(self, parent=None):
        super(OPCROptionsWindow, self).__init__(parent)
        #=======================================================================
        # Submenu layout
        #=======================================================================
        self.layout = QtGui.QVBoxLayout()
        self.layout.setSpacing(20)

        #=======================================================================
        # Submenu widgets
        #=======================================================================
        self.OKbutton = QtGui.QPushButton("OK")
        self.OKbutton.clicked.connect(self.OKClose)

        # Visualization and minimum patch size controls
        self.visualizeopcrcheck = QtGui.QCheckBox("Visualize OPCR")
        self.opcrlabel = QtGui.QLabel("Minimum patch count")
        self.opcrminpatch = QtGui.QLineEdit("3")
        self.opcrminpatch.setFixedWidth(40)
        self.minpatchhbox = HBoxWidget([self.opcrlabel, self.opcrminpatch], spacing=15)

        #=======================================================================
        # Building the submenu layout
        #=======================================================================
        self.layout.addWidget(self.minpatchhbox)
        self.layout.addWidget(self.visualizeopcrcheck)
        self.layout.addWidget(self.OKbutton)
```

```
        self.layout.setContentsMargins(20,20,20,20)
        self.setLayout(self.layout)
        self.setSizePolicy(0, 0)

        self.setWindowTitle('OPCR Options')

    def OKClose(self):
        """Closes submenu on OK."""
        self.close()

class HBoxWidget(QtGui.QWidget):
    """Generic class for creating QWidgets with QHBoxLayout with standard properties.

    Args:
        widgetlist (list): List of QWidget objects to be displayed.
        indent (int): Left marginal indentation of HBoxWidget.
        spacing (int): Component spacing of HBoxWidget contents.
    """
    def __init__(self, widgetlist, indent=0, spacing=10):
        super(HBoxWidget,self).__init__()

        self.initUI(widgetlist, indent, spacing)

    def initUI(self, widgetlist, indent, spacing):
        """Adds widgets to and sets layout of HBoxWidget object."""
        self.hbox = QtGui.QHBoxLayout()
        map(lambda x: self.hbox.addWidget(x), widgetlist)
        self.hbox.setContentsMargins(indent,0,0,0)
        self.hbox.setSpacing(spacing)
        self.setLayout(self.hbox)

class VGroupBoxWidget(QtGui.QGroupBox):
    """Generic class for creating QGroupBox with QVBoxLayout with standard properties.

    Args:
        widgetlist (list): List of QWidget objects to be displayed.
        title (str): Title for QGroupBox.
    """
    def __init__(self, title, widgetlist):
        super(VGroupBoxWidget, self).__init__(title)

        self.initUI(widgetlist)

    def initUI(self, widgetlist):
        """Adds widgets to and sets layout of VGroupBoxWidget object."""
        self.vbox = QtGui.QVBoxLayout()
        self.vbox.setContentsMargins(10,10,10,10)
        self.vbox.setSpacing(10)
        map(lambda x: self.vbox.addWidget(x), widgetlist)
        self.setLayout(self.vbox)
        self.setCheckable(1)
        self.setStyleSheet('QGroupBox::title {background-color: transparent}')

class OutLog:
    def __init__(self, edit, out=None, color=None):
        """(edit, out=None, color=None) -> can write stdout, stderr to a
        QTextEdit.

        Args:
            edit (QTextEdit) = QTextEdit object for writing stdout and stderr to.
            out = Alternate stream (can be the original sys.stdout).
            color = Alternate color (i.e. color stderr, a different color).
        """
        self.edit = edit
        self.out = None
        self.color = color

    def write(self, m):
```

```
        if self.color:
            tc = self.edit.textColor()
            self.edit.setTextColor(self.color)

        self.edit.moveCursor(QtGui.QTextCursor.End)
        self.edit.insertPlainText( m )

        if self.color:
            self.edit.setTextColor(tc)

        if self.out:
            self.out.write(m)

def main():
    """Main application loop."""
    window = MainWidget()
    window.show()
    sys.exit(QtGui.qApp.exec_())

if __name__ == "__main__":
    main()
```

v. *normcore.py*: Functions for calculating normal vectors

```
'''
Created on Oct 1, 2015

Functions for the creation and manipulation of normal vectors.

@author: Julia M. Winchester
'''

from numpy import cross, array, sqrt, column_stack, spacing, zeros, isnan, mean, sum

def normal(plane):
    """Given triangle vertices, returns normal vector for triangle as XYZ coordinates."""

    a = plane[0]
    b = plane[1]
    c = plane[2]

    ab = [(b[0]-a[0]),(b[1]-a[1]),(b[2]-a[2])]
    ac = [(c[0]-a[0]),(c[1]-a[1]),(c[2]-a[2])]

    return cross(ab,ac)

def normalmap(varray,farray):
    """Given a list of vertices and polygons, returns array of polygon normal vectors."""
    return array([normal(varray[verts]) for verts in farray])

def normalize(vects):
    """Normalizes (sets magnitude to 1) given vectors."""
    d = sqrt((vects**2).sum(axis=1)) # Square roots of sums of squares of normal vectors,
        i.e. magnitudes of normal vectors
    d = [1 if m < spacing(1) else m for m in d]
    return vects/column_stack((d,d,d)) # each face has its normal vector XYZ divided by
        that vector's magnitude. this normalizes the vector, i.e. gives it a magnitude of
        1.

def computenormal(varray, faceindex, fvarray, vfarray):
    """Given a polygonal mesh, returns unit normals for polygons and unit normals of
    vertices (approximated as average of associated polygon normals)."""
    nvert = len(varray)

    fnormal = normalmap(varray,faceindex)
    # normalize face normals
    fnormal4 = normalize(fnormal)

    # unit normals of vertices
    vnormal = zeros([nvert,3],float)
    for vindex, faces in vfarray.iteritems():
        vnormal[vindex] = sum(fnormal4[faces], axis=0)
        if isnan(fnormal4[faces]).any(): print "nan found during vertex normal creation
            at vertex #: " + str(vindex)

    # normalize vertex normals
    vnormal4 = normalize(vnormal)

    # check for nan values in vnormal4
    for i, norm in enumerate(vnormal4):
        if isnan(norm).any():
            print "nan vnormal 4 entry found"
            print "corresponding vnormal entry:"
            print norm

    # enforce that normals are outward
    mvertex = mean(varray,1)
    repmvertex = column_stack((mvertex,mvertex,mvertex))
    v = varray - repmvertex
    s = sum((v*vnormal4),0)
```

```
s2 = 0
s3 = 0

for i in s:
    if i > 0:
        s2 += 1
    if i < 0:
        s3 += 1
if s2 < s3:
    print 'Outward normal flipping has occurred'
    vnormal4 = -vnormal4
    fnormal4 = -fnormal4

return [vnormal4, fnormal4]
```

vi. *OPC.py*: Orientation patch count rotated algorithm

```
'''
Created on Sep 2, 2011

This module calculates Orientation Patch Count Rotated for a provided 3D mesh
through MeshOPCR class. See Evans et al. 2007 and Winchester (in review) for
details on method.

@author: Julia M. Winchester
'''

from copy import copy as pcopy
from numpy import array, matrix, mat, transpose, average, subtract, row_stack
from numpy import mean as amean
from collections import defaultdict

import math
import normcore

class MeshOPCR(object):
    """Class for calculating and storing Orientation patch count rotated values for
    polygonal mesh data.

    When instanced, this class calculates OPCR and associated variables
    and stores them. All attributes listed below are populated on instantiation.

    Args:
        TopoMesh (TopoMesh object): Triangulated polygon mesh data.
        minpatch (int): Minimum size in polygons for patches to be counted.

    Attributes:
        Mesh (TopoMesh object): Triangulated polygon mesh data.
        theta (float): Radians of OPC rotations for OPCR calculation.
        n_rotations (int, 8): Number of OPC rotations for OPCR calculation.
        opc_list (list): List of OPC at each of 8 rotations. The average
            of these values is OPCR.
        patches_list (list): List of lists. Contains 8 lists (one per
            rotation), each of which lists all counted surface patches for
            that rotation.
        colormap_list (list): List of lists. Contains 8 lists (one per
            rotation), each of which lists polygons sorted into colors
            based on XY aspect (direction that polygon faces) for that
            rotation.
        vert_tri_dict (dict): Associates vertex index keys with related
            face index values.
        fnormal (ndarray): Normalized unit normals of surface polygons.
        vnormal (ndarray): Normalized approximated unit normals of surface
            vertices (approximated as average of normals of associated faces).
        OPCR (float): Orientation patch count rotated. Average of opc_list.
    """
    def __init__(self, TopoMesh, minpatch):
        self.Mesh = TopoMesh
        self.MeshRotated = None
        self.min_patch_size = int(minpatch)
        self.theta = math.radians(5.625)
        self.n_rotations = 8
        self.opc_list = [None, None, None, None, None, None, None, None]
        self.patches_list = [None, None, None, None, None, None, None, None]
        self.colormap_list = [None, None, None, None, None, None, None, None]
        self.vert_tri_dict = None
        self.fnormal = None
        self.vnormal = None
        self.OPCR = None

        self.calcopcr()

    def calcopcr(self):
```

```
    """Method for calculating OPCR and associated variables from surface mesh. Calls
    internal methods."""
    self.Mesh = pcopy(self.Mesh)
    self.Mesh.vertices = self._centermesh(self.Mesh.vertices)
    self.MeshRotated = pcopy(self.Mesh)

    self._get_vert_tri_dict()

    self.opc_list[0], self.patches_list[0], self.colormap_list[0] =
    self._get_opc(self.Mesh.vertices, self.Mesh.faces, self.Mesh.triverts)

    for i in range(1,self.n_rotations):
            self._rotatemesh()
            self.opc_list[i], self.patches_list[i], self.colormap_list[i] =
                self._get_opc(self.MeshRotated.vertices, self.MeshRotated.faces,
                self.MeshRotated.triverts)

    self.OPCR = average(self.opc_list)

def _get_opc(self, vertices, faces, triverts):
    """Calculates and returns OPC, list of patches, and list of polygons sorted into
    color bins by XY aspect."""
    self.vnormal, self.fnormal = normcore.computenormal(vertices, faces, triverts,
        self.vert_tri_dict)

    flatfaces = array([i for i, norm in enumerate(self.fnormal) if (norm[0:1] ==
        0).all()], dtype=int)
    orientation_map = array([self._xydegrees(norm[1],norm[0]) for norm in
        self.fnormal])

    color_map = array([self._sort_to_colors(aspect_theta) for aspect_theta in
        orientation_map])
    color_map[flatfaces] = '#000000'

    pairdict = defaultdict(list) #lists per vertex all possible pairs of polygons
        that include that vertex
    for vertex, faces in self.vert_tri_dict.iteritems():
        pairdict[vertex] = self._pair_faces(faces)

    adjacent_face_pairs = self._adjacent_face_pairs(pairdict)

    same_color_pairs = [pair for pair in adjacent_face_pairs if color_map[pair[0]] ==
        color_map[pair[1]]]

    color_face_dict = defaultdict(list) # lists adjacent polygon pairs for each color
        bin
    for item in same_color_pairs:
        color_face_dict[color_map[item[0]]].append(item)

    colorlist = ['#FF0000','#964B00','#FFFF00','#00FFFF','#0000FF','#90EE90',
        '#014421','#FFC0CB']

    patches = [self._build_patches(color_face_dict[color]) for color in colorlist]

    patches = [self._cull_small_patches(subpat,self.min_patch_size) for subpat in
        patches]

    opc = sum([len(subpat) for subpat in patches])

    return [opc, patches, color_map]

def _centermesh(self, vert_sequence):
    """Translates mesh centroid to XYZ coordinate origin."""
    centroid = amean(vert_sequence, axis=0)
    return array([subtract(vert,centroid) for vert in vert_sequence])

def _get_vert_tri_dict(self):
    """Generates dictionary associating vertex index keys with related polygon index
```

```
    values."""
    self.vert_tri_dict = defaultdict(list)

    for findex, face in enumerate(self.Mesh.faces):
        for vertex in face:
            self.vert_tri_dict[vertex].append(findex)

def _rotatemesh(self):
    """Rotates mesh theta radians around Z-axis."""
    zrotmat = matrix([[math.cos(self.theta),(-
        1*math.sin(self.theta)),0],[math.sin(self.theta),math.cos(self.theta),0],
        [0,0,1]])

    vert_matrix = mat(self.MeshRotated.vertices)
    rotated_verts = row_stack([transpose(zrotmat * transpose(vert)) for vert in
        vert_matrix])
    self.MeshRotated.vertices = array(rotated_verts)

def _xydegrees(self, y, x):
    """Given a vector (x,y) returns angle of vector from the positive X-axis."""
    vectangle = math.degrees(math.atan2(y,x))
    if vectangle < 0:
        return vectangle+360
    else:
        return vectangle

def _sort_to_colors(self, aspect_theta):
    """Given a polygon XY aspect angle, returns the appropriate bin for color
    sorting."""
    colorlist = ['#FF0000','#964B00','#FFFF00','#00FFFF','#0000FF','#90EE90',
        '#014421','#FFC0CB']
    modtheta = (aspect_theta + 22.5) % 360
    group = int(modtheta//45)
    return colorlist[group]

def _pair_faces(self, inputlist):
    """Given a list of numbers, returns all possible pairs of numbers without
        replication or identical-number pairs."""
    return [(x,y) for x in set(inputlist) for y in set(inputlist) if x < y]

def _adjacent_face_pairs(self, pairdict):
    """Given a list of polygon face pairs sharing vertices, returns the subset of
       polygon pairs where pair members share an edge."""
    touching_list = list()
    seen = set()
    seentwice = set()
    for item in pairdict:
        for pair in pairdict[item]:
            if pair in seen:
                touching_list.append(pair)
                if pair in seentwice:
                    print "WARNING: POSSIBLE IDENTICAL TRIANGLES AT ", pair
                else:
                    seentwice.add(pair)
            else:
                seen.add(pair)
    return touching_list

def _build_patches(self, face_pairs):
    """Given a list of adjacent pairs of polygons on a surface, returns list of all
       contiguous patches of polygons involving provided pairs."""
    patcheslist = list()
    for pair in face_pairs:
        wassorted = list()
        for i, clumppatch in enumerate(patcheslist):
            if pair[0] in clumppatch or pair[1] in clumppatch:
                clumppatch.add(pair[0])
                clumppatch.add(pair[1])
```

```
                wassorted.append(i)
                continue

        if len(wassorted) == 0:
            patcheslist.append(set([pair[0],pair[1]]))

        if len(wassorted) > 1:
            tempset = set()
            for sortpair in wassorted:
                tempset = tempset | patcheslist[sortpair]
            patcheslist[wassorted[0]] = tempset
            for i in wassorted[1:]:
                del patcheslist[i]

    return patcheslist

def _cull_small_patches(self, patches, minsize):
    """Given a list of patches, returns only patches with numbers of polygons equal
        to or greater than minsize."""
    return [patch for patch in patches if len(patch) >= minsize]
```

vii. *plython.py*: Module for creation and saving of .ply polygonal meshes

```
'''
Created on Sep 1, 2011

Plython opens .ply files and produces simple numpy arrays with polygon vertex and face
data. Using the createarray() function, this module reads ASCII-format .ply (binary is
not supported to date) and returns numpy arrays representing position of mesh vertices
and connections between vertices to produce interconnected triangular polygon faces. A
savearray() function is also provided to save arrays of mesh data (formatted similarly to
arrays returned by the createarray() function).

Mesh .ply files are initiated with headers defining basic mesh properties and subsequent
lists of mesh property data. To read mesh files, the functions included here first
retrieve the number of polygon vertices and faces from the header. XYZ coordinate
triplets for polygon vertices are then read and stored as an i x 3 array where i equals
number of vertices and assuming triangular polygons. After this lists of polygon vertices
(identified as indices from the first array) comprising each mesh are read and stored in
two arrays. One array stores XYZ coordinate triplets for each vertex comprising each
polygon, producing a j x i x 3 array where i equals vertex number and j equals face
number. For greater efficiency, this data is also stored in a j x 3 array listing vertex
indices (from the first array described above) comprising each face. createarray()
returns these three arrays as a list in the order described.

@author: Julia M. Winchester
'''
from numpy import array
from struct import unpack

class PlythonMesh(object):
    """A class for creating and interacting with triangulated polygon meshes.

    Creates a list of Numpy ndarray objects containing triangulated polygon
    mesh data if provided with a path to a .ply file.

    Args:
        filepath (str): Path to a .ply polygon mesh file.

    Attributes:
        mesh (list): Triangulated polygon mesh data. Contains three ndarrays:
            vertex XYZ points, polygons with component vertex XYZ points,
            and polygons with component vertex indices.
        vertices (ndarray): Vertex XYZ points for mesh.
        faces (ndarray): Polygons with component vertex indices for mesh.
        triverts (ndarray): Polygons with component vertex XYZ points for mesh.
        nvert (int): Number of vertices in mesh.
        nface (int): Number of polygons in mesh.

    """
    def __init__(self, filepath=""):
        self.mesh = None
        self.vertices = None
        self.faces = None
        self.triverts = None
        self.nvert = 0
        self.nface = 0

        if filepath is not "":
            self.CreateArray(filepath)

    def CreateArray(self, filepath):
        """Creates triangulated polygon mesh data objects from .ply file.

        Args:
            filepath (str): Path to a .ply polygon mesh file.

        """
        meshfile = open(filepath, 'r')
```

```
        meshstring = meshfile.read()
        meshfile.close()


        datamode = self._StringAfter(meshstring, 'format')
        self.nvert = int(self._StringAfter(meshstring,'element vertex'))
        self.nface = int(self._StringAfter(meshstring,'element face'))

        if datamode == "ascii" or datamode == "ASCII":
            self.vertices, self.faces, self.triverts = self._read_ascii(meshstring)
        else:
            self.vertices, self.faces, self.triverts = self._read_bin(meshstring,
                datamode)

        self.mesh = [self.vertices, self.triverts, self.faces]

        self.check_mesh_consistency()

    def _read_ascii(self, meshstring):
        """Reads ASCII mesh data."""
        meshdata = meshstring[meshstring.find('end_header'):].splitlines()[1:]

        if len(meshdata) < self.nvert:
            raise EOFError('Unexpected end of .PLY file in list of vertices.')

        vlist = meshdata[0:self.nvert]

        if len(meshdata[self.nvert:]) < self.nface:
            raise EOFError('Unexpected end of .PLY in list of polygon vertex indices.')

        flist = meshdata[self.nvert:(self.nvert+self.nface)]

        if flist[0][0] != '3':
            raise ValueError('Non-triangular polygons found within .PLY file.')

        varray = array([vertices.split() for vertices in vlist], float)
        farray = array([vertices.split()[1:4] for vertices in flist], int)
        vfarray = array([[varray[vindex] for vindex in vertices] for vertices in farray],
            float)

        return varray, farray, vfarray

    def _read_bin(self, meshstring, mode):
        """Reads binary mesh data."""
        if mode == "binary_little_endian":
            byteorder = "<"
        elif mode == "binary_big_endian":
            byteorder = ">"

        meshdata = meshstring[meshstring.find('end_header')+11:]

        # Expected number of bytes for vertex data, assumes 3 XYZ coordinate float values
        vertbytes = self.nvert*3*4
        # Expected number of bytes for face data, assumes unsigned char (= 3) and 3
            integer vertex index values
        facebytes = self.nface*(3*4+1)

        if len(meshdata) < vertbytes:
            raise EOFError('Unexpected end of .PLY file in list of vertices.')

        vertdata = meshdata[0:vertbytes]

        if len(meshdata[vertbytes:]) < facebytes:
            raise EOFError('Unexpected end of .PLY in list of polygon vertex indices.')

        facedata = meshdata[vertbytes:vertbytes+facebytes]

        if unpack(byteorder+'B', facedata[0])[0] != 3:
```

```
            raise ValueError('Non-triangular polygons found within .PLY file.')

        vert_xyz_split = [vertdata[i:i+4] for i in range(0, vertbytes, 4)]
        vert_xyz_points = map(lambda x: unpack(byteorder+'f', x)[0], vert_xyz_split)
        vert_array = array(vert_xyz_points)
        vert_array = vert_array.reshape([self.nvert,3])

        face_split = [facedata[i:i+13] for i in range(0, facebytes, 13)]
        face_index_split = [[face[i:i+4] for i in range(1, len(face), 4)] for face in
            face_split]
        face_index_value = [[unpack(byteorder+'i', index)[0] for index in face] for face
            in face_index_split]
        face_array = array(face_index_value)
        face_array = face_array.reshape([self.nface,3])

        vert_face_array = array([[vert_array[vertex] for vertex in face] for face in
            face_array], float)

        return vert_array, face_array, vert_face_array

    def check_mesh_consistency(self):
        """Checks mesh data produced by CreateArray for consistency, raises exceptions if
        mesh is inconsistent or nonexistent."""
        if self.vertices is None or self.faces is None or self.triverts is None:
            raise ValueError('Mesh data is missing.')
        if len(self.vertices) != self.nvert or len(self.faces) != self.nface or
            len(self.triverts) != self.nface:
            raise ValueError('Unexpected vertex, face, or face-vertex index length, mesh
                is inconsistent.')
        for i, trivert in enumerate(self.triverts):
            if (trivert != self.vertices[self.faces[i]]).any():
                raise ValueError("Mesh vertex and face arrays do not contain identical
                    vertices, mesh is inconsistent.")

    def SaveArray(self, filepath):
        """Saves mesh as an ASCII .ply format triangulated surface file.

        Args:
            filepath (str): Path to a .ply polygon mesh file to be created.

        """
        self.check_mesh_consistency()

        arrayfile = open(filepath,'w')
        arrayfile.write("ply\nformat ascii 1.0\nelement vertex %s\n" % self.nvert)
        arrayfile.write("property float32 x\nproperty float32 y\nproperty float32
            z\nelement face %s\nproperty list uint8 int32 vertex_indices\nend_header\n" %
            self.nface)

        for xyz in self.Vertices():
            arrayfile.write(str(xyz[0])+" "+str(xyz[1])+" "+str(xyz[2])+"\n")

        for vertexindices in self.Triangles():
            arrayfile.write("3 " + str(int(vertexindices[0]))+"
            "+str(int(vertexindices[1]))+" "+str(int(vertexindices[2]))+"\n")

        arrayfile.close()

    def Vertices(self):
        """Returns vertex XYZ data points."""
        return self.vertices

    def TriVert(self):
        """Returns polygons with component vertex XYZ data points."""
        return self.triverts

    def Triangles(self):
        """Returns polygons with component vertex indices."""
```

```
    return self.faces

def Mesh(self):
    """Returns triangulated polygon mesh data."""
    return self.mesh

def _StringAfter(self,text,phrase):
    """Internal method for finding first discrete word or number (separated by
        spaces) after phrase in text."""
    try:
        return text[text.index(phrase)+len(phrase):].split()[0]
    except (ValueError, IndexError) as err:
        err.args += ('Phrase %s is not in text %s, is longer than text, or is last
            element in text.' % (phrase, text),)
        raise
```

viii. *render.py*: Functions for plotting 2D outline of 3D surface mesh

```
'''
Created on Sep 8, 2011

This module contains three functions that plot the 2D projection of a 3D mesh in
the XY plane and measure the absolute area of the mesh projection. The function
plotmeshoutline() plots a) the provided mesh in blue over the X and Y axes and
b) a red scalebar where length is known in coordinate units and pixels. This
produces a "flat" 2D projection of the 3D mesh input on the XY plane. The plot
is then returned as a StringIO file-like object and the scalebar pixel length
is returned as a float. The function areafromrender() uses the image buffer and
the scalebar pixel length to derive the absolute projection area ("outline
area") of the 3D mesh in the XY plane.

@author: Julia M. Winchester
'''
import matplotlib
matplotlib.use('AGG')

import matplotlib.pyplot as plt
from StringIO import StringIO
from numpy import array,amax,amin,square

try:
       import Image
except ImportError:
       from PIL import Image

def countpixels(image, colorlist): # Returns the number of pixels in a list of
    RGB+transparency values that match the colors (RGB+transparency) given in colorlist
    return sum(list(image).count(color) for color in colorlist)

def areafromrender(linelength, strbuffer): # Receives image plot from StringIO object and
    returns absolute area covered by mesh as projected on XY plane
    strbuffer.seek(0) # Rewind image buffer back to beginning to allow Image.open() to
        identify it
    img = Image.open(strbuffer).getdata()
    strbuffer.close()
    redpixie = countpixels(img, [(255,0,0,255),(255,127,127,255)])

    bluepixie = len(list(img)) - countpixels(img, [(255, 0, 0, 255), (255, 255, 255,
        255), (255, 155, 155, 255), (255, 188, 188, 255), (255, 230, 230, 255), (255,
        205, 205, 255)])
    print "blue pixels = " + str(bluepixie)

    rope = float(linelength)
    print "line = " + str(rope)

    redballoon = float(redpixie)
    print "red pixels = " + str(redballoon)

    # This is a very verbose explanation of the returned value
    #pixel_length_ratio = float(red_balloons/line)
    #print "pixel length ratio = " + str(pixel_length_ratio)
    #red_height_mm = line
    #red_width_mm = float(1*(1/pixel_length_ratio))
    #red_area_mm2 = red_height_mm*red_width_mm
    #pixel_area_ratio = float(red_balloons/red_area_mm2)
    #blue_area_mm2 = float(blue_pixels)*(1.0/pixel_area_ratio)

    return float(bluepixie)*(square(rope)/square(redballoon))

def plotmeshoutline(mesh): # Returns pixel length of scalebar and image plot as StringIO
file-like object
    xarray = mesh[0][:,0]
    yarray = mesh[0][:,1]
```

```
    xaxismin = amin(xarray) - 0.5
    xaxismax = amax(xarray) + 0.5
    yaxismin = amin(yarray) - 0.5
    yaxismax = amax(yarray) + 0.5
    linelength = amax(yarray) - amin(yarray) + 1

    fig = plt.figure()
    ax = fig.add_subplot(111)

    linesquare = matplotlib.patches.Polygon([[xaxismin,yaxismin],[xaxismin,yaxismax]],
        ec='r',fc='r')
    plt.axis([xaxismin,xaxismax,yaxismin,yaxismax])
    ax.add_patch(linesquare)

    ax.set_xscale('linear')
    ax.set_yscale('linear')
    ax.set_aspect(1)
    ax.axis('off')

    vert = array([face[:,[0,1]] for face in mesh[1]]) # makes a copy of mesh[1] including
        only XY coordinate points for vertices comprising faces

    polygons = matplotlib.collections.PolyCollection(vert,facecolor='b',edgecolor='b')

    ax.add_collection(polygons)

    imgbuffer = StringIO()
    plt.savefig(imgbuffer,format='png')
    return linelength, imgbuffer

def meshprojectionarea(mesh):
    linelength, imgbuffer = plotmeshoutline(mesh)
    return areafromrender(linelength, imgbuffer)
```

ix. *RFI.py*: Relief index algorithm

```
'''
Created on Sep 2, 2011

This module calculates relief index (3D surface area/2D area of surface
projected on XY plane) for a provided 3D mesh using the MeshRFI class.

@author: Julia M. Winchester
'''

import matplotlib
matplotlib.use('AGG')

import warnings
import matplotlib.pyplot as plt
from StringIO import StringIO
from numpy import sqrt, square, amin, amax, array, array_equal
from numpy.linalg import det

try:
    import Image
except ImportError:
    from PIL import Image

class MeshRFI(object):
    """Class for calculating and storing relief index values for polygonal mesh data.

    When instanced, this class calculates relief index and associated variables
    and stores them. All attributes below are populated on instantiation.

    Args:
        TopoMesh (TopoMesh object): Triangulated polygon mesh data.

    Attributes:
        Mesh (TopoMesh object): Triangulated polygon mesh data.
        RFI (float): Mesh surface relief index (surfarea/projarea).
        surfarea (float): 3D mesh surface area.
        projarea (float): 2D mesh surface area projected on XY plane.
        linelin (float): Reference line for building pixel/area unit ratio.
        bluepixie (float): Number of blue pixels (mesh) on projected area render.
        redpixie (float): Number of red pixels (reference line) on projected area render.
        pixelratio (float): Pixel/area unit ratio, used for converting number of
                            blue pixels to area units.
        imgbuffer (StringIO object): 2D plot of surface mesh with reference line for
                                     determining projected XY-plane surface area.
    """
    def __init__(self, TopoMesh):
        self.Mesh = TopoMesh
        self.RFI = None
        self.surfarea = None
        self.projarea = None
        self.linelen = None
        self.bluepixie = None
        self.redpixie = None
        self.pixelratio = None
        self.imgbuffer = None

        self._check_mesh_consistency()

        self.calcrfi()

    def calcrfi(self):
        """Calls methods for calculating surface and projected areas, then derives relief
        index value."""
        self.surfarea = round(sum(self._triangle_area(face) for face in
            self.Mesh.triverts),3)
        self._get_projection_area()
```

```
    self.RFI = round(self.surfarea/self.projarea, 3)

def _get_projection_area(self):
    """Creates 2D plot of surface mesh and derives projection area from this plot."""
    self._plot_surface()
    self._get_2d_area()

def _plot_surface(self): # Returns pixel length of scalebar and image plot as
    StringIO file-like object
    """Plots 3D polygonal mesh as 2D raster shape on the XY plane with reference line
    for area units."""
    xarray = self.Mesh.vertices[:,0]
    yarray = self.Mesh.vertices[:,1]

    xaxismin = amin(xarray) - 0.5
    xaxismax = amax(xarray) + 0.5
    yaxismin = amin(yarray) - 0.5
    yaxismax = amax(yarray) + 0.5
    self.linelen = amax(yarray) - amin(yarray) + 1.0

    if self.linelen == 1.0:
        raise ValueError("Polygon mesh has a zero area projected in the XY plane.")

    fig = plt.figure()
    ax = fig.add_subplot(111)

    linesquare =
        matplotlib.patches.Polygon([[xaxismin,yaxismin],[xaxismin,yaxismax]],
        ec='r',fc='r')
    plt.axis([xaxismin,xaxismax,yaxismin,yaxismax])
    ax.add_patch(linesquare)

    ax.set_xscale('linear')
    ax.set_yscale('linear')
    ax.set_aspect(1)
    ax.axis('off')

    vert = array([face[:,[0,1]] for face in self.Mesh.triverts]) # makes a copy of
        self.Mesh.triverts including only XY coordinate points for vertices
        comprising faces

    polygons =
        matplotlib.collections.PolyCollection(vert,facecolor='b',edgecolor='b')

    ax.add_collection(polygons)

    self.imgbuffer = StringIO()
    plt.savefig(self.imgbuffer,format='png')

def _get_2d_area(self): # Receives image plot from StringIO object and returns
    absolute area covered by mesh as projected on XY plane
    """Derives 2D surface area of polygonal mesh projected on XY plane given a 2D
       raster plot and area-unit reference line."""
    if isinstance(self.imgbuffer, StringIO) is not True:
        raise TypeError("Non-StringIO object provided for imgbuffer.")

    self.imgbuffer.seek(0) # Rewind image buffer back to beginning to allow
        Image.open() to identify it
    img = Image.open(self.imgbuffer).getdata()


    self.redpixie = self._count_pixels(img, (255,0,0,255), (255,127,127,255))
    self.bluepixie = len(list(img)) - self._count_pixels(img, (255, 0, 0, 255), (255,
        255, 255, 255), (255, 155, 155, 255), (255, 188, 188, 255), (255, 230, 230,
        255), (255, 205, 205, 255))

    rope = float(self.linelen)
    redballoon = float(self.redpixie)
```

```
    self.pixelratio = redballoon/rope

    self.projarea = round(float(self.bluepixie)*(square(rope)/square(redballoon)), 3)

def _count_pixels(self, image, *args): # Returns the number of pixels in a list of
    RGB+transparency values that match the colors (RGB+transparency) given in
    colorlist
    """Returns the number of pixels in an image that match colors given as *args.

    Args:
        image (StringIO object): Image string buffer object from which pixels are
            counted.
        *args: Series of lists or tuples of RGB+transparency value color data. Pixels
            in image that match these colors will be counted.
    """
    return sum([list(image).count(color) for color in set(args)])

def _triangle_area(self, verts):
    """Returns the area of a triangle defined by vertices.

    Args:
        verts(ndarray): A set of three XYZ point triplets forming a triangle.
    """
    fx = verts[:,0]
    fy = verts[:,1]
    fz = verts[:,2]
    fc = [1,1,1]

    a = [fx, fy, fc]
    b = [fy, fz, fc]
    c = [fz, fx, fc]

    return 0.5*sqrt(square(det(a))+square(det(b))+square(det(c)))

def _check_mesh_consistency(self):
    """Checks mesh vertex and face-vertex arrays to ensure identical vertices
    throughout."""
    for i, trivert in enumerate(self.Mesh.triverts):
        if (trivert != self.Mesh.vertices[self.Mesh.faces[i]]).any():
            raise ValueError("Mesh vertex and face arrays do not contain identical
                vertices.")
```

x. *topomesh.py*: Class for storing polygonal surface meshes and associated topographic data

```
'''
Created on Jan 10, 2016

@author: Julia M. Winchester
'''
import plython
import DNE
import OPC
import RFI
import implicitfair

from collections import defaultdict

class TopoMesh(plython.PlythonMesh):
    """A class for creating and interacting with triangulated polygon meshes and
    topographic variables.

    Class inherits from plython.PlythonMesh. Creates a list of Numpy ndarray objects
    containing triangulated polygon mesh data if provided with a path to a .ply file.
    Topographic variables are instanced as None and take the data types specified below
    when generated using the ProcessSurface method.

    Args:
        filepath (str): Path to a .ply polygon mesh file

    Attributes:
        mesh (list): Triangulated polygon mesh data. Contains three ndarrays:
            vertex XYZ points, polygons with component vertex XYZ points,
            and polygons with component vertex indices.
        nvert (int): Number of vertices in mesh.
        nface (int): Number of polygons in mesh.
        vertices (ndarray): Vertex XYZ points for mesh.
        faces (ndarray): Polygons with component vertex indices for mesh.
        triverts (ndarray): Polygons with component vertex XYZ points for mesh.
        DNE (float): Total Dirichlet normal energy of mesh.
        DNEscalars (ndarray): Scalars for visualizing DNE.
        conditionfaces (list): List of polygon face indices with high matrix condition
            numbers.
        boundaryfaces (list): List of polygon face indices forming mesh edges.
        outlierfaces (list): List of polygon face indices removed as outliers, with DNE
            values and face areas.
        RFI (float): Relief index of mesh (surface area/projected area).
        surfarea (float): 3D surface area of mesh.
        projarea (float): 2D surface area of mesh projected on XY plane.
        OPCR (float): Orientation patch count rotated for mesh.
        OPClist (list): Orientation patch counts at 8 rotations for mesh.
        OPCscalars: Scalars for visualizing OPC.

    """
    def __init__(self, filepath=""):
        super(TopoMesh,self).__init__(filepath)

        self.DNE = None
        self.DNEscalars = None
        self.conditionfaces = None
        self.boundaryfaces = None
        self.outlierfaces = None

        self.RFI = None
        self.surfarea = None
        self.projarea = None
        self.linelen = None
        self.bluepixie = None
        self.redpixie = None
        self.pixelratio = None
```

```
        self.OPCR = None
        self.OPClist = None
        self.OPCscalars = None

    def GenerateDNE(self, dosmooth, smoothit, smoothstep, docondition, dooutlier,
        outlierperc, outliertype, filename):
        """Calculates Dirichlet normal energy (surface bending) from mesh data.

        For details on args, see DNE.MeshDNE class.

        Args:
            doSmooth (bool): If true, do implicit fair smooth.
            SmoothIt (int): Iterations of smoothing
            SmoothStep (float): Smoothing step size.
            doCondition (bool): If true, do polygon condition number control.
            doOutlier (bool): If true, do outlier removal.
            OutlierPerc (float): Outlier percentile.
            OutlierType (bool): If true, outliers as energy*area. If false, outliers as
energy.

        """
        self.check_for_mesh(self.GenerateDNE)

        surfcurv = DNE.MeshDNE(self, dosmooth, smoothit, smoothstep, docondition,
            dooutlier, outlierperc, outliertype, filename)
        self.DNE = surfcurv.DNE
        self.DNEscalars = surfcurv.equantity
        self.conditionfaces = surfcurv.high_condition_faces
        self.boundaryfaces = surfcurv.boundary_faces
        self.outlierfaces = surfcurv.outlier_faces

    def GenerateRFI(self):
        """Calculates relief index (surface relief) from mesh data."""
        self.check_for_mesh(self.GenerateRFI)

        surfrelf = RFI.MeshRFI(self)
        self.RFI = surfrelf.RFI
        self.surfarea = surfrelf.surfarea
        self.projarea = surfrelf.projarea
        self.linelen = surfrelf.linelen
        self.bluepixie = surfrelf.bluepixie
        self.redpixie = surfrelf.redpixie
        self.pixelratio = surfrelf.pixelratio

    def GenerateOPCR(self, minpatch):
        """Calculates orientation patch count rotated (surface complexity) from mesh
            data.

        For details on args see OPC.MeshOPCR class.

        Args:
            minpatch (int): Minimum size for counting patches.

        """
        self.check_for_mesh(self.GenerateOPCR)

        surfcomp = OPC.MeshOPCR(self, minpatch)
        self.OPCR = surfcomp.OPCR
        self.OPClist = surfcomp.opc_list
        self.OPCscalars = surfcomp.colormap_list[0]

    def implicit_fair_mesh(self, iterations, step):
        self.get_vert_tri_dict()
        faired_vertices = implicitfair.smooth(self.vertices, self.faces, iterations,
            step, self.vert_tri_dict)
        self.vertices = faired_vertices
        self.mesh[0] = faired_vertices
```

```
    for i in range(len(self.triverts)):
        self.triverts[i] = self.vertices[self.faces[i]]

    self.mesh[1] = self.triverts

def get_vert_tri_dict(self):
    """Generates dictionary associating vertex index keys with related polygon index
        values."""
    self.vert_tri_dict = defaultdict(list)

    for findex, face in enumerate(self.faces):
        for vertex in face:
            self.vert_tri_dict[vertex].append(findex)

def check_for_mesh(self, function="function"):
    if self.mesh == None:
        raise ValueError('A mesh has not been imported, %s cannot proceed.' %
            function)
```

A1.2.2: Supporting scripts for MorphoTester

Supporting scripts for MorphoTester are listed alphabetically and include:

i. *BINtoASC*.py: Script to convert binary .ply format files to ASCII .ply format, requires *meshconv* (Min, 2016)
ii. *meshrotate*.py: Rotates mesh or meshes around X, Y, or Z axes
iii. *meshrotate*-batch.py: Rotates meshes around X and Y axes in steps from 0 to 30 degrees (0, 2, 4, 6, …, 30)
iv. *PLYtoOFF*.py: Script to convert .ply format surfaces to .off format, requires *meshconv* (Min, 2016)

i. *BINtoASC*.py: Script to convert binary .ply format files to ASCII .ply format, requires *meshconv* (Min, 2016)

```
'''
Created on Jan 21, 2015

@author: Julia M. Winchester

Script requires meshconv (http://www.cs.princeton.edu/~min/meshconv/) for usage.
'''

import sys
import os

# Replace with desired directory
dirpath = "/Users/Username/meshes"

# Replace with location of meshconv
meshconv = "/Users/Username/meshconv"

for filename in os.listdir(dirpath):
    fullpath = os.path.join(dirpath,filename)
    newfilename = filename[0:-4]
    os.system(meshconv + " " + fullpath + " -c ply -o " +
        os.path.join(dirpath,newfilename) + "-asc " + "-ascii")
```

ii. *meshrotate*.py: Rotates mesh or meshes around X, Y, or Z axes

```
'''
Created on Jun 25, 2014

@author: Julia M. Winchester

Command line utility for rotating meshes around X/Y/Z axes. It will batch rotate all
ascii ply files in the given directory the supplied number of degrees around the supplied
axis.

Usage: python meshrotate.py <directory> <degrees> <x/y/z> <output addendum>
'''

import plython
import math
import numpy
import os
from sys import argv

dirpath = argv[1]
degrees = argv[2]
axis = argv[3]
addendum = argv[4]

def Check_Zero_Centroid(mesh):
    # Calculates centroid by averaging X Y and Z coordinates
    mesht = numpy.transpose(mesh[0])

    X = numpy.average(mesht[0])
    Y = numpy.average(mesht[1])
    Z = numpy.average(mesht[2])

    centroid = [X,Y,Z]

    # If Centroid isn't at the origin, translates coordinates to origin

    if centroid[0] != 0 or centroid[1] != 0 or centroid[2] != 0:
        mesht[0] = numpy.subtract(mesht[0],centroid[0])
        mesht[1] = numpy.subtract(mesht[1],centroid[1])
        mesht[2] = numpy.subtract(mesht[2],centroid[2])

    # Retransposes mesh to achieve original dimensions
    mesh[0] = numpy.transpose(mesht)

    return mesh

def RotateMesh(mesh, theta, axis):
    # z rotation matrix using theta supplied in radians
    xrotmat = numpy.matrix([[1,0,0],[0,math.cos(theta),-
        1*math.sin(theta)],[0,math.sin(theta),math.cos(theta)]])
    yrotmat = numpy.matrix([[math.cos(theta), 0, math.sin(theta)],[0,1,0],[-
        1*math.sin(theta),0,math.cos(theta)]])
    zrotmat = numpy.matrix([[math.cos(theta),(-
        1*math.sin(theta)),0],[math.sin(theta),math.cos(theta),0],[0,0,1]])
    specialrotmat = numpy.matrix([[0.98675376,-0.1486028,0.06507106],[-0.15098283,-
        0.9879753,0.03330231],[-0.05933978,0.0426858,0.99732478]])

    meshm = numpy.mat(mesh[0])

    if axis == "z":
        rotmat = zrotmat
    if axis == "y":
        rotmat = yrotmat
    if axis == "x":
        rotmat = xrotmat
    if axis == "special":
        rotmat = specialrotmat
```

```
    # using matrix multiplication, multiplies xyz triplets by rotation matrix to rotate
entire xyz point cloud
    for i in range(len(mesh[0])):
        XYZ = numpy.transpose(meshm[i])
        XYZprime = rotmat * XYZ
        meshm[i] = numpy.transpose(XYZprime)

    mesh[0] = numpy.asarray(meshm)

    return mesh

def Main():
    dirpath = argv[1]
    degrees = argv[2]
    axis = argv[3]
    addendum = argv[4]

    radians = math.radians(float(degrees))

    for filename in os.listdir(dirpath):
        if filename[-3:] == "ply":
            mesh = plython.CreateArray(os.path.join(dirpath,filename))
            mesh = Check_Zero_Centroid(mesh)
            mesh = RotateMesh(mesh,radians,axis)
            newfilename = filename[:-4] + addendum + ".ply"
            plython.SaveArray(mesh[0],mesh[2],os.path.join(dirpath,newfilename))
        else:
            print str(filename)+" is not a .ply file. Continuing to next file in
                directory."

if __name__ == "__main__":
    Main()
```

iii. *meshrotate*-batch.py: Rotates meshes around X and Y axes in steps from 0 to 30 degrees (0, 2, 4, 6, …, 30)

```
'''
Created on Apr 16, 2015

@author: Julia M. Winchester

Command line utility for creating a "population" of meshes rotated in the X and Y
directions independently and combined
in steps of 2 from 0 to 30 (0 degrees, 2, 4, ..., 30) to create a matrix of 225 meshes of
various rotations to check
against topography.
'''

import plython
import numpy
import math

def Check_Zero_Centroid(cmesh):
    # Calculates centroid by averaging X Y and Z coordinates
    mesht = numpy.transpose(cmesh[0])

    Xc = numpy.average(mesht[0])
    Yc = numpy.average(mesht[1])
    Zc = numpy.average(mesht[2])

    centroid = [Xc,Yc,Zc]

    # If Centroid isn't at the origin, translates coordinates to origin

    if centroid[0] != 0 or centroid[1] != 0 or centroid[2] != 0:
        mesht[0] = numpy.subtract(mesht[0],centroid[0])
        mesht[1] = numpy.subtract(mesht[1],centroid[1])
        mesht[2] = numpy.subtract(mesht[2],centroid[2])

    # Retransposes mesh to achieve original dimensions
    cmesh[0] = numpy.transpose(mesht)

    return cmesh

def RotateMesh(rmesh, theta, axis):
    # z rotation matrix using theta supplied in radians
    xrotmat = numpy.matrix([[1,0,0],[0,math.cos(theta),-
        1*math.sin(theta)],[0,math.sin(theta),math.cos(theta)]])
    yrotmat = numpy.matrix([[math.cos(theta), 0, math.sin(theta)],[0,1,0],[-
        1*math.sin(theta),0,math.cos(theta)]])
    zrotmat = numpy.matrix([[math.cos(theta),(-
        1*math.sin(theta)),0],[math.sin(theta),math.cos(theta),0],[0,0,1]])

    meshm = numpy.mat(rmesh[0])

    if axis == "z":
        rotmat = zrotmat
    if axis == "y":
        rotmat = yrotmat
    if axis == "x":
        rotmat = xrotmat

    # using matrix multiplication, multiplies xyz triplets by rotation matrix to rotate
        entire xyz point cloud
    for i in range(len(rmesh[0])):
        XYZ = numpy.transpose(meshm[i])
        XYZprime = rotmat * XYZ
        meshm[i] = numpy.transpose(XYZprime)

    rmesh[0] = numpy.asarray(meshm)
```

```
    return rmesh

# This is an example filename, should be replaced with desired file
filename = "/Users/Username/mesh.ply"

stepsx = [0,2,4,6,8,10,12,14,16,18,20,22,24,26,28,30]

stepsy = [0,2,4,6,8,10,12,14,16,18,20,22,24,26,28,30]

for x in stepsx:
    for y in stepsy:
        mesh = plython.CreateArray(filename)
        mesh2 = Check_Zero_Centroid(mesh)

        newmesh = RotateMesh(mesh2, math.radians(float(x)), "x")
        newmesh2 = Check_Zero_Centroid(newmesh)
        newmesh3 = RotateMesh(newmesh2, math.radians(float(y)), "y")
        newmesh4 = Check_Zero_Centroid(newmesh3)
        plython.SaveArray(newmesh4[0],newmesh4[2],"/Users/Username/mesh-rotx" +str(x)+"-
roty" + str(y) + ".ply")
        newmesh = 0
        newmesh2 = 0
        newmesh3 = 0
        newmesh4 = 0
        mesh = 0
        mesh2 = 0
```

iv. *PLYtoOFF*.py: Script to convert .ply format surfaces to .off format, requires *meshconv* (Min, 2016)

```
'''
Created on May 22, 2015

@author: Julia M. Winchester

Script requires meshconv (http://www.cs.princeton.edu/~min/meshconv/) for usage.
'''

import sys
import os

# Replace with desired directory
dirpath = "/Users/Username/meshes"

# Replace with meshconv.exe
meshconv = "/Users/Username/meshtools/meshconv"

for filename in os.listdir(dirpath):
    fullpath = os.path.join(dirpath,filename)
    os.system("sed -i '' '16,18d' " + fullpath)
    os.system("sed -i '' '$d' " + fullpath)
    os.system("sed -i '' '$d' " + fullpath)
    newfilename = filename[0:-4]
    os.system(meshconv + " " + fullpath + " -c off")
```

A1.2.3: Simple geometric object creation script

The script used to create simple geometric objects, *shapemaker.py*, is provided below. Some applications interpret the meshes created by this script as having incoherent faces – that is, interpreted "outer" or "external" sides of polygon faces are not coherent across meshes. Free open-source software, such as Meshlab, can re-orient polygon faces coherently if needed.

```
'''
Created on Aug 31, 2014

This is a script to create a flat mesh with a variable number of ridges and heights to
those ridges

@author: Julia M. Winchester
'''

# script to create a single-row flat strip of vertices and faces
import numpy
import Plython
import os

def rowvertexlist(y, z, n):
    vertexlist = list()
    for i in range(n):
        vertexlist.append([int(i),int(y),int(z)])
    return vertexlist

def createvertices(length, nfeatures, altvertheight):
    altvert = 0
    currenty = 0
    fullvertexlist = list()
    for i in range(length+1):
        if altvert == 0:
            altvert += 1
            fullvertexlist.extend(rowvertexlist(currenty,0,6))
            currenty +=1
        else:
            altvert = 0
            if nfeatures != 0:
                fullvertexlist.extend(rowvertexlist(currenty,altvertheight,6))
                nfeatures -= 1
                currenty += 1
            else:
                fullvertexlist.extend(rowvertexlist(currenty,0,6))
                currenty += 1
    return fullvertexlist

def createfaces(length):
    nvert = (length+1)*6
    currentrow = 0
    facelist = list()
    while currentrow != length:
        stitchverts = range((6*currentrow),(12+(6*currentrow)))
        facelist.append([stitchverts[6],stitchverts[0],stitchverts[1]])
        facelist.append([stitchverts[6],stitchverts[7],stitchverts[1]])
        facelist.append([stitchverts[7],stitchverts[1],stitchverts[2]])
        facelist.append([stitchverts[7],stitchverts[8],stitchverts[2]])
        facelist.append([stitchverts[8],stitchverts[2],stitchverts[3]])
        facelist.append([stitchverts[8],stitchverts[9],stitchverts[3]])
        facelist.append([stitchverts[9],stitchverts[3],stitchverts[4]])
        facelist.append([stitchverts[9],stitchverts[10],stitchverts[4]])
        facelist.append([stitchverts[10],stitchverts[4],stitchverts[5]])
        facelist.append([stitchverts[10],stitchverts[11],stitchverts[5]])
        currentrow += 1
```

```
    return facelist

def createmesh(length,nfeatures,altvertheight,filename):
    fullvertexlist = createvertices(length,nfeatures,altvertheight)
    vertexarray = numpy.asarray(fullvertexlist)

    fullfacelist = createfaces(length)
    facearray = numpy.asarray(fullfacelist)

    Plython.SaveArray(vertexarray,facearray,filename)

filestem = "/Users/Username/Research/SimpleShapes/ShapeMaker/"
for nfeatures in range(1,11):
    filename1 = str(nfeatures)+"features"
    for height in range(1,11):
        filename2 = str(height) + "height.ply"
        createmesh((2*nfeatures),nfeatures,height,str(filestem+filename1+filename2))
        print "saving " + str(filestem+filename1+filename2)
        #os.system("/Applications/meshlab.app/Contents/MacOS/meshlabserver - i " +
            str(filestem+filename1+filename2) + " - o " +
            str(filestem+"binary"+filename1+filename2) + " -s
            /Users/Username/Research/SimpleShapes/ShapeMaker/
            ReOrientFacesCoherently.mlx")
```

A1.2.4: Amira scripts for mesh simplification and smoothing

Amira scripts for producing variably simplified and smoothed surfaces for the example *Cercocebus atys* and *Theropithecus gelada* specimens discussed in chapter one are provided below. They are given in alphabetical order by species.

i. Amira script for *Cercocebus atys*

```
# AmiraScript

load /Users/Moocow/Cercocebus/full/Cercocebus.ply
create HxSimplifier Simplifier
Simplifier attach {Cercocebus.ply}
Simplifier simplifyParameters setValue faces 2500
Simplifier simplifyAction setIndex 0
Simplifier fire
Cercocebus.ply save “Stanford PLY” /Users/Moocow/Cercocebus/full/Cercocebus2500simp.ply

create HxSurfaceSmooth SmoothSurface
SmoothSurface data connect Cercocebus.2500simp.ply
SmoothSurface parameters setValue iterations 1
SmoothSurface action setIndex 0
SmoothSurface fire
Cercocebus.2500simp.smooth save “Stanford PLY”
/Users/Moocow/Cercocebus/full/Cercocebus.2500simp.smooth1.ply
remove Cercocebus.2500simp.smooth1.ply

SmoothSurface parameters setValue iterations 2
SmoothSurface action setIndex 0
SmoothSurface fire
Cercocebus.2500simp.smooth save “Stanford PLY”
/Users/Moocow/Cercocebus/full/Cercocebus.2500simp.smooth2.ply
remove Cercocebus.2500simp.smooth2.ply

SmoothSurface parameters setValue iterations 3
SmoothSurface action setIndex 0
SmoothSurface fire
Cercocebus.2500simp.smooth save “Stanford PLY”
/Users/Moocow/Cercocebus/full/Cercocebus.2500simp.smooth3.ply
remove Cercocebus.2500simp.smooth3.ply

SmoothSurface parameters setValue iterations 6
SmoothSurface action setIndex 0
SmoothSurface fire
Cercocebus.2500simp.smooth save “Stanford PLY”
/Users/Moocow/Cercocebus/full/Cercocebus.2500simp.smooth6.ply
remove Cercocebus.2500simp.smooth6.ply

SmoothSurface parameters setValue iterations 12
SmoothSurface action setIndex 0
SmoothSurface fire
Cercocebus.2500simp.smooth save “Stanford PLY”
/Users/Moocow/Cercocebus/full/Cercocebus.2500simp.smooth12.ply
remove Cercocebus.2500simp.smooth12.ply

SmoothSurface parameters setValue iterations 25
SmoothSurface action setIndex 0
SmoothSurface fire
Cercocebus.2500simp.smooth save “Stanford PLY”
/Users/Moocow/Cercocebus/full/Cercocebus.2500simp.smooth25.ply
remove Cercocebus.2500simp.smooth25.ply

SmoothSurface parameters setValue iterations 50
SmoothSurface action setIndex 0
SmoothSurface fire
```

```
Cercocebus.2500simp.smooth save “Stanford PLY”
/Users/Moocow/Cercocebus/full/Cercocebus.2500simp.smooth50.ply
remove Cercocebus.2500simp.smooth50.ply

SmoothSurface parameters setValue iterations 75
SmoothSurface action setIndex 0
SmoothSurface fire
Cercocebus.2500simp.smooth save “Stanford PLY”
/Users/Moocow/Cercocebus/full/Cercocebus.2500simp.smooth75.ply
remove Cercocebus.2500simp.smooth75.ply

SmoothSurface parameters setValue iterations 100
SmoothSurface action setIndex 0
SmoothSurface fire
Cercocebus.2500simp.smooth save “Stanford PLY”
/Users/Moocow/Cercocebus/full/Cercocebus.2500simp.smooth100.ply
remove Cercocebus.2500simp.smooth100.ply

SmoothSurface parameters setValue iterations 125
SmoothSurface action setIndex 0
SmoothSurface fire
Cercocebus.2500simp.smooth save “Stanford PLY”
/Users/Moocow/Cercocebus/full/Cercocebus.2500simp.smooth125.ply
remove Cercocebus.2500simp.smooth125.ply

SmoothSurface parameters setValue iterations 150
SmoothSurface action setIndex 0
SmoothSurface fire
Cercocebus.2500simp.smooth save “Stanford PLY”
/Users/Moocow/Cercocebus/full/Cercocebus.2500simp.smooth150.ply
remove Cercocebus.2500simp.smooth150.ply

remove Cercocebus.2500simp.ply

load /Users/Moocow/Cercocebus/full/Cercocebus.ply
create HxSimplifier Simplifier
Simplifier attach {Cercocebus.ply}
Simplifier simplifyParameters setValue faces 5000
Simplifier simplifyAction setIndex 0
Simplifier fire
Cercocebus.ply save “Stanford PLY” /Users/Moocow/Cercocebus/full/Cercocebus.5000simp.ply

create HxSurfaceSmooth SmoothSurface
SmoothSurface data connect Cercocebus.5000simp.ply
SmoothSurface parameters setValue iterations 1
SmoothSurface action setIndex 0
SmoothSurface fire
Cercocebus.5000simp.smooth save “Stanford PLY”
/Users/Moocow/Cercocebus/full/Cercocebus.5000simp.smooth1.ply
remove Cercocebus.5000simp.smooth1.ply

SmoothSurface parameters setValue iterations 2
SmoothSurface action setIndex 0
SmoothSurface fire
Cercocebus.5000simp.smooth save “Stanford PLY”
/Users/Moocow/Cercocebus/full/Cercocebus.5000simp.smooth2.ply
remove Cercocebus.5000simp.smooth2.ply

SmoothSurface parameters setValue iterations 3
SmoothSurface action setIndex 0
SmoothSurface fire
Cercocebus.5000simp.smooth save “Stanford PLY”
/Users/Moocow/Cercocebus/full/Cercocebus.5000simp.smooth3.ply
remove Cercocebus.5000simp.smooth3.ply

SmoothSurface parameters setValue iterations 6
SmoothSurface action setIndex 0
SmoothSurface fire
```

```
Cercocebus.5000simp.smooth save “Stanford PLY”
/Users/Moocow/Cercocebus/full/Cercocebus.5000simp.smooth6.ply
remove Cercocebus.5000simp.smooth6.ply

SmoothSurface parameters setValue iterations 12
SmoothSurface action setIndex 0
SmoothSurface fire
Cercocebus.5000simp.smooth save “Stanford PLY”
/Users/Moocow/Cercocebus/full/Cercocebus.5000simp.smooth12.ply
remove Cercocebus.5000simp.smooth12.ply

SmoothSurface parameters setValue iterations 25
SmoothSurface action setIndex 0
SmoothSurface fire
Cercocebus.5000simp.smooth save “Stanford PLY”
/Users/Moocow/Cercocebus/full/Cercocebus.5000simp.smooth25.ply
remove Cercocebus.5000simp.smooth25.ply

SmoothSurface parameters setValue iterations 50
SmoothSurface action setIndex 0
SmoothSurface fire
Cercocebus.5000simp.smooth save “Stanford PLY”
/Users/Moocow/Cercocebus/full/Cercocebus.5000simp.smooth50.ply
remove Cercocebus.5000simp.smooth50.ply

SmoothSurface parameters setValue iterations 75
SmoothSurface action setIndex 0
SmoothSurface fire
Cercocebus.5000simp.smooth save “Stanford PLY”
/Users/Moocow/Cercocebus/full/Cercocebus.5000simp.smooth75.ply
remove Cercocebus.5000simp.smooth75.ply

SmoothSurface parameters setValue iterations 100
SmoothSurface action setIndex 0
SmoothSurface fire
Cercocebus.5000simp.smooth save “Stanford PLY”
/Users/Moocow/Cercocebus/full/Cercocebus.5000simp.smooth100.ply
remove Cercocebus.5000simp.smooth100.ply

SmoothSurface parameters setValue iterations 125
SmoothSurface action setIndex 0
SmoothSurface fire
Cercocebus.5000simp.smooth save “Stanford PLY”
/Users/Moocow/Cercocebus/full/Cercocebus.5000simp.smooth125.ply
remove Cercocebus.5000simp.smooth125.ply

SmoothSurface parameters setValue iterations 150
SmoothSurface action setIndex 0
SmoothSurface fire
Cercocebus.5000simp.smooth save “Stanford PLY”
/Users/Moocow/Cercocebus/full/Cercocebus.5000simp.smooth150.ply
remove Cercocebus.5000simp.smooth150.ply

remove Cercocebus.5000simp.ply

load /Users/Moocow/Cercocebus/full/Cercocebus.ply
create HxSimplifier Simplifier
Simplifier attach {Cercocebus.ply}
Simplifier simplifyParameters setValue faces 7500
Simplifier simplifyAction setIndex 0
Simplifier fire
Cercocebus.ply save “Stanford PLY” /Users/Moocow/Cercocebus/full/Cercocebus.7500simp.ply

create HxSurfaceSmooth SmoothSurface
SmoothSurface data connect Cercocebus.7500simp.ply
SmoothSurface parameters setValue iterations 1
SmoothSurface action setIndex 0
SmoothSurface fire
```

```
Cercocebus.7500simp.smooth save “Stanford PLY”
/Users/Moocow/Cercocebus/full/Cercocebus.7500simp.smooth1.ply
remove Cercocebus.7500simp.smooth1.ply

SmoothSurface parameters setValue iterations 2
SmoothSurface action setIndex 0
SmoothSurface fire
Cercocebus.7500simp.smooth save “Stanford PLY”
/Users/Moocow/Cercocebus/full/Cercocebus.7500simp.smooth2.ply
remove Cercocebus.7500simp.smooth2.ply

SmoothSurface parameters setValue iterations 3
SmoothSurface action setIndex 0
SmoothSurface fire
Cercocebus.7500simp.smooth save “Stanford PLY”
/Users/Moocow/Cercocebus/full/Cercocebus.7500simp.smooth3.ply
remove Cercocebus.7500simp.smooth3.ply

SmoothSurface parameters setValue iterations 6
SmoothSurface action setIndex 0
SmoothSurface fire
Cercocebus.7500simp.smooth save “Stanford PLY”
/Users/Moocow/Cercocebus/full/Cercocebus.7500simp.smooth6.ply
remove Cercocebus.7500simp.smooth6.ply

SmoothSurface parameters setValue iterations 12
SmoothSurface action setIndex 0
SmoothSurface fire
Cercocebus.7500simp.smooth save “Stanford PLY”
/Users/Moocow/Cercocebus/full/Cercocebus.7500simp.smooth12.ply
remove Cercocebus.7500simp.smooth12.ply

SmoothSurface parameters setValue iterations 25
SmoothSurface action setIndex 0
SmoothSurface fire
Cercocebus.7500simp.smooth save “Stanford PLY”
/Users/Moocow/Cercocebus/full/Cercocebus.7500simp.smooth25.ply
remove Cercocebus.7500simp.smooth25.ply

SmoothSurface parameters setValue iterations 50
SmoothSurface action setIndex 0
SmoothSurface fire
Cercocebus.7500simp.smooth save “Stanford PLY”
/Users/Moocow/Cercocebus/full/Cercocebus.7500simp.smooth50.ply
remove Cercocebus.7500simp.smooth50.ply

SmoothSurface parameters setValue iterations 75
SmoothSurface action setIndex 0
SmoothSurface fire
Cercocebus.7500simp.smooth save “Stanford PLY”
/Users/Moocow/Cercocebus/full/Cercocebus.7500simp.smooth75.ply
remove Cercocebus.7500simp.smooth75.ply

SmoothSurface parameters setValue iterations 100
SmoothSurface action setIndex 0
SmoothSurface fire
Cercocebus.7500simp.smooth save “Stanford PLY”
/Users/Moocow/Cercocebus/full/Cercocebus.7500simp.smooth100.ply
remove Cercocebus.7500simp.smooth100.ply

SmoothSurface parameters setValue iterations 125
SmoothSurface action setIndex 0
SmoothSurface fire
Cercocebus.7500simp.smooth save “Stanford PLY”
/Users/Moocow/Cercocebus/full/Cercocebus.7500simp.smooth125.ply
remove Cercocebus.7500simp.smooth125.ply

SmoothSurface parameters setValue iterations 150
```

```
SmoothSurface action setIndex 0
SmoothSurface fire
Cercocebus.7500simp.smooth save “Stanford PLY”
/Users/Moocow/Cercocebus/full/Cercocebus.7500simp.smooth150.ply
remove Cercocebus.7500simp.smooth150.ply

remove Cercocebus.7500simp.ply

load /Users/Moocow/Cercocebus/full/Cercocebus.ply
create HxSimplifier Simplifier
Simplifier attach {Cercocebus.ply}
Simplifier simplifyParameters setValue faces 10000
Simplifier simplifyAction setIndex 0
Simplifier fire
Cercocebus.ply save “Stanford PLY” /Users/Moocow/Cercocebus/full/Cercocebus.10000simp.ply

create HxSurfaceSmooth SmoothSurface
SmoothSurface data connect Cercocebus.10000simp.ply
SmoothSurface parameters setValue iterations 1
SmoothSurface action setIndex 0
SmoothSurface fire
Cercocebus.10000simp.smooth save “Stanford PLY”
/Users/Moocow/Cercocebus/full/Cercocebus.10000simp.smooth1.ply
remove Cercocebus.10000simp.smooth1.ply

SmoothSurface parameters setValue iterations 2
SmoothSurface action setIndex 0
SmoothSurface fire
Cercocebus.10000simp.smooth save “Stanford PLY”
/Users/Moocow/Cercocebus/full/Cercocebus.10000simp.smooth2.ply
remove Cercocebus.10000simp.smooth2.ply

SmoothSurface parameters setValue iterations 3
SmoothSurface action setIndex 0
SmoothSurface fire
Cercocebus.10000simp.smooth save “Stanford PLY”
/Users/Moocow/Cercocebus/full/Cercocebus.10000simp.smooth3.ply
remove Cercocebus.10000simp.smooth3.ply

SmoothSurface parameters setValue iterations 6
SmoothSurface action setIndex 0
SmoothSurface fire
Cercocebus.10000simp.smooth save “Stanford PLY”
/Users/Moocow/Cercocebus/full/Cercocebus.10000simp.smooth6.ply
remove Cercocebus.10000simp.smooth6.ply

SmoothSurface parameters setValue iterations 12
SmoothSurface action setIndex 0
SmoothSurface fire
Cercocebus.10000simp.smooth save “Stanford PLY”
/Users/Moocow/Cercocebus/full/Cercocebus.10000simp.smooth12.ply
remove Cercocebus.10000simp.smooth12.ply

SmoothSurface parameters setValue iterations 25
SmoothSurface action setIndex 0
SmoothSurface fire
Cercocebus.10000simp.smooth save “Stanford PLY”
/Users/Moocow/Cercocebus/full/Cercocebus.10000simp.smooth25.ply
remove Cercocebus.10000simp.smooth25.ply

SmoothSurface parameters setValue iterations 50
SmoothSurface action setIndex 0
SmoothSurface fire
Cercocebus.10000simp.smooth save “Stanford PLY”
/Users/Moocow/Cercocebus/full/Cercocebus.10000simp.smooth50.ply
remove Cercocebus.10000simp.smooth50.ply

SmoothSurface parameters setValue iterations 75
```

```
SmoothSurface action setIndex 0
SmoothSurface fire
Cercocebus.10000simp.smooth save “Stanford PLY”
/Users/Moocow/Cercocebus/full/Cercocebus.10000simp.smooth75.ply
remove Cercocebus.10000simp.smooth75.ply

SmoothSurface parameters setValue iterations 100
SmoothSurface action setIndex 0
SmoothSurface fire
Cercocebus.10000simp.smooth save “Stanford PLY”
/Users/Moocow/Cercocebus/full/Cercocebus.10000simp.smooth100.ply
remove Cercocebus.10000simp.smooth100.ply

SmoothSurface parameters setValue iterations 125
SmoothSurface action setIndex 0
SmoothSurface fire
Cercocebus.10000simp.smooth save “Stanford PLY”
/Users/Moocow/Cercocebus/full/Cercocebus.10000simp.smooth125.ply
remove Cercocebus.10000simp.smooth125.ply

SmoothSurface parameters setValue iterations 150
SmoothSurface action setIndex 0
SmoothSurface fire
Cercocebus.10000simp.smooth save “Stanford PLY”
/Users/Moocow/Cercocebus/full/Cercocebus.10000simp.smooth150.ply
remove Cercocebus.10000simp.smooth150.ply

remove Cercocebus.10000simp.ply

load /Users/Moocow/Cercocebus/full/Cercocebus.ply
create HxSimplifier Simplifier
Simplifier attach {Cercocebus.ply}
Simplifier simplifyParameters setValue faces 15000
Simplifier simplifyAction setIndex 0
Simplifier fire
Cercocebus.ply save “Stanford PLY” /Users/Moocow/Cercocebus/full/Cercocebus.15000simp.ply

create HxSurfaceSmooth SmoothSurface
SmoothSurface data connect Cercocebus.15000simp.ply
SmoothSurface parameters setValue iterations 1
SmoothSurface action setIndex 0
SmoothSurface fire
Cercocebus.15000simp.smooth save “Stanford PLY”
/Users/Moocow/Cercocebus/full/Cercocebus.15000simp.smooth1.ply
remove Cercocebus.15000simp.smooth1.ply

SmoothSurface parameters setValue iterations 2
SmoothSurface action setIndex 0
SmoothSurface fire
Cercocebus.15000simp.smooth save “Stanford PLY”
/Users/Moocow/Cercocebus/full/Cercocebus.15000simp.smooth2.ply
remove Cercocebus.15000simp.smooth2.ply

SmoothSurface parameters setValue iterations 3
SmoothSurface action setIndex 0
SmoothSurface fire
Cercocebus.15000simp.smooth save “Stanford PLY”
/Users/Moocow/Cercocebus/full/Cercocebus.15000simp.smooth3.ply
remove Cercocebus.15000simp.smooth3.ply

SmoothSurface parameters setValue iterations 6
SmoothSurface action setIndex 0
SmoothSurface fire
Cercocebus.15000simp.smooth save “Stanford PLY”
/Users/Moocow/Cercocebus/full/Cercocebus.15000simp.smooth6.ply
remove Cercocebus.15000simp.smooth6.ply

SmoothSurface parameters setValue iterations 12
```

```
SmoothSurface action setIndex 0
SmoothSurface fire
Cercocebus.15000simp.smooth save “Stanford PLY”
/Users/Moocow/Cercocebus/full/Cercocebus.15000simp.smooth12.ply
remove Cercocebus.15000simp.smooth12.ply

SmoothSurface parameters setValue iterations 25
SmoothSurface action setIndex 0
SmoothSurface fire
Cercocebus.15000simp.smooth save “Stanford PLY”
/Users/Moocow/Cercocebus/full/Cercocebus.15000simp.smooth25.ply
remove Cercocebus.15000simp.smooth25.ply

SmoothSurface parameters setValue iterations 50
SmoothSurface action setIndex 0
SmoothSurface fire
Cercocebus.15000simp.smooth save “Stanford PLY”
/Users/Moocow/Cercocebus/full/Cercocebus.15000simp.smooth50.ply
remove Cercocebus.15000simp.smooth50.ply

SmoothSurface parameters setValue iterations 75
SmoothSurface action setIndex 0
SmoothSurface fire
Cercocebus.15000simp.smooth save “Stanford PLY”
/Users/Moocow/Cercocebus/full/Cercocebus.15000simp.smooth75.ply
remove Cercocebus.15000simp.smooth75.ply

SmoothSurface parameters setValue iterations 100
SmoothSurface action setIndex 0
SmoothSurface fire
Cercocebus.15000simp.smooth save “Stanford PLY”
/Users/Moocow/Cercocebus/full/Cercocebus.15000simp.smooth100.ply
remove Cercocebus.15000simp.smooth100.ply

SmoothSurface parameters setValue iterations 125
SmoothSurface action setIndex 0
SmoothSurface fire
Cercocebus.15000simp.smooth save “Stanford PLY”
/Users/Moocow/Cercocebus/full/Cercocebus.15000simp.smooth125.ply
remove Cercocebus.15000simp.smooth125.ply

SmoothSurface parameters setValue iterations 150
SmoothSurface action setIndex 0
SmoothSurface fire
Cercocebus.15000simp.smooth save “Stanford PLY”
/Users/Moocow/Cercocebus/full/Cercocebus.15000simp.smooth150.ply
remove Cercocebus.15000simp.smooth150.ply

remove Cercocebus.15000simp.ply

load /Users/Moocow/Cercocebus/full/Cercocebus.ply
create HxSimplifier Simplifier
Simplifier attach {Cercocebus.ply}
Simplifier simplifyParameters setValue faces 20000
Simplifier simplifyAction setIndex 0
Simplifier fire
Cercocebus.ply save “Stanford PLY” /Users/Moocow/Cercocebus/full/Cercocebus.20000simp.ply

create HxSurfaceSmooth SmoothSurface
SmoothSurface data connect Cercocebus.20000simp.ply
SmoothSurface parameters setValue iterations 1
SmoothSurface action setIndex 0
SmoothSurface fire
Cercocebus.20000simp.smooth save “Stanford PLY”
/Users/Moocow/Cercocebus/full/Cercocebus.20000simp.smooth1.ply
remove Cercocebus.20000simp.smooth1.ply

SmoothSurface parameters setValue iterations 2
```

```
SmoothSurface action setIndex 0
SmoothSurface fire
Cercocebus.20000simp.smooth save “Stanford PLY”
/Users/Moocow/Cercocebus/full/Cercocebus.20000simp.smooth2.ply
remove Cercocebus.20000simp.smooth2.ply

SmoothSurface parameters setValue iterations 3
SmoothSurface action setIndex 0
SmoothSurface fire
Cercocebus.20000simp.smooth save “Stanford PLY”
/Users/Moocow/Cercocebus/full/Cercocebus.20000simp.smooth3.ply
remove Cercocebus.20000simp.smooth3.ply

SmoothSurface parameters setValue iterations 6
SmoothSurface action setIndex 0
SmoothSurface fire
Cercocebus.20000simp.smooth save “Stanford PLY”
/Users/Moocow/Cercocebus/full/Cercocebus.20000simp.smooth6.ply
remove Cercocebus.20000simp.smooth6.ply

SmoothSurface parameters setValue iterations 12
SmoothSurface action setIndex 0
SmoothSurface fire
Cercocebus.20000simp.smooth save “Stanford PLY”
/Users/Moocow/Cercocebus/full/Cercocebus.20000simp.smooth12.ply
remove Cercocebus.20000simp.smooth12.ply

SmoothSurface parameters setValue iterations 25
SmoothSurface action setIndex 0
SmoothSurface fire
Cercocebus.20000simp.smooth save “Stanford PLY”
/Users/Moocow/Cercocebus/full/Cercocebus.20000simp.smooth25.ply
remove Cercocebus.20000simp.smooth25.ply

SmoothSurface parameters setValue iterations 50
SmoothSurface action setIndex 0
SmoothSurface fire
Cercocebus.20000simp.smooth save “Stanford PLY”
/Users/Moocow/Cercocebus/full/Cercocebus.20000simp.smooth50.ply
remove Cercocebus.20000simp.smooth50.ply

SmoothSurface parameters setValue iterations 75
SmoothSurface action setIndex 0
SmoothSurface fire
Cercocebus.20000simp.smooth save “Stanford PLY”
/Users/Moocow/Cercocebus/full/Cercocebus.20000simp.smooth75.ply
remove Cercocebus.20000simp.smooth75.ply

SmoothSurface parameters setValue iterations 100
SmoothSurface action setIndex 0
SmoothSurface fire
Cercocebus.20000simp.smooth save “Stanford PLY”
/Users/Moocow/Cercocebus/full/Cercocebus.20000simp.smooth100.ply
remove Cercocebus.20000simp.smooth100.ply

SmoothSurface parameters setValue iterations 125
SmoothSurface action setIndex 0
SmoothSurface fire
Cercocebus.20000simp.smooth save “Stanford PLY”
/Users/Moocow/Cercocebus/full/Cercocebus.20000simp.smooth125.ply
remove Cercocebus.20000simp.smooth125.ply

SmoothSurface parameters setValue iterations 150
SmoothSurface action setIndex 0
SmoothSurface fire
Cercocebus.20000simp.smooth save “Stanford PLY”
/Users/Moocow/Cercocebus/full/Cercocebus.20000simp.smooth150.ply
remove Cercocebus.20000simp.smooth150.ply
```

```
remove Cercocebus.20000simp.ply

load /Users/Moocow/Cercocebus/full/Cercocebus.ply
create HxSimplifier Simplifier
Simplifier attach {Cercocebus.ply}
Simplifier simplifyParameters setValue faces 30000
Simplifier simplifyAction setIndex 0
Simplifier fire
Cercocebus.ply save “Stanford PLY” /Users/Moocow/Cercocebus/full/Cercocebus.30000simp.ply

create HxSurfaceSmooth SmoothSurface
SmoothSurface data connect Cercocebus.30000simp.ply
SmoothSurface parameters setValue iterations 1
SmoothSurface action setIndex 0
SmoothSurface fire
Cercocebus.30000simp.smooth save “Stanford PLY”
/Users/Moocow/Cercocebus/full/Cercocebus.30000simp.smooth1.ply
remove Cercocebus.30000simp.smooth1.ply

SmoothSurface parameters setValue iterations 2
SmoothSurface action setIndex 0
SmoothSurface fire
Cercocebus.30000simp.smooth save “Stanford PLY”
/Users/Moocow/Cercocebus/full/Cercocebus.30000simp.smooth2.ply
remove Cercocebus.30000simp.smooth2.ply

SmoothSurface parameters setValue iterations 3
SmoothSurface action setIndex 0
SmoothSurface fire
Cercocebus.30000simp.smooth save “Stanford PLY”
/Users/Moocow/Cercocebus/full/Cercocebus.30000simp.smooth3.ply
remove Cercocebus.30000simp.smooth3.ply

SmoothSurface parameters setValue iterations 6
SmoothSurface action setIndex 0
SmoothSurface fire
Cercocebus.30000simp.smooth save “Stanford PLY”
/Users/Moocow/Cercocebus/full/Cercocebus.30000simp.smooth6.ply
remove Cercocebus.30000simp.smooth6.ply

SmoothSurface parameters setValue iterations 12
SmoothSurface action setIndex 0
SmoothSurface fire
Cercocebus.30000simp.smooth save “Stanford PLY”
/Users/Moocow/Cercocebus/full/Cercocebus.30000simp.smooth12.ply
remove Cercocebus.30000simp.smooth12.ply

SmoothSurface parameters setValue iterations 25
SmoothSurface action setIndex 0
SmoothSurface fire
Cercocebus.30000simp.smooth save “Stanford PLY”
/Users/Moocow/Cercocebus/full/Cercocebus.30000simp.smooth25.ply
remove Cercocebus.30000simp.smooth25.ply

SmoothSurface parameters setValue iterations 50
SmoothSurface action setIndex 0
SmoothSurface fire
Cercocebus.30000simp.smooth save “Stanford PLY”
/Users/Moocow/Cercocebus/full/Cercocebus.30000simp.smooth50.ply
remove Cercocebus.30000simp.smooth50.ply

SmoothSurface parameters setValue iterations 75
SmoothSurface action setIndex 0
SmoothSurface fire
Cercocebus.30000simp.smooth save “Stanford PLY”
/Users/Moocow/Cercocebus/full/Cercocebus.30000simp.smooth75.ply
remove Cercocebus.30000simp.smooth75.ply
```

```
SmoothSurface parameters setValue iterations 100
SmoothSurface action setIndex 0
SmoothSurface fire
Cercocebus.30000simp.smooth save “Stanford PLY”
/Users/Moocow/Cercocebus/full/Cercocebus.30000simp.smooth100.ply
remove Cercocebus.30000simp.smooth100.ply

SmoothSurface parameters setValue iterations 125
SmoothSurface action setIndex 0
SmoothSurface fire
Cercocebus.30000simp.smooth save “Stanford PLY”
/Users/Moocow/Cercocebus/full/Cercocebus.30000simp.smooth125.ply
remove Cercocebus.30000simp.smooth125.ply

SmoothSurface parameters setValue iterations 150
SmoothSurface action setIndex 0
SmoothSurface fire
Cercocebus.30000simp.smooth save “Stanford PLY”
/Users/Moocow/Cercocebus/full/Cercocebus.30000simp.smooth150.ply
remove Cercocebus.30000simp.smooth150.ply

remove Cercocebus.30000simp.ply

load /Users/Moocow/Cercocebus/full/Cercocebus.ply
create HxSimplifier Simplifier
Simplifier attach {Cercocebus.ply}
Simplifier simplifyParameters setValue faces 50000
Simplifier simplifyAction setIndex 0
Simplifier fire
Cercocebus.ply save “Stanford PLY” /Users/Moocow/Cercocebus/full/Cercocebus.50000simp.ply

create HxSurfaceSmooth SmoothSurface
SmoothSurface data connect Cercocebus.50000simp.ply
SmoothSurface parameters setValue iterations 1
SmoothSurface action setIndex 0
SmoothSurface fire
Cercocebus.50000simp.smooth save “Stanford PLY”
/Users/Moocow/Cercocebus/full/Cercocebus.50000simp.smooth1.ply
remove Cercocebus.50000simp.smooth1.ply

SmoothSurface parameters setValue iterations 2
SmoothSurface action setIndex 0
SmoothSurface fire
Cercocebus.50000simp.smooth save “Stanford PLY”
/Users/Moocow/Cercocebus/full/Cercocebus.50000simp.smooth2.ply
remove Cercocebus.50000simp.smooth2.ply

SmoothSurface parameters setValue iterations 3
SmoothSurface action setIndex 0
SmoothSurface fire
Cercocebus.50000simp.smooth save “Stanford PLY”
/Users/Moocow/Cercocebus/full/Cercocebus.50000simp.smooth3.ply
remove Cercocebus.50000simp.smooth3.ply

SmoothSurface parameters setValue iterations 6
SmoothSurface action setIndex 0
SmoothSurface fire
Cercocebus.50000simp.smooth save “Stanford PLY”
/Users/Moocow/Cercocebus/full/Cercocebus.50000simp.smooth6.ply
remove Cercocebus.50000simp.smooth6.ply

SmoothSurface parameters setValue iterations 12
SmoothSurface action setIndex 0
SmoothSurface fire
Cercocebus.50000simp.smooth save “Stanford PLY”
/Users/Moocow/Cercocebus/full/Cercocebus.50000simp.smooth12.ply
remove Cercocebus.50000simp.smooth12.ply
```

```
SmoothSurface parameters setValue iterations 25
SmoothSurface action setIndex 0
SmoothSurface fire
Cercocebus.50000simp.smooth save “Stanford PLY”
/Users/Moocow/Cercocebus/full/Cercocebus.50000simp.smooth25.ply
remove Cercocebus.50000simp.smooth25.ply

SmoothSurface parameters setValue iterations 50
SmoothSurface action setIndex 0
SmoothSurface fire
Cercocebus.50000simp.smooth save “Stanford PLY”
/Users/Moocow/Cercocebus/full/Cercocebus.50000simp.smooth50.ply
remove Cercocebus.50000simp.smooth50.ply

SmoothSurface parameters setValue iterations 75
SmoothSurface action setIndex 0
SmoothSurface fire
Cercocebus.50000simp.smooth save “Stanford PLY”
/Users/Moocow/Cercocebus/full/Cercocebus.50000simp.smooth75.ply
remove Cercocebus.50000simp.smooth75.ply

SmoothSurface parameters setValue iterations 100
SmoothSurface action setIndex 0
SmoothSurface fire
Cercocebus.50000simp.smooth save “Stanford PLY”
/Users/Moocow/Cercocebus/full/Cercocebus.50000simp.smooth100.ply
remove Cercocebus.50000simp.smooth100.ply

SmoothSurface parameters setValue iterations 125
SmoothSurface action setIndex 0
SmoothSurface fire
Cercocebus.50000simp.smooth save “Stanford PLY”
/Users/Moocow/Cercocebus/full/Cercocebus.50000simp.smooth125.ply
remove Cercocebus.50000simp.smooth125.ply

SmoothSurface parameters setValue iterations 150
SmoothSurface action setIndex 0
SmoothSurface fire
Cercocebus.50000simp.smooth save “Stanford PLY”
/Users/Moocow/Cercocebus/full/Cercocebus.50000simp.smooth150.ply
remove Cercocebus.50000simp.smooth150.ply

remove Cercocebus.50000simp.ply

load /Users/Moocow/Cercocebus/full/Cercocebus.ply
create HxSimplifier Simplifier
Simplifier attach {Cercocebus.ply}
Simplifier simplifyParameters setValue faces 80000
Simplifier simplifyAction setIndex 0
Simplifier fire
Cercocebus.ply save “Stanford PLY” /Users/Moocow/Cercocebus/full/Cercocebus.80000simp.ply

create HxSurfaceSmooth SmoothSurface
SmoothSurface data connect Cercocebus.80000simp.ply
SmoothSurface parameters setValue iterations 1
SmoothSurface action setIndex 0
SmoothSurface fire
Cercocebus.80000simp.smooth save “Stanford PLY”
/Users/Moocow/Cercocebus/full/Cercocebus.80000simp.smooth1.ply
remove Cercocebus.80000simp.smooth1.ply

SmoothSurface parameters setValue iterations 2
SmoothSurface action setIndex 0
SmoothSurface fire
Cercocebus.80000simp.smooth save “Stanford PLY”
/Users/Moocow/Cercocebus/full/Cercocebus.80000simp.smooth2.ply
remove Cercocebus.80000simp.smooth2.ply
```

```
SmoothSurface parameters setValue iterations 3
SmoothSurface action setIndex 0
SmoothSurface fire
Cercocebus.80000simp.smooth save “Stanford PLY”
/Users/Moocow/Cercocebus/full/Cercocebus.80000simp.smooth3.ply
remove Cercocebus.80000simp.smooth3.ply

SmoothSurface parameters setValue iterations 6
SmoothSurface action setIndex 0
SmoothSurface fire
Cercocebus.80000simp.smooth save “Stanford PLY”
/Users/Moocow/Cercocebus/full/Cercocebus.80000simp.smooth6.ply
remove Cercocebus.80000simp.smooth6.ply

SmoothSurface parameters setValue iterations 12
SmoothSurface action setIndex 0
SmoothSurface fire
Cercocebus.80000simp.smooth save “Stanford PLY”
/Users/Moocow/Cercocebus/full/Cercocebus.80000simp.smooth12.ply
remove Cercocebus.80000simp.smooth12.ply

SmoothSurface parameters setValue iterations 25
SmoothSurface action setIndex 0
SmoothSurface fire
Cercocebus.80000simp.smooth save “Stanford PLY”
/Users/Moocow/Cercocebus/full/Cercocebus.80000simp.smooth25.ply
remove Cercocebus.80000simp.smooth25.ply

SmoothSurface parameters setValue iterations 50
SmoothSurface action setIndex 0
SmoothSurface fire
Cercocebus.80000simp.smooth save “Stanford PLY”
/Users/Moocow/Cercocebus/full/Cercocebus.80000simp.smooth50.ply
remove Cercocebus.80000simp.smooth50.ply

SmoothSurface parameters setValue iterations 75
SmoothSurface action setIndex 0
SmoothSurface fire
Cercocebus.80000simp.smooth save “Stanford PLY”
/Users/Moocow/Cercocebus/full/Cercocebus.80000simp.smooth75.ply
remove Cercocebus.80000simp.smooth75.ply

SmoothSurface parameters setValue iterations 100
SmoothSurface action setIndex 0
SmoothSurface fire
Cercocebus.80000simp.smooth save “Stanford PLY”
/Users/Moocow/Cercocebus/full/Cercocebus.80000simp.smooth100.ply
remove Cercocebus.80000simp.smooth100.ply

SmoothSurface parameters setValue iterations 125
SmoothSurface action setIndex 0
SmoothSurface fire
Cercocebus.80000simp.smooth save “Stanford PLY”
/Users/Moocow/Cercocebus/full/Cercocebus.80000simp.smooth125.ply
remove Cercocebus.80000simp.smooth125.ply

SmoothSurface parameters setValue iterations 150
SmoothSurface action setIndex 0
SmoothSurface fire
Cercocebus.80000simp.smooth save “Stanford PLY”
/Users/Moocow/Cercocebus/full/Cercocebus.80000simp.smooth150.ply
remove Cercocebus.80000simp.smooth150.ply

remove Cercocebus.80000simp.ply

load /Users/Moocow/Cercocebus/full/Cercocebus.ply
create HxSimplifier Simplifier
```

```
Simplifier attach {Cercocebus.ply}
Simplifier simplifyParameters setValue faces 120000
Simplifier simplifyAction setIndex 0
Simplifier fire
Cercocebus.ply save “Stanford PLY”
/Users/Moocow/Cercocebus/full/Cercocebus.120000simp.ply

create HxSurfaceSmooth SmoothSurface
SmoothSurface data connect Cercocebus.120000simp.ply
SmoothSurface parameters setValue iterations 1
SmoothSurface action setIndex 0
SmoothSurface fire
Cercocebus.120000simp.smooth save “Stanford PLY”
/Users/Moocow/Cercocebus/full/Cercocebus.120000simp.smooth1.ply
remove Cercocebus.120000simp.smooth1.ply

SmoothSurface parameters setValue iterations 2
SmoothSurface action setIndex 0
SmoothSurface fire
Cercocebus.120000simp.smooth save “Stanford PLY”
/Users/Moocow/Cercocebus/full/Cercocebus.120000simp.smooth2.ply
remove Cercocebus.120000simp.smooth2.ply

SmoothSurface parameters setValue iterations 3
SmoothSurface action setIndex 0
SmoothSurface fire
Cercocebus.120000simp.smooth save “Stanford PLY”
/Users/Moocow/Cercocebus/full/Cercocebus.120000simp.smooth3.ply
remove Cercocebus.120000simp.smooth3.ply

SmoothSurface parameters setValue iterations 6
SmoothSurface action setIndex 0
SmoothSurface fire
Cercocebus.120000simp.smooth save “Stanford PLY”
/Users/Moocow/Cercocebus/full/Cercocebus.120000simp.smooth6.ply
remove Cercocebus.120000simp.smooth6.ply

SmoothSurface parameters setValue iterations 12
SmoothSurface action setIndex 0
SmoothSurface fire
Cercocebus.120000simp.smooth save “Stanford PLY”
/Users/Moocow/Cercocebus/full/Cercocebus.120000simp.smooth12.ply
remove Cercocebus.120000simp.smooth12.ply

SmoothSurface parameters setValue iterations 25
SmoothSurface action setIndex 0
SmoothSurface fire
Cercocebus.120000simp.smooth save “Stanford PLY”
/Users/Moocow/Cercocebus/full/Cercocebus.120000simp.smooth25.ply
remove Cercocebus.120000simp.smooth25.ply

SmoothSurface parameters setValue iterations 50
SmoothSurface action setIndex 0
SmoothSurface fire
Cercocebus.120000simp.smooth save “Stanford PLY”
/Users/Moocow/Cercocebus/full/Cercocebus.120000simp.smooth50.ply
remove Cercocebus.120000simp.smooth50.ply

SmoothSurface parameters setValue iterations 75
SmoothSurface action setIndex 0
SmoothSurface fire
Cercocebus.120000simp.smooth save “Stanford PLY”
/Users/Moocow/Cercocebus/full/Cercocebus.120000simp.smooth75.ply
remove Cercocebus.120000simp.smooth75.ply

SmoothSurface parameters setValue iterations 100
SmoothSurface action setIndex 0
SmoothSurface fire
```

```
Cercocebus.120000simp.smooth save “Stanford PLY”
/Users/Moocow/Cercocebus/full/Cercocebus.120000simp.smooth100.ply
remove Cercocebus.120000simp.smooth100.ply

SmoothSurface parameters setValue iterations 125
SmoothSurface action setIndex 0
SmoothSurface fire
Cercocebus.120000simp.smooth save “Stanford PLY”
/Users/Moocow/Cercocebus/full/Cercocebus.120000simp.smooth125.ply
remove Cercocebus.120000simp.smooth125.ply

SmoothSurface parameters setValue iterations 150
SmoothSurface action setIndex 0
SmoothSurface fire
Cercocebus.120000simp.smooth save “Stanford PLY”
/Users/Moocow/Cercocebus/full/Cercocebus.120000simp.smooth150.ply
remove Cercocebus.120000simp.smooth150.ply

remove Cercocebus.120000simp.ply
```

ii. Amira script for *Theropithecus gelada*

```
# AmiraScript

load /Users/Moocow/Theropithecus/full/Theropithecus.ply
create HxSimplifier Simplifier
Simplifier attach {Theropithecus.ply}
Simplifier simplifyParameters setValue faces 2500
Simplifier simplifyAction setIndex 0
Simplifier fire
Theropithecus.ply save "Stanford PLY"
/Users/Moocow/Theropithecus/full/Theropithecus.2500simp.ply

create HxSurfaceSmooth SmoothSurface
SmoothSurface data connect Theropithecus.2500simp.ply
SmoothSurface parameters setValue iterations 1
SmoothSurface action setIndex 0
SmoothSurface fire
Theropithecus.2500simp.smooth save "Stanford PLY"
/Users/Moocow/Theropithecus/full/Theropithecus.2500simp.smooth1.ply
remove Theropithecus.2500simp.smooth1.ply

SmoothSurface parameters setValue iterations 2
SmoothSurface action setIndex 0
SmoothSurface fire
Theropithecus.2500simp.smooth save "Stanford PLY"
/Users/Moocow/Theropithecus/full/Theropithecus.2500simp.smooth2.ply
remove Theropithecus.2500simp.smooth2.ply

SmoothSurface parameters setValue iterations 3
SmoothSurface action setIndex 0
SmoothSurface fire
Theropithecus.2500simp.smooth save "Stanford PLY"
/Users/Moocow/Theropithecus/full/Theropithecus.2500simp.smooth3.ply
remove Theropithecus.2500simp.smooth3.ply

SmoothSurface parameters setValue iterations 6
SmoothSurface action setIndex 0
SmoothSurface fire
Theropithecus.2500simp.smooth save "Stanford PLY"
/Users/Moocow/Theropithecus/full/Theropithecus.2500simp.smooth6.ply
remove Theropithecus.2500simp.smooth6.ply

SmoothSurface parameters setValue iterations 12
SmoothSurface action setIndex 0
SmoothSurface fire
Theropithecus.2500simp.smooth save "Stanford PLY"
/Users/Moocow/Theropithecus/full/Theropithecus.2500simp.smooth12.ply
```

```
remove Theropithecus.2500simp.smooth12.ply

SmoothSurface parameters setValue iterations 25
SmoothSurface action setIndex 0
SmoothSurface fire
Theropithecus.2500simp.smooth save "Stanford PLY"
/Users/Moocow/Theropithecus/full/Theropithecus.2500simp.smooth25.ply
remove Theropithecus.2500simp.smooth25.ply

SmoothSurface parameters setValue iterations 50
SmoothSurface action setIndex 0
SmoothSurface fire
Theropithecus.2500simp.smooth save "Stanford PLY"
/Users/Moocow/Theropithecus/full/Theropithecus.2500simp.smooth50.ply
remove Theropithecus.2500simp.smooth50.ply

SmoothSurface parameters setValue iterations 75
SmoothSurface action setIndex 0
SmoothSurface fire
Theropithecus.2500simp.smooth save "Stanford PLY"
/Users/Moocow/Theropithecus/full/Theropithecus.2500simp.smooth75.ply
remove Theropithecus.2500simp.smooth75.ply

SmoothSurface parameters setValue iterations 100
SmoothSurface action setIndex 0
SmoothSurface fire
Theropithecus.2500simp.smooth save "Stanford PLY"
/Users/Moocow/Theropithecus/full/Theropithecus.2500simp.smooth100.ply
remove Theropithecus.2500simp.smooth100.ply

SmoothSurface parameters setValue iterations 125
SmoothSurface action setIndex 0
SmoothSurface fire
Theropithecus.2500simp.smooth save "Stanford PLY"
/Users/Moocow/Theropithecus/full/Theropithecus.2500simp.smooth125.ply
remove Theropithecus.2500simp.smooth125.ply

SmoothSurface parameters setValue iterations 150
SmoothSurface action setIndex 0
SmoothSurface fire
Theropithecus.2500simp.smooth save "Stanford PLY"
/Users/Moocow/Theropithecus/full/Theropithecus.2500simp.smooth150.ply
remove Theropithecus.2500simp.smooth150.ply

remove Theropithecus.2500simp.ply

load /Users/Moocow/Theropithecus/full/Theropithecus.ply
create HxSimplifier Simplifier
Simplifier attach {Theropithecus.ply}
Simplifier simplifyParameters setValue faces 5000
Simplifier simplifyAction setIndex 0
Simplifier fire
Theropithecus.ply save "Stanford PLY"
/Users/Moocow/Theropithecus/full/Theropithecus.5000simp.ply

create HxSurfaceSmooth SmoothSurface
SmoothSurface data connect Theropithecus.5000simp.ply
SmoothSurface parameters setValue iterations 1
SmoothSurface action setIndex 0
SmoothSurface fire
Theropithecus.5000simp.smooth save "Stanford PLY"
/Users/Moocow/Theropithecus/full/Theropithecus.5000simp.smooth1.ply
remove Theropithecus.5000simp.smooth1.ply

SmoothSurface parameters setValue iterations 2
SmoothSurface action setIndex 0
SmoothSurface fire
```

```
Theropithecus.5000simp.smooth save "Stanford PLY"
/Users/Moocow/Theropithecus/full/Theropithecus.5000simp.smooth2.ply
remove Theropithecus.5000simp.smooth2.ply

SmoothSurface parameters setValue iterations 3
SmoothSurface action setIndex 0
SmoothSurface fire
Theropithecus.5000simp.smooth save "Stanford PLY"
/Users/Moocow/Theropithecus/full/Theropithecus.5000simp.smooth3.ply
remove Theropithecus.5000simp.smooth3.ply

SmoothSurface parameters setValue iterations 6
SmoothSurface action setIndex 0
SmoothSurface fire
Theropithecus.5000simp.smooth save "Stanford PLY"
/Users/Moocow/Theropithecus/full/Theropithecus.5000simp.smooth6.ply
remove Theropithecus.5000simp.smooth6.ply

SmoothSurface parameters setValue iterations 12
SmoothSurface action setIndex 0
SmoothSurface fire
Theropithecus.5000simp.smooth save "Stanford PLY"
/Users/Moocow/Theropithecus/full/Theropithecus.5000simp.smooth12.ply
remove Theropithecus.5000simp.smooth12.ply

SmoothSurface parameters setValue iterations 25
SmoothSurface action setIndex 0
SmoothSurface fire
Theropithecus.5000simp.smooth save "Stanford PLY"
/Users/Moocow/Theropithecus/full/Theropithecus.5000simp.smooth25.ply
remove Theropithecus.5000simp.smooth25.ply

SmoothSurface parameters setValue iterations 50
SmoothSurface action setIndex 0
SmoothSurface fire
Theropithecus.5000simp.smooth save "Stanford PLY"
/Users/Moocow/Theropithecus/full/Theropithecus.5000simp.smooth50.ply
remove Theropithecus.5000simp.smooth50.ply

SmoothSurface parameters setValue iterations 75
SmoothSurface action setIndex 0
SmoothSurface fire
Theropithecus.5000simp.smooth save "Stanford PLY"
/Users/Moocow/Theropithecus/full/Theropithecus.5000simp.smooth75.ply
remove Theropithecus.5000simp.smooth75.ply

SmoothSurface parameters setValue iterations 100
SmoothSurface action setIndex 0
SmoothSurface fire
Theropithecus.5000simp.smooth save "Stanford PLY"
/Users/Moocow/Theropithecus/full/Theropithecus.5000simp.smooth100.ply
remove Theropithecus.5000simp.smooth100.ply

SmoothSurface parameters setValue iterations 125
SmoothSurface action setIndex 0
SmoothSurface fire
Theropithecus.5000simp.smooth save "Stanford PLY"
/Users/Moocow/Theropithecus/full/Theropithecus.5000simp.smooth125.ply
remove Theropithecus.5000simp.smooth125.ply

SmoothSurface parameters setValue iterations 150
SmoothSurface action setIndex 0
SmoothSurface fire
Theropithecus.5000simp.smooth save "Stanford PLY"
/Users/Moocow/Theropithecus/full/Theropithecus.5000simp.smooth150.ply
remove Theropithecus.5000simp.smooth150.ply

remove Theropithecus.5000simp.ply
```

```
load /Users/Moocow/Theropithecus/full/Theropithecus.ply
create HxSimplifier Simplifier
Simplifier attach {Theropithecus.ply}
Simplifier simplifyParameters setValue faces 7500
Simplifier simplifyAction setIndex 0
Simplifier fire
Theropithecus.ply save "Stanford PLY"
/Users/Moocow/Theropithecus/full/Theropithecus.7500simp.ply

create HxSurfaceSmooth SmoothSurface
SmoothSurface data connect Theropithecus.7500simp.ply
SmoothSurface parameters setValue iterations 1
SmoothSurface action setIndex 0
SmoothSurface fire
Theropithecus.7500simp.smooth save "Stanford PLY"
/Users/Moocow/Theropithecus/full/Theropithecus.7500simp.smooth1.ply
remove Theropithecus.7500simp.smooth1.ply

SmoothSurface parameters setValue iterations 2
SmoothSurface action setIndex 0
SmoothSurface fire
Theropithecus.7500simp.smooth save "Stanford PLY"
/Users/Moocow/Theropithecus/full/Theropithecus.7500simp.smooth2.ply
remove Theropithecus.7500simp.smooth2.ply

SmoothSurface parameters setValue iterations 3
SmoothSurface action setIndex 0
SmoothSurface fire
Theropithecus.7500simp.smooth save "Stanford PLY"
/Users/Moocow/Theropithecus/full/Theropithecus.7500simp.smooth3.ply
remove Theropithecus.7500simp.smooth3.ply

SmoothSurface parameters setValue iterations 6
SmoothSurface action setIndex 0
SmoothSurface fire
Theropithecus.7500simp.smooth save "Stanford PLY"
/Users/Moocow/Theropithecus/full/Theropithecus.7500simp.smooth6.ply
remove Theropithecus.7500simp.smooth6.ply

SmoothSurface parameters setValue iterations 12
SmoothSurface action setIndex 0
SmoothSurface fire
Theropithecus.7500simp.smooth save "Stanford PLY"
/Users/Moocow/Theropithecus/full/Theropithecus.7500simp.smooth12.ply
remove Theropithecus.7500simp.smooth12.ply

SmoothSurface parameters setValue iterations 25
SmoothSurface action setIndex 0
SmoothSurface fire
Theropithecus.7500simp.smooth save "Stanford PLY"
/Users/Moocow/Theropithecus/full/Theropithecus.7500simp.smooth25.ply
remove Theropithecus.7500simp.smooth25.ply

SmoothSurface parameters setValue iterations 50
SmoothSurface action setIndex 0
SmoothSurface fire
Theropithecus.7500simp.smooth save "Stanford PLY"
/Users/Moocow/Theropithecus/full/Theropithecus.7500simp.smooth50.ply
remove Theropithecus.7500simp.smooth50.ply

SmoothSurface parameters setValue iterations 75
SmoothSurface action setIndex 0
SmoothSurface fire
Theropithecus.7500simp.smooth save "Stanford PLY"
/Users/Moocow/Theropithecus/full/Theropithecus.7500simp.smooth75.ply
remove Theropithecus.7500simp.smooth75.ply
```

```
SmoothSurface parameters setValue iterations 100
SmoothSurface action setIndex 0
SmoothSurface fire
Theropithecus.7500simp.smooth save "Stanford PLY"
/Users/Moocow/Theropithecus/full/Theropithecus.7500simp.smooth100.ply
remove Theropithecus.7500simp.smooth100.ply

SmoothSurface parameters setValue iterations 125
SmoothSurface action setIndex 0
SmoothSurface fire
Theropithecus.7500simp.smooth save "Stanford PLY"
/Users/Moocow/Theropithecus/full/Theropithecus.7500simp.smooth125.ply
remove Theropithecus.7500simp.smooth125.ply

SmoothSurface parameters setValue iterations 150
SmoothSurface action setIndex 0
SmoothSurface fire
Theropithecus.7500simp.smooth save "Stanford PLY"
/Users/Moocow/Theropithecus/full/Theropithecus.7500simp.smooth150.ply
remove Theropithecus.7500simp.smooth150.ply

remove Theropithecus.7500simp.ply

load /Users/Moocow/Theropithecus/full/Theropithecus.ply
create HxSimplifier Simplifier
Simplifier attach {Theropithecus.ply}
Simplifier simplifyParameters setValue faces 10000
Simplifier simplifyAction setIndex 0
Simplifier fire
Theropithecus.ply save "Stanford PLY"
/Users/Moocow/Theropithecus/full/Theropithecus.10000simp.ply

create HxSurfaceSmooth SmoothSurface
SmoothSurface data connect Theropithecus.10000simp.ply
SmoothSurface parameters setValue iterations 1
SmoothSurface action setIndex 0
SmoothSurface fire
Theropithecus.10000simp.smooth save "Stanford PLY"
/Users/Moocow/Theropithecus/full/Theropithecus.10000simp.smooth1.ply
remove Theropithecus.10000simp.smooth1.ply

SmoothSurface parameters setValue iterations 2
SmoothSurface action setIndex 0
SmoothSurface fire
Theropithecus.10000simp.smooth save "Stanford PLY"
/Users/Moocow/Theropithecus/full/Theropithecus.10000simp.smooth2.ply
remove Theropithecus.10000simp.smooth2.ply

SmoothSurface parameters setValue iterations 3
SmoothSurface action setIndex 0
SmoothSurface fire
Theropithecus.10000simp.smooth save "Stanford PLY"
/Users/Moocow/Theropithecus/full/Theropithecus.10000simp.smooth3.ply
remove Theropithecus.10000simp.smooth3.ply

SmoothSurface parameters setValue iterations 6
SmoothSurface action setIndex 0
SmoothSurface fire
Theropithecus.10000simp.smooth save "Stanford PLY"
/Users/Moocow/Theropithecus/full/Theropithecus.10000simp.smooth6.ply
remove Theropithecus.10000simp.smooth6.ply

SmoothSurface parameters setValue iterations 12
SmoothSurface action setIndex 0
SmoothSurface fire
Theropithecus.10000simp.smooth save "Stanford PLY"
/Users/Moocow/Theropithecus/full/Theropithecus.10000simp.smooth12.ply
remove Theropithecus.10000simp.smooth12.ply
```

```
SmoothSurface parameters setValue iterations 25
SmoothSurface action setIndex 0
SmoothSurface fire
Theropithecus.10000simp.smooth save "Stanford PLY"
/Users/Moocow/Theropithecus/full/Theropithecus.10000simp.smooth25.ply
remove Theropithecus.10000simp.smooth25.ply

SmoothSurface parameters setValue iterations 50
SmoothSurface action setIndex 0
SmoothSurface fire
Theropithecus.10000simp.smooth save "Stanford PLY"
/Users/Moocow/Theropithecus/full/Theropithecus.10000simp.smooth50.ply
remove Theropithecus.10000simp.smooth50.ply

SmoothSurface parameters setValue iterations 75
SmoothSurface action setIndex 0
SmoothSurface fire
Theropithecus.10000simp.smooth save "Stanford PLY"
/Users/Moocow/Theropithecus/full/Theropithecus.10000simp.smooth75.ply
remove Theropithecus.10000simp.smooth75.ply

SmoothSurface parameters setValue iterations 100
SmoothSurface action setIndex 0
SmoothSurface fire
Theropithecus.10000simp.smooth save "Stanford PLY"
/Users/Moocow/Theropithecus/full/Theropithecus.10000simp.smooth100.ply
remove Theropithecus.10000simp.smooth100.ply

SmoothSurface parameters setValue iterations 125
SmoothSurface action setIndex 0
SmoothSurface fire
Theropithecus.10000simp.smooth save "Stanford PLY"
/Users/Moocow/Theropithecus/full/Theropithecus.10000simp.smooth125.ply
remove Theropithecus.10000simp.smooth125.ply

SmoothSurface parameters setValue iterations 150
SmoothSurface action setIndex 0
SmoothSurface fire
Theropithecus.10000simp.smooth save "Stanford PLY"
/Users/Moocow/Theropithecus/full/Theropithecus.10000simp.smooth150.ply
remove Theropithecus.10000simp.smooth150.ply

remove Theropithecus.10000simp.ply

load /Users/Moocow/Theropithecus/full/Theropithecus.ply
create HxSimplifier Simplifier
Simplifier attach {Theropithecus.ply}
Simplifier simplifyParameters setValue faces 15000
Simplifier simplifyAction setIndex 0
Simplifier fire
Theropithecus.ply save "Stanford PLY"
/Users/Moocow/Theropithecus/full/Theropithecus.15000simp.ply

create HxSurfaceSmooth SmoothSurface
SmoothSurface data connect Theropithecus.15000simp.ply
SmoothSurface parameters setValue iterations 1
SmoothSurface action setIndex 0
SmoothSurface fire
Theropithecus.15000simp.smooth save "Stanford PLY"
/Users/Moocow/Theropithecus/full/Theropithecus.15000simp.smooth1.ply
remove Theropithecus.15000simp.smooth1.ply

SmoothSurface parameters setValue iterations 2
SmoothSurface action setIndex 0
SmoothSurface fire
Theropithecus.15000simp.smooth save "Stanford PLY"
/Users/Moocow/Theropithecus/full/Theropithecus.15000simp.smooth2.ply
```

```
remove Theropithecus.15000simp.smooth2.ply

SmoothSurface parameters setValue iterations 3
SmoothSurface action setIndex 0
SmoothSurface fire
Theropithecus.15000simp.smooth save "Stanford PLY"
/Users/Moocow/Theropithecus/full/Theropithecus.15000simp.smooth3.ply
remove Theropithecus.15000simp.smooth3.ply

SmoothSurface parameters setValue iterations 6
SmoothSurface action setIndex 0
SmoothSurface fire
Theropithecus.15000simp.smooth save "Stanford PLY"
/Users/Moocow/Theropithecus/full/Theropithecus.15000simp.smooth6.ply
remove Theropithecus.15000simp.smooth6.ply

SmoothSurface parameters setValue iterations 12
SmoothSurface action setIndex 0
SmoothSurface fire
Theropithecus.15000simp.smooth save "Stanford PLY"
/Users/Moocow/Theropithecus/full/Theropithecus.15000simp.smooth12.ply
remove Theropithecus.15000simp.smooth12.ply

SmoothSurface parameters setValue iterations 25
SmoothSurface action setIndex 0
SmoothSurface fire
Theropithecus.15000simp.smooth save "Stanford PLY"
/Users/Moocow/Theropithecus/full/Theropithecus.15000simp.smooth25.ply
remove Theropithecus.15000simp.smooth25.ply

SmoothSurface parameters setValue iterations 50
SmoothSurface action setIndex 0
SmoothSurface fire
Theropithecus.15000simp.smooth save "Stanford PLY"
/Users/Moocow/Theropithecus/full/Theropithecus.15000simp.smooth50.ply
remove Theropithecus.15000simp.smooth50.ply

SmoothSurface parameters setValue iterations 75
SmoothSurface action setIndex 0
SmoothSurface fire
Theropithecus.15000simp.smooth save "Stanford PLY"
/Users/Moocow/Theropithecus/full/Theropithecus.15000simp.smooth75.ply
remove Theropithecus.15000simp.smooth75.ply

SmoothSurface parameters setValue iterations 100
SmoothSurface action setIndex 0
SmoothSurface fire
Theropithecus.15000simp.smooth save "Stanford PLY"
/Users/Moocow/Theropithecus/full/Theropithecus.15000simp.smooth100.ply
remove Theropithecus.15000simp.smooth100.ply

SmoothSurface parameters setValue iterations 125
SmoothSurface action setIndex 0
SmoothSurface fire
Theropithecus.15000simp.smooth save "Stanford PLY"
/Users/Moocow/Theropithecus/full/Theropithecus.15000simp.smooth125.ply
remove Theropithecus.15000simp.smooth125.ply

SmoothSurface parameters setValue iterations 150
SmoothSurface action setIndex 0
SmoothSurface fire
Theropithecus.15000simp.smooth save "Stanford PLY"
/Users/Moocow/Theropithecus/full/Theropithecus.15000simp.smooth150.ply
remove Theropithecus.15000simp.smooth150.ply

remove Theropithecus.15000simp.ply

load /Users/Moocow/Theropithecus/full/Theropithecus.ply
```

```
create HxSimplifier Simplifier
Simplifier attach {Theropithecus.ply}
Simplifier simplifyParameters setValue faces 20000
Simplifier simplifyAction setIndex 0
Simplifier fire
Theropithecus.ply save "Stanford PLY"
/Users/Moocow/Theropithecus/full/Theropithecus.20000simp.ply

create HxSurfaceSmooth SmoothSurface
SmoothSurface data connect Theropithecus.20000simp.ply
SmoothSurface parameters setValue iterations 1
SmoothSurface action setIndex 0
SmoothSurface fire
Theropithecus.20000simp.smooth save "Stanford PLY"
/Users/Moocow/Theropithecus/full/Theropithecus.20000simp.smooth1.ply
remove Theropithecus.20000simp.smooth1.ply

SmoothSurface parameters setValue iterations 2
SmoothSurface action setIndex 0
SmoothSurface fire
Theropithecus.20000simp.smooth save "Stanford PLY"
/Users/Moocow/Theropithecus/full/Theropithecus.20000simp.smooth2.ply
remove Theropithecus.20000simp.smooth2.ply

SmoothSurface parameters setValue iterations 3
SmoothSurface action setIndex 0
SmoothSurface fire
Theropithecus.20000simp.smooth save "Stanford PLY"
/Users/Moocow/Theropithecus/full/Theropithecus.20000simp.smooth3.ply
remove Theropithecus.20000simp.smooth3.ply

SmoothSurface parameters setValue iterations 6
SmoothSurface action setIndex 0
SmoothSurface fire
Theropithecus.20000simp.smooth save "Stanford PLY"
/Users/Moocow/Theropithecus/full/Theropithecus.20000simp.smooth6.ply
remove Theropithecus.20000simp.smooth6.ply

SmoothSurface parameters setValue iterations 12
SmoothSurface action setIndex 0
SmoothSurface fire
Theropithecus.20000simp.smooth save "Stanford PLY"
/Users/Moocow/Theropithecus/full/Theropithecus.20000simp.smooth12.ply
remove Theropithecus.20000simp.smooth12.ply

SmoothSurface parameters setValue iterations 25
SmoothSurface action setIndex 0
SmoothSurface fire
Theropithecus.20000simp.smooth save "Stanford PLY"
/Users/Moocow/Theropithecus/full/Theropithecus.20000simp.smooth25.ply
remove Theropithecus.20000simp.smooth25.ply

SmoothSurface parameters setValue iterations 50
SmoothSurface action setIndex 0
SmoothSurface fire
Theropithecus.20000simp.smooth save "Stanford PLY"
/Users/Moocow/Theropithecus/full/Theropithecus.20000simp.smooth50.ply
remove Theropithecus.20000simp.smooth50.ply

SmoothSurface parameters setValue iterations 75
SmoothSurface action setIndex 0
SmoothSurface fire
Theropithecus.20000simp.smooth save "Stanford PLY"
/Users/Moocow/Theropithecus/full/Theropithecus.20000simp.smooth75.ply
remove Theropithecus.20000simp.smooth75.ply

SmoothSurface parameters setValue iterations 100
SmoothSurface action setIndex 0
```

```
SmoothSurface fire
Theropithecus.20000simp.smooth save "Stanford PLY"
/Users/Moocow/Theropithecus/full/Theropithecus.20000simp.smooth100.ply
remove Theropithecus.20000simp.smooth100.ply

SmoothSurface parameters setValue iterations 125
SmoothSurface action setIndex 0
SmoothSurface fire
Theropithecus.20000simp.smooth save "Stanford PLY"
/Users/Moocow/Theropithecus/full/Theropithecus.20000simp.smooth125.ply
remove Theropithecus.20000simp.smooth125.ply

SmoothSurface parameters setValue iterations 150
SmoothSurface action setIndex 0
SmoothSurface fire
Theropithecus.20000simp.smooth save "Stanford PLY"
/Users/Moocow/Theropithecus/full/Theropithecus.20000simp.smooth150.ply
remove Theropithecus.20000simp.smooth150.ply

remove Theropithecus.20000simp.ply

load /Users/Moocow/Theropithecus/full/Theropithecus.ply
create HxSimplifier Simplifier
Simplifier attach {Theropithecus.ply}
Simplifier simplifyParameters setValue faces 30000
Simplifier simplifyAction setIndex 0
Simplifier fire
Theropithecus.ply save "Stanford PLY"
/Users/Moocow/Theropithecus/full/Theropithecus.30000simp.ply

create HxSurfaceSmooth SmoothSurface
SmoothSurface data connect Theropithecus.30000simp.ply
SmoothSurface parameters setValue iterations 1
SmoothSurface action setIndex 0
SmoothSurface fire
Theropithecus.30000simp.smooth save "Stanford PLY"
/Users/Moocow/Theropithecus/full/Theropithecus.30000simp.smooth1.ply
remove Theropithecus.30000simp.smooth1.ply

SmoothSurface parameters setValue iterations 2
SmoothSurface action setIndex 0
SmoothSurface fire
Theropithecus.30000simp.smooth save "Stanford PLY"
/Users/Moocow/Theropithecus/full/Theropithecus.30000simp.smooth2.ply
remove Theropithecus.30000simp.smooth2.ply

SmoothSurface parameters setValue iterations 3
SmoothSurface action setIndex 0
SmoothSurface fire
Theropithecus.30000simp.smooth save "Stanford PLY"
/Users/Moocow/Theropithecus/full/Theropithecus.30000simp.smooth3.ply
remove Theropithecus.30000simp.smooth3.ply

SmoothSurface parameters setValue iterations 6
SmoothSurface action setIndex 0
SmoothSurface fire
Theropithecus.30000simp.smooth save "Stanford PLY"
/Users/Moocow/Theropithecus/full/Theropithecus.30000simp.smooth6.ply
remove Theropithecus.30000simp.smooth6.ply

SmoothSurface parameters setValue iterations 12
SmoothSurface action setIndex 0
SmoothSurface fire
Theropithecus.30000simp.smooth save "Stanford PLY"
/Users/Moocow/Theropithecus/full/Theropithecus.30000simp.smooth12.ply
remove Theropithecus.30000simp.smooth12.ply

SmoothSurface parameters setValue iterations 25
```

```
SmoothSurface action setIndex 0
SmoothSurface fire
Theropithecus.30000simp.smooth save "Stanford PLY"
/Users/Moocow/Theropithecus/full/Theropithecus.30000simp.smooth25.ply
remove Theropithecus.30000simp.smooth25.ply

SmoothSurface parameters setValue iterations 50
SmoothSurface action setIndex 0
SmoothSurface fire
Theropithecus.30000simp.smooth save "Stanford PLY"
/Users/Moocow/Theropithecus/full/Theropithecus.30000simp.smooth50.ply
remove Theropithecus.30000simp.smooth50.ply

SmoothSurface parameters setValue iterations 75
SmoothSurface action setIndex 0
SmoothSurface fire
Theropithecus.30000simp.smooth save "Stanford PLY"
/Users/Moocow/Theropithecus/full/Theropithecus.30000simp.smooth75.ply
remove Theropithecus.30000simp.smooth75.ply

SmoothSurface parameters setValue iterations 100
SmoothSurface action setIndex 0
SmoothSurface fire
Theropithecus.30000simp.smooth save "Stanford PLY"
/Users/Moocow/Theropithecus/full/Theropithecus.30000simp.smooth100.ply
remove Theropithecus.30000simp.smooth100.ply

SmoothSurface parameters setValue iterations 125
SmoothSurface action setIndex 0
SmoothSurface fire
Theropithecus.30000simp.smooth save "Stanford PLY"
/Users/Moocow/Theropithecus/full/Theropithecus.30000simp.smooth125.ply
remove Theropithecus.30000simp.smooth125.ply

SmoothSurface parameters setValue iterations 150
SmoothSurface action setIndex 0
SmoothSurface fire
Theropithecus.30000simp.smooth save "Stanford PLY"
/Users/Moocow/Theropithecus/full/Theropithecus.30000simp.smooth150.ply
remove Theropithecus.30000simp.smooth150.ply

remove Theropithecus.30000simp.ply

load /Users/Moocow/Theropithecus/full/Theropithecus.ply
create HxSimplifier Simplifier
Simplifier attach {Theropithecus.ply}
Simplifier simplifyParameters setValue faces 50000
Simplifier simplifyAction setIndex 0
Simplifier fire
Theropithecus.ply save "Stanford PLY"
/Users/Moocow/Theropithecus/full/Theropithecus.50000simp.ply

create HxSurfaceSmooth SmoothSurface
SmoothSurface data connect Theropithecus.50000simp.ply
SmoothSurface parameters setValue iterations 1
SmoothSurface action setIndex 0
SmoothSurface fire
Theropithecus.50000simp.smooth save "Stanford PLY"
/Users/Moocow/Theropithecus/full/Theropithecus.50000simp.smooth1.ply
remove Theropithecus.50000simp.smooth1.ply

SmoothSurface parameters setValue iterations 2
SmoothSurface action setIndex 0
SmoothSurface fire
Theropithecus.50000simp.smooth save "Stanford PLY"
/Users/Moocow/Theropithecus/full/Theropithecus.50000simp.smooth2.ply
remove Theropithecus.50000simp.smooth2.ply
```

```
SmoothSurface parameters setValue iterations 3
SmoothSurface action setIndex 0
SmoothSurface fire
Theropithecus.50000simp.smooth save "Stanford PLY"
/Users/Moocow/Theropithecus/full/Theropithecus.50000simp.smooth3.ply
remove Theropithecus.50000simp.smooth3.ply

SmoothSurface parameters setValue iterations 6
SmoothSurface action setIndex 0
SmoothSurface fire
Theropithecus.50000simp.smooth save "Stanford PLY"
/Users/Moocow/Theropithecus/full/Theropithecus.50000simp.smooth6.ply
remove Theropithecus.50000simp.smooth6.ply

SmoothSurface parameters setValue iterations 12
SmoothSurface action setIndex 0
SmoothSurface fire
Theropithecus.50000simp.smooth save "Stanford PLY"
/Users/Moocow/Theropithecus/full/Theropithecus.50000simp.smooth12.ply
remove Theropithecus.50000simp.smooth12.ply

SmoothSurface parameters setValue iterations 25
SmoothSurface action setIndex 0
SmoothSurface fire
Theropithecus.50000simp.smooth save "Stanford PLY"
/Users/Moocow/Theropithecus/full/Theropithecus.50000simp.smooth25.ply
remove Theropithecus.50000simp.smooth25.ply

SmoothSurface parameters setValue iterations 50
SmoothSurface action setIndex 0
SmoothSurface fire
Theropithecus.50000simp.smooth save "Stanford PLY"
/Users/Moocow/Theropithecus/full/Theropithecus.50000simp.smooth50.ply
remove Theropithecus.50000simp.smooth50.ply

SmoothSurface parameters setValue iterations 75
SmoothSurface action setIndex 0
SmoothSurface fire
Theropithecus.50000simp.smooth save "Stanford PLY"
/Users/Moocow/Theropithecus/full/Theropithecus.50000simp.smooth75.ply
remove Theropithecus.50000simp.smooth75.ply

SmoothSurface parameters setValue iterations 100
SmoothSurface action setIndex 0
SmoothSurface fire
Theropithecus.50000simp.smooth save "Stanford PLY"
/Users/Moocow/Theropithecus/full/Theropithecus.50000simp.smooth100.ply
remove Theropithecus.50000simp.smooth100.ply

SmoothSurface parameters setValue iterations 125
SmoothSurface action setIndex 0
SmoothSurface fire
Theropithecus.50000simp.smooth save "Stanford PLY"
/Users/Moocow/Theropithecus/full/Theropithecus.50000simp.smooth125.ply
remove Theropithecus.50000simp.smooth125.ply

SmoothSurface parameters setValue iterations 150
SmoothSurface action setIndex 0
SmoothSurface fire
Theropithecus.50000simp.smooth save "Stanford PLY"
/Users/Moocow/Theropithecus/full/Theropithecus.50000simp.smooth150.ply
remove Theropithecus.50000simp.smooth150.ply

remove Theropithecus.50000simp.ply

load /Users/Moocow/Theropithecus/full/Theropithecus.ply
create HxSimplifier Simplifier
Simplifier attach {Theropithecus.ply}
```

```
Simplifier simplifyParameters setValue faces 80000
Simplifier simplifyAction setIndex 0
Simplifier fire
Theropithecus.ply save "Stanford PLY"
/Users/Moocow/Theropithecus/full/Theropithecus.80000simp.ply

create HxSurfaceSmooth SmoothSurface
SmoothSurface data connect Theropithecus.80000simp.ply
SmoothSurface parameters setValue iterations 1
SmoothSurface action setIndex 0
SmoothSurface fire
Theropithecus.80000simp.smooth save "Stanford PLY"
/Users/Moocow/Theropithecus/full/Theropithecus.80000simp.smooth1.ply
remove Theropithecus.80000simp.smooth1.ply

SmoothSurface parameters setValue iterations 2
SmoothSurface action setIndex 0
SmoothSurface fire
Theropithecus.80000simp.smooth save "Stanford PLY"
/Users/Moocow/Theropithecus/full/Theropithecus.80000simp.smooth2.ply
remove Theropithecus.80000simp.smooth2.ply

SmoothSurface parameters setValue iterations 3
SmoothSurface action setIndex 0
SmoothSurface fire
Theropithecus.80000simp.smooth save "Stanford PLY"
/Users/Moocow/Theropithecus/full/Theropithecus.80000simp.smooth3.ply
remove Theropithecus.80000simp.smooth3.ply

SmoothSurface parameters setValue iterations 6
SmoothSurface action setIndex 0
SmoothSurface fire
Theropithecus.80000simp.smooth save "Stanford PLY"
/Users/Moocow/Theropithecus/full/Theropithecus.80000simp.smooth6.ply
remove Theropithecus.80000simp.smooth6.ply

SmoothSurface parameters setValue iterations 12
SmoothSurface action setIndex 0
SmoothSurface fire
Theropithecus.80000simp.smooth save "Stanford PLY"
/Users/Moocow/Theropithecus/full/Theropithecus.80000simp.smooth12.ply
remove Theropithecus.80000simp.smooth12.ply

SmoothSurface parameters setValue iterations 25
SmoothSurface action setIndex 0
SmoothSurface fire
Theropithecus.80000simp.smooth save "Stanford PLY"
/Users/Moocow/Theropithecus/full/Theropithecus.80000simp.smooth25.ply
remove Theropithecus.80000simp.smooth25.ply

SmoothSurface parameters setValue iterations 50
SmoothSurface action setIndex 0
SmoothSurface fire
Theropithecus.80000simp.smooth save "Stanford PLY"
/Users/Moocow/Theropithecus/full/Theropithecus.80000simp.smooth50.ply
remove Theropithecus.80000simp.smooth50.ply

SmoothSurface parameters setValue iterations 75
SmoothSurface action setIndex 0
SmoothSurface fire
Theropithecus.80000simp.smooth save "Stanford PLY"
/Users/Moocow/Theropithecus/full/Theropithecus.80000simp.smooth75.ply
remove Theropithecus.80000simp.smooth75.ply

SmoothSurface parameters setValue iterations 100
SmoothSurface action setIndex 0
SmoothSurface fire
```

```
Theropithecus.80000simp.smooth save "Stanford PLY"
/Users/Moocow/Theropithecus/full/Theropithecus.80000simp.smooth100.ply
remove Theropithecus.80000simp.smooth100.ply

SmoothSurface parameters setValue iterations 125
SmoothSurface action setIndex 0
SmoothSurface fire
Theropithecus.80000simp.smooth save "Stanford PLY"
/Users/Moocow/Theropithecus/full/Theropithecus.80000simp.smooth125.ply
remove Theropithecus.80000simp.smooth125.ply

SmoothSurface parameters setValue iterations 150
SmoothSurface action setIndex 0
SmoothSurface fire
Theropithecus.80000simp.smooth save "Stanford PLY"
/Users/Moocow/Theropithecus/full/Theropithecus.80000simp.smooth150.ply
remove Theropithecus.80000simp.smooth150.ply

remove Theropithecus.80000simp.ply

load /Users/Moocow/Theropithecus/full/Theropithecus.ply
create HxSimplifier Simplifier
Simplifier attach {Theropithecus.ply}
Simplifier simplifyParameters setValue faces 120000
Simplifier simplifyAction setIndex 0
Simplifier fire
Theropithecus.ply save "Stanford PLY"
/Users/Moocow/Theropithecus/full/Theropithecus.120000simp.ply

create HxSurfaceSmooth SmoothSurface
SmoothSurface data connect Theropithecus.120000simp.ply
SmoothSurface parameters setValue iterations 1
SmoothSurface action setIndex 0
SmoothSurface fire
Theropithecus.120000simp.smooth save "Stanford PLY"
/Users/Moocow/Theropithecus/full/Theropithecus.120000simp.smooth1.ply
remove Theropithecus.120000simp.smooth1.ply

SmoothSurface parameters setValue iterations 2
SmoothSurface action setIndex 0
SmoothSurface fire
Theropithecus.120000simp.smooth save "Stanford PLY"
/Users/Moocow/Theropithecus/full/Theropithecus.120000simp.smooth2.ply
remove Theropithecus.120000simp.smooth2.ply

SmoothSurface parameters setValue iterations 3
SmoothSurface action setIndex 0
SmoothSurface fire
Theropithecus.120000simp.smooth save "Stanford PLY"
/Users/Moocow/Theropithecus/full/Theropithecus.120000simp.smooth3.ply
remove Theropithecus.120000simp.smooth3.ply

SmoothSurface parameters setValue iterations 6
SmoothSurface action setIndex 0
SmoothSurface fire
Theropithecus.120000simp.smooth save "Stanford PLY"
/Users/Moocow/Theropithecus/full/Theropithecus.120000simp.smooth6.ply
remove Theropithecus.120000simp.smooth6.ply

SmoothSurface parameters setValue iterations 12
SmoothSurface action setIndex 0
SmoothSurface fire
Theropithecus.120000simp.smooth save "Stanford PLY"
/Users/Moocow/Theropithecus/full/Theropithecus.120000simp.smooth12.ply
remove Theropithecus.120000simp.smooth12.ply

SmoothSurface parameters setValue iterations 25
SmoothSurface action setIndex 0
```

```
SmoothSurface fire
Theropithecus.120000simp.smooth save "Stanford PLY"
/Users/Moocow/Theropithecus/full/Theropithecus.120000simp.smooth25.ply
remove Theropithecus.120000simp.smooth25.ply

SmoothSurface parameters setValue iterations 50
SmoothSurface action setIndex 0
SmoothSurface fire
Theropithecus.120000simp.smooth save "Stanford PLY"
/Users/Moocow/Theropithecus/full/Theropithecus.120000simp.smooth50.ply
remove Theropithecus.120000simp.smooth50.ply

SmoothSurface parameters setValue iterations 75
SmoothSurface action setIndex 0
SmoothSurface fire
Theropithecus.120000simp.smooth save "Stanford PLY"
/Users/Moocow/Theropithecus/full/Theropithecus.120000simp.smooth75.ply
remove Theropithecus.120000simp.smooth75.ply

SmoothSurface parameters setValue iterations 100
SmoothSurface action setIndex 0
SmoothSurface fire
Theropithecus.120000simp.smooth save "Stanford PLY"
/Users/Moocow/Theropithecus/full/Theropithecus.120000simp.smooth100.ply
remove Theropithecus.120000simp.smooth100.ply

SmoothSurface parameters setValue iterations 125
SmoothSurface action setIndex 0
SmoothSurface fire
Theropithecus.120000simp.smooth save "Stanford PLY"
/Users/Moocow/Theropithecus/full/Theropithecus.120000simp.smooth125.ply
remove Theropithecus.120000simp.smooth125.ply

SmoothSurface parameters setValue iterations 150
SmoothSurface action setIndex 0
SmoothSurface fire
Theropithecus.120000simp.smooth save "Stanford PLY"
/Users/Moocow/Theropithecus/full/Theropithecus.120000simp.smooth150.ply
remove Theropithecus.120000simp.smooth150.ply

remove Theropithecus.120000simp.ply
```

A1.3: Source code referenced in chapter four

The following source code details modifications made to the *auto3dgm* R package (Boyer et al., 2015a) to permit optional disabling of specimen mirroring, based on initial user input. Though this package includes numerous files, three were modified and will be included here: *align_shapes.R*, *gpd.R*, and *principle_component_alignment.R*. These files are current with the official version of *auto3dgm* as of the time of writing (4/11/2016), and a complete modified forked version of this software package is repositoried at $githublink.

i. *align_shapes.R*

```
align_shapes <-
function(Data_dir, Output_dir, Levels, Ids, Names, Mirror = 1){

##############################################################################################
#####
# R Code for Shape Alignment
# Chris Glynn, Jesus Puente, Doug Boyer,Sayan Mukherjee, Ingrid Daubechies, and Justin
Gladman
# Departments of Statistical Science, Mathematics, and Evolutionary Anthropology
# Duke University
# September 6, 2013
##############################################################################################
#####

# Additional modifications made by Julia M. Winchester, 2016

#-----------------------------------------------------------------------------------------
--

ds = list(N=c(), ids=c(), names=c(), n = NA, K = NA, msc = list(mesh_dir=NA,
output_dir=NA), shape=list())

ds$N = Levels
ds$ids = Ids
ds$names = Names



#-------------YOU DO NOT NEED TO MODIFY ANYTHING AFTER THIS POINT ----------------------
-#

#Variables not to be changed

ds$n = length(ds$ids)
ds$K = length(ds$N)

#ds.msc.general_dir


ds$msc$mesh_dir = Data_dir
ds$msc$output_dir = Output_dir

if(!file.exists(ds$msc$output_dir)){
  Attempt = tryCatch({
    dir.create(ds$msc$output_dir)
  },warning=function(warn){
    return(stop(paste("Cannot Create:",ds$msc$output_dir,sep=" ")))
  },error=function(err){
    return(stop(paste("Cannot Create:",ds$msc$output_dir,sep=" ")))
  }
```

```
  )
}


#Initialization

#Fill in X with subsampled shapes
#Center and Standardize them
#Compute Singular Value Decompositions

mat = matrix(nrow=1, ncol=1)
shape.prototype = list(list(mat,mat), matrix(nrow=3, ncol=1), NA, c(NA, NA, NA),
list(mat,mat), list(mat,mat), list(mat,mat), list(mat), list(V = mat, FF = mat)  )
names(shape.prototype) = c("X", "center", "scale", "epsilon", "U_X", "D_X", "V_X",
"neigh", "lowres")


for (ii in 1:ds$n){

  ds$shape=list.add(ds$shape,shape.prototype)


  ds$shape[[ii]]$X[[ ds$K ]] = get_subsampled_shape(ds$msc$mesh_dir, ds$ids[ii], ds$N[
ds$K ])
  ds$shape[[ii]]$center = matrix(apply(ds$shape[[ii]]$X[[ ds$K ]], 1, mean), nrow=3,
ncol=1)
  ds$shape[[ii]]$scale=f_scale(ds$shape[[ii]]$X[[ ds$K ]])
  ds$shape[[ii]]$epsilon = rep(0, ds$K)

  for (kk in 1:ds$K){
    ds$shape[[ii]]$X[[kk]] = ds$shape[[ii]]$X[[ ds$K ]][ , (1:ds$N[kk]) ]
    ds$shape[[ii]]$X[[kk]] =
f_center(ds$shape[[ii]]$X[[kk]])/f_scale(ds$shape[[ii]]$X[[kk]])
    SVD = svd(ds$shape[[ii]]$X[[kk]])
    ds$shape[[ii]]$U_X[[kk]] = SVD$u
    tmpD_X = SVD$d
    tmpV_X = SVD$v
    ds$shape[[ii]]$D_X[[kk]] = diag(tmpD_X)
    ds$shape[[ii]]$V_X[[kk]] = tmpV_X[,1:3]
  }

  for (kk in 2:ds$K){
    ds$shape[[ii]]$epsilon[kk] = 1.0001*hausdorff(ds$shape[[ii]]$X[[kk]][, (1:ds$N[kk-1])
], ds$shape[[ii]]$X[[kk]] )[[1]]
    M.MD2= crangesearch(ds$shape[[ii]]$X[[kk]][, (1:ds$N[kk-
1])],ds$shape[[ii]]$X[[kk]],ds$shape[[ii]]$epsilon[kk])
    ds$shape[[ii]]$neigh[kk] = M.MD2[[1]]
  }
}

ds_unscaled = ds
for (ii in 1:ds$n){
  for (kk in 1:ds$K){
    ds_unscaled$shape[[ii]]$X[[kk]] = (ds$shape[[ii]]$scale / sqrt( ds$N[ ds$K ] )) *
ds$shape[[ii]]$X[[kk]]
  }
}
############################################################
#Read the low resolution files.  For display purposes only.

for (ii in 1:ds$n){
  #Read the files
  lowres_off_fn = paste(ds$msc$mesh_dir, "/lowres/", ds$ids[ii], ".off", sep="")
  if (file.exists( lowres_off_fn ) || url.exists(lowres_off_fn) ){
    tmpVF= read_off(lowres_off_fn)
    ds$shape[[ii]]$lowres$V = tmpVF[[1]]
    ds$shape[[ii]]$lowres$FF = tmpVF[[2]]
```

```
    ds$shape[[ii]]$lowres$V = ds$shape[[ii]]$lowres$V -
repmat(ds$shape[[ii]]$center,1,dim(ds$shape[[ii]]$lowres$V)[2]);
    ds$shape[[ii]]$lowres$V = ds$shape[[ii]]$lowres$V / ( ds$shape[[ii]]$scale / sqrt(
ds$N[ ds$K ] ) );


  }else{
    stop(paste("Cannot find low resolution file: ", lowres_off_fn,sep=""))
  }


}


# Alignment
# 'pa' stands for pairwise alignment
# 1. Compute a pairwise alignment of all pairs, then compute minimum
#    spanning tree
pa = list()
pa = list.add(pa, upper_triangle(ds$n) )  # a 1 entry in this matrix indicates the
pairwise distance should be computed

# Number of positions to test, the number of possibilities for aligning the principal
axes
# 8 positions are used if mirroring is on, 4 positions used otherwise
if (Mirror){
  pa = list.add(pa, 8)
}else{
  pa = list.add(pa, 4)
}

pa = list.add(pa,paste(ds$msc$output_dir, "/jobs/", sep="") )
names(pa)=c("A","L","pfj")



k = 1;

# Break up all the pairwise distances into a a bunch of different
# computations, to be computed either in the same machine or in different
# ones
# Remember to remove all previous jobs in the output/jobs folder!
unlink(paste(ds$msc$output_dir,"/jobs", sep=""), recursive=TRUE)
dir.create(paste(ds$ms$output_dir,"/jobs", sep=""))

compute_alignment(ds, k, pa , 1, FALSE )

pa = reduce( ds, pa, 1 );
pw_rotations = pa;

mst = graphminspantree(pa$d + t(pa$d))
ga = globalize(pa, mst + t(mst), 2)
ga = list.add(ga, k)
names(ga)=c(names(ga)[1:2],"k")

plot_tree(mst, ds$names, "Minimum Spanning Tree")

#now output the graph
jpeg(paste(ds$msc$output_dir,"/MST.jpg",sep=""), height=625, width=625)
plot_tree(mst, ds$names, "Minimum Spanning Tree")
dev.off()


theta = pi/2
rotation_matrix = matrix(c(cos(theta), -sin(theta), 0, sin(theta), cos(theta), 0, 0, 0,
1), nrow=3, byrow=T)
rotation_matrix = rotation_matrix%*%matrix(c(0,0,1,0,-1,0,1,0,0), nrow=3,
byrow=T)%*%t(ds$shape[[1]]$U_X[[k]])
```

```
#This will write the aligned files
unlink(paste(ds$msc$output_dir, "/", "Aligned_Shapes", sep=""), recursive=TRUE)
dir.create(paste(ds$msc$output_dir, "/", "Aligned_Shapes", sep=""))
write_aligned_files(ds, ga, ds$msc$mesh_dir, paste(ds$msc$output_dir, "/",
"Aligned_Shapes", sep=""), FALSE )

#create the variable argument for write_off_global_alignment
varargin = list(1:ds$n, 10, rotation_matrix,3.0, 1 )
write_off_global_alignment(paste(ds$msc$output_dir,"/alignment.off", sep="" ), ds, ga,
varargin)

varargin= list()
write_morphologika(paste(ds$msc$output_dir, "/morphologika.txt", sep=""), ds, ga,
varargin)
write_morphologika(paste(ds$msc$output_dir, "/morphologika_unscaled.txt", sep=""),
ds_unscaled, ga, varargin)



save(ds, pa, ga, mst, file = paste(ds$msc$output_dir, "/session.RData", sep=""))

##-----------------------------------------------------------------------------
##-----------------------------------------------------------------------------
##-----------------------------------------------------------------------------
##-----------------------------------------------------------------------------
##-----------------------------------------------------------------------------


#Compute the edges in the MST with higher number of points.

message("\n\nComputing alignment at second subsampling level\n\n")
pa_tmp = localize(ga)
pa$R = pa_tmp$R

k = 2 #Which level to run next
pa$A = upper_triangle(ds$n)
pa$pfj = paste(ds$msc$output_dir, '/jobs/', sep="")
tmpR = pa$R
tmpP = pa$P

#Remember to remove all previous jobs in the output/jobs folder
#Auto delete files from output/jobs folder
unlink(paste(ds$msc$output_dir,"/jobs", sep=""), recursive=TRUE)
dir.create(paste(ds$msc$output_dir,"/jobs", sep=""))

compute_alignment(ds, k, pa , 1, FALSE )
pa = reduce(ds, pa, 1)


#mst is same as before.
ga = globalize(pa, mst, 1)

ga = list.add(ga, k)
names(ga)=c(names(ga)[1:2],"k")

#output higher resolution
#create the variable argument for write_off_global_alignment
varargin = list(1:ds$n, 10, rotation_matrix,3.0, 1 )
write_off_global_alignment(paste(ds$msc$output_dir,"/alignment_2.off", sep="" ), ds, ga,
varargin)

varargin= list()
write_morphologika(paste(ds$msc$output_dir, "/morphologika_2.txt", sep=""), ds, ga,
varargin)
write_morphologika(paste(ds$msc$output_dir, "/morphologika_2_unscaled.txt", sep=""),
ds_unscaled, ga, varargin)
```

```
save(ds, pa, ga, mst, file = paste(ds$msc$output_dir, "/session_2.RData", sep=""))

#Compute all pairwise Procrustes distances

proc_d = matrix(rep(0, ds$n^2), nrow=ds$n)

for (ii in 1:ds$n){
  for (jj in ii:ds$n){
    if(ii==jj){next}
    PRO = cprocrustes(ds$shape[[ii]]$X[[k]] %*% ga$P[[ii]], ds$shape[[jj]]$X[[k]] %*%
ga$P[[jj]] )
    tmpR = PRO[[1]]
    proc_d[ii,jj]=PRO[[2]]
  }
}

mst_proc_d = graphminspantree(proc_d + t(proc_d) )
plot_tree(mst_proc_d, ds$names, "Minimum Spanning Tree")

proc_d = .5*(proc_d + t(proc_d))

#very close to what Matlab gives but not exact.  Not sure why.
#non-metric MDS in each case.  Need to take the negative to get it close.
coords = -t(isoMDS(proc_d, k=2, maxit=200, tol=1e-4)$points)

varargin = list(diag(c(1,1,1)), mst_proc_d)
filename = paste(ds$msc$output_dir, "/map.off", sep="")
write_off_placed_shapes(filename, coords, ds, ga, varargin)



Retx = list(ds, ga, pa)
closeAllConnections()
return(Retx)
}
```

ii. *gpd.R*

```
gpd <-
function(X_arg,Y_arg,L_arg){


  #Generalized Procrustes Distance
  #L: the number of samples from the ambiguity distribution
  # If L is 8, the first 8 samples are forced to be exactly the 8 elements
  # of the ambiguity set when the singular values are different. Since this
  # involves surface mirroring, it is only used when mirroring is on. If
  # mirroring is off, a subset of 4 elements is used.

  N = dim(X_arg)[2]

  #Initialize tests
  tst = list()
  R_0 = 1
  mat = matrix()

  tst = list.add(tst, principal_component_alignment(X_arg,Y_arg,L_arg))

  d = 2
  tst = list.add(tst, rep(0,L_arg))

  R=3
  R.prototype =list(); for (i in 1:L_arg){R.prototype = list.add(R.prototype, mat)}
  tst = list.add(tst, R.prototype)

  P=4
  P.prototype = list(); for (i in 1:L_arg){P.prototype =list.add(P.prototype, mat)}
  tst = list.add(tst, P.prototype)
```

```
  gamma = 5
  tst = list.add(tst, rep(0,L_arg))

  names(tst) = c("R_0", "d", "R", "P", "gamma")

  M_0 = matrix(rep(1,N*N),nrow=N, ncol=N, byrow=T)
  for (ii in 1:L_arg){
    GPD = locgpd(X_arg,Y_arg,tst$R_0[[ii]], M_0)
    tst$d[[ii]]=GPD[[1]]
    tst$R[[ii]]=GPD[[2]]
    tst$P[[ii]]=GPD[[3]]
    tst$gamma[[ii]]=GPD[[4]]
  }
  jmin = min(tst$d)
  jarg = which(tst$d==jmin)[1]

  # Return values
  d = tst$d[[jarg]]
  R = tst$R[[jarg]]
  P = tst$P[[jarg]]
  gamma = tst$gamma[[jarg]]

  GPD = list(d,R,P,gamma)
  return(GPD)
}
```

iii. *principle_component_alignment.R*

```
principal_component_alignment <-
function(X_arg,Y_arg,L_arg){
  X = as.matrix(X_arg)
  Y = as.matrix(Y_arg)

  SVD.X = svd(X)
  u.X = SVD.X$u
  d.X =diag(SVD.X$d)
  v.X =SVD.X$v

  SVD.Y = svd(Y)
  u.Y = SVD.Y$u
  d.Y =diag(SVD.Y$d)
  v.Y =SVD.Y$v

  R = list()

  tmp = u.X%*%diag(c(1,1,1))%*%t(u.Y)
  R = list.add(R, tmp)

  tmp = u.X%*%diag(c(-1,1,1))%*%t(u.Y)
  R = list.add(R, tmp)

  tmp = u.X%*%diag(c(1,-1,1))%*%t(u.Y)
  R = list.add(R, tmp)

  tmp = u.X%*%diag(c(1,1,-1))%*%t(u.Y)
  R = list.add(R, tmp)

  tmp = u.X%*%diag(c(-1,-1,1))%*%t(u.Y)
  R = list.add(R, tmp)

  tmp = u.X%*%diag(c(1,-1,-1))%*%t(u.Y)
  R = list.add(R, tmp)

  tmp = u.X%*%diag(c(-1,1,-1))%*%t(u.Y)
  R = list.add(R, tmp)

  tmp = u.X%*%diag(c(-1,-1,-1))%*%t(u.Y)
```

```
  R = list.add(R, tmp)

  if (L_arg == 8){
    return(R)
  }else if (L_arg == 4){
    newR = list()
    for (i in 1:length(R)) {
      if (det(R[[i]]) != -1) {
        newR = list.add(newR, R[[i]])
      }
    }
    return(newR)
  }
}
```

Table A2.1. Museum attributions and specimen numbers for test cercopithecoid sample.

Species	Museum	Specimen
Cercocebus atys	AMNH	70063
Cercocebus atys	AMNH	70385
Cercocebus atys	AMNH	77777
Cercocebus atys	AMNH	89373
Cercocebus atys	MNHN	1982-1065
Cercocebus atys	MNHN	1962-1437
Cercocebus atys	MNHN	1962-1431
Cercopithecus mitis	AMNH	52354
Cercopithecus mitis	AMNH	52355
Cercopithecus mitis	AMNH	52364
Cercopithecus mitis	NMNH	236996
Cercopithecus mitis	NMNH	259446
Cercopithecus mitis	NMNH	452544
Cercopithecus mitis	NMNH	452547
Cercopithecus mitis	NMNH	452548
Cercopithecus mitis	NMNH	452552
Cercopithecus mitis	NMNH	452554
Colobus guereza	AMNH	52236
Colobus guereza	BMNH	28.11.11.2
Colobus guereza	BMNH	14.1.24.1
Colobus guereza	BMNH	72.152
Colobus guereza	BMNH	40.8
Colobus guereza	BMNH	1.4.6.1
Colobus guereza	BMNH	54.762

Colobus guereza	BMNH	24.8.6.4
Colobus guereza	BMNH	1938.9.9.4
Colobus guereza	MNHN	163627
Theropithecus gelada	MNHN	1971-10
Theropithecus gelada	MNHN	1934-1419
Theropithecus gelada	MNHN	A-1.440
Theropithecus gelada	MNHN	1962-1467
Theropithecus gelada	MNHN	1972-360
Theropithecus gelada	MNHN	1969-451
Theropithecus gelada	MNHN	1963-58
Theropithecus gelada	MNHN	1931-836
Theropithecus gelada	NMNH	305107

* Museum attributions: AMNH - American Museum of Natural History, New York City; BMNH - Natural History Museum, London; MNHN - Muséum national d'Histoire naturelle, Paris; NMNH, National Museum of Natural History, Washington. D.C.

Table A2.2. 3D-OPCR and DEM-OPCR values by specimen.

Species	Museum	Specimen	DEM-OPCR	3D-OPCR	Δ-OPCR
Cercocebus atys	AMNH	70063	52.750	68.250	15.500
Cercocebus atys	AMNH	70385	54.500	63.625	9.125
Cercocebus atys	AMNH	77777	52.875	63.000	10.125
Cercocebus atys	AMNH	89373	53.375	68.000	14.625
Cercocebus atys	MNHN	1982-1065	54.375	87.500	33.125
Cercocebus atys	MNHN	1962-1437	63.250	80.250	17.000
Cercocebus atys	MNHN	1962-1431	70.750	99.375	28.625
Cercopithecus mitis	AMNH	52354	57.250	60.500	3.250
Cercopithecus mitis	AMNH	52355	57.625	75.500	17.875
Cercopithecus mitis	AMNH	52364	56.750	64.000	7.250

Cercopithecus mitis	NMNH	236996	62.250	84.750	22.500
Cercopithecus mitis	NMNH	259446	53.375	66.750	13.375
Cercopithecus mitis	NMNH	452544	54.250	71.750	17.500
Cercopithecus mitis	NMNH	452547	54.625	62.125	7.500
Cercopithecus mitis	NMNH	452548	56.750	77.875	21.125
Cercopithecus mitis	NMNH	452552	51.000	62.500	11.500
Cercopithecus mitis	NMNH	452554	57.125	71.750	14.625
Colobus guereza	AMNH	52236	51.375	64.250	12.875
Colobus guereza	BMNH	28.11.11.2	55.375	68.250	12.875
Colobus guereza	BMNH	14.1.24.1	57.875	85.250	27.375
Colobus guereza	BMNH	72.152	60.250	77.000	16.750
Colobus guereza	BMNH	40.8	54.500	70.625	16.125
Colobus guereza	BMNH	1.4.6.1	56.125	86.750	30.625
Colobus guereza	BMNH	54.762	56.375	66.250	9.875
Colobus guereza	BMNH	24.8.6.4	49.125	63.250	14.125
Colobus guereza	BMNH	1938.9.9.4	52.750	67.125	14.375
Colobus guereza	MNHN	163627	47.250	60.375	13.125
Theropithecus gelada	MNHN	1971-10	48.375	82.125	33.750
Theropithecus gelada	MNHN	1934-1419	55.375	83.125	27.750
Theropithecus gelada	MNHN	A-1.440	60.500	89.250	28.750
Theropithecus gelada	MNHN	1962-1467	61.875	96.375	34.500
Theropithecus gelada	MNHN	1972-360	59.500	91.750	32.250
Theropithecus gelada	MNHN	1969-451	61.125	101.500	40.375
Theropithecus gelada	MNHN	1963-58	55.125	76.500	21.375
Theropithecus gelada	MNHN	1931-836	53.875	81.625	27.750
Theropithecus gelada	NMNH	305107	52.875	74.875	22.000

* Museum attributions: AMNH - American Museum of Natural History, New York City; BMNH - Natural History Museum, London; MNHN - Muséum national d'Histoire naturelle, Paris; NMNH, National Museum of Natural History, Washington. D.C.

Table A2.3. DNE, RFI, and OPCR of simple geometric objects.

a. Constant-Length assemblage

i. DNE

Features	1	2	3	4	5	6	7	8	9	10
Height										
1	2.036	2.326	2.616	2.907	3.197	3.487	3.778	4.068	4.358	4.415
2	3.536	5.038	6.540	8.042	9.544	11.047	12.549	14.051	15.553	16.248
3	4.820	8.525	12.230	15.935	19.639	23.344	27.049	30.754	34.459	36.926
4	6.304	12.901	19.498	26.095	32.692	39.289	45.886	52.483	59.080	64.141
5	7.966	17.869	27.771	37.674	47.576	57.478	67.381	77.283	87.185	95.334

ii. RFI

Features	1	2	3	4	5	6	7	8	9	10
Height										
1	1.020	1.060	1.101	1.141	1.182	1.222	1.263	1.304	1.344	1.385
2	1.100	1.221	1.342	1.463	1.584	1.705	1.826	1.947	2.068	2.189
3	1.191	1.403	1.614	1.826	2.038	2.249	2.461	2.673	2.884	3.096
4	1.285	1.591	1.896	2.202	2.508	2.814	3.120	3.425	3.731	4.037
5	1.380	1.782	2.183	2.584	2.986	3.387	3.788	4.190	4.591	4.992

iii. OPCR

Features	1	2	3	4	5	6	7	8	9	10
Height										
1	2.000	4.000	6.000	8.000	10.000	12.000	14.000	16.000	18.000	20.000

2	2.000	4.000	6.000	8.000	10.000	12.000	14.000	16.000	18.000	20.000
3	2.000	4.000	6.000	8.000	10.000	12.000	14.000	16.000	18.000	20.000
4	2.000	4.000	6.000	8.000	10.000	12.000	14.000	16.000	18.000	20.000
5	2.000	4.000	6.000	8.000	10.000	12.000	14.000	16.000	18.000	20.000

b. Delta-Length assemblage

i. DNE

Features	1	2	3	4	5	6	7	8	9	10
Height										
1	1.802	2.092	2.383	2.673	2.963	3.253	3.544	3.834	4.124	4.415
2	2.729	4.231	5.733	7.235	8.738	10.240	11.742	13.244	14.746	16.248
3	3.582	7.287	10.992	14.697	18.402	22.106	25.811	29.516	33.221	36.926
4	4.768	11.365	17.962	24.559	31.156	37.753	44.350	50.947	57.544	64.141
5	6.212	16.115	26.017	35.920	45.822	55.724	65.627	75.529	85.431	95.334
6	7.824	21.274	34.724	48.174	61.623	75.073	88.523	101.973	115.423	128.873
7	9.543	26.685	43.828	60.970	78.113	95.255	112.398	129.541	146.683	163.826
8	11.332	32.258	53.183	74.109	95.035	115.960	136.886	157.812	178.737	199.663
9	13.170	37.937	62.704	87.471	112.239	137.006	161.773	186.541	211.308	236.075
10	15.041	43.689	72.337	100.986	129.634	158.282	186.931	215.579	244.227	272.875

ii. DNE/polygon

Features	1	2	3	4	5	6	7	8	9	10
Height										
1	0.090	0.052	0.040	0.033	0.030	0.027	0.025	0.024	0.023	0.022
2	0.136	0.106	0.096	0.090	0.087	0.085	0.084	0.083	0.082	0.081
3	0.179	0.182	0.183	0.184	0.184	0.184	0.184	0.184	0.185	0.185

4	0.238	0.284	0.299	0.307	0.312	0.315	0.317	0.318	0.320	0.321
5	0.311	0.403	0.434	0.449	0.458	0.464	0.469	0.472	0.475	0.477
6	0.391	0.532	0.579	0.602	0.616	0.626	0.632	0.637	0.641	0.644
7	0.477	0.667	0.730	0.762	0.781	0.794	0.803	0.810	0.815	0.819
8	0.567	0.806	0.886	0.926	0.950	0.966	0.978	0.986	0.993	0.998
9	0.659	0.948	1.045	1.093	1.122	1.142	1.156	1.166	1.174	1.180
10	0.752	1.092	1.206	1.262	1.296	1.319	1.335	1.347	1.357	1.364

iii. RFI

Features	1	2	3	4	5	6	7	8	9	10
Height										
1	1.383	1.401	1.393	1.386	1.397	1.380	1.391	1.380	1.386	1.385
2	2.187	2.215	2.202	2.191	2.209	2.182	2.199	2.181	2.191	2.189
3	3.092	3.133	3.114	3.099	3.124	3.085	3.109	3.085	3.098	3.096
4	4.032	4.085	4.060	4.041	4.074	4.023	4.054	4.022	4.040	4.037
5	4.986	5.052	5.021	4.997	5.038	4.975	5.014	4.974	4.996	4.992
6	5.948	6.026	5.990	5.961	6.010	5.934	5.981	5.934	5.960	5.956
7	6.914	7.005	6.963	6.930	6.986	6.899	6.953	6.898	6.928	6.923
8	7.884	7.987	7.940	7.901	7.966	7.866	7.927	7.865	7.899	7.894
9	8.855	8.971	8.918	8.875	8.947	8.834	8.904	8.834	8.873	8.866
10	9.827	9.956	9.897	9.849	9.930	9.805	9.882	9.804	9.847	9.840

iv. OPCR

Features	1	2	3	4	5	6	7	8	9	10
Height										
1	1.875	3.750	5.500	7.250	9.000	10.875	12.625	14.375	16.125	17.875
2	1.875	3.750	5.500	7.250	9.000	10.875	12.625	14.375	16.125	17.875

3	1.875	3.750	5.500	7.250	9.000	10.875	12.625	14.375	16.125	17.875
4	1.875	3.750	5.500	7.250	9.000	10.875	12.625	14.375	16.125	17.875
5	1.875	3.750	5.500	7.250	9.000	10.875	12.625	14.375	16.125	17.875
6	1.875	3.750	5.500	7.250	9.000	10.875	12.625	14.375	16.125	17.875
7	2.000	3.875	5.500	7.375	9.125	11.000	12.750	14.500	16.250	18.000
8	1.875	3.750	5.500	7.250	9.000	10.875	12.625	14.375	16.125	17.875
9	1.875	3.750	5.500	7.250	9.000	10.875	12.625	14.375	16.125	17.875
10	1.875	3.750	5.500	7.250	9.000	10.875	12.625	14.375	16.125	17.875

Table A2.4. DNE, RFI, and OPCR by specimen per cropping treatment.

		OC			CC			BC		
Species	Specimen	DNE	RFI	OPCR	DNE	RFI	OPCR	DNE	RFI	OPCR
Cercocebus atys	1065	171.593	0.263	87.500	158.310	0.411	73.000	168.770	0.329	77.125
Cercocebus atys	1437	209.777	0.308	81.250	213.781	0.519	70.625	211.455	0.470	72.375
Cercocebus atys	1431	204.567	0.229	99.375	194.953	0.485	78.875	190.596	0.411	84.750
Cercocebus atys	70063	199.279	0.297	69.000	219.017	0.560	56.375	215.545	0.472	60.750
Cercocebus atys	70385	180.458	0.276	63.625	180.053	0.552	55.125	182.749	0.504	56.375
Cercocebus atys	77777	201.461	0.279	63.000	204.997	0.554	58.250	257.061	0.459	58.625
Cercocebus atys	89373	208.763	0.308	68.000	209.080	0.550	57.375	213.674	0.504	61.000
Cercopithecus mitis	236996	197.171	0.276	84.750	187.117	0.511	64.000	194.185	0.386	72.750
Cercopithecus mitis	259446	232.836	0.352	66.500	215.650	0.524	58.250	231.017	0.425	62.875
Cercopithecus mitis	452544	162.861	0.303	71.750	154.974	0.468	55.500	154.865	0.405	62.000
Cercopithecus mitis	452547	194.377	0.303	62.125	194.853	0.491	54.375	192.321	0.406	54.125
Cercopithecus mitis	452548	225.175	0.254	77.875	211.561	0.478	71.250	224.423	0.292	80.750
Cercopithecus mitis	452552	138.265	0.251	62.500	153.439	0.510	61.375	135.158	0.436	57.500
Cercopithecus mitis	452554	224.102	0.316	71.750	206.338	0.526	58.000	214.017	0.458	60.875
Cercopithecus mitis	52354	188.483	0.299	60.500	189.210	0.554	55.375	200.174	0.411	55.750

Cercopithecus mitis	52355	231.539	0.328	79.625	231.965	0.532	68.250	238.370	0.410	72.625
Cercopithecus mitis	52364	207.213	0.346	64.000	207.431	0.520	60.375	213.971	0.482	65.500
Colobus guereza	52236	199.571	0.328	64.250	192.429	0.524	53.250	195.916	0.421	56.625
Colobus guereza	11112	198.751	0.351	68.250	202.788	0.551	59.125	207.237	0.498	60.375
Colobus guereza	1241	231.574	0.372	85.250	241.756	0.512	66.875	240.703	0.459	75.000
Colobus guereza	152	237.805	0.351	77.000	244.029	0.497	68.250	242.556	0.449	73.250
Colobus guereza	163627	195.950	0.389	60.375	197.064	0.581	52.125	197.484	0.472	54.500
Colobus guereza	408	218.999	0.321	70.625	214.055	0.488	57.375	212.583	0.420	60.625
Colobus guereza	461	230.718	0.341	86.750	226.142	0.528	69.125	224.729	0.456	70.625
Colobus guereza	762	231.524	0.386	66.250	224.614	0.543	53.500	224.633	0.517	55.375
Colobus guereza	864	196.928	0.362	63.250	200.541	0.499	53.000	200.408	0.465	53.250
Colobus guereza	994	226.918	0.389	67.125	215.189	0.493	61.250	221.375	0.445	61.375
Theropithecus gelada	10	259.089	0.439	82.125	238.456	0.602	60.375	236.119	0.561	64.000
Theropithecus gelada	1419	245.234	0.405	83.125	230.640	0.489	73.250	241.155	0.491	72.250
Theropithecus gelada	1440	202.216	0.335	89.250				202.714	0.414	82.500
Theropithecus gelada	1467	253.949	0.352	96.375	238.922	0.523	78.250	245.296	0.455	82.125
Theropithecus gelada	305107	236.020	0.382	74.875	217.981	0.543	59.750	216.297	0.493	59.375
Theropithecus gelada	360	245.809	0.314	91.750	239.498	0.435	77.500	243.358	0.395	77.000
Theropithecus gelada	451	259.781	0.231	101.500	215.094	0.437	75.125	220.505	0.388	82.875
Theropithecus gelada	58	247.938	0.389	76.500	251.681	0.518	64.750	255.169	0.497	66.500
Theropithecus gelada	836	244.730	0.337	81.625	239.363	0.492	66.500	244.761	0.447	70.625

Table A2.5. DNE, DNE/polygon, 2DA, 3DA, RFI, and OPCR across levels of smoothing and decimation.

a. *Cercocebus atys* specimen 89373

Decimation level	Smoothing iterations	DNE	DNE/polygon	2DA	3DA	RFI	OPCR
2500	0	183.382	0.073	42.639	78.434	0.305	53.500

2500	1	167.214	0.067	42.639	77.667	0.300	52.625
2500	2	158.669	0.063	42.647	77.358	0.298	53.500
2500	3	152.939	0.061	42.654	77.178	0.296	53.250
2500	6	142.643	0.057	42.670	76.893	0.294	51.375
2500	12	132.658	0.053	42.728	76.693	0.292	49.000
2500	25	123.212	0.049	42.859	76.717	0.291	46.625
2500	50	116.144	0.046	43.110	77.228	0.292	44.875
2500	75	113.234	0.045	43.362	77.943	0.293	45.500
2500	100	111.969	0.045	43.614	78.758	0.296	43.875
2500	100	111.969	0.045	43.614	78.758	0.296	43.875
2500	125	111.627	0.045	43.867	79.641	0.298	43.000
2500	150	111.907	0.045	44.121	80.582	0.301	42.750
5000	0	250.068	0.050	42.745	79.009	0.307	69.750
5000	1	223.332	0.045	42.740	78.414	0.303	62.750
5000	2	210.381	0.042	42.745	78.182	0.302	61.625
5000	3	202.030	0.040	42.748	78.050	0.301	59.875
5000	6	187.492	0.038	42.762	77.848	0.300	58.750
5000	12	173.827	0.035	42.790	77.716	0.298	58.125
5000	25	161.462	0.032	42.862	77.746	0.298	58.125
5000	50	153.005	0.031	43.000	78.121	0.299	55.750
5000	75	149.488	0.030	43.145	78.643	0.300	54.875
5000	100	148.211	0.030	43.274	79.236	0.302	54.875
5000	100	148.211	0.030	43.274	79.236	0.302	54.875
5000	125	148.031	0.030	43.408	79.878	0.305	54.000
5000	150	148.540	0.030	43.556	80.559	0.307	54.250
7500	0	307.730	0.041	42.775	79.346	0.309	90.375
7500	1	265.395	0.035	42.759	78.735	0.305	78.125
7500	2	247.719	0.033	42.758	78.522	0.304	72.750

7500	3	236.961	0.032	42.755	78.405	0.303	72.000
7500	6	218.468	0.029	42.763	78.229	0.302	68.375
7500	12	202.733	0.027	42.798	78.115	0.301	67.500
7500	25	190.290	0.025	42.839	78.145	0.301	66.125
7500	50	181.658	0.024	42.923	78.472	0.302	62.500
7500	75	178.540	0.024	43.010	78.913	0.303	60.875
7500	100	177.527	0.024	43.106	79.407	0.305	60.750
7500	100	177.527	0.024	43.106	79.407	0.305	60.750
7500	125	177.636	0.024	43.203	79.935	0.308	60.500
7500	150	178.462	0.024	43.287	80.491	0.310	61.500
10000	0	367.767	0.037	42.797	79.557	0.310	112.500
10000	0	367.767	0.037	42.797	79.557	0.310	112.500
10000	1	310.990	0.031	42.791	78.953	0.306	89.750
10000	1	310.990	0.031	42.791	78.953	0.306	89.750
10000	2	287.849	0.029	42.787	78.750	0.305	85.250
10000	2	287.849	0.029	42.787	78.750	0.305	85.250
10000	3	274.045	0.027	42.788	78.640	0.304	81.500
10000	3	274.045	0.027	42.788	78.640	0.304	81.500
10000	6	250.616	0.025	42.793	78.472	0.303	75.625
10000	6	250.616	0.025	42.793	78.472	0.303	75.625
10000	12	229.934	0.023	42.813	78.357	0.302	73.125
10000	12	229.934	0.023	42.813	78.357	0.302	73.125
10000	25	212.983	0.021	42.847	78.365	0.302	70.000
10000	25	212.983	0.021	42.847	78.365	0.302	70.000
10000	50	201.744	0.020	42.915	78.632	0.303	68.250
10000	50	201.744	0.020	42.915	78.632	0.303	68.250
10000	75	197.611	0.020	42.983	79.006	0.304	68.375
10000	75	197.611	0.020	42.983	79.006	0.304	68.375

10000	100	196.151	0.020	43.059	79.429	0.306	68.125
10000	100	196.151	0.020	43.059	79.429	0.306	68.125
10000	125	196.192	0.020	43.137	79.883	0.308	66.625
10000	125	196.192	0.020	43.137	79.883	0.308	66.625
10000	150	197.200	0.020	43.213	80.361	0.310	66.875
10000	150	197.200	0.020	43.213	80.361	0.310	66.875
15000	0	495.426	0.033	42.825	79.944	0.312	155.750
15000	1	391.808	0.026	42.822	79.207	0.308	114.875
15000	2	353.976	0.024	42.821	78.997	0.306	102.875
15000	3	332.900	0.022	42.820	78.891	0.306	96.250
15000	6	301.588	0.020	42.823	78.735	0.305	91.625
15000	12	275.544	0.018	42.832	78.625	0.304	84.375
15000	25	253.055	0.017	42.854	78.610	0.303	75.375
15000	50	237.687	0.016	42.902	78.800	0.304	74.750
15000	75	232.393	0.016	42.943	79.083	0.305	73.125
15000	100	230.784	0.015	42.983	79.407	0.307	72.750
15000	100	230.784	0.015	42.983	79.407	0.307	72.750
15000	125	230.969	0.015	43.028	79.756	0.309	71.625
15000	150	232.306	0.015	43.071	80.124	0.310	70.750
20000	0	645.274	0.032	42.836	80.392	0.315	217.750
20000	1	471.459	0.024	42.826	79.387	0.309	145.250
20000	2	415.391	0.021	42.819	79.145	0.307	115.875
20000	3	386.939	0.019	42.820	79.036	0.306	106.750
20000	6	344.349	0.017	42.822	78.886	0.305	97.000
20000	12	310.019	0.016	42.830	78.784	0.305	93.875
20000	25	282.215	0.014	42.842	78.763	0.304	87.000
20000	50	263.913	0.013	42.877	78.916	0.305	81.000
20000	75	258.036	0.013	42.904	79.151	0.306	80.125

20000	100	256.403	0.013	42.934	79.423	0.308	80.500
20000	100	256.403	0.013	42.934	79.423	0.308	80.500
20000	125	256.903	0.013	42.966	79.716	0.309	78.625
20000	150	258.676	0.013	43.000	80.027	0.311	79.875
30000	0	1074.641	0.036	42.857	81.367	0.321	397.375
30000	1	670.392	0.022	42.837	79.699	0.310	223.750
30000	2	558.802	0.019	42.827	79.358	0.308	168.625
30000	3	507.291	0.017	42.826	79.222	0.308	151.375
30000	6	438.209	0.015	42.819	79.052	0.307	128.875
30000	12	388.080	0.013	42.825	78.936	0.306	113.500
30000	25	344.961	0.012	42.826	78.890	0.305	103.625
30000	50	320.275	0.011	42.847	78.982	0.306	97.125
30000	75	312.033	0.010	42.857	79.148	0.307	92.875
30000	100	309.249	0.010	42.872	79.347	0.308	93.625
30000	100	309.249	0.010	42.872	79.347	0.308	93.625
30000	125	309.295	0.010	42.888	79.565	0.309	91.875
30000	150	310.992	0.010	42.908	79.798	0.310	90.875
50000	0	2399.193	0.048	42.888	83.474	0.333	963.875
50000	1	1216.608	0.024	42.853	80.225	0.314	438.125
50000	2	925.366	0.019	42.840	79.657	0.310	305.625
50000	3	799.507	0.016	42.835	79.464	0.309	247.500
50000	6	645.771	0.013	42.828	79.253	0.308	193.750
50000	12	539.494	0.011	42.827	79.123	0.307	162.500
50000	25	473.544	0.009	42.828	79.061	0.307	144.875
50000	50	432.235	0.009	42.831	79.116	0.307	130.000
50000	75	418.685	0.008	42.837	79.234	0.308	122.500
50000	100	412.751	0.008	42.849	79.380	0.308	120.500
50000	100	412.751	0.008	42.849	79.380	0.308	120.500

50000	125	411.774	0.008	42.857	79.541	0.309	118.000
50000	150	413.314	0.008	42.866	79.713	0.310	118.750
80000	0	5290.402	0.066	42.906	86.111	0.348	2172.250
80000	1	2350.358	0.029	42.867	80.883	0.317	893.250
80000	2	1660.414	0.021	42.851	80.005	0.312	559.875
80000	3	1365.974	0.017	42.847	79.726	0.310	437.500
80000	6	1024.584	0.013	42.844	79.445	0.309	313.625
80000	12	816.108	0.010	42.837	79.283	0.308	244.250
80000	25	690.170	0.009	42.835	79.195	0.307	204.250
80000	50	608.402	0.008	42.838	79.209	0.307	181.125
80000	75	579.743	0.007	42.842	79.286	0.308	172.375
80000	100	567.454	0.007	42.845	79.389	0.308	169.250
80000	100	567.454	0.007	42.845	79.389	0.308	169.250
80000	125	562.958	0.007	42.851	79.507	0.309	164.125
80000	150	562.424	0.007	42.856	79.635	0.310	161.250
120000	0	10678.478	0.089	42.911	88.256	0.361	3752.875
120000	1	4644.911	0.039	42.872	81.638	0.322	1656.625
120000	2	3147.543	0.026	42.857	80.447	0.315	1016.125
120000	3	2500.984	0.021	42.848	80.060	0.313	791.875
120000	6	1752.676	0.015	42.842	79.678	0.310	535.250
120000	12	1321.436	0.011	42.834	79.464	0.309	395.250
120000	25	1057.275	0.009	42.831	79.341	0.308	313.000
120000	50	897.561	0.007	42.834	79.322	0.308	265.875
120000	75	840.832	0.007	42.833	79.372	0.308	246.250
120000	100	814.900	0.007	42.837	79.449	0.309	234.750
120000	100	814.900	0.007	42.837	79.449	0.309	234.750
120000	125	803.804	0.007	42.838	79.541	0.309	232.125
120000	150	799.841	0.007	42.843	76.641	0.291	228.000

b. *Theropithecus gelada* specimen 1963-58

Decimation level	Smoothing iterations	DNE	DNE/polygon	2D Area	3D Area	RFI	OPCR
2500	0	230.681	0.092	97.155	210.124	0.386	66.875
2500	1	202.952	0.081	97.116	207.662	0.380	64.000
2500	2	190.413	0.076	97.127	206.626	0.377	61.750
2500	3	182.362	0.073	97.151	205.993	0.376	60.250
2500	6	168.210	0.067	97.201	204.910	0.373	56.500
2500	12	154.723	0.062	97.296	204.012	0.370	51.625
2500	25	143.249	0.057	97.538	203.758	0.368	50.000
2500	50	136.944	0.055	97.973	204.968	0.369	47.125
2500	75	135.844	0.054	98.413	206.860	0.371	46.125
2500	100	136.259	0.055	98.862	209.046	0.374	46.500
2500	100	136.259	0.055	98.862	209.046	0.374	46.500
2500	125	137.308	0.055	99.309	211.413	0.378	46.875
2500	150	138.664	0.055	99.778	213.915	0.381	46.750
5000	0	320.077	0.064	97.171	211.486	0.389	87.250
5000	1	279.173	0.056	97.136	209.640	0.385	79.375
5000	2	261.659	0.052	97.124	208.968	0.383	75.000
5000	3	250.712	0.050	97.140	208.578	0.382	74.500
5000	6	231.868	0.046	97.135	207.936	0.381	72.875
5000	12	213.731	0.043	97.171	207.429	0.379	70.625
5000	25	196.866	0.039	97.320	207.316	0.378	66.625
5000	50	183.844	0.037	97.564	208.188	0.379	62.500
5000	75	178.455	0.036	97.833	209.595	0.381	59.250
5000	100	176.263	0.035	98.092	211.272	0.384	57.875
5000	100	176.263	0.035	98.092	211.272	0.384	57.875

5000	125	175.827	0.035	98.344	213.127	0.387	57.750
5000	150	176.461	0.035	98.610	215.116	0.390	58.250
7500	0	389.338	0.052	97.194	212.182	0.390	103.625
7500	1	333.247	0.044	97.176	210.463	0.386	94.500
7500	2	310.811	0.041	97.180	209.873	0.385	89.625
7500	3	296.657	0.040	97.175	209.543	0.384	88.500
7500	6	272.788	0.036	97.188	209.020	0.383	84.375
7500	12	250.334	0.033	97.207	208.620	0.382	79.250
7500	25	229.875	0.031	97.315	208.568	0.381	74.875
7500	50	215.682	0.029	97.547	209.353	0.382	71.625
7500	75	210.154	0.028	97.773	210.537	0.384	70.125
7500	100	207.744	0.028	97.980	211.913	0.386	68.375
7500	100	207.744	0.028	97.980	211.913	0.386	68.375
7500	125	206.924	0.028	98.215	213.415	0.388	67.625
7500	150	207.131	0.028	98.443	215.015	0.391	67.500
10000	0	471.328	0.047	97.227	212.761	0.392	128.500
10000	0	471.328	0.047	97.227	212.761	0.392	128.500
10000	1	387.248	0.039	97.187	210.959	0.388	111.000
10000	1	387.248	0.039	97.187	210.959	0.388	111.000
10000	2	355.807	0.036	97.188	210.367	0.386	105.000
10000	2	355.807	0.036	97.188	210.367	0.386	105.000
10000	3	337.399	0.034	97.196	210.040	0.385	101.000
10000	3	337.399	0.034	97.196	210.040	0.385	101.000
10000	6	307.828	0.031	97.186	209.527	0.384	93.875
10000	6	307.828	0.031	97.186	209.527	0.384	93.875
10000	12	282.092	0.028	97.219	209.145	0.383	87.750
10000	12	282.092	0.028	97.219	209.145	0.383	87.750
10000	25	259.550	0.026	97.285	209.081	0.383	84.875

10000	25	259.550	0.026	97.285	209.081	0.383	84.875
10000	50	244.449	0.024	97.427	209.743	0.383	78.500
10000	50	244.449	0.024	97.427	209.743	0.383	78.500
10000	75	239.235	0.024	97.567	210.744	0.385	76.375
10000	75	239.235	0.024	97.567	210.744	0.385	76.375
10000	100	237.511	0.024	97.714	211.897	0.387	76.000
10000	100	237.511	0.024	97.714	211.897	0.387	76.000
10000	125	237.529	0.024	97.871	213.146	0.389	76.250
10000	125	237.529	0.024	97.871	213.146	0.389	76.250
10000	150	238.583	0.024	98.034	214.468	0.391	76.375
10000	150	238.583	0.024	98.034	214.468	0.391	76.375
15000	0	636.429	0.042	97.250	213.942	0.394	180.750
15000	1	482.605	0.032	97.229	211.525	0.389	133.375
15000	2	438.381	0.029	97.226	210.911	0.387	120.625
15000	3	414.509	0.028	97.225	210.601	0.386	115.125
15000	6	376.335	0.025	97.217	210.132	0.385	106.875
15000	12	342.800	0.023	97.243	209.781	0.384	99.875
15000	25	313.885	0.021	97.294	209.687	0.384	94.750
15000	50	294.918	0.020	97.397	210.186	0.385	91.750
15000	75	288.866	0.019	97.522	210.985	0.386	89.875
15000	100	287.622	0.019	97.639	211.921	0.387	88.375
15000	100	287.622	0.019	97.639	211.921	0.387	88.375
15000	125	288.942	0.019	97.760	212.942	0.389	88.875
15000	150	291.884	0.019	97.860	214.024	0.391	88.250
20000	0	856.518	0.043	97.313	215.495	0.398	262.125
20000	1	587.274	0.029	97.257	212.050	0.390	167.125
20000	2	518.170	0.026	97.252	211.320	0.388	141.250
20000	3	484.384	0.024	97.227	210.991	0.387	132.875

20000	6	434.862	0.022	97.232	210.522	0.386	122.000
20000	12	393.887	0.020	97.230	210.184	0.385	114.125
20000	25	361.725	0.018	97.256	210.096	0.385	107.500
20000	50	340.007	0.017	97.300	210.534	0.386	99.625
20000	75	332.944	0.017	97.378	211.234	0.387	95.500
20000	100	331.321	0.017	97.462	212.055	0.389	94.375
20000	100	331.321	0.017	97.462	212.055	0.389	94.375
20000	125	332.751	0.017	97.541	212.953	0.390	93.000
20000	150	336.329	0.017	97.618	213.909	0.392	93.375
30000	0	1372.312	0.046	97.375	218.871	0.405	467.000
30000	1	795.884	0.027	97.291	212.896	0.392	226.750
30000	2	675.530	0.023	97.252	211.865	0.389	184.125
30000	3	627.581	0.021	97.237	211.485	0.389	167.125
30000	6	559.119	0.019	97.216	211.003	0.387	151.625
30000	12	502.440	0.017	97.224	210.668	0.387	136.000
30000	25	460.701	0.015	97.236	210.552	0.386	126.625
30000	50	432.485	0.014	97.267	210.881	0.387	121.000
30000	75	424.315	0.014	97.311	211.440	0.388	119.750
30000	100	423.296	0.014	97.371	212.101	0.389	119.375
30000	100	423.296	0.014	97.371	212.101	0.389	119.375
30000	125	425.957	0.014	97.423	212.825	0.391	118.125
30000	150	431.050	0.014	97.473	213.598	0.392	118.500
50000	0	2751.524	0.055	97.435	224.168	0.417	1051.250
50000	1	1285.673	0.026	97.337	214.092	0.394	405.000
50000	2	1021.931	0.020	97.288	212.532	0.391	278.250
50000	3	920.552	0.018	97.277	212.032	0.390	236.875
50000	6	801.102	0.016	97.246	211.459	0.388	207.500
50000	12	712.542	0.014	97.224	211.058	0.388	187.375

50000	25	651.200	0.013	97.223	210.852	0.387	172.250
50000	50	600.835	0.012	97.235	211.030	0.387	159.000
50000	75	586.640	0.012	97.255	211.429	0.388	156.375
50000	100	584.431	0.012	97.290	211.922	0.389	152.250
50000	100	584.431	0.012	97.290	211.922	0.389	152.250
50000	125	587.780	0.012	97.307	212.471	0.390	151.500
50000	150	594.595	0.012	97.327	213.059	0.392	150.875
80000	0	5243.121	0.066	97.473	227.948	0.425	1887.750
80000	1	2107.700	0.026	97.355	215.126	0.396	742.500
80000	2	1528.618	0.019	97.324	213.070	0.392	449.625
80000	3	1306.662	0.016	97.299	212.442	0.390	367.500
80000	6	1077.351	0.013	97.255	211.815	0.389	291.375
80000	12	940.612	0.012	97.231	211.431	0.388	246.500
80000	25	851.333	0.011	97.218	211.222	0.388	222.375
80000	50	784.140	0.010	97.221	211.314	0.388	209.500
80000	75	759.907	0.010	97.229	211.599	0.389	199.750
80000	100	752.140	0.009	97.234	211.967	0.390	196.250
80000	100	752.140	0.009	97.234	211.967	0.390	196.250
80000	125	752.485	0.009	97.236	212.383	0.391	193.500
80000	150	757.529	0.009	97.244	212.835	0.392	192.250
120000	0	7609.455	0.063	97.484	229.457	0.428	2657.500
120000	1	3147.268	0.026	97.355	216.102	0.399	1214.875
120000	2	2121.601	0.018	97.323	213.699	0.393	731.750
120000	3	1714.970	0.014	97.291	212.945	0.392	569.500
120000	6	1288.783	0.011	97.269	212.243	0.390	403.875
120000	12	1059.886	0.009	97.252	211.876	0.389	318.750
120000	25	925.813	0.008	97.234	211.696	0.389	266.375
120000	50	838.602	0.007	97.239	211.764	0.389	239.250

120000	75	804.860	0.007	97.250	211.982	0.390	220.250
120000	100	790.195	0.007	97.249	212.263	0.390	218.375
120000	100	790.195	0.007	97.249	212.263	0.390	218.375
120000	125	784.786	0.007	97.266	212.580	0.391	218.625
120000	150	784.907	0.007	97.277	212.922	0.392	219.625

c. Percent differences between *C. atys* and *T. gelada* specimens by metric

Decimation level	Smoothing iterations	DNE	DNE/polygon	2D Area	3D Area	RFI	OPCR
2500	0	25.793	25.742	127.855	167.899	26.564	25.000
2500	1	21.373	21.324	127.763	167.375	26.739	21.615
2500	2	20.006	19.958	127.746	167.104	26.769	15.421
2500	3	19.238	19.191	127.765	166.906	26.743	13.146
2500	6	17.924	17.877	127.797	166.487	26.637	9.976
2500	12	16.633	16.586	127.710	166.011	26.577	5.357
2500	25	16.262	16.216	127.579	165.597	26.534	7.239
2500	50	17.909	17.862	127.263	165.406	26.613	5.014
2500	75	19.968	19.920	126.957	165.399	26.684	1.374
2500	100	21.694	21.645	126.675	165.428	26.705	5.983
2500	100	21.694	21.645	126.675	165.428	26.705	5.983
2500	125	23.006	22.957	126.387	165.457	26.697	9.012
2500	150	23.910	23.860	126.146	165.463	26.612	9.357
5000	0	27.996	27.919	127.327	167.673	26.595	25.090
5000	1	25.004	24.929	127.272	167.350	26.762	26.494
5000	2	24.374	24.299	127.217	167.284	26.898	21.704
5000	3	24.096	24.022	127.239	167.236	26.931	24.426
5000	6	23.668	23.594	127.153	167.105	27.044	24.043
5000	12	22.956	22.882	127.088	166.906	27.073	21.505

5000	25	21.927	21.854	127.054	166.658	27.001	14.624
5000	50	20.156	20.083	126.893	166.494	26.944	12.108
5000	75	19.377	19.306	126.754	166.515	26.911	7.973
5000	100	18.927	18.856	126.677	166.636	26.842	5.467
5000	100	18.927	18.856	126.677	166.636	26.842	5.467
5000	125	18.777	18.706	126.557	166.816	26.819	6.944
5000	150	18.797	18.726	126.398	167.029	26.842	7.373
7500	0	26.519	26.502	127.222	167.414	26.360	14.661
7500	1	25.566	25.550	127.264	167.306	26.581	20.960
7500	2	25.469	25.452	127.279	167.279	26.671	23.196
7500	3	25.192	25.176	127.283	167.257	26.717	22.917
7500	6	24.864	24.847	127.271	167.190	26.792	23.400
7500	12	23.480	23.463	127.130	167.068	26.921	17.407
7500	25	20.802	20.786	127.164	166.899	26.816	13.233
7500	50	18.730	18.714	127.260	166.787	26.578	14.600
7500	75	17.707	17.691	127.326	166.796	26.379	15.195
7500	100	17.021	17.005	127.300	166.869	26.270	12.551
7500	100	17.021	17.005	127.300	166.869	26.270	12.551
7500	125	16.488	16.472	127.334	166.986	26.129	11.777
7500	150	16.064	16.049	127.419	167.129	25.945	9.756
10000	0	28.159	28.121	127.182	167.432	26.309	14.222
10000	0	28.159	28.121	127.182	167.432	26.309	14.222
10000	1	24.521	24.484	127.120	167.196	26.530	23.677
10000	1	24.521	24.484	127.120	167.196	26.530	23.677
10000	2	23.609	23.572	127.144	167.133	26.582	23.167
10000	2	23.609	23.572	127.144	167.133	26.582	23.167
10000	3	23.118	23.081	127.157	167.091	26.609	23.926
10000	3	23.118	23.081	127.157	167.091	26.609	23.926

10000	6	22.829	22.792	127.107	167.009	26.693	24.132
10000	6	22.829	22.792	127.107	167.009	26.693	24.132
10000	12	22.684	22.647	127.078	166.913	26.740	20.000
10000	12	22.684	22.647	127.078	166.913	26.740	20.000
10000	25	21.864	21.828	127.052	166.804	26.723	21.250
10000	25	21.864	21.828	127.052	166.804	26.723	21.250
10000	50	21.168	21.132	127.023	166.740	26.624	15.018
10000	50	21.168	21.132	127.023	166.740	26.624	15.018
10000	75	21.064	21.027	126.990	166.744	26.512	11.700
10000	75	21.064	21.027	126.990	166.744	26.512	11.700
10000	100	21.086	21.049	126.930	166.775	26.419	11.560
10000	100	21.086	21.049	126.930	166.775	26.419	11.560
10000	125	21.070	21.033	126.884	166.823	26.314	14.447
10000	125	21.070	21.033	126.884	166.823	26.314	14.447
10000	150	20.985	20.949	126.862	166.881	26.187	14.206
10000	150	20.985	20.949	126.862	166.881	26.187	14.206
15000	0	28.461	28.418	127.087	167.615	26.308	16.051
15000	1	23.174	23.133	127.054	167.053	26.383	16.104
15000	2	23.845	23.804	127.052	166.986	26.457	17.254
15000	3	24.515	24.473	127.055	166.952	26.491	19.610
15000	6	24.784	24.743	127.021	166.885	26.564	16.644
15000	12	24.408	24.367	127.034	166.812	26.580	18.370
15000	25	24.038	23.997	127.036	166.743	26.566	25.705
15000	50	24.078	24.037	127.022	166.734	26.514	22.742
15000	75	24.301	24.259	127.096	166.789	26.380	22.906
15000	100	24.628	24.587	127.157	166.879	26.256	21.478
15000	100	24.628	24.587	127.157	166.879	26.256	21.478
15000	125	25.100	25.058	127.201	166.992	26.151	24.084

15000	150	25.646	25.604	127.206	167.116	26.070	24.735
20000	0	32.737	32.717	127.176	168.055	26.284	20.379
20000	1	24.565	24.547	127.098	167.109	26.293	15.060
20000	2	24.743	24.724	127.123	167.004	26.334	21.899
20000	3	25.184	25.165	127.060	166.956	26.410	24.473
20000	6	26.285	26.266	127.061	166.869	26.440	25.773
20000	12	27.053	27.033	127.014	166.785	26.487	21.571
20000	25	28.174	28.154	127.011	166.745	26.488	23.563
20000	50	28.833	28.814	126.928	166.782	26.522	22.994
20000	75	29.030	29.011	126.967	166.875	26.449	19.189
20000	100	29.219	29.174	127.004	166.994	26.378	17.236
20000	100	29.219	29.199	127.004	166.994	26.378	17.236
20000	125	29.524	29.505	127.019	167.140	26.330	18.283
20000	150	30.019	30.000	127.019	167.296	26.293	16.901
30000	0	27.700	27.666	127.209	168.992	26.332	17.521
30000	1	18.719	18.688	127.119	167.125	26.132	1.341
30000	2	20.889	20.857	127.081	166.974	26.239	9.192
30000	3	23.712	23.679	127.051	166.952	26.320	10.405
30000	6	27.592	27.558	127.039	166.917	26.392	17.653
30000	12	29.468	29.434	127.026	166.885	26.451	19.824
30000	25	33.552	33.516	127.049	166.893	26.466	22.195
30000	50	35.036	34.999	127.010	166.999	26.529	24.582
30000	75	35.984	35.948	127.060	167.145	26.502	28.937
30000	100	36.879	36.842	127.120	167.308	26.465	27.503
30000	100	36.879	36.842	127.120	167.308	26.465	27.503
30000	125	37.719	37.682	127.157	167.486	26.445	28.571
30000	150	38.605	38.568	127.167	167.673	26.446	30.399
50000	0	14.685	14.777	127.185	168.548	25.117	9.065

50000	1	5.677	5.762	127.142	166.864	25.702	-7.561
50000	2	10.435	10.524	127.096	166.809	25.983	-8.957
50000	3	15.140	15.232	127.097	166.828	26.091	-4.293
50000	6	24.054	24.153	127.062	166.815	26.214	7.097
50000	12	32.076	32.182	127.016	166.747	26.274	15.308
50000	25	37.516	37.626	127.008	166.695	26.283	18.896
50000	50	39.007	39.118	127.020	166.735	26.272	22.308
50000	75	40.115	40.227	127.035	166.841	26.268	27.653
50000	100	41.594	41.708	127.053	166.972	26.268	26.349
50000	100	41.594	41.708	127.053	166.972	26.268	26.349
50000	125	42.743	42.858	127.050	167.121	26.282	28.390
50000	150	43.860	43.976	127.049	167.283	26.298	27.053
80000	0	-0.894	-0.911	127.178	164.714	21.951	-13.097
80000	1	-10.324	-10.340	127.109	165.972	24.879	-16.877
80000	2	-7.938	-7.954	127.122	166.321	25.501	-19.692
80000	3	-4.342	-4.359	127.085	166.465	25.754	-16.000
80000	6	5.150	5.132	126.998	166.618	26.053	-7.094
80000	12	15.256	15.236	126.979	166.679	26.183	0.921
80000	25	23.351	23.330	126.959	166.711	26.262	8.874
80000	50	28.885	28.863	126.950	166.780	26.306	15.666
80000	75	31.077	31.054	126.948	166.881	26.331	15.881
80000	100	32.546	32.523	126.944	166.998	26.353	15.953
80000	100	32.546	32.523	126.944	166.998	26.353	15.953
80000	125	33.666	33.643	126.917	167.125	26.392	17.898
80000	150	34.690	34.666	126.909	167.263	26.418	19.225
120000	0	-28.740	-28.774	127.177	159.990	18.709	-29.188
120000	1	-32.243	-32.274	127.083	164.708	23.803	-26.666
120000	2	-32.595	-32.626	127.088	165.639	24.900	-27.986

120000	3	-31.428	-31.460	127.061	165.982	25.309	-28.082
120000	6	-26.468	-26.502	127.041	166.376	25.751	-24.545
120000	12	-19.793	-19.830	127.044	166.631	26.008	-19.355
120000	25	-12.434	-12.475	127.018	166.818	26.203	-14.896
120000	50	-6.569	-6.612	127.014	166.968	26.310	-10.014
120000	75	-4.278	-4.323	127.045	167.074	26.325	-10.558
120000	100	-3.032	-3.077	127.021	167.169	26.361	-6.976
120000	100	-3.032	-3.077	127.021	167.169	26.361	-6.976
120000	125	-2.366	-2.412	127.055	167.258	26.343	-5.816
120000	150	-1.867	-1.913	127.055	177.817	34.693	-3.673

Table A2.6. DNE, RFI, and OPCR across degrees of X and Y axis rotation.

a. *Cercocebys atys* specimen 89373

i. DNE

X	0	2	4	6	8	10	12	14	16	18	20	22	24	26	28	30
Y																
0	196.151	196.151	196.151	196.151	196.151	196.151	196.151	196.151	196.151	196.151	196.151	196.151	196.151	196.151	196.151	196.151
2	196.151	196.151	196.151	196.151	196.151	196.151	196.151	196.151	196.151	196.151	196.151	196.151	196.151	196.151	196.151	196.151
4	196.151	196.151	196.151	196.151	196.151	196.151	196.151	196.151	196.151	196.151	196.151	196.151	196.151	196.151	196.151	196.151
6	196.151	196.151	196.151	196.151	196.151	196.151	196.151	196.151	196.151	196.151	196.151	196.151	196.151	196.151	196.151	196.151
8	196.151	196.151	196.151	196.151	196.151	196.151	196.151	196.151	196.151	196.151	196.151	196.151	196.151	196.151	196.151	196.151
10	196.151	196.151	196.151	196.151	196.151	196.151	196.151	196.151	196.151	196.151	196.151	196.151	196.151	196.151	196.151	196.151
12	196.151	196.151	196.151	196.151	196.151	196.151	196.151	196.151	196.151	196.151	196.151	196.151	196.151	196.151	196.151	196.151
14	196.151	196.151	196.151	196.151	196.151	196.151	196.151	196.151	196.151	196.151	196.151	196.151	196.151	196.151	196.151	196.151
16	196.151	196.151	196.151	196.151	196.151	196.151	196.151	196.151	196.151	196.151	196.151	196.151	196.151	196.151	196.151	196.151

18	196.151	196.151	196.151	196.151	196.151	196.151	196.151	196.151	196.151	196.151	196.151	196.151	196.151	196.151	196.151	196.151
20	196.151	196.151	196.151	196.151	196.151	196.151	196.151	196.151	196.151	196.151	196.151	196.151	196.151	196.151	196.151	196.151
22	196.151	196.151	196.151	196.151	196.151	196.151	196.151	196.151	196.151	196.151	196.151	196.151	196.151	196.151	196.151	196.151
24	196.151	196.151	196.151	196.151	196.151	196.151	196.151	196.151	196.151	196.151	196.151	196.151	196.151	196.151	196.151	196.151
26	196.151	196.151	196.151	196.151	196.151	196.151	196.151	196.151	196.151	196.151	196.151	196.151	196.151	196.151	196.151	196.151
28	196.151	196.151	196.151	196.151	196.151	196.151	196.151	196.151	196.151	196.151	196.151	196.151	196.151	196.151	196.151	196.151
30	196.151	196.151	196.151	196.151	196.151	196.151	196.151	196.151	196.151	196.151	196.151	196.151	196.151	196.151	196.151	196.151

ii. RFI

1. Absolute Values

X	0	2	4	6	8	10	12	14	16	18	20	22	24	26	28	30
Y																
0	0.306	0.307	0.308	0.310	0.312	0.315	0.319	0.323	0.328	0.332	0.338	0.343	0.349	0.356	0.363	0.370
2	0.306	0.307	0.308	0.310	0.313	0.316	0.319	0.323	0.328	0.333	0.338	0.343	0.349	0.356	0.363	0.370
4	0.307	0.308	0.309	0.311	0.313	0.316	0.320	0.324	0.329	0.333	0.338	0.344	0.350	0.356	0.363	0.370
6	0.309	0.309	0.311	0.313	0.315	0.318	0.321	0.325	0.330	0.334	0.340	0.345	0.351	0.357	0.364	0.371
8	0.311	0.311	0.313	0.314	0.317	0.320	0.323	0.327	0.332	0.336	0.341	0.347	0.352	0.359	0.366	0.373
10	0.313	0.314	0.315	0.317	0.320	0.323	0.326	0.330	0.334	0.339	0.343	0.349	0.354	0.361	0.367	0.375
12	0.316	0.317	0.318	0.320	0.323	0.326	0.329	0.333	0.337	0.341	0.346	0.351	0.357	0.363	0.370	0.377
14	0.320	0.321	0.322	0.324	0.327	0.329	0.333	0.336	0.340	0.345	0.349	0.354	0.360	0.366	0.373	0.380
16	0.324	0.325	0.326	0.328	0.331	0.334	0.337	0.340	0.344	0.348	0.353	0.358	0.364	0.370	0.376	0.383
18	0.329	0.330	0.331	0.333	0.336	0.339	0.342	0.345	0.349	0.353	0.357	0.362	0.367	0.373	0.380	0.387
20	0.334	0.335	0.337	0.339	0.341	0.344	0.347	0.350	0.353	0.357	0.362	0.366	0.372	0.378	0.384	0.391
22	0.340	0.341	0.342	0.344	0.347	0.349	0.352	0.355	0.359	0.362	0.366	0.371	0.376	0.382	0.388	0.395
24	0.346	0.347	0.348	0.350	0.353	0.355	0.358	0.361	0.364	0.368	0.372	0.376	0.381	0.387	0.393	0.400
26	0.352	0.353	0.355	0.357	0.359	0.361	0.364	0.366	0.370	0.373	0.377	0.382	0.387	0.393	0.399	0.406

28	0.359	0.360	0.361	0.363	0.365	0.367	0.370	0.373	0.376	0.379	0.384	0.388	0.393	0.399	0.405	0.411
30	0.366	0.367	0.368	0.370	0.372	0.374	0.377	0.379	0.382	0.386	0.390	0.395	0.400	0.405	0.411	0.418

2. Percent difference from origin (0 degrees X and Y rotation)

X	0	2	4	6	8	10	12	14	16	18	20	22	24	26	28	30
Y																
0	0.000	0.201	0.600	1.245	2.007	3.036	4.195	5.489	6.982	8.549	10.289	12.125	14.127	16.275	18.511	20.942
2	0.106	0.292	0.707	1.318	2.103	3.098	4.285	5.563	7.037	8.621	10.305	12.150	14.082	16.254	18.456	20.890
4	0.346	0.551	1.001	1.597	2.396	3.369	4.515	5.830	7.303	8.821	10.515	12.321	14.268	16.388	18.622	21.015
6	0.783	1.020	1.432	2.080	2.862	3.834	5.003	6.283	7.716	9.234	10.920	12.698	14.636	16.703	18.920	21.318
8	1.471	1.677	2.119	2.723	3.543	4.507	5.626	6.915	8.314	9.821	11.461	13.224	15.085	17.195	19.389	21.768
10	2.307	2.557	2.982	3.585	4.378	5.363	6.472	7.724	9.078	10.588	12.195	13.912	15.760	17.816	19.992	22.358
12	3.357	3.593	4.028	4.604	5.445	6.389	7.474	8.717	10.059	11.497	13.072	14.773	16.594	18.626	20.770	23.117
14	4.534	4.807	5.261	5.877	6.666	7.613	8.705	9.845	11.160	12.571	14.131	15.765	17.579	19.577	21.733	24.090
16	5.913	6.184	6.638	7.299	8.082	9.005	10.067	11.168	12.444	13.805	15.306	16.922	18.745	20.701	22.798	25.082
18	7.442	7.752	8.266	8.861	9.656	10.580	11.591	12.645	13.867	15.189	16.669	18.235	19.988	21.963	24.033	26.262
20	9.206	9.511	9.978	10.645	11.383	12.281	13.203	14.264	15.418	16.728	18.091	19.637	21.426	23.335	25.383	27.591
22	11.046	11.371	11.811	12.469	13.253	14.061	14.977	15.957	17.111	18.312	19.658	21.197	22.933	24.826	26.869	29.089
24	12.990	13.314	13.805	14.454	15.197	15.969	16.854	17.761	18.843	20.061	21.387	22.890	24.600	26.481	28.474	30.674
26	15.052	15.422	15.907	16.518	17.204	17.964	18.754	19.667	20.744	21.889	23.257	24.777	26.423	28.293	30.262	32.478
28	17.216	17.562	18.066	18.656	19.286	19.988	20.778	21.690	22.785	23.949	25.290	26.753	28.433	30.276	32.205	34.391
30	19.414	19.859	20.344	20.886	21.495	22.184	22.999	23.875	24.932	26.098	27.425	28.912	30.578	32.362	34.335	36.497

iii. OPCR

1. Absolute values

X	0	2	4	6	8	10	12	14	16	18	20	22	24	26	28	30
Y																
0	68.125	67.625	67.375	67.375	66.125	64.375	63.500	64.625	65.125	64.875	65.500	66.375	65.125	64.125	63.375	60.875
2	68.625	68.625	68.000	68.375	66.250	65.625	64.875	65.000	66.375	65.125	66.250	66.500	65.500	63.875	63.375	62.500
4	70.375	69.250	68.125	68.000	67.125	66.250	66.375	65.625	66.625	66.625	66.250	66.250	65.125	63.750	63.625	62.250
6	69.625	69.500	68.750	67.500	66.375	65.750	66.625	66.500	67.000	65.375	66.125	64.750	65.750	63.000	63.250	60.750
8	69.250	69.125	68.875	67.375	66.750	67.750	66.625	67.375	66.625	66.125	66.500	65.250	64.375	61.750	61.750	60.000
10	68.250	68.875	69.000	68.000	66.625	66.375	66.375	65.750	65.750	65.125	65.375	63.375	61.250	61.625	61.250	60.125
12	68.250	69.000	68.750	67.500	67.375	67.500	66.000	64.875	65.625	64.500	63.625	61.625	60.500	59.500	59.750	60.000
14	68.500	69.625	68.125	67.000	67.125	66.625	65.625	65.750	63.625	63.875	60.875	60.500	59.875	59.125	58.625	59.125
16	67.875	68.750	68.000	67.625	66.125	67.000	65.000	64.375	63.250	61.500	60.375	59.875	58.875	58.125	58.250	56.875
18	67.250	66.875	66.750	65.500	66.000	65.375	64.125	63.000	61.750	61.375	59.375	57.875	57.250	57.125	57.500	55.875
20	67.125	67.125	66.250	64.875	65.125	62.625	62.500	60.875	60.625	58.750	57.375	56.750	55.625	56.000	56.000	55.750
22	65.000	65.000	64.750	64.625	61.500	60.875	60.125	58.750	58.750	57.250	56.375	55.250	55.000	55.000	55.750	54.500
24	63.750	63.000	63.250	62.625	59.500	58.500	57.500	56.625	55.500	55.750	55.125	54.625	52.750	54.250	54.500	54.125
26	61.500	61.875	60.375	59.125	59.125	56.625	54.500	54.625	54.125	53.750	54.250	52.125	52.750	52.625	54.000	52.125
28	61.250	60.500	59.000	57.750	57.875	54.500	52.125	52.125	52.375	52.000	52.000	52.625	53.000	53.250	52.000	51.625
30	58.750	57.875	57.250	56.000	54.375	54.250	53.125	50.875	49.625	51.125	50.375	52.375	52.750	51.250	52.500	51.250

2. Percent difference from origin (0 degrees X and Y rotation)

X	0	2	4	6	8	10	12	14	16	18	20	22	24	26	28	30
Y																
0	0.000	-0.734	-1.101	-1.101	-2.936	-5.505	-6.789	-5.138	-4.404	-4.771	-3.853	-2.569	-4.404	-5.872	-6.972	-10.642
2	0.734	0.734	-0.183	0.367	-2.752	-3.670	-4.771	-4.587	-2.569	-4.404	-2.752	-2.385	-3.853	-6.239	-6.972	-8.257
4	3.303	1.651	0.000	-0.183	-1.468	-2.752	-2.569	-3.670	-2.202	-2.202	-2.752	-2.752	-4.404	-6.422	-6.606	-8.624
6	2.202	2.018	0.917	-0.917	-2.569	-3.486	-2.202	-2.385	-1.651	-4.037	-2.936	-4.954	-3.486	-7.523	-7.156	-10.826
8	1.651	1.468	1.101	-1.101	-2.018	-0.550	-2.202	-1.101	-2.202	-2.936	-2.385	-4.220	-5.505	-9.358	-9.358	-11.927

10	0.183	1.101	1.284	-0.183	-2.202	-2.569	-2.569	-3.486	-3.486	-4.404	-4.037	-6.972	-10.092	-9.541	-10.092	-11.743
12	0.183	1.284	0.917	-0.917	-1.101	-0.917	-3.119	-4.771	-3.670	-5.321	-6.606	-9.541	-11.193	-12.661	-12.294	-11.927
14	0.550	2.202	0.000	-1.651	-1.468	-2.202	-3.670	-3.486	-6.606	-6.239	-10.642	-11.193	-12.110	-13.211	-13.945	-13.211
16	-0.367	0.917	-0.183	-0.734	-2.936	-1.651	-4.587	-5.505	-7.156	-9.725	-11.376	-12.110	-13.578	-14.679	-14.495	-16.514
18	-1.284	-1.835	-2.018	-3.853	-3.119	-4.037	-5.872	-7.523	-9.358	-9.908	-12.844	-15.046	-15.963	-16.147	-15.596	-17.982
20	-1.468	-1.468	-2.752	-4.771	-4.404	-8.073	-8.257	-10.642	-11.009	-13.761	-15.780	-16.697	-18.349	-17.798	-17.798	-18.165
22	-4.587	-4.587	-4.954	-5.138	-9.725	-10.642	-11.743	-13.761	-13.761	-15.963	-17.248	-18.899	-19.266	-19.266	-18.165	-20.000
24	-6.422	-7.523	-7.156	-8.073	-12.661	-14.128	-15.596	-16.881	-18.532	-18.165	-19.083	-19.817	-22.569	-20.367	-20.000	-20.550
26	-9.725	-9.174	-11.376	-13.211	-13.211	-16.881	-20.000	-19.817	-20.550	-21.101	-20.367	-23.486	-22.569	-22.752	-20.734	-23.486
28	-10.092	-11.193	-13.394	-15.229	-15.046	-20.000	-23.486	-23.486	-23.119	-23.670	-23.670	-22.752	-22.202	-21.835	-23.670	-24.220
30	-13.761	-15.046	-15.963	-17.798	-20.183	-20.367	-22.018	-25.321	-27.156	-24.954	-26.055	-23.119	-22.569	-24.771	-22.936	-24.771

b. *Theropithecus gelada* specimen
1963-58

i. DNE

X	0	2	4	6	8	10	12	14	16	18	20	22	24	26	28	30
Y																
0	237.511	237.511	237.511	237.511	237.511	237.511	237.511	237.511	237.511	237.511	237.511	237.511	237.511	237.511	237.511	237.511
2	237.511	237.511	237.511	237.511	237.511	237.511	237.511	237.511	237.511	237.511	237.511	237.511	237.511	237.511	237.511	237.511
4	237.511	237.511	237.511	237.511	237.511	237.511	237.511	237.511	237.511	237.511	237.511	237.511	237.511	237.511	237.511	237.511
6	237.511	237.511	237.511	237.511	237.511	237.511	237.511	237.511	237.511	237.511	237.511	237.511	237.511	237.511	237.511	237.511
8	237.511	237.511	237.511	237.511	237.511	237.511	237.511	237.511	237.511	237.511	237.511	237.511	237.511	237.511	237.511	237.511
10	237.511	237.511	237.511	237.511	237.511	237.511	237.511	237.511	237.511	237.511	237.511	237.511	237.511	237.511	237.511	237.511
12	237.511	237.511	237.511	237.511	237.511	237.511	237.511	237.511	237.511	237.511	237.511	237.511	237.511	237.511	237.511	237.511
14	237.511	237.511	237.511	237.511	237.511	237.511	237.511	237.511	237.511	237.511	237.511	237.511	237.511	237.511	237.511	237.511
16	237.511	237.511	237.511	237.511	237.511	237.511	237.511	237.511	237.511	237.511	237.511	237.511	237.511	237.511	237.511	237.511
18	237.511	237.511	237.511	237.511	237.511	237.511	237.511	237.511	237.511	237.511	237.511	237.511	237.511	237.511	237.511	237.511

20	237.511	237.511	237.511	237.511	237.511	237.511	237.511	237.511	237.511	237.511	237.511	237.511	237.511	237.511	237.511	237.511
22	237.511	237.511	237.511	237.511	237.511	237.511	237.511	237.511	237.511	237.511	237.511	237.511	237.511	237.511	237.511	237.511
24	237.511	237.511	237.511	237.511	237.511	237.511	237.511	237.511	237.511	237.511	237.511	237.511	237.511	237.511	237.511	237.511
26	237.511	237.511	237.511	237.511	237.511	237.511	237.511	237.511	237.511	237.511	237.511	237.511	237.511	237.511	237.511	237.511
28	237.511	237.511	237.511	237.511	237.511	237.511	237.511	237.511	237.511	237.511	237.511	237.511	237.511	237.511	237.511	237.511
30	237.511	237.511	237.511	237.511	237.511	237.511	237.511	237.511	237.511	237.511	237.511	237.511	237.511	237.511	237.511	237.511

ii. RFI

1. Absolute values

X	0	2	4	6	8	10	12	14	16	18	20	22	24	26	28	30
Y																
0	0.387	0.388	0.390	0.392	0.394	0.397	0.399	0.402	0.405	0.408	0.412	0.416	0.420	0.425	0.431	0.437
2	0.387	0.388	0.390	0.392	0.394	0.396	0.399	0.401	0.404	0.407	0.411	0.415	0.419	0.424	0.430	0.435
4	0.387	0.388	0.390	0.392	0.394	0.397	0.399	0.401	0.404	0.407	0.411	0.414	0.419	0.423	0.429	0.434
6	0.388	0.389	0.391	0.393	0.395	0.397	0.399	0.401	0.404	0.407	0.410	0.414	0.418	0.423	0.428	0.434
8	0.389	0.391	0.392	0.394	0.396	0.398	0.400	0.402	0.405	0.407	0.411	0.414	0.418	0.423	0.428	0.434
10	0.391	0.392	0.394	0.395	0.397	0.399	0.401	0.403	0.405	0.408	0.411	0.415	0.419	0.424	0.429	0.434
12	0.393	0.394	0.395	0.397	0.399	0.400	0.402	0.404	0.406	0.409	0.412	0.416	0.420	0.424	0.429	0.435
14	0.394	0.396	0.397	0.399	0.400	0.402	0.404	0.406	0.408	0.411	0.414	0.417	0.421	0.426	0.431	0.436
16	0.396	0.398	0.399	0.401	0.402	0.404	0.405	0.407	0.410	0.412	0.415	0.419	0.423	0.427	0.432	0.438
18	0.398	0.400	0.402	0.403	0.404	0.406	0.408	0.410	0.412	0.414	0.417	0.421	0.425	0.429	0.434	0.439
20	0.400	0.402	0.404	0.405	0.407	0.408	0.410	0.412	0.414	0.417	0.420	0.423	0.427	0.431	0.436	0.442
22	0.403	0.404	0.406	0.408	0.409	0.411	0.412	0.415	0.417	0.419	0.423	0.426	0.430	0.434	0.439	0.444
24	0.405	0.407	0.408	0.410	0.412	0.413	0.415	0.418	0.420	0.422	0.426	0.429	0.433	0.437	0.442	0.447
26	0.408	0.410	0.411	0.413	0.415	0.416	0.419	0.421	0.423	0.426	0.429	0.432	0.436	0.441	0.445	0.451
28	0.412	0.413	0.415	0.416	0.418	0.420	0.422	0.424	0.427	0.429	0.432	0.436	0.440	0.444	0.449	0.454

30	0.416	0.417	0.418	0.419	0.421	0.423	0.425	0.428	0.430	0.433	0.437	0.440	0.444	0.448	0.453	0.459

2. Percent different from origin (0 degrees X and Y rotation)

X	0	2	4	6	8	10	12	14	16	18	20	22	24	26	28	30
Y																
0	0.000	0.293	0.740	1.290	1.850	2.480	3.118	3.785	4.564	5.427	6.403	7.435	8.624	9.922	11.341	12.845
2	-0.028	0.281	0.724	1.257	1.839	2.415	3.037	3.697	4.447	5.232	6.173	7.186	8.339	9.586	10.992	12.508
4	0.062	0.363	0.802	1.350	1.925	2.468	3.052	3.651	4.358	5.181	6.081	7.037	8.171	9.421	10.780	12.258
6	0.242	0.584	1.001	1.539	2.072	2.603	3.135	3.718	4.390	5.141	6.035	7.023	8.078	9.340	10.676	12.152
8	0.582	0.905	1.317	1.812	2.290	2.811	3.321	3.845	4.518	5.243	6.109	7.049	8.125	9.340	10.680	12.147
10	0.953	1.278	1.722	2.167	2.611	3.093	3.567	4.094	4.719	5.431	6.261	7.186	8.261	9.452	10.772	12.220
12	1.437	1.789	2.172	2.606	2.999	3.413	3.874	4.399	5.012	5.710	6.541	7.445	8.493	9.661	10.953	12.383
14	1.923	2.281	2.677	3.072	3.450	3.839	4.265	4.818	5.414	6.083	6.892	7.787	8.809	10.000	11.247	12.658
16	2.395	2.788	3.207	3.587	3.973	4.329	4.764	5.288	5.891	6.548	7.346	8.213	9.243	10.400	11.640	13.042
18	2.857	3.294	3.742	4.136	4.508	4.899	5.314	5.835	6.423	7.086	7.858	8.717	9.713	10.875	12.125	13.537
20	3.413	3.840	4.306	4.711	5.095	5.462	5.930	6.418	7.005	7.672	8.463	9.307	10.351	11.459	12.706	14.083
22	4.033	4.421	4.873	5.341	5.728	6.121	6.571	7.108	7.685	8.370	9.167	10.018	11.021	12.149	13.385	14.772
24	4.736	5.104	5.521	5.948	6.395	6.837	7.344	7.893	8.457	9.137	9.947	10.805	11.830	12.952	14.191	15.568
26	5.518	5.883	6.281	6.672	7.121	7.596	8.142	8.713	9.316	9.985	10.789	11.667	12.693	13.836	15.094	16.422
28	6.405	6.745	7.111	7.482	7.907	8.401	8.981	9.539	10.218	10.926	11.746	12.636	13.667	14.799	16.044	17.415
30	7.360	7.655	8.012	8.359	8.777	9.269	9.865	10.468	11.182	11.938	12.791	13.687	14.737	15.878	17.106	18.495

iii. OPCR

1. Absolute values

X	0	2	4	6	8	10	12	14	16	18	20	22	24	26	28	30

Y																
0	76.000	77.500	79.375	78.875	80.375	81.125	83.750	83.500	84.250	84.375	83.500	82.750	81.750	82.375	80.750	79.500
2	76.750	78.250	81.000	80.625	81.000	83.250	84.750	85.375	84.625	83.375	83.375	82.625	84.375	82.375	81.375	81.000
4	76.500	79.000	80.125	79.875	81.125	81.875	84.000	86.000	85.875	83.750	85.375	85.500	84.125	83.875	83.375	81.625
6	76.750	78.750	80.125	80.500	82.500	83.750	84.000	84.375	84.750	84.750	86.000	86.000	85.875	83.500	81.375	80.500
8	77.250	79.750	81.250	81.750	83.875	84.875	84.250	85.750	85.250	86.375	85.875	85.750	86.250	84.125	81.125	80.500
10	77.250	79.750	82.750	82.625	84.000	83.625	84.500	85.375	86.875	87.125	85.500	84.875	84.000	83.000	81.500	81.125
12	79.125	79.750	81.250	83.000	83.000	83.750	85.375	86.000	86.750	84.875	84.000	84.375	83.500	81.125	80.625	81.500
14	78.875	80.375	81.250	82.750	82.875	83.500	84.875	84.750	82.125	81.625	83.000	82.000	82.250	79.875	80.125	79.125
16	79.000	79.625	80.250	82.000	82.000	81.500	81.625	82.000	80.375	80.125	81.375	80.125	79.375	79.000	77.500	77.625
18	78.875	79.500	79.375	79.500	78.875	78.875	80.000	79.500	78.875	79.250	79.500	79.625	77.375	76.625	77.250	75.500
20	79.625	77.750	77.500	78.750	78.625	80.250	78.250	78.000	76.750	77.875	77.375	75.250	75.250	74.375	74.750	73.375
22	77.375	77.125	76.125	76.625	76.000	76.250	76.375	75.375	75.875	76.250	73.750	74.875	75.000	73.375	72.750	74.125
24	76.000	76.000	74.750	74.125	74.750	75.250	74.875	74.000	73.625	73.000	73.000	73.625	72.125	72.000	70.750	72.500
26	74.500	73.250	73.125	72.625	73.250	73.625	72.875	73.375	71.500	71.125	70.250	70.625	70.875	69.625	69.125	69.750
28	72.875	72.875	73.375	72.125	71.625	72.000	71.000	71.375	70.625	70.125	69.625	70.000	69.125	68.750	68.000	66.750
30	72.875	72.250	71.500	71.875	69.875	70.375	69.250	69.750	69.375	68.125	67.000	66.875	67.500	67.625	67.625	66.500

2. Percent difference from origin (0 degrees X and Y rotation)

X	0	2	4	6	8	10	12	14	16	18	20	22	24	26	28	30
Y																
0	0.000	1.974	4.441	3.783	5.757	6.743	10.197	9.868	10.855	11.020	9.868	8.882	7.566	8.388	6.250	4.605
2	0.987	2.961	6.579	6.086	6.579	9.539	11.513	12.336	11.349	9.704	9.704	8.717	11.020	8.388	7.072	6.579
4	0.658	3.947	5.428	5.099	6.743	7.730	10.526	13.158	12.993	10.197	12.336	12.500	10.691	10.362	9.704	7.401
6	0.987	3.618	5.428	5.921	8.553	10.197	10.526	11.020	11.513	11.513	13.158	13.158	12.993	9.868	7.072	5.921
8	1.645	4.934	6.908	7.566	10.362	11.678	10.855	12.829	12.171	13.651	12.993	12.829	13.487	10.691	6.743	5.921
10	1.645	4.934	8.882	8.717	10.526	10.033	11.184	12.336	14.309	14.638	12.500	11.678	10.526	9.211	7.237	6.743

12	4.112	4.934	6.908	9.211	9.211	10.197	12.336	13.158	14.145	11.678	10.526	11.020	9.868	6.743	6.086	7.237
14	3.783	5.757	6.908	8.882	9.046	9.868	11.678	11.513	8.059	7.401	9.211	7.895	8.224	5.099	5.428	4.112
16	3.947	4.770	5.592	7.895	7.895	7.237	7.401	7.895	5.757	5.428	7.072	5.428	4.441	3.947	1.974	2.138
18	3.783	4.605	4.441	4.605	3.783	3.783	5.263	4.605	3.783	4.276	4.605	4.770	1.809	0.822	1.645	-0.658
20	4.770	2.303	1.974	3.618	3.454	5.592	2.961	2.632	0.987	2.467	1.809	-0.987	-0.987	-2.138	-1.645	-3.454
22	1.809	1.480	0.164	0.822	0.000	0.329	0.493	-0.822	-0.164	0.329	-2.961	-1.480	-1.316	-3.454	-4.276	-2.467
24	0.000	0.000	-1.645	-2.467	-1.645	-0.987	-1.480	-2.632	-3.125	-3.947	-3.947	-3.125	-5.099	-5.263	-6.908	-4.605
26	-1.974	-3.618	-3.783	-4.441	-3.618	-3.125	-4.112	-3.454	-5.921	-6.414	-7.566	-7.072	-6.743	-8.388	-9.046	-8.224
28	-4.112	-4.112	-3.454	-5.099	-5.757	-5.263	-6.579	-6.086	-7.072	-7.730	-8.388	-7.895	-9.046	-9.539	-10.526	-12.171
30	-4.112	-4.934	-5.921	-5.428	-8.059	-7.401	-8.882	-8.224	-8.717	-10.362	-11.842	-12.007	-11.184	-11.020	-11.020	-12.500

Table A3.1. Sample specimens with museum attributions.

Genus	Species	Collection	Specimen Number	Wear Score	Primary sample	Secondary sample
Allenopithecus	*nigroviridis*	BMNH	1938.1134	1	x	
Allenopithecus	*nigroviridis*	BMNH	28.11.11.4A	1.5	x	
Allenopithecus	*nigroviridis*	BMNH	28.11.11.4B	1.5	x	
Allenopithecus	*nigroviridis*	NMNH	300808	1.5	x	
Allenopithecus	*nigroviridis*	NMNH	395131	3.5	x	
Allenopithecus	*nigroviridis*	NMNH	537780	1	x	
Cercocebus	*atys*	AMNH	70063	1	x	
Cercocebus	*atys*	AMNH	70385	1	x	
Cercocebus	*atys*	AMNH	77777	2	x	
Cercocebus	*atys*	AMNH	89373	3	x	
Cercocebus	*atys*	MNHNP	1962-1431	3	x	
Cercocebus	*atys*	MNHNP	1962-1437	4	x	
Cercocebus	*atys*	MNHNP	1982-1065	1.5	x	
Cercopithecus	*campbelli*	MNHNP	1908-57	1		x
Cercopithecus	*campbelli*	MNHNP	1967-65	0.5		x
Cercopithecus	*campbelli*	MNHNP	2009-337	0.5		x
Cercopithecus	*campbelli*	MNHNP	2009-339	1.5		x
Cercopithecus	*campbelli*	NMNH	16105	1		x
Cercopithecus	*campbelli*	SMNK	4220	1.5		x
Cercopithecus	*campbelli*	SMNK	4226	2.5		x
Cercopithecus	*mitis*	AMNH	52354	1	x	
Cercopithecus	*mitis*	AMNH	52355	1	x	
Cercopithecus	*mitis*	AMNH	52364	1	x	
Cercopithecus	*mitis*	NMNH	236996	2	x	
Cercopithecus	*mitis*	NMNH	259446	2	x	

Cercopithecus	*mitis*	NMNH	452544	2	x	
Cercopithecus	*mitis*	NMNH	452547	1	x	
Cercopithecus	*mitis*	NMNH	452548	2	x	
Cercopithecus	*mitis*	NMNH	452552	2	x	
Cercopithecus	*mitis*	NMNH	452554	1	x	
Chlorocebus	*aethiops*	NMNH	182161	2.5	x	
Chlorocebus	*aethiops*	NMNH	182164	3	x	
Chlorocebus	*aethiops*	NMNH	182166	1.5	x	
Chlorocebus	*aethiops*	NMNH	252703	2	x	
Chlorocebus	*aethiops*	NMNH	342069	2.5	x	
Chlorocebus	*aethiops*	NMNH	396326	1.5	x	
Chlorocebus	*aethiops*	NMNH	397230	1	x	
Chlorocebus	*aethiops*	NMNH	397717	4	x	
Chlorocebus	*aethiops*	NMNH	397720	1	x	
Chlorocebus	*aethiops*	NMNH	397721	3.5	x	
Colobus	*guereza*	AMNH	52236	1.5	x	
Colobus	*guereza*	BMNH	40.1	3		x
Colobus	*guereza*	BMNH	40.8	1	x	x
Colobus	*guereza*	BMNH	54.762	1.5	x	x
Colobus	*guereza*	BMNH	72.152	2.5	x	x
Colobus	*guereza*	BMNH	1.4.6.1	2	x	x
Colobus	*guereza*	BMNH	11.7.25.15	1		x
Colobus	*guereza*	BMNH	12.5.18.2	4		x
Colobus	*guereza*	BMNH	14.1.24.1	1	x	x
Colobus	*guereza*	BMNH	1938.9.9.4	1	x	x
Colobus	*guereza*	BMNH	24.8.6.4	2	x	x
Colobus	*guereza*	BMNH	28.11.11.2	1.5	x	x
Colobus	*guereza*	MNHNP	163627	1.5	x	x

Colobus	*guereza*	NMNH	148579	4		x
Colobus	*guereza*	NMNH	163124	2		x
Colobus	*guereza*	NMNH	163273	2.5		x
Colobus	*satanas*	BMNH	30.12.15.7	1	x	
Colobus	*satanas*	MNHNP	1856-28	0.5	x	
Colobus	*satanas*	MNHNP	1885-891	1	x	
Colobus	*satanas*	NMNH	598556	3.5	x	
Colobus	*satanas*	NMNH	598557	2	x	
Colobus	*satanas*	NMNH	598560	1	x	
Colobus	*satanas*	NMNH	598561	0.5	x	
Lophocebus	*albigena*	AMNH	52603	1.5	x	
Lophocebus	*albigena*	AMNH	52611	1.5	x	
Lophocebus	*albigena*	AMNH	52613	1	x	
Lophocebus	*albigena*	AMNH	52615	1.5	x	
Lophocebus	*albigena*	NMNH	220086	0.5	x	
Lophocebus	*albigena*	NMNH	220087	2	x	
Lophocebus	*albigena*	NMNH	220089	1	x	
Lophocebus	*albigena*	NMNH	220375	1	x	
Lophocebus	*albigena*	NMNH	220376	2	x	
Lophocebus	*albigena*	NMNH	598484	0.5	x	
Macaca	*fascicularis*	AMNH	102768	2	x	
Macaca	*fascicularis*	AMNH	103649	2	x	
Macaca	*fascicularis*	AMNH	103655	2	x	
Macaca	*fascicularis*	AMNH	106025	2	x	
Macaca	*fascicularis*	MNHNP	1876-411	0.5		x
Macaca	*fascicularis*	MNHNP	1890-37	0.5		x
Macaca	*fascicularis*	MNHNP	1899-278	1		x
Macaca	*fascicularis*	MNHNP	1906-125	1		x

Macaca	*fascicularis*	MNHNP	2009-385	1.5		x
Macaca	*fascicularis*	NMNH	34913	2.5	x	x
Macaca	*fascicularis*	NMNH	114411	2.5	x	x
Macaca	*fascicularis*	NMNH	114505	3		x
Macaca	*fascicularis*	NMNH	121803	2	x	x
Macaca	*fascicularis*	NMNH	125102	3.5	x	x
Macaca	*fascicularis*	NMNH	196817	4		x
Macaca	*fascicularis*	NMNH	196824	3	x	x
Macaca	*fascicularis*	NMNH	198300	4		x
Macaca	*fascicularis*	NMNH	317191	2	x	x
Macaca	*sylvanus*	MNHNP	1926-251	3	x	
Macaca	*sylvanus*	MNHNP	1926-299	2	x	
Macaca	*sylvanus*	MNHNP	1931-835	2.5	x	
Macaca	*sylvanus*	MNHNP	1962-1473	1	x	
Macaca	*sylvanus*	MNHNP	1995-1252	4	x	
Macaca	*sylvanus*	MNHNP	2009-364	1	x	
Macaca	*sylvanus*	NMNH	255979	5	x	
Macaca	*sylvanus*	NMNH	476783	5	x	
Mandrillus	*sphinx*	AMNH	274	1.5	x	
Mandrillus	*sphinx*	AMNH	120387	2	x	
Mandrillus	*sphinx*	AMNH	903418	1.5	x	
Mandrillus	*sphinx*	MNHNP	1934-1418	2	x	
Mandrillus	*sphinx*	MNHNP	1962-1466	4.5	x	
Mandrillus	*sphinx*	MNHNP	1971-303	1	x	
Mandrillus	*sphinx*	MNHNP	1995-238	1.5	x	
Mandrillus	*sphinx*	NMNH	598493	5	x	
Mandrillus	*sphinx*	NMNH	598494	5	x	
Mandrillus	*sphinx*	NMNH	598554	5	x	

Miopithecus	*ogouensis*	BMNH	5.5.23.8	1	x	
Miopithecus	*ogouensis*	BMNH	5.5.23.9	1.5	x	
Miopithecus	*ogouensis*	BMNH	8.2.4.3	2.5	x	
Miopithecus	*ogouensis*	BMNH	97.7.1.1	1	x	
Miopithecus	*ogouensis*	NMNH	220338	2	x	
Miopithecus	*ogouensis*	NMNH	395340	1	x	
Miopithecus	*ogouensis*	NMNH	395343	2.5	x	
Miopithecus	*ogouensis*	NMNH	397625	1.5	x	
Miopithecus	*ogouensis*	NMNH	397649	1	x	
Nasalis	*larvatus*	AMNH	103461	3.5	x	
Nasalis	*larvatus*	AMNH	103466	3.5	x	
Nasalis	*larvatus*	AMNH	103468	3	x	
Nasalis	*larvatus*	AMNH	103668	2	x	
Nasalis	*larvatus*	AMNH	103671	3.5	x	
Nasalis	*larvatus*	NMNH	142216	3	x	
Nasalis	*larvatus*	NMNH	142219	4	x	
Nasalis	*larvatus*	NMNH	145323	4	x	
Nasalis	*larvatus*	NMNH	196789	2	x	
Nasalis	*larvatus*	NMNH	198277	3	x	
Papio	*cynocephalus*	BMNH	1966.494	1.5	x	x
Papio	*cynocephalus*	BMNH	1897.10.1.10	1	x	x
Papio	*cynocephalus*	BMNH	1897.10.1.11	2.5	x	x
Papio	*cynocephalus*	NMNH	313783			x
Papio	*cynocephalus*	NMNH	384211	1	x	x
Papio	*cynocephalus*	NMNH	384216	2	x	x
Papio	*cynocephalus*	NMNH	384217	2	x	x
Papio	*cynocephalus*	NMNH	384218	4	x	x

Papio	*cynocephalus*	NMNH	452507	1	x	x
Papio	*cynocephalus*	NMNH	452509	2	x	x
Piliocolobus	*badius*	AMNH	89421	1.5	x	
Piliocolobus	*badius*	MNHNP	1895-9	2	x	
Piliocolobus	*badius*	MNHNP	1939-705	1.5	x	
Piliocolobus	*badius*	MNHNP	1962-1195	1.5	x	
Piliocolobus	*badius*	MNHNP	2009-288	2	x	
Presbytis	*melalophos*	AMNH	102755	1	x	
Presbytis	*melalophos*	AMNH	102757	2	x	
Presbytis	*melalophos*	AMNH	102882	2	x	
Presbytis	*melalophos*	AMNH	102883	1	x	
Presbytis	*melalophos*	AMNH	102891	1	x	
Presbytis	*melalophos*	AMNH	102895	1	x	
Presbytis	*melalophos*	AMNH	106600	1	x	
Presbytis	*melalophos*	AMNH	106603	2	x	
Presbytis	*melalophos*	AMNH	106605	1.5	x	
Presbytis	*melalophos*	AMNH	106671	2	x	
Presbytis	*melalophos*	AMNH	107086	1.5	x	
Procolobus	*verus*	MNHNP	1962-178	1	x	
Procolobus	*verus*	NMNH	477329	3	x	
Procolobus	*verus*	NMNH	477330	5	x	
Procolobus	*verus*	NMNH	481799	1.5	x	
Procolobus	*verus*	NMNH	481800	2	x	
Procolobus	*verus*	NMNH	481801	3	x	
Procolobus	*verus*	NMNH	481802	2.5	x	
Pygathrix	*nigripes*	BMNH	27.12.1.10	2.5	x	
Pygathrix	*nigripes*	BMNH	6.11.6.1	1.5	x	
Pygathrix	*nigripes*	BMNH	8.11.1.2	2	x	

Pygathrix	*nigripes*	BMNH	8.11.1.4	1.5	x	
Pygathrix	*nigripes*	MNHNP	1877-695	4	x	
Pygathrix	*nigripes*	MNHNP	1878-1123	4.5	x	
Pygathrix	*nigripes*	MNHNP	1896-2422	2	x	
Pygathrix	*nigripes*	MNHNP	1929-443	2	x	
Rhinopithecus	*roxellana*	AMNH	110456	0.5	x	
Rhinopithecus	*roxellana*	AMNH	119648	2	x	
Rhinopithecus	*roxellana*	BMNH	8.10.9.1	1	x	
Rhinopithecus	*roxellana*	BMNH	8.10.9.2	1.5	x	
Rhinopithecus	*roxellana*	NMNH	258986	1	x	
Rhinopithecus	*roxellana*	NMNH	268888	2	x	
Rhinopithecus	*roxellana*	NMNH	268891	4	x	
Rhinopithecus	*roxellana*	NMNH	268894	4	x	
Rhinopithecus	*roxellana*	NMNH	268897	3	x	
Semnopithecus	*entellus*	AMNH	90328	2	x	
Semnopithecus	*entellus*	AMNH	150044	3	x	
Semnopithecus	*entellus*	BMNH	12.2.8.6	2.5	x	
Semnopithecus	*entellus*	BMNH	14.11.18.17	2.5	x	
Semnopithecus	*entellus*	BMNH	14.11.18.25	1.5	x	
Semnopithecus	*entellus*	BMNH	14.7.10.14	3.5	x	
Semnopithecus	*entellus*	BMNH	15.3.1.8	2.5	x	
Semnopithecus	*entellus*	MNHNP	1958-162	2.5	x	
Semnopithecus	*entellus*	MNHNP	1964-1615	0.5	x	
Semnopithecus	*entellus*	MNHNP	2009-412	2	x	
Theropithecus	*gelada*	MNHNP	1904-161	4		x
Theropithecus	*gelada*	MNHNP	1904-174	1		x
Theropithecus	*gelada*	MNHNP	1931-836	4	x	x
Theropithecus	*gelada*	MNHNP	1934-1419	3.5	x	x

Theropithecus	*gelada*	MNHNP	1934-251	5		x
Theropithecus	*gelada*	MNHNP	1942-162	5		x
Theropithecus	*gelada*	MNHNP	1962-1467	3	x	x
Theropithecus	*gelada*	MNHNP	1963-58	2	x	x
Theropithecus	*gelada*	MNHNP	1969-448	4.5		x
Theropithecus	*gelada*	MNHNP	1969-451	5	x	x
Theropithecus	*gelada*	MNHNP	1969-453	4.5		x
Theropithecus	*gelada*	MNHNP	1971-10	2	x	x
Theropithecus	*gelada*	MNHNP	1972-360	4	x	x
Theropithecus	*gelada*	MNHNP	A-1.440	3.5	x	x
Theropithecus	*gelada*	NMNH	240885	5		x
Theropithecus	*gelada*	NMNH	283190	2.5		x
Theropithecus	*gelada*	NMNH	305107	4	x	x
Theropithecus	*gelada*	NMNH	319992	5		x
Theropithecus	*gelada*	NMNH	354990	5	x	x
Trachypithecus	*obscurus*	AMNH	54967	1.5	x	
Trachypithecus	*obscurus*	AMNH	54969	5	x	
Trachypithecus	*obscurus*	AMNH	54970	5	x	
Trachypithecus	*obscurus*	AMNH	119492	3	x	
Trachypithecus	*obscurus*	NMNH	37304	4	x	
Trachypithecus	*obscurus*	NMNH	83258	1	x	
Trachypithecus	*obscurus*	NMNH	104445	1.5	x	
Trachypithecus	*obscurus*	NMNH	124177	2	x	
Trachypithecus	*obscurus*	NMNH	236623	2	x	
Trachypithecus (Kasi)	*vetulus*	BMNH	66.5544	2	x	
Trachypithecus (Kasi)	*vetulus*	BMNH	66.5545	1	x	
Trachypithecus (Kasi)	*vetulus*	BMNH	1975.1086	1	x	
Trachypithecus (Kasi)	*vetulus*	BMNH	1950.7.17.7	2	x	

Trachypithecus (Kasi)	*vetulus*	BMNH	20.5.1.1	5	x
Trachypithecus (Kasi)	*vetulus*	BMNH	23.1.18.2	1	x
Trachypithecus (Kasi)	*vetulus*	BMNH	23.1.18.3	1.5	x
Trachypithecus (Kasi)	*vetulus*	BMNH	28.7.12.3	3	x
Trachypithecus (Kasi)	*vetulus*	BMNH	79.9.5.2	2	x

* Museum attributions. AMNH: American Museum of Natural History, New York. BMNH: Natural History Museum, London. MNHNP: Museum nationale d'Histoire naturelle, Paris. NMNH: National Museum of Natural History, Washington D.C. SMNK: State Museum of Natural History, Karlsruhe.

Table A3.2. Raw topographic variable data for individual specimens of primary (relatively unworn) sample.

Specimen	Species	Polygons	DNE	DNE/Polygons	RFI	OPCR	Ln 2D Area	Ln 3D Area
Allne300808-m2-or-uc-10ksimp-100sm-h-gm-asc.ply	*Allenopithecus nigroviridis*	9878	263.281	234.614	0.352	66	3.372	4.077
Allne395131b-m2-or-uc-10ksimp-100sm-h-gm-asc.ply	*Allenopithecus nigroviridis*	10284	170.583	165.872	0.247	77	3.171	3.666
Allne537780-m2-or-uc-10ksimp-100sm-h-gm-q-asc.ply	*Allenopithecus nigroviridis*				0.338	82.25	3.128	3.804
Allni11114A-m2-or-uc-10ksimp-100sm-h-gm-asc.ply	*Allenopithecus nigroviridis*	9945	209.328	210.486	0.353	61.25	3.178	3.885
Allni11114B-m2-or-uc-10ksimp-100sm-gm-asc.ply	*Allenopithecus nigroviridis*	9998	173.496	173.531	0.324	61.375	3.170	3.819
Cerat1065-m2-or-uc-10ksimp-100sm-gm-asc.ply	*Cercocebus atys*	10000	171.593	171.593	0.263	87.5	3.754	4.280
Cerat1437-m2-or-uc-10ksimp-100sm-gm-asc-e.ply	*Cercocebus atys*	9958	209.779	210.664	0.308	80.25	3.115	3.731
Certoat1431-m2-or-uc-10ksimp-100sm-h-gm-asc.ply	*Cercocebus atys*	9855	204.604	207.614	0.229	99.375	3.491	3.948
Cetorat70063-m2-or-uc-10ksimp-100sm-h-gm-asc-e.ply	*Cercocebus atys*	9716	199.282	205.107	0.296	68.25	4.053	4.646
Cetorat70385-m2-or-uc-10ksimp-100sm-h-gm-asc.ply	*Cercocebus atys*	9872	180.458	182.798	0.276	63.625	4.003	4.556
Cetorat77777-m2-or-uc-10ksimp-100sm-h-gm-asc.ply	*Cercocebus atys*	10109	201.462	199.290	0.279	63	3.572	4.129
Cetorat89373-m2-or-uc-10ksimp-100sm-h-gm-asc.ply	*Cercocebus atys*	9900	208.763	210.872	0.308	68	3.762	4.379
Cermi236996-m2-or-uc-10ksimp-100sm-h-gm-asc.ply	*Cercopithecus mitis*	9789	197.171	201.421	0.276	84.75	3.105	3.657
Cermi259446-m2-or-uc-10ksimp-100sm-gm-asc-e.ply	*Cercopithecus mitis*	9887	232.882	235.544	0.351	66.75	3.194	3.896
Cermi452544-m2-or-uc-10ksimp-100sm-gm-asc.ply	*Cercopithecus mitis*	9998	162.861	162.894	0.303	71.75	3.327	3.933
Cermi452547-m2-or-uc-10ksimp-100sm-gm-asc.ply	*Cercopithecus mitis*	9998	194.377	194.416	0.303	62.125	3.257	3.863
Cermi452548-m2-or-uc-10ksimp-100sm-h-gm-asc.ply	*Cercopithecus mitis*	9931	225.176	226.741	0.254	77.875	3.609	4.117

Cermi452552-m2-or-uc-10ksimp-100sm-h-gm-asc.ply	*Cercopithecus mitis*	9887	138.265	139.845	0.251	62.5	3.009	3.511
Cermi452554-m2-or-uc-10ksimp-100sm-h-gm-asc.ply	*Cercopithecus mitis*	9936	224.239	225.683	0.316	71.75	3.449	4.082
Cermi52354-m2-or-uc-10ksimp-100sm-h-gm-asc.ply	*Cercopithecus mitis*	9749	188.483	193.336	0.299	60.5	3.333	3.932
Cermi52355-m2-or-uc-10ksimp-100sm-h-gm-asc-e.ply	*Cercopithecus mitis*	9975	231.539	232.119	0.327	75.5	3.464	4.117
Cermi52364-m2-or-uc-10ksimp-100sm-h-gm-asc.ply	*Cercopithecus mitis*	9954	207.213	208.171	0.346	64	3.485	4.176
Chlae182161-m2-or-uc-10ksimp-100sm-gm-asc.ply	*Chlorocebus aethiops*	9998	177.626	177.662	0.273	80	3.249	3.795
Chlae182164-m2-or-uc-10ksimp-100sm-gm-asc.ply	*Chlorocebus aethiops*	9998	167.214	167.247	0.276	73.375		
Chlae182166-m2-or-uc-10ksimp-100sm-h-gm-asc.ply	*Chlorocebus aethiops*	10063	235.13	233.658	0.325	76.25	3.225	3.876
Chlae252703-m2-or-uc-10ksimp-100sm-gm-asc.ply	*Chlorocebus aethiops*	9995	178.302	178.391	0.273	72.875	3.403	3.948
Chlae342069-m2-or-uc-10ksimp-100sm-gm-asc.ply	*Chlorocebus aethiops*	9995	179.096	179.186	0.239	88.25	3.352	3.830
Chlae396326-m2-or-uc-10ksimp-100sm-gm-asc.ply	*Chlorocebus aethiops*	9998	189.819	189.857	0.324	63.125	3.310	3.958
Chlae397230-m2-or-uc-10ksimp-100sm-gm-asc.ply	*Chlorocebus aethiops*	9998	228.089	228.135	0.329	84.125	3.324	3.982
Chlae397717-m2-or-uc-10ksimp-100sm-gm-asc.ply	*Chlorocebus aethiops*	9986	209.147	209.440	0.240	105.5	3.468	3.948
Chlae397720-m2-or-uc-10ksimp-100sm-gm-asc.ply	*Chlorocebus aethiops*	9998	163.419	163.452	0.243	78.375	2.969	3.455
Chlae397721-m2-or-uc-10ksimp-100sm-gm-asc.ply	*Chlorocebus aethiops*	9990	214.395	214.610	0.238	97.75	3.259	3.736
Cogue52236-m2-or-uc-10ksimp-100sm-h-gm-asc.ply	*Colobus guereza*	10112	199.571	197.361	0.328	64.25	3.601	4.257
Colgu11112-m2-or-uc-10ksimp-100sm-gm-asc.ply	*Colobus guereza*	10000	198.762	198.762	0.350	68.25	3.562	4.263
Colgu1241-m2-or-uc-10ksimp-100sm-gm-asc.ply	*Colobus guereza*	9997	231.574	231.643	0.372	85.25	3.689	4.433
Colgu152-m2-or-uc-10ksimp-100sm-gm-asc.ply	*Colobus guereza*	9997	237.85	237.921	0.351	77	3.465	4.168
Colgu163627-m2-or-uc-10ksimp-100sm-gm-asc.ply	*Colobus guereza*	10000	195.988	195.988	0.389	60.375	3.466	4.243
Colgu408-m2-or-uc-10ksimp-100sm-gm-asc.ply	*Colobus guereza*	9989	218.999	219.240	0.321	70.625	3.556	4.197
Colgu461-m2-or-uc-10ksimp-100sm-h-gm-asc.ply	*Colobus guereza*	9978	230.718	231.227	0.341	86.75	3.440	4.121
Colgu762-m2-or-uc-10ksimp-100sm-h-gm-asc.ply	*Colobus guereza*	10190	231.524	227.207	0.386	66.25	3.619	4.390
Colgu864-m2-or-uc-10k-100sm-gm-asc.ply	*Colobus guereza*	9994	196.928	197.046	0.362	63.25	3.669	4.394
Colgu994-m2-or-uc-10ksimp-100sm-gm-asc.ply	*Colobus guereza*	9992	226.935	227.117	0.389	67.125	3.540	4.317
Colsa12157-m2-or-uc-10ksimp-100sm-gm-asc.ply	*Colobus satanas*	9994	228.67	228.807	0.310	87.75	3.497	4.117
Colsa28-m2-or-uc-10ksimp-100sm-h-gm-asc.ply	*Colobus satanas*	9999	234.157	234.180	0.319	86.625	3.410	4.049
Colsa598556-m2-or-uc-10ksimp-100sm-h-gm-asc.ply	*Colobus satanas*	10022	223.366	222.876	0.329	80	3.420	4.078

Colsa598557-2-m2-or-uc-10ksimp-100sm-h-gm-asc.ply	*Colobus satanas*	10000	206.043	206.043	0.304	73.5	3.491	4.100
Colsa598560-m2-or-uc-10ksimp-100sm-gm-asc.ply	*Colobus satanas*	9990	229.647	229.877	0.352	71	3.432	4.136
Colsa598561-m2-or-uc-10ksimp-100sm-gm-asc.ply	*Colobus satanas*	9996	212.468	212.553	0.361	69.875	3.502	4.224
Colsa891-m2-or-uc-10ksimp-100sm-gm-asc.ply	*Colobus satanas*	10000	198.541	198.541	0.304	78.25	3.442	4.050
Lopal220086-m2-or-uc-10ksimp-100sm-h-gm-asc.ply	*Lophocebus albigena*	9929	201.437	202.877	0.281	77.625	3.564	4.127
Lopal220087-m2-or-uc-10ksimp-100sm-gm-asc.ply	*Lophocebus albigena*	9974	200.851	201.375	0.267	77.125	3.183	3.716
Lopal220089-m2-or-uc-10ksimp-100sm-h-gm-asc.ply	*Lophocebus albigena*	10360	199.65	192.712	0.242	82	3.505	3.988
Lopal220375-m2-or-uc-10ksimp-100sm-h-gm-asc.ply	*Lophocebus albigena*	10171	202.097	198.699	0.288	76.625	3.276	3.852
Lopal220376-m2-or-uc-10ksimp-100sm-h-gm-asc.ply	*Lophocebus albigena*	10065	169.708	168.612	0.241	75.875	3.356	3.837
Lopal52603-m2-or-uc-10ksimp-100sm-h-gm-asc.ply	*Lophocebus albigena*	9990	209.622	209.832	0.285	81.625	3.575	4.144
Lopal52611-m2-or-uc-10ksimp-100sm-h-gm-asc.ply	*Lophocebus albigena*	9863	219.204	222.249	0.263	92	3.383	3.910
Lopal52613-m2-or-uc-10ksimp-100sm-gm-asc.ply	*Lophocebus albigena*	9998	188.711	188.749	0.275	71.5	3.534	4.083
Lopal52615-m2-or-uc-10ksimp-100sm-gm-asc.ply	*Lophocebus albigena*	9995	185.014	185.107	0.213	82.5	3.574	4.001
Lopal598484-m2-or-uc-10ksimp-100sm-h-gm-asc.ply	*Lophocebus albigena*	10075	161.303	160.102	0.237	73.5	3.465	3.940
Macfa102768-m2-or-uc-10ksimp-100sm-gm-asc.ply	*Macaca fascicularis*	10112	241.864	235.535	0.340	83.75	3.400	4.079
Macfa103649-m2-or-uc-10ksimp-100sm-gm-asc.ply	*Macaca fascicularis*	9987	220.466	220.753	0.301	97.75	3.408	4.009
Macfa103655-m2-or-uc-10ksimp-100sm-gm-asc.ply	*Macaca fascicularis*	9996	186.052	186.126	0.316	74.5	3.227	3.858
Macfa106025-m2-or-uc-10ksimp-100sm-h-gm-asc.ply	*Macaca fascicularis*	9948	227.262	228.450	0.295	90.875	3.488	4.078
Macfa114411-m2-or-uc-10ksimp-100sm-h-gm-asc.ply	*Macaca fascicularis*	10210	215.815	211.376	0.329	90.25	3.393	4.051
Macfa121803-m2-or-uc-10ksimp-100sm-h-gm-asc.ply	*Macaca fascicularis*	10183	230.451	226.310	0.258	97.375	3.438	3.954
Macfa125102-m2-or-uc-10ksimp-100sm-h-gm-asc.ply	*Macaca fascicularis*	10430	225.367	216.076	0.278	93.625	3.312	3.868
Macfa196824-m2-or-uc-10ksimp-100sm-h-gm-asc.ply	*Macaca fascicularis*	9973	188.932	189.443	0.273	85.75	3.319	3.865
Macfa317191-m2-or-uc-10ksimp-100sm-h-gm-asc.ply	*Macaca fascicularis*	10162	228.487	224.845	0.298	78.75	3.466	4.062
Macfa34913-m2-or-uc-10ksimp-100sm-h-gm-asc.ply	*Macaca fascicularis*	10100	189.925	188.045	0.247	81.75	3.338	3.833
Macsy1252-m2-or-uc-e-10ksimp-100sm-h-gm-asc.ply	*Macaca sylvanus*	10054	150.842	150.032	0.286	64	3.969	4.542
Macsy1473-m2-or-uc-10ksimp-100sm-h-gm-asc.ply	*Macaca sylvanus*	10276	212.02	206.325	0.274	96	3.890	4.438
Macsy251-m2-or-uc-10ksimp-100sm-h-gm-asc.ply	*Macaca sylvanus*	9825	203.104	206.722	0.338	76.875		
Macsy255979-m2-or-uc-10ksimp-100sm-h-gm-asc.ply	*Macaca sylvanus*	9941	211.628	212.884	0.221	98	4.101	4.543

Macsy299-m2-or-uc-10ksimp-100sm-h-gm-asc.ply	*Macaca sylvanus*	10363	222.592	214.795	0.305	93.875	4.076	4.687
Macsy476783-m2-or-uc-10ksimp-100sm-gm-asc.ply	*Macaca sylvanus*	9994	181.949	182.058	0.281	76.625	3.787	4.348
Macsy835-m2-or-uc-10ksimp-100sm-h-gm-asc.ply	*Macaca sylvanus*	9949	198.249	199.265	0.244	99.625	3.960	4.448
Mansp120387-m2-or-uc-10ksimp-100sm-gm-asc.ply	*Mandrillus sphinx*	10244	262.304	228.681	0.315	79.125	4.627	5.257
Mansp1418-Lm2-or-uc-10ksimp-100sm-gm-asc.ply	*Mandrillus sphinx*	9991	212.352	212.543	0.223	95.875	4.534	4.980
Mansp1466-m2-or-uc-10ksimp-100sm-gm-asc.ply	*Mandrillus sphinx*	9997	176.096	176.149	0.221	82.25	4.351	4.793
Mansp238-m2-or-uc-10ksimp-100sm-gm-asc.ply	*Mandrillus sphinx*	9985	188.404	188.687	0.247	79.125	4.272	4.766
Mansp274-m2-or-uc-10ksimp-100sm-h-gm-asc.ply	*Mandrillus sphinx*	9633	236.998	246.027	0.288	81	4.180	4.757
Mansp303-m2-or-uc-10ksimp-100sm-h-gm-asc.ply	*Mandrillus sphinx*	10047	248.573	247.410	0.314	75.25	4.274	4.901
Mansp598493-m2-or-uc-10ksimp-100sm-gm-asc.ply	*Mandrillus sphinx*	9996	189.985	190.061	0.281	89	4.292	4.855
Mansp598494-m2-or-uc-10ksimp-100sm-gm-asc.ply	*Mandrillus sphinx*	9996	201.639	201.720	0.219	98	4.445	4.883
Mansp598554-m2-or-uc-10ksimp-100sm-gm-asc.ply	*Mandrillus sphinx*	10000	197.626	197.626	0.242	91	4.403	4.887
Mansp903418-m2-or-uc-10ksimp-100sm-gm-asc.ply	*Mandrillus sphinx*	9994	251.017	240.336	0.318	72.5	4.485	5.122
Mioog220338-m2-or-uc-10ksimp-100sm-gm-asc.ply	*Miopithecus ogouensis*	9978	230.987	231.496	0.278	102.125	2.344	2.900
Mioog243-m2-or-uc-10ksimp-100sm-h-gm-asc.ply	*Miopithecus ogouensis*	9690	216.079	222.992	0.223	133	2.282	2.728
Mioog395340-m2-or-uc-10ksimp-100sm-h-gm-asc.ply	*Miopithecus ogouensis*	10250	265.505	251.651	0.375	75.5	2.354	3.104
Mioog395343-m2-or-uc-10ksimp-100sm-h-gm-asc.ply	*Miopithecus ogouensis*	9987	223.635	223.926	0.327	81.875	2.428	3.082
Mioog397625-m2-or-uc-10ksimp-100sm-h-gm-asc.ply	*Miopithecus ogouensis*	10228	232.213	227.037	0.331	78.625	2.408	3.070
Mioog397649-m2-or-uc-10ksimp-100sm-h-gm-asc.ply	*Miopithecus ogouensis*	10093	189.024	187.282	0.293	75.25	2.329	2.915
Mioog5238-m2-or-uc-10ksimp-100sm-h-gm-asc.ply	*Miopithecus ogouensis*	9570	256.811	255.751	0.356	94.25	2.417	3.130
Mioog5239-m2-or-uc-10ksimp-100sm-gm-asc.ply	*Miopithecus ogouensis*				0.343	83.625	2.474	3.159
Mioog711-m2-or-uc-10ksimp-100sm-h-gm-asc.ply	*Miopithecus ogouensis*				0.387	87.5	2.313	3.088
Nalar103461-m2-or-uc-10ksimp-100sm-h-gm-asc.ply	*Nasalis larvatus*	9967	246.286	247.101	0.369	68.75	3.844	4.582
Nalar103466-m2-or-uc-10ksimp-100sm-h-gm-asc.ply	*Nasalis larvatus*	9950	308.115	278.434	0.426	87	3.682	4.533
Nalar103468-m2-or-uc-10ksimp-100sm-h-gm-asc.ply	*Nasalis larvatus*	10038	245.72	244.790	0.395	70.875	3.717	4.507
Nalar103668-m2-or-uc-10ksimp-100sm-h-gm-asc.ply	*Nasalis larvatus*	9964	365.76	337.124	0.448	86.375	3.852	4.749
Nalar103671-m2-or-uc-10ksimp-100sm-h-gm-asc.ply	*Nasalis larvatus*	9852	237.11	240.672	0.390	80.5	3.765	4.545
Nasla142216-m2-or-uc-10ksimp-100sm-h-gm-asc.ply	*Nasalis larvatus*	10076	244.766	242.920	0.395	79.25	3.672	4.461

Nasla142219-m2-or-uc-10ksimp-100sm-h-gm-asc.ply	*Nasalis larvatus*	10168	165.289	162.558	0.356	55	3.843	4.555
Nasla145323-m2-or-uc-10ksimp-100sm-gm-asc.ply	*Nasalis larvatus*	9975	222.104	222.661	0.387	67.75	3.753	4.526
Nasla196789-m2-or-uc-10ksimp-100sm-h-gm-asc.ply	*Nasalis larvatus*	10067	208.13	206.745	0.404	61.625	3.830	4.639
Nasla198277-m2-or-uc-10ksimp-100sm-gm-asc.ply	*Nasalis larvatus*	9994	223.578	223.712	0.334	82.75	3.701	4.369
Papcy10110-m2-or-uc-10ksimp-100sm-h-gm-asc.ply	*Papio cynocephalus*	9824	224.815	228.843	0.321	73.75	4.412	5.054
Papcy10111-m2-or-uc-10ksimp-100sm-gm-asc.ply	*Papio cynocephalus*	10000	207.714	207.714	0.220	92	4.427	4.867
Papcy384211-m2-or-uc-10ksimp-10sm-h-gm-asc.ply	*Papio cynocephalus*	10021	232.063	231.577	0.250	89.75	4.458	4.958
Papcy384216-m2-or-uc-10ksimp-100sm-h-gm-asc.ply	*Papio cynocephalus*	10056	168.866	167.926	0.215	87	4.541	4.971
Papcy384217-m2-or-uc-10ksimp-100sm-hh-gm-asc.ply	*Papio cynocephalus*	9999	184.084	184.102	0.218	83.125	4.394	4.830
Papcy384218-m2-or-uc-10ksimp-100sm-h-gm-asc.ply	*Papio cynocephalus*	10151	178.815	176.155	0.274	82.875	4.603	5.150
Papcy452507-m2-or-uc-10ksimp-100sm-gm-asc.ply	*Papio cynocephalus*	9992	196.457	196.614	0.241	89.375	4.472	4.953
Papcy452509-m2-or-uc-10ksimp-100sm-gm-asc.ply	*Papio cynocephalus*	9995	178.041	178.130	0.254	83.5	4.506	5.014
Papcy494-m2-or-uc-10ksimp-100sm-gm-asc.ply	*Papio cynocephalus*	10000	203.047	203.047	0.298	72.75	4.361	4.958
Pilba1195-m2-or-uc-10ksimp-100sm-gm-asc.ply	*Piliocolobus badius*	9996	239.895	239.991	0.398	80.375	3.693	4.489
Pilba288-m2-or-uc-10ksimp-100sm-gm-asc.ply	*Piliocolobus badius*	9999	241.275	241.299	0.418	74.5	3.556	4.393
Pilba705-m2-or-uc-10ksimp-100sm-h-gm-asc.ply	*Piliocolobus badius*	10010	254.163	253.909	0.377	73.25	3.295	4.049
Pilba89421-m2-or-uc-10ksimp-100sm-h-gm-asc.ply	*Piliocolobus badius*	9811	252.527	257.392	0.388	58.125	3.543	4.320
Pilba9-m2-or-uc-10ksimp-100sm-gm-asc.ply	*Piliocolobus badius*	9996	231.432	231.525	0.430	62.875	3.472	4.333
Preme102755-m2-or-uc-10k-100sm-h-gm-asc.ply	*Presbytis melalophos*	10029	228.09	227.430	0.366	68.5	3.250	3.981
Preme102757-m2-or-uc-10ksimp-100sm-h-gm-asc.ply	*Presbytis melalophos*	9706	235.306	242.434	0.326	74.375	2.977	3.628
Preme102882-m2-or-uc-10ksimp-100sm-h-gm-asc.ply	*Presbytis melalophos*	10145	241.108	237.662	0.364	76.875	3.224	3.952
Preme102883-m2-or-uc-10ksimp-100sm-h-gm-asc.ply	*Presbytis melalophos*	10046	209.372	208.413	0.385	65.375	3.200	3.971
Preme102891-m2-or-uc-10ksimp-100sm-h-gm-asc.ply	*Presbytis melalophos*	10000	222.209	222.209	0.326	71.625	3.213	3.864
Preme102895-m2-or-uc-10ksimp-100sm-h-gm-asc.ply	*Presbytis melalophos*				0.405	86.125	3.193	4.003
Preme106600-m2-or-uc-10ksimp-100sm-h-gm-asc.ply	*Presbytis melalophos*	9898	280.274	262.446	0.437	71.375	3.290	4.164
Preme106603-m2-or-uc-10ksimp-100sm-h-gm-asc.ply	*Presbytis melalophos*	9948	242.746	244.015	0.352	82.875	3.237	3.941
Preme106605-m2-or-uc-10ksimp-100sm-h-gm-asc.ply	*Presbytis melalophos*	10000	205.325	205.325	0.372	57.625	3.224	3.968
Preme106671-m2-or-uc-10ksimp-100sm-h-gm-asc.ply	*Presbytis melalophos*	9961	239.435	240.372	0.326	87	3.224	3.876

Preme107086-m2-or-uc-10ksimp-100sm-h-gm-asc.ply	*Presbytis melalophos*	9755	251.191	257.500	0.375	80	3.130	3.880
Prove178-m2-or-uc-10ksimp-100sm-h-gm-asc.ply	*Procolobus verus*	10409	205.34	197.272	0.375	57	3.244	3.993
Prove477329-m2-or-uc-10ksimp-100sm-gm-asc.ply	*Procolobus verus*	9978	193.783	194.210	0.376	64.25	2.988	3.740
Prove477330-m2-or-uc-10ksimp-100sm-gm-asc.ply	*Procolobus verus*	9988	190.78	191.009	0.386	65.5	3.100	3.873
Prove481799-m2-or-uc-10ksimp-100sm-h-gm-asc.ply	*Procolobus verus*	9513	264.455	277.993	0.419	70.375	3.096	3.935
Prove481800-m2-or-uc-10ksimp-100sm-h-gm-asc.ply	*Procolobus verus*	9774	215.294	220.272	0.355	81.5	3.151	3.861
Prove481802-m2-or-uc-10ksimp-100sm-h-gm-asc.ply	*Procolobus verus*	9652	209.211	216.754	0.318	83.5	3.113	3.748
Pygni1114-m2-or-uc-10ksimp-100sm-gm-asc.ply	*Pygathrix nigripes*	9988	234.929	235.211	0.327	70.625	3.612	4.266
Pygni1161-m2-or-uc-10ksimp-100sm-h-gm-asc.ply	*Pygathrix nigripes*	10165	215.403	211.907	0.341	76	3.581	4.264
Pygni12110-m2-or-uc-10ksimp-100sm-gm-asc.ply	*Pygathrix nigripes*	10000	209.423	209.423	0.332	76.75	3.432	4.096
Pygni2422-m2-or-uc-10ksimp-100sm-gm-asc.ply	*Pygathrix nigripes*	9980	233.007	233.474	0.358	72.5	3.483	4.198
Pygni443-m2-or-uc-10ksimp-100sm-gm-asc.ply	*Pygathrix nigripes*	9987	219.391	219.677	0.302	85.25	3.460	4.064
Pygni695-m2-or-uc-10ksimp-100sm-gm-asc.ply	*Pygathrix nigripes*	9988	218.403	218.665	0.300	102.625	3.591	4.192
Rhiro1091-m2-or-uc-10ksimp-100sm-gm-asc.ply	*Rhinopithecus roxellana*	9977	176.05	176.456	0.357	62.875	4.153	4.866
Rhiro1092-m2-or-uc-10ksimp-100sm-gm-asc.ply	*Rhinopithecus roxellana*	9993	222.627	222.783	0.341	70.5	3.920	4.601
Rhiro110456-m2-or-uc-10ksimp-100sm-gm-asc.ply	*Rhinopithecus roxellana*	9996	285.107	285.221	0.405	69.375	3.887	4.697
Rhiro119648-m2-or-uc-10ksimp-100sm-gm-asc.ply	*Rhinopithecus roxellana*	9893	171.253	173.105	0.341	55	4.062	4.743
Rhiro258986-m2-or-uc-10ksimp-100sm-gm-asc.ply	*Rhinopithecus roxellana*	10000	249.246	249.246	0.363	68.875	4.174	4.900
Rhiro268888-m2-or-uc-10ksimp-100sm-gm-asc.ply	*Rhinopithecus roxellana*	9932	203.507	204.900	0.385	63.625	3.862	4.631
Rhiro268891-m2-or-uc-10ksimp-100sm-gm-asc.ply	*Rhinopithecus roxellana*	9998	193.927	193.966	0.290	72.75	3.918	4.498
Rhiro268894-m2-or-uc-10ksimp-100sm-h-gm-asc.ply	*Rhinopithecus roxellana*	10000	204.508	204.508	0.334	66.125	3.902	4.571
Rhiro268897-m2-or-uc-10ksimp-100sm-gm-asc.ply	*Rhinopithecus roxellana*	10000	166.532	166.532	0.314	73.25	3.902	4.531
Semen111817-m2-or-uc-10ksimp-100sm-h-gm-asc.ply	*Semnopithecus entellus*	9808	260.028	222.338	0.360	63.5	3.876	4.595
Semen111825-m2-or-uc-10ksimp-100sm-h-gm-asc.ply	*Semnopithecus entellus*	10109	181.145	179.192	0.368	63	3.777	4.514
Semen150044-m2-or-uc-10ksimp-100sm-h-gm-asc.ply	*Semnopithecus entellus*	9938	213.377	214.708	0.346	65.375	3.723	4.415
Semen1615-m2-or-uc-10ksimp-100sm-gm-asc.ply	*Semnopithecus entellus*	9998	268.469	231.421	0.375	64.125	3.534	4.285
Semen162-m2-or-uc-10ksimp-100sm-gm-asc.ply	*Semnopithecus entellus*	9991	160.893	161.038	0.310	61.5	3.846	4.466
Semen286-m2-or-uc-10ksimp-100sm-h-gm-asc.ply	*Semnopithecus entellus*	9960	259.62	238.111	0.383	69.5	3.872	4.639

Semen318-m2-or-uc-10ksimp-100sm-h-gm-asc.ply	*Semnopithecus entellus*	9877	204.511	207.058	0.364	67.125	3.748	4.477
Semen412-m2-or-uc-10ksimp-100sm-gm-asc.ply	*Semnopithecus entellus*	9998	163.593	163.626	0.322	58.625	3.920	4.564
Semen71014-m2-or-uc-10ksimp-100sm-h-gm-asc.ply	*Semnopithecus entellus*	9904	197.473	199.387	0.383	66	4.065	4.830
Semen90328-m2-or-uc-10ksimp-100sm-gm-asc.ply	*Semnopithecus entellus*	9985	229.185	229.529	0.417	60.875	3.800	4.635
Thege10-m2-or-uc-10ksimp-100sm-gm-asc.ply	*Theropithecus gelada*	10077	259.089	257.109	0.439	82.125	4.358	5.236
Thege1419-m2-or-uc-10ksimp-100sm-gm-asc.ply	*Theropithecus gelada*	9753	245.234	251.445	0.405	83.125	4.524	5.335
Thege1440-m2-or-uc-10ksimp-100sm-h-gm-asc.ply	*Theropithecus gelada*	10301	202.231	196.322	0.335	89.25	4.453	5.122
Thege1467-m2-or-uc-10ksimp-100sm-gm-asc.ply	*Theropithecus gelada*	9997	253.949	254.025	0.352	96.375	4.625	5.329
Thege174-or-uc-10ksimp-100sm-gm-asc.ply	*Theropithecus gelada*	9998	279.833	279.889	0.373	77	4.067	4.812
Thege305107-m2-or-uc-10ksimp-100sm-h-gm-asc.ply	*Theropithecus gelada*	9922	236.033	237.889	0.382	74.875	4.496	5.261
Thege354990-or-uc-10ksimp-100sm-h-gm-asc.ply	*Theropithecus gelada*	9999	237.537	237.561	0.301	83.5	4.374	4.977
Thege360-m2-or-uc-10ksimp-100sm-gm-asc.ply	*Theropithecus gelada*	9997	245.838	245.912	0.314	91.75	4.472	5.100
Thege451-m2-or-uc-10ksimp-100sm-gm-asc.ply	*Theropithecus gelada*	10000	259.785	259.785	0.231	101.5	4.470	4.932
Thege58-m2-or-uc-10ksimp-100sm-gm-asc.ply	*Theropithecus gelada*	10040	247.938	246.950	0.389	76.5	4.586	5.364
Thege836-m2-or-uc-10ksimp-100sm-h-gm-asc.ply	*Theropithecus gelada*	10300	244.73	237.602	0.337	81.625	4.487	5.162
TraKave1086-m2-or-uc-10ksimp-100sm-h-gm-asc.ply	*Trachypithecus (Kavi) vetulus*	9797	180.234	183.969	0.348	58.625	3.340	4.036
TraKave1182-m2-or-uc-10ksimp-100sm-gm-asc.ply	*Trachypithecus (Kavi) vetulus*				0.397	86.125	3.253	4.046
TraKave1183-m2-or-uc-10ksimp-100sm-h-gm-asc.ply	*Trachypithecus (Kavi) vetulus*	9946	248.537	249.886	0.427	65.125	3.304	4.158
TraKave511-m2-or-uc-10ksimp-100sm-gm-asc.ply	*Trachypithecus (Kavi) vetulus*	9998	229.771	229.817	0.305	86.375	3.297	3.906
TraKave5544-m2-or-uc-10ksimp-100sm-gm-asc.ply	*Trachypithecus (Kavi) vetulus*	9987	206.434	206.703	0.341	70.5	3.462	4.144
TraKave5545-m2-or-uc-10ksimp-100sm-gm-asc.ply	*Trachypithecus (Kavi) vetulus*	10077	273.121	271.034	0.357	76.25	3.274	3.989
TraKave7177-m2-or-uc-10ksimp-100sm-gm-asc.ply	*Trachypithecus (Kavi) vetulus*				0.430	84.125	3.281	4.142
TraKave952-m2-or-uc-10ksimp-100-h-gm-asc.ply	*Trachypithecus (Kavi) vetulus*	9899	213.305	215.481	0.276	96.75	3.403	3.956
Traob104445-m2-or-uc-10ksimp-100sm-gm-asc.ply	*Trachypithecus obscurus*	9997	190.945	191.002	0.374	64	3.362	4.110
Traob119492-m2-or-uc-10ksimp-100sm-h-gm-asc.ply	*Trachypithecus obscurus*	9921	244.694	246.642	0.363	77.625	3.359	4.086
Traob124177-m2-or-uc-10ksimp-100sm-gm-asc.ply	*Trachypithecus obscurus*	9990	224.929	225.154	0.376	73.625	3.452	4.205
Traob236623-m2-or-uc-10ksimp-100sm-gm-asc.ply	*Trachypithecus obscurus*				0.251	86.375	3.251	3.753
Traob37304-m2-or-uc-10ksimp-100sm-h-gm-asc.ply	*Trachypithecus obscurus*	9876	209.762	212.396	0.320	82.75	3.227	3.867

Traob54967-m2-or-uc-10ksimp-100sm-gm-asc.ply	*Trachypithecus obscurus*	9999	222.232	222.254	0.408	52.75	3.265	4.082
Traob54969-m2-or-uc-10ksimp-100sm-h-gm-asc.ply	*Trachypithecus obscurus*	9949	222.084	223.222	0.331	85	3.173	3.836
Traob54970-m2-or-uc-10ksimp-100sm-h-gm-asc.ply	*Trachypithecus obscurus*	10289	220.658	214.460	0.311	86.375	3.256	3.879
Traob83258-m2-or-uc-10ksimp-100sm-h-gm-asc.ply	*Trachypithecus obscurus*	10052	262.401	261.044	0.408	75.125	3.333	4.149

* Specimens are named using a taxon code comprised of the first three letters (usually) of the specimen's genus followed by the first two letters of the specimen's species, and a numeric code consisting of the specimen's museum attribution number excluding year (if present).

Table A3.3. Raw topographic variable data for individual specimens of secondary (variably worn) sample.

Specimen	Species	Polygons	DNE	DNE/Polygons	RFI	OPCR
Cerca16105	*Cercopithecus campbelli*	9989	249.123	249.397	0.320	79
Cerca337	*Cercopithecus campbelli*	10000	212.093	212.093	0.276	84
Cerca339	*Cercopithecus campbelli*	9998	196.133	196.172	0.285	80
Cerca4220	*Cercopithecus campbelli*	9988	261.9	263.587	0.289	82.25
Cerca4226	*Cercopithecus campbelli*	9991	188.498	188.668	0.279	67.125
Cerca57	*Cercopithecus campbelli*	9996	182.374	182.447	0.299	72.75
Cerca65	*Cercopithecus campbelli*	9999	177.004	177.022	0.335	63.5
Colgu11112-m2-or-uc-10ksimp-100sm-gm-asc.ply	*Colobus guereza*	10000	198.762	198.762	0.350	68.25
Colgu1241-m2-or-uc-10ksimp-100sm-gm-asc.ply	*Colobus guereza*	9997	231.574	231.643	0.372	85.25
Colgu148579	*Colobus guereza*	9987	196.544	196.800	0.261	92.875
Colgu152-m2-or-uc-10ksimp-100sm-gm-asc.ply	*Colobus guereza*	9997	237.85	237.921	0.351	77
Colgu163124	*Colobus guereza*	9997	212.249	212.313	0.312	72.125
Colgu163273	*Colobus guereza*	9945	197.601	198.694	0.297	84.5
Colgu163627-m2-or-uc-10ksimp-100sm-gm-asc.ply	*Colobus guereza*	10000	195.988	195.988	0.389	60.375
Colgu401	*Colobus guereza*	10176	171.437	168.472	0.260	63.625
Colgu408-m2-or-uc-10ksimp-100sm-gm-asc.ply	*Colobus guereza*	9989	218.999	219.240	0.321	70.625
Colgu461-m2-or-uc-10ksimp-100sm-h-gm-asc.ply	*Colobus guereza*	9978	230.718	231.227	0.341	86.75
Colgu5182	*Colobus guereza*	9982	211.646	212.028	0.211	105.375

Colgu72515	*Colobus guereza*	9988	226.755	227.027	0.259	73.75
Colgu762-m2-or-uc-10ksimp-100sm-h-gm-asc.ply	*Colobus guereza*	10190	231.524	227.207	0.386	66.25
Colgu864-m2-or-uc-10k-100sm-gm-asc.ply	*Colobus guereza*	9994	196.928	197.046	0.362	63.25
Colgu994-m2-or-uc-10ksimp-100sm-gm-asc.ply	*Colobus guereza*	9992	226.935	227.117	0.389	67.125
Macfa114411-m2-or-uc-10ksimp-100sm-h-gm-asc.ply	*Macaca fascicularis*	10210	215.815	211.376	0.329	90.25
Macfa114505	*Macaca fascicularis*	9939	273.283	274.960	0.278	85.625
Macfa121803-m2-or-uc-10ksimp-100sm-h-gm-asc.ply	*Macaca fascicularis*	10183	230.451	226.310	0.258	97.375
Macfa125	*Macaca fascicularis*	9614	256.13	266.414	0.245	98.625
Macfa125102-m2-or-uc-10ksimp-100sm-h-gm-asc.ply	*Macaca fascicularis*	10430	225.367	216.076	0.278	93.625
Macfa196817	*Macaca fascicularis*	9992	215.201	215.373	0.257	81.5
Macfa196824-m2-or-uc-10ksimp-100sm-h-gm-asc.ply	*Macaca fascicularis*	9973	188.932	189.443	0.273	85.75
Macfa198300	*Macaca fascicularis*	9954	208.557	209.521	0.329	72.625
Macfa278	*Macaca fascicularis*	9685	216.642	223.688	0.325	77.375
Macfa317191-m2-or-uc-10ksimp-100sm-h-gm-asc.ply	*Macaca fascicularis*	10162	228.487	224.845	0.298	78.75
Macfa34913-m2-or-uc-10ksimp-100sm-h-gm-asc.ply	*Macaca fascicularis*	10100	189.925	188.045	0.247	81.75
Macfa37	*Macaca fascicularis*	9955	214.395	215.364	0.252	90.25
Macfa385	*Macaca fascicularis*	9868	278.345	282.068	0.375	84
Macfa411	*Macaca fascicularis*	9513	296.143	311.303	0.248	112.5
Papcy10110-m2-or-uc-10ksimp-100sm-h-gm-asc.ply	*Papio cynocephalus*	9824	224.815	228.843	0.321	73.75
Papcy10111-m2-or-uc-10ksimp-100sm-gm-asc.ply	*Papio cynocephalus*	10000	207.714	207.714	0.220	92
Papcy384211-m2-or-uc-10ksimp-10sm-h-gm-asc.ply	*Papio cynocephalus*	10021	232.063	231.577	0.250	89.75
Papcy384216-m2-or-uc-10ksimp-100sm-h-gm-asc.ply	*Papio cynocephalus*	10056	168.866	167.926	0.215	87
Papcy384217-m2-or-uc-10ksimp-100sm-hh-gm-asc.ply	*Papio cynocephalus*	9999	184.084	184.102	0.218	83.125
Papcy384218-m2-or-uc-10ksimp-100sm-h-gm-asc.ply	*Papio cynocephalus*	10151	178.815	176.155	0.274	82.875
Papcy452507-m2-or-uc-10ksimp-100sm-gm-asc.ply	*Papio cynocephalus*	9992	196.457	196.614	0.241	89.375
Papcy452509-m2-or-uc-10ksimp-100sm-gm-asc.ply	*Papio cynocephalus*	9995	178.041	178.130	0.254	83.5
Papcy494-m2-or-uc-10ksimp-100sm-gm-asc.ply	*Papio cynocephalus*	10000	203.047	203.047	0.298	72.75
Thege10	*Theropithecus gelada*	10077	259.089	257.109	0.439	82.125

Thege1419	*Theropithecus gelada*	9753	245.234	251.445	0.405	83.125
Thege1440	*Theropithecus gelada*	10301	202.231	196.322	0.335	89.25
Thege1467	*Theropithecus gelada*	9997	253.949	254.025	0.352	96.375
Thege161	*Theropithecus gelada*	9997	258.298	258.376	0.346	78.25
Thege162	*Theropithecus gelada*	9994	207.141	207.265	0.281	88.25
Thege174	*Theropithecus gelada*	9998	279.833	279.889	0.373	77
Thege251	*Theropithecus gelada*	9960	260.813	261.860	0.263	83.5
Thege283190	*Theropithecus gelada*	9886	228.41	231.044	0.320	67.5
Thege305107	*Theropithecus gelada*	9922	236.033	237.889	0.382	74.875
Thege319992	*Theropithecus gelada*	9909	285.13	287.749	0.249	105.5
Thege354990	*Theropithecus gelada*	9999	237.537	237.561	0.301	83.5
Thege360	*Theropithecus gelada*	9997	245.838	245.912	0.314	91.75
Thege448	*Theropithecus gelada*	9852	257.604	261.474	0.206	107.5
Thege451	*Theropithecus gelada*	10000	259.785	259.785	0.231	101.5
Thege453	*Theropithecus gelada*	9930	232.128	233.764	0.219	90.125
Thege58	*Theropithecus gelada*	10040	247.938	246.950	0.389	76.5
Thege836	*Theropithecus gelada*	10300	244.73	237.602	0.337	81.625
Thege240885	*Theropithecus gelada*	9945	261.4	262.846	0.242	105.375

Table A3.4. Raw data for species-mean relative M_2 area.

Species	Ln mean body mass	Ln mean 2D area	Estimated Ln mean 2D area	Estimated mean 2D area	Relative M_2 area*
Allenopithecus nigroviridis	1.556	3.209	3.221	25.065	-1.279
Cercocebus atys	2.152	3.720	3.652	38.556	7.069
Cercopithecus mitis	1.797	3.338	3.395	29.829	-5.541
Chlorocebus aethiops	1.445	3.848	3.141	23.124	102.771
Colobus guereza	2.315	3.564	3.770	43.377	-18.611

Colobus satanas	2.187	3.457	3.678	39.556	-19.798
Lophocebus albigena	1.965	3.450	3.517	33.687	-6.527
Macaca fascicularis	1.499	3.382	3.180	24.044	22.356
Macaca sylvanus	2.407	4.551	3.837	46.367	104.375
Mandrillus sphinx	3.102	4.395	4.339	76.653	5.739
Miopithecus ogouensis	0.560	2.374	2.501	12.196	-11.942
Nasalis larvatus	2.715	3.768	4.060	57.947	-25.277
Papio cynocephalus	2.725	4.466	4.067	58.369	49.113
Piliocolobus badius	2.114	3.520	3.625	37.530	-9.953
Presbytis melalophos	1.876	3.200	3.453	31.597	-22.395
Procolobus verus	1.493	3.101	3.176	23.946	-7.201
Pygathrix nemaeus	2.274	3.538	3.741	42.124	-18.353
Rhinopithecus roxellana	2.691	3.982	4.042	56.946	-5.819
Semnopithecus entellus	2.528	3.825	3.924	50.621	-9.480
Theropithecus gelada	2.731	4.456	4.071	58.611	46.950
Trachypithecus obscurus	1.957	3.301	3.512	33.499	-18.982
Trachypithecus (Kasi) vetulus	2.451	3.326	3.868	47.867	-41.859

* Relative M_2 area is calculated as the percent difference between actual and estimated mean 2DA values.

Table A4.1. Species for which mesiodistal length means were gathered from Swindler (2002).

Species
Cercocebus galeritus
Cercocebus torquatus
Cercopithecus ascanius
Cercopithecus cephus
Cercopithecus mitis
Cercopithecus mona
Cercopithecus neglectus
Cercopithecus nictitans
Chlorocebus aethiops
Colobus polykomos
Kasi johnii
Lophocebus albigena
Macaca fascicularis
Macaca mulatta
Macaca nemestrina
Macaca nigra
Nasalis larvatus
Papio cynocephalus
Piliocolobus badius
Presbytis comata
Pygathrix nemaeus
Rhinopithecus roxellana
Simias concolor
Theropithecus gelada
Trachypithecus cristata

Trachypithecus phayrei

Table A4.2. Specimens comprising 3D surface mesh sample. Intermolar indicates specimens used for intermolar analyses, intramolar indicates specimens used for intramolar analyses.

Species	**Museum**	**Specimen**	**M_1**	**M_2**	**M_3**	**Intermolar**	**Intramolar**
Cercopithecus campbelli	MNHNP	1908-57	x	x	x	x	
Cercopithecus campbelli	MNHNP	1962-1420	x	x	x	x	
Cercopithecus campbelli	MNHNP	1967-65	x	x	x	x	
Cercopithecus campbelli	MNHNP	2009-337	x	x	x	x	
Cercopithecus campbelli	MNHNP	2009-339	x	x	x	x	
Cercopithecus campbelli	NMNH	16105	x	x	x	x	
Cercopithecus campbelli	SMNK	4220	x	x	x	x	
Cercopithecus campbelli	SMNK	4226	x	x	x	x	
Cercopithecus mitis	AMNH	52384			x		x
Cercopithecus mitis	AMNH	52386			x		x
Cercopithecus mitis	NMNH	259446	x	x	x	x	x
Cercopithecus mitis	NMNH	452544	x	x	x	x	x
Cercopithecus mitis	NMNH	452547	x	x	x	x	x
Cercopithecus mitis	NMNH	452548	x	x	x	x	x
Cercopithecus mitis	NMNH	452552	x	x	x	x	x
Cercopithecus mitis	NMNH	452554	x	x	x	x	x
Cercopithecus mitis	NMNH	452-1	x	x	x	x	x
Cercopithecus mitis	NMNH	236996			x		x
Cercopithecus mona	NMNH	480930	x	x	x	x	
Cercopithecus mona	NMNH	480931	x	x	x	x	
Cercopithecus mona	NMNH	480944	x	x	x	x	
Cercopithecus mona	NMNH	480975	x	x	x	x	

Cercopithecus mona	NMNH	480998	x	x	x	x	
Cercopithecus mona	NMNH	480999	x	x	x	x	
Cercopithecus mona	NMNH	481006	x	x	x	x	
Colobus guereza	AMNH	52237			x		x
Colobus guereza	AMNH	119768			x		x
Colobus guereza	BMNH	40.8	x	x	x	x	x
Colobus guereza	BMNH	54.762	x	x	x	x	x
Colobus guereza	BMNH	1.4.6.1	x	x	x	x	
Colobus guereza	BMNH	14.1.24.1	x	x	x	x	x
Colobus guereza	BMNH	1938.9.9.4	x	x	x	x	x
Colobus guereza	BMNH	24.8.6.4	x	x	x	x	x
Colobus guereza	BMNH	28.11.11.2	x	x	x	x	x
Colobus guereza	BMNH	40.1			x		x
Colobus guereza	MNHNP	163627			x		x
Colobus guereza	NMNH	148579	x	x	x	x	
Colobus guereza	NMNH	163124	x	x	x	x	x
Colobus guereza	NMNH	163273			x		x
Colobus polykomos	SMNK	5878	x	x	x	x	
Colobus polykomos	SMNK	5892	x	x	x	x	
Colobus polykomos	SMNK	10944	x	x	x	x	
Colobus polykomos	SMNK	10956	x	x	x	x	
Colobus polykomos	SMNK	10961	x	x	x	x	
Colobus polykomos	SMNK	10967	x	x	x	x	
Colobus satanas	BMNH	30.12.15.7	x	x	x	x	
Colobus satanas	MNHNP	1856-28	x	x	x	x	
Colobus satanas	MNHNP	1885-891	x	x	x	x	
Colobus satanas	NMNH	598556	x	x	x	x	

Colobus satanas	NMNH	598557	x	x	x	x	
Colobus satanas	NMNH	598560	x	x	x	x	
Colobus satanas	NMNH	598561	x	x	x	x	
Macaca fascicularis	AMNH	102768			x		x
Macaca fascicularis	AMNH	103649			x		x
Macaca fascicularis	AMNH	103655			x		x
Macaca fascicularis	AMNH	103658			x		x
Macaca fascicularis	AMNH	106025			x		x
Macaca fascicularis	AMNH	106384			x		x
Macaca fascicularis	MNHNP	1876-411			x		x
Macaca fascicularis	MNHNP	1899-278			x		x
Macaca fascicularis	MNHNP	1906-125			x		x
Macaca fascicularis	MNHNP	2009-385			x		x
Macaca fascicularis	NMNH	114411			x		x
Macaca fascicularis	NMNH	114505			x		x
Macaca fascicularis	NMNH	121803			x		x
Macaca fascicularis	NMNH	125102			x		x
Macaca fascicularis	NMNH	196817			x		x
Macaca fascicularis	NMNH	196824			x		x
Macaca fascicularis	NMNH	198300			x		x
Macaca fascicularis	NMNH	317191			x		x
Presbytis melalophos	AMNH	102755			x		x
Presbytis melalophos	AMNH	102757			x		x
Presbytis melalophos	AMNH	102882			x		x
Presbytis melalophos	AMNH	102883			x		x
Presbytis melalophos	AMNH	102891			x		x
Presbytis melalophos	AMNH	102895			x		x

Presbytis melalophos	AMNH	106600			x		x
Presbytis melalophos	AMNH	106605			x		x
Presbytis melalophos	AMNH	106671			x		x
Presbytis melalophos	AMNH	107086			x		x
Presbytis melalophos	AMNH	107088			x		x

Table A4.3. DNE, RFI, and OPCR of M_1s, M_2s, and M_3s for intermolar shape variability analyses.

		M1			**M2**			**M3**		
Species	**Specimen**	**DNE**	**RFI**	**OPCR**	**DNE**	**RFI**	**OPCR**	**DNE**	**RFI**	**OPCR**
Cercopithecus campbelli	1908-57	142.917	0.173	103.500	182.374	0.299	72.750	222.205	0.340	62.125
Cercopithecus campbelli	1962-1420	274.590	0.282	101.500	345.547	0.241	109.250	346.796	0.369	104.250
Cercopithecus campbelli	1967-65	192.929	0.249	68.500	177.004	0.335	63.500	221.982	0.386	65.500
Cercopithecus campbelli	2009-337	164.127	0.229	81.375	212.093	0.276	84.000	252.904	0.314	79.000
Cercopithecus campbelli	2009-339	155.721	0.205	107.125	196.133	0.285	80.000	206.383	0.328	63.625
Cercopithecus campbelli	16105	230.151	0.216	105.000	249.123	0.320	79.000	390.102	0.359	98.250
Cercopithecus campbelli	4220	149.003	0.251	78.000	290.554	0.289	82.250	258.697	0.345	69.125
Cercopithecus campbelli	4226	101.584	0.193	79.250	188.498	0.279	67.125	279.203	0.317	81.500
Cercopithecus mitis	259446	241.535	0.309	86.125	235.333	0.349	66.125	264.919	0.392	58.000
Cercopithecus mitis	452544	137.915	0.264	62.875	162.861	0.303	71.750	181.936	0.340	55.625
Cercopithecus mitis	452547	174.132	0.258	82.750	194.377	0.302	62.125	200.581	0.322	63.500
Cercopithecus mitis	452548	210.238	0.279	83.375	225.153	0.253	77.875	262.588	0.316	78.125
Cercopithecus mitis	452552	335.185	0.199	94.750	138.265	0.249	62.500	160.740	0.280	62.250
Cercopithecus mitis	452554	157.578	0.315	55.875	224.239	0.316	71.750	397.277	0.340	75.250
Cercopithecus mitis	452-1	166.274	0.288	64.500	218.485	0.325	68.375	277.364	0.354	71.000
Cercopithecus mona	480930	126.999	0.175	95.250	207.019	0.295	65.375	244.076	0.339	68.750
Cercopithecus mona	480931	176.993	0.254	72.875	183.524	0.345	60.375	196.552	0.334	58.625
Cercopithecus mona	480944	126.281	0.215	64.875	223.995	0.299	69.625	273.126	0.336	74.125

Cercopithecus mona	480975	168.327	0.276	64.750	184.333	0.306	64.500	227.953	0.338	75.125
Cercopithecus mona	480998	190.309	0.205	100.750	163.707	0.292	72.625	165.479	0.323	55.625
Cercopithecus mona	480999	152.483	0.186	80.625	183.225	0.277	64.125	285.492	0.338	67.000
Cercopithecus mona	481006	144.137	0.184	96.375	167.554	0.224	83.000	196.130	0.264	65.750
Colobus guereza	40.8	181.018	0.259	79.125	218.999	0.321	70.625	241.787	0.315	73.625
Colobus guereza	54.762	218.000	0.294	77.250	231.524	0.386	66.250	254.074	0.363	75.625
Colobus guereza	1.4.6.1	222.171	0.359	67.625	230.718	0.341	86.750	261.941	0.342	92.375
Colobus guereza	14.1.24.1	213.422	0.322	77.500	231.574	0.372	85.250	260.631	0.320	95.000
Colobus guereza	1938.9.9.4	187.464	0.285	79.000	226.935	0.389	67.125	281.982	0.381	74.750
Colobus guereza	24.8.6.4	150.852	0.275	63.625	197.371	0.362	63.250	271.321	0.411	77.750
Colobus guereza	28.11.11.2	144.828	0.327	68.375	198.762	0.350	68.250	284.437	0.408	71.000
Colobus guereza	148579	180.888	0.233	76.875	196.544	0.263	92.875	223.955	0.302	83.500
Colobus guereza	163124	168.562	0.263	72.375	212.249	0.313	72.125	308.527	0.353	86.625
Colobus polykomos	5878	203.217	0.357	68.000	207.730	0.333	76.125	268.795	0.336	83.500
Colobus polykomos	5892	203.483	0.348	68.000	340.275	0.373	76.625	329.972	0.409	76.000
Colobus polykomos	10944	336.452	0.301	81.375	227.760	0.316	75.250	429.458	0.351	89.875
Colobus polykomos	10956	281.297	0.332	64.375	179.020	0.344	60.625	240.749	0.325	78.375
Colobus polykomos	10961	212.247	0.338	80.250	302.992	0.348	73.000	379.384	0.334	98.125
Colobus polykomos	10967	458.576	0.320	78.125	210.465	0.330	76.000	260.147	0.375	75.500
Colobus satanas	30.12.15.7	225.681	0.264	107.000	228.670	0.310	87.750	262.531	0.320	95.125
Colobus satanas	1856-28	211.857	0.312	81.250	234.157	0.319	86.625	304.527	0.318	90.250
Colobus satanas	1885-891	245.558	0.263	87.000	198.541	0.304	78.250	264.268	0.362	83.750
Colobus satanas	598556	185.334	0.292	76.125	223.366	0.329	80.000	226.734	0.343	72.000
Colobus satanas	598557	179.455	0.297	71.250	206.043	0.304	73.500	291.040	0.391	75.375
Colobus satanas	598560	201.881	0.326	71.750	229.647	0.352	71.000	286.326	0.367	82.375
Colobus satanas	598561	185.956	0.339	68.500	212.468	0.361	69.875	232.186	0.330	88.125

Table A4.4. Average specimen pairwise landmark distances for M_1s, M_2s, and M_3s for intermolar shape variability analyses.

a. *Cercopithecus*

i. M_1

Specimen	1	2	3	4	5	6	7	8	9	10	11	12	13	14	15	16	17	18	19	20	21
1	0.263	0.186	0.212	0.206	0.219	0.228	0.258	0.271	0.245	0.298	0.288	0.311	0.174	0.342	0.153	0.318	0.242	0.314	0.236	0.145	0.268
2		0.288	0.184	0.299	0.249	0.221	0.187	0.236	0.275	0.257	0.221	0.278	0.222	0.303	0.278	0.252	0.221	0.242	0.142	0.275	0.192
3			0.250	0.159	0.242	0.249	0.293	0.295	0.256	0.310	0.321	0.331	0.219	0.370	0.134	0.344	0.271	0.340	0.267	0.221	0.303
4				0.257	0.173	0.151	0.167	0.161	0.215	0.200	0.208	0.209	0.139	0.241	0.234	0.252	0.150	0.246	0.142	0.226	0.177
5					0.245	0.264	0.301	0.294	0.266	0.312	0.330	0.335	0.234	0.365	0.190	0.351	0.274	0.355	0.277	0.227	0.309
6						0.212	0.238	0.209	0.165	0.248	0.269	0.249	0.150	0.282	0.234	0.309	0.214	0.303	0.225	0.250	0.246
7							0.216	0.199	0.244	0.233	0.252	0.228	0.181	0.268	0.235	0.274	0.175	0.268	0.195	0.245	0.212
8								0.228	0.262	0.251	0.154	0.278	0.214	0.314	0.278	0.201	0.205	0.184	0.136	0.268	0.180
9									0.238	0.212	0.257	0.167	0.206	0.207	0.277	0.285	0.189	0.280	0.210	0.285	0.231
10										0.268	0.295	0.290	0.193	0.329	0.242	0.315	0.229	0.314	0.238	0.270	0.278
11											0.286	0.252	0.229	0.278	0.289	0.304	0.166	0.297	0.239	0.313	0.248
12												0.299	0.251	0.331	0.311	0.176	0.243	0.159	0.189	0.296	0.212
13													0.252	0.153	0.320	0.329	0.239	0.326	0.259	0.332	0.253
14														0.283	0.192	0.275	0.190	0.276	0.193	0.203	0.226
15															0.357	0.366	0.270	0.357	0.298	0.365	0.287
16																0.322	0.247	0.320	0.253	0.189	0.282
17																	0.263	0.185	0.214	0.327	0.242
18																		0.256	0.190	0.257	0.200
19																			0.209	0.316	0.229
20																				0.250	0.149
21																					0.279

* Specimens in order from 1 to 21: Cerca57, Cerca65, Cerca337, Cerca339, Cerca1420, Cerca4220, Cerca4226, Cerca016105, Cermi4521, Cermi259446, Cermi452544, Cermi452547, Cermi452548, Cermi452552, Cermi452554, Cermo480930, Cermo480931, Cermo480944, Cermo480975, Cermo480998, Cermo480999. Specimen identifications are coded with the first three letters of genus, the first two letters of species, and the museum attribution number excluding leading year values (for BMNH and MNHNP).

ii. M_2

Specimen	1	2	3	4	5	6	7	8	9	10	11	12	13	14	15	16	17	18	19	20	21
1	0.276	0.259	0.310	0.216	0.267	0.208	0.173	0.266	0.266	0.312	0.197	0.301	0.257	0.304	0.261	0.242	0.283	0.224	0.207	0.229	0.282
2		0.314	0.348	0.271	0.290	0.206	0.248	0.290	0.297	0.212	0.278	0.213	0.159	0.324	0.324	0.305	0.290	0.260	0.262	0.288	0.307
3			0.165	0.265	0.234	0.256	0.229	0.174	0.252	0.317	0.230	0.318	0.284	0.275	0.287	0.263	0.243	0.191	0.264	0.249	0.262
4				0.308	0.259	0.303	0.275	0.207	0.296	0.342	0.281	0.349	0.316	0.303	0.322	0.303	0.258	0.248	0.300	0.290	0.279
5					0.256	0.196	0.185	0.267	0.260	0.293	0.214	0.287	0.241	0.283	0.270	0.256	0.277	0.227	0.229	0.227	0.274
6						0.247	0.212	0.193	0.232	0.297	0.241	0.300	0.267	0.240	0.298	0.277	0.213	0.167	0.237	0.262	0.148
7							0.161	0.254	0.242	0.228	0.205	0.218	0.163	0.277	0.265	0.243	0.247	0.191	0.196	0.227	0.268
8								0.209	0.211	0.264	0.153	0.259	0.208	0.255	0.227	0.193	0.216	0.155	0.157	0.184	0.245
9									0.231	0.288	0.229	0.293	0.269	0.254	0.286	0.256	0.212	0.162	0.247	0.247	0.240
10										0.287	0.239	0.286	0.272	0.178	0.285	0.251	0.245	0.159	0.230	0.256	0.254
11											0.291	0.193	0.168	0.319	0.322	0.308	0.302	0.265	0.267	0.288	0.309
12												0.284	0.245	0.277	0.198	0.157	0.252	0.183	0.203	0.147	0.266
13													0.160	0.314	0.320	0.300	0.289	0.255	0.273	0.286	0.307
14														0.296	0.288	0.269	0.261	0.229	0.235	0.253	0.282
15															0.320	0.289	0.260	0.205	0.277	0.288	0.267
16																0.235	0.298	0.251	0.258	0.159	0.317
17																	0.262	0.216	0.232	0.202	0.297
18																		0.183	0.249	0.269	0.235
19																			0.194	0.211	0.205

20																			0.218	0.260
21																				0.283

* Specimens in order from 1 to 21: Cerca57, Cerca65, Cerca337, Cerca339, Cerca1420, Cerca4220, Cerca4226, Cerca016105, Cermi4521, Cermi259446, Cermi452544, Cermi452547, Cermi452548, Cermi452552, Cermi452554, Cermo480930, Cermo480931, Cermo480944, Cermo480975, Cermo480998, Cermo480999. Specimen identifications are coded with the first three letters of genus, the first two letters of species, and the museum attribution number excluding leading year values (for BMNH and MNHNP).

iii. M_3

Specimen	1	2	3	4	5	6	7	8	9	10	11	12	13	14	15	16	17	18	19	20	21
1	0.242	0.160	0.290	0.328	0.245	0.171	0.148	0.286	0.314	0.295	0.260	0.297	0.189	0.217	0.206	0.273	0.271	0.337	0.239	0.153	0.233
2		0.233	0.284	0.228	0.218	0.294	0.265	0.363	0.387	0.365	0.258	0.388	0.185	0.315	0.306	0.358	0.353	0.405	0.225	0.286	0.320
3			0.273	0.312	0.217	0.224	0.197	0.315	0.352	0.337	0.237	0.332	0.147	0.255	0.252	0.306	0.307	0.367	0.212	0.214	0.270
4				0.341	0.286	0.324	0.323	0.376	0.425	0.357	0.160	0.392	0.253	0.356	0.348	0.394	0.357	0.441	0.243	0.328	0.331
5					0.290	0.373	0.354	0.413	0.443	0.425	0.321	0.448	0.269	0.371	0.355	0.410	0.407	0.444	0.308	0.363	0.394
6						0.310	0.269	0.378	0.396	0.386	0.250	0.401	0.181	0.315	0.302	0.360	0.370	0.410	0.234	0.294	0.342
7							0.228	0.297	0.330	0.297	0.290	0.305	0.250	0.254	0.255	0.308	0.283	0.349	0.275	0.197	0.239
8								0.316	0.340	0.326	0.287	0.326	0.218	0.259	0.261	0.306	0.309	0.366	0.256	0.209	0.267
9									0.366	0.267	0.357	0.207	0.324	0.295	0.282	0.350	0.163	0.400	0.351	0.254	0.224
10										0.387	0.387	0.385	0.352	0.226	0.317	0.175	0.367	0.183	0.377	0.261	0.326
11											0.348	0.254	0.339	0.324	0.309	0.381	0.225	0.412	0.355	0.269	0.198
12												0.370	0.215	0.323	0.314	0.357	0.341	0.404	0.194	0.292	0.310
13													0.346	0.325	0.288	0.365	0.156	0.412	0.375	0.274	0.229
14														0.270	0.260	0.316	0.316	0.361	0.166	0.230	0.271
15															0.229	0.169	0.290	0.266	0.318	0.172	0.259
16																0.275	0.264	0.333	0.302	0.180	0.254
17																	0.347	0.216	0.350	0.229	0.307

18																		0.393	0.348	0.243	0.193
19																			0.385	0.291	0.343
20																				0.268	0.296
21																					0.189

* Specimens in order from 1 to 21: Cerca57, Cerca65, Cerca337, Cerca339, Cerca1420, Cerca4220, Cerca4226, Cerca016105, Cermi4521, Cermi259446, Cermi452544, Cermi452547, Cermi452548, Cermi452552, Cermi452554, Cermo480930, Cermo480931, Cermo480944, Cermo480975, Cermo480998, Cermo480999. Specimen identifications are coded with the first three letters of genus, the first two letters of species, and the museum attribution number excluding leading year values (for BMNH and MNHNP).

b. *Colobus*

i. M_1

Specimen	1	2	3	4	5	6	7	8	9	10	11	12	13	14	15	16	17	18	19	20	21
1	0.265	0.341	0.154	0.310	0.250	0.326	0.313	0.269	0.320	0.337	0.263	0.297	0.237	0.262	0.195	0.223	0.304	0.284	0.311	0.235	0.204
2		0.265	0.246	0.243	0.136	0.258	0.253	0.164	0.265	0.246	0.228	0.193	0.291	0.185	0.261	0.186	0.226	0.215	0.220	0.263	0.226
3			0.325	0.255	0.253	0.269	0.266	0.201	0.331	0.260	0.293	0.286	0.361	0.280	0.343	0.289	0.165	0.235	0.232	0.354	0.315
4				0.292	0.228	0.312	0.296	0.245	0.283	0.314	0.233	0.271	0.201	0.251	0.145	0.188	0.287	0.266	0.290	0.203	0.167
5					0.247	0.222	0.206	0.177	0.316	0.255	0.267	0.286	0.342	0.270	0.311	0.255	0.214	0.134	0.226	0.326	0.292
6						0.257	0.261	0.163	0.244	0.250	0.208	0.156	0.263	0.158	0.239	0.152	0.220	0.212	0.205	0.250	0.208
7							0.163	0.195	0.343	0.285	0.296	0.296	0.347	0.290	0.323	0.281	0.241	0.192	0.251	0.347	0.310
8								0.192	0.336	0.271	0.292	0.303	0.340	0.283	0.307	0.277	0.237	0.172	0.254	0.334	0.293
9									0.265	0.200	0.217	0.217	0.300	0.200	0.269	0.188	0.146	0.140	0.155	0.287	0.241
10										0.329	0.164	0.255	0.322	0.256	0.303	0.214	0.297	0.294	0.295	0.314	0.270
11											0.296	0.272	0.354	0.280	0.328	0.282	0.231	0.243	0.162	0.343	0.315
12												0.230	0.281	0.213	0.258	0.161	0.251	0.250	0.263	0.276	0.227
13													0.298	0.210	0.288	0.203	0.264	0.259	0.242	0.287	0.258

14														0.300	0.147	0.249	0.331	0.320	0.329	0.265	0.238
15															0.276	0.182	0.244	0.240	0.248	0.273	0.235
16																0.215	0.305	0.287	0.302	0.231	0.196
17																	0.235	0.225	0.243	0.216	0.168
18																		0.183	0.185	0.323	0.283
19																			0.208	0.305	0.269
20																				0.317	0.286
21																					0.148

* Specimens in order from 1 to 21: Colgu148579, Colgu408, Colgu461, Colgu762, Colgu864, Colgu994, Colgu1241, Colgu11112, Colgu163124, Colpo5878, Colpo5892, Colpo10944, Colpo10956, Colpo10967, Colsa28, Colsa891, Colsa12157, Colsa598556, Colsa598557, Colsa598560. Specimen identifications are coded with the first three letters of genus, the first two letters of species, and the museum attribution number excluding leading year values (for BMNH and MNHNP).

ii. M_2

Specimen	1	2	3	4	5	6	7	8	9	10	11	12	13	14	15	16	17	18	19	20	21
1	0.269	0.271	0.305	0.236	0.267	0.306	0.171	0.310	0.277	0.300	0.278	0.265	0.171	0.244	0.247	0.282	0.292	0.247	0.293	0.176	0.214
2		0.196	0.163	0.255	0.282	0.265	0.245	0.208	0.156	0.263	0.269	0.261	0.319	0.152	0.291	0.230	0.162	0.238	0.281	0.303	0.201
3			0.251	0.260	0.291	0.274	0.242	0.257	0.229	0.257	0.278	0.260	0.315	0.169	0.296	0.243	0.255	0.252	0.280	0.289	0.212
4				0.289	0.315	0.305	0.288	0.271	0.216	0.310	0.300	0.305	0.349	0.204	0.332	0.273	0.214	0.271	0.324	0.338	0.244
5					0.160	0.291	0.223	0.305	0.268	0.282	0.164	0.264	0.268	0.228	0.288	0.263	0.284	0.149	0.226	0.280	0.204
6						0.310	0.260	0.312	0.292	0.304	0.207	0.295	0.293	0.251	0.310	0.277	0.305	0.197	0.263	0.304	0.237
7							0.291	0.324	0.294	0.248	0.307	0.272	0.322	0.236	0.335	0.186	0.305	0.252	0.305	0.340	0.222
8								0.273	0.253	0.267	0.263	0.222	0.228	0.207	0.170	0.244	0.269	0.209	0.240	0.206	0.172
9									0.167	0.296	0.313	0.285	0.354	0.224	0.306	0.280	0.233	0.291	0.301	0.323	0.256
10										0.283	0.281	0.270	0.326	0.187	0.311	0.261	0.204	0.260	0.292	0.307	0.228
11											0.303	0.249	0.322	0.244	0.311	0.205	0.295	0.247	0.273	0.323	0.219

12												0.281	0.312	0.244	0.307	0.275	0.303	0.195	0.247	0.311	0.236
13													0.296	0.225	0.273	0.230	0.293	0.223	0.231	0.295	0.179
14														0.283	0.284	0.308	0.328	0.279	0.328	0.230	0.249
15															0.263	0.189	0.200	0.196	0.247	0.279	0.152
16																0.281	0.304	0.259	0.277	0.246	0.228
17																	0.275	0.200	0.252	0.308	0.157
18																		0.266	0.310	0.324	0.237
19																			0.172	0.283	0.149
20																				0.313	0.205
21																					0.260

* Specimens in order from 1 to 21: Colgu148579, Colgu408, Colgu461, Colgu762, Colgu864, Colgu994, Colgu1241, Colgu11112, Colgu163124, Colpo5878, Colpo5892, Colpo10944, Colpo10956, Colpo10967, Colsa28, Colsa891, Colsa12157, Colsa598556, Colsa598557, Colsa598560. Specimen identifications are coded with the first three letters of genus, the first two letters of species, and the museum attribution number excluding leading year values (for BMNH and MNHNP).

iii. M_3

Specimen	1	2	3	4	5	6	7	8	9	10	11	12	13	14	15	16	17	18	19	20	21
1	0.305	0.176	0.288	0.305	0.236	0.156	0.267	0.201	0.258	0.167	0.160	0.153	0.242	0.218	0.226	0.171	0.256	0.249	0.284	0.293	0.221
2		0.276	0.157	0.389	0.390	0.336	0.376	0.333	0.358	0.325	0.321	0.327	0.394	0.347	0.209	0.302	0.233	0.245	0.214	0.292	0.288
3			0.237	0.318	0.291	0.193	0.282	0.242	0.279	0.224	0.209	0.217	0.294	0.246	0.182	0.202	0.221	0.214	0.254	0.287	0.196
4				0.367	0.376	0.313	0.354	0.323	0.339	0.315	0.301	0.305	0.386	0.326	0.175	0.276	0.206	0.221	0.162	0.279	0.262
5					0.385	0.341	0.172	0.342	0.232	0.336	0.272	0.324	0.364	0.267	0.346	0.308	0.374	0.369	0.373	0.409	0.339
6						0.278	0.358	0.182	0.355	0.284	0.279	0.280	0.308	0.322	0.333	0.236	0.346	0.346	0.364	0.360	0.310
7							0.303	0.235	0.292	0.208	0.212	0.190	0.277	0.249	0.262	0.225	0.295	0.285	0.309	0.333	0.259
8								0.317	0.187	0.295	0.232	0.292	0.322	0.215	0.323	0.284	0.351	0.340	0.358	0.391	0.320
9									0.299	0.243	0.223	0.237	0.292	0.271	0.273	0.150	0.293	0.288	0.317	0.326	0.261

10										0.285	0.202	0.281	0.317	0.147	0.305	0.272	0.329	0.325	0.341	0.380	0.311
11											0.198	0.203	0.287	0.248	0.248	0.221	0.279	0.268	0.323	0.314	0.255
12												0.192	0.222	0.152	0.246	0.193	0.280	0.269	0.298	0.324	0.249
13													0.273	0.240	0.254	0.211	0.281	0.278	0.302	0.318	0.259
14														0.275	0.340	0.290	0.356	0.367	0.375	0.377	0.329
15															0.284	0.244	0.313	0.307	0.326	0.365	0.289
16																0.229	0.146	0.148	0.212	0.230	0.199
17																	0.252	0.253	0.282	0.304	0.234
18																		0.187	0.226	0.175	0.238
19																			0.240	0.262	0.235
20																				0.288	0.284
21																					0.277

* Specimens in order from 1 to 21: Colgu148579, Colgu408, Colgu461, Colgu762, Colgu864, Colgu994, Colgu1241, Colgu11112, Colgu163124, Colpo5878, Colpo5892, Colpo10944, Colpo10956, Colpo10967, Colsa28, Colsa891, Colsa12157, Colsa598556, Colsa598557, Colsa598560. Specimen identifications are coded with the first three letters of genus, the first two letters of species, and the museum attribution number excluding leading year values (for BMNH and MNHNP).

Table A4.5. DNE, RFI, and OPCR of anterior and posterior sections of M_1s and M_3s for intramolar shape variability analyses.

	M_1						**M_3**					
	Anterior			**Posterior**			**Anterior**			**Posterior**		
Specimen	**DNE**	**RFI**	**OPCR**	**DNE**	**RFI**	**OPCR**	**DNE**	**RFI**	**OPCR**	**DNE**	**RFI**	**OPCR**
Colgu148579	114.804	0.242	62.875	124.652	0.227	60.375	108.694	0.318	37.375	174.960	0.296	67.250
Colgu11112	88.097	0.360	41.875	83.678	0.293	40.250	162.902	0.419	46.000	183.553	0.406	53.000
Colgu1241	141.208	0.352	45.750	136.787	0.301	60.250	179.785	0.336	57.625	178.889	0.317	71.125
Colgu163124	101.492	0.291	40.875	106.614	0.240	58.500	195.793	0.361	49.625	223.144	0.358	70.625
Colgu408	109.523	0.273	56.625	126.122	0.244	64.625	237.379	0.314	74.125	155.081	0.310	56.125
Colgu461	146.702	0.371	48.000	175.862	0.354	51.250	173.797	0.365	62.250	190.538	0.326	68.250

Colgu762	121.068	0.315	49.250	140.839	0.277	51.750	146.794	0.368	45.875	217.732	0.363	58.000
Colgu864	94.354	0.298	47.250	101.820	0.253	46.375	269.612	0.411	77.125	217.345	0.393	64.500
Colgu994	129.323	0.283	58.750	125.725	0.289	48.750	187.087	0.401	53.125	230.063	0.376	65.000
Colpo10944	251.027	0.329	53.000	211.186	0.277	67.000	182.868	0.363	49.875	354.740	0.346	80.875
Colpo10956	275.821	0.336	43.000	102.945	0.331	48.625	129.478	0.346	53.625	199.329	0.318	67.875
Colpo10961	185.683	0.356	66.500	131.317	0.329	62.000	422.100	0.355	56.500	487.506	0.332	89.500
Colpo10967	117.536	0.338	43.125	130.543	0.308	66.375	141.265	0.374	48.750	232.574	0.379	53.500
Colpo5878	114.247	0.359	44.375	136.484	0.360	56.750	553.713	0.342	63.875	230.456	0.337	69.375
Colpo5892	127.127	0.367	41.375	146.586	0.332	48.625	344.693	0.410	46.750	240.258	0.416	55.000
Colsa12157	164.121	0.279	74.375	152.093	0.254	82.375	272.276	0.320	99.000	189.035	0.308	71.000
Colsa28	180.241	0.316	70.000	161.067	0.316	74.625	318.063	0.330	68.875	289.280	0.318	84.250
Colsa598556	127.963	0.290	51.250	141.050	0.299	50.250	165.311	0.385	51.375	218.337	0.350	66.750
Colsa598557	239.202	0.297	54.000	124.661	0.299	54.250	147.382	0.350	47.875	167.744	0.339	56.375
Colsa598560	147.360	0.329	55.875	149.162	0.325	44.875	293.445	0.391	73.125	196.474	0.387	52.875
Colsa598561	112.698	0.349	44.250	118.071	0.334	47.000	222.733	0.380	58.375	194.947	0.364	56.625
Colsa891	253.001	0.269	76.375	174.415	0.266	69.500	174.599	0.364	62.750	176.054	0.310	74.875

* Specimen identifications are coded with the first three letters of genus, the first two letters of species, and the museum attribution number excluding leading year values (for BMNH and MNHNP).

Table A4.6. Raw cusp-tip landmarks of M_3s for intramolar cusp position variability analyses.

	Protoconid			**Metaconid**			**Entoconid**			**Hypoconid**			**Hypoconulid**		
Specimen*	**X**	**Y**	**Z**	**X**	**Y**	**Z**	**X**	**Y**	**Z**	**X**	**Y**	**Z**	**X**	**Y**	**Z**
Cermi236996	6.988	5.612	25.273	5.279	7.468	24.516	5.215	7.682	27.131	6.700	6.198	27.773	*5.250*	*6.287*	*29.024*
Cermi259446	3.767	1.432	10.356	1.264	3.438	10.670	2.192	4.492	7.831	4.223	2.887	7.492	*4.830*	*4.765*	*7.166*
Cermi4521	4.790	7.929	13.936	1.656	6.471	14.324	1.741	6.630	11.263	4.022	8.021	10.879	*3.607*	*6.252*	*9.114*
Cermi452544	3.789	5.465	12.548	6.603	3.257	13.375	6.709	3.740	10.064	4.517	5.242	9.370	*6.214*	*5.832*	*8.479*
Cermi452547	4.285	7.659	27.916	2.073	6.358	26.929	1.126	6.707	30.011	3.238	7.891	30.690	*2.473*	*6.794*	*31.795*

Cermi452548	2.045	5.411	27.271	0.686	1.910	26.185	1.259	1.650	29.996	1.443	4.583	30.366	*2.675*	*3.038*	*31.527*
Cermi452552	2.118	1.195	11.487	4.088	1.359	10.117	1.287	0.847	8.994	2.665	1.082	8.132	*1.769*	*1.332*	*7.837*
Cermi452554	2.355	1.958	11.131	5.810	1.518	10.905	4.410	1.446	7.560	2.156	1.712	8.091	*3.044*	*2.663*	*6.759*
Cermi52386	4.645	1.679	8.504	1.881	2.094	10.180	0.712	2.283	7.307	2.995	1.439	5.924	*1.838*	*3.420*	*4.992*
Cermi52384	6.883	4.756	7.766	6.603	1.932	9.151	6.486	1.052	6.106	7.143	3.329	5.006	*5.294*	*1.958*	*4.001*
Cogue119768	6.864	3.468	15.288	7.280	7.036	16.185	7.454	7.717	13.490	7.539	4.097	11.727	7.991	6.482	8.902
Cogue52237	4.510	6.238	25.635	8.268	6.072	24.468	8.830	5.798	27.927	5.110	6.614	29.051	6.272	5.605	31.657
Colgu11112	8.412	2.792	13.454	9.688	6.619	14.336	9.572	6.842	10.787	8.858	3.200	9.966	8.643	4.792	7.379
Colgu1241	3.533	6.278	17.316	3.433	1.763	18.496	3.388	1.380	14.832	2.819	5.747	13.485	2.855	3.263	10.488
Colgu163124	4.518	1.279	15.180	1.109	4.555	15.920	0.670	4.390	11.991	3.429	0.918	11.340	2.313	2.485	7.893
Colgu163273	7.231	8.192	25.759	4.052	10.401	24.284	3.353	10.943	28.156	6.794	9.008	29.327	4.850	9.717	32.356
Colgu163627	6.818	3.110	15.950	3.388	1.569	17.035	2.723	0.972	13.306	6.290	1.984	12.115	4.415	1.248	9.569
Colgu401	7.279	7.485	29.683	3.920	7.133	29.052	4.248	6.969	32.383	6.686	8.106	32.926	5.786	6.636	35.022
Colgu408	6.642	2.509	10.584	3.378	3.190	12.214	2.242	3.448	8.951	5.509	2.513	7.353	4.280	4.211	5.938
Colgu762	8.305	5.547	33.210	8.713	2.151	31.661	8.749	1.428	35.085	8.763	4.500	36.331	7.995	3.160	38.222
Colgu864	7.501	6.167	26.877	5.569	9.375	25.552	5.377	9.700	29.410	7.499	6.983	30.565	6.460	7.793	33.155
Colgu994	2.200	4.307	25.787	2.064	7.617	24.599	2.189	8.467	27.847	1.763	5.179	29.139	1.997	7.284	31.906
Macfa102768	2.464	1.567	12.606	5.570	0.955	13.283	5.680	1.233	9.427	2.545	1.591	8.818	3.688	2.626	6.321
Macfa103649	2.443	5.814	13.372	3.217	8.529	14.392	3.324	9.330	11.158	2.560	6.909	10.242	3.315	8.017	7.738
Macfa103655	3.832	5.970	12.808	5.306	8.065	13.534	6.240	8.026	10.736	4.302	6.207	9.964	5.925	6.965	8.069
Macfa103658	5.540	3.686	13.484	8.472	5.129	13.457	7.721	4.753	10.197	5.206	3.434	10.365	5.658	4.177	7.843
Macfa106025	7.330	8.008	10.509	10.275	6.303	10.852	9.556	5.261	7.679	7.225	6.876	6.848	7.269	5.027	4.516
Macfa106384	4.530	8.300	12.071	1.647	7.237	13.037	1.353	6.798	9.977	3.561	7.934	8.831	2.387	6.698	6.640
Macfa114411	1.257	4.392	9.739	2.287	1.439	10.298	2.733	1.485	7.008	1.283	3.752	6.343	2.576	3.302	4.412
Macfa114505	2.696	6.899	10.818	1.669	3.113	11.408	2.274	3.217	7.936	2.549	6.523	7.344	3.007	5.663	4.632
Macfa121803	6.692	6.408	10.266	4.434	8.096	10.697	3.974	7.768	7.596	6.403	6.730	7.084	5.540	6.837	4.439
Macfa125	9.013	4.337	10.879	8.169	7.394	12.256	8.212	8.502	8.884	9.168	5.810	7.682	8.256	7.439	5.223

Macfa125102	4.100	3.221	9.448	6.618	2.792	10.358	7.027	3.687	6.855	4.561	3.630	6.650	5.616	4.466	4.157
Macfa196817	1.915	6.752	10.432	4.578	7.955	11.616	5.259	8.325	8.553	2.504	7.233	7.681	4.347	7.875	5.876
Macfa196824	2.769	5.632	9.544	0.992	2.814	10.578	1.110	2.343	7.394	2.420	4.832	6.627	1.876	3.359	3.919
Macfa198300	3.866	5.727	25.353	6.374	5.288	24.703	6.363	4.431	27.529	4.381	5.303	27.781	5.096	4.516	30.040
Macfa278	1.332	3.939	16.700	3.618	1.318	17.550	3.741	1.512	14.114	1.535	3.404	13.591	2.846	3.366	10.869
Macfa317191	7.029	4.941	11.745	5.956	7.303	12.356	5.373	6.922	8.865	7.050	4.737	8.553	6.145	4.645	6.414
Macfa385	3.001	6.684	33.947	4.653	10.214	33.111	4.525	9.795	37.177	3.048	7.461	37.520	4.317	8.069	41.328
Macfa411	8.811	6.653	11.898	7.335	10.341	12.717	6.028	10.162	8.517	7.956	6.906	7.717	5.850	7.798	4.329
Preme102755	6.227	4.287	24.619	5.159	1.258	22.948	4.981	0.692	26.073	6.336	2.949	27.517	5.067	1.179	28.877
Preme102757	2.984	5.327	22.366	5.845	4.679	21.236	5.797	4.034	24.019	3.495	5.055	24.842	4.685	3.610	25.819
Preme102882	1.701	5.012	5.387	1.972	1.429	7.035	1.437	0.930	3.932	0.767	4.079	2.909	1.760	2.385	1.585
Preme102883	2.712	1.379	7.919	5.854	1.222	9.029	6.191	0.646	5.707	3.003	0.456	5.203	4.657	1.209	3.430
Preme102891	6.649	3.728	23.252	7.261	6.460	21.586	7.452	7.572	24.553	7.452	4.685	25.658	6.893	6.517	26.687
Preme102895	1.766	5.125	8.411	1.020	2.097	10.105	0.530	1.365	6.691	0.792	4.415	5.950	1.275	2.519	4.359
Preme106600	6.157	9.622	31.579	3.355	8.628	29.909	1.965	8.371	33.006	4.816	10.031	34.232	2.904	7.796	35.660
Preme106605	5.945	8.881	33.802	8.402	6.056	33.558	7.899	6.541	37.127	6.042	8.908	37.109	5.794	6.907	38.858
Preme106671	5.761	1.771	19.671	8.431	3.137	21.248	9.072	3.724	18.538	6.830	1.945	17.166	8.607	3.597	15.785
Preme107086	3.812	3.099	22.780	7.349	2.099	23.351	6.716	2.180	20.513	3.964	3.012	20.413	5.293	3.685	18.960
Preme107088	5.119	6.329	22.409	2.250	5.146	23.987	2.068	4.411	21.409	3.829	5.884	20.181	3.131	4.458	19.592

* Specimen identifications are coded with the first three letters of genus, the first two letters of species, and the museum attribution number excluding leading year values (for BMNH and MNHNP).

Table A4.7. Cusp-tip landmarks Procrustes-transformed using entire sample (including dummy hypoconulid values).

	Protoconid			**Metaconid**			**Entoconid**			**Hypoconid**			**Hypoconulid/post. margin**		
Specimen*	**X**	**Y**	**Z**	**X**	**Y**	**Z**	**X**	**Y**	**Z**	**X**	**Y**	**Z**	**X**	**Y**	**Z**
Cermi236996	0.248	-0.233	-0.331	-0.137	0.184	-0.501	-0.151	0.232	0.087	0.183	-0.101	0.231	*-0.143*	*-0.082*	*0.513*
Cermi259446	0.263	-0.266	-0.336	-0.147	0.172	-0.487	-0.156	0.276	0.111	0.177	-0.071	0.249	*-0.138*	*-0.111*	*0.464*

Cermi4521	0.264	-0.268	-0.332	-0.146	0.197	-0.472	-0.157	0.235	0.087	0.197	-0.085	0.210	*-0.158*	*-0.080*	*0.507*
Cermi452544	0.260	-0.267	-0.304	-0.163	0.211	-0.513	-0.154	0.241	0.099	0.185	-0.092	0.263	*-0.128*	*-0.093*	*0.454*
Cermi452547	0.251	-0.227	-0.342	-0.120	0.164	-0.519	-0.181	0.251	0.142	0.168	-0.116	0.255	*-0.119*	*-0.073*	*0.464*
Cermi452548	0.249	-0.293	-0.294	-0.130	0.222	-0.519	-0.199	0.229	0.147	0.207	-0.075	0.226	*-0.127*	*-0.082*	*0.441*
Cermi452552	0.284	-0.247	-0.342	-0.146	0.195	-0.536	-0.159	0.213	0.176	0.118	-0.114	0.283	*-0.096*	*-0.047*	*0.419*
Cermi452554	0.276	-0.265	-0.313	-0.166	0.200	-0.532	-0.140	0.227	0.172	0.171	-0.094	0.246	*-0.142*	*-0.068*	*0.425*
Cermi52386	0.239	-0.269	-0.319	-0.138	0.187	-0.485	-0.165	0.259	0.096	0.227	-0.070	0.225	*-0.162*	*-0.107*	*0.481*
Cermi52384	0.241	-0.258	-0.339	-0.137	0.183	-0.487	-0.150	0.234	0.114	0.222	-0.075	0.225	*-0.176*	*-0.084*	*0.487*
Cogue119768	0.247	-0.191	-0.337	-0.100	0.202	-0.420	-0.210	0.190	-0.036	0.171	-0.184	0.185	-0.108	-0.018	0.609
Cogue52237	0.229	-0.225	-0.291	-0.097	0.205	-0.485	-0.225	0.238	0.009	0.173	-0.131	0.205	-0.080	-0.088	0.562
Colgu11112	0.253	-0.232	-0.303	-0.113	0.216	-0.480	-0.216	0.217	0.031	0.170	-0.147	0.202	-0.094	-0.055	0.550
Colgu1241	0.255	-0.219	-0.306	-0.115	0.228	-0.454	-0.225	0.194	0.004	0.188	-0.184	0.193	-0.103	-0.019	0.563
Colgu163124	0.244	-0.229	-0.306	-0.110	0.211	-0.468	-0.215	0.223	0.016	0.187	-0.144	0.197	-0.106	-0.060	0.560
Colgu163273	0.236	-0.211	-0.302	-0.100	0.205	-0.479	-0.214	0.217	0.014	0.174	-0.150	0.191	-0.096	-0.060	0.576
Colgu163627	0.229	-0.207	-0.331	-0.090	0.208	-0.463	-0.225	0.200	-0.002	0.173	-0.157	0.226	-0.087	-0.045	0.569
Colgu401	0.199	-0.223	-0.325	-0.095	0.204	-0.516	-0.169	0.182	0.061	0.193	-0.081	0.230	-0.129	-0.082	0.550
Colgu408	0.243	-0.255	-0.302	-0.134	0.200	-0.486	-0.206	0.275	0.049	0.198	-0.113	0.262	-0.100	-0.107	0.477
Colgu762	0.242	-0.237	-0.295	-0.114	0.207	-0.508	-0.203	0.237	0.050	0.161	-0.117	0.223	-0.086	-0.090	0.530
Colgu864	0.227	-0.203	-0.309	-0.082	0.200	-0.505	-0.215	0.206	0.030	0.140	-0.135	0.210	-0.069	-0.068	0.574
Colgu994	0.237	-0.199	-0.335	-0.081	0.196	-0.461	-0.212	0.186	0.020	0.162	-0.153	0.176	-0.106	-0.030	0.601
Macfa102768	0.212	-0.184	-0.342	-0.083	0.163	-0.512	-0.171	0.211	0.060	0.152	-0.110	0.220	-0.110	-0.080	0.573
Macfa103649	0.241	-0.194	-0.351	-0.078	0.166	-0.488	-0.179	0.204	0.057	0.116	-0.112	0.181	-0.099	-0.063	0.600
Macfa103655	0.231	-0.198	-0.354	-0.073	0.188	-0.477	-0.216	0.179	0.067	0.175	-0.152	0.192	-0.116	-0.017	0.571
Macfa103658	0.249	-0.200	-0.327	-0.109	0.194	-0.505	-0.177	0.191	0.069	0.150	-0.147	0.201	-0.112	-0.038	0.561
Macfa106025	0.238	-0.207	-0.363	-0.087	0.188	-0.476	-0.175	0.179	0.041	0.132	-0.110	0.207	-0.108	-0.050	0.591
Macfa106384	0.244	-0.208	-0.354	-0.098	0.196	-0.477	-0.173	0.174	0.041	0.141	-0.122	0.203	-0.115	-0.040	0.587
Macfa114411	0.231	-0.232	-0.351	-0.087	0.195	-0.494	-0.195	0.197	0.072	0.155	-0.093	0.228	-0.104	-0.067	0.546

Macfa114505	0.243	-0.229	-0.304	-0.094	0.223	-0.491	-0.215	0.194	0.022	0.134	-0.125	0.199	-0.069	-0.062	0.574
Macfa121803	0.225	-0.198	-0.354	-0.051	0.188	-0.478	-0.215	0.170	0.038	0.119	-0.116	0.182	-0.079	-0.044	0.611
Macfa125	0.248	-0.211	-0.344	-0.093	0.179	-0.481	-0.185	0.209	0.060	0.143	-0.119	0.183	-0.114	-0.058	0.582
Macfa125102	0.218	-0.178	-0.334	-0.051	0.167	-0.525	-0.194	0.173	0.100	0.125	-0.118	0.159	-0.097	-0.045	0.600
Macfa196817	0.263	-0.211	-0.323	-0.106	0.198	-0.483	-0.219	0.206	0.080	0.174	-0.180	0.187	-0.111	-0.013	0.540
Macfa196824	0.260	-0.209	-0.320	-0.096	0.208	-0.477	-0.198	0.177	0.039	0.130	-0.149	0.158	-0.097	-0.027	0.600
Macfa198300	0.241	-0.210	-0.335	-0.058	0.198	-0.495	-0.214	0.160	0.080	0.119	-0.120	0.150	-0.088	-0.028	0.601
Macfa278	0.235	-0.219	-0.306	-0.099	0.202	-0.502	-0.181	0.199	0.042	0.150	-0.108	0.179	-0.105	-0.074	0.587
Macfa317191	0.190	-0.177	-0.329	-0.046	0.168	-0.534	-0.210	0.198	0.065	0.131	-0.108	0.222	-0.067	-0.082	0.576
Macfa385	0.234	-0.201	-0.327	-0.093	0.193	-0.497	-0.140	0.154	0.053	0.130	-0.093	0.144	-0.131	-0.053	0.626
Macfa411	0.232	-0.196	-0.346	-0.073	0.182	-0.480	-0.196	0.183	0.052	0.148	-0.129	0.174	-0.111	-0.040	0.601
Preme102755	0.254	-0.237	-0.320	-0.134	0.235	-0.489	-0.187	0.173	0.062	0.193	-0.150	0.229	-0.126	-0.021	0.517
Preme102757	0.252	-0.249	-0.293	-0.145	0.235	-0.507	-0.193	0.198	0.091	0.220	-0.150	0.232	-0.133	-0.034	0.477
Preme102882	0.262	-0.278	-0.257	-0.164	0.239	-0.495	-0.208	0.250	0.076	0.233	-0.139	0.227	-0.123	-0.071	0.449
Preme102883	0.236	-0.235	-0.294	-0.126	0.197	-0.509	-0.201	0.243	0.096	0.226	-0.136	0.217	-0.135	-0.068	0.490
Preme102891	0.249	-0.263	-0.294	-0.119	0.214	-0.499	-0.237	0.241	0.110	0.223	-0.136	0.219	-0.116	-0.057	0.463
Preme102895	0.246	-0.254	-0.280	-0.124	0.210	-0.515	-0.211	0.236	0.113	0.217	-0.126	0.196	-0.127	-0.066	0.486
Preme106600	0.241	-0.246	-0.319	-0.123	0.183	-0.465	-0.200	0.243	0.107	0.265	-0.130	0.178	-0.184	-0.050	0.499
Preme106605	0.261	-0.248	-0.318	-0.157	0.196	-0.501	-0.150	0.230	0.115	0.209	-0.116	0.225	-0.163	-0.063	0.478
Preme106671	0.261	-0.240	-0.310	-0.126	0.230	-0.461	-0.220	0.191	0.056	0.219	-0.175	0.190	-0.135	-0.007	0.526
Preme107086	0.282	-0.265	-0.236	-0.195	0.234	-0.508	-0.168	0.260	0.071	0.206	-0.150	0.216	-0.125	-0.079	0.457
Preme107088	0.273	-0.310	-0.278	-0.155	0.269	-0.487	-0.223	0.210	0.085	0.205	-0.116	0.245	-0.101	-0.053	0.434

* Specimen identifications are coded with the first three letters of genus, the first two letters of species, and the museum attribution number excluding leading year values (for BMNH and MNHNP).

Table A4.8. 2D and 3D specimen pairwise cusp distances within species for intramolar intraspecies cusp position variability analyses.

a. 2D

i. *Cercopithecus mitis*

Specimen 1	Specimen 2	Protoconid distance	Metaconid distance	Entoconid distance	Hypoconid distance	Hypoconulid distance
Cermi236996-fakeHC	Cermi259446-fakeHC	0.036	0.016	0.045	0.031	*0.030*
Cermi236996-fakeHC	Cermi4521-fakeHC	0.038	0.016	0.007	0.022	*0.015*
Cermi259446-fakeHC	Cermi4521-fakeHC	0.002	0.026	0.042	0.024	*0.038*
Cermi236996-fakeHC	Cermi452544-fakeHC	0.036	0.038	0.009	0.010	*0.020*
Cermi259446-fakeHC	Cermi452544-fakeHC	0.004	0.043	0.036	0.022	*0.021*
Cermi4521-fakeHC	Cermi452544-fakeHC	0.004	0.022	0.007	0.014	*0.034*
Cermi236996-fakeHC	Cermi452547-fakeHC	0.007	0.026	0.035	0.020	*0.026*
Cermi259446-fakeHC	Cermi452547-fakeHC	0.041	0.028	0.035	0.045	*0.043*
Cermi4521-fakeHC	Cermi452547-fakeHC	0.043	0.042	0.029	0.042	*0.040*
Cermi452544-fakeHC	Cermi452547-fakeHC	0.041	0.064	0.029	0.029	*0.022*
Cermi236996-fakeHC	Cermi452548-fakeHC	0.059	0.038	0.049	0.036	*0.016*
Cermi259446-fakeHC	Cermi452548-fakeHC	0.030	0.052	0.064	0.030	*0.031*
Cermi4521-fakeHC	Cermi452548-fakeHC	0.029	0.029	0.043	0.014	*0.032*
Cermi452544-fakeHC	Cermi452548-fakeHC	0.028	0.034	0.047	0.028	*0.011*
Cermi452547-fakeHC	Cermi452548-fakeHC	0.066	0.058	0.029	0.056	*0.012*
Cermi236996-fakeHC	Cermi452552-fakeHC	0.039	0.014	0.021	0.066	*0.058*
Cermi259446-fakeHC	Cermi452552-fakeHC	0.028	0.023	0.064	0.073	*0.077*
Cermi4521-fakeHC	Cermi452552-fakeHC	0.029	0.003	0.022	0.084	*0.070*
Cermi452544-fakeHC	Cermi452552-fakeHC	0.032	0.024	0.029	0.071	*0.056*
Cermi452547-fakeHC	Cermi452552-fakeHC	0.038	0.040	0.044	0.051	*0.034*
Cermi452548-fakeHC	Cermi452552-fakeHC	0.058	0.031	0.043	0.098	*0.047*
Cermi236996-fakeHC	Cermi452554-fakeHC	0.043	0.033	0.012	0.014	*0.014*
Cermi259446-fakeHC	Cermi452554-fakeHC	0.013	0.034	0.052	0.023	*0.044*

Cermi4521-fakeHC	Cermi452554-fakeHC	0.013	0.020	0.019	0.027	*0.020*
Cermi452544-fakeHC	Cermi452554-fakeHC	0.017	0.012	0.020	0.014	*0.029*
Cermi452547-fakeHC	Cermi452554-fakeHC	0.046	0.058	0.047	0.022	*0.024*
Cermi452548-fakeHC	Cermi452554-fakeHC	0.039	0.041	0.059	0.040	*0.021*
Cermi452552-fakeHC	Cermi452554-fakeHC	0.020	0.020	0.024	0.057	*0.050*
Cermi236996-fakeHC	Cermi52384-bs-fakeHC	0.037	0.003	0.030	0.054	*0.031*
Cermi259446-fakeHC	Cermi52384-bs-fakeHC	0.025	0.017	0.020	0.050	*0.024*
Cermi4521-fakeHC	Cermi52384-bs-fakeHC	0.025	0.013	0.025	0.033	*0.027*
Cermi452544-fakeHC	Cermi52384-bs-fakeHC	0.021	0.035	0.021	0.047	*0.037*
Cermi452547-fakeHC	Cermi52384-bs-fakeHC	0.044	0.029	0.017	0.074	*0.054*
Cermi452548-fakeHC	Cermi52384-bs-fakeHC	0.026	0.036	0.045	0.020	*0.043*
Cermi452552-fakeHC	Cermi52384-bs-fakeHC	0.051	0.011	0.046	0.118	*0.089*
Cermi452554-fakeHC	Cermi52384-bs-fakeHC	0.038	0.030	0.041	0.060	*0.044*
Cermi236996-fakeHC	Cermi52384b-bs-fakeHC	0.026	0.001	0.002	0.048	*0.033*
Cermi259446-fakeHC	Cermi52384b-bs-fakeHC	0.023	0.014	0.043	0.045	*0.047*
Cermi4521-fakeHC	Cermi52384b-bs-fakeHC	0.024	0.016	0.007	0.027	*0.019*
Cermi452544-fakeHC	Cermi52384b-bs-fakeHC	0.020	0.038	0.008	0.041	*0.050*
Cermi452547-fakeHC	Cermi52384b-bs-fakeHC	0.033	0.026	0.035	0.068	*0.058*
Cermi452548-fakeHC	Cermi52384b-bs-fakeHC	0.035	0.039	0.050	0.015	*0.050*
Cermi452552-fakeHC	Cermi52384b-bs-fakeHC	0.044	0.014	0.023	0.112	*0.088*

Cermi452554-fakeHC	Cermi52384b-bs-fakeHC	0.036	0.033	0.012	0.054	*0.038*
Cermi52384-bs-fakeHC	Cermi52384b-bs-fakeHC	0.011	0.004	0.029	0.007	*0.027*

ii. *Colobus guereza*

Specimen 1	**Specimen 2**	**Protoconid distance**	**Metaconid distance**	**Entoconid distance**	**Hypoconid distance**	**Hypoconulid distance**
Cogue119768-bs	Cogue52237-bs	0.038	0.004	0.050	0.053	0.075
Cogue119768-bs	Colgu11112	0.041	0.019	0.028	0.037	0.040
Cogue52237-bs	Colgu11112	0.026	0.020	0.023	0.016	0.036
Cogue119768-bs	Colgu1241	0.029	0.030	0.015	0.017	0.005
Cogue52237-bs	Colgu1241	0.027	0.029	0.044	0.055	0.073
Colgu11112	Colgu1241	0.013	0.011	0.025	0.041	0.037
Cogue119768-bs	Colgu163124-mirL	0.038	0.014	0.033	0.043	0.043
Cogue52237-bs	Colgu163124-mirL	0.016	0.015	0.018	0.019	0.037
Colgu11112	Colgu163124-mirL	0.010	0.006	0.006	0.017	0.013
Colgu1241	Colgu163124-mirL	0.015	0.018	0.031	0.040	0.042
Cogue119768-bs	Colgu163273-mirL	0.023	0.002	0.026	0.034	0.044
Cogue52237-bs	Colgu163273-mirL	0.015	0.003	0.024	0.019	0.032
Colgu11112	Colgu163273-mirL	0.027	0.018	0.002	0.006	0.006
Colgu1241	Colgu163273-mirL	0.020	0.027	0.025	0.036	0.042
Colgu163124-mirL	Colgu163273-mirL	0.019	0.012	0.007	0.014	0.009
Cogue119768-bs	Colgu163627-mirL	0.024	0.011	0.018	0.027	0.034
Cogue52237-bs	Colgu163627-mirL	0.018	0.007	0.038	0.026	0.044
Colgu11112	Colgu163627-mirL	0.035	0.025	0.019	0.010	0.012
Colgu1241	Colgu163627-mirL	0.028	0.032	0.006	0.031	0.031
Colgu163124-mirL	Colgu163627-mirL	0.027	0.021	0.025	0.019	0.024
Colgu163273-mirL	Colgu163627-mirL	0.008	0.010	0.019	0.007	0.017
Cogue119768-bs	Colgu401-mirL	0.057	0.005	0.042	0.105	0.067
Cogue52237-bs	Colgu401-mirL	0.029	0.002	0.080	0.054	0.049
Colgu11112	Colgu401-mirL	0.054	0.022	0.059	0.070	0.044
Colgu1241	Colgu401-mirL	0.055	0.031	0.057	0.104	0.068

Colgu163124-mirL	Colgu401-mirL	0.045	0.017	0.062	0.064	0.031
Colgu163273-mirL	Colgu401-mirL	0.038	0.005	0.057	0.072	0.039
Colgu163627-mirL	Colgu401-mirL	0.034	0.007	0.059	0.079	0.056
Cogue119768-bs	Colgu408-mirL	0.064	0.035	0.085	0.076	0.089
Cogue52237-bs	Colgu408-mirL	0.034	0.038	0.041	0.030	0.028
Colgu11112	Colgu408-mirL	0.025	0.027	0.059	0.044	0.053
Colgu1241	Colgu408-mirL	0.038	0.034	0.083	0.072	0.088
Colgu163124-mirL	Colgu408-mirL	0.026	0.026	0.053	0.033	0.047
Colgu163273-mirL	Colgu408-mirL	0.045	0.035	0.059	0.044	0.047
Colgu163627-mirL	Colgu408-mirL	0.050	0.045	0.077	0.050	0.064
Colgu401-mirL	Colgu408-mirL	0.054	0.039	0.100	0.032	0.038
Cogue119768-bs	Colgu762	0.045	0.015	0.047	0.068	0.076
Cogue52237-bs	Colgu762	0.018	0.018	0.022	0.019	0.006
Colgu11112	Colgu762	0.012	0.010	0.023	0.031	0.036
Colgu1241	Colgu762	0.022	0.021	0.048	0.072	0.074
Colgu163124-mirL	Colgu762	0.008	0.006	0.018	0.038	0.036
Colgu163273-mirL	Colgu762	0.026	0.015	0.023	0.036	0.032
Colgu163627-mirL	Colgu762	0.032	0.024	0.042	0.042	0.046
Colgu401-mirL	Colgu762	0.044	0.019	0.065	0.048	0.044
Colgu408-mirL	Colgu762	0.019	0.021	0.039	0.037	0.022
Cogue119768-bs	Colgu864-mirL	0.024	0.018	0.016	0.058	0.063
Cogue52237-bs	Colgu864-mirL	0.021	0.015	0.034	0.034	0.023
Colgu11112	Colgu864-mirL	0.039	0.035	0.011	0.032	0.028
Colgu1241	Colgu864-mirL	0.032	0.043	0.015	0.069	0.060
Colgu163124-mirL	Colgu864-mirL	0.031	0.030	0.017	0.048	0.037
Colgu163273-mirL	Colgu864-mirL	0.012	0.018	0.010	0.038	0.028
Colgu163627-mirL	Colgu864-mirL	0.004	0.011	0.011	0.039	0.029
Colgu401-mirL	Colgu864-mirL	0.034	0.014	0.052	0.076	0.061
Colgu408-mirL	Colgu864-mirL	0.055	0.052	0.070	0.062	0.050
Colgu762	Colgu864-mirL	0.037	0.033	0.033	0.028	0.028
Cogue119768-bs	Colgu994	0.013	0.019	0.005	0.031	0.012
Cogue52237-bs	Colgu994	0.027	0.018	0.054	0.025	0.063
Colgu11112	Colgu994	0.037	0.037	0.032	0.010	0.028
Colgu1241	Colgu994	0.027	0.046	0.015	0.040	0.012

Colgu163124-mirL	Colgu994	0.031	0.032	0.038	0.026	0.031
Colgu163273-mirL	Colgu994	0.013	0.020	0.031	0.012	0.031
Colgu163627-mirL	Colgu994	0.011	0.014	0.019	0.011	0.024
Colgu401-mirL	Colgu994	0.045	0.016	0.044	0.079	0.057
Colgu408-mirL	Colgu994	0.057	0.053	0.090	0.054	0.077
Colgu762	Colgu994	0.038	0.034	0.052	0.037	0.064
Colgu864-mirL	Colgu994	0.011	0.003	0.021	0.029	0.053

iii. *Macaca fascicularis*

Specimen 1	**Specimen 2**	**Protoconid distance**	**Metaconid distance**	**Entoconid distance**	**Hypoconid distance**	**Hypoconulid distance**
Macfa102768	Macfa103649	0.030	0.006	0.011	0.036	0.019
Macfa102768	Macfa103655	0.024	0.027	0.056	0.047	0.063
Macfa103649	Macfa103655	0.010	0.023	0.045	0.071	0.050
Macfa102768	Macfa103658	0.040	0.040	0.021	0.036	0.042
Macfa103649	Macfa103658	0.010	0.042	0.012	0.048	0.028
Macfa103655	Macfa103658	0.018	0.036	0.041	0.025	0.022
Macfa102768	Macfa106025	0.035	0.025	0.033	0.020	0.030
Macfa103649	Macfa106025	0.013	0.024	0.025	0.016	0.016
Macfa103655	Macfa106025	0.011	0.014	0.041	0.060	0.035
Macfa103658	Macfa106025	0.013	0.023	0.013	0.041	0.013
Macfa102768	Macfa106384	0.040	0.036	0.037	0.016	0.039
Macfa103649	Macfa106384	0.014	0.036	0.030	0.027	0.028
Macfa103655	Macfa106384	0.016	0.026	0.044	0.045	0.024
Macfa103658	Macfa106384	0.009	0.012	0.018	0.026	0.003
Macfa106025	Macfa106384	0.006	0.013	0.005	0.015	0.012
Macfa102768	Macfa114411	0.051	0.032	0.028	0.018	0.014
Macfa103649	Macfa114411	0.039	0.030	0.017	0.043	0.006

Macfa103655	Macfa114411	0.034	0.015	0.028	0.062	0.052
Macfa103658	Macfa114411	0.036	0.022	0.019	0.054	0.030
Macfa106025	Macfa114411	0.026	0.007	0.028	0.028	0.018
Macfa106384	Macfa114411	0.027	0.011	0.032	0.032	0.029
Macfa102768	Macfa114505	0.055	0.061	0.047	0.023	0.045
Macfa103649	Macfa114505	0.035	0.059	0.037	0.023	0.030
Macfa103655	Macfa114505	0.033	0.040	0.015	0.048	0.066
Macfa103658	Macfa114505	0.029	0.033	0.038	0.026	0.049
Macfa106025	Macfa114505	0.023	0.035	0.043	0.016	0.041
Macfa106384	Macfa114505	0.021	0.027	0.047	0.008	0.051
Macfa114411	Macfa114505	0.013	0.029	0.020	0.038	0.035
Macfa102768	Macfa121803	0.019	0.041	0.060	0.034	0.047
Macfa103649	Macfa121803	0.016	0.035	0.048	0.005	0.028
Macfa103655	Macfa121803	0.006	0.023	0.008	0.066	0.046
Macfa103658	Macfa121803	0.024	0.059	0.043	0.044	0.034
Macfa106025	Macfa121803	0.015	0.037	0.040	0.015	0.030
Macfa106384	Macfa121803	0.021	0.048	0.042	0.023	0.036
Macfa114411	Macfa121803	0.034	0.037	0.033	0.043	0.034
Macfa114505	Macfa121803	0.036	0.056	0.023	0.018	0.021
Macfa102768	Macfa125	0.045	0.018	0.014	0.012	0.022
Macfa103649	Macfa125	0.018	0.019	0.008	0.028	0.015
Macfa103655	Macfa125	0.021	0.022	0.044	0.046	0.041
Macfa103658	Macfa125	0.011	0.023	0.019	0.029	0.020
Macfa106025	Macfa125	0.010	0.011	0.032	0.014	0.009
Macfa106384	Macfa125	0.005	0.018	0.037	0.004	0.017
Macfa114411	Macfa125	0.027	0.017	0.015	0.028	0.014
Macfa114505	Macfa125	0.019	0.044	0.033	0.011	0.045

Macfa121803	Macfa125	0.026	0.043	0.048	0.025	0.037
Macfa102768	Macfa125102	0.009	0.032	0.044	0.029	0.037
Macfa103649	Macfa125102	0.028	0.027	0.033	0.011	0.019
Macfa103655	Macfa125102	0.025	0.030	0.023	0.060	0.034
Macfa103658	Macfa125102	0.038	0.064	0.024	0.038	0.016
Macfa106025	Macfa125102	0.035	0.042	0.019	0.011	0.012
Macfa106384	Macfa125102	0.040	0.055	0.021	0.017	0.018
Macfa114411	Macfa125102	0.056	0.045	0.024	0.039	0.023
Macfa114505	Macfa125102	0.057	0.070	0.029	0.012	0.033
Macfa121803	Macfa125102	0.022	0.020	0.021	0.006	0.018
Macfa125	Macfa125102	0.045	0.043	0.036	0.019	0.021
Macfa102768	Macfa196817	0.057	0.042	0.049	0.073	0.067
Macfa103649	Macfa196817	0.027	0.043	0.040	0.090	0.052
Macfa103655	Macfa196817	0.034	0.034	0.027	0.028	0.006
Macfa103658	Macfa196817	0.017	0.005	0.044	0.041	0.025
Macfa106025	Macfa196817	0.025	0.021	0.052	0.082	0.037
Macfa106384	Macfa196817	0.019	0.009	0.056	0.067	0.028
Macfa114411	Macfa196817	0.038	0.019	0.025	0.089	0.055
Macfa114505	Macfa196817	0.027	0.027	0.013	0.068	0.065
Macfa121803	Macfa196817	0.039	0.056	0.035	0.085	0.045
Macfa125	Macfa196817	0.015	0.024	0.035	0.069	0.045
Macfa125102	Macfa196817	0.055	0.063	0.041	0.079	0.035
Macfa102768	Macfa196824	0.054	0.047	0.044	0.045	0.055
Macfa103649	Macfa196824	0.025	0.046	0.033	0.040	0.037
Macfa103655	Macfa196824	0.031	0.030	0.019	0.045	0.022
Macfa103658	Macfa196824	0.014	0.019	0.025	0.020	0.019
Macfa106025	Macfa196824	0.022	0.022	0.023	0.040	0.026

Macfa106384	Macfa196824	0.017	0.012	0.025	0.030	0.023
Macfa114411	Macfa196824	0.037	0.016	0.021	0.062	0.041
Macfa114505	Macfa196824	0.026	0.015	0.024	0.024	0.045
Macfa121803	Macfa196824	0.037	0.050	0.018	0.035	0.025
Macfa125	Macfa196824	0.013	0.030	0.034	0.034	0.035
Macfa125102	Macfa196824	0.053	0.060	0.005	0.032	0.018
Macfa196817	Macfa196824	0.003	0.014	0.036	0.054	0.020
Macfa102768	Macfa198300	0.039	0.043	0.067	0.035	0.056
Macfa103649	Macfa198300	0.016	0.037	0.056	0.008	0.037
Macfa103655	Macfa198300	0.015	0.018	0.019	0.065	0.031
Macfa103658	Macfa198300	0.012	0.051	0.048	0.041	0.027
Macfa106025	Macfa198300	0.004	0.030	0.043	0.017	0.030
Macfa106384	Macfa198300	0.003	0.039	0.044	0.023	0.030
Macfa114411	Macfa198300	0.024	0.029	0.042	0.045	0.043
Macfa114505	Macfa198300	0.019	0.044	0.034	0.017	0.039
Macfa121803	Macfa198300	0.020	0.013	0.011	0.004	0.018
Macfa125	Macfa198300	0.007	0.039	0.057	0.025	0.040
Macfa125102	Macfa198300	0.040	0.031	0.024	0.006	0.020
Macfa196817	Macfa198300	0.022	0.048	0.046	0.082	0.028
Macfa196824	Macfa198300	0.019	0.039	0.023	0.031	0.009
Macfa102768	Macfa278	0.041	0.042	0.015	0.003	0.007
Macfa103649	Macfa278	0.025	0.042	0.005	0.035	0.013
Macfa103655	Macfa278	0.021	0.030	0.041	0.050	0.059
Macfa103658	Macfa278	0.023	0.013	0.008	0.039	0.037
Macfa106025	Macfa278	0.012	0.018	0.021	0.018	0.024
Macfa106384	Macfa278	0.014	0.006	0.026	0.017	0.035
Macfa114411	Macfa278	0.014	0.014	0.015	0.015	0.007

Macfa114505	Macfa278	0.014	0.022	0.035	0.024	0.038
Macfa121803	Macfa278	0.023	0.051	0.044	0.033	0.040
Macfa125	Macfa278	0.015	0.024	0.011	0.013	0.019
Macfa125102	Macfa278	0.044	0.059	0.029	0.028	0.030
Macfa196817	Macfa278	0.029	0.008	0.039	0.076	0.062
Macfa196824	Macfa278	0.027	0.007	0.028	0.046	0.049
Macfa198300	Macfa278	0.011	0.041	0.051	0.034	0.050
Macfa102768	Macfa317191	0.023	0.038	0.040	0.021	0.043
Macfa103649	Macfa317191	0.053	0.032	0.031	0.016	0.038
Macfa103655	Macfa317191	0.046	0.034	0.021	0.062	0.082
Macfa103658	Macfa317191	0.063	0.069	0.033	0.043	0.063
Macfa106025	Macfa317191	0.056	0.046	0.040	0.002	0.052
Macfa106384	Macfa317191	0.062	0.059	0.044	0.017	0.064
Macfa114411	Macfa317191	0.068	0.049	0.014	0.028	0.040
Macfa114505	Macfa317191	0.074	0.073	0.007	0.018	0.020
Macfa121803	Macfa317191	0.041	0.020	0.029	0.015	0.040
Macfa125	Macfa317191	0.067	0.048	0.026	0.016	0.053
Macfa125102	Macfa317191	0.027	0.006	0.030	0.013	0.048
Macfa196817	Macfa317191	0.080	0.067	0.012	0.084	0.082
Macfa196824	Macfa317191	0.077	0.064	0.025	0.042	0.063
Macfa198300	Macfa317191	0.060	0.032	0.039	0.018	0.058
Macfa278	Macfa317191	0.061	0.063	0.029	0.019	0.039
Macfa102768	Macfa385	0.028	0.032	0.065	0.028	0.034
Macfa103649	Macfa385	0.009	0.031	0.063	0.023	0.033
Macfa103655	Macfa385	0.004	0.020	0.080	0.074	0.039
Macfa103658	Macfa385	0.015	0.017	0.053	0.057	0.024
Macfa106025	Macfa385	0.007	0.007	0.043	0.017	0.023

Macfa106384	Macfa385	0.012	0.006	0.038	0.031	0.020
Macfa114411	Macfa385	0.031	0.006	0.070	0.025	0.031
Macfa114505	Macfa385	0.030	0.030	0.085	0.033	0.063
Macfa121803	Macfa385	0.009	0.042	0.076	0.025	0.053
Macfa125	Macfa385	0.017	0.015	0.071	0.029	0.018
Macfa125102	Macfa385	0.028	0.049	0.057	0.026	0.034
Macfa196817	Macfa385	0.030	0.014	0.095	0.098	0.044
Macfa196824	Macfa385	0.027	0.015	0.062	0.056	0.043
Macfa198300	Macfa385	0.011	0.035	0.074	0.029	0.050
Macfa278	Macfa385	0.018	0.011	0.061	0.026	0.033
Macfa317191	Macfa385	0.050	0.053	0.082	0.015	0.071
Macfa102768	Macfa411	0.023	0.021	0.038	0.019	0.040
Macfa103649	Macfa411	0.009	0.017	0.027	0.037	0.027
Macfa103655	Macfa411	0.003	0.006	0.021	0.035	0.024
Macfa103658	Macfa411	0.017	0.038	0.021	0.018	0.002
Macfa106025	Macfa411	0.013	0.015	0.021	0.025	0.011
Macfa106384	Macfa411	0.017	0.028	0.025	0.010	0.004
Macfa114411	Macfa411	0.036	0.019	0.015	0.037	0.029
Macfa114505	Macfa411	0.035	0.046	0.022	0.015	0.048
Macfa121803	Macfa411	0.007	0.023	0.022	0.032	0.032
Macfa125	Macfa411	0.022	0.020	0.028	0.012	0.018
Macfa125102	Macfa411	0.023	0.026	0.009	0.026	0.015
Macfa196817	Macfa411	0.034	0.037	0.033	0.057	0.027
Macfa196824	Macfa411	0.031	0.035	0.006	0.027	0.020
Macfa198300	Macfa411	0.017	0.022	0.029	0.031	0.026
Macfa278	Macfa411	0.023	0.033	0.022	0.022	0.035
Macfa317191	Macfa411	0.046	0.031	0.021	0.028	0.062

Macfa385	Macfa411	0.006	0.023	0.063	0.041	0.024

iv. *Presbytis melalophos*

Specimen 1	**Specimen 2**	**Protoconid distance**	**Metaconid distance**	**Entoconid distance**	**Hypoconid distance**	**Hypoconulid distance**
Preme102755	Preme102757	0.012	0.012	0.026	0.026	0.015
Preme102755	Preme102882	0.041	0.031	0.080	0.041	0.051
Preme102757	Preme102882	0.030	0.019	0.054	0.017	0.038
Preme102755	Preme102883	0.018	0.039	0.071	0.036	0.048
Preme102757	Preme102883	0.021	0.043	0.046	0.015	0.034
Preme102882	Preme102883	0.050	0.057	0.009	0.008	0.012
Preme102755	Preme102891	0.026	0.025	0.084	0.032	0.038
Preme102757	Preme102891	0.014	0.033	0.061	0.014	0.028
Preme102882	Preme102891	0.019	0.051	0.030	0.011	0.016
Preme102883	Preme102891	0.031	0.019	0.035	0.004	0.022
Preme102755	Preme102895	0.019	0.026	0.068	0.034	0.046
Preme102757	Preme102895	0.008	0.032	0.043	0.023	0.033
Preme102882	Preme102895	0.028	0.049	0.014	0.021	0.006
Preme102883	Preme102895	0.022	0.014	0.012	0.014	0.008
Preme102891	Preme102895	0.009	0.007	0.026	0.011	0.015
Preme102755	Preme106600	0.016	0.053	0.072	0.074	0.065
Preme102757	Preme106600	0.011	0.056	0.046	0.049	0.054
Preme102882	Preme106600	0.038	0.069	0.010	0.033	0.064
Preme102883	Preme106600	0.012	0.014	0.002	0.039	0.052
Preme102891	Preme106600	0.019	0.032	0.037	0.043	0.068
Preme102895	Preme106600	0.009	0.027	0.014	0.048	0.059
Preme102755	Preme106605	0.013	0.046	0.068	0.037	0.056

Preme102757	Preme106605	0.010	0.041	0.054	0.036	0.041
Preme102882	Preme106605	0.030	0.043	0.060	0.034	0.040
Preme102883	Preme106605	0.029	0.032	0.053	0.027	0.028
Preme102891	Preme106605	0.020	0.042	0.087	0.025	0.047
Preme102895	Preme106605	0.017	0.036	0.061	0.013	0.036
Preme106600	Preme106605	0.020	0.036	0.051	0.058	0.024
Preme102755	Preme106671	0.007	0.009	0.037	0.036	0.016
Preme102757	Preme106671	0.013	0.020	0.027	0.026	0.027
Preme102882	Preme106671	0.038	0.039	0.059	0.038	0.065
Preme102883	Preme106671	0.025	0.034	0.054	0.039	0.061
Preme102891	Preme106671	0.026	0.017	0.053	0.039	0.053
Preme102895	Preme106671	0.021	0.020	0.046	0.049	0.060
Preme106600	Preme106671	0.021	0.047	0.055	0.064	0.065
Preme106605	Preme106671	0.008	0.046	0.079	0.060	0.062
Preme102755	Preme107086	0.040	0.061	0.089	0.013	0.059
Preme102757	Preme107086	0.034	0.049	0.067	0.014	0.046
Preme102882	Preme107086	0.024	0.031	0.040	0.029	0.008
Preme102883	Preme107086	0.055	0.079	0.037	0.024	0.016
Preme102891	Preme107086	0.034	0.078	0.070	0.022	0.024
Preme102895	Preme107086	0.038	0.074	0.048	0.026	0.013
Preme106600	Preme107086	0.045	0.088	0.035	0.062	0.066
Preme106605	Preme107086	0.027	0.054	0.035	0.034	0.042
Preme106671	Preme107086	0.033	0.069	0.085	0.029	0.073
Preme102755	Preme107088	0.076	0.040	0.052	0.036	0.041
Preme102757	Preme107088	0.065	0.036	0.032	0.037	0.037
Preme102882	Preme107088	0.035	0.032	0.043	0.037	0.029
Preme102883	Preme107088	0.084	0.078	0.039	0.030	0.038

Preme102891	Preme107088	0.053	0.066	0.034	0.027	0.016
Preme102895	Preme107088	0.062	0.066	0.029	0.016	0.030
Preme106600	Preme107088	0.072	0.092	0.041	0.062	0.083
Preme106605	Preme107088	0.064	0.074	0.075	0.004	0.063
Preme106671	Preme107088	0.072	0.049	0.019	0.061	0.057
Preme107086	Preme107088	0.046	0.053	0.073	0.034	0.036

b. 3D

i. *Cercopithecus mitis*

Specimen 1	**Specimen 2**	**Protoconid distance**	**Metaconid distance**	**Entoconid distance**	**Hypoconid distance**	**Hypoconulid distance**
Cermi236996-fakeHC	Cermi259446-fakeHC	0.037	0.021	0.051	0.035	0.058
Cermi236996-fakeHC	Cermi4521-fakeHC	0.038	0.033	0.007	0.030	0.017
Cermi259446-fakeHC	Cermi4521-fakeHC	0.005	0.030	0.048	0.045	0.057
Cermi236996-fakeHC	Cermi452544-fakeHC	0.045	0.040	0.015	0.033	0.062
Cermi259446-fakeHC	Cermi452544-fakeHC	0.033	0.050	0.038	0.026	0.023
Cermi4521-fakeHC	Cermi452544-fakeHC	0.028	0.046	0.014	0.054	0.062
Cermi236996-fakeHC	Cermi452547-fakeHC	0.014	0.032	0.065	0.031	0.055
Cermi259446-fakeHC	Cermi452547-fakeHC	0.041	0.042	0.047	0.046	0.043
Cermi4521-fakeHC	Cermi452547-fakeHC	0.044	0.063	0.062	0.061	0.058
Cermi452544-fakeHC	Cermi452547-fakeHC	0.056	0.064	0.052	0.030	0.024
Cermi236996-fakeHC	Cermi452548-fakeHC	0.070	0.042	0.077	0.036	0.074
Cermi259446-fakeHC	Cermi452548-fakeHC	0.052	0.061	0.073	0.038	0.039
Cermi4521-fakeHC	Cermi452548-fakeHC	0.048	0.055	0.073	0.021	0.073
Cermi452544-fakeHC	Cermi452548-fakeHC	0.030	0.035	0.067	0.046	0.018
Cermi452547-fakeHC	Cermi452548-fakeHC	0.082	0.058	0.030	0.064	0.026
Cermi236996-fakeHC	Cermi452552-fakeHC	0.041	0.038	0.091	0.084	0.111
Cermi259446-fakeHC	Cermi452552-fakeHC	0.029	0.053	0.091	0.081	0.089
Cermi4521-fakeHC	Cermi452552-fakeHC	0.031	0.064	0.092	0.111	0.112

Cermi452544-fakeHC	Cermi452552-fakeHC	0.050	0.033	0.082	0.074	0.066
Cermi452547-fakeHC	Cermi452552-fakeHC	0.038	0.044	0.056	0.058	0.057
Cermi452548-fakeHC	Cermi452552-fakeHC	0.075	0.035	0.052	0.113	0.052
Cermi236996-fakeHC	Cermi452554-fakeHC	0.047	0.045	0.086	0.020	0.088
Cermi259446-fakeHC	Cermi452554-fakeHC	0.027	0.056	0.080	0.023	0.058
Cermi4521-fakeHC	Cermi452554-fakeHC	0.023	0.063	0.088	0.045	0.084
Cermi452544-fakeHC	Cermi452554-fakeHC	0.019	0.022	0.076	0.022	0.041
Cermi452547-fakeHC	Cermi452554-fakeHC	0.055	0.060	0.056	0.024	0.045
Cermi452548-fakeHC	Cermi452554-fakeHC	0.043	0.043	0.065	0.045	0.026
Cermi452552-fakeHC	Cermi452554-fakeHC	0.036	0.021	0.024	0.068	0.051
Cermi236996-fakeHC	Cermi52384-bs-fakeHC	0.039	0.017	0.032	0.054	0.044
Cermi259446-fakeHC	Cermi52384-bs-fakeHC	0.031	0.017	0.025	0.055	0.030
Cermi4521-fakeHC	Cermi52384-bs-fakeHC	0.028	0.018	0.027	0.037	0.037
Cermi452544-fakeHC	Cermi52384-bs-fakeHC	0.026	0.045	0.021	0.060	0.045
Cermi452547-fakeHC	Cermi52384-bs-fakeHC	0.050	0.045	0.049	0.080	0.057
Cermi452548-fakeHC	Cermi52384-bs-fakeHC	0.036	0.050	0.068	0.020	0.059
Cermi452552-fakeHC	Cermi52384-bs-fakeHC	0.056	0.052	0.092	0.131	0.109
Cermi452554-fakeHC	Cermi52384-bs-fakeHC	0.038	0.056	0.086	0.064	0.071
Cermi236996-fakeHC	Cermi52384b-bs-fakeHC	0.027	0.014	0.027	0.048	0.042
Cermi259446-fakeHC	Cermi52384b-bs-fakeHC	0.023	0.014	0.043	0.051	0.052
Cermi4521-fakeHC	Cermi52384b-bs-fakeHC	0.025	0.022	0.028	0.031	0.027
Cermi452544-fakeHC	Cermi52384b-bs-fakeHC	0.040	0.046	0.017	0.056	0.059
Cermi452547-fakeHC	Cermi52384b-bs-fakeHC	0.033	0.041	0.045	0.074	0.063

Cermi452548-fakeHC	Cermi52384b-bs-fakeHC	0.057	0.051	0.059	0.015	0.068
Cermi452552-fakeHC	Cermi52384b-bs-fakeHC	0.045	0.051	0.066	0.126	0.111
Cermi452554-fakeHC	Cermi52384b-bs-fakeHC	0.044	0.056	0.060	0.059	0.072
Cermi52384-bs-fakeHC	Cermi52384b-bs-fakeHC	0.023	0.004	0.034	0.007	0.027

ii. *Colobus guereza*

Specimen 1	**Specimen 2**	**Protoconid distance**	**Metaconid distance**	**Entoconid distance**	**Hypoconid distance**	**Hypoconulid distance**
Cogue119768-bs	Cogue52237-bs	0.060	0.065	0.068	0.056	0.089
Cogue119768-bs	Colgu11112	0.054	0.063	0.073	0.040	0.071
Cogue52237-bs	Colgu11112	0.028	0.020	0.032	0.017	0.038
Cogue119768-bs	Colgu1241	0.043	0.045	0.043	0.019	0.046
Cogue52237-bs	Colgu1241	0.030	0.042	0.045	0.056	0.073
Colgu11112	Colgu1241	0.013	0.028	0.037	0.042	0.040
Cogue119768-bs	Colgu163124-mirL	0.049	0.050	0.062	0.044	0.065
Cogue52237-bs	Colgu163124-mirL	0.022	0.022	0.020	0.020	0.037
Colgu11112	Colgu163124-mirL	0.010	0.014	0.016	0.018	0.016
Colgu1241	Colgu163124-mirL	0.015	0.022	0.033	0.040	0.042
Cogue119768-bs	Colgu163273-mirL	0.042	0.059	0.057	0.034	0.055
Cogue52237-bs	Colgu163273-mirL	0.019	0.006	0.025	0.024	0.035
Colgu11112	Colgu163273-mirL	0.027	0.018	0.018	0.012	0.027
Colgu1241	Colgu163273-mirL	0.021	0.037	0.027	0.036	0.044
Colgu163124-mirL	Colgu163273-mirL	0.020	0.017	0.007	0.015	0.019
Cogue119768-bs	Colgu163627-mirL	0.025	0.044	0.038	0.050	0.052
Cogue52237-bs	Colgu163627-mirL	0.044	0.023	0.040	0.034	0.044
Colgu11112	Colgu163627-mirL	0.044	0.030	0.039	0.027	0.023
Colgu1241	Colgu163627-mirL	0.038	0.033	0.009	0.046	0.031
Colgu163124-mirL	Colgu163627-mirL	0.037	0.021	0.031	0.035	0.026
Colgu163273-mirL	Colgu163627-mirL	0.030	0.020	0.025	0.036	0.019
Cogue119768-bs	Colgu401-mirL	0.059	0.096	0.106	0.115	0.089

Cogue52237-bs	Colgu401-mirL	0.045	0.031	0.095	0.060	0.050
Colgu11112	Colgu401-mirL	0.059	0.042	0.066	0.076	0.044
Colgu1241	Colgu401-mirL	0.059	0.069	0.081	0.110	0.070
Colgu163124-mirL	Colgu401-mirL	0.049	0.051	0.076	0.072	0.033
Colgu163273-mirL	Colgu401-mirL	0.045	0.037	0.074	0.082	0.047
Colgu163627-mirL	Colgu401-mirL	0.034	0.053	0.086	0.079	0.059
Cogue119768-bs	Colgu408-mirL	0.073	0.075	0.120	0.108	0.159
Cogue52237-bs	Colgu408-mirL	0.036	0.038	0.057	0.065	0.089
Colgu11112	Colgu408-mirL	0.025	0.028	0.061	0.075	0.090
Colgu1241	Colgu408-mirL	0.038	0.047	0.094	0.100	0.123
Colgu163124-mirL	Colgu408-mirL	0.027	0.032	0.062	0.073	0.095
Colgu163273-mirL	Colgu408-mirL	0.045	0.035	0.069	0.083	0.110
Colgu163627-mirL	Colgu408-mirL	0.058	0.051	0.092	0.062	0.112
Colgu401-mirL	Colgu408-mirL	0.059	0.049	0.101	0.045	0.082
Cogue119768-bs	Colgu762	0.062	0.089	0.098	0.078	0.110
Cogue52237-bs	Colgu762	0.018	0.029	0.047	0.026	0.033
Colgu11112	Colgu762	0.015	0.030	0.030	0.038	0.042
Colgu1241	Colgu762	0.024	0.058	0.067	0.078	0.081
Colgu163124-mirL	Colgu762	0.014	0.040	0.038	0.045	0.047
Colgu163273-mirL	Colgu762	0.027	0.032	0.043	0.048	0.057
Colgu163627-mirL	Colgu762	0.048	0.051	0.067	0.042	0.060
Colgu401-mirL	Colgu762	0.054	0.021	0.065	0.049	0.048
Colgu408-mirL	Colgu762	0.020	0.030	0.039	0.054	0.057
Cogue119768-bs	Colgu864-mirL	0.037	0.086	0.068	0.063	0.072
Cogue52237-bs	Colgu864-mirL	0.028	0.025	0.040	0.034	0.026
Colgu11112	Colgu864-mirL	0.040	0.043	0.011	0.033	0.037
Colgu1241	Colgu864-mirL	0.032	0.066	0.030	0.071	0.061
Colgu163124-mirL	Colgu864-mirL	0.031	0.048	0.022	0.049	0.040
Colgu163273-mirL	Colgu864-mirL	0.014	0.031	0.019	0.042	0.028
Colgu163627-mirL	Colgu864-mirL	0.022	0.043	0.034	0.043	0.030
Colgu401-mirL	Colgu864-mirL	0.038	0.018	0.060	0.079	0.066
Colgu408-mirL	Colgu864-mirL	0.055	0.055	0.072	0.081	0.109
Colgu762	Colgu864-mirL	0.039	0.033	0.039	0.031	0.053
Cogue119768-bs	Colgu994	0.013	0.046	0.057	0.032	0.015

Cogue52237-bs	Colgu994	0.052	0.029	0.055	0.038	0.075
Colgu11112	Colgu994	0.049	0.042	0.034	0.028	0.058
Colgu1241	Colgu994	0.040	0.046	0.022	0.043	0.040
Colgu163124-mirL	Colgu994	0.043	0.033	0.038	0.034	0.051
Colgu163273-mirL	Colgu994	0.036	0.027	0.032	0.020	0.040
Colgu163627-mirL	Colgu994	0.012	0.014	0.030	0.052	0.039
Colgu401-mirL	Colgu994	0.046	0.056	0.060	0.096	0.076
Colgu408-mirL	Colgu994	0.066	0.058	0.094	0.102	0.146
Colgu762	Colgu994	0.056	0.058	0.060	0.060	0.096
Colgu864-mirL	Colgu994	0.028	0.043	0.023	0.045	0.059

iii. *Macaca fascicularis*

Specimen 1	**Specimen 2**	**Protoconid distance**	**Metaconid distance**	**Entoconid distance**	**Hypoconid distance**	**Hypoconulid distance**
Macfa102768	Macfa103649	0.032	0.025	0.012	0.053	0.033
Macfa102768	Macfa103655	0.027	0.045	0.056	0.055	0.063
Macfa103649	Macfa103655	0.011	0.025	0.046	0.072	0.058
Macfa102768	Macfa103658	0.043	0.041	0.023	0.041	0.043
Macfa103649	Macfa103658	0.026	0.045	0.017	0.052	0.048
Macfa103655	Macfa103658	0.032	0.046	0.041	0.027	0.024
Macfa102768	Macfa106025	0.041	0.045	0.038	0.024	0.034
Macfa103649	Macfa106025	0.018	0.027	0.030	0.031	0.018
Macfa103655	Macfa106025	0.014	0.014	0.049	0.062	0.040
Macfa103658	Macfa106025	0.038	0.037	0.032	0.042	0.032
Macfa102768	Macfa106384	0.042	0.051	0.042	0.023	0.042
Macfa103649	Macfa106384	0.015	0.038	0.034	0.035	0.031
Macfa103655	Macfa106384	0.016	0.026	0.051	0.046	0.028
Macfa103658	Macfa106384	0.028	0.030	0.034	0.026	0.025
Macfa106025	Macfa106384	0.010	0.013	0.005	0.016	0.012
Macfa102768	Macfa114411	0.052	0.037	0.030	0.019	0.031
Macfa103649	Macfa114411	0.039	0.031	0.023	0.063	0.055
Macfa103655	Macfa114411	0.034	0.023	0.029	0.071	0.058
Macfa103658	Macfa114411	0.043	0.025	0.019	0.060	0.034
Macfa106025	Macfa114411	0.029	0.020	0.042	0.035	0.048

Macfa106384	Macfa114411	0.027	0.021	0.045	0.040	0.050
Macfa102768	Macfa114505	0.067	0.064	0.061	0.032	0.045
Macfa103649	Macfa114505	0.059	0.059	0.051	0.029	0.040
Macfa103655	Macfa114505	0.060	0.043	0.047	0.049	0.066
Macfa103658	Macfa114505	0.038	0.035	0.060	0.026	0.051
Macfa106025	Macfa114505	0.063	0.039	0.047	0.018	0.044
Macfa106384	Macfa114505	0.055	0.031	0.050	0.009	0.052
Macfa114411	Macfa114505	0.049	0.029	0.054	0.048	0.045
Macfa102768	Macfa121803	0.023	0.053	0.063	0.051	0.061
Macfa103649	Macfa121803	0.016	0.036	0.052	0.005	0.030
Macfa103655	Macfa121803	0.006	0.023	0.030	0.067	0.061
Macfa103658	Macfa121803	0.035	0.065	0.053	0.048	0.060
Macfa106025	Macfa121803	0.018	0.037	0.040	0.030	0.036
Macfa106384	Macfa121803	0.021	0.048	0.042	0.032	0.044
Macfa114411	Macfa121803	0.034	0.041	0.047	0.063	0.074
Macfa114505	Macfa121803	0.062	0.058	0.029	0.025	0.042
Macfa102768	Macfa125	0.045	0.036	0.014	0.039	0.024
Macfa103649	Macfa125	0.020	0.020	0.008	0.028	0.024
Macfa103655	Macfa125	0.023	0.022	0.044	0.047	0.042
Macfa103658	Macfa125	0.020	0.033	0.021	0.034	0.028
Macfa106025	Macfa125	0.021	0.012	0.037	0.028	0.013
Macfa106384	Macfa125	0.012	0.019	0.041	0.020	0.018
Macfa114411	Macfa125	0.028	0.022	0.019	0.052	0.038
Macfa114505	Macfa125	0.044	0.045	0.050	0.019	0.045
Macfa121803	Macfa125	0.027	0.043	0.053	0.025	0.048
Macfa102768	Macfa125102	0.012	0.034	0.059	0.068	0.045
Macfa103649	Macfa125102	0.033	0.046	0.054	0.025	0.019
Macfa103655	Macfa125102	0.032	0.057	0.041	0.069	0.044
Macfa103658	Macfa125102	0.039	0.067	0.039	0.057	0.042
Macfa106025	Macfa125102	0.046	0.064	0.063	0.050	0.015
Macfa106384	Macfa125102	0.045	0.073	0.063	0.048	0.022
Macfa114411	Macfa125102	0.058	0.054	0.037	0.079	0.059
Macfa114505	Macfa125102	0.065	0.077	0.083	0.042	0.042
Macfa121803	Macfa125102	0.029	0.051	0.065	0.024	0.022

Macfa125	Macfa125102	0.046	0.061	0.054	0.031	0.027
Macfa102768	Macfa196817	0.060	0.051	0.052	0.080	0.075
Macfa103649	Macfa196817	0.039	0.043	0.046	0.090	0.080
Macfa103655	Macfa196817	0.046	0.035	0.030	0.029	0.032
Macfa103658	Macfa196817	0.018	0.022	0.046	0.044	0.033
Macfa106025	Macfa196817	0.047	0.023	0.065	0.084	0.063
Macfa106384	Macfa196817	0.037	0.011	0.068	0.069	0.054
Macfa114411	Macfa196817	0.047	0.022	0.027	0.098	0.055
Macfa114505	Macfa196817	0.033	0.029	0.059	0.069	0.074
Macfa121803	Macfa196817	0.050	0.057	0.054	0.085	0.084
Macfa125	Macfa196817	0.026	0.024	0.040	0.069	0.061
Macfa125102	Macfa196817	0.056	0.075	0.046	0.084	0.069
Macfa102768	Macfa196824	0.059	0.058	0.049	0.077	0.061
Macfa103649	Macfa196824	0.040	0.047	0.037	0.046	0.037
Macfa103655	Macfa196824	0.046	0.030	0.034	0.057	0.036
Macfa103658	Macfa196824	0.016	0.034	0.039	0.048	0.044
Macfa106025	Macfa196824	0.049	0.022	0.023	0.064	0.028
Macfa106384	Macfa196824	0.039	0.012	0.025	0.055	0.027
Macfa114411	Macfa196824	0.049	0.023	0.039	0.093	0.068
Macfa114505	Macfa196824	0.031	0.021	0.030	0.048	0.052
Macfa121803	Macfa196824	0.050	0.050	0.018	0.043	0.027
Macfa125	Macfa196824	0.028	0.030	0.040	0.042	0.040
Macfa125102	Macfa196824	0.055	0.077	0.061	0.032	0.018
Macfa196817	Macfa196824	0.005	0.015	0.055	0.062	0.064
Macfa102768	Macfa198300	0.039	0.046	0.069	0.078	0.063
Macfa103649	Macfa198300	0.022	0.038	0.060	0.032	0.037
Macfa103655	Macfa198300	0.024	0.026	0.023	0.077	0.043
Macfa103658	Macfa198300	0.015	0.052	0.049	0.066	0.048
Macfa106025	Macfa198300	0.028	0.036	0.058	0.060	0.032
Macfa106384	Macfa198300	0.019	0.043	0.058	0.058	0.033
Macfa114411	Macfa198300	0.029	0.029	0.042	0.090	0.070
Macfa114505	Macfa198300	0.037	0.044	0.067	0.051	0.047
Macfa121803	Macfa198300	0.027	0.022	0.042	0.032	0.021
Macfa125	Macfa198300	0.011	0.042	0.060	0.042	0.044

Macfa125102	Macfa198300	0.040	0.043	0.032	0.011	0.020
Macfa196817	Macfa198300	0.025	0.049	0.046	0.090	0.067
Macfa196824	Macfa198300	0.025	0.043	0.047	0.032	0.009
Macfa102768	Macfa278	0.054	0.043	0.024	0.041	0.015
Macfa103649	Macfa278	0.051	0.044	0.015	0.035	0.018
Macfa103655	Macfa278	0.052	0.039	0.048	0.052	0.061
Macfa103658	Macfa278	0.031	0.013	0.028	0.045	0.045
Macfa106025	Macfa278	0.058	0.032	0.021	0.034	0.025
Macfa106384	Macfa278	0.050	0.026	0.026	0.030	0.035
Macfa114411	Macfa278	0.047	0.016	0.033	0.051	0.042
Macfa114505	Macfa278	0.014	0.024	0.040	0.031	0.040
Macfa121803	Macfa278	0.053	0.056	0.045	0.033	0.047
Macfa125	Macfa278	0.041	0.032	0.020	0.014	0.019
Macfa125102	Macfa278	0.052	0.064	0.064	0.034	0.033
Macfa196817	Macfa278	0.034	0.020	0.054	0.077	0.078
Macfa196824	Macfa278	0.030	0.025	0.028	0.051	0.050
Macfa198300	Macfa278	0.031	0.042	0.063	0.045	0.052
Macfa102768	Macfa317191	0.026	0.044	0.041	0.021	0.043
Macfa103649	Macfa317191	0.057	0.056	0.032	0.044	0.045
Macfa103655	Macfa317191	0.052	0.067	0.021	0.069	0.083
Macfa103658	Macfa317191	0.063	0.075	0.033	0.048	0.065
Macfa106025	Macfa317191	0.066	0.074	0.047	0.015	0.054
Macfa106384	Macfa317191	0.066	0.082	0.050	0.026	0.065
Macfa114411	Macfa317191	0.072	0.063	0.016	0.028	0.050
Macfa114505	Macfa317191	0.079	0.084	0.044	0.030	0.020
Macfa121803	Macfa317191	0.048	0.060	0.039	0.043	0.054
Macfa125	Macfa317191	0.068	0.072	0.027	0.042	0.053
Macfa125102	Macfa317191	0.028	0.011	0.046	0.065	0.054
Macfa196817	Macfa317191	0.080	0.084	0.019	0.091	0.090
Macfa196824	Macfa317191	0.078	0.086	0.036	0.077	0.068
Macfa198300	Macfa317191	0.061	0.051	0.041	0.074	0.063
Macfa278	Macfa317191	0.065	0.071	0.037	0.047	0.041
Macfa102768	Macfa385	0.031	0.035	0.066	0.081	0.063
Macfa103649	Macfa385	0.025	0.032	0.063	0.044	0.042

Macfa103655	Macfa385	0.027	0.029	0.081	0.088	0.068
Macfa103658	Macfa385	0.015	0.018	0.055	0.081	0.069
Macfa106025	Macfa385	0.036	0.022	0.045	0.065	0.043
Macfa106384	Macfa385	0.029	0.021	0.040	0.067	0.045
Macfa114411	Macfa385	0.039	0.007	0.073	0.087	0.086
Macfa114505	Macfa385	0.038	0.030	0.090	0.063	0.082
Macfa121803	Macfa385	0.028	0.047	0.078	0.045	0.055
Macfa125	Macfa385	0.024	0.022	0.071	0.049	0.048
Macfa125102	Macfa385	0.029	0.056	0.074	0.029	0.044
Macfa196817	Macfa385	0.030	0.020	0.098	0.107	0.098
Macfa196824	Macfa385	0.028	0.025	0.063	0.058	0.051
Macfa198300	Macfa385	0.014	0.035	0.078	0.030	0.056
Macfa278	Macfa385	0.028	0.012	0.062	0.043	0.052
Macfa317191	Macfa385	0.050	0.065	0.083	0.079	0.087
Macfa102768	Macfa411	0.024	0.038	0.039	0.050	0.049
Macfa103649	Macfa411	0.010	0.018	0.027	0.038	0.027
Macfa103655	Macfa411	0.008	0.007	0.025	0.039	0.038
Macfa103658	Macfa411	0.026	0.045	0.027	0.033	0.040
Macfa106025	Macfa411	0.021	0.016	0.025	0.042	0.015
Macfa106384	Macfa411	0.018	0.029	0.028	0.031	0.015
Macfa114411	Macfa411	0.036	0.023	0.024	0.065	0.062
Macfa114505	Macfa411	0.055	0.047	0.037	0.029	0.055
Macfa121803	Macfa411	0.010	0.023	0.026	0.033	0.034
Macfa125	Macfa411	0.022	0.020	0.029	0.015	0.026
Macfa125102	Macfa411	0.026	0.051	0.049	0.030	0.015
Macfa196817	Macfa411	0.041	0.037	0.043	0.059	0.067
Macfa196824	Macfa411	0.041	0.035	0.015	0.032	0.020
Macfa198300	Macfa411	0.020	0.026	0.040	0.039	0.026
Macfa278	Macfa411	0.046	0.039	0.025	0.022	0.038
Macfa317191	Macfa411	0.049	0.062	0.024	0.056	0.067
Macfa385	Macfa411	0.020	0.028	0.063	0.050	0.035

iv. *Presbytis melalophos*

Specimen 1	Specimen 2	Protoconid distance	Metaconid distance	Entoconid distance	Hypoconid distance	Hypoconulid distance
Preme102755	Preme102757	0.029	0.022	0.039	0.027	0.043
Preme102755	Preme102882	0.075	0.031	0.081	0.041	0.085
Preme102757	Preme102882	0.047	0.022	0.056	0.018	0.047
Preme102755	Preme102883	0.031	0.044	0.079	0.038	0.055
Preme102757	Preme102883	0.021	0.043	0.046	0.021	0.037
Preme102882	Preme102883	0.062	0.059	0.023	0.013	0.043
Preme102755	Preme102891	0.037	0.027	0.097	0.034	0.066
Preme102757	Preme102891	0.014	0.034	0.064	0.019	0.031
Preme102882	Preme102891	0.042	0.051	0.046	0.014	0.022
Preme102883	Preme102891	0.031	0.022	0.038	0.004	0.035
Preme102755	Preme102895	0.044	0.037	0.085	0.047	0.056
Preme102757	Preme102895	0.015	0.033	0.048	0.043	0.034
Preme102882	Preme102895	0.036	0.053	0.040	0.038	0.037
Preme102883	Preme102895	0.026	0.015	0.021	0.025	0.009
Preme102891	Preme102895	0.017	0.018	0.026	0.026	0.027
Preme102755	Preme106600	0.016	0.058	0.084	0.090	0.067
Preme102757	Preme106600	0.028	0.070	0.048	0.073	0.058
Preme102882	Preme106600	0.073	0.076	0.033	0.059	0.081
Preme102883	Preme106600	0.028	0.046	0.011	0.055	0.053
Preme102891	Preme106600	0.031	0.046	0.037	0.059	0.077
Preme102895	Preme106600	0.040	0.057	0.015	0.051	0.060
Preme102755	Preme106605	0.013	0.047	0.086	0.038	0.068
Preme102757	Preme106605	0.027	0.041	0.059	0.036	0.041
Preme102882	Preme106605	0.068	0.044	0.072	0.034	0.050
Preme102883	Preme106605	0.037	0.033	0.056	0.028	0.031
Preme102891	Preme106605	0.031	0.042	0.087	0.025	0.050

Preme102895	Preme106605	0.042	0.039	0.061	0.032	0.036
Preme106600	Preme106605	0.020	0.051	0.051	0.074	0.032
Preme102755	Preme106671	0.012	0.029	0.038	0.054	0.018
Preme102757	Preme106671	0.021	0.050	0.044	0.050	0.056
Preme102882	Preme106671	0.065	0.052	0.063	0.054	0.101
Preme102883	Preme106671	0.030	0.059	0.068	0.048	0.071
Preme102891	Preme106671	0.031	0.041	0.076	0.050	0.082
Preme102895	Preme106671	0.037	0.058	0.074	0.050	0.072
Preme106600	Preme106671	0.023	0.047	0.076	0.065	0.071
Preme106605	Preme106671	0.012	0.061	0.099	0.070	0.078
Preme102755	Preme107086	0.092	0.064	0.089	0.018	0.084
Preme102757	Preme107086	0.066	0.049	0.070	0.021	0.050
Preme102882	Preme107086	0.032	0.033	0.040	0.031	0.011
Preme102883	Preme107086	0.080	0.079	0.045	0.024	0.037
Preme102891	Preme107086	0.067	0.079	0.080	0.022	0.025
Preme102895	Preme107086	0.058	0.074	0.064	0.033	0.031
Preme106600	Preme107086	0.094	0.098	0.050	0.073	0.078
Preme106605	Preme107086	0.086	0.054	0.057	0.035	0.047
Preme106671	Preme107086	0.081	0.083	0.086	0.040	0.100
Preme102755	Preme107088	0.086	0.040	0.057	0.039	0.093
Preme102757	Preme107088	0.067	0.041	0.032	0.039	0.056
Preme102882	Preme107088	0.041	0.033	0.044	0.041	0.033
Preme102883	Preme107088	0.086	0.081	0.041	0.041	0.067
Preme102891	Preme107088	0.056	0.067	0.042	0.037	0.033
Preme102895	Preme107088	0.062	0.072	0.040	0.052	0.059
Preme106600	Preme107088	0.083	0.094	0.046	0.091	0.105
Preme106605	Preme107088	0.075	0.075	0.081	0.021	0.077

Preme106671	Preme107088	0.078	0.055	0.035	0.083	0.108
Preme107086	Preme107088	0.063	0.057	0.075	0.044	0.042

Table A4.9. Interspecies pairwise cusp-tip landmark distances for intramolar interspecies cusp position variability analyses.

Specimen identifications are coded with the first three letters of genus, the first two letters of species, and the museum attribution number excluding leading year values (for BMNH and MNHNP).

a. *Cercopithecus* - *Colobus*

Specimen 1	**Specimen 2**	**Protoconid distance**	**Metaconid distance**	**Entoconid distance**	**Hypoconid distance**
Cermi236996-fakeHC	Cogue119768-bs	0.042	0.091	0.143	0.095
Cermi259446-fakeHC	Cogue119768-bs	0.076	0.088	0.179	0.129
Cermi4521-fakeHC	Cogue119768-bs	0.078	0.070	0.141	0.105
Cermi452544-fakeHC	Cogue119768-bs	0.084	0.113	0.155	0.121
Cermi452547-fakeHC	Cogue119768-bs	0.036	0.108	0.191	0.098
Cermi452548-fakeHC	Cogue119768-bs	0.110	0.106	0.187	0.122
Cermi452552-fakeHC	Cogue119768-bs	0.067	0.125	0.220	0.132
Cermi452554-fakeHC	Cogue119768-bs	0.083	0.130	0.223	0.109
Cermi52384-bs-fakeHC	Cogue119768-bs	0.080	0.077	0.156	0.133
Cermi52384b-bs-fakeHC	Cogue119768-bs	0.067	0.079	0.168	0.127
Cermi236996-fakeHC	Cogue52237-bs	0.045	0.048	0.108	0.041
Cermi259446-fakeHC	Cogue52237-bs	0.071	0.060	0.129	0.074
Cermi4521-fakeHC	Cogue52237-bs	0.069	0.051	0.103	0.052
Cermi452544-fakeHC	Cogue52237-bs	0.054	0.072	0.115	0.071
Cermi452547-fakeHC	Cogue52237-bs	0.057	0.058	0.141	0.053
Cermi452548-fakeHC	Cogue52237-bs	0.071	0.051	0.140	0.069

Cermi452552-fakeHC	Cogue52237-bs	0.079	0.072	0.182	0.098
Cermi452554-fakeHC	Cogue52237-bs	0.067	0.084	0.185	0.056
Cermi52384-bs-fakeHC	Cogue52237-bs	0.053	0.046	0.108	0.084
Cermi52384b-bs-fakeHC	Cogue52237-bs	0.060	0.046	0.129	0.077
Cermi236996-fakeHC	Colgu11112	0.028	0.045	0.087	0.056
Cermi259446-fakeHC	Colgu11112	0.048	0.056	0.116	0.089
Cermi4521-fakeHC	Colgu11112	0.047	0.039	0.083	0.068
Cermi452544-fakeHC	Colgu11112	0.035	0.060	0.095	0.084
Cermi452547-fakeHC	Colgu11112	0.040	0.065	0.121	0.062
Cermi452548-fakeHC	Colgu11112	0.061	0.043	0.117	0.085
Cermi452552-fakeHC	Colgu11112	0.052	0.069	0.156	0.102
Cermi452554-fakeHC	Colgu11112	0.042	0.076	0.161	0.069
Cermi52384-bs-fakeHC	Colgu11112	0.042	0.039	0.092	0.099
Cermi52384b-bs-fakeHC	Colgu11112	0.046	0.042	0.107	0.092
Cermi236996-fakeHC	Colgu1241	0.029	0.067	0.118	0.091
Cermi259446-fakeHC	Colgu1241	0.057	0.072	0.152	0.126
Cermi4521-fakeHC	Colgu1241	0.056	0.047	0.114	0.101
Cermi452544-fakeHC	Colgu1241	0.048	0.078	0.127	0.116
Cermi452547-fakeHC	Colgu1241	0.038	0.091	0.156	0.094
Cermi452548-fakeHC	Colgu1241	0.075	0.067	0.149	0.116
Cermi452552-fakeHC	Colgu1241	0.054	0.093	0.185	0.134
Cermi452554-fakeHC	Colgu1241	0.052	0.097	0.191	0.106
Cermi52384-bs-fakeHC	Colgu1241	0.054	0.056	0.127	0.125
Cermi52384b-bs-fakeHC	Colgu1241	0.053	0.060	0.139	0.119
Cermi236996-fakeHC	Colgu163124-mirL	0.025	0.050	0.096	0.055
Cermi259446-fakeHC	Colgu163124-mirL	0.052	0.056	0.124	0.090
Cermi4521-fakeHC	Colgu163124-mirL	0.051	0.038	0.092	0.061

Cermi452544-fakeHC	Colgu163124-mirL	0.041	0.069	0.104	0.084
Cermi452547-fakeHC	Colgu163124-mirL	0.038	0.069	0.133	0.067
Cermi452548-fakeHC	Colgu163124-mirL	0.065	0.056	0.131	0.078
Cermi452552-fakeHC	Colgu163124-mirL	0.057	0.078	0.169	0.114
Cermi452554-fakeHC	Colgu163124-mirL	0.049	0.085	0.173	0.072
Cermi52384-bs-fakeHC	Colgu163124-mirL	0.042	0.040	0.101	0.089
Cermi52384b-bs-fakeHC	Colgu163124-mirL	0.044	0.043	0.118	0.083
Cermi236996-fakeHC	Colgu163273-mirL	0.038	0.047	0.098	0.064
Cermi259446-fakeHC	Colgu163273-mirL	0.070	0.058	0.128	0.098
Cermi4521-fakeHC	Colgu163273-mirL	0.070	0.047	0.095	0.071
Cermi452544-fakeHC	Colgu163273-mirL	0.061	0.072	0.107	0.093
Cermi452547-fakeHC	Colgu163273-mirL	0.046	0.060	0.137	0.073
Cermi452548-fakeHC	Colgu163273-mirL	0.083	0.053	0.134	0.089
Cermi452552-fakeHC	Colgu163273-mirL	0.072	0.074	0.172	0.114
Cermi452554-fakeHC	Colgu163273-mirL	0.069	0.084	0.176	0.079
Cermi52384-bs-fakeHC	Colgu163273-mirL	0.060	0.043	0.105	0.102
Cermi52384b-bs-fakeHC	Colgu163273-mirL	0.060	0.044	0.121	0.095
Cermi236996-fakeHC	Colgu163627-mirL	0.032	0.065	0.120	0.056
Cermi259446-fakeHC	Colgu163627-mirL	0.069	0.071	0.153	0.088
Cermi4521-fakeHC	Colgu163627-mirL	0.070	0.057	0.117	0.077
Cermi452544-fakeHC	Colgu163627-mirL	0.073	0.089	0.130	0.075
Cermi452547-fakeHC	Colgu163627-mirL	0.032	0.077	0.159	0.050
Cermi452548-fakeHC	Colgu163627-mirL	0.096	0.071	0.154	0.089
Cermi452552-fakeHC	Colgu163627-mirL	0.069	0.093	0.191	0.090
Cermi452554-fakeHC	Colgu163627-mirL	0.078	0.103	0.196	0.066
Cermi52384-bs-fakeHC	Colgu163627-mirL	0.064	0.057	0.129	0.102
Cermi52384b-bs-fakeHC	Colgu163627-mirL	0.054	0.059	0.142	0.096

Cermi236996-fakeHC	Colgu401-mirL	0.050	0.048	0.059	0.023
Cermi259446-fakeHC	Colgu401-mirL	0.078	0.067	0.108	0.026
Cermi4521-fakeHC	Colgu401-mirL	0.079	0.067	0.060	0.021
Cermi452544-fakeHC	Colgu401-mirL	0.077	0.069	0.072	0.035
Cermi452547-fakeHC	Colgu401-mirL	0.055	0.046	0.107	0.050
Cermi452548-fakeHC	Colgu401-mirL	0.091	0.040	0.102	0.016
Cermi452552-fakeHC	Colgu401-mirL	0.089	0.056	0.120	0.098
Cermi452554-fakeHC	Colgu401-mirL	0.089	0.072	0.124	0.030
Cermi52384-bs-fakeHC	Colgu401-mirL	0.061	0.056	0.085	0.036
Cermi52384b-bs-fakeHC	Colgu401-mirL	0.056	0.055	0.077	0.030
Cermi236996-fakeHC	Colgu408-mirL	0.037	0.022	0.080	0.036
Cermi259446-fakeHC	Colgu408-mirL	0.042	0.031	0.080	0.048
Cermi4521-fakeHC	Colgu408-mirL	0.039	0.019	0.074	0.059
Cermi452544-fakeHC	Colgu408-mirL	0.021	0.041	0.080	0.024
Cermi452547-fakeHC	Colgu408-mirL	0.050	0.050	0.100	0.030
Cermi452548-fakeHC	Colgu408-mirL	0.039	0.040	0.109	0.053
Cermi452552-fakeHC	Colgu408-mirL	0.058	0.051	0.150	0.083
Cermi452554-fakeHC	Colgu408-mirL	0.037	0.055	0.149	0.036
Cermi52384-bs-fakeHC	Colgu408-mirL	0.022	0.014	0.065	0.064
Cermi52384b-bs-fakeHC	Colgu408-mirL	0.037	0.017	0.096	0.059
Cermi236996-fakeHC	Colgu762	0.037	0.033	0.064	0.028
Cermi259446-fakeHC	Colgu762	0.055	0.052	0.087	0.055
Cermi4521-fakeHC	Colgu762	0.053	0.049	0.059	0.049
Cermi452544-fakeHC	Colgu762	0.037	0.049	0.069	0.053
Cermi452547-fakeHC	Colgu762	0.050	0.044	0.096	0.033
Cermi452548-fakeHC	Colgu762	0.057	0.025	0.097	0.062
Cermi452552-fakeHC	Colgu762	0.064	0.044	0.136	0.074

Cermi452554-fakeHC	Colgu762	0.049	0.057	0.138	0.034
Cermi52384-bs-fakeHC	Colgu762	0.040	0.039	0.063	0.081
Cermi52384b-bs-fakeHC	Colgu762	0.049	0.039	0.083	0.074
Cermi236996-fakeHC	Colgu864-mirL	0.042	0.057	0.090	0.059
Cermi259446-fakeHC	Colgu864-mirL	0.078	0.072	0.122	0.084
Cermi4521-fakeHC	Colgu864-mirL	0.078	0.071	0.086	0.076
Cermi452544-fakeHC	Colgu864-mirL	0.072	0.082	0.099	0.082
Cermi452547-fakeHC	Colgu864-mirL	0.048	0.054	0.126	0.057
Cermi452548-fakeHC	Colgu864-mirL	0.094	0.055	0.120	0.092
Cermi452552-fakeHC	Colgu864-mirL	0.079	0.071	0.157	0.080
Cermi452554-fakeHC	Colgu864-mirL	0.080	0.088	0.162	0.064
Cermi52384-bs-fakeHC	Colgu864-mirL	0.068	0.061	0.098	0.110
Cermi52384b-bs-fakeHC	Colgu864-mirL	0.064	0.061	0.110	0.103
Cermi236996-fakeHC	Colgu994	0.036	0.069	0.102	0.079
Cermi259446-fakeHC	Colgu994	0.072	0.074	0.140	0.111
Cermi4521-fakeHC	Colgu994	0.074	0.065	0.100	0.084
Cermi452544-fakeHC	Colgu994	0.078	0.098	0.113	0.109
Cermi452547-fakeHC	Colgu994	0.032	0.076	0.142	0.088
Cermi452548-fakeHC	Colgu994	0.103	0.080	0.134	0.103
Cermi452552-fakeHC	Colgu994	0.068	0.099	0.167	0.123
Cermi452554-fakeHC	Colgu994	0.081	0.110	0.173	0.093
Cermi52384-bs-fakeHC	Colgu994	0.072	0.062	0.116	0.117
Cermi52384b-bs-fakeHC	Colgu994	0.060	0.063	0.123	0.110

b. *Cercopithecus – Macaca*

Specimen 1	**Specimen 2**	**Protoconid distance**	**Metaconid distance**	**Entoconid distance**	**Hypoconid distance**
Cermi236996-fakeHC	Macfa102768	0.062	0.059	0.040	0.034

Cermi259446-fakeHC	Macfa102768	0.097	0.069	0.084	0.055
Cermi4521-fakeHC	Macfa102768	0.099	0.082	0.038	0.052
Cermi452544-fakeHC	Macfa102768	0.103	0.094	0.052	0.057
Cermi452547-fakeHC	Macfa102768	0.058	0.037	0.091	0.039
Cermi452548-fakeHC	Macfa102768	0.124	0.076	0.092	0.066
Cermi452552-fakeHC	Macfa102768	0.095	0.074	0.116	0.072
Cermi452554-fakeHC	Macfa102768	0.108	0.093	0.117	0.037
Cermi52384-bs-fakeHC	Macfa102768	0.092	0.066	0.060	0.085
Cermi52384b-bs-fakeHC	Macfa102768	0.080	0.063	0.062	0.079
Cermi236996-fakeHC	Macfa103649	0.045	0.063	0.050	0.084
Cermi259446-fakeHC	Macfa103649	0.077	0.069	0.094	0.100
Cermi4521-fakeHC	Macfa103649	0.079	0.076	0.049	0.090
Cermi452544-fakeHC	Macfa103649	0.089	0.100	0.062	0.109
Cermi452547-fakeHC	Macfa103649	0.035	0.052	0.097	0.090
Cermi452548-fakeHC	Macfa103649	0.114	0.083	0.095	0.108
Cermi452552-fakeHC	Macfa103649	0.069	0.088	0.121	0.102
Cermi452554-fakeHC	Macfa103649	0.088	0.104	0.124	0.087
Cermi52384-bs-fakeHC	Macfa103649	0.082	0.064	0.069	0.127
Cermi52384b-bs-fakeHC	Macfa103649	0.065	0.062	0.071	0.121
Cermi236996-fakeHC	Macfa103655	0.045	0.068	0.087	0.064
Cermi259446-fakeHC	Macfa103655	0.077	0.076	0.123	0.099
Cermi4521-fakeHC	Macfa103655	0.080	0.073	0.084	0.073
Cermi452544-fakeHC	Macfa103655	0.089	0.100	0.094	0.093
Cermi452547-fakeHC	Macfa103655	0.037	0.067	0.110	0.073
Cermi452548-fakeHC	Macfa103655	0.113	0.079	0.096	0.090
Cermi452552-fakeHC	Macfa103655	0.073	0.094	0.128	0.114
Cermi452554-fakeHC	Macfa103655	0.091	0.108	0.139	0.080
Cermi52384-bs-fakeHC	Macfa103655	0.079	0.066	0.099	0.103
Cermi52384b-bs-fakeHC	Macfa103655	0.063	0.065	0.099	0.096
Cermi236996-fakeHC	Macfa103658	0.033	0.029	0.052	0.064
Cermi259446-fakeHC	Macfa103658	0.068	0.047	0.097	0.093
Cermi4521-fakeHC	Macfa103658	0.069	0.049	0.051	0.078
Cermi452544-fakeHC	Macfa103658	0.071	0.057	0.062	0.090
Cermi452547-fakeHC	Macfa103658	0.031	0.034	0.094	0.065

Cermi452548-fakeHC	Macfa103658	0.098	0.038	0.088	0.095
Cermi452552-fakeHC	Macfa103658	0.060	0.048	0.110	0.094
Cermi452554-fakeHC	Macfa103658	0.072	0.063	0.115	0.073
Cermi52384-bs-fakeHC	Macfa103658	0.070	0.036	0.073	0.112
Cermi52384b-bs-fakeHC	Macfa103658	0.060	0.035	0.068	0.105
Cermi236996-fakeHC	Macfa106025	0.043	0.056	0.075	0.057
Cermi259446-fakeHC	Macfa106025	0.069	0.063	0.122	0.073
Cermi4521-fakeHC	Macfa106025	0.073	0.059	0.075	0.070
Cermi452544-fakeHC	Macfa106025	0.087	0.088	0.088	0.079
Cermi452547-fakeHC	Macfa106025	0.031	0.059	0.125	0.060
Cermi452548-fakeHC	Macfa106025	0.110	0.070	0.120	0.085
Cermi452552-fakeHC	Macfa106025	0.064	0.084	0.141	0.077
Cermi452554-fakeHC	Macfa106025	0.086	0.097	0.145	0.058
Cermi52384-bs-fakeHC	Macfa106025	0.076	0.052	0.098	0.104
Cermi52384b-bs-fakeHC	Macfa106025	0.057	0.052	0.096	0.098
Cermi236996-fakeHC	Macfa106384	0.035	0.047	0.077	0.054
Cermi259446-fakeHC	Macfa106384	0.064	0.056	0.125	0.077
Cermi4521-fakeHC	Macfa106384	0.067	0.048	0.078	0.067
Cermi452544-fakeHC	Macfa106384	0.079	0.076	0.090	0.080
Cermi452547-fakeHC	Macfa106384	0.024	0.057	0.127	0.059
Cermi452548-fakeHC	Macfa106384	0.104	0.059	0.122	0.084
Cermi452552-fakeHC	Macfa106384	0.057	0.077	0.141	0.083
Cermi452554-fakeHC	Macfa106384	0.078	0.088	0.145	0.060
Cermi52384-bs-fakeHC	Macfa106384	0.071	0.043	0.101	0.103
Cermi52384b-bs-fakeHC	Macfa106384	0.053	0.043	0.097	0.096
Cermi236996-fakeHC	Macfa114411	0.026	0.051	0.058	0.030
Cermi259446-fakeHC	Macfa114411	0.049	0.064	0.097	0.038
Cermi4521-fakeHC	Macfa114411	0.052	0.063	0.056	0.046
Cermi452544-fakeHC	Macfa114411	0.065	0.080	0.066	0.046
Cermi452547-fakeHC	Macfa114411	0.023	0.051	0.090	0.038
Cermi452548-fakeHC	Macfa114411	0.085	0.057	0.081	0.055
Cermi452552-fakeHC	Macfa114411	0.056	0.073	0.111	0.070
Cermi452554-fakeHC	Macfa114411	0.068	0.087	0.119	0.025
Cermi52384-bs-fakeHC	Macfa114411	0.050	0.053	0.072	0.076

Cermi52384b-bs-fakeHC	Macfa114411	0.031	0.053	0.072	0.070
Cermi236996-fakeHC	Macfa114505	0.028	0.058	0.099	0.063
Cermi259446-fakeHC	Macfa114505	0.053	0.073	0.135	0.085
Cermi4521-fakeHC	Macfa114505	0.052	0.061	0.096	0.075
Cermi452544-fakeHC	Macfa114505	0.041	0.073	0.109	0.088
Cermi452547-fakeHC	Macfa114505	0.040	0.070	0.137	0.066
Cermi452548-fakeHC	Macfa114505	0.065	0.046	0.130	0.093
Cermi452552-fakeHC	Macfa114505	0.059	0.074	0.165	0.087
Cermi452554-fakeHC	Macfa114505	0.050	0.085	0.171	0.068
Cermi52384-bs-fakeHC	Macfa114505	0.043	0.058	0.110	0.111
Cermi52384b-bs-fakeHC	Macfa114505	0.046	0.059	0.120	0.105
Cermi236996-fakeHC	Macfa121803	0.047	0.089	0.101	0.083
Cermi259446-fakeHC	Macfa121803	0.079	0.098	0.141	0.100
Cermi4521-fakeHC	Macfa121803	0.082	0.096	0.099	0.089
Cermi452544-fakeHC	Macfa121803	0.091	0.120	0.111	0.108
Cermi452547-fakeHC	Macfa121803	0.040	0.084	0.136	0.089
Cermi452548-fakeHC	Macfa121803	0.114	0.096	0.124	0.107
Cermi452552-fakeHC	Macfa121803	0.077	0.112	0.154	0.101
Cermi452554-fakeHC	Macfa121803	0.094	0.128	0.163	0.086
Cermi52384-bs-fakeHC	Macfa121803	0.080	0.088	0.116	0.125
Cermi52384b-bs-fakeHC	Macfa121803	0.064	0.088	0.118	0.120
Cermi236996-fakeHC	Macfa125	0.026	0.049	0.050	0.065
Cermi259446-fakeHC	Macfa125	0.058	0.055	0.090	0.088
Cermi4521-fakeHC	Macfa125	0.060	0.057	0.047	0.069
Cermi452544-fakeHC	Macfa125	0.070	0.084	0.059	0.094
Cermi452547-fakeHC	Macfa125	0.016	0.049	0.093	0.076
Cermi452548-fakeHC	Macfa125	0.096	0.069	0.090	0.088
Cermi452552-fakeHC	Macfa125	0.051	0.078	0.119	0.103
Cermi452554-fakeHC	Macfa125	0.069	0.092	0.123	0.073
Cermi52384-bs-fakeHC	Macfa125	0.064	0.047	0.065	0.105
Cermi52384b-bs-fakeHC	Macfa125	0.048	0.046	0.069	0.099
Cermi236996-fakeHC	Macfa125102	0.063	0.090	0.074	0.095
Cermi259446-fakeHC	Macfa125102	0.099	0.102	0.110	0.114
Cermi4521-fakeHC	Macfa125102	0.101	0.112	0.072	0.095

Cermi452544-fakeHC	Macfa125102	0.103	0.121	0.078	0.123
Cermi452547-fakeHC	Macfa125102	0.060	0.069	0.089	0.106
Cermi452548-fakeHC	Macfa125102	0.125	0.096	0.072	0.115
Cermi452552-fakeHC	Macfa125102	0.096	0.099	0.092	0.125
Cermi452554-fakeHC	Macfa125102	0.107	0.119	0.105	0.102
Cermi52384-bs-fakeHC	Macfa125102	0.095	0.098	0.090	0.131
Cermi52384b-bs-fakeHC	Macfa125102	0.084	0.096	0.076	0.126
Cermi236996-fakeHC	Macfa196817	0.028	0.038	0.074	0.091
Cermi259446-fakeHC	Macfa196817	0.057	0.048	0.100	0.125
Cermi4521-fakeHC	Macfa196817	0.058	0.041	0.069	0.101
Cermi452544-fakeHC	Macfa196817	0.060	0.066	0.077	0.117
Cermi452547-fakeHC	Macfa196817	0.028	0.051	0.086	0.094
Cermi452548-fakeHC	Macfa196817	0.088	0.049	0.073	0.117
Cermi452552-fakeHC	Macfa196817	0.046	0.066	0.114	0.130
Cermi452554-fakeHC	Macfa196817	0.058	0.077	0.124	0.105
Cermi52384-bs-fakeHC	Macfa196817	0.063	0.034	0.077	0.128
Cermi52384b-bs-fakeHC	Macfa196817	0.055	0.035	0.082	0.122
Cermi236996-fakeHC	Macfa196824	0.029	0.053	0.087	0.103
Cermi259446-fakeHC	Macfa196824	0.059	0.063	0.130	0.129
Cermi4521-fakeHC	Macfa196824	0.060	0.051	0.086	0.107
Cermi452544-fakeHC	Macfa196824	0.060	0.076	0.098	0.132
Cermi452547-fakeHC	Macfa196824	0.030	0.065	0.128	0.110
Cermi452548-fakeHC	Macfa196824	0.088	0.056	0.119	0.127
Cermi452552-fakeHC	Macfa196824	0.050	0.078	0.147	0.131
Cermi452554-fakeHC	Macfa196824	0.059	0.089	0.154	0.113
Cermi52384-bs-fakeHC	Macfa196824	0.064	0.048	0.105	0.143
Cermi52384b-bs-fakeHC	Macfa196824	0.056	0.049	0.106	0.137
Cermi236996-fakeHC	Macfa198300	0.025	0.080	0.096	0.105
Cermi259446-fakeHC	Macfa198300	0.060	0.092	0.134	0.125
Cermi4521-fakeHC	Macfa198300	0.062	0.090	0.094	0.105
Cermi452544-fakeHC	Macfa198300	0.068	0.107	0.102	0.134
Cermi452547-fakeHC	Macfa198300	0.021	0.074	0.115	0.116
Cermi452548-fakeHC	Macfa198300	0.093	0.080	0.097	0.125
Cermi452552-fakeHC	Macfa198300	0.057	0.097	0.123	0.133

Cermi452554-fakeHC	Macfa198300	0.070	0.114	0.136	0.113
Cermi52384-bs-fakeHC	Macfa198300	0.061	0.082	0.111	0.141
Cermi52384b-bs-fakeHC	Macfa198300	0.049	0.081	0.104	0.136
Cermi236996-fakeHC	Macfa278	0.031	0.041	0.063	0.062
Cermi259446-fakeHC	Macfa278	0.063	0.058	0.106	0.083
Cermi4521-fakeHC	Macfa278	0.062	0.055	0.062	0.061
Cermi452544-fakeHC	Macfa278	0.054	0.066	0.075	0.092
Cermi452547-fakeHC	Macfa278	0.041	0.046	0.113	0.079
Cermi452548-fakeHC	Macfa278	0.076	0.041	0.110	0.081
Cermi452552-fakeHC	Macfa278	0.067	0.059	0.136	0.109
Cermi452554-fakeHC	Macfa278	0.063	0.073	0.139	0.072
Cermi52384-bs-fakeHC	Macfa278	0.052	0.045	0.082	0.097
Cermi52384b-bs-fakeHC	Macfa278	0.052	0.045	0.086	0.091
Cermi236996-fakeHC	Macfa317191	0.080	0.098	0.071	0.053
Cermi259446-fakeHC	Macfa317191	0.115	0.111	0.105	0.064
Cermi4521-fakeHC	Macfa317191	0.117	0.121	0.067	0.070
Cermi452544-fakeHC	Macfa317191	0.116	0.127	0.077	0.069
Cermi452547-fakeHC	Macfa317191	0.080	0.076	0.097	0.050
Cermi452548-fakeHC	Macfa317191	0.134	0.101	0.087	0.083
Cermi452552-fakeHC	Macfa317191	0.118	0.104	0.122	0.063
Cermi452554-fakeHC	Macfa317191	0.125	0.124	0.131	0.049
Cermi52384-bs-fakeHC	Macfa317191	0.105	0.107	0.081	0.103
Cermi52384b-bs-fakeHC	Macfa317191	0.096	0.105	0.085	0.097
Cermi236996-fakeHC	Macfa385	0.035	0.045	0.086	0.103
Cermi259446-fakeHC	Macfa385	0.072	0.059	0.137	0.117
Cermi4521-fakeHC	Macfa385	0.073	0.059	0.089	0.095
Cermi452544-fakeHC	Macfa385	0.074	0.075	0.099	0.131
Cermi452547-fakeHC	Macfa385	0.034	0.045	0.138	0.120
Cermi452548-fakeHC	Macfa385	0.099	0.052	0.133	0.114
Cermi452552-fakeHC	Macfa385	0.069	0.066	0.138	0.141
Cermi452554-fakeHC	Macfa385	0.078	0.081	0.140	0.110
Cermi52384-bs-fakeHC	Macfa385	0.069	0.048	0.116	0.129
Cermi52384b-bs-fakeHC	Macfa385	0.059	0.047	0.101	0.124
Cermi236996-fakeHC	Macfa411	0.043	0.067	0.075	0.073

Cermi259446-fakeHC	Macfa411	0.077	0.074	0.118	0.099
Cermi4521-fakeHC	Macfa411	0.080	0.075	0.074	0.075
Cermi452544-fakeHC	Macfa411	0.087	0.100	0.086	0.103
Cermi452547-fakeHC	Macfa411	0.037	0.063	0.114	0.085
Cermi452548-fakeHC	Macfa411	0.111	0.080	0.105	0.096
Cermi452552-fakeHC	Macfa411	0.073	0.093	0.132	0.115
Cermi452554-fakeHC	Macfa411	0.089	0.107	0.140	0.084
Cermi52384-bs-fakeHC	Macfa411	0.079	0.066	0.093	0.111
Cermi52384b-bs-fakeHC	Macfa411	0.064	0.065	0.093	0.105

c. *Cercopithecus – Presbytis*

Specimen 1	**Specimen 2**	**Protoconid distance**	**Metaconid distance**	**Entoconid distance**	**Hypoconid distance**
Cermi236996-fakeHC	Preme102755	0.013	0.052	0.074	0.050
Cermi259446-fakeHC	Preme102755	0.034	0.064	0.119	0.083
Cermi4521-fakeHC	Preme102755	0.034	0.043	0.073	0.068
Cermi452544-fakeHC	Preme102755	0.034	0.045	0.084	0.068
Cermi452547-fakeHC	Preme102755	0.025	0.078	0.112	0.050
Cermi452548-fakeHC	Preme102755	0.061	0.034	0.102	0.076
Cermi452552-fakeHC	Preme102755	0.039	0.063	0.124	0.100
Cermi452554-fakeHC	Preme102755	0.037	0.064	0.131	0.063
Cermi52384-bs-fakeHC	Preme102755	0.035	0.048	0.095	0.087
Cermi52384b-bs-fakeHC	Preme102755	0.031	0.052	0.088	0.081
Cermi236996-fakeHC	Preme102757	0.041	0.052	0.055	0.060
Cermi259446-fakeHC	Preme102757	0.048	0.066	0.089	0.091
Cermi4521-fakeHC	Preme102757	0.045	0.051	0.052	0.072
Cermi452544-fakeHC	Preme102757	0.022	0.030	0.059	0.074
Cermi452547-fakeHC	Preme102757	0.054	0.076	0.075	0.066
Cermi452548-fakeHC	Preme102757	0.044	0.024	0.063	0.076

Cermi452552-fakeHC	Preme102757	0.059	0.049	0.093	0.120
Cermi452554-fakeHC	Preme102757	0.036	0.047	0.101	0.075
Cermi52384-bs-fakeHC	Preme102757	0.035	0.053	0.067	0.080
Cermi52384b-bs-fakeHC	Preme102757	0.048	0.056	0.061	0.075
Cermi236996-fakeHC	Preme102882	0.087	0.061	0.060	0.063
Cermi259446-fakeHC	Preme102882	0.080	0.069	0.068	0.091
Cermi4521-fakeHC	Preme102882	0.075	0.051	0.053	0.067
Cermi452544-fakeHC	Preme102882	0.048	0.032	0.059	0.076
Cermi452547-fakeHC	Preme102882	0.100	0.090	0.071	0.075
Cermi452548-fakeHC	Preme102882	0.042	0.045	0.074	0.070
Cermi452552-fakeHC	Preme102882	0.093	0.062	0.117	0.131
Cermi452554-fakeHC	Preme102882	0.059	0.053	0.120	0.079
Cermi52384-bs-fakeHC	Preme102882	0.066	0.059	0.047	0.070
Cermi52384b-bs-fakeHC	Preme102882	0.086	0.062	0.071	0.066
Cermi236996-fakeHC	Preme102883	0.038	0.019	0.052	0.057
Cermi259446-fakeHC	Preme102883	0.059	0.039	0.058	0.087
Cermi4521-fakeHC	Preme102883	0.057	0.042	0.046	0.059
Cermi452544-fakeHC	Preme102883	0.041	0.041	0.047	0.076
Cermi452547-fakeHC	Preme102883	0.051	0.034	0.051	0.072
Cermi452548-fakeHC	Preme102883	0.059	0.027	0.052	0.065
Cermi452552-fakeHC	Preme102883	0.069	0.034	0.095	0.129
Cermi452554-fakeHC	Preme102883	0.054	0.046	0.099	0.075
Cermi52384-bs-fakeHC	Preme102883	0.042	0.029	0.039	0.067
Cermi52384b-bs-fakeHC	Preme102883	0.050	0.029	0.055	0.062
Cermi236996-fakeHC	Preme102891	0.047	0.035	0.089	0.054
Cermi259446-fakeHC	Preme102891	0.045	0.052	0.087	0.084
Cermi4521-fakeHC	Preme102891	0.041	0.041	0.083	0.058

Cermi452544-fakeHC	Preme102891	0.015	0.046	0.083	0.072
Cermi452547-fakeHC	Preme102891	0.060	0.054	0.065	0.068
Cermi452548-fakeHC	Preme102891	0.030	0.025	0.053	0.063
Cermi452552-fakeHC	Preme102891	0.062	0.050	0.105	0.125
Cermi452554-fakeHC	Preme102891	0.033	0.059	0.115	0.072
Cermi52384-bs-fakeHC	Preme102891	0.027	0.036	0.074	0.066
Cermi52384b-bs-fakeHC	Preme102891	0.045	0.038	0.087	0.061
Cermi236996-fakeHC	Preme102895	0.055	0.032	0.066	0.055
Cermi259446-fakeHC	Preme102895	0.060	0.052	0.068	0.086
Cermi4521-fakeHC	Preme102895	0.057	0.050	0.060	0.048
Cermi452544-fakeHC	Preme102895	0.031	0.039	0.059	0.082
Cermi452547-fakeHC	Preme102895	0.069	0.047	0.044	0.077
Cermi452548-fakeHC	Preme102895	0.041	0.013	0.036	0.060
Cermi452552-fakeHC	Preme102895	0.074	0.034	0.085	0.133
Cermi452554-fakeHC	Preme102895	0.046	0.046	0.093	0.075
Cermi52384-bs-fakeHC	Preme102895	0.042	0.041	0.053	0.064
Cermi52384b-bs-fakeHC	Preme102895	0.059	0.042	0.061	0.059
Cermi236996-fakeHC	Preme106600	0.018	0.038	0.053	0.102
Cermi259446-fakeHC	Preme106600	0.034	0.034	0.054	0.127
Cermi4521-fakeHC	Preme106600	0.034	0.028	0.047	0.087
Cermi452544-fakeHC	Preme106600	0.032	0.068	0.046	0.122
Cermi452547-fakeHC	Preme106600	0.032	0.057	0.040	0.124
Cermi452548-fakeHC	Preme106600	0.054	0.067	0.042	0.093
Cermi452552-fakeHC	Preme106600	0.049	0.075	0.085	0.181
Cermi452554-fakeHC	Preme106600	0.041	0.081	0.090	0.121
Cermi52384-bs-fakeHC	Preme106600	0.023	0.025	0.039	0.085
Cermi52384b-bs-fakeHC	Preme106600	0.023	0.026	0.051	0.084

Cermi236996-fakeHC	Preme106605	0.024	0.024	0.028	0.030
Cermi259446-fakeHC	Preme106605	0.026	0.029	0.047	0.059
Cermi4521-fakeHC	Preme106605	0.024	0.031	0.030	0.036
Cermi452544-fakeHC	Preme106605	0.024	0.021	0.020	0.051
Cermi452547-fakeHC	Preme106605	0.034	0.052	0.046	0.050
Cermi452548-fakeHC	Preme106605	0.053	0.042	0.058	0.041
Cermi452552-fakeHC	Preme106605	0.033	0.037	0.064	0.108
Cermi452554-fakeHC	Preme106605	0.024	0.032	0.058	0.048
Cermi52384-bs-fakeHC	Preme106605	0.031	0.026	0.037	0.049
Cermi52384b-bs-fakeHC	Preme106605	0.031	0.027	0.004	0.043
Cermi236996-fakeHC	Preme106671	0.025	0.062	0.085	0.092
Cermi259446-fakeHC	Preme106671	0.038	0.067	0.119	0.127
Cermi4521-fakeHC	Preme106671	0.036	0.040	0.082	0.095
Cermi452544-fakeHC	Preme106671	0.028	0.066	0.093	0.116
Cermi452547-fakeHC	Preme106671	0.036	0.088	0.112	0.102
Cermi452548-fakeHC	Preme106671	0.057	0.059	0.100	0.107
Cermi452552-fakeHC	Preme106671	0.041	0.085	0.136	0.151
Cermi452554-fakeHC	Preme106671	0.030	0.086	0.145	0.110
Cermi52384-bs-fakeHC	Preme106671	0.038	0.051	0.095	0.112
Cermi52384b-bs-fakeHC	Preme106671	0.040	0.055	0.100	0.106
Cermi236996-fakeHC	Preme107086	0.105	0.077	0.037	0.055
Cermi259446-fakeHC	Preme107086	0.102	0.081	0.045	0.089
Cermi4521-fakeHC	Preme107086	0.097	0.071	0.032	0.065
Cermi452544-fakeHC	Preme107086	0.071	0.039	0.037	0.077
Cermi452547-fakeHC	Preme107086	0.117	0.103	0.073	0.064
Cermi452548-fakeHC	Preme107086	0.072	0.066	0.088	0.075
Cermi452552-fakeHC	Preme107086	0.107	0.068	0.116	0.116

Cermi452554-fakeHC	Preme107086	0.077	0.050	0.111	0.072
Cermi52384-bs-fakeHC	Preme107086	0.093	0.077	0.026	0.083
Cermi52384b-bs-fakeHC	Preme107086	0.111	0.079	0.054	0.077
Cermi236996-fakeHC	Preme107088	0.097	0.088	0.075	0.030
Cermi259446-fakeHC	Preme107088	0.074	0.098	0.097	0.053
Cermi4521-fakeHC	Preme107088	0.069	0.074	0.070	0.047
Cermi452544-fakeHC	Preme107088	0.052	0.064	0.076	0.036
Cermi452547-fakeHC	Preme107088	0.107	0.115	0.082	0.038
Cermi452548-fakeHC	Preme107088	0.034	0.063	0.068	0.046
Cermi452552-fakeHC	Preme107088	0.091	0.090	0.111	0.095
Cermi452554-fakeHC	Preme107088	0.056	0.083	0.121	0.040
Cermi52384-bs-fakeHC	Preme107088	0.067	0.084	0.076	0.055
Cermi52384b-bs-fakeHC	Preme107088	0.086	0.088	0.082	0.049

d. *Colobus – Macaca*

Specimen 1	**Specimen 2**	**Protoconid distance**	**Metaconid distance**	**Entoconid distance**	**Hypoconid distance**	**Hypoconulid distance**
Cogue119768-bs	Macfa102768	0.036	0.101	0.106	0.083	0.071
Cogue52237-bs	Macfa102768	0.067	0.052	0.079	0.033	0.033
Colgu11112	Macfa102768	0.074	0.069	0.054	0.044	0.038
Colgu1241	Macfa102768	0.066	0.092	0.08	0.086	0.062
Colgu163124-mirL	Macfa102768	0.066	0.07	0.063	0.054	0.024
Colgu163273-mirL	Macfa102768	0.054	0.056	0.064	0.054	0.024
Colgu163627-mirL	Macfa102768	0.03	0.067	0.083	0.051	0.042
Colgu401-mirL	Macfa102768	0.044	0.042	0.029	0.052	0.03
Colgu408-mirL	Macfa102768	0.087	0.068	0.074	0.062	0.101
Colgu762	Macfa102768	0.076	0.054	0.042	0.011	0.051
Colgu864-mirL	Macfa102768	0.04	0.037	0.054	0.029	0.042

Colgu994	Macfa102768	0.029	0.061	0.063	0.063	0.057
Cogue119768-bs	Macfa103649	0.015	0.08	0.099	0.09	0.047
Cogue52237-bs	Macfa103649	0.069	0.043	0.075	0.065	0.049
Colgu11112	Macfa103649	0.062	0.062	0.047	0.067	0.051
Colgu1241	Macfa103649	0.053	0.079	0.07	0.102	0.058
Colgu163124-mirL	Macfa103649	0.057	0.058	0.057	0.08	0.041
Colgu163273-mirL	Macfa103649	0.052	0.045	0.057	0.07	0.025
Colgu163627-mirL	Macfa103649	0.027	0.05	0.075	0.085	0.038
Colgu401-mirL	Macfa103649	0.057	0.05	0.024	0.097	0.061
Colgu408-mirL	Macfa103649	0.079	0.065	0.077	0.115	0.13
Colgu762	Macfa103649	0.07	0.058	0.041	0.062	0.077
Colgu864-mirL	Macfa103649	0.045	0.038	0.045	0.043	0.04
Colgu994	Macfa103649	0.017	0.04	0.053	0.062	0.034
Cogue119768-bs	Macfa103655	0.024	0.064	0.104	0.033	0.038
Cogue52237-bs	Macfa103655	0.068	0.03	0.084	0.025	0.081
Colgu11112	Macfa103655	0.065	0.049	0.053	0.012	0.049
Colgu1241	Macfa103655	0.057	0.061	0.065	0.035	0.016
Colgu163124-mirL	Macfa103655	0.058	0.044	0.067	0.015	0.047
Colgu163273-mirL	Macfa103655	0.054	0.031	0.065	0.002	0.048
Colgu163627-mirL	Macfa103655	0.025	0.029	0.073	0.034	0.041
Colgu401-mirL	Macfa103655	0.05	0.048	0.048	0.083	0.07
Colgu408-mirL	Macfa103655	0.078	0.063	0.099	0.083	0.132
Colgu762	Macfa103655	0.071	0.055	0.062	0.049	0.09
Colgu864-mirL	Macfa103655	0.045	0.032	0.046	0.042	0.07
Colgu994	Macfa103655	0.019	0.019	0.048	0.021	0.034
Cogue119768-bs	Macfa103658	0.014	0.086	0.111	0.045	0.052
Cogue52237-bs	Macfa103658	0.048	0.026	0.09	0.029	0.059

Colgu11112	Macfa103658	0.04	0.034	0.06	0.02	0.027
Colgu1241	Macfa103658	0.029	0.061	0.081	0.054	0.022
Colgu163124-mirL	Macfa103658	0.036	0.04	0.072	0.037	0.023
Colgu163273-mirL	Macfa103658	0.031	0.029	0.071	0.027	0.031
Colgu163627-mirL	Macfa103658	0.021	0.048	0.086	0.035	0.027
Colgu401-mirL	Macfa103658	0.055	0.02	0.015	0.084	0.048
Colgu408-mirL	Macfa103658	0.061	0.031	0.091	0.085	0.109
Colgu762	Macfa103658	0.049	0.014	0.056	0.039	0.066
Colgu864-mirL	Macfa103658	0.029	0.028	0.056	0.018	0.054
Colgu994	Macfa103658	0.015	0.052	0.061	0.029	0.041
Cogue119768-bs	Macfa106025	0.031	0.059	0.085	0.086	0.037
Cogue52237-bs	Macfa106025	0.075	0.021	0.084	0.046	0.055
Colgu11112	Macfa106025	0.066	0.038	0.057	0.053	0.043
Colgu1241	Macfa106025	0.061	0.053	0.063	0.094	0.042
Colgu163124-mirL	Macfa106025	0.061	0.033	0.064	0.066	0.033
Colgu163273-mirL	Macfa106025	0.061	0.021	0.061	0.061	0.021
Colgu163627-mirL	Macfa106025	0.033	0.023	0.069	0.065	0.03
Colgu401-mirL	Macfa106025	0.056	0.044	0.021	0.072	0.055
Colgu408-mirL	Macfa106025	0.078	0.049	0.102	0.086	0.127
Colgu762	Macfa106025	0.074	0.046	0.065	0.034	0.076
Colgu864-mirL	Macfa106025	0.055	0.032	0.05	0.026	0.045
Colgu994	Macfa106025	0.029	0.017	0.043	0.062	0.023
Cogue119768-bs	Macfa106384	0.024	0.057	0.087	0.071	0.032
Cogue52237-bs	Macfa106384	0.067	0.012	0.089	0.033	0.064
Colgu11112	Macfa106384	0.057	0.026	0.062	0.038	0.044
Colgu1241	Macfa106384	0.051	0.042	0.067	0.078	0.034
Colgu163124-mirL	Macfa106384	0.053	0.021	0.069	0.051	0.035

Colgu163273-mirL	Macfa106384	0.053	0.009	0.065	0.045	0.029
Colgu163627-mirL	Macfa106384	0.028	0.02	0.073	0.052	0.033
Colgu401-mirL	Macfa106384	0.055	0.04	0.021	0.072	0.057
Colgu408-mirL	Macfa106384	0.071	0.038	0.107	0.082	0.129
Colgu762	Macfa106384	0.066	0.037	0.07	0.029	0.081
Colgu864-mirL	Macfa106384	0.048	0.032	0.054	0.014	0.054
Colgu994	Macfa106384	0.022	0.022	0.046	0.047	0.02
Cogue119768-bs	Macfa114411	0.046	0.076	0.109	0.101	0.08
Cogue52237-bs	Macfa114411	0.061	0.017	0.081	0.048	0.035
Colgu11112	Macfa114411	0.052	0.037	0.05	0.061	0.017
Colgu1241	Macfa114411	0.053	0.059	0.074	0.103	0.052
Colgu163124-mirL	Macfa114411	0.047	0.039	0.064	0.067	0.016
Colgu163273-mirL	Macfa114411	0.054	0.022	0.064	0.07	0.032
Colgu163627-mirL	Macfa114411	0.032	0.034	0.08	0.066	0.037
Colgu401-mirL	Macfa114411	0.042	0.025	0.033	0.04	0.029
Colgu408-mirL	Macfa114411	0.056	0.048	0.082	0.058	0.079
Colgu762	Macfa114411	0.057	0.033	0.046	0.025	0.033
Colgu864-mirL	Macfa114411	0.051	0.012	0.047	0.048	0.045
Colgu994	Macfa114411	0.037	0.033	0.056	0.08	0.067
Cogue119768-bs	Macfa114505	0.051	0.074	0.059	0.07	0.069
Cogue52237-bs	Macfa114505	0.02	0.019	0.047	0.04	0.031
Colgu11112	Macfa114505	0.01	0.023	0.025	0.041	0.035
Colgu1241	Macfa114505	0.015	0.043	0.021	0.079	0.056
Colgu163124-mirL	Macfa114505	0.002	0.031	0.03	0.056	0.039
Colgu163273-mirL	Macfa114505	0.019	0.023	0.024	0.048	0.027
Colgu163627-mirL	Macfa114505	0.038	0.033	0.027	0.057	0.026
Colgu401-mirL	Macfa114505	0.05	0.031	0.061	0.081	0.067

Colgu408-mirL	Macfa114505	0.026	0.046	0.086	0.091	0.111
Colgu762	Macfa114505	0.012	0.031	0.053	0.037	0.055
Colgu864-mirL	Macfa114505	0.031	0.029	0.014	0.015	0.006
Colgu994	Macfa114505	0.044	0.042	0.009	0.046	0.056
Cogue119768-bs	Macfa121803	0.028	0.077	0.078	0.085	0.039
Cogue52237-bs	Macfa121803	0.068	0.05	0.075	0.061	0.066
Colgu11112	Macfa121803	0.067	0.069	0.047	0.063	0.064
Colgu1241	Macfa121803	0.06	0.079	0.043	0.097	0.059
Colgu163124-mirL	Macfa121803	0.06	0.065	0.057	0.075	0.06
Colgu163273-mirL	Macfa121803	0.055	0.052	0.052	0.066	0.042
Colgu163627-mirL	Macfa121803	0.025	0.047	0.052	0.081	0.043
Colgu401-mirL	Macfa121803	0.046	0.061	0.052	0.096	0.088
Colgu408-mirL	Macfa121803	0.079	0.085	0.105	0.113	0.15
Colgu762	Macfa121803	0.072	0.073	0.068	0.059	0.094
Colgu864-mirL	Macfa121803	0.045	0.043	0.037	0.04	0.045
Colgu994	Macfa121803	0.022	0.036	0.024	0.058	0.032
Cogue119768-bs	Macfa125	0.021	0.066	0.101	0.07	0.049
Cogue52237-bs	Macfa125	0.058	0.027	0.071	0.039	0.049
Colgu11112	Macfa125	0.046	0.043	0.043	0.043	0.037
Colgu1241	Macfa125	0.04	0.06	0.07	0.079	0.045
Colgu163124-mirL	Macfa125	0.042	0.039	0.055	0.052	0.023
Colgu163273-mirL	Macfa125	0.044	0.027	0.055	0.045	0.018
Colgu163627-mirL	Macfa125	0.023	0.034	0.074	0.064	0.032
Colgu401-mirL	Macfa125	0.053	0.043	0.031	0.078	0.043
Colgu408-mirL	Macfa125	0.061	0.047	0.071	0.096	0.116
Colgu762	Macfa125	0.056	0.045	0.035	0.043	0.067
Colgu864-mirL	Macfa125	0.041	0.033	0.042	0.031	0.046

Colgu994	Macfa125	0.019	0.029	0.053	0.04	0.035
Cogue119768-bs	Macfa125102	0.032	0.12	0.138	0.084	0.031
Cogue52237-bs	Macfa125102	0.064	0.071	0.116	0.068	0.06
Colgu11112	Macfa125102	0.072	0.09	0.085	0.068	0.051
Colgu1241	Macfa125102	0.062	0.112	0.103	0.097	0.045
Colgu163124-mirL	Macfa125102	0.064	0.093	0.099	0.078	0.044
Colgu163273-mirL	Macfa125102	0.05	0.076	0.099	0.067	0.028
Colgu163627-mirL	Macfa125102	0.031	0.083	0.11	0.091	0.032
Colgu401-mirL	Macfa125102	0.05	0.058	0.047	0.106	0.069
Colgu408-mirL	Macfa125102	0.087	0.097	0.115	0.127	0.137
Colgu762	Macfa125102	0.074	0.076	0.081	0.074	0.084
Colgu864-mirL	Macfa125102	0.036	0.049	0.08	0.056	0.044
Colgu994	Macfa125102	0.028	0.076	0.083	0.054	0.017
Cogue119768-bs	Macfa196817	0.029	0.064	0.118	0.005	0.07
Cogue52237-bs	Macfa196817	0.049	0.012	0.078	0.052	0.084
Colgu11112	Macfa196817	0.031	0.02	0.05	0.037	0.047
Colgu1241	Macfa196817	0.021	0.042	0.077	0.015	0.026
Colgu163124-mirL	Macfa196817	0.032	0.02	0.066	0.04	0.052
Colgu163273-mirL	Macfa196817	0.034	0.01	0.067	0.03	0.061
Colgu163627-mirL	Macfa196817	0.035	0.028	0.082	0.046	0.05
Colgu401-mirL	Macfa196817	0.065	0.035	0.059	0.11	0.072
Colgu408-mirL	Macfa196817	0.053	0.028	0.077	0.104	0.113
Colgu762	Macfa196817	0.044	0.027	0.046	0.074	0.082
Colgu864-mirL	Macfa196817	0.039	0.032	0.05	0.061	0.077
Colgu994	Macfa196817	0.031	0.033	0.063	0.031	0.064
Cogue119768-bs	Macfa196824	0.028	0.058	0.078	0.06	0.017
Cogue52237-bs	Macfa196824	0.046	0.008	0.074	0.067	0.074

Colgu11112	Macfa196824	0.029	0.019	0.045	0.059	0.058
Colgu1241	Macfa196824	0.018	0.035	0.047	0.076	0.038
Colgu163124-mirL	Macfa196824	0.029	0.017	0.054	0.07	0.054
Colgu163273-mirL	Macfa196824	0.031	0.006	0.05	0.056	0.041
Colgu163627-mirL	Macfa196824	0.033	0.016	0.055	0.082	0.037
Colgu401-mirL	Macfa196824	0.063	0.039	0.037	0.119	0.081
Colgu408-mirL	Macfa196824	0.053	0.04	0.099	0.13	0.147
Colgu762	Macfa196824	0.041	0.036	0.061	0.08	0.096
Colgu864-mirL	Macfa196824	0.036	0.032	0.035	0.055	0.056
Colgu994	Macfa196824	0.03	0.025	0.025	0.038	0.01
Cogue119768-bs	Macfa198300	0.02	0.086	0.12	0.089	0.025
Cogue52237-bs	Macfa198300	0.049	0.04	0.106	0.078	0.072
Colgu11112	Macfa198300	0.041	0.059	0.075	0.077	0.058
Colgu1241	Macfa198300	0.034	0.076	0.084	0.103	0.042
Colgu163124-mirL	Macfa198300	0.035	0.06	0.089	0.087	0.055
Colgu163273-mirL	Macfa198300	0.034	0.045	0.087	0.076	0.041
Colgu163627-mirL	Macfa198300	0.013	0.046	0.092	0.101	0.035
Colgu401-mirL	Macfa198300	0.045	0.043	0.054	0.117	0.085
Colgu408-mirL	Macfa198300	0.057	0.076	0.12	0.137	0.147
Colgu762	Macfa198300	0.048	0.058	0.083	0.085	0.095
Colgu864-mirL	Macfa198300	0.031	0.026	0.068	0.065	0.051
Colgu994	Macfa198300	0.012	0.041	0.065	0.061	0.018
Cogue119768-bs	Macfa278	0.043	0.081	0.084	0.079	0.061
Cogue52237-bs	Macfa278	0.018	0.017	0.068	0.042	0.038
Colgu11112	Macfa278	0.023	0.029	0.042	0.049	0.043
Colgu1241	Macfa278	0.02	0.056	0.059	0.086	0.061
Colgu163124-mirL	Macfa278	0.014	0.036	0.049	0.055	0.03

Colgu163273-mirL	Macfa278	0.009	0.022	0.048	0.05	0.02
Colgu163627-mirL	Macfa278	0.028	0.04	0.063	0.072	0.039
Colgu401-mirL	Macfa278	0.04	0.015	0.028	0.072	0.044
Colgu408-mirL	Macfa278	0.038	0.038	0.081	0.096	0.114
Colgu762	Macfa278	0.022	0.017	0.045	0.046	0.062
Colgu864-mirL	Macfa278	0.018	0.018	0.037	0.042	0.039
Colgu994	Macfa278	0.035	0.044	0.041	0.047	0.047
Cogue119768-bs	Macfa317191	0.059	0.13	0.102	0.093	0.084
Cogue52237-bs	Macfa317191	0.072	0.08	0.071	0.051	0.02
Colgu11112	Macfa317191	0.087	0.099	0.039	0.058	0.046
Colgu1241	Macfa317191	0.08	0.121	0.063	0.099	0.074
Colgu163124-mirL	Macfa317191	0.078	0.102	0.055	0.071	0.047
Colgu163273-mirL	Macfa317191	0.063	0.085	0.055	0.068	0.037
Colgu163627-mirL	Macfa317191	0.049	0.093	0.069	0.064	0.043
Colgu401-mirL	Macfa317191	0.047	0.064	0.044	0.068	0.067
Colgu408-mirL	Macfa317191	0.098	0.105	0.078	0.078	0.107
Colgu762	Macfa317191	0.086	0.083	0.042	0.031	0.051
Colgu864-mirL	Macfa317191	0.049	0.056	0.037	0.031	0.015
Colgu994	Macfa317191	0.052	0.086	0.047	0.072	0.07
Cogue119768-bs	Macfa385	0.019	0.078	0.119	0.107	0.045
Cogue52237-bs	Macfa385	0.044	0.017	0.128	0.084	0.089
Colgu11112	Macfa385	0.044	0.035	0.101	0.088	0.085
Colgu1241	Macfa385	0.035	0.059	0.106	0.118	0.077
Colgu163124-mirL	Macfa385	0.037	0.038	0.108	0.093	0.072
Colgu163273-mirL	Macfa385	0.028	0.022	0.105	0.086	0.062
Colgu163627-mirL	Macfa385	0.009	0.037	0.111	0.112	0.072
Colgu401-mirL	Macfa385	0.041	0.022	0.041	0.108	0.082

Colgu408-mirL	Macfa385	0.061	0.043	0.138	0.138	0.162
Colgu762	Macfa385	0.049	0.028	0.104	0.088	0.113
Colgu864-mirL	Macfa385	0.02	0.015	0.094	0.078	0.082
Colgu994	Macfa385	0.009	0.037	0.085	0.076	0.042
Cogue119768-bs	Macfa411	0.018	0.069	0.09	0.06	0.023
Cogue52237-bs	Macfa411	0.063	0.033	0.076	0.04	0.069
Colgu11112	Macfa411	0.06	0.053	0.045	0.039	0.056
Colgu1241	Macfa411	0.052	0.067	0.057	0.07	0.044
Colgu163124-mirL	Macfa411	0.054	0.049	0.057	0.048	0.046
Colgu163273-mirL	Macfa411	0.047	0.035	0.054	0.038	0.035
Colgu163627-mirL	Macfa411	0.019	0.035	0.064	0.064	0.04
Colgu401-mirL	Macfa411	0.048	0.047	0.029	0.087	0.068
Colgu408-mirL	Macfa411	0.075	0.064	0.093	0.103	0.141
Colgu762	Macfa411	0.066	0.055	0.054	0.052	0.091
Colgu864-mirL	Macfa411	0.038	0.031	0.037	0.037	0.057
Colgu994	Macfa411	0.012	0.025	0.036	0.028	0.011

e. *Colobus – Presbytis*

Specimen 1	**Specimen 2**	**Protoconid distance**	**Metaconid distance**	**Entoconid distance**	**Hypoconid distance**	**Hypoconulid distance**
Cogue119768-bs	Preme102755	0.05	0.083	0.103	0.06	0.093
Cogue52237-bs	Preme102755	0.041	0.048	0.093	0.037	0.093
Colgu11112	Preme102755	0.017	0.029	0.062	0.036	0.058
Colgu1241	Preme102755	0.023	0.04	0.073	0.05	0.051
Colgu163124-mirL	Preme102755	0.019	0.04	0.073	0.033	0.062
Colgu163273-mirL	Preme102755	0.037	0.046	0.071	0.042	0.077
Colgu163627-mirL	Preme102755	0.041	0.058	0.08	0.022	0.069
Colgu401-mirL	Preme102755	0.057	0.056	0.02	0.069	0.069
Colgu408-mirL	Preme102755	0.028	0.035	0.105	0.05	0.099
Colgu762	Preme102755	0.028	0.039	0.067	0.046	0.082

Colgu864-mirL	Preme102755	0.045	0.064	0.054	0.059	0.093
Colgu994	Preme102755	0.045	0.071	0.051	0.062	0.086
Cogue119768-bs	Preme102757	0.073	0.104	0.129	0.076	0.135
Cogue52237-bs	Preme102757	0.034	0.061	0.097	0.057	0.113
Colgu11112	Preme102757	0.02	0.046	0.067	0.058	0.086
Colgu1241	Preme102757	0.033	0.061	0.093	0.061	0.093
Colgu163124-mirL	Preme102757	0.025	0.058	0.082	0.048	0.091
Colgu163273-mirL	Preme102757	0.042	0.061	0.082	0.061	0.109
Colgu163627-mirL	Preme102757	0.061	0.076	0.099	0.048	0.104
Colgu401-mirL	Preme102757	0.067	0.06	0.042	0.074	0.087
Colgu408-mirL	Preme102757	0.014	0.042	0.089	0.052	0.08
Colgu762	Preme102757	0.016	0.042	0.057	0.068	0.09
Colgu864-mirL	Preme102757	0.055	0.072	0.066	0.084	0.121
Colgu994	Preme102757	0.067	0.088	0.075	0.08	0.127
Cogue119768-bs	Preme102882	0.119	0.106	0.127	0.088	0.169
Cogue52237-bs	Preme102882	0.071	0.076	0.07	0.065	0.122
Colgu11112	Preme102882	0.065	0.058	0.056	0.069	0.106
Colgu1241	Preme102882	0.076	0.065	0.093	0.073	0.127
Colgu163124-mirL	Preme102882	0.071	0.067	0.066	0.055	0.112
Colgu163273-mirL	Preme102882	0.084	0.075	0.071	0.07	0.13
Colgu163627-mirL	Preme102882	0.107	0.087	0.094	0.063	0.128
Colgu401-mirL	Preme102882	0.107	0.08	0.079	0.071	0.101
Colgu408-mirL	Preme102882	0.053	0.05	0.037	0.056	0.051
Colgu762	Preme102882	0.059	0.061	0.029	0.076	0.091
Colgu864-mirL	Preme102882	0.097	0.091	0.064	0.095	0.136
Colgu994	Preme102882	0.114	0.099	0.085	0.089	0.158
Cogue119768-bs	Preme102883	0.062	0.093	0.143	0.08	0.132
Cogue52237-bs	Preme102883	0.013	0.039	0.091	0.054	0.092
Colgu11112	Preme102883	0.019	0.038	0.071	0.059	0.074
Colgu1241	Preme102883	0.027	0.064	0.107	0.066	0.094
Colgu163124-mirL	Preme102883	0.015	0.046	0.083	0.044	0.076
Colgu163273-mirL	Preme102883	0.025	0.04	0.088	0.059	0.095
Colgu163627-mirL	Preme102883	0.046	0.06	0.11	0.058	0.095
Colgu401-mirL	Preme102883	0.049	0.032	0.078	0.066	0.062

Colgu408-mirL	Preme102883	0.023	0.025	0.058	0.058	0.054
Colgu762	Preme102883	0.006	0.015	0.047	0.068	0.067
Colgu864-mirL	Preme102883	0.036	0.044	0.077	0.087	0.107
Colgu994	Preme102883	0.055	0.065	0.096	0.078	0.121
Cogue119768-bs	Preme102891	0.084	0.082	0.157	0.078	0.151
Cogue52237-bs	Preme102891	0.044	0.028	0.102	0.052	0.109
Colgu11112	Preme102891	0.032	0.02	0.085	0.057	0.09
Colgu1241	Preme102891	0.046	0.046	0.117	0.065	0.108
Colgu163124-mirL	Preme102891	0.036	0.032	0.098	0.043	0.097
Colgu163273-mirL	Preme102891	0.054	0.029	0.102	0.058	0.115
Colgu163627-mirL	Preme102891	0.07	0.047	0.12	0.054	0.111
Colgu401-mirL	Preme102891	0.071	0.031	0.103	0.063	0.091
Colgu408-mirL	Preme102891	0.012	0.024	0.076	0.055	0.054
Colgu762	Preme102891	0.027	0.013	0.069	0.064	0.08
Colgu864-mirL	Preme102891	0.066	0.04	0.09	0.083	0.121
Colgu994	Preme102891	0.077	0.056	0.109	0.076	0.141
Cogue119768-bs	Preme102895	0.085	0.099	0.157	0.075	0.134
Cogue52237-bs	Preme102895	0.036	0.042	0.105	0.045	0.092
Colgu11112	Preme102895	0.033	0.038	0.084	0.052	0.074
Colgu1241	Preme102895	0.045	0.064	0.118	0.065	0.094
Colgu163124-mirL	Preme102895	0.036	0.049	0.098	0.035	0.078
Colgu163273-mirL	Preme102895	0.049	0.044	0.102	0.049	0.096
Colgu163627-mirL	Preme102895	0.072	0.063	0.122	0.062	0.095
Colgu401-mirL	Preme102895	0.072	0.03	0.087	0.062	0.066
Colgu408-mirL	Preme102895	0.022	0.032	0.075	0.07	0.05
Colgu762	Preme102895	0.024	0.013	0.064	0.063	0.065
Colgu864-mirL	Preme102895	0.062	0.045	0.089	0.079	0.106
Colgu994	Preme102895	0.079	0.07	0.106	0.064	0.123
Cogue119768-bs	Preme106600	0.058	0.054	0.153	0.109	0.138
Cogue52237-bs	Preme106600	0.038	0.04	0.102	0.095	0.127
Colgu11112	Preme106600	0.024	0.038	0.082	0.1	0.104
Colgu1241	Preme106600	0.033	0.047	0.117	0.095	0.108
Colgu163124-mirL	Preme106600	0.022	0.03	0.094	0.082	0.1
Colgu163273-mirL	Preme106600	0.039	0.035	0.098	0.094	0.117

Colgu163627-mirL	Preme106600	0.043	0.041	0.12	0.107	0.12
Colgu401-mirL	Preme106600	0.048	0.061	0.083	0.101	0.082
Colgu408-mirL	Preme106600	0.02	0.029	0.067	0.109	0.103
Colgu762	Preme106600	0.026	0.05	0.057	0.114	0.11
Colgu864-mirL	Preme106600	0.046	0.059	0.087	0.129	0.138
Colgu994	Preme106600	0.05	0.044	0.105	0.105	0.13
Cogue119768-bs	Preme106605	0.061	0.099	0.168	0.087	0.148
Cogue52237-bs	Preme106605	0.049	0.063	0.13	0.043	0.12
Colgu11112	Preme106605	0.023	0.053	0.108	0.055	0.1
Colgu1241	Preme106605	0.032	0.07	0.139	0.078	0.113
Colgu163124-mirL	Preme106605	0.028	0.059	0.118	0.045	0.1
Colgu163273-mirL	Preme106605	0.047	0.062	0.121	0.059	0.118
Colgu163627-mirL	Preme106605	0.054	0.078	0.142	0.054	0.12
Colgu401-mirL	Preme106605	0.067	0.064	0.075	0.039	0.082
Colgu408-mirL	Preme106605	0.026	0.027	0.098	0.039	0.077
Colgu762	Preme106605	0.033	0.045	0.084	0.047	0.097
Colgu864-mirL	Preme106605	0.057	0.075	0.11	0.073	0.134
Colgu994	Preme106605	0.057	0.085	0.122	0.077	0.139
Cogue119768-bs	Preme106671	0.057	0.056	0.093	0.05	0.088
Cogue52237-bs	Preme106671	0.04	0.045	0.066	0.066	0.104
Colgu11112	Preme106671	0.013	0.027	0.036	0.059	0.068
Colgu1241	Preme106671	0.022	0.013	0.052	0.033	0.051
Colgu163124-mirL	Preme106671	0.02	0.026	0.051	0.046	0.07
Colgu163273-mirL	Preme106671	0.039	0.041	0.049	0.052	0.083
Colgu163627-mirL	Preme106671	0.05	0.043	0.059	0.062	0.075
Colgu401-mirL	Preme106671	0.065	0.068	0.052	0.106	0.079
Colgu408-mirL	Preme106671	0.025	0.04	0.085	0.098	0.116
Colgu762	Preme106671	0.024	0.054	0.048	0.089	0.097
Colgu864-mirL	Preme106671	0.05	0.069	0.03	0.091	0.102
Colgu994	Preme106671	0.054	0.056	0.037	0.063	0.084
Cogue119768-bs	Preme107086	0.13	0.133	0.134	0.058	0.165
Cogue52237-bs	Preme107086	0.086	0.105	0.087	0.039	0.114
Colgu11112	Preme107086	0.08	0.088	0.075	0.039	0.101
Colgu1241	Preme107086	0.088	0.097	0.109	0.046	0.124

Colgu163124-mirL	Preme107086	0.087	0.096	0.08	0.027	0.106
Colgu163273-mirL	Preme107086	0.097	0.103	0.085	0.04	0.124
Colgu163627-mirL	Preme107086	0.123	0.117	0.11	0.035	0.123
Colgu401-mirL	Preme107086	0.129	0.104	0.079	0.071	0.093
Colgu408-mirL	Preme107086	0.077	0.073	0.046	0.059	0.042
Colgu762	Preme107086	0.077	0.085	0.046	0.056	0.083
Colgu864-mirL	Preme107086	0.111	0.118	0.082	0.068	0.13
Colgu994	Preme107086	0.127	0.128	0.1	0.06	0.153
Cogue119768-bs	Preme107088	0.135	0.109	0.124	0.097	0.178
Cogue52237-bs	Preme107088	0.097	0.087	0.082	0.053	0.134
Colgu11112	Preme107088	0.084	0.068	0.055	0.064	0.116
Colgu1241	Preme107088	0.097	0.066	0.083	0.088	0.133
Colgu163124-mirL	Preme107088	0.091	0.076	0.071	0.058	0.126
Colgu163273-mirL	Preme107088	0.108	0.085	0.072	0.071	0.142
Colgu163627-mirL	Preme107088	0.124	0.093	0.088	0.055	0.136
Colgu401-mirL	Preme107088	0.123	0.093	0.066	0.04	0.122
Colgu408-mirL	Preme107088	0.067	0.072	0.077	0.018	0.069
Colgu762	Preme107088	0.082	0.078	0.048	0.049	0.103
Colgu864-mirL	Preme107088	0.121	0.102	0.056	0.076	0.144
Colgu994	Preme107088	0.13	0.107	0.071	0.09	0.168

f. *Macaca – Presbytis*

Specimen 1	**Specimen 2**	**Protoconid distance**	**Metaconid distance**	**Entoconid distance**	**Hypoconid distance**	**Hypoconulid distance**
Macfa102768	Preme102755	0.071	0.091	0.041	0.058	0.083
Macfa103649	Preme102755	0.055	0.089	0.032	0.098	0.097
Macfa103655	Preme102755	0.056	0.077	0.031	0.041	0.055
Macfa103658	Preme102755	0.038	0.05	0.022	0.052	0.049
Macfa106025	Preme102755	0.055	0.067	0.025	0.076	0.081
Macfa106384	Preme102755	0.046	0.054	0.026	0.064	0.073
Macfa114411	Preme102755	0.039	0.062	0.028	0.068	0.059
Macfa114505	Preme102755	0.021	0.042	0.053	0.07	0.091
Macfa121803	Preme102755	0.059	0.096	0.037	0.094	0.108
Macfa125	Preme102755	0.036	0.07	0.036	0.074	0.075

Macfa125102	Preme102755	0.071	0.112	0.039	0.103	0.091
Macfa196817	Preme102755	0.028	0.046	0.049	0.055	0.028
Macfa196824	Preme102755	0.029	0.048	0.026	0.095	0.088
Macfa198300	Preme102755	0.034	0.084	0.035	0.113	0.092
Macfa278	Preme102755	0.03	0.049	0.033	0.078	0.09
Macfa317191	Preme102755	0.088	0.119	0.034	0.075	0.104
Macfa385	Preme102755	0.042	0.059	0.051	0.12	0.114
Macfa411	Preme102755	0.054	0.081	0.017	0.074	0.087
Macfa102768	Preme102757	0.09	0.095	0.04	0.079	0.109
Macfa103649	Preme102757	0.081	0.098	0.037	0.121	0.131
Macfa103655	Preme102757	0.082	0.091	0.039	0.06	0.097
Macfa103658	Preme102757	0.06	0.055	0.028	0.076	0.087
Macfa106025	Preme102757	0.083	0.081	0.057	0.099	0.118
Macfa106384	Preme102757	0.074	0.069	0.059	0.088	0.111
Macfa114411	Preme102757	0.064	0.072	0.02	0.086	0.082
Macfa114505	Preme102757	0.024	0.055	0.073	0.095	0.12
Macfa121803	Preme102757	0.083	0.11	0.063	0.118	0.145
Macfa125	Preme102757	0.064	0.081	0.034	0.095	0.109
Macfa125102	Preme102757	0.089	0.117	0.026	0.124	0.128
Macfa196817	Preme102757	0.05	0.059	0.03	0.071	0.07
Macfa196824	Preme102757	0.049	0.064	0.057	0.117	0.129
Macfa198300	Preme102757	0.059	0.095	0.045	0.133	0.132
Macfa278	Preme102757	0.037	0.057	0.051	0.097	0.12
Macfa317191	Preme102757	0.101	0.123	0.031	0.098	0.128
Macfa385	Preme102757	0.062	0.068	0.079	0.138	0.151
Macfa411	Preme102757	0.078	0.093	0.042	0.094	0.126
Macfa102768	Preme102882	0.135	0.112	0.055	0.086	0.125
Macfa103649	Preme102882	0.127	0.113	0.057	0.129	0.153
Macfa103655	Preme102882	0.129	0.106	0.072	0.069	0.134
Macfa103658	Preme102882	0.105	0.072	0.066	0.088	0.117
Macfa106025	Preme102882	0.129	0.094	0.086	0.107	0.144
Macfa106384	Preme102882	0.121	0.081	0.09	0.097	0.141
Macfa114411	Preme102882	0.109	0.089	0.054	0.091	0.098
Macfa114505	Preme102882	0.07	0.072	0.078	0.104	0.137

Macfa121803	Preme102882	0.13	0.126	0.088	0.125	0.17
Macfa125	Preme102882	0.11	0.095	0.049	0.102	0.133
Macfa125102	Preme102882	0.133	0.137	0.081	0.13	0.155
Macfa196817	Preme102882	0.094	0.072	0.046	0.082	0.108
Macfa196824	Preme102882	0.093	0.077	0.082	0.125	0.16
Macfa198300	Preme102882	0.105	0.113	0.09	0.14	0.162
Macfa278	Preme102882	0.081	0.075	0.066	0.101	0.139
Macfa317191	Preme102882	0.143	0.143	0.052	0.107	0.139
Macfa385	Preme102882	0.107	0.085	0.119	0.141	0.178
Macfa411	Preme102882	0.125	0.108	0.072	0.101	0.155
Macfa102768	Preme102883	0.073	0.054	0.057	0.079	0.088
Macfa103649	Preme102883	0.07	0.061	0.06	0.118	0.116
Macfa103655	Preme102883	0.07	0.062	0.072	0.059	0.098
Macfa103658	Preme102883	0.05	0.017	0.063	0.079	0.08
Macfa106025	Preme102883	0.074	0.052	0.089	0.098	0.105
Macfa106384	Preme102883	0.066	0.043	0.093	0.087	0.102
Macfa114411	Preme102883	0.057	0.042	0.052	0.084	0.064
Macfa114505	Preme102883	0.013	0.045	0.09	0.094	0.107
Macfa121803	Preme102883	0.07	0.082	0.094	0.115	0.136
Macfa125	Preme102883	0.056	0.047	0.053	0.091	0.094
Macfa125102	Preme102883	0.072	0.081	0.07	0.118	0.118
Macfa196817	Preme102883	0.046	0.032	0.045	0.074	0.078
Macfa196824	Preme102883	0.044	0.045	0.088	0.114	0.124
Macfa198300	Preme102883	0.048	0.069	0.085	0.128	0.127
Macfa278	Preme102883	0.02	0.028	0.073	0.089	0.101
Macfa317191	Preme102883	0.082	0.088	0.055	0.099	0.11
Macfa385	Preme102883	0.047	0.035	0.116	0.128	0.137
Macfa411	Preme102883	0.065	0.062	0.075	0.089	0.117
Macfa102768	Preme102891	0.099	0.064	0.087	0.075	0.113
Macfa103649	Preme102891	0.09	0.064	0.087	0.116	0.138
Macfa103655	Preme102891	0.09	0.057	0.079	0.057	0.115
Macfa103658	Preme102891	0.071	0.024	0.087	0.076	0.1
Macfa106025	Preme102891	0.089	0.047	0.112	0.095	0.128
Macfa106384	Preme102891	0.082	0.036	0.115	0.084	0.124

Macfa114411	Preme102891	0.067	0.038	0.071	0.08	0.084
Macfa114505	Preme102891	0.036	0.027	0.102	0.091	0.121
Macfa121803	Preme102891	0.091	0.077	0.103	0.112	0.153
Macfa125	Preme102891	0.072	0.048	0.079	0.089	0.118
Macfa125102	Preme102891	0.099	0.087	0.081	0.117	0.138
Macfa196817	Preme102891	0.061	0.026	0.05	0.073	0.088
Macfa196824	Preme102891	0.061	0.032	0.104	0.112	0.142
Macfa198300	Preme102891	0.068	0.063	0.09	0.126	0.143
Macfa278	Preme102891	0.048	0.024	0.097	0.087	0.125
Macfa317191	Preme102891	0.11	0.094	0.067	0.095	0.125
Macfa385	Preme102891	0.072	0.034	0.142	0.127	0.164
Macfa411	Preme102891	0.087	0.059	0.091	0.087	0.139
Macfa102768	Preme102895	0.099	0.063	0.071	0.071	0.09
Macfa103649	Preme102895	0.093	0.07	0.073	0.103	0.118
Macfa103655	Preme102895	0.094	0.068	0.075	0.05	0.1
Macfa103658	Preme102895	0.072	0.025	0.071	0.071	0.082
Macfa106025	Preme102895	0.096	0.059	0.1	0.087	0.108
Macfa106384	Preme102895	0.088	0.049	0.103	0.076	0.105
Macfa114411	Preme102895	0.076	0.046	0.059	0.077	0.065
Macfa114505	Preme102895	0.035	0.041	0.101	0.083	0.106
Macfa121803	Preme102895	0.095	0.086	0.1	0.1	0.136
Macfa125	Preme102895	0.077	0.057	0.066	0.075	0.097
Macfa125102	Preme102895	0.098	0.085	0.067	0.1	0.12
Macfa196817	Preme102895	0.064	0.039	0.046	0.07	0.078
Macfa196824	Preme102895	0.062	0.048	0.096	0.098	0.125
Macfa198300	Preme102895	0.071	0.07	0.084	0.109	0.128
Macfa278	Preme102895	0.046	0.03	0.086	0.071	0.104
Macfa317191	Preme102895	0.107	0.091	0.061	0.092	0.11
Macfa385	Preme102895	0.072	0.041	0.124	0.107	0.142
Macfa411	Preme102895	0.09	0.068	0.083	0.072	0.119
Macfa102768	Preme106600	0.072	0.065	0.063	0.122	0.109
Macfa103649	Preme106600	0.061	0.053	0.067	0.15	0.133
Macfa103655	Preme106600	0.06	0.051	0.078	0.094	0.105
Macfa103658	Preme106600	0.047	0.043	0.068	0.119	0.096

Macfa106025	Preme106600	0.059	0.038	0.096	0.137	0.119
Macfa106384	Preme106600	0.052	0.031	0.099	0.126	0.112
Macfa114411	Preme106600	0.036	0.048	0.058	0.126	0.094
Macfa114505	Preme106600	0.023	0.056	0.1	0.132	0.138
Macfa121803	Preme106600	0.061	0.074	0.101	0.147	0.154
Macfa125	Preme106600	0.043	0.035	0.06	0.122	0.109
Macfa125102	Preme106600	0.073	0.095	0.07	0.142	0.133
Macfa196817	Preme106600	0.042	0.029	0.051	0.104	0.091
Macfa196824	Preme106600	0.042	0.039	0.095	0.138	0.136
Macfa198300	Preme106600	0.04	0.073	0.089	0.149	0.142
Macfa278	Preme106600	0.031	0.047	0.081	0.117	0.12
Macfa317191	Preme106600	0.086	0.105	0.062	0.142	0.144
Macfa385	Preme106600	0.046	0.045	0.12	0.144	0.138
Macfa411	Preme106600	0.058	0.052	0.082	0.117	0.126
Macfa102768	Preme106605	0.084	0.082	0.062	0.057	0.11
Macfa103649	Preme106605	0.066	0.085	0.07	0.103	0.137
Macfa103655	Preme106605	0.068	0.088	0.097	0.059	0.114
Macfa103658	Preme106605	0.05	0.048	0.066	0.071	0.1
Macfa106025	Preme106605	0.065	0.075	0.094	0.079	0.126
Macfa106384	Preme106605	0.057	0.064	0.096	0.071	0.121
Macfa114411	Preme106605	0.047	0.071	0.071	0.058	0.09
Macfa114505	Preme106605	0.03	0.069	0.119	0.079	0.134
Macfa121803	Preme106605	0.071	0.109	0.117	0.1	0.158
Macfa125	Preme106605	0.047	0.07	0.069	0.077	0.115
Macfa125102	Preme106605	0.084	0.112	0.073	0.107	0.139
Macfa196817	Preme106605	0.037	0.054	0.082	0.082	0.094
Macfa196824	Preme106605	0.039	0.067	0.105	0.109	0.143
Macfa198300	Preme106605	0.046	0.099	0.101	0.117	0.148
Macfa278	Preme106605	0.041	0.058	0.085	0.075	0.123
Macfa317191	Preme106605	0.101	0.12	0.084	0.078	0.138
Macfa385	Preme106605	0.055	0.065	0.099	0.115	0.152
Macfa411	Preme106605	0.066	0.087	0.091	0.08	0.135
Macfa102768	Preme106671	0.08	0.095	0.052	0.098	0.09
Macfa103649	Preme106671	0.064	0.084	0.042	0.121	0.1

Macfa103655	Preme106671	0.067	0.069	0.017	0.05	0.05
Macfa103658	Preme106671	0.045	0.059	0.044	0.076	0.053
Macfa106025	Preme106671	0.066	0.059	0.048	0.111	0.082
Macfa106384	Preme106671	0.057	0.047	0.052	0.096	0.072
Macfa114411	Preme106671	0.051	0.062	0.029	0.111	0.071
Macfa114505	Preme106671	0.021	0.045	0.034	0.099	0.099
Macfa121803	Preme106671	0.07	0.088	0.028	0.117	0.109
Macfa125	Preme106671	0.046	0.065	0.038	0.095	0.078
Macfa125102	Preme106671	0.079	0.116	0.054	0.115	0.091
Macfa196817	Preme106671	0.032	0.044	0.028	0.046	0.028
Macfa196824	Preme106671	0.032	0.041	0.031	0.099	0.086
Macfa198300	Preme106671	0.044	0.082	0.04	0.122	0.091
Macfa278	Preme106671	0.033	0.056	0.042	0.097	0.096
Macfa317191	Preme106671	0.096	0.125	0.015	0.116	0.113
Macfa385	Preme106671	0.05	0.061	0.088	0.13	0.111
Macfa411	Preme106671	0.064	0.074	0.025	0.086	0.085
Macfa102768	Preme107086	0.15	0.132	0.05	0.066	0.117
Macfa103649	Preme107086	0.141	0.137	0.059	0.103	0.146
Macfa103655	Preme107086	0.144	0.134	0.094	0.039	0.131
Macfa103658	Preme107086	0.117	0.094	0.069	0.058	0.113
Macfa106025	Preme107086	0.146	0.121	0.087	0.084	0.138
Macfa106384	Preme107086	0.137	0.109	0.091	0.071	0.135
Macfa114411	Preme107086	0.13	0.115	0.068	0.077	0.092
Macfa114505	Preme107086	0.086	0.103	0.094	0.077	0.131
Macfa121803	Preme107086	0.147	0.154	0.106	0.099	0.165
Macfa125	Preme107086	0.125	0.119	0.055	0.077	0.127
Macfa125102	Preme107086	0.146	0.159	0.095	0.104	0.149
Macfa196817	Preme107086	0.104	0.099	0.075	0.053	0.107
Macfa196824	Preme107086	0.103	0.107	0.094	0.096	0.155
Macfa198300	Preme107086	0.12	0.142	0.11	0.113	0.157
Macfa278	Preme107086	0.096	0.101	0.068	0.079	0.131
Macfa317191	Preme107086	0.158	0.165	0.074	0.086	0.132
Macfa385	Preme107086	0.121	0.11	0.111	0.119	0.171
Macfa411	Preme107086	0.139	0.135	0.084	0.074	0.15

Macfa102768	Preme107088	0.154	0.131	0.057	0.059	0.142
Macfa103649	Preme107088	0.141	0.129	0.052	0.11	0.166
Macfa103655	Preme107088	0.141	0.115	0.037	0.071	0.143
Macfa103658	Preme107088	0.123	0.09	0.051	0.077	0.128
Macfa106025	Preme107088	0.138	0.106	0.073	0.082	0.156
Macfa106384	Preme107088	0.131	0.093	0.076	0.076	0.153
Macfa114411	Preme107088	0.115	0.101	0.033	0.058	0.112
Macfa114505	Preme107088	0.09	0.077	0.066	0.085	0.144
Macfa121803	Preme107088	0.143	0.133	0.062	0.107	0.178
Macfa125	Preme107088	0.122	0.11	0.046	0.087	0.148
Macfa125102	Preme107088	0.154	0.15	0.049	0.118	0.166
Macfa196817	Preme107088	0.11	0.086	0.008	0.092	0.113
Macfa196824	Preme107088	0.11	0.085	0.062	0.12	0.168
Macfa198300	Preme107088	0.12	0.12	0.051	0.129	0.169
Macfa278	Preme107088	0.103	0.089	0.061	0.086	0.154
Macfa317191	Preme107088	0.165	0.156	0.027	0.077	0.148
Macfa385	Preme107088	0.126	0.099	0.105	0.128	0.195
Macfa411	Preme107088	0.139	0.12	0.05	0.092	0.167

Table A4.10. Distances between protoconid and metaconid (PM), entoconid and hypoconid (EH), and hypoconulid and geometric centroid of non-hypoconulid cusps (HC).

				Centroid (PMEH)			
Specimen*	PM	EH	PM/EH	X	Y	Z	HC
Cermi236996	0.592	0.494	1.200	0.143	0.082	-0.513	1.077
Cermi259446	0.618	0.501	1.234	0.138	0.111	-0.464	0.993
Cermi4521	0.635	0.493	1.288	0.158	0.080	-0.507	1.073
Cermi452544	0.672	0.502	1.337	0.128	0.093	-0.454	0.962
Cermi452547	0.567	0.519	1.093	0.119	0.073	-0.464	0.970
Cermi452548	0.678	0.514	1.320	0.126	0.083	-0.441	0.932
Cermi452552	0.646	0.441	1.465	0.138	-0.002	-0.409	0.864

Cermi452554	0.678	0.453	1.498	0.142	0.068	-0.425	0.907
Cermi52386	0.615	0.528	1.164	0.162	0.107	-0.481	1.038
Cermi52384	0.600	0.496	1.209	0.176	0.084	-0.487	1.049
Cogue119768	0.531	0.577	0.919	0.109	0.017	-0.609	1.237
Cogue52237	0.573	0.577	0.992	0.081	0.088	-0.562	1.149
Colgu11112	0.605	0.557	1.086	0.094	0.055	-0.550	1.121
Colgu1241	0.598	0.590	1.014	0.103	0.018	-0.563	1.146
Colgu163124	0.587	0.574	1.024	0.106	0.060	-0.560	1.146
Colgu163273	0.563	0.563	1.000	0.096	0.060	-0.576	1.174
Colgu163627	0.539	0.581	0.928	0.088	0.044	-0.569	1.156
Colgu401	0.553	0.478	1.155	0.129	0.082	-0.550	1.141
Colgu408	0.619	0.600	1.033	0.100	0.107	-0.477	0.998
Colgu762	0.607	0.536	1.132	0.086	0.090	-0.530	1.088
Colgu864	0.544	0.524	1.038	0.070	0.068	-0.574	1.165
Colgu994	0.523	0.529	0.989	0.106	0.030	-0.601	1.222
Macfa102768	0.487	0.483	1.007	0.110	0.079	-0.573	1.179
Macfa103649	0.500	0.450	1.112	0.100	0.063	-0.600	1.223
Macfa103655	0.507	0.527	0.962	0.116	0.017	-0.571	1.167
Macfa103658	0.561	0.489	1.149	0.112	0.038	-0.561	1.147
Macfa106025	0.524	0.453	1.157	0.108	0.050	-0.591	1.205
Macfa106384	0.543	0.461	1.178	0.115	0.040	-0.587	1.198
Macfa114411	0.551	0.481	1.146	0.104	0.067	-0.546	1.119
Macfa114505	0.595	0.505	1.177	0.069	0.062	-0.574	1.164
Macfa121803	0.490	0.462	1.060	0.079	0.044	-0.611	1.236
Macfa125	0.535	0.480	1.115	0.114	0.058	-0.582	1.191
Macfa125102	0.478	0.436	1.096	0.097	0.045	-0.600	1.218
Macfa196817	0.573	0.561	1.021	0.111	0.013	-0.540	1.102

Macfa196824	0.571	0.477	1.197	0.097	0.026	-0.600	1.217
Macfa198300	0.531	0.440	1.205	0.087	0.028	-0.601	1.215
Macfa278	0.572	0.472	1.212	0.105	0.074	-0.587	1.201
Macfa317191	0.466	0.484	0.961	0.067	0.082	-0.576	1.171
Macfa385	0.540	0.377	1.432	0.131	0.053	-0.626	1.284
Macfa411	0.504	0.480	1.049	0.111	0.040	-0.601	1.225
Preme102755	0.634	0.526	1.206	0.127	0.021	-0.517	1.066
Preme102757	0.662	0.558	1.186	0.133	0.034	-0.477	0.992
Preme102882	0.710	0.607	1.170	0.123	0.072	-0.449	0.943
Preme102883	0.603	0.584	1.032	0.135	0.068	-0.490	1.026
Preme102891	0.636	0.604	1.054	0.116	0.057	-0.463	0.962
Preme102895	0.639	0.567	1.127	0.127	0.067	-0.486	1.013
Preme106600	0.581	0.600	0.969	0.184	0.051	-0.499	1.068
Preme106605	0.637	0.510	1.247	0.163	0.063	-0.478	1.018
Preme106671	0.627	0.587	1.068	0.135	0.007	-0.526	1.085
Preme107086	0.742	0.574	1.293	0.125	0.080	-0.457	0.961
Preme107088	0.750	0.561	1.337	0.101	0.053	-0.434	0.898